THE EMERGING FORM OF SMART GRID: SMART INTEGRATED ENERGY SYSTEMS AND PROSUMER CENTRED ENERGY COMMUNITY

EDITED BY: Tao Huang, Ciwei Gao, Chenghong Gu and Yingjun Wu
PUBLISHED IN: Frontiers in Energy Research

frontiers Research Topics

frontiers

ISSN 1664-8714
ISBN 978-2-88976-540-9
DOI 10.3389/978-2-88976-540-9

About Frontiers

Frontiers is more than just an open-access publisher of scholarly articles: it is a pioneering approach to the world of academia, radically improving the way scholarly research is managed. The grand vision of Frontiers is a world where all people have an equal opportunity to seek, share and generate knowledge. Frontiers provides immediate and permanent online open access to all its publications, but this alone is not enough to realize our grand goals.

Frontiers Journal Series

The Frontiers Journal Series is a multi-tier and interdisciplinary set of open-access, online journals, promising a paradigm shift from the current review, selection and dissemination processes in academic publishing. All Frontiers journals are driven by researchers for researchers; therefore, they constitute a service to the scholarly community. At the same time, the Frontiers Journal Series operates on a revolutionary invention, the tiered publishing system, initially addressing specific communities of scholars, and gradually climbing up to broader public understanding, thus serving the interests of the lay society, too.

Dedication to Quality

Each Frontiers article is a landmark of the highest quality, thanks to genuinely collaborative interactions between authors and review editors, who include some of the world's best academicians. Research must be certified by peers before entering a stream of knowledge that may eventually reach the public - and shape society; therefore, Frontiers only applies the most rigorous and unbiased reviews.
Frontiers revolutionizes research publishing by freely delivering the most outstanding research, evaluated with no bias from both the academic and social point of view. By applying the most advanced information technologies, Frontiers is catapulting scholarly publishing into a new generation.

What are Frontiers Research Topics?

Frontiers Research Topics are very popular trademarks of the Frontiers Journals Series: they are collections of at least ten articles, all centered on a particular subject. With their unique mix of varied contributions from Original Research to Review Articles, Frontiers Research Topics unify the most influential researchers, the latest key findings and historical advances in a hot research area! Find out more on how to host your own Frontiers Research Topic or contribute to one as an author by contacting the Frontiers Editorial Office: frontiersin.org/about/contact

THE EMERGING FORM OF SMART GRID: SMART INTEGRATED ENERGY SYSTEMS AND PROSUMER CENTRED ENERGY COMMUNITY

Topic Editors:
Tao Huang, Politecnico di Torino, Italy
Ciwei Gao, Southeast University, China
Chenghong Gu, University of Bath, United Kingdom
Yingjun Wu, Hohai University, China

Citation: Huang, T., Gao, C., Gu, C., Wu, Y., eds. (2022). The Emerging Form of Smart Grid: Smart Integrated Energy Systems and Prosumer Centred Energy Community. Lausanne: Frontiers Media SA. doi: 10.3389/978-2-88976-540-9

Table of Contents

frontiers in Energy Research

ORIGINAL RESEARCH
published: 18 February 2021
doi: 10.3389/fenrg.2020.633334

Stability Analysis for Distributed Secondary Control with Consideration of Diverse Input and Communication Delays for Distributed Generations in a DC Integrated Energy System

Tao Wang[1], *Chunyan Rong*[1], *Shuai Tang*[1] *and Yinqiu Hong*[2]*

[1]*Institute of State Grid Hebei Electric Power Company Economic and Technological Research, Shijiazhuang, China,* [2]*School of Electrical Engineering, Southeast University, Nanjing, China*

An integrated energy system is a promising approach to synthesize various forms of energy, where cooperative control is indispensable for stable and efficient operation. During the information exchange of cooperative distributed secondary control (DSC) in an integrated energy system, the effect of time delays on system performance cannot be ignored, which mainly consist of input delays and communication delays. Compared with most of the existing literature which only address DSC considering communication delays, this paper investigates the stability robustness of an integrated energy system in the case of both input and communication delays. First, the impacts of input and communication delays on DSC are analyzed based on the Gerschgorin theorem and Nyquist criterion, where the system stability is principally dependent on input delays while has little correlation with communication delays and the inconsistency of the two delays may result in steady-state deviation. Then, on the assumption of identical input and communication delays, a closed-loop small-signal model equipped with a distributed secondary controller is established for stability analysis and the delay-dependent criteria are formulated to determine the stability margin of the system based on critical characteristic root tracking. By a series of trial declarations, the delay margins with regard to different controller gains are determined and the qualitative relationship between delay margins and controller gains can be utilized to guide the controller design for improved system performance. The effectiveness of the theoretical results is verified by case studies on a test system.

Keywords: communication delay, input delay, secondary control, stability analysis, integrated energy system

OPEN ACCESS

Edited by:
Yingjun Wu,
Hohai University, China

Reviewed by:
Yuhua Du,
Temple University, United States
Wei Liu,
Nanjing University of Science and Technology, China

***Correspondence:**
Yinqiu Hong
hyq97820@163.com

Specialty section:
This article was submitted to Smart Grids, a section of the journal Frontiers in Energy Research

Received: *25 November 2020*
Accepted: *17 December 2020*
Published: *18 February 2021*

Citation:
Wang T, Rong C, Tang S and Hong Y (2021) Stability Analysis for Distributed Secondary Control with Consideration of Diverse Input and Communication Delays for Distributed Generations in a DC Integrated Energy System. Front. Energy Res. 8:633334. doi: 10.3389/fenrg.2020.633334

INTRODUCTION

The concept of an integrated system installed with multiple forms of renewable energy has been promoted for better exploitation of its advantages. However, the stochasticity and intermittency of distributed generations (DGs) could degrade the reliability and power quality of the system. Besides, considerable differences between the peak and valley loads would lead to an inefficient energy utilization. To address these challenges, the storages within the integrated system are equipped to smooth out the fluctuation of output power as well as implement power dispatch (He and Li, 2011;

Yu et al., 2016; Wang et al., 2019a). As one of the most attractive features, the integrated system can be operated in island mode in case of planned or spontaneous events, to provide an uninterrupted power supply to customers (Jin et al., 2014; Han et al., 2018). With the superiority of low complexity and energy loss, the integrated system has a promising future to be evolved into a possible DC structure (Morstyn et al., 2016; Yoo et al., 2020). A reliable control scheme is of great significance in ensuring the safe and stable operation of the system. To meet the requirement of spontaneous power sharing without communication, droop control, which takes the virtue of the relationship between power and voltage/frequency, is widely utilized. However, the presence of droop characteristics would produce poor power sharing due to the distinct output impedances of individual DGs, as well as diverse voltage deviation (Guo et al., 2014; Wang et al., 2019b).

To deal with the aforementioned defects, secondary control is introduced, varying from a centralized control structure to a distributed control structure. Centralized secondary control assumes a microgrid centralized controller (MGCC), which requires a global information collection and calculation (Lopes et al., 2006; Mehdi et al., 2020); however, it is sensitive to a single-point-of-failure. In recent years, inspired by multi-agent technology, distributed secondary control, in which each DG exchanges information with its immediate neighbors via local networks, has gained a lot of popularity (Simpson-Porco et al., 2015; Guo et al., 2018; Kang et al., 2018; Lu et al., 2018). Nasirian et al. (2015), developed a complete dynamic model of the DC integrated system with a distributed control framework, and the guidelines for the controller design were given to optimize the dynamic performance. A novel distributed control strategy was proposed by Trip et al. (2018), where the secondary control objectives were achieved with consideration of the requirement of plug-and-play. Baranwal et al. (2019) proposed to improve system robustness under various uncertainties by distributed control methods based on robust algorithms. Moreover, distributed secondary schemes based on a smooth adaptive method was proposed to reinforce system robustness (Zuo et al., 2020), and the adaptive virtual resistance was introduced by Kumar and Pathak (2020) to reduce the overshoot during secondary control. Dou et al. (2017) presented H_∞ algorithms to provide further system performance improvements.

The main feature of the existing literature on distributed control lies in the local-neighboring information exchange. During information collection and exchange, the time delays are unavoidable and it is important to study the impact of time delays on system performance, especially considering the increasing utilization of open communication infrastructures and the low inertia of inverter-interfaced DGs (Lou et al., 2018; Li and Shahidehpour, 2019). Broadly speaking, there exists two kinds of time delays among DGs, i.e., input delays and communication delays, where the former is in regard to the information collected and processed by the local DG and the latter is related to communication from one DG to another. Although the impact of communication delays on an integrated DG system have been extensively researched by Lou et al. (2018) and Liu et al. (2015) based on a small signal model through the critical characteristic root tracking method, there are few studies on the secondary control of an integrated energy system with input delays, to the best of our knowledge. Olfati-Saber and Murray (2004) proposed a delay-dependent distributed control, in which each agent delays its local measurements as the same number as communication delays, that is, matched input and communication delays are assumed. However, these two delays generate from different sources and they are not the same number in many cases. Therefore, it is necessary to investigate the impact of both input delays and communication delays on the distributed secondary control of an integrated energy system.

Motivated by the aforementioned research gap, this paper investigates the stability robustness of a DC microgrid taking both input and communication delays into consideration. First, upon the consensus-based secondary control of the integrated energy system, input delays and communication delays are separately introduced, compared to most of the existing DSC literature which only addresses communication delays. Then, based on the Nyquist criterion and Gerschgorin theorem, the sufficient condition for delayed-system consensus is derived, from which we can observe that the stability of the integrated system mainly depends on input delays, and the system performance in the presence of communication delay could be ameliorated in company with a moderate input delay. For the sake of better system performance, a synchronous interaction case with an identical number of input delays and communication delays is expected and discussed, where a closed-loop small-signal model for a DC integrated energy system is established and the delay margin calculation method is provided by virtue of tracing the critical characteristic root. By a series of trial declarations, the relationship between control parameters and stability robustness is determined to guide the controller design.

The remainder of this paper is organized as follows: **Problem Formulation** section reviews the hierarchical control of DC integrated energy systems and delay-dependent secondary control. The respective formulation and impacts of input delays and communication delays are investigated in **Impact of Input and Communication Delays on System Performance** section, and the sufficient condition for system stability is derived. In **Stability Robustness with Identical Input and Communication Delays** section, the procedures for delay margin determination are introduced considering the concurrence of input and communication delays. A case study based on a test DC MG is conducted to investigate the relationship between the control gains and delay margins and the effectiveness of the theoretical results are demonstrated by simulation in **Simulation Results** section.

PROBLEM FORMULATION

Hierarchical Control of a DC Integrated Energy System

The hierarchical control structure is displayed in **Figure 1**, which includes primary control and secondary control, with droop control widely adopted as primary control to ensure system stability:

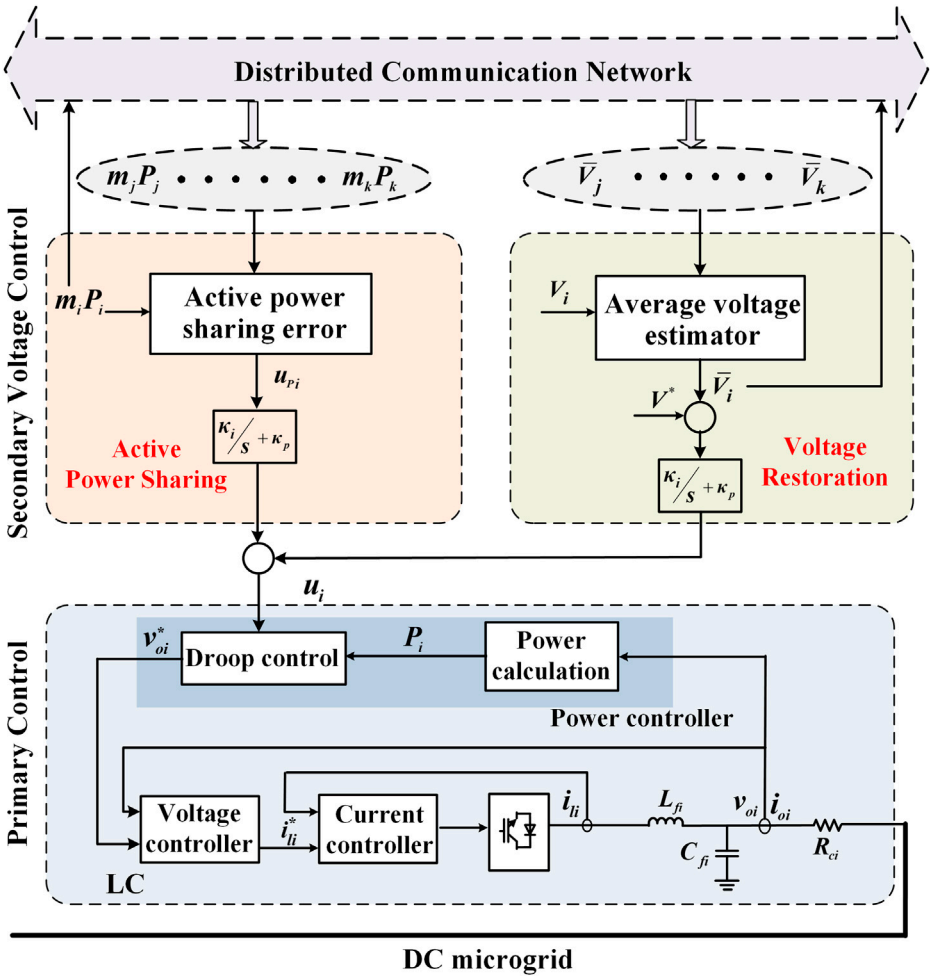

FIGURE 1 | Hierarchical control structure of the DC microgrid.

$$V_i = V_{ni} - m_iP_i \tag{1}$$

where V_i and V_{ni} represent the actual output and nominal voltages of the ith DG, m_i denotes the droop coefficient, and P_i denotes the measured active power.

To achieve accurate power sharing and eliminate voltage deviation in the presence of droop control, secondary control is introduced by adding an auxiliary term u_i on the basis of **Eq. 1**:

$$V_i = V_{ni} - m_iP_i + u_i \tag{2}$$

The control objective of proportional sharing requires active power to allocate according to the inverse of the droop coefficient between DGs, i.e., $m_1P_1 = m_2P_2 = \ldots = m_nP_n$. Based on average consensus protocol, the controller for power sharing can be designed as:

$$u_{Pi} = k_{i1}\int \sum_{j=1,j\neq i}^{n} a_{ij}\left(m_jP_j - m_iP_i\right)dt \tag{3}$$

where k_{i1} represents the integral gain of power sharing controller and a_{ij} represents the communication weight, with $a_{ij} = 1$ implying the existence of a communication link between the ith and jth DG and $a_{ij} = 0$ implying otherwise.

In view of the contradiction between voltage restoration and proportional power sharing, the average voltage is always taken to be regulated to the nominal value in practice. Given the absence of a global controller, the average voltage will be estimated locally utilizing a distributed observer:

$$\overline{V}_i = V_i + k_{i3}\int \sum_{j=1,j\neq i}^{n} a_{ij}\left(\overline{V}_j - \overline{V}_i\right)dt \tag{4}$$

where $\overline{V}_i$ denotes the average voltage observed by the ith DG and k_{i3} denotes the integral gain. Recalling the expectation of voltage deviation compensation, the corresponding controller can be constructed and then the secondary control input can be formulated based on a combination of the two controllers:

$$u_i = u_{Pi} + k_{i2}\int \left(V_n - \overline{V}_i\right)dt \tag{5}$$

where k_{i2} denotes the integral gain of the voltage restoration controller. It can be observed from **Eq. 3** and **Eq. 4**, based on the

distributed information exchange, the active powers and estimated average voltages of DGs converge to a common state.

Delay-Dependent Consensus Algorithm

In most of the existing literature on DSC, the time delays with regard to the transmission among local-neighboring DGs are considered for system stability analysis. Then, each DG obtains decision control based on the delayed state information from neighbors and its current state, i.e., mismatched time delays. Alternatively, based on the delayed-consensus protocol put forward by Olfati-Saber and Murray (2004), active power sharing can be formulated in a symmetric format as follows:

$$\boldsymbol{u_i(t)} = \sum_{j=1,j\neq i}^{n} \boldsymbol{a_{ij}}\left(\boldsymbol{m_jP_j}\left(\boldsymbol{t-\tau_{ij}}\right) - \boldsymbol{m_iP_i}\left(\boldsymbol{t-\tau_{ij}}\right)\right) \tag{6}$$

where τ_{ij} is denoted as communication delays in regard to the information exchange between DG_i and DG_j. It can be observed that the local DG_i delayed its own measurements by the same amount as the communication delays so that the states of its own and its neighbors were with the same time instant. Actually, the delays intentionally introduced by the agent itself during the processing of local data can be considered as input delays, which refer to signal collection and signal modulation/demodulation, while the communication delays contain not only signal collection and signal modulation/demodulation, but also packet organization format and signal transmission. Generally, communication delays for signals from neighboring DGs are larger than those from local DGs. Protocol (6) is applicable upon the assumption of identical input and communication delays; however, the time delay can be affected by multiple factors in practice, e.g., communication link and hardware facilities and it does not apply to the case of diverse delays. Therefore, a more universal form of the consensus algorithm can be formulated as:

$$\boldsymbol{u_i(t)} = \sum_{j=1,j\neq i}^{n} \boldsymbol{a_{ij}}\left(\boldsymbol{m_jP_j}\left(\boldsymbol{t-\tau_{ij}}\right) - \boldsymbol{m_iP_i(t-\tau)}\right) \tag{7}$$

where τ represents the local input delay, which is related to the procedure of information collecting and processing as well as actuator and controllers. Employing consensus protocol **Eq. 7** in microgrids, the power sharing controller can be designed as:

$$\boldsymbol{u_{Pi}} = \boldsymbol{k_{i1}}\int \sum_{j=1,j\neq i}^{n} \boldsymbol{a_{ij}}\left(\boldsymbol{m_jP_j}\left(\boldsymbol{t-\tau_{ij}}\right) - \boldsymbol{m_iP_i(t-\tau)}\right)\boldsymbol{dt} \tag{8}$$

Homoplastically, the average voltage estimation can be given by:

$$\overline{\boldsymbol{V}}_{\boldsymbol{i}} = \boldsymbol{V_i} + \boldsymbol{k_{i3}}\int \sum_{j=1,j\neq i}^{n} \boldsymbol{a_{ij}}\left(\overline{\boldsymbol{V}}_{\boldsymbol{j}}\left(\boldsymbol{t-\tau_{ij}}\right) - \overline{\boldsymbol{V}}_{\boldsymbol{i}}\boldsymbol{(t-\tau)}\right)\boldsymbol{dt} \tag{9}$$

As can be deduced from **Eq. 8** and **Eq. 9**, these two kinds of delays could exert diverse influence on system performance, which indicates the significance of stability analysis of the MG system taking both input and communication delays into consideration.

IMPACT OF INPUT AND COMMUNICATION DELAYS ON SYSTEM PERFORMANCE

In this section, the stability issue with regard to input and communication delays will be thoroughly investigated. Firstly, some useful lemmas are introduced.

Lemma 1 (Ren and Beard, 2005): 0 is a single root of the Laplacian matrix L if there exists a global reachable node.

Lemma 2 (Massoulie, 2002): For any $\gamma \in [0,1)$, $-1+j0$ is not included in the convex hull $\gamma Co(0 \cup \{Ei(j\omega), i\in N\})$ if $\omega\in R$, where $E_i(j\omega) = \frac{\pi}{2T}\cdot\frac{e^{-j\omega T}}{j\omega}$.

Lemma 3 (Meng et al., 2011): For $\omega \in R$, the disc is contained in the convex hull $\gamma Co(0 \cup \{W_i(j\omega), i\in N\})$.

Theorem 1: Once the inequality **Eq. 10** holds, the states will converge to the consensus value asymptotically, where $d_i = \sum_{vj\in Ni} a_{ij}$.

$$\max\{di\tau\} < \pi/4 \tag{10}$$

Proof: Under the unified consensus protocol in **Eq. 7**, the dynamic of active power can be modeled as:

$$\boldsymbol{m_i\dot{P}_i} = \boldsymbol{C_P}\sum_{j=1,j\neq i}^{n} \boldsymbol{a_{ij}}\left(\boldsymbol{m_jP_j}\left(\boldsymbol{t-\tau_{ij}}\right) - \boldsymbol{m_iP_i(t-\tau)}\right) \tag{11}$$

where C_p denotes the interaction strength. Performing Laplace transformation on **Eqs 11, 12** follows:

$$\boldsymbol{sm_iP_i(s)} - \boldsymbol{m_iP_i(0)} = \boldsymbol{C_P}\sum_{j=1,j\neq i}^{n} \boldsymbol{a_{ij}}\left(\boldsymbol{m_jP_j(s)e^{-s\tau_{ij}}} - \boldsymbol{m_iP_i(s)e^{-s\tau}}\right) \tag{12}$$

Then, the characteristic equation of the system can be derived as $\det(sI + L(s)) = 0$. Where I is an identity matrix with n dimensions and $L(s)$ is defined as:

$$\boldsymbol{L(s)} = \begin{cases} -\boldsymbol{a_{ij}e^{-s\tau_{ij}}}, & \boldsymbol{V_j\in N_i} \\ \sum_{j=1,j\neq i}^{n}\boldsymbol{a_{ij}e^{-s\tau}}, & \boldsymbol{j=i} \\ 0, & \text{otherwise} \end{cases}$$

It can be deduced from lemma 1 that 0 is a single root of the characteristic equation. Defining $P(s) = \det(I + G(s))$, where $G(s) = L(s)/s$, then obviously, the zeros of $P(s)$ are equivalent to the non-zero roots of the characteristic equation.

According to the Gerschgorin theory, the eigenvalues of $G(j\omega)$ lie in a disc:

$$\boldsymbol{\lambda\left(G(j\omega)\right)} \in \cup_{\,i\,\in\,N}\boldsymbol{G_i}$$

where

$$\boldsymbol{G_i} = \left\{\boldsymbol{\zeta}:\boldsymbol{\zeta}\in\boldsymbol{C},\left|\boldsymbol{\zeta} - \sum_{j=1,j\neq i}^{n}\boldsymbol{a_{ij}}\frac{\boldsymbol{e^{-j\omega T}}}{\boldsymbol{j\omega}}\right| \leq \left|\sum_{j=1,j\neq i}^{n}\boldsymbol{a_{ij}}\frac{\boldsymbol{e^{-j\omega T}}}{\boldsymbol{j\omega}}\right|\right\}$$

and C represents the complex field. Premising the line between the origin and the center of disc, which can be obtained as $G_{i0}(j\omega) = d_i\frac{e^{-j\omega T}}{j\omega}$ intersects the boundary of the disk at W_i, then, the trajectory of W_i can be expressed as:

$$W_i(j\omega) = 2d_i\frac{e^{-j\omega T}}{j\omega} \tag{13}$$

According to Lemma 2, it can be derived that $W_i(j\omega) = \gamma_i E_i(j\omega)$ with $\gamma_i = 4d_iT/\pi$. On account of the condition $\max\{d_i\tau\}<\pi/4$, defining $\gamma = \max\{\gamma_i,\ i\in N\}$ and apparently, the following relationship holds:

$$Co\left(0\cup\{W_i(j\omega),\ i\in N\}\right)\subseteq \gamma Co\left(0\cup\{E_i\}(j\omega),\ i\in N\right) \tag{14}$$

Employing Lemma 2, it can be deduced that $-1+j0$ is not included in the set $Co(0\cup\{W_i(j\omega), i\in N\})$. Further combined with lemma 3 as well as the Gerschgorin theory, the conclusion can be drawn that the root locus of $G(j\omega)$ will not pass $-1+j0$. According to the generalized Nyquist criterion, all zeros of $P(s)$ will have negative real parts, i.e., the system will converge asymptotically and the proof of Theorem 1 are completed.

From the sufficient condition for system stability **Eq. 10**, we can conclude that whether the system under the consensus protocol in **Eq. 7** achieves consensus mainly depends on the input delays while it has a weak association with communication delays. Therefore, it is critically important to investigate the impact of input delays on system performance rather than only considering communication delays, in contrast to most of the existing delay-dependent analyses of distributed secondary control in MGs. Generally, input delays are relatively negligible compared to communication delays in practice. However, great distinction between the two kinds of delays will introduce information disorder for decision-making due to local-neighboring state interaction, which could definitely give rise to steady state deviation (Fatihcan, 2010). To avoid the aforementioned steady deviation, auxiliary methods are usually applied to ensure that the local and neighbors' information comes from the same time instant, that is, the local information is delayed in an identical way to the communication delays. In practical implementation, the previous information of each DG is saved by signal storage devices and the local information with the same timestamp as the neighboring information can be obtained from the device once the signal from neighboring nodes is received. Thus, the control decision will be made using the local and neighboring information from the same timestamp, i.e., the communication and input delays are controlled so they are uniform.

STABILITY ROBUSTNESS WITH IDENTICAL INPUT AND COMMUNICATION DELAYS

In this section, we consider secondary voltage control under the theoretical assumption of identical communication delays and input delays. Considering that the communication delays during information exchange are inevitable and much larger than input delays in practice, whereas the inconformity between the input and communication delays may result in equilibrium deviation, the state in local DG is usually delayed similarly to communication delay, to come at an agreement of information instants. It should be noted that the communication delay can be determined based on the offset between the sending timestamp T1 and the receiving timestamp T2.

With the increase of input delays, the system performance is degraded and even leads to instability in the worst case. In this section, the stability robustness of distributed secondary control with input and communication delays is addressed. Firstly, a small signal model of MG is derived, taking time delays and controller parameters into consideration. Then, the delay margin as the maximum delay under which the system can maintain stable is determined and the relationship between the controller gains and delay margin is investigated to guide the controller design.

Small-Signal Modeling of a DC Integrated System

The closed loop small-signal model of a DC microgrid installed with time delays is established first, consisting of three parts: the inverters, network, and loads.

The inverters are controlled by the hierarchical control strategy mentioned in **Impact of Input and Communication Delays on System Performance** section. The voltage regulation to the reference value can be implemented with the assistance of the voltage and current double-loop controller:

$$\begin{aligned}
&\frac{d\theta}{dt} = V_i - V_{oi}\\
&i_{ref} = k_{pv}(V_i - V_{oi}) + k_{iv}\theta\\
&\frac{d\vartheta}{dt} = i_{ref} - i_{oi}\\
&d_i = k_{pi}\left(i_{ref} - i_{oi}\right) + k_{ii}\theta
\end{aligned} \tag{15}$$

where V_{oi} denotes the actual output voltage; i_{oi} and i_{ref} denote the actual output and reference currents, respectively; k_{pv}, k_{iv}, k_{pi}, and k_{ii} are the proportional and integral gains of the PI controllers; and d_i represents the duty cycle. Whereas in practice, considering the much faster response of voltage and current loop compared with the power loop, the dynamic of primary control can be assumed to be equivalent to that of the power controller. Further considering the employment of the virtual resistance technique, the reference for the virtual output voltage of the inverter can be obtained from the droop equation and the actual output voltage reference can be provided by:

$$V_i = V_{vi} - r_{vi}i_i = V_{ni} - m_iP_i + u_i - r_{vi}I_i \tag{16}$$

where V_{vi} represents the virtual output voltage; r_{vi} represents the virtual resistance; I_i denotes the output current, and u_i can be obtained from **Eqs 3–5** in **Impact of Input and Communication Delays on System Performance** section. As can be deduced from the equation, the effect of adding the virtual resistance is equivalent to essentially changing the droop gain in DC systems. Hence, the term in regard to virtual resistance can be omitted in subsequent analysis for simplification. Besides, the

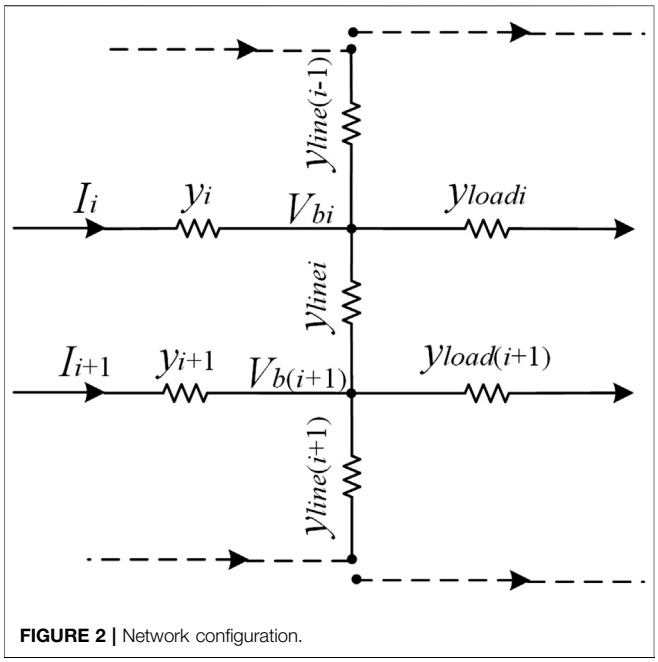

FIGURE 2 | Network configuration.

active power in the equation can be measured through a low-pass filter:

$$\dot{\boldsymbol{P}}_i = -\boldsymbol{\omega}_f \boldsymbol{P}_i + \boldsymbol{\omega}_f \boldsymbol{V}_i \boldsymbol{I}_i \tag{17}$$

where ω_f is the cutoff frequency.

By differentiating and linearizing the above **Eqs. 16, 17**, the small-signal model of inverters can be established as:

$$\Delta\dot{\boldsymbol{x}} = \boldsymbol{A}^{'}\Delta\boldsymbol{x} + \boldsymbol{B}\Delta\boldsymbol{I} \tag{18}$$

where $\Delta x = [\Delta P_1, \Delta P_2, \ldots, \Delta P_n, \Delta V_1, \Delta V_2, \ldots, \Delta V_n, \Delta\overline{V}_1, \Delta\overline{V}_2, \ldots, \Delta\overline{V}_n]^T$ represents the system state variables, $\Delta I = [\Delta I_1, \Delta I_2, \ldots, \Delta I_n]^T$ and A', B are parameter matrices listed in the Appendix.

The inverters are supposed to be connected to the network as depicted in **Figure 2**.

According to the circuit configuration, the output current can be modeled as:

$$\boldsymbol{I} = \boldsymbol{Y}(\boldsymbol{V} - \boldsymbol{V}_b) \tag{19}$$

where $Y = \mathrm{diag}(y_i)$, with y_i denoting the output admittance of the ith DG and $V_b = [V_{b1}, V_{b2}, \ldots, V_{bn}]^T$ with V_{bi} denoting the ith bus voltage. The relationship between the bus voltage and the output voltage of DGs can be established using the node voltage equation:

$$\boldsymbol{y}_{si}\boldsymbol{V}_{bi} = \boldsymbol{y}_{line(i-1)}\boldsymbol{V}_{bi(i-1)} + \boldsymbol{y}_{linei}\boldsymbol{V}_{bi(i+1)} + \boldsymbol{y}_i\boldsymbol{V}_i \tag{20}$$

where $y_{si} = y_{\mathrm{line}i} + y_{\mathrm{line}(i\text{-}1)} + y_i + y_{\mathrm{load}i}$; $y_{\mathrm{line}i}$ represents the line admittance between the ith and $(i+1)$th DG and $y_{\mathrm{load}i}$ represents the admittance of the ith load.

Further, based on the integration of **Eqs 19** and **20**, the small-signal model of output current can be established as:

$$\Delta\boldsymbol{I} = \boldsymbol{Y}'\Delta\boldsymbol{V} \tag{21}$$

where $Y' = Y(1-Y_s^{-1}Y)$ is the admittance matrix with

$$\boldsymbol{Y}_s = \begin{bmatrix} \boldsymbol{y}_{s1} & -\boldsymbol{y}_{line1} & 0 & \cdots & 0 \\ -\boldsymbol{y}_{line1} & \boldsymbol{y}_{s2} & -\boldsymbol{y}_{line2} & \ddots & \vdots \\ 0 & \ddots & \ddots & \ddots & 0 \\ \vdots & \ddots & -\boldsymbol{y}_{line(n-1)} & \boldsymbol{y}_{s(n-1)} & -\boldsymbol{y}_{linen} \\ 0 & \cdots & 0 & -\boldsymbol{y}_{linen} & \boldsymbol{y}_{sn} \end{bmatrix}$$

By substituting (**Eq. 20**) into (**Eq. 17**), the closed-loop small-signal model for the whole system without delay can be obtained as:

$$\Delta\dot{\boldsymbol{x}} = \boldsymbol{A}\Delta\boldsymbol{x} \tag{22}$$

where A is the system parameter matrix and can be derived as $A = A'+BY'H$, where $H = [\boldsymbol{0}_{n\times n}\ I_{n\times n}\ \boldsymbol{0}_{n\times n}]$.

Further, we assume a uniform delay of τ during local data processing and information interaction, then **Eqs 3 and 4** can be replaced as:

$$\Delta\dot{\boldsymbol{u}}_{Pi} = \boldsymbol{k}_{i1}\sum_{j=1,j\neq i}^{n}\boldsymbol{a}_{ij}\left(\boldsymbol{m}_j\Delta\boldsymbol{P}_j(\boldsymbol{t}-\boldsymbol{\tau}) - \boldsymbol{m}_i\Delta\boldsymbol{P}_i(\boldsymbol{t}-\boldsymbol{\tau})\right) \tag{23}$$

$$\Delta\dot{\overline{\boldsymbol{V}}}_i = \Delta\dot{\boldsymbol{V}}_i + \boldsymbol{k}_{i3}\int\sum_{j=1,j\neq i}^{n}\boldsymbol{a}_{ij}\left(\Delta\overline{\boldsymbol{V}}_j(\boldsymbol{t}-\boldsymbol{\tau}) - \Delta\overline{\boldsymbol{V}}_i(\boldsymbol{t}-\boldsymbol{\tau})\right)\boldsymbol{dt} \tag{24}$$

Correspondingly, (**Eq. 22**) can be modified and the complete delay-dependent small-signal model can be acquired as:

$$\Delta\dot{\boldsymbol{x}} = \boldsymbol{A}_1\Delta\boldsymbol{x}(\boldsymbol{t}) + \boldsymbol{A}_d\Delta\boldsymbol{x}(\boldsymbol{t}-\boldsymbol{\tau}) \tag{25}$$

where A_1 and A_d are coefficient matrices given in the Appendix.

Critical Characteristic Root Tracking Method

The stability of a DC microgrid installed with delay will be analyzed based on the small-signal model established previously in this section. **Equation 25** yields the characteristic equation of the system:

$$\boldsymbol{det}(\boldsymbol{sI} - \boldsymbol{A}_1 - \boldsymbol{A}_d\boldsymbol{e}^{-\tau\boldsymbol{s}}) = 0 \tag{26}$$

According to the stability criterion for a closed-loop system, it can be deduced that the system is stable when all the eigenvalues of **Eq. 26** have a negative real component. Whereas the solution of **Eq. 26** would be challenging to acquire directly due to the existence of the transcendental item. Therefore, the method of critical characteristic root tracking will be introduced to reduce the complexity of this problem (Jia and Yu, 2008).

Considering the pure imaginary root corresponds to the critical stable state of the system, the stability switch can be assumed to take place accompanied by the occurrence of a pure imaginary root. Provided the equation has a pure imaginary solution $j\omega_c$, then there is

$$\boldsymbol{det}\left(\boldsymbol{sI} - \boldsymbol{A}_1 - \boldsymbol{A}_d\boldsymbol{e}^{-j\omega_c\tau}\right) = 0 \tag{27}$$

and $j\omega_c$ will be one of the eigenvalues of **Eq. 26**. It can be noticed that the transcendental item $e^{-j\omega_c\tau}$ presents a periodic

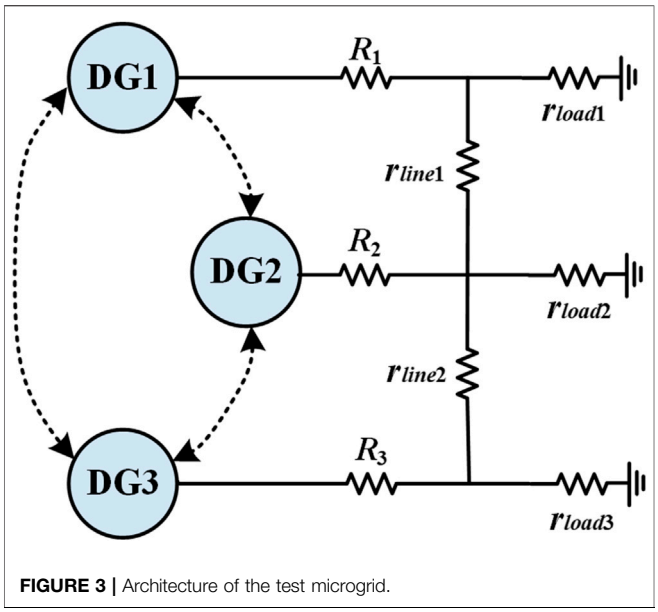

FIGURE 3 | Architecture of the test microgrid.

characteristic to τ with a period of $2\pi/\omega_c$, i.e., infinite cases can be covered by those when τ changes within the limited range. Defining $\xi = \omega_c\tau$ and the transcendental item in **Eq. 27** can be replaced by $e^{-j\xi}$. Thus, the problem of calculating all roots of **Eq. 26** can be simplified to the search of the possible imaginary solution of the equation when parameter ξ varies within the finite region $[0,2\pi]$. Recording feasible imaginary roots and the corresponding ξ as $j\omega_c$ and ξ_c respectively, then the candidate delay margin can be calculated as $\tau_c = \xi_c/\text{abs}(\omega_c)$. Thus, multiple sets of ω_c and ξ_c will be obtained, hence, an extra restriction in terms of transition direction will be applied to exclude undesirable results. Introducing the definition of transition direction around the critical characteristic root $j\omega_c$ as:

$$RT|_{s=j\omega_c} = sgn\left(Re\left(\frac{\partial s}{\partial \tau}\Big|_{s=j\omega_c}\right)\right) \tag{28}$$

where $sgn(\cdot)$ represents the sign function, with possible values of 0, 1, and −1 corresponding to zero, positives, and negatives, respectively; $\text{Re}(\cdot)$ represents the real component of a complex. It can be deduced from the definition that the condition $RT = 1$ ensures a state transition of the system from instability to stability as the communication delay τ increases.

Ultimately, n satisfactory values of delay margin will be calculated and screened out as $\tau_{c1}, \tau_{c2}, \ldots, \tau_{cn}$ and the delay margin can then be determined as the minimum of the feasible values, i.e., $\tau_d = \min\{\tau_{c1}, \tau_{c2}, \ldots, \tau_{cn}\}$.

To summarize, the delay-dependent stability analysis includes the following steps:

Step 1: Establish the closed-loop small-signal model for the whole system considering communication delays;

Step 2: Designate control parameters and acquire the characteristic equation related to ξ;

Step 3: Change ξ within $[0,2\pi]$ and track the root of the characteristic equation, calculate the corresponding τ_c as the candidate delay margin once the equation has a pure imaginary root;

Step 4: Calculate RT for each τ_c and screen out those with RT = 1 as $\tau_{c1}, \tau_{c2}, \ldots, \tau_{cn}$;

Step 5: Determine the delay margin as $\tau_d = \min\{\tau_{c1}, \tau_{c2}, \ldots, \tau_{cn}\}$;

Step 6: Change control parameters and repeat steps 2–5. Investigate the impact of control parameters on delay margin.

In addition, it is worth noting that the aforementioned analysis is performed on the assumption that the dynamic of the inner loop is ignorable, whereas considering the premise is decided by the controller of the inner loop and is irrelevant to the major concern of secondary control in this paper, the analytical method in this section is still effective.

SIMULATION RESULTS

In this section, simulations are performed for stability analysis with consideration of both input and communication delays by a test DC microgrid as presented in **Figure 3**, where three DGs are connected and communicate with each other. The control and system parameters are listed in **Table 1**, and active power is desired to be 1:1:1. The separate and comprehensive impacts of communication and input delays are investigated by employing various time delays. Then, to investigate the quantitative effect of controller gains on the system stability, the cases of different controller gain sets are performed. Simulation results using MATLAB/Simulink are utilized to verify the theoretical results. For the sake of simplicity, the controller gains of the two DGs are assumed to be same, and due to the small number of proportional gains in the PI controller, only the integral terms are utilized.

Impact of Input and Communication Delays on System Performance

In this case, the impact of input and communication delays on system performance is investigated. The islanded MG is controlled by droop control at the first stage and the distributed secondary control is launched at t = 3s. For a more intuitive comparison, simulation results of the delay-free case are displayed in **Figure 4**, from which we can see that stability is

TABLE 1 | Control and system parameters.

Parameter	Value	Parameter	Value
MG voltage	800 V	Connection impedances	
DG power ratings		R_1/R_2	0.1 Ω/ 0.3 Ω/ 0.25 Ω
DG1, DG2, DG3	25 kW	Line impedances	
Voltage droop coefficient		r_{line1}/r_{line2}	0.3 Ω
$m_1/m_2/m_3$	$2*10^{-3}$ V/W	Load ratings	
Observer parameters		$r_{load1}/r_{load2}/r_{load3}$	50 Ω/ 40 Ω/ 40 Ω
k_{i3}	3		

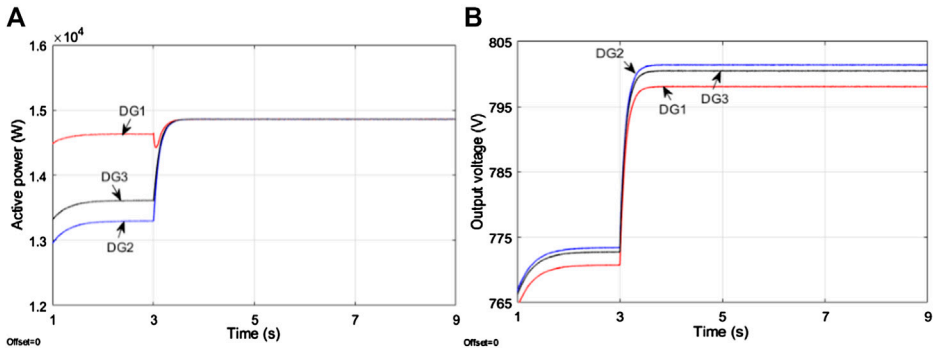

FIGURE 4 | Simulation results of the case without time delay **(A)** Active powers **(B)** Output voltages.

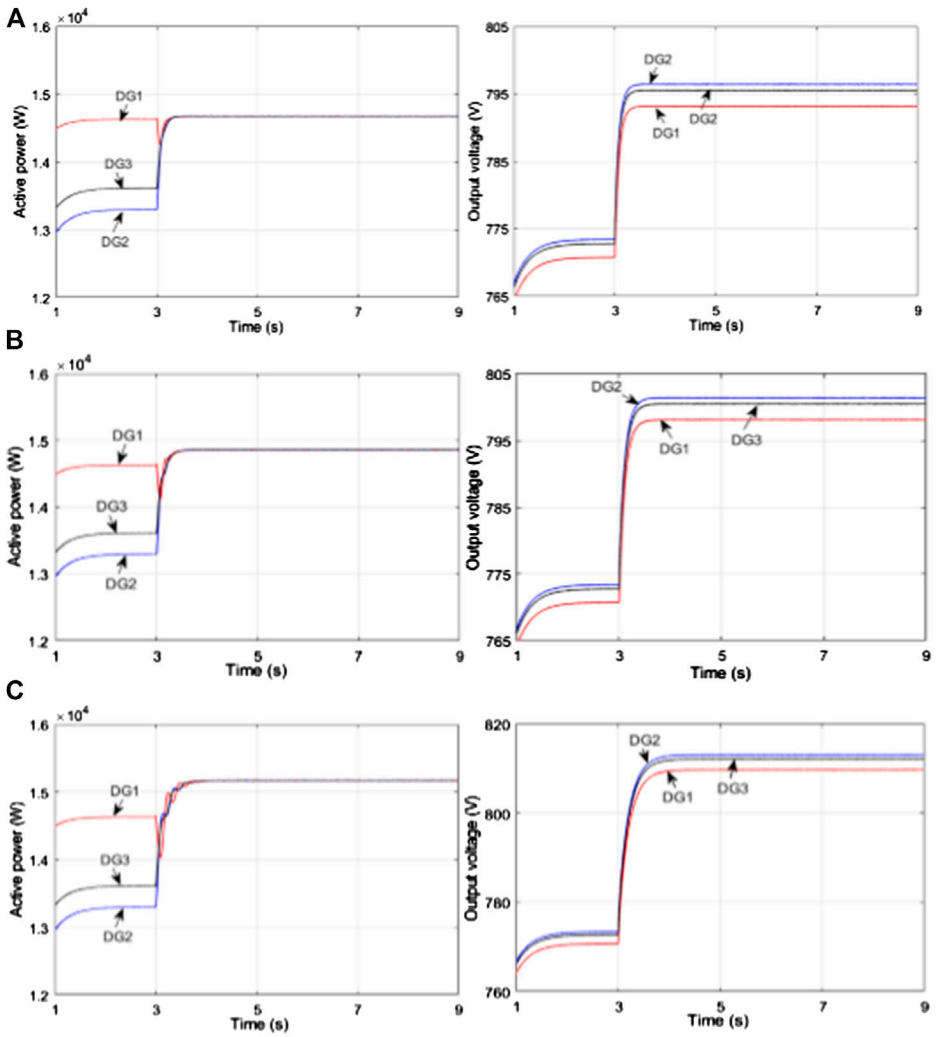

FIGURE 5 | Simulation results of active powers and actual output voltages with different communication delays and a fixed input delay of τ = 30 ms **(A)** τ_{ij} = 0 ms **(B)** τ_{ij} = 30 ms **(C)** τ_{ij} = 100 ms.

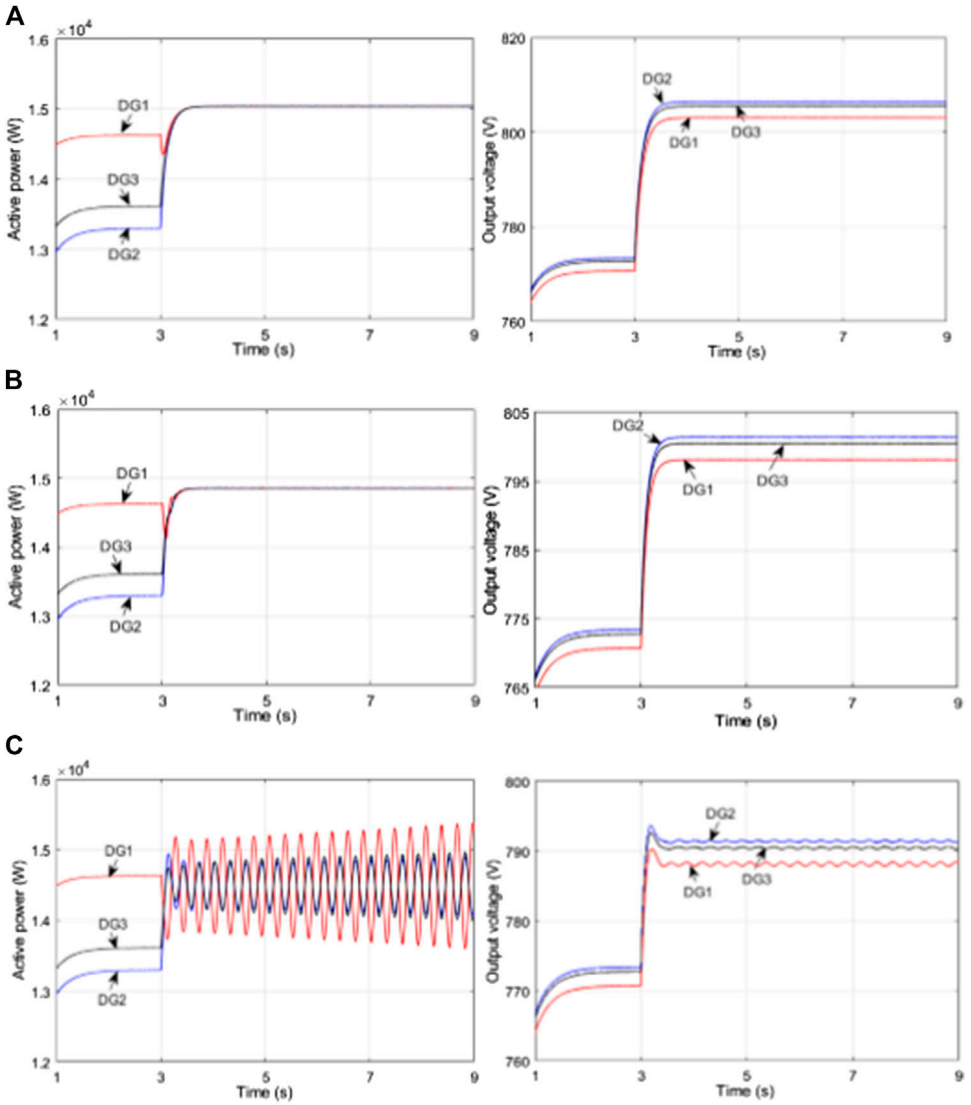

FIGURE 6 | Simulation results of active powers and actual output voltages with various input delays and a fixed communication delay of τ_{ij} = 30 ms **(A)** τ = 0 ms **(B)** τ = 30 ms **(C)** τ = 60 ms.

primarily guaranteed by droop control, whereas the system suffers from inaccurate power allocation and different voltage deviation. With the aid of secondary control at t = 3s, active power reallocates between DGs and voltage rises gradually. After a while, the system reaches a new equilibrium where active power has a 1:1:1 sharing between DGs and the average voltage arrives at the expected reference value, 800 V. Firstly, the input delay for each DG is set as τ = 30 ms, and different communication delays of τ_{ij} = 0 ms, 30 ms, and 100 ms are performed, with the results shown in **Figure 5**. As can be visualized from **Figure 5**, the system remains stable regardless of the gradual increase of communication delay, implying that communication delays have negligible influence on system stability, which is consistent with the theoretical conclusion drawn in **Stability Robustness with Identical Input and Communication Delays** section. However, due to the inconsistency between input and communication delays (i.e., 0 ms or 100 ms for communication delays, 30 ms for input delays), the voltages and active powers deviate from the responses of the delay-free case shown in **Figure 4**, which indicates that communication delays could exert an influence on the steady-state error. Only when τ_{ij} = τ = 30 ms do the responses appear to be the same as the accurate ones in **Figure 4**.

Further, the impact of input delays on the MG system is studied and the simulation operation is the same as above. The communication delay during individual information exchange is fixed as τ_{ij} = 30 ms and different input delays of τ_i = 0 ms, 30 ms, and 60 ms are performed with the results shown in **Figure 6**. As

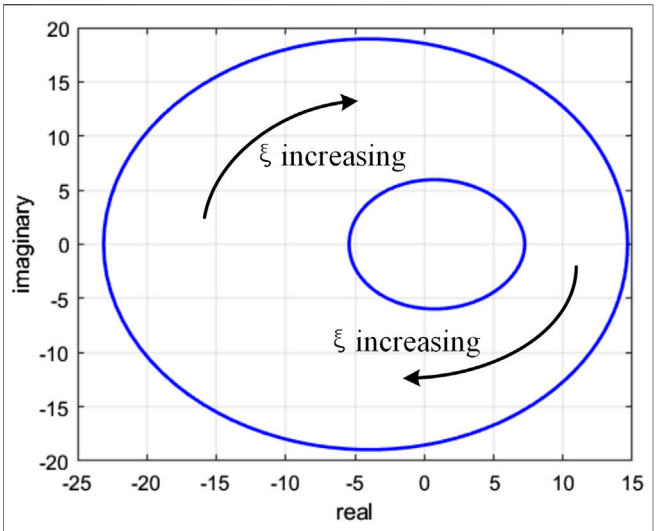

FIGURE 7 | Dominant root loci of the case with k_{i1} = 12, k_{i2} = 10.

can be observed from **Figure 6**, the MG system experiences steady-state deviation with τ_i = 0 ms, τ_{ij} = 30 ms but reaches an accurate convergence with τ_i = 30 ms, τ_{ij} = 30 ms. Therefore, a certain input delay would facilitate system performance. With an increase in the input delay, the responses undergo growing oscillations with τ_i = 60 ms, τ_{ij} = 30 ms, which is in accordance with the theoretical stability constraint for input delay as τ < 39.3 ms derived from the stability sufficient condition **Eq. 10** in this case. Therefore, the stability of the MG system is mainly dependent on input delays but has little correlation with communication delays, and moreover, the inconsistency between input delays and communication delays would result in convergence deviation, indicating that a moderate increase of input delays can contribute to the elimination of steady-state deviation in some practical cases.

Relationship Between Control Gains and Delay Margin

Considering that the communication delays cannot be negligible and could cause precision degradation, the consensus protocol was proposed where the information of the local DG is delayed at the same rate as the communication delays of its neighbors. In this case, we will investigate the performance of distributed secondary control with the same input and communication delays to avoid the occurrence of convergence error due to mismatched states.

Theoretical Calculation of Delay Margin

Considering that the stability condition for delay is dependent on controller gains, the delay margin of the test system with various control gains will be calculated adopting the analysis method proposed in **Simulation Results** section. We will first take the case of k_{i1} = 12, k_{i2} = 10 as an example to illustrate the determination of the delay margin. The corresponding dominant root loci of the characteristic equation is displayed in **Figure 7**. Four feasible sets of {ω, ξ} are obtained, among which two sets satisfying the condition RT = 1 are singled out as {ω_{c1}, ξ_{c1}} = {1.443, 5.931} and {ω_{c2}, ξ_{c2}} = {1.628,18.550}, yielding a corresponding communication delay as τ_{c1} = 243.3 ms and τ_{c2} = 87.9 ms. Hence, the delay margin in this case can be obtained as τ_d = 87.9 ms. Then, similar operations are performed as the above procedures with different controller sets k_{i1} and k_{i2}, the delay stability posture is generated as shown in **Table 2**. As can be observed from the table, the upper bound of the stability region shows a slight increase with a larger k_{i2} while the delay margin decreases apparently when k_{i1} becomes larger, i.e., a larger integral gain of the power sharing controller would lead to a worse stability robustness to delay while the integral gain of the voltage regulation controller has relatively less impact on system stability.

Simulation Results of Delay Margin

Simulations will be undertaken with two sets of controller gains in the presence of identical delays to verify the effectiveness of the proposed methodology. The selected sets of control parameters are marked in the table as k_{i1} = 12, k_{i2} = 10 and k_{i1} = 16, k_{i2} = 4. Initially, droop control operates in the DC microgrid and secondary control is launched at t = 3 s, with the simulation results depicted in **Figures 8** and **9**, respectively. It can be observed that in the delay-free case, accurate active power sharing and average voltage regulation is achieved after the secondary control is activated. In the case of k_{i1} = 12, k_{i2} = 10, considering the presence of time delay as shown in **Figures 8(B),(C)**, the curves of active powers and output voltages show a decaying oscillation with time delay τ = 83 ms and recover to stability about 3 s later. However, as the time delay further increases to τ = 98 ms, oscillation enlarges and the MG system fails to remain stable. Then the delay margin with regard to this set of controller gains lies between τ = 83 ms and τ = 98 ms, according to the theoretical delay margin τ_d = 87.9 ms obtained from **Table 2**.

Similarly, for the case of controller set k_{i1} = 16, k_{i2} = 4 as depicted in **Figure 6**, the system tends to be stable with a relatively small delay τ = 55 ms while the MG system becomes unstable when the delay increases to τ = 65 ms. Querying the theoretical result τ_d = 58.4 ms in **Table 2**, the effectiveness of the proposed analysis method is verified.

As can be visualized from the figures, similar dynamic performance is shown in the above two cases, whereas the control parameter set k_{i1} = 12, k_{i2} = 10 enjoys great superiority over that of k_{i1} = 16, k_{i2} = 4 in terms of delay-

TABLE 2 | Theoretical delay margin of the DC microgrid.

τ_d (s)		k_{i1}				
		4	8	12	16	20
k_{i2}	2	0.2421	0.1215	0.0777	0.0570	0.0446
	4	0.2452	0.1270	0.0802	0.0584	0.0457
	6	0.2477	0.1321	0.0828	0.0598	0.0466
	8	0.2512	0.1385	0.0853	0.0612	0.0475
	10	0.2535	0.1432	0.0879	0.0626	0.0485

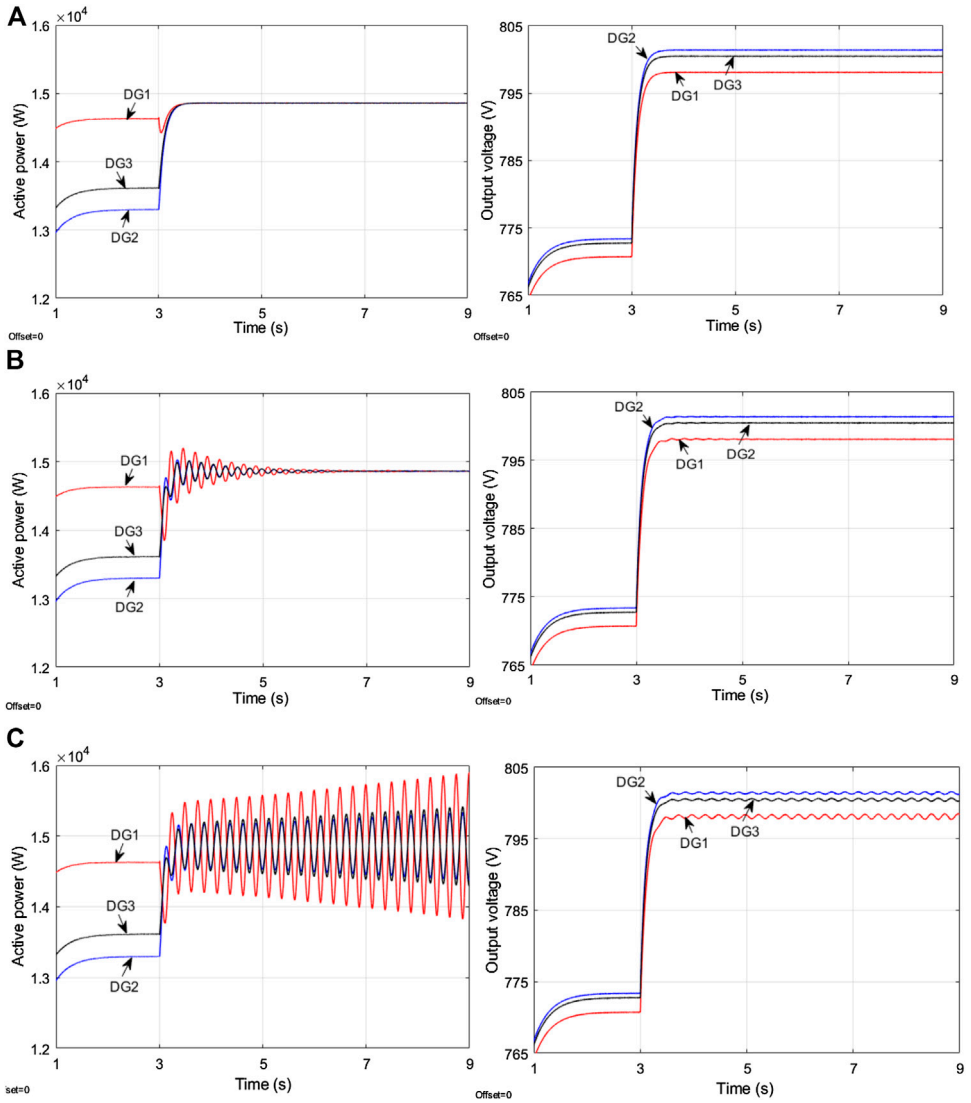

FIGURE 8 | Simulation results of active powers and actual output voltages with various time delays under $k_{i1} = 12$, $k_{i2} = 10$ **(A)** Without delay **(B)** $\tau = 83$ ms **(C)** $\tau = 98$ ms.

dependent stability. Therefore, the proposed stability analysis theory would be instructional for the design of control gains, to achieve a compromise between the dynamic performance and delay margin.

CONCLUSION

This paper addresses the stability analysis of distributed secondary control in DC integrated energy systems, taking both input and communication delays into consideration. Based on the Gerschgorin theorem and Nyquist criterion, the impact of input and communication delays on system stability is investigated and the stability condition is derived, from which we can observe that the stable operation mainly depends on input delays while is almost impervious to communication delays. However, the distinction between input and communication delays could give rise to steady-state error, indicating that a moderate increase of input delay can contribute to the elimination of steady-state deviation in some cases. The conclusion would be of great significance for control performance optimization in practice. Then, a small-signal model for stability analysis considering identical input and communication delays is derived and the delay margin corresponding to different control parameters can be calculated based on the critical characteristic root tracking method. The qualitative relationship between controller gains and delay margin can be utilized to guide the control design. Simulation cases are carried out to verify the effectiveness of the theoretical

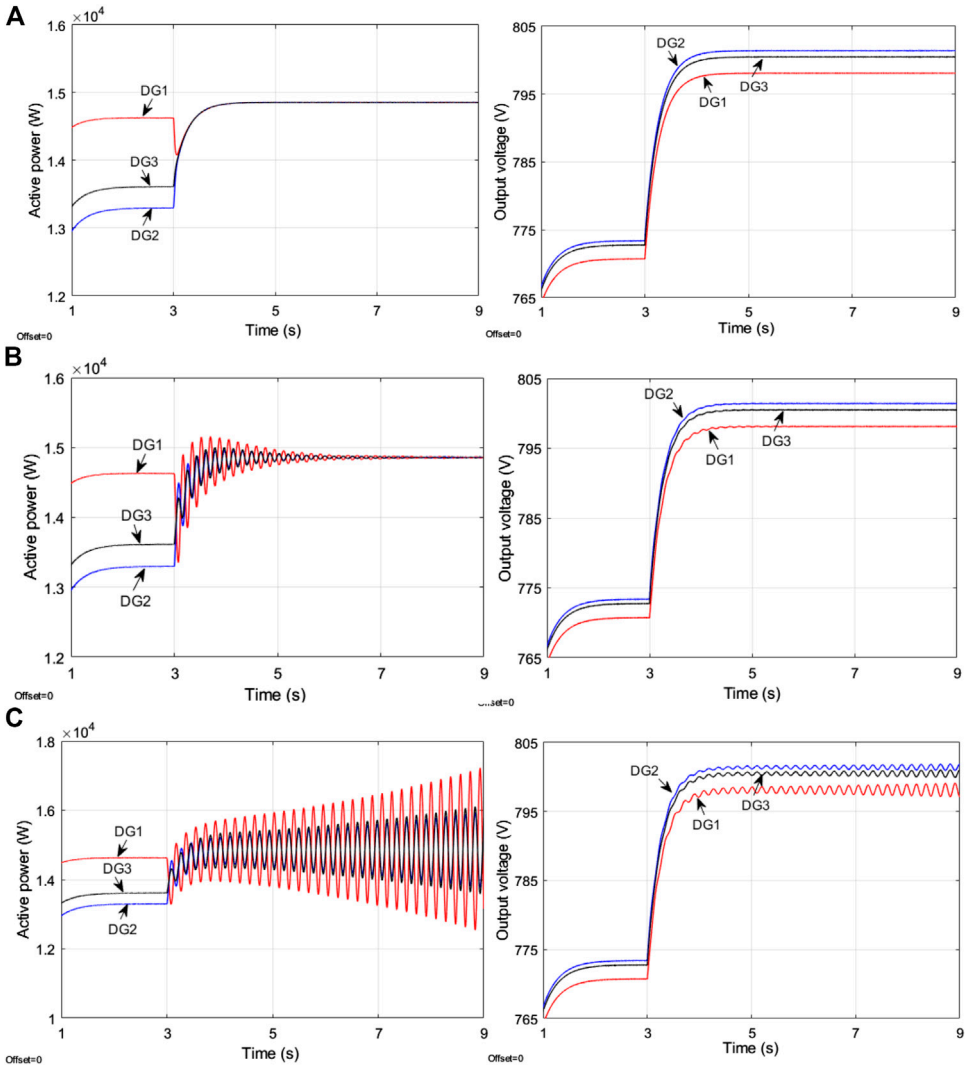

FIGURE 9 | Simulation results of active powers and actual output voltages with various time delays under $k_{i1} = 16$, $k_{i2} = 4$ **(A)** Without delay **(B)** $\tau = 55$ ms **(C)** $\tau = 65$ ms.

conclusions. Although the small-signal modeling is implemented in a small-scale system in this paper, the effectiveness of the approach remains regardless of the increasing number of DGs, considering that the small-signal method is always applicable for modeling DGs, and both the establishment and solution of the model can be executed by computers.

DATA AVAILABILITY STATEMENT

The original contributions presented in the study are included in the article/Supplementary Material, further inquiries can be directed to the corresponding author.

AUTHOR CONTRIBUTIONS

TW and CR proposed the methodology. TW and ST conducted the theoretical analysis as well as the simulation verification. QH wrote the original draft which was reviewed and edited by TW and CR All authors agree to be accountable for the content of the work.

FUNDING

This research was supported by the science and technology project of the State Grid Corporation of China, Grant 5204JY20000B.

REFERENCES

Baranwal, M., Askarian, A., Salapaka, S., and Salapaka, M. (2019). A distributed architecture for robust and optimal control of DC microgrids. *IEEE Trans. Ind. Electron.* 66, 3082–3092. doi:10.1109/TIE.2018.2840506

Dou, C., Yue, D., Guerrero, J. M., Xie, X., and Hu, S. (2017). Multiagent system-based distributed coordinated control for radial DC microgrid considering transmission time delays. *IEEE Trans. Smart Grid* 8, 2370–2381. doi:10.1007/s12555-019-0610-7

Fatihcan, A. M. (2010). Consensus in networks under transmission delays and the normalized Laplacian. *IFAC Proc. Vol.* 43, 277–282. doi:10.1098/rsta.2012.0460

Guo, F., Wen, C., Mao, J., and Song, Y. (2014). Distributed secondary voltage and frequency restoration control of drop-controlled inverter-based microgrids. *IEEE Trans. Ind. Electron.* 62, 4355–4364. doi:10.1109/TIE.2014.2379211

Guo, F., Xu, Q., Wen, C., Wang, L., and Wang, P. (2018). Distributed secondary control for power allocation and voltage restoration in islanded DC microgrids. *IEEE Trans. Sustain. Energy* 9, 1857–1869. doi:10.1007/s12555-019-0929-0

Han, Y., Zhang, K., Li, H., Coelho, E. A. A., and Guerrero, J. M. (2018). MAS-based distributed coordinated control and optimization in microgrid and microgrid clusters. *Comprehens. Overview* 33, 6488–6508. doi:10.1109/TPEL.2017.2761438

He, J., and Li, Y. W. (2011). Analysis, design, and implementation of virtual impedance for power electronics interfaced distributed generation. *IEEE Trans. Ind. Appl.* 47, 2525–2538. doi:10.3390/en11071801

Jia, H. J., and Yu, X. D. (2008). "A simple method for power system stability analysis with multiple time delays", in Proceedings of 2008 IEEE power and energy society general meeting - conversion and delivery of electrical energy in the 21st century. Pittsburgh, PA, 20–24.

Jin, C., Wang, P., Xiao, J., Tang, Y., and Choo, F. H. (2014). Implementation of hierarchical control in DC microgrids. *IEEE Trans. Ind. Electron.* 61, 4032–4042. doi:10.1109/TIE.2013.2286563

Kang, W., Li, Q., Gao, M., Li, X., Wang, X., Xu, R., and Chen, X. (2018). Distributed secondary control method for islanded microgrids with communication constraints. *IEEE Access* 6, 5812–5821. doi:10.1109/ACCESS.2017.2762356

Kumar, R., and Pathak, M. K. (2020). Distributed droop control of dc microgrid for improved voltage regulation and current sharing. *IET Renew. Power Gener.* 14, 2499–2506. doi:10.22266/ijies2019.0630.23

Li, Z., and Shahidehpour, M. (2019). Small-signal modeling and stability analysis of hybrid AC/DC microgrids. *IEEE Trans. Smart Grid* 10, 2080–2095. doi:10.1002/2050-7038.12683

Liu, S., Wang, X., and Liu, P. X. (2015). Impact of communication delays on secondary frequency control in an islanded microgrid. *IEEE Trans. Ind. Electron.* 62, 2021–2031. doi:10.3390/en12152926

Lopes, J. A. P., Moreria, C. L., and Madureira, A. G. (2006). Defining control strategies for microgrids islanded operation. *IEEE Trans. Power Syst.* 21, 916–924. doi:10.1109/TPWRS.2006.873018

Lou, G., Gu, W., Xu, Y., Jin, W., and Du, X. (2018). Stability robustness for secondary voltage control in autonomous microgrids with consideration of communication delays. *IEEE Trans. Power Syst.* 33, 4164–4178. doi:10.1109/TPWRS.2017.2782243

Lu, X., Yu, X., Lai, J., Wang, Y., and Guerrero, J. M. (2018). A novel distributed secondary coordination control approach for islanded microgrids. *IEEE Transactions on Smart Grid* 9, 2726–2740. doi:10.1109/TSG.2016.2618120

Massoulie, L. (2002). Stability of distributed congestion control with heterogeneous feedback delays. *IEEE Trans. Automat. Contr.* 47, 895–902. doi:10.1109/TNET.2003.820246

Mehdi, M., Kim, C., and Saad, M. (2020). Robust centralized control for DC islanded microgrid considering communication network delay. *IEEE Access* 8, 77765–77778. doi:10.3390/su12187628

Meng, Z., Ren, W., Cao, Y., and You, Z. (2011). Leaderless and leader-following consensus with communication and input delays under a directed network topology. *IEEE Trans. Syst. Man Cybern. B Cybern.* 41, 75–88. doi:10.1109/TSMCB.2010.2045891

Morstyn, T., Hredzak, B., Demetriades, G. D., and Agelidis, V. G. (2016). Unified distributed control for DC microgrid operating modes. *IEEE Trans. Power Syst.* 31, 802–812. doi:10.1007/s40565-018-0466-5

Nasirian, V., Moayedi, S., Davoudi, A., and Lewis, F. L. (2015). Distributed cooperative control of DC microgrids. *IEEE Trans. Power Electron.* 30, 2288–2303. doi:10.1109/TIE.2019.2898606

Olfati-Saber, R., and Murray, R. M. (2004). Consensus problems in networks of agents with switching topology and time-delays. *IEEE Trans. Automat. Contr.* 49, 1520–1533. doi:10.1109/TAC.2004.834113

Ren, W., and Beard, R. W. (2005). Consensus seeking in multiagent systems under dynamically changing interaction topologies. *IEEE Trans. Autom. Contr.* 50, 655–661. doi:10.1109/TAC.2005.846556

Simpson-Porco, J. W., Shafiee, Q., and Dörfler, F. (2015). Secondary frequency and voltage control of islanded microgrids via distributed averaging. *IEEE Trans. Ind. Electron.* 62, 7025–7038. doi:10.1109/TIE.2015.2436879

Trip, S., Cucuzzella, M., Cheng, X., and Scherpen, J. (2018). Distributed averaging control for voltage regulation and current sharing in DC microgrids. *IEEE Control Syst. Lett.* 3, 174–179. doi:10.1109/LCSYS.2018.2857559

Wang, C., Duan, J., Fan, B., Yang, Q., and Liu, W. (2019a). Decentralized high-performance control of DC microgrids. *IEEE Trans. Smart Grid* 10, 3355–3363. doi:10.1109/TSG.2018.2825199

Wang, Z., Liu, F., Chen, Y., Low, S. H., and Mei, S. (2019b). Unified distributed control of stand-alone DC microgrids. *IEEE Trans. Smart Grid* 10, 1013–1024. doi:10.3390/electronics8111265

Yoo, H., Nguyen, T., and Kim, H. (2020). Consensus-based distributed coordination control of hybrid AC/DC microgrids. *IEEE Trans. Sustain. Energy* 11, 629–639. doi:10.3390/en13123209

Yu, K., Ai, Q., Wang, S., Ni, J., and Lv, T. (2016). Analysis and optimization of droop controller for microgrid system based on small-signal dynamic model. *IEEE Trans. Smart Grid* 7, 695–705. doi:10.1109/ACCESS.2020.3014977

Zuo, S., Altun, T., Lewis, F. L., and Davoudi, A. (2020). Distributed resilient secondary control of DC microgrids against unbounded attacks. *IEEE Trans. Smart Grid* 11, 3850–3859. doi:10.1109/tsg.2020.2992118

Conflict of Interest: The authors declare that this study received funding from the science and technology project of the State Grid Corporation of China. The funder had the following involvement with the study: provide practical application scenario for the case study.

APPENDIX

$A' = R^{-1}D$, $B = R^{-1}E$ where

$$R = \begin{bmatrix} I_{n\times n} & \mathbf{0}_{n\times n} & \mathbf{0}_{n\times n} \\ M_{n\times n} + k_{p1}LM_{n\times n} & I_{n\times n} & k_{p2}\cdot I_{n\times n} \\ \mathbf{0}_{n\times n} & -I_{n\times n} & I_{n\times n} \end{bmatrix}, \quad D = \begin{bmatrix} -\omega_f \cdot I_{n\times n} & \omega_f \widehat{I} & \mathbf{0}_{n\times n} \\ -k_{i1}LM_{n\times n} & \mathbf{0}_{n\times n} & -k_{i2}\cdot I_{n\times n} \\ \mathbf{0}_{n\times n} & \mathbf{0}_{n\times n} & -k_3 L \end{bmatrix}, \quad E = \begin{bmatrix} \omega_f \widehat{V} \\ \mathbf{0}_{n\times n} \\ \mathbf{0}_{n\times n} \end{bmatrix}$$

$$\mathrm{M} = \ = \mathrm{diag}(\mathrm{mi}), \ I_{n\times n} = \begin{bmatrix} 1 & 0 & \cdots & 0 \\ 0 & 1 & & \vdots \\ \vdots & & \ddots & 0 \\ 0 & \cdots & 0 & 1 \end{bmatrix}_{n\times n}, \ \widehat{I} = \begin{bmatrix} I_1 & 0 & \cdots & 0 \\ 0 & I_2 & & \vdots \\ \vdots & & \ddots & 0 \\ 0 & \cdots & 0 & I_n \end{bmatrix}, \ \widehat{V} = \begin{bmatrix} V_1 & 0 & \cdots & 0 \\ 0 & V_2 & & \vdots \\ \vdots & & \ddots & 0 \\ 0 & \cdots & 0 & V_n \end{bmatrix}$$

$A_1 = R^{-1}D_1$, $A_1 = R^{-1}D_d$ where

$$D_1 = \begin{bmatrix} -\omega_f \cdot I_{n\times n} & \omega_f\left(\widehat{V}\cdot Y + \widehat{I}\right) & \mathbf{0}_{n\times n} \\ \mathbf{0}_{n\times n} & \mathbf{0}_{n\times n} & -k_{i2}\cdot I_{n\times n} \\ \mathbf{0}_{n\times n} & \mathbf{0}_{n\times n} & \mathbf{0}_{n\times n} \end{bmatrix}, \quad D_d = \begin{bmatrix} \mathbf{0}_{n\times n} & \mathbf{0}_{n\times n} & \mathbf{0}_{n\times n} \\ -k_1 \cdot L \cdot M & \mathbf{0}_{n\times n} & \mathbf{0}_{n\times n} \\ \mathbf{0}_{n\times n} & \mathbf{0}_{n\times n} & -k_3 \cdot L \end{bmatrix}$$

frontiers in Energy Research

ORIGINAL RESEARCH
published: 07 May 2021
doi: 10.3389/fenrg.2021.673228

Optimal Electricity Allocation Model Under China's Planning-Market Double-Track Mechanism Considering Bidding Game of Generation Companies

*Jinrui Cui[1,2], Yating Li[3], Chuan He[1,2], Zhi Zhang[3], Haichao Wang[1,2], Jiajun Tang[3], Yongbo Li[1,2], Hualin Cai[1], Zhenzhi Lin[3,4] and Li Yang[3]**

[1] State Grid Anhui Electric Power Co., Ltd., Hefei, China, [2] Anhui Power Exchange Center Company, Hefei, China, [3] Department of Electrical Engineering, College of Electrical Engineering, Zhejiang University, Hangzhou, China, [4] Department of Electrical Engineering, College of Electrical Engineering, Shandong University, Jinan, China

In China, under the planning-market double-track mechanism implemented on the generation side of electricity, unreasonable market-oriented power generation proportion may lead to unnecessary vicious competition and market price changes, and it is against the will of power exchange (PX). Given this background, in this study, a bi-level model for planning-market electricity allocation that considers the bidding game of generation companies is proposed for a smooth transition of power system reform. In the upper level of the model, the proportion of planned electricity is optimized by PX to minimize the average social electricity purchase price. In the lower level of the model, considering the impact of market power on the bidding strategy of generation companies, the bidding strategy of generation companies set as price makers is proposed using the residual demand curve analysis method, while the price takers adopt the lowest bidding strategy. Simulations based on data from a provincial electricity market in China illustrate that the proposed model can effectively reflect the impact of market-oriented electricity proportion on market power and market-clearing price, thus providing a quantitative basis for PX to determine the proportion of market-oriented electricity in total electricity consumption.

Keywords: planning-market double-track mechanism, electricity allocation, market power, residual demand curve, bidding game

OPEN ACCESS

Edited by:
Yingjun Wu,
Hohai University, China

Reviewed by:
Jiajia Yang,
University of New South Wales, Australia
Qin Wang,
Electric Power Research Institute (EPRI), United States

****Correspondence:***
Li Yang
eeyangli@zju.edu.cn

Specialty section:
This article was submitted to Smart Grids, a section of the journal Frontiers in Energy Research

Received: *27 February 2021*
Accepted: *12 April 2021*
Published: *07 May 2021*

Citation:
Cui J, Li Y, He C, Zhang Z, Wang H, Tang J, Li Y, Cai H, Lin Z and Yang L (2021) Optimal Electricity Allocation Model Under China's Planning-Market Double-Track Mechanism Considering Bidding Game of Generation Companies. Front. Energy Res. 9:673228. doi: 10.3389/fenrg.2021.673228

INTRODUCTION

In China, the planning-market double-track mechanism (PMDM) is implemented for electric power system reform. Orderly deregulation of the electricity market and implementation of priority generation/utilization mechanisms can ensure stable construction of a competitive electricity market in China. Under the PMDM, the total electricity provided by the generation side is divided into planned electricity and market electricity. Planned electricity is guaranteed by the base power-supply contract signed by the power grid company (GC) and generation companies, and is settled at a regulated price. Market-oriented electricity demand is met by wholesale market transactions and settled according to market price (National Development and Reform Commission National Energy Administration, 2017). Under a given market structure, the proportion of planned electricity is the key that affects market operation and interests of market entities.

Liberalization rates of power generation and utilization plan are different with the development of the electricity market in different provinces of China, and the proportion of market-oriented electricity is determined partly according to access conditions of market entities. By the end of 2020, coal-fired and gas-fired power plants and users with a voltage level of 10 kV or higher were allowed to participate in an electricity market transaction in Guangdong, China. In Anhui province of China, users with an annual power consumption of more than 500 MWh and units with a capacity of 100 MW or higher can apply to be a market entity. Users in Shandong province of China need to meet the requirements for voltage level (i.e., 10 kV and higher) and electricity consumption (4,000 MWh and higher) if they wish to participate in market transactions. On the power generation side, coal-fired and cogeneration units are the main entities in the Shandong electricity market.

Similarly, the electricity market has been liberalized in other countries by gradually relaxing the access conditions of users. In the United Kingdon, in 1990, users with a power level of 1 MW or higher were allowed to participate in electricity market transactions. Then, in 1994, users with a power level of 100 kW or higher were allowed to participate in market transactions, while in 1998 all users were allowed to apply to be a market entity. In Texas, USA, in the second year of wholesale electricity market operation, all users were allowed to participate in the market. At present, generation companies and most power users are allowed to participate in market transactions, with no planned power generation and consumption guaranteed by the government. For example, in the United States resident users in PJM, ERCOT and NYISO are given. In the United Kingdom, the United States, and Australia, renewable energy is introduced into the wholesale electricity market through a renewable portfolio standard or contract for difference. At Nord Pool, power exchange between countries is realized through cross-border transactions (Fereidoon, 2017).

Most existing research studies have focused on the distribution and adjustment of planned electricity and market electricity in a time sequence from the perspective of a power system operator based on the fact that annual planned electricity has been determined (Li et al., 2020). An optimal allocation model of contract electricity and bidding electricity in each period of the trading day is established to minimize total power purchase cost, and it considers constraints in unit operation and network congestion by Jiang et al. (2004). An intra-day rolling generation scheduling model of a wind power system considering the uncertainty of wind power is established by Sun et al. (2020) to cooperatively optimize the target electricity and generation plan of generation units. With full consideration of the impact of power uncertainty of renewable energy, a time-sequence simulation method for monthly energy trading schedule is proposed by Zhang Q. et al. (2020). A two-stage optimization model for annual rolling generation scheduling with consideration of the influence of electric power direct trading on open and impartial dispatching is proposed by Xie et al. (2018). However, there are few research studies on the degree of liberalization of the regulated electricity market, and there is no appropriate method to determine the proportion of planned electricity to total electricity consumption. In addition, market bidding strategies of generation companies are the key to reflect the effectiveness of market rule design and parameter setting. Existing research on the bidding strategy of generation companies has based on cost analysis, market price forecast, or bidding estimation of rival generation companies (Huang and Li, 2015; De et al., 2018; Guo et al., 2021). A multi-objective joint bidding model for wind-thermal-photovoltaic hybrid generation system is established with the goal of maximizing the total profit of power and reserve markets and minimizing emissions of thermal power units, and it considers the cost of different types of units by Khaloie et al. (2020). A bidding strategy for generation companies in a sequential dual market is proposed to maximize the utility that makes a tradeoff between revenues and risks in the electricity and balancing markets by Jiang et al. (2019), and it considers the uncertainties of electricity consumption and bidding strategies of rival companies. Under the conditions of risk constraints, a two-stage bidding game model for wind power suppliers in the day-ahead and balancing markets is established by Schneider and Roozbehani (2016) and Baringo and Conejo (2016), in which the market behaviors and performance of wind power suppliers are studied from the perspective of price sensitivity. In fact, the proportion of planned electricity will affect the supply and demand of the electricity market, and then affect the market power of generation companies. However, the impact of market power on biddings of generation companies is rarely considered in the studies mentioned above.

Given this background, in this study, a bi-level planning-market electricity allocation model for the PMDM of China is established. In the upper level of the model, the proportion of planned electricity is optimized by PX to minimize the social average purchase price (SAPP). In the lower level of the model, bidding strategies for generation companies with different market power are proposed, and the bidding game process of generation companies is simulated to solve the market equilibrium. Finally, the effectiveness and rationality of the proposed model are verified by a provincial electricity market in China.

PLANNING-MARKET ELECTRICITY ALLOCATION PROBLEM CONSIDERING MARKET POWER OF GENERATION COMPANIES

In order to support the orderly development of the social economy, the power generation side in China has been regulated by the government for a long time. Only a few direct-purchasing forward bilateral contracts are allowed between power producers and large users before the electricity market restructuring started in 2015, which accounting for a low proportion of consumption power (Zhang Z. et al., 2020). In 2017, the phased planning-market double-track mechanism was proposed by the government to guide the gradual liberalization of the power market of China. Thermal power units have been allowed to participate in the market in most of the provincial power markets, while renewable energy (mainly wind power

and photovoltaics) and hydropower have been arranged by an independent system operator (ISO) to generate electricity preferentially (National Development and Reform Commission National Energy Administration, 2017). The priority power generation mechanism is implemented in China in order to ensure the consumption of renewable energy and hydropower.

A two-level market system for the national unified power market and the provincial power market is established in China to realize the optimal allocation of resources nationwide. The transaction sequence of the national unified power market, organized by Beijing Trading Center, is prior to the provincial power market. In order to implement the national strategy of power transmission from west to east and the clean energy consumption policy, cross-provincial, and cross-regional transactions are divided into the power within the government framework agreement and the market-oriented transaction (State Electricity Regulatory Commission, 2012). The implementation of the electricity quantity by cross-provincial and cross-regional trading should be guaranteed when the provincial electricity market is carried out inside the province (Lei and Song, 2016).

The allocation of planned electricity and market electricity is undertaken by PX. Before the start of the annual transaction, the annual planned electricity of thermal power producers is arranged by local PX after deduction of imported energy and priority generation energy according to the predicted annual electricity consumption. Then, total planned electricity is allocated to each unit in proportion according to its capacity (Min and Li, 2016). At present, the spot market pilot has been launched in eight provinces and cities in China. By the end of 2020, three spot market trials had been carried out in Zhejiang province. The full power bidding mode is adopted by the spot market in Zhejiang, and it draws lessons from PJM. The annual planned electricity of each unit is decomposed into each period of the bidding day by PX in advance as the minimum output. Then the residual load demand of each period is released to provide a reference for the quotation of thermal power units (Lei and Song, 2016). The trading process of the electricity market under PMDM is shown in **Figure 1**.

In general, the proportion of planned electricity to total electricity consumption will affect the supply and demand of the market, and then affect the market power. As a quick case study, it is assumed that the annual total electricity consumption is 100 billion kWh and that the maximum generation quantity is 150 billion kWh. Q_L represents the total market demand, and Q_G represents the total market supply. A is the market supply–demand ratio, which can be calculated as $A = Q_G/Q_L$. As shown in **Table 1**, with the increase in the planned electricity proportion, the market supply–demand ratio increases, and the market power decreases.

Since the first round of power system reform was carried out in 2002, the separation of power plants and power grids has been initially realized, and five power generation groups have been established in China. Due to historical reasons, there is a high concentration rate in the power generation side of China (Lei and Song, 2016). The proportion of installed capacity of thermal power producers in Zhejiang and Anhui provinces of China is shown in **Figure 2**. Among these producers, the installed capacity of the Zheneng group accounts for 51.1% of the total capacity of Zhejiang, and there are three generation companies whose capacity accounts for more than 15% of the total capacity in Anhui. The Herfindahl-Hirschman index (HHI) is an index reflecting market concentration. The HHI in the Zhejiang power generation market is 3,144 and that in the Anhui power generation market is 1,525; both of which are more than 1,000, indicating that the market power is high and that it is difficult to develop effective competition. In a highly concentrated market, large-capacity generation companies may use market power to raise market prices, resulting in market price distortion and social welfare losses (Bagchi et al., 2019; Hajiabadi and Samadi, 2019). It is necessary for PX to consider the market structure of the generation side when allocating planned electricity and market electricity, so as to ensure appropriate market adequacy, restrain market power, and realize full market competition (Hakam et al., 2020).

PLANNING-MARKET ELECTRICITY ALLOCATION MODEL OF PX

The equivalent load demand, i.e., the total amount of planned electricity and market electricity, is obtained by deduction of imported energy and priority generation energy based on annual total electricity consumption. The priority generation energy mainly includes renewable energy and hydropower energy. Wind power and photovoltaics fluctuate randomly (Liu et al., 2020; Xing et al., 2021). The output of hydropower plants and pumped storage plants are adjustable and are pre-dispatched by ISO considering the demand of peak load cutting and valley load filling. Among them, hydropower plants are flexible in start-up and shut-down and low in start-up costs and are usually arranged by ISO during peak load period to ease the tension in power generation. Pumped storage plants are in the power generation state in peak load period and load state in low load period, which can reduce load peak valley difference (Fekete et al., 2019; Song et al., 2020).

The equivalent load duration curve after deduction of the imported energy and priority generation energy is shown in **Figure 3**. Due to limitation in reservoir capacity and unit rated power, power and energy constraints of hydropower and pumped storage plants can be expressed as (Hu et al., 2021).

$$0 \le P_H(s,t) \le P_H^{\max} \tag{1}$$

$$\sum_{t \in T_p} P_H(s,t) \triangle t \le E_H^{\max} \tag{2}$$

$$-P_P^{\max} \le P_P(s,t) \le P_P^{\max} \tag{3}$$

$$\sum_{t \in T_p} P_P(s,t) \triangle t \le E_P^{\max} \tag{4}$$

$$\sum_{t \in T_v} \left| P_P(s,t) \triangle t \right| \le E_P^{\max} \tag{5}$$

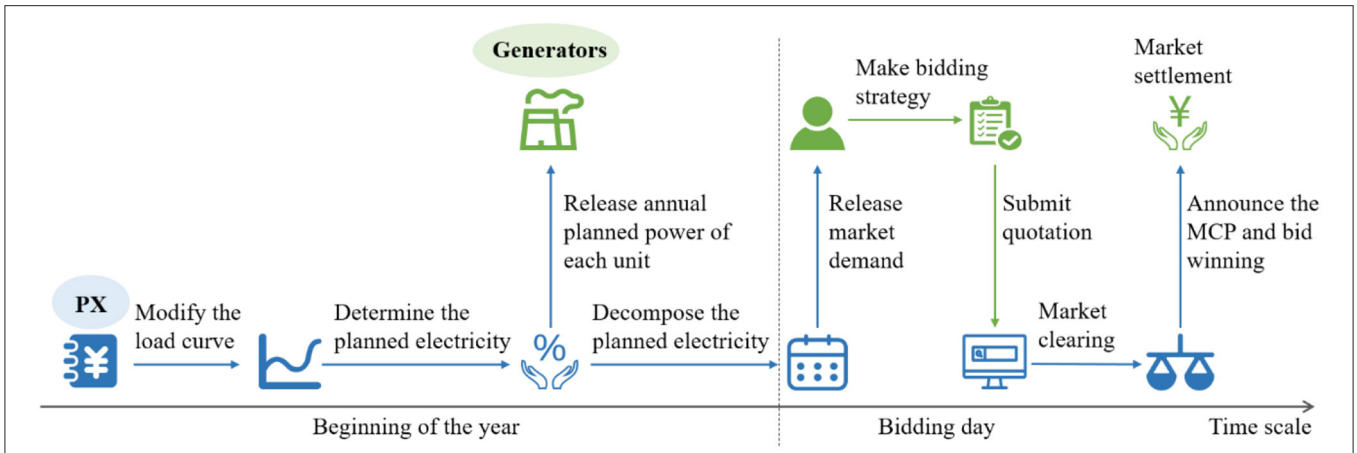

FIGURE 1 | Electricity market transaction process.

TABLE 1 | Market supply–demand ratio under different proportions of planned electricity.

Proportion of planned electricity	Q_G	Q_L	A
0%	1,500	1,000	1.5
10%	1,400	900	1.56
20%	1,300	800	1.63
30%	1,200	700	1.71

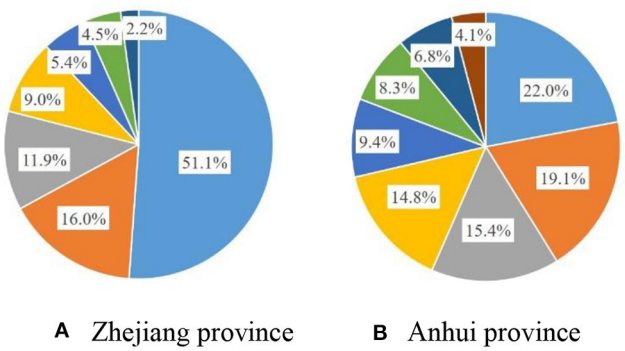

FIGURE 2 | Structure of installed generator. **(A)** Zhejiang province; **(B)** Anhui province.

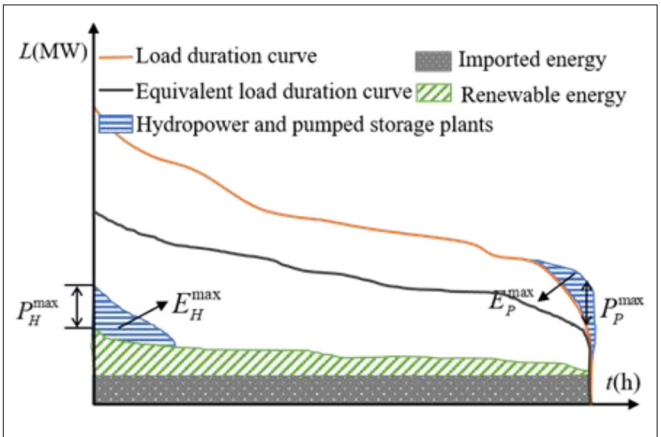

FIGURE 3 | Equivalent load duration curve.

where $P_H(s,t)$ and $P_P(s,t)$ represent the output of hydropower plant and pumped storage plant, respectively, in period t under scenario s. $P_H^{\max}$ and $P_P^{\max}$ represent the maximum output of hydropower plant and pumped storage plant, respectively. $E_H^{\max}$ and $E_P^{\max}$ represent the maximum storage energy for hydropower plants and pumped storage plants, respectively. T_p and T_v are the peak and valley time sets, respectively.

At present, the power market in China is similar to the pool mode, and there is no awareness in market bidding on the demand side. In this study, the load curve is considered to be inelastic, i.e., the load curve does not change with a change in market price. The load curve is modified according to imported energy and priority generation energy, and the equivalent load curve $L_{eq}(s,t)$ is obtained, which is expressed as

$$L_{eq}(s,t) = L(s,t) - P_R(s,t) - P_I(s,t) - P_H(s,t) - P_P(s,t) \quad (6)$$

where $L(s,t)$ denotes the load in period t under scenario s. $P_R(s,t)$ and $P_I(s,t)$ are the output of renewable energy and imported electricity in period t under scenario s, respectively.

Equivalent load demand is divided into planned electricity and market electricity by PX. The decision variable of PX is the proportion of planned electricity γ, and the objective function is to minimize SAPP $\bar{\lambda}$. Therefore, the optimal decision model of

PX can be expressed as

$$\min \ \overline{\lambda} = \frac{\lambda^P \gamma Q_{eq} + \sum_s N_s \sum_t \sum_{i \in \Omega_{M,s,t}} \lambda^M(s,t) P_i^M(s,t)}{Q_{eq}} \quad (7)$$

$$s.t.\ 0 \le \gamma \le \gamma_{\max} \quad (8)$$

$$Q_{eq} = \sum_s N_s \sum_t L_{eq}(s,t) \quad (9)$$

where Q_{eq} is the equivalent load demand after deduction of imported energy and priority generation energy. λ^P denotes the settlement price of planned electricity. $\lambda^M(s,t)$ represents the market clearing price (MCP) in period t under scenario s. $P_i^M(s,t)$ indicates the winning bid of unit i in period t under scenario s. N_s is the number of days of scenario s in a year. $\Omega_{M,s,t}$ denotes the set of all winning units in period t under scenario s. $\gamma_{\max}$ is the upper limit of planned electricity proportion.

Annual planned electricity is distributed to each unit in proportion according to unit capacity. Let Q_i^P represent the total annual planned electricity of unit i and be expressed as

$$Q_i^P = \gamma Q_{eq} \frac{P_i^N h_i}{\sum_{i \in \Omega} P_i^N h_i} \quad (10)$$

where P_i^N is the rated capacity of unit i. h_i represents the annual utilization hours of unit i. Ω denotes the set of all thermal power units.

The total annual planned electricity is decomposed into each period of the bidding day by PX in advance through the deterministic power decomposition algorithm based on the typical daily load curve. Then, the planned power of each unit in different periods $P_i^P(s,t)$ is obtained in proportion (Chen et al., 2009) and can be expressed as:

$$P_i^P(s,t) = \beta_{d,t} Q_i^P \quad (11)$$

where $\beta_{d,t}$ is the proportion of electricity consumption in period t of day d to annual electricity consumption and can be calculated from the typical daily load curve.

In the centralized market, PX receives the quotation of each generation company and determines the winning bid of each generation company through the specified market-clearing algorithm. The goal of market clearing is to minimize the total generation cost and determine a unified market-clearing price for all generation companies (Yang et al., 2019; Zhang and Yan, 2019). Without considering network constraints, the optimal model of market-clearing can be expressed as (Faraji et al., 2020).

$$\min \sum_{i \in \Omega_{M,s,t}} \lambda^M(s,t) P_i^M(s,t) \quad (12)$$

$$s.t. \sum_{i \in \Omega_{M,s,t}} P_i^M(s,t) + \sum_{i \in \Omega} P_i^P(s,t) = L_{eq}(s,t) \quad (13)$$

$$\lambda^M(s,t) \ge \rho_i(s,t) (i \in \Omega_M) \quad (14)$$

where $\rho_i(s,t)$ is the bidding price of unit i in period t under scenario s. Ω_M denotes the set of units participating in the bidding. When multiple units are marginal and offer the same price, the amount of electricity is allocated according to the bidding capacity of the units (Guo et al., 2019).

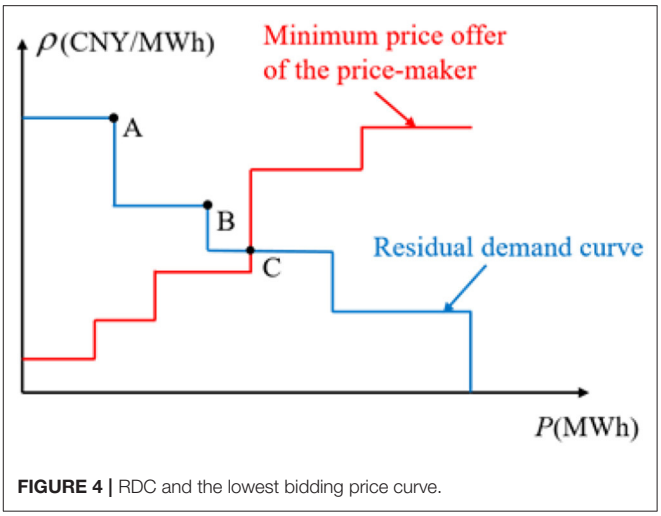

FIGURE 4 | RDC and the lowest bidding price curve.

BIDDING GAME MODEL OF GENERATION COMPANIES CONSIDERING MARKET POWER

Price Makers and Price Takers

Among the generation companies in the electricity market, some large ones have the ability to raise the MCP because of their strong market power, and they are defined as price makers. The others are regarded as price takers (Ilak et al., 2014). Price makers often make bidding strategies with the goal of maximizing revenue, while price takers often choose cost-based bidding strategies to ensure generation (Nieta et al., 2014; Shafie-khah et al., 2015).

Must run ratio (MRR) is a kind of prior evaluation index to measure the market power, which considers the impact of market supply and demand, and can evaluate the market power of a single generation company (Lei and Song, 2016). Therefore, in this study, MRR is used to define whether a generation company is a price maker or a price taker. Assuming that there are J generation companies in the market and all the competitors of generation company j are recorded as $\widehat{j}$, $M_j(s,t)$ is let to represent the MRR of generation company $j$in period t under scenario s and can be expressed as

$$M_j(s,t) = [L_{eq}(s,t) - \sum_{i \in \widehat{j}} P_i^N] / \sum_{i \in j} P_i^N \quad (15)$$

The greater M_j is, the more likely generation company j is to exercise market power (Lei and Song, 2016). In this study, the generation company that satisfies $M_j > 0$ is selected as the price maker.

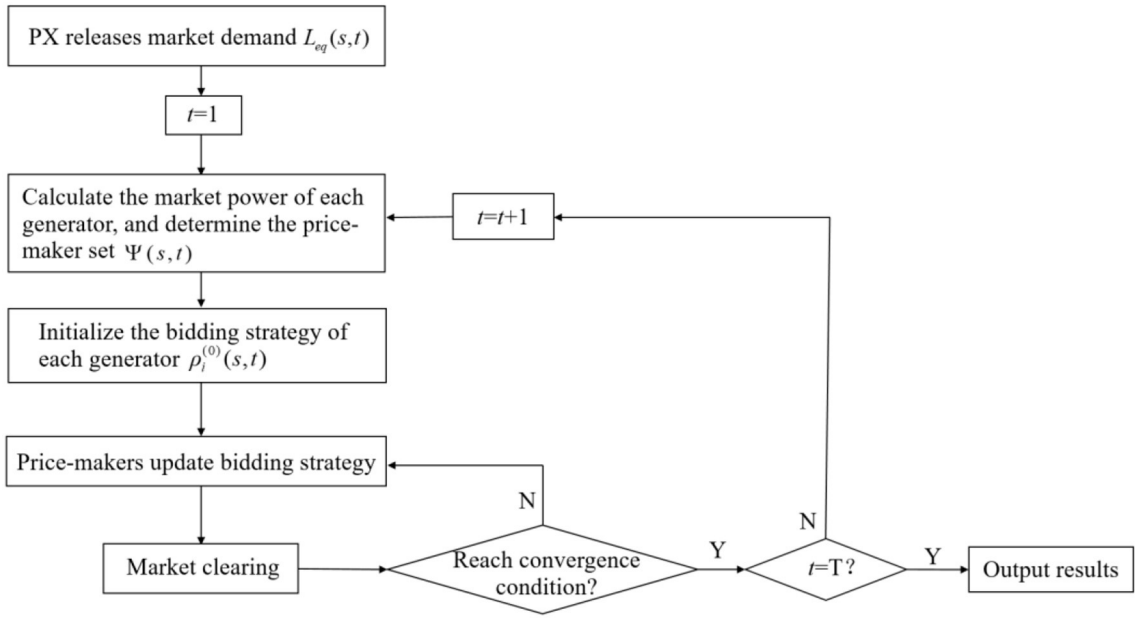

FIGURE 5 | Flow chart for solving generation companies bidding game model.

Bidding Strategies of Price Takers Based on the Lowest Bidding Price

In the centralized market, generation companies are required to declare a minimum output, a price and a capacity $[P_i^P(s,t), \rho_i(s,t), P_i(s,t)]$ for each unit. The minimum output $P_i^P(s,t)$ is the output of the unit to meet the planned power and is provided at zero price to ensure that power is dispatched but settled at the planned power price λ^P. The bidding price $\rho_i(s,t)$ of the unit should be less than the upper limit of the market price $\overline{\rho}$.

The lowest bidding price varies with the power generation cost of each unit. Unit cost includes fuel cost, which is measured by the marginal cost $C_{M,i}$ of the unit and fixed cost $C_{F,i}$, which consists of investment cost $C_{I,i}$ and operation and maintenance cost $C_{O,i}$. In order to include the fixed cost in the bidding price, it is necessary to convert the multi-year and annual fixed costs into hourly fixed cost, whose conversion formula is

$$C_{F,i} = [C_{I,i} + C_{O,i}\frac{(1+i_y)^{Y_i}-1}{i_y(1+i_y)^{Y_i}}] \times \frac{i_h(1+i_h)^{Y_h Y_i}}{(1+i_h)^{Y_h Y_i}-1} \quad (16)$$

$$i_h = (1+i_y)^{\frac{1}{Y_h}} - 1 \quad (17)$$

where i_y is the annual interest rate, and i_h is the hourly interest rate. Y_i is the lifetime of unit i, and $Y_h = 8760$ h.

In conclusion, the lowest bidding price $\rho_i^{\min}$ of unit i is:

$$\rho_i^{\min} = C_{M,i} + C_{F,i} \quad (18)$$

Bidding Strategies of Price Makers Based on the Residual Demand Curve

Residual demand curve (RDC) refers to the demand curve faced by a specific generation company in the competitive electricity market, and it can be calculated by subtracting the bidding curves of all competitors of the company from the total demand curve. The bidding strategies of generation companies acting as price markers are based on RDC (Bompard et al., 2008).

In this study, the single period bidding problem of generation companies is analyzed, and there is no correlation among the biddings of different periods. The profit of generation company j in period t is equal to the income of planned electricity and market electricity minus generation cost. The goal of strategic bidding is to maximize profit $F_j(s,t)$, and the bidding optimization problem can be described as

$$\max\ F_j(s,t) = \sum_{i\in j}[\lambda^P P_i^P(s,t) + \lambda^M(s,t)P_i^M(s,t) - C_i(s,t) - C_{F,i}] \quad (19)$$

$$s.t.\ C_i(s,t) = C_{M,i}([P_i^P(s,t) + P_i^M(s,t)] \quad (20)$$

$$P_i^{\min} \le P_i^P(s,t) + P_i^M(s,t) \le P_i^{\max} \quad (21)$$

where $C_i(s,t)$ is the fuel cost of unit i in period t under scenario s. $P_i^{\min}$ and $P_i^{\max}$ represent the minimum and maximum technological outputs of the unit, respectively.

In the electricity market, large-capacity generation companies can exercise their market power through capacity gaming or price gaming (Wang et al., 2016; Tong et al., 2019). In this study, the price game model is used to solve the optimal bidding strategy for price makers by exploring their RDC (Bompard et al., 2008). As shown in **Figure 4**, the blue curve is the RDC of the generation company j, and the red curve is the quotation curve of all units of the generation company j according to the lowest bidding price. The points with discontinuous slope (points A and B) are proved to be potential best biddings of price makers (Bompard et al., 2008). Generation company j starts from the highest bidding benchmark (point A) and then goes down to the intersection

(point C) of the lowest bidding price curve and the RDC to find the point to maximize its profit. For example, when a generation company chooses point B as the bidding benchmark, its units whose cost is lower than B will be quoted at the price of B, and units whose cost is higher than B will be quoted at the lowest bidding price.

The solution steps of generation companies bidding game model considering market power can be summarized as follows; and for ease of understanding, a flow chart for solving the proposed model is shown in **Figure 5**.

1) The set of price makers $\Psi(s,t)$ in a specific period is determined by calculating the market power of each generation company.
2) We initialize the bidding strategy $\rho_i^{(0)}(s,t)$ of each generation company to the lowest bidding price $\rho_i^{\min}$ of each unit. The biddings of price takers remain unchanged.
3) For each price maker $j \in \Psi(s,t)$, it is assumed that the price quoted by its competitor $\widehat{j}$ is the result of the last iteration, and the RDC of price maker j is calculated.
4) The optimal bidding strategy of price maker j is determined based on its RDC considering the cost of each unit.
5) We judge whether the market is in equilibrium. If no price maker wants to change the bidding strategies or the number of iterations exceeds the maximum limit, it ends. If not, return to step 3.

CASE STUDIES

In this study, the actual power market data of a province in China are used to demonstrate the proposed model. The settlement price of planned electricity λ^P is 360 CNY/MWh, and the market price cap $\overline{\rho}$ is 450 CNY/MWh. The unit capacity and cost information of each generation group are shown in **Table 2**. The maximum unit technical output is 1, and the maximum unit technical output is 0.3. According to the typical load curve of the province and the output of imported energy, renewable energy and hydropower, the typical daily equivalent load curve is obtained and shown in **Figure 6**, with the probability of typical scenarios. By solving the proposed model, it is found that the optimal proportion of planned electricity is 0.4, the minimum SAPP is 334 CNY/MWh, and the average MCP ($\overline{\lambda^M}$) is 310 CNY/MWh.

Impacts of the Proportion of Planned Electricity on MCP and Market Power

As shown in **Figure 7**, $\overline{\lambda^M}$ decreases when γ increases. This implies that when the proportion of planned electricity increases, the generation adequacy in the market increases and the market power of generation companies becomes lesser, and that the companies tend to quote according to cost, so the MCP decreases. First, $\overline{\lambda}$ decreases and then increases when γ increases. When the proportion of planned electricity increases, the purchasing cost of planned electricity increases, while that of market electricity decreases due to the decrease in market electricity quantity and MCP. Under the combined effect of the two, first, the SAPP decreases and then increases, and there is a minimum value.

TABLE 2 | Unit capacity and cost of power generation groups.

Name of power generation group	Unit capacity (MW)	Marginal cost (CNY/MWh)
WN	1,320	230
	1,260	232
	1,110	238
	600	290
	330	300
	330	300
GD	1,260	232
	1,050	238
	640	280
	640	280
	320	300
GT	1,000	240
	1,000	240
	640	280
	640	280
HD	1,000	240
	1,000	240
	320	300
	320	300
DT	1,320	230
	320	300
	320	300
SW	1,260	232
	600	290
HN	660	270
	330	300
	330	300

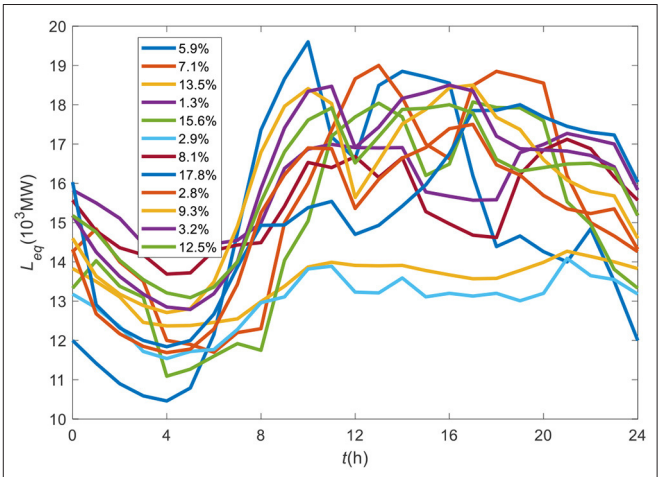

FIGURE 6 | Typical daily equivalent load curve and scenario probability.

The number of price makers in each period under different proportions of planned electricity is shown in **Figure 8**. When $\gamma = 0.3$, the period without price makers accounted for 27.4%, and the period with 7 price makers accounted for 32.1%, in which

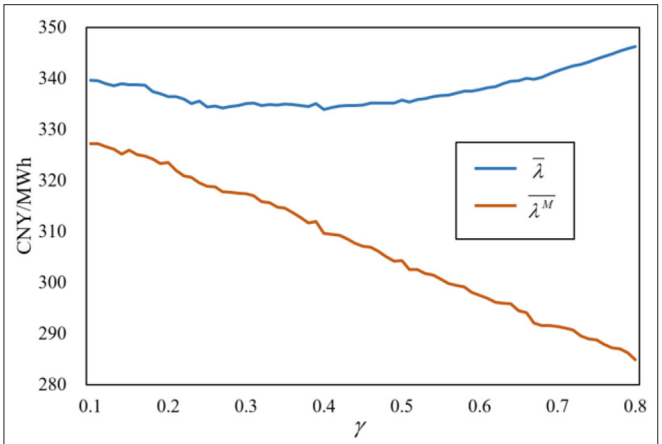

FIGURE 7 | SAPP and MCP under different proportions of planned electricity.

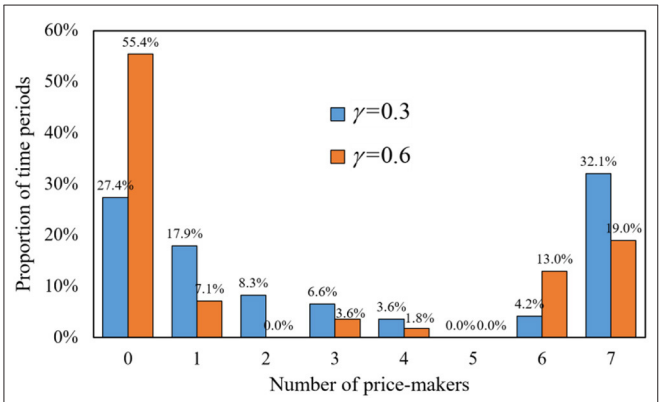

FIGURE 8 | The number of price makers under different proportions of planned electricity.

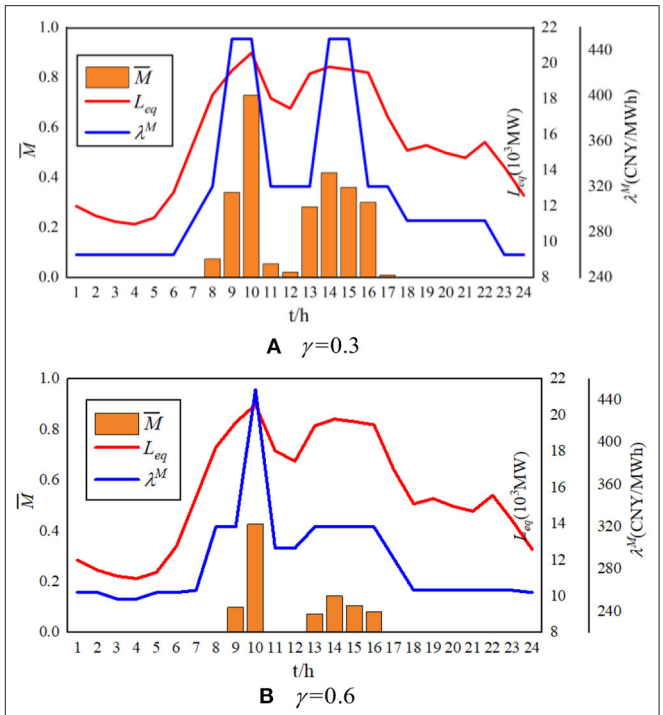

FIGURE 9 | MCP and market power on a typical day. **(A)** $\gamma = 0.3$; **(B)** $\gamma = 0.6$.

TABLE 3 | Optimal proportion of planned electricity under different load growth rates.

Load growth rates	γ	$\overline{M_1}$	$\overline{\lambda^M}$(CNY/MWh)	$\overline{\lambda}$(CNY/MWh)
0%	0.40	0.04	310	332
3%	0.52	0.07	313	341
6%	0.64	0.12	318	348
9%	0.69	0.17	324	352

there is great market power in the market. When $\gamma = 0.6$, the proportion of time periods without price makers increased from 27.4 to 55.4%, and the number of price makers also decreased in other periods. This implies that the higher the proportion of planned electricity, the lesser the number of price makers in the market and the lesser the market power.

Impacts of the Load Level on MCP and Market Power

Under the conditions of constant power generation, different load levels mean different market demands and generation adequacy. Therefore, the load level will also affect the market power of generation companies. The MCP and market power of a typical day with a different proportion of planned electricity is shown in **Figure 9**, where $\overline{M}$ is the average value of the MRR of seven generation companies. It can be seen from **Figure 9** that when $\gamma = 0.3$, $\overline{M}$is positive from 8:00 to 17:00, while when $\gamma = 0.6$, there are only 6 periods of 9:00–10:00 and 13:00–16:00, in which market power exists and the value of $\overline{M}$ is lesser. When $\gamma = 0.3$ for 9:00–10:00 and 14:00–15:00, and $\gamma = 0.6$ for 10:00, $\overline{M}$ is above 0.3; and the MCP reaches the market price cap. In the period of $\overline{M} = 0$, all generation companies in the market are price takers and quote according to the lowest bidding price, so the MCP is lower.

It can also be seen from **Figure 9** that $\overline{M}$ and λ^M vary in different periods, and they are both high in peak load period no matter what γ is. In peak load periods, more units with high costs and high quotations win the bid because of the high load. At the same time, market generation adequacy is low and the market power of generation companies is high, which lead to high MCP due to the bidding strategies of price takers. In contrast, the market generation adequacy is high in low load periods, so the MCP is low.

We let $\overline{M_1}$ be the average MRR of seven generation companies in all periods under the optimal proportion of planned electricity. $\overline{\lambda^M}$ and $\overline{\lambda}$ are the average MCP and SAPP, respectively, in all periods under the optimal proportion of planned electricity. It can be seen in **Table 3** that a higher proportion of planned electricity is required to cope with the increased load growth

rate, so as to ensure minimum SAPP. When the load growth rate increases, $\overline{M_1}$ and $\overline{\lambda^M}$ become higher. This implies that under the conditions of the unchanged generation structure, the load growth causes the generation capacity to be tenser, which leads to higher MCP and further causes an increase in $\overline{\lambda}$.

Profit of Generation Companies Under Different Bidding Strategies

The profit of seven generation companies (namely, WN, GD, GT, HD, DT, SW, and HN) under different bidding strategies are shown in **Table 4**. Compared with cost-based bidding, when strategy-based bidding is adopted, the profit of all generation companies increases by more than 2%. Among them, the growth rate of WN is the highest, i.e., 7%, and the profit increases from 10.06 to 10.82 million CNY. At the same time, $\overline{\lambda^M}$ has increased from 306 to 310 CNY/MWh. Under the settlement mode of unified clearing price, although price takers have no ability to raise the price, their profit will also increase.

At a certain period, WN and GD are price makers; and GT, HD, DT, SW, and HN are price takers. The bidding curve of WN under different bidding strategies is shown in **Figure 10**. When WN bids according to the lowest bidding price, the bidding curve is divided into six segments according to the different costs of each unit, and the planned electricity (1,823 MWh) is quoted at 0 CNY/MWh. When adopting strategy-based bidding, the bidding curve of WN is only divided into three segments, which are quoted at 0, 310, and 320 CNY/MWh, respectively. Among the six units of WN, the bidding price of four units is higher than the lowest bidding price, which indicates that WN has made use of market power to increase MCP to 310 CNY/MWh, thus obtaining more profits.

TABLE 4 | Profit of generation companies and MCP.

	Quotation strategy	Cost-based quotation	Strategy-based quotation
$\overline{\lambda}^M$ (CNY/MWh)		306	310
Profit	WN	10.06	10.82
(million CNY)	GD	8.93	9.4
	GT	7.66	8.06
	HD	6.89	7.1
	DT	5.78	5.9
	SW	5.31	5.42
	HN	5.07	5.17

CONCLUSION

In this study, a planning-market electricity allocation model is established, and it considers the objectives of minimizing electricity purchase price for PX and maximizing profits for generation companies. Bidding strategies for price makers and price takers are proposed considering the market power of generation companies. The game process of generation companies is simulated, and the MCP and the optimal bidding strategy of each generation company in the market equilibrium state are obtained. The proposed model is demonstrated in the case of a provincial electricity market in China, and the main findings are as follows:

1) The proportion of planned electricity affects the market power of generation companies, and it further affects MCP. The higher the proportion, the lesser the market power and the lower the MCP. In addition, PX should comprehensively consider market power and power purchasing cost when determining the proportion of planned electricity.
2) The level of load affects the market power of generation companies and the optimal proportion of planned electricity. Under the conditions of unchanged generation structure, with the growth in future load, PX should gradually increase the proportion of planned electricity.
3) The bidding strategy that price makers adopt to pursue profit maximization will lead to an increase in MCP. At this time, more profits can also be obtained when price takers bid based on cost.

In this study, the allocation of planned electricity and market electricity in China is analyzed under the PMDM. In the future, the convergence of the market in different stages considering the requirements of orderly releasing the plan of power generation and power utilization can be studied. In addition, with the deepening reform on the electricity sale side, the impact of electricity demand elasticity on the bidding strategy of generation companies can also be considered.

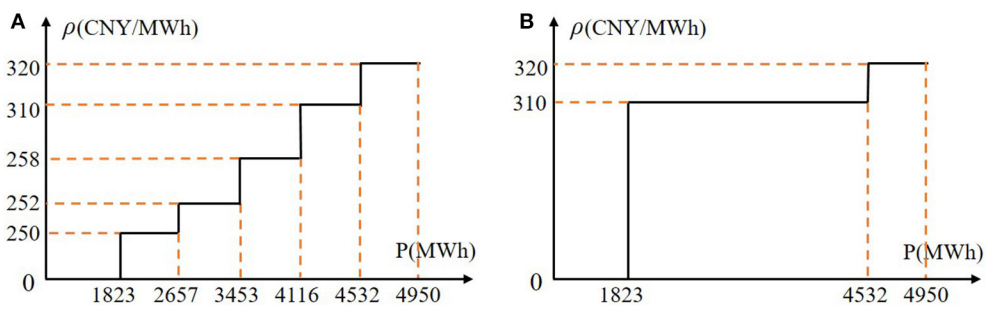

FIGURE 10 | Bidding curve of WN under different bidding strategies. **(A)** Cost-based bidding; **(B)** strategy-based bidding.

DATA AVAILABILITY STATEMENT

The original contributions presented in the study are included in the article/supplementary material, further inquiries can be directed to the corresponding author/s.

AUTHOR CONTRIBUTIONS

JC, LY, and ZL conceptualized the study. YaL, CH, and ZZ performed the analysis. YaL, HW, and JT performed investigations. YoL and HC acquired resources. JC, CH, HW, YoL, and HC acquired funding. JC wrote the original draft. YaL, ZZ, and ZL reviewed and edited the manuscript. All authors agreed to be accountable for the content of the work.

FUNDING

This study was supported by the National Key R&D Program of China (No. 2016YFB0901100) and the Science and Technology Program of State Grid Zhejiang Electric Power Co., Ltd. (No. B31200200006).

REFERENCES

Bagchi, A., Goel, L., and Wang, P. (2019). Adequacy assessment of generating systems incorporating storage integrated virtual power plants. *IEEE Trans. Smart Grid* 10, 3440–3451. doi: 10.1109/TSG.2018.2827107

Baringo, L., and Conejo, A. J. (2016). Offering strategy of wind-power producer: a multi-stage risk-constrained approach. *IEEE Trans. Power Syst.* 31, 1420–1429. doi: 10.1109/TPWRS.2015.2411332

Bompard, E., Carpaneto, E., Ciwei, G., Napoli, R., Benini, M., Gallanti, M., et al. (2008). A game theory simulator for assessing the performances of competitive electricity markets. *Electric Power Syst. Res*. 78, 217–227. doi: 10.1016/j.epsr.2007.02.007

Chen, J., Yang, L., Zhang, N., Dai, T., and Gan, D. (2009). Decomposition of contract for difference based on generation companies declaration. *Autom. Electric Power Syst.* 33, 30–34. doi: 10.7500/AEPS200807079

De, G., Tan, Z., Li, M., Huang, L., and Song, X. (2018). Two-Stage stochastic optimization for the strategic bidding of a generation company considering wind power uncertainty.*Energies* 11:3527. doi: 10.3390/en11123527

Faraji, J., Abazari, A., Babaei, M., Muyeen, S. M., and Benbouzid, M. (2020). Day-ahead optimization of prosumer considering battery depreciation and weather prediction for renewable energy sources. *Appl. Sci.* 10:2774. doi: 10.3390/app10082774

Fekete, K., Nikolovski, S., Klaić, Z., and Androjić, A. (2019). Optimal re-dispatching of cascaded hydropower plants using quadratic programming and chance-constrained programming. *Energies* 12:1604. doi: 10.3390/en12091604

Fereidoon, P. (2017). *Evolution of Global Electricity Markets: New Paradigms, New Challenges, New Approaches*. Beijing: China Machine Press.

Guo, H., Chen, Q., Xia, Q., and Kang, C. (2019). Market power mitigation clearing mechanism based on constrained bidding capacities. *IEEE Trans. Power Syst.* 34, 4817–4827. doi: 10.1109/TPWRS.2019.2913334

Guo, L., Ding, Y., Bao, M., and Zeng, D. (2021). A bi-level model for the bidding strategy of an inter-regional electricity trading aggregator considering reliability requirements and transmission losses. *IEEE Access* 9, 13476–13487. doi: 10.1109/ACCESS.2021.3051654

Hajiabadi, M. E., and Samadi, M. (2019). Locational marginal price share: a new structural market power index. *J. Mod. Power Syst. Clean Energy* 7, 1709–1720. doi: 10.1007/s40565-019-0532-7

Hakam, D. F., Wiyono, S. K., and Hariyanto, N. (2020). Competition in power generation: ex-ante analysis of indonesia's electricity market. *Energies* 13:6741. doi: 10.3390/en13246741

Hu, S., Xiang, Y., Li, J., and Liu, J. (2021). A two-stage dispatching method for a wind-hydropower-pumped storage integrated energy system. *Front. Energy Res*. 9:646975. doi: 10.3389/fenrg.2021.646975

Huang, H., and Li, F. (2015). Bidding strategy for wind generation considering conventional generation and transmission constraints. *J. Mod. Power Syst. Clean Energy*. 3, 51–62. doi: 10.1007/s40565-015-0100-8

Ilak, P., Krajcar, S., Rajšl, I., and Delimar, M. (2014). Pricing energy and ancillary services in a day-ahead market for a price taker hydro generating company using a risk-constrained approach. *Energies* 7, 2317–2342. doi: 10.3390/en7042317

Jiang, D., Liu, X., and Li, Q. (2004). Economically distributing strategies for daily generation scheduling in a power system under power market environment. *Proc. CSEE* 24, 90–94. doi: 10.13334/j.0258-8013.pcsee.2004.07.017

Jiang, Y., Hou, J., Lin, Z., Wen, F., Li, J., He, C., et al. (2019). Optimal bidding strategy for a power producer under monthly pre-listing balancing mechanism in actual sequential energy dual-market in China. *IEEE Access* 7, 70986–70998. doi: 10.1109/ACCESS.2019.2919347

Khaloie, H., Abdollahi, A., Shafie-Khah, M., Siano, P., Nojavan, S., Anvari-Moghaddam, A., et al. (2020). Co-optimized bidding strategy of an integrated wind-thermal-photovoltaic system in deregulated electricity market under uncertainties. *J. Clean. Prod.* 242:118434. doi: 10.1016/j.jclepro.2019.118434

Lei, G., and Song, X. (2016). "Provincial electricity market orderly operating evaluation model adapting to the new round of electricity reform requirements," in *Conference Papers. China International Conference on Electricity Distribution* (Xian: IEEE).

Li, P., Fan, Y., Huang, Y., Sun, Y., Wang, W., and Liu, C. (2020). Monthly generation scheduling method of renewable energy power system based on power plant aggregation and decomposition models. *Power Syst. Technol*. 44, 3281–3293. doi: 10.13335/j.1000-3673.pst.2020.0509

Liu, W., Zhang, X., Wu, Y., and Feng, S. (2020). Economic analysis of renewable energy in the electricity marketization framework: a case study in Guangdong, China. *Front. Energy Res*. 8:98. doi: 10.3389/fenrg.2020.00098

Min, W., and Li, X. (2016). "An efficient pricing mechanism of the inter-area electricity market based on the special transforming period in China," in *Conference Papers. China International Conference on Electricity Distribution* (Xian: IEEE).

National Development and Reform Commission National Energy Administration (2017). *Notice on Orderly Releasing Plans of Power Generation and Power Utilization*. Available online at: https://www.ndrc.gov.cn/fzggw/jgsj/yxj/sjdt/201704/t20170410_986939.html (accessed February 26, 2021).

Nieta, A. A. S., Contreras, J., Munoz, J. I., and O'Malley, M. (2014). Modeling the impact of a wind power producer as a price maker. *IEEE Trans. Power Syst.* 29, 2723–2732. doi: 10.1109/TPWRS.2014.2313960

Schneider, I., and Roozbehani, M. (2016). Energy market design for renewable resources: imbalance settlements and efficiency–robustness tradeoffs. *IEEE Trans. Power Syst.* 33, 3757–3767. doi: 10.1109/TPWRS.2017.2782638

Shafie-khah, M., Heydarian-Forushani, E., Golshan, M. E. H., Moghaddam, M. P., Sheikh-El-Eslami, M. K., and Catalao, J. P. S. (2015). Strategic offering for a price maker wind power producer in oligopoly markets considering demand response exchange. *IEEE Trans. Ind. Inform.* 11, 1542–1553. doi: 10.1109/TII.2015.2472339

Song, X., Lin, C., Zhang, R., Jiang, T., and Chen, H. (2020). Two-stage stochastic scheduling of integrated electricity and natural gas systems considering ramping costs with power-to-gas storage and wind power. *Front. Energy Res*. 8:596774. doi: 10.3389/fenrg.2020.596774

State Electricity Regulatory Commission (2012). *Basic Rules for Inter Provincial and Inter Regional Electric Energy Trading (Trial)*. Policy. Available online at: http://www.law-lib.com/law/law_view.asp?id=404865 (accessed February 26, 2021).

Sun, L., Zhang, N., Li, N., Liu, X., and Li, W. (2020). An intra-day rolling scheduling considering energy equity based on gini coefficient. *Power Syst. Technol*. 44, 340–347. doi: 10.13335/j.1000-3673.pst.2019.1459

Tong, X., Hu, C., Zheng, C., Rui, T., Wang, B., and Shen, W. (2019). Energy market management for distribution network with a multi-microgrid system: a dynamic game approach. *Appl. Sci.* 9:5436. doi: 10.3390/app9245436

Wang, Y., Ai, X., Tan, Z., Yan, L., and Liu, S. (2016). Interactive dispatch modes and bidding strategy of multiple virtual power plants based on demand response and game theory. *IEEE Trans. Smart Grid.* 7, 510–519. doi: 10.1109/TSG.2015.2409121

Xie, B., Yang, X., Yu, Z., Luo, G., and Guo, R. (2018). Two-stage optimization model for annual rolling generation scheduling considering open and impartial dispatching. *Electr. Power Autom. Equip*. 38, 155–161. doi: 10.16081/j.issn.1006-6047.2018.12.023

Xing, Q., Cheng, M., Liu, S., Xiang, Q., Xie, H., and Chen, T. (2021). Multi-objective optimization and dispatch of distributed energy resources for renewable power utilization considering market mechanism. *Front. Energy Res.* 9:647199. doi: 10.3389/fenrg.2021.647199

Yang, J., Tan, Z., Pu, D., Pu, L., Tan, C., and Guo, H. (2019). Robust optimization model for energy purchase and sale of electric–gas interconnection system in multi-energy market. *Appl. Sci.* 9:5497. doi: 10.3390/app9245497

Zhang, C., and Yan, W. (2019). Spot market mechanism design for the electricity market in china considering the impact of a contract market. *Energies* 12:1064. doi: 10.3390/en12061064

Zhang, Q., Sun, L., Shen, J., Li, P., and Li, W. (2020). Four-stage modeling of monthty energy trading schedule considering fairness of power scheduling progress. *Autom. Electr. Power Syst.* 44, 101–110. doi: 10.7500/AEPS20191219006

Zhang, Z., Jiang, Y., Lin, Z., Wen, F., Ding, Y., Yang, L., et al. (2020). Optimal alliance strategies among retailers under energy deviation settlement mechanism in China's forward electricity market. *IEEE Trans. Power Syst.* 35, 2059–2071. doi: 10.1109/TPWRS.2019.2955479

Conflict of Interest: JC, CH, HW, and YoL were employed by State Grid Anhui Electric Power Co., Ltd. and Anhui Power Exchange Center Company. HC was employed by State Grid Anhui Electric Power Co.

The remaining authors declare that the research was conducted in the absence of any commercial or financial relationships that could be construed as a potential conflict of interest.

frontiers in Energy Research

ORIGINAL RESEARCH
published: 18 May 2021
doi: 10.3389/fenrg.2021.686890

Comprehensive Benefit/Cost Analysis of Utilizing PEV Parking Lots as Virtual Energy Storage for the Energy Supply Sustainability of Future Distribution Systems

Bo Zeng[1], Bo Sun[1], Hongwei Mu[1], Yuqing Wang[2], Xuan Wei[3] and Libin Wang[4]*

[1] State Key Laboratory of Alternate Electrical Power System with Renewable Energy Sources, North China Electric Power University, Beijing, China, [2] School of Economics and Management, North China Electric Power University, Baoding, China, [3] Tsinghua-Berkeley Shenzhen Institute, Tsinghua University, Shenzhen, China, [4] Economic and Electrical Research Institute, Shanxi Electrical Power Company of SGCC, Taiyuan, China

OPEN ACCESS

Edited by:
Tao Huang,
Politecnico di Torino, Italy

Reviewed by:
Fei Xue,
Xi'an Jiaotong-Liverpool University, China
Ouyang Shaojie,
China Southern Power Grid, China

***Correspondence:**
Bo Sun
sunboncepu@163.com

Specialty section:
This article was submitted to Smart Grids, a section of the journal Frontiers in Energy Research

Received: *28 March 2021*
Accepted: *19 April 2021*
Published: *18 May 2021*

Citation:
Zeng B, Sun B, Mu H, Wang Y, Wei X and Wang L (2021) Comprehensive Benefit/Cost Analysis of Utilizing PEV Parking Lots as Virtual Energy Storage for the Energy Supply Sustainability of Future Distribution Systems. Front. Energy Res. 9:686890. doi: 10.3389/fenrg.2021.686890

The proliferation of plug-in electric vehicles has led to increased public charging infrastructure in cities worldwide. Grid-connected parking lot spaces are the most common charging option due to their technological readiness and convenience of adoption. Since the batteries aggregated by parking lots can be regarded as virtual energy storage, grid-connected parking lots are expected to provide many benefits to the urban distribution grid. This paper proposes a comprehensive methodological framework to evaluate the potential benefits and costs of utilizing grid-connected parking lot infrastructures to promote energy supply sustainability in future power distribution grids. Capacity-value-based and cost-effectiveness indexes are developed, which quantify the potential contribution of parking lots to power supply reliability and the associated economic implications. To realistically describe the available generation capacity of parking lot resources, a comprehensive model is presented, which explicitly considers the impact of external stimuli (incentive rates) on the behavioral patterns of lot users. Vehicle user responsiveness to incentive grades is derived from social field surveys. To conduct the evaluation, a hybrid algorithm based on Monte Carlo simulations is employed. The proposed methodology is illustrated on a real distribution grid in Beijing. The results confirm the effectiveness of our proposed approach and support practical policy suggestions.

Keywords: grid-connected parking lot, distribution system, sustainability, economy, plug-in electric vehicle, virtual energy storage

INTRODUCTION

Worsening environmental problems are increasingly promoting the transformation of the global energy system. Transportation in the current system accounts for a large proportion of the energy consumption sector, so transportation plays a vital role in achieving the sustainable development of the energy system. The electrification of transportation needs can effectively solve the problem

of dependence on fossil fuels and exhaust emissions. Given this, in the past ten years, the electric vehicle industry has achieved remarkable development worldwide (Du et al., 2019).

In future smart cities, the information and intelligence of the power supply system are necessary requirements, and the sustainability of the energy supply is also an essential aspect. Therefore, an urban power supply system is needed to provide users with reliable and stable power services (Xu and Chung, 2016). At present, newly added power generation units ensure that the sustainable power supply target is reached. These redundant power generating units can provide end-users with the required backup power in an emergency (Silva et al., 2018). However, a redundant power generation unit added to a system requires additional investment and remains in a hot standby state for a long time after installation. The overall utilization rate is shallow, so plug-in electric vehicles (PEVs) are expected to play an important role. Since most family cars are parked more than 95% of each day (Heydarian-Forushani et al., 2016), a grid-connected parking lot (GPL) can act as a controllable load during charging or as a virtual energy storage unit during discharging. In future smart cities, different types of GPLs could be used to meet the energy needs of PEVs (Moradijoz et al., 2020). Intelligent charging piles will play a vital role as connection devices between electric vehicles and the grid. GPLs can obtain the battery status of electric vehicles in real time through intelligent charging piles. Using electric vehicle batteries to absorb new energy is a promising research direction for smart grids (Farzin and Monadi, 2019). There have been some studies on the impact of vehicle-to-grid (V2G) systems on the power grid by electric vehicles as a movable load or energy storage unit. Utilizing the energy stored in the batteries of electric cars increases the ability of the power system to resist natural disasters by participating in V2G systems and improving the resilience of the power system (Momen et al., 2020). When a power supply or feeder fails, the GPL is used as the power supply of the distribution network, which can increase the reliability of the distribution network and reduce the failure time of the distribution network (Guner and Ozdemir, 2020). Participation in V2G systems can shift the charging demand of PEVs from peak hours to off-peak hours, which can significantly increase the economic and environmental benefits of power systems (Onishi et al., 2020). In distribution system planning, an investment in system expansion can be deferred by exploiting the storage capacity of the GPL (Al-Rubaye et al., 2019). By controlling the active power injected or released by the GPL to achieve stable voltage fluctuation, the reliability and stability of the power grid can be improved (Singh et al., 2018).

However, the aforementioned research does not address the impact of GPLs on the overall sustainability of smart cities. To fill this gap, some scholars have studied this issue. Sequential Monte Carlo simulation technology is used to determine the sufficiency of the power supply when participating in V2G through GPLs under different urban power system (UPS) operation modes in Xu and Chung (2016). When considering GPL participation in auxiliary services, random methods are used to determine the impact of GPLs on UPS reliability (Mohammadi-Hosseininejad et al., 2018). A GPL is used as a backup unit to restore power to a faulty area or as a storage unit to address downstream blockages of feeders, thereby helping to restore power. There is also a framework based on nonsequential Monte Carlo simulations that can assess the sustainability of GPLs and consider the role of renewable energy (Farzin et al., 2017). This work fully captures the volatility related to electric vehicles and renewable energy and probabilistically simulates the V2G capability of providing grid-to-vehicle (G2V) resources during an emergency for research purposes. The use of PEVs can increase the flexibility of a power system, and this effect is related to the popularity of PEVs (Bozic and Pantos, 2015). There is also an article that considers the total charging load of electric vehicles in a GPL and the travel mode of electric vehicles and combines the charging load and system load of electric vehicles to evaluate the reliability of the system (Irshad et al., 2020). Some researchers have also considered the uncertainty of incentive policies regarding the charging behavior of private car owners and their impact on public transportation plans (Zeng et al., 2021a). Additionally, considering the charging decisions of PEV users at the bottom layer of the two-tier model can effectively capture the uncertainty and self-interested behavior of electric vehicle owners (Zeng et al., 2020a). The results show that considering uncertainty in electric vehicles could have a significant impact on the results of the final evaluation. Similarly, a cost/value evaluation framework is proposed in Neyestani et al. (2015), and other improvements are made in Shaukat et al. (2018).

The above researches show that GPL is an emerging element of future smart cities and a new choice to enhance the sustainable operation of future urban power grids. However, none of them consider the potential economic value of GPLs. From a system perspective, due to the use of a two-way charger, a GPL can be regarded as a virtual energy storage unit, which can provide capacity support for the grid by extracting energy from PEV batteries in an emergency. Therefore, the GPL responds to potential emergencies (such as generator failures and fluctuations in load demand) by improving the operating level (generation capacity) of the power system and provides important assistance for the sustainability of energy services. Compared with traditional expansion-based solutions, this solution does not require additional asset investment, reduces the risk of load loss, and has the opportunity to achieve better urban energy system sustainability performance (in economic and environmental terms).

However, the above-mentioned works provide an incomplete assessment of the impact of GPLs in future smart city power supply systems and do not involve the economic impact of GPLs on the power grid. The economy is the most intuitive manifestation of the impact of GPLs on the power grid. Therefore, this paper proposes a new evaluation framework based on capacity value, which uses GPLs as virtual energy storage to evaluate the sustainable power supply capability of GPLs for future smart cities. The capacity value is used to evaluate the ability of a specific power generation resource to contribute sufficient power (Keane et al., 2011). However, in this research, we extend the concept of capability value to the context of GPLs. The goal is to quantify the potential benefits of GPLs in increasing the reliability and sustainability of power supplies and then to quantify the economic value that GPLs can provide in

virtual energy storage. To achieve this goal, this article develops a new model to characterize a GPL's available generation capacity and considers the role of critical parameters in the operation process. Unlike existing works, in our research, we propose a framework in which a GPL is regarded as a virtual energy storage unit to evaluate the capacity power and the economy of the energy storage device.

The main contributions and innovations of this paper are as follows:

(1) A comprehensive methodological framework is proposed to quantify the potential costs and benefits of utilizing GPLs as virtual energy storage to improve the sustainability of urban distribution systems.
(2) This study creatively associates capacity value indicators with economic indicators, which has reference significance for the planning of GPLs in future smart city contexts.
(3) This study puts forward corresponding policy recommendations based on the results of case studies of GPLs.

The rest of this paper is organized as follows: first, the capacity value metrics defined for GPLs is introduced in Section "Capacity Value Metrics," and then the method for estimating the available GPL generation capacity is presented in Section "Modeling of GPLs." Section "Economic Analysis" presents the economic analysis model of GPLs. Section "Evaluation Algorithm" provides the algorithm framework used to perform the capacity value calculation. Section "Case Study" presents case studies and a discussion about the evaluation results. Finally, the conclusions of this study are drawn in Section "Conclusion."

CAPACITY VALUE METRICS

The capacity value is initially used to quantify the capacity of generator sets (Keane et al., 2011). This article regards a GPL as a virtual energy storage unit similar to a power generation resource. This is because PEVs use power batteries as the source and can participate in V2G through charging piles, which can be regarded as virtual energy storage units, and when the power grid needs them, the energy in PEV batteries can be injected back to the power grid. Therefore, the concept of capacity value can be reasonably extended to the evaluation of GPLs.

In fact, in existing research, there are two commonly used evaluation indicators, the equivalent firm capacity and the equivalent conventional capacity (ECC). These two indicators can operate well in a wide range of applications (Keane et al., 2011; Dent et al., 2015; Ding and Xu, 2017; Zeng et al., 2020a,b). To keep the description uniform, in this article, the same method is used to present the capacity value. A detailed introduction is given below.

In this study, the definition of the equivalent firm capacity is the generator capacity that can be replaced by GPL resources, where the forced outage rate (FOR) of the generator is 0, which means that the generator is completely reliable. First, let the GPL participate in V2G and calculate the UPS (with V2G) reliability index E_1 in this state, which represents the UPS reliability of the GPL participating in V2G; then calculate the UPS (without V2G) reliability index E_2 of the GPL not participating in V2G. By comparing the reliability index, it can be judged whether GPL has the ability to increase UPS reliability when participating in V2G. If V2G can improve the reliability of UPS, calculate the reliability of this system by gradually adding the new generator capacity of the UPS (without V2G) until it is the same as the reliability index of the UPS (with V2G) system. Then, the generator capacity value that can be replaced by GPL can be determined by the increased capacity value.

The concept of the ECC metric is defined according to the principles of the equivalent firm capacity metric. However, a "real" conventional generator, which is different from the equivalent firm capacity, is adopted by the ECC, and the specific reliability characteristics for capacity value estimation are possessed by the ECC.

From the above, the mathematical expression of the ECC is as follows:

$$E_1^{\mathrm{ECC}} = \Re\left[(C^{\mathrm{T}} + C^{\mathrm{PL}}); \mathbf{D}\right] \tag{2.1}$$

Where E_1^{ECC} is the UPS reliability index concerning the GPL's V2G. In this paper, the well-known expected energy not supplied (EENS) (Zeng et al., 2020a,b) is adopted and FOR is non-zero. Then calculate the reliability index E_2^{ECC} of the UPS with GPL not participating in V2G, the formula is as follows:

$$E_2^{\mathrm{ECC}} = \Re\left[(C^{\mathrm{T}} + C^{\mathrm{E}}); \mathbf{D}\right] \tag{2.2}$$

where C^{E} indicates the installed capacity of the generator unit. To estimate the ECC, C^{E} can be adjusted so that the EENS of the system will reach the same level as that of the system which GPL participating in V2G, $E_1^{\mathrm{ECC}} = E_2^{\mathrm{ECC}}$. Finally, the result for C^{E} tends to stabilize; the value of C^{E} is considered the ECC of the GPL here.

MODELING OF GPLS

The distribution network studied in this paper includes transformers, transmission lines, renewable energy units, loads, and GPLs. For renewable energy power generation (such as wind or solar energy), the power output depends on weather conditions, so these generator sets cannot guarantee stable output power. In reliability studies, the impact of uncertainties in the renewable energy supply can be represented by using a proper probability distribution function (PDF). The impact of these uncertainties can be appropriately considered and reflected in our developed evaluation framework by using the Monte Carlo simulation method, which is presented in detail in Section "Evaluation Algorithm." Regarding transformers, this paper uses a Monte Carlo model to represent the normal/fault state of the transformer in actual operation. It is also assumed that the available power from the grid considering the installed capacity of the distribution transformer obeys a uniform distribution, which is consistent with Zeng et al. (2020a). Additionally, it is assumed that the charging pile of the GPL is equipped with a bilateral charger and the GPL operator can automatically and

remotely obtain all the necessary information of the PEV user (Yilmaz and Krein, 2013). Furthermore, it has been assumed that the GPL is owned and operated by a private entity, which is independent of the power grid. The GPL owner has independent economic revenues and makes profits from both providing recharging service to PEV users and providing flexibility (capacity support) to the grid.

To express the operating characteristics of the GPL, this paper proposes a comprehensive modeling framework, as described below.

Modeling of Bilateral Chargers

The available capacity of a GPL depends on the hardware of its charging equipment. During operation, if there is no mechanical failure, a single bilateral charger can provide any required output power within its rated discharge capacity; otherwise, its output power is 0.

Therefore, considering the faulty operation status of the bilateral charger and the number of installations in the GPL, the maximum power output that the PEV GPL can provide in period t can be expressed as:

$$P_t^{\mathrm{M}} = \sum_{k \in \Omega_{CP}} \left(\beta_{k,t}^{\mathrm{C}} \times P_k^{\mathrm{DC}}\right) \tag{3.1}$$

where P_k^{DC}, Ω_{CP} and P_k^{DC} are the maximum rated power of the GPL at time t, the collection of all bilateral chargers of the GPL, and the rated discharge rate of the bilateral charger. Additionally, $\beta_{k,t}^{\mathrm{C}}$ is a 0/1 variable that represents the availability of the k-th bilateral charger at time t. During operation, if the charger is working under the normal state, the value of β would be assigned to unity; otherwise, it would be set to zero. In practice, since "whether the charging pile is working in the normal or failure state" is a random event, hence the value of β is an uncertain variable. In the evaluation, the value of β is determined by using a sampling simulation procedure presented in Section "Evaluation Algorithm."

Modeling of PEV Behaviors

In this study, we characterize the behaviors of PEV users through three characteristics, as shown in **Figure 1**, namely, traffic uptake, energy demand, and customer willingness. The traffic uptake includes the arrival time and departure time. The energy demand includes the initial Soc and target Soc. The customer willingness refers to the incentive rate. These three parts are mutually independent and can be superimposed, and together they define the characteristics of PEV behaviors.

To model the uncertainties of PEV behavior, truncated Gaussian distributions are widely employed for arrival and departure times and the arrival Soc (Shafie-Khah et al., 2015). This paper uses a Gaussian distribution to simulate the arrival departure times of electric vehicles and the Soc of arrival (Shafie-Khah et al., 2015). The relevant data are in **Table 1**.

TABLE 1 | Data of electric vehicles.

	Mean	Standard deviation	Min	max
Initial PEV Soc (%)	50	25	30	90
Arrival time (h)	8	3	5	17
Departure time (h)	16	3	11	24

Initial Soc

The initial Soc of the PEVs when individuals arrive at the GPLs can be described by the following PDF (Shafie-Khah et al., 2015):

$$f\left(Soc_n^{\mathrm{Ini}}\right) = \begin{cases} 0 & Soc_n^{\mathrm{Ini}} < Soc^{\mathrm{PEV\,min}} \\ \frac{1}{\sqrt{2\pi}\sigma^{\mathrm{Soc}}} \exp\left[-\frac{\left(Soc_n^{\mathrm{Ini}}-\mu^{\mathrm{Soc}}\right)^2}{2\left(\sigma^{\mathrm{Soc}}\right)^2}\right] & Soc^{\mathrm{PEV\,min}} \le Soc_n^{\mathrm{Ini}} \le Soc^{\mathrm{PEV\,max}} \\ 0 & Soc_n^{\mathrm{Ini}} > Soc^{\mathrm{PEV\,max}} \end{cases} \tag{3.2}$$

where Soc_n^{Ini}, μ^{Soc} and σ^{Soc}, $Soc^{\mathrm{PEV,min}}$ and $Soc^{\mathrm{PEV,max}}$ are the battery power (%) when the n-th electric vehicle reaches the GPL, the mean and variance of the random variables of the initial Soc of the PEV, and the lower and upper limit of the value area, respectively.

Arrival Time

The time needed for the PEV users to reach the GPL can be represented by the following PDF (Shafie-Khah et al., 2015):

$$f\left(t_n^{\mathrm{Ar}}\right) = \begin{cases} 0 & t_n^{\mathrm{Ar}} < t^{\mathrm{Ar,min}} \\ \frac{1}{\sqrt{2\pi}\sigma^{\mathrm{Ar}}} \exp\left[-\frac{\left(t_n^{\mathrm{Ar}}-\mu^{\mathrm{Ar}}\right)^2}{2\left(\sigma^{\mathrm{Ar}}\right)^2}\right] & t^{\mathrm{Ar,min}} \le t_n^{\mathrm{Ar}} \le t^{\mathrm{Ar,max}} \\ 0 & t_i^{\mathrm{Ar}} > t^{\mathrm{Ar,max}} \end{cases} \tag{3.3}$$

where t_n^{Ar}, μ^{Ar}, σ^{Ar}, $t^{\mathrm{Ar,min}}$ and $t^{\mathrm{Ar,max}}$ are the arrival time of the n-th PEV, the mean and variance of the random variables of the initial arrival time of the PEVs, and the lower and upper limits of the area of t_n^{Ar}.

Departure Time

The time when a PEV user leaves the GPL can be represented by the following PDF (Shafie-Khah et al., 2015):

$$f\left(t_n^{\mathrm{De}}\right) = \begin{cases} 0 & t_n^{\mathrm{De}} < \mathrm{Max}\left\{t^{\mathrm{De,min}}, t^{\mathrm{Ar,min}}\right\} \\ \frac{1}{\sqrt{2\pi}\sigma^{\mathrm{De}}} \exp\left[-\frac{\left(t_n^{\mathrm{De}}-\mu^{\mathrm{De}}\right)^2}{2\left(\sigma^{\mathrm{De}}\right)^2}\right] & \mathrm{Max}\left\{t^{De,\mathrm{min}}, t^{\mathrm{Ar}}\right\} \le t_n^{\mathrm{De}} \le t^{De,\mathrm{max}} \\ 0 & t_n^{\mathrm{De}} > t^{De,\mathrm{max}} \end{cases} \tag{3.4}$$

where t_n^{De}, μ^{De}, σ^{De}, $t^{\mathrm{De,min}}$, $t^{\mathrm{De,max}}$ and $\mathrm{Max}\left\{t^{\mathrm{De,min}}, t^{\mathrm{Ar}}\right\}$ are the time when the first PEV leaves, the mean and variance of the random variables of the initial arrival time of the PEVs, the lower and upper limits of the range of t_n^{De}, and the maximum of the time at which the PEV arrives at the GPL and the time it leaves.

Participation Rate of PEV Users

Plug-in electric vehicle users have two ways to provide backup for the power grid: load reduction and V2G. The willingness of a PEV user will directly affect the user's participation, and the user's decision to participate in V2G is related to the GPL's

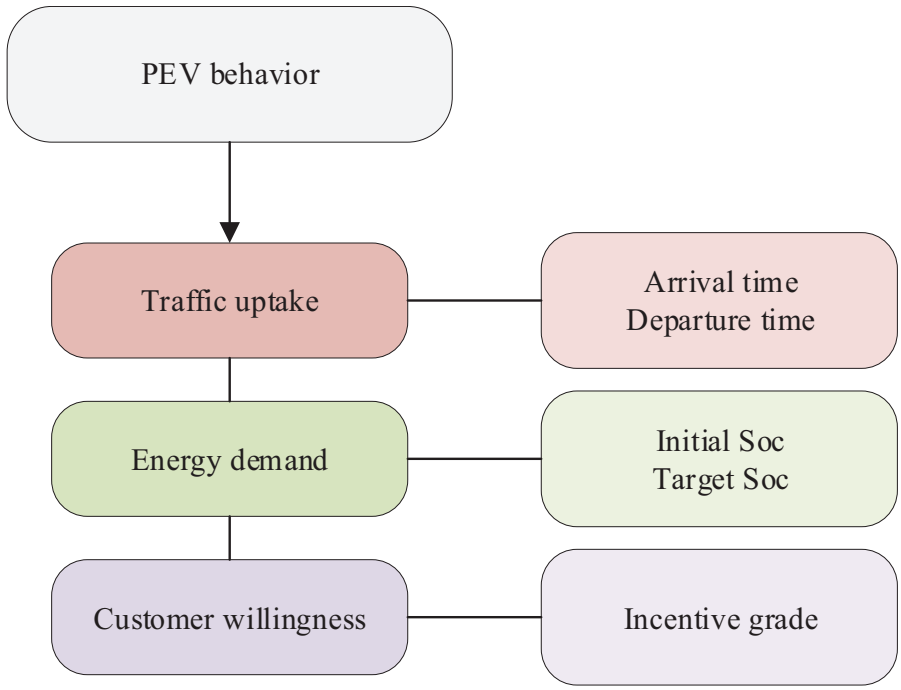

FIGURE 1 | Illustration of PEV behavior model.

incentive grade. We can simply assume that the GPL charges a certain service fee. When the incentive grade is higher, users will have a greater willingness to participate in V2G. According to the elastic relationship between electric vehicle user participation and price compensation, the participation of electric vehicle users in the V2G market in a single electricity sales scenario is a concave function of the power company's compensation price. Finally, as the compensation increases, the user participation rate gradually approaches.

In this study, due to the lack of statistical data on PEV customer preferences, we conducted a field survey. We sent 300 questionnaires to selected Beijing PEV owners to investigate the users' willingness to participate in load shedding and V2G under different incentive levels. Taking a single price for the electricity sold by the grid as an example, the compensation prices are ¥1.0, 1.25, 1.5, 1.75, and 2.0 per kWh. We further processed the questionnaire to determine its accuracy. The 150 questionnaires were first analyzed, and then the sample size was gradually increased in intervals of 25; then, the error between the participation degrees after 25 questionnaires and the previous statistical results was determined. The difference between the last a pair of result for questionnaire data is less than 1%, so it is concluded that these statistics are credible. The statistical error results of the data are shown in **Table 2**:

Figure 2 shows the relationship between user participation willingness and the compensation price, including load reduction willingness and V2G willingness. The abscissa in the figure represents the unit electricity compensation price when the grid purchases electricity from users. As seen from the figure, as the compensation continues to increase, user participation continues to increase. Considering that battery discharge has a great impact on users, V2G needs a high price incentive.

TABLE 2 | Statistical error of the questionnaire.

Number of questionnaires	150	175	200	225	250	275	300
Statistical error	–	5.102	4.332	3.421	2.287	1.629	0.993

In actual situations, different incentive grades produce different degrees of participation, so this article will analyze and compare different situations below.

Calculation of a GPL's Capacity for V2G Participation

According to the above model, at time t, the available capacity of the GPL is expressed as follows:

$$P_t^{\mathrm{AG}} = \sum_{n \in \Omega_{\mathrm{EV}}} P^{\mathrm{DC}} \gamma_{n,t}^{\mathrm{V2G}} \tag{3.5}$$

where P_t^{AG} is the total available capacity of the GPL and $\gamma_{n,t}^{\mathrm{V2G}}$ is a 0/1 variable indicating whether the n-th electric vehicle participates in V2G during period t. If it does, $\gamma_{n,t}^{\mathrm{V2G}}$ 1; otherwise, $\gamma_{n,t}^{\mathrm{V2G}}$ 0. Eqs. (3.5) shows that the available capacity of the GPL is the total capacity of the PEVs participating in the V2G project.

In practice, the value of $\gamma_{n,t}^{\mathrm{V2G}}$ depends on the Soc of the PEV battery (Soc > 90%), the participation of PEV users, and the operating strategy of the GPL operator. Therefore, it can be

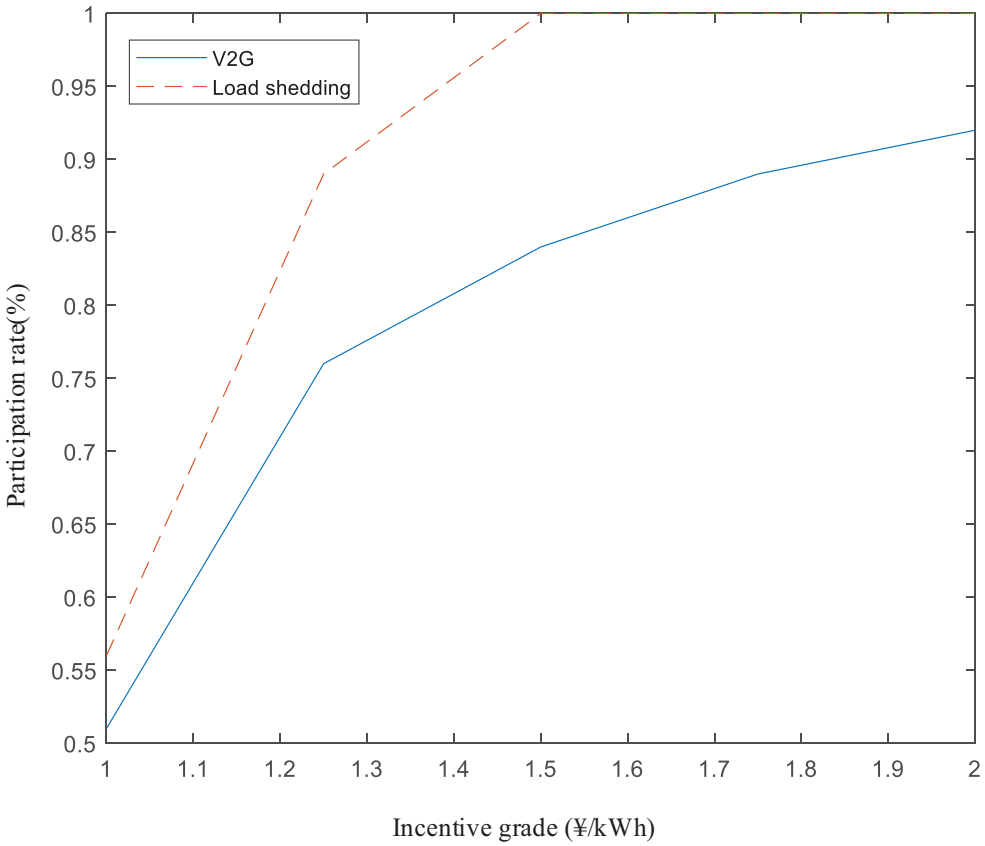

FIGURE 2 | Participation rates vs. incentive rates.

written in a decomposed form as follows:

$$\gamma_{n,t}^{\mathrm{V2G}} = \gamma_{n,t}^{\mathrm{C}} \times \gamma_{n,t}^{\mathrm{OP}} \tag{3.6}$$

where $\gamma_{n,t}^{\mathrm{C}}$ and $\gamma_{n,t}^{\mathrm{OP}}$ are 0/1 variables that indicate whether the PEV participates in the V2G project and whether the GPL operator implements the V2G project, respectively. The method used to determine $\gamma_{n,t}^{\mathrm{C}}$ and $\gamma_{n,t}^{\mathrm{OP}}$ is introduced below.

According to Eq. (3.5), for PEV users, vehicle participation in V2G has the following two prerequisites: (1) The PEV is in the GPL and the Soc of the PEV battery > 90%; (2) The individual agrees to participate in the V2G project. Therefore, the calculation of $\gamma_{n,t}^{\mathrm{C}}$ in Eqs. (3.6) is as follows: through Monte Carlo simulation of the willing behavior of a PEV user under the determined participation degree, the generated user's willingness is α_n^{E}.

$$\gamma_{n,t}^{\mathrm{C}} = \alpha_{n,t}^{\mathrm{P}} \times \alpha_n^{\mathrm{E}} \tag{3.7}$$

In this study, the Monte Carlo simulation method is used to simulate the willing behavior of a PEV user under the determined participation degree. The generated user willingness is in terms of $\alpha_{n,t}^{\mathrm{P}}$ and α_n^{E}, which are all 0/1 variables that indicate whether the Soc of the n-th PEV battery is > 90% and whether the PEV user is willing to participate in V2G, respectively. In addition, $\alpha_{n,t}^{\mathrm{P}}$ is obtained by the following formula:

$$\alpha_{n,t}^{\mathrm{P}} = \begin{cases} 1\ , & t_n^{\mathrm{Ar}} + t_n^{\mathrm{Ch}} \le t \le t_n^{\mathrm{De}} \\ 0\ , & otherwise \end{cases} \tag{3.8}$$

$$t_n^{\mathrm{Ch}} = (Soc^{\mathrm{Tar}} - Soc^{\mathrm{Ini}})E^{\mathrm{EV}} / \left(P^{\mathrm{C}}\eta^{\mathrm{BC}}\right) \tag{3.9}$$

where $t_n^{\mathrm{Ar}}$and t_n^{De} are the sample values obtained from Eqs. (3.3) and (3.4), respectively, and t_n^{Ch} is the time needed to charge the kth car to the target Soc.

On the other hand, the available capacity of the GPL also depends on the operator's operating plan, which is represented by the variable $\gamma_{n,t}^{\mathrm{OP}}$ in Eq. (3.10). It is judged whether the GPL needs to participate in V2G at time t, and the judgment standard is the electricity price signal given by the grid. In the regular operation of the power grid, the GPL exists as a load unit to charge the electric vehicle to the target state (Soc = 90%). When the grid fails, the GPL will be given a higher electricity price in order to attract the GPL to participate in the V2G. The GPL is used as an energy storage device to support grid electricity. Therefore, while improving the reliability of the power grid, the investment cost and the operation and maintenance cost of the power grid for energy storage equipment are avoided due to the role of the GPL as virtual energy storage, thereby increasing the economy of the power grid.

Based on the operating strategy of the GPL operator, $\gamma_{n,t}^{\mathrm{OP}}$ in Eq. (3.6) can be expressed as:

$$\gamma_{n,t}^{\mathrm{OP}} = \begin{cases} 1 & \omega^{\mathrm{V2G}} > \omega^{\mathrm{Pay}} \\ 0 & \text{otherwise} \end{cases} \tag{3.10}$$

where ω^{V2G} and ω^{Pay} are the electricity price when the GPL participates in V2G and the marginal price of deciding V2G whether the GPL participates. Equation (3.10) shows that from the perspective of the PEV GPL operator, the GPL will participate in V2G only if the price of electricity purchased by the grid from the GPL is larger than ω^{Pay}.

In summary, combining Eqs. (3.5) - (3.10), the total available capacity of the GPL for participating in V2G at each time can be obtained.

ECONOMIC ANALYSIS

Without increasing the installed capacity of power generation, the current urban energy system mainly improves its flexibility and reliability by configuring energy storage equipment. The cost of energy storage equipment is mainly composed of investment and maintenance costs. Compared with energy storage equipment, when a GPL is used as virtual energy storage through participation in V2G, although there are corresponding scheduling costs, there are no investment, operation or maintenance costs. Therefore, theoretically speaking, it is more economical to increase the system reliability through GPL participation in V2G than to build new energy storage equipment. In this section, the investment, operation, and maintenance costs of energy storage equipment minus the cost of calling GPLs to participate in V2G dispatch are used as economic indicators to evaluate the economic benefits of GPLs. Lithium batteries are more suitable than other batteries for installation in urban centers due to their small size and simple operation. Therefore, this article uses lithium batteries as energy storage devices to analyze economic indicators. Since the service life of lithium batteries is 10 years, the cost of the energy storage equipment must be shared every year according to its investment, operation, and maintenance costs (Zaisen, 2018).

Therefore, the total economic function of the power grid is:

$$E^{\mathrm{G}} = S^{\mathrm{P,E}} + S^{\mathrm{m}} - E^{\mathrm{V2G}} \tag{4.1}$$

where $S^{\mathrm{P,E}}$ represents the energy storage investment cost, S^{m} represents the energy storage operating cost, and E^{V2G} represents the cost of the power grid when parking lots participate in V2G.

The energy storage investment cost allocated each year can be expressed as follows:

$$S^{\mathrm{P},E} = \left(C^{\mathrm{P}} \cdot P^{St} + C^{\mathrm{E}} \cdot E^{St}\right)/10 \tag{4.2}$$

where C^{P} is the power cost of the energy storage device, P^{St} is the power of the energy storage device, C^{E} is the capacity cost of the energy storage device, and E^{St} is the capacity of the energy storage device. C^{P} 2000 ¥/kW, and C^{E} 1500 ¥/kWh (Zaisen, 2018).

According to engineering requirements, different battery device types are selected. Due to different production processes and the production of raw materials, there is a large difference in the costs of energy storage device capacity.

The annual operating cost of the energy storage system is mainly determined by the scale of the energy storage system, and it is expressed as follows:

$$S^{\mathrm{m}} = C^{\mathrm{m}} \cdot E^{\mathrm{St}} \tag{4.3}$$

where C^{m} represents the annual operation and maintenance cost per unit capacity. In this study, we assume that C^{m} 0.05 ¥/kWh (Zaisen, 2018).

The cost that the grid needs to pay when parking lots participate in V2G is as follows:

$$E^{\mathrm{V2G}} = \sum_{t=0}^{8760} \lambda_t^{\mathrm{V2G}} P_t^{\mathrm{V2G}} \Delta t \tag{4.4}$$

where λ_t^{V2G} is the incentive reward offered for GPL owners; P_t^{V2G} is the V2G power provided by GPLs in time-period t, and E^{V2G} is the energy in one year during operation for which the grid needs to pay subsidies to the GPL owner.

EVALUATION ALGORITHM

In this section, the algorithm used for evaluating the benefits/costs of utilizing GPLs as virtual energy storage to promote the sustainability of distribution systems is described based on the metrics in Section "Capacity Value Metrics" and the system models described in Section "Modeling of GPLs and Economic Analysis."

By analyzing and comparing the UPS reliability level depending on whether the GPL participates in V2G, the capacity value of the GPL can be estimated. This study uses a comprehensive evaluation algorithm based on the sequential Monte Carlo simulation method. The following presents a detailed description about the main steps of our evaluation algorithm. The flowchart is shown in **Figure 3**.

Step 1: According to the forced outage rate of each element in the distribution system, sample the state duration sequence of the system components by using the Monte Carlo simulation method.

Step 2: Generate the time series of the renewable energy supply according to its PDF with the inverse transform method (Billinton and Allan, 1996), if applicable.

Step 3: According to the status data obtained from the above steps, determine the power output of the generator set and transformer in each time period.

Step 4: Obtain the available capacity of the GPL according to Eqs. (3.5) – (3.10).

Step 5: According to the traditional reliability calculation method (Billinton and Allan, 1996), calculate the reliability index of the smart distribution network when the GPL does not participate in the V2G; the result obtained is used as the benchmark EENS $^{\mathrm{base}}$.

Step 6: According to the following substeps, perform sequential Monte Carlo sampling on the smart distribution

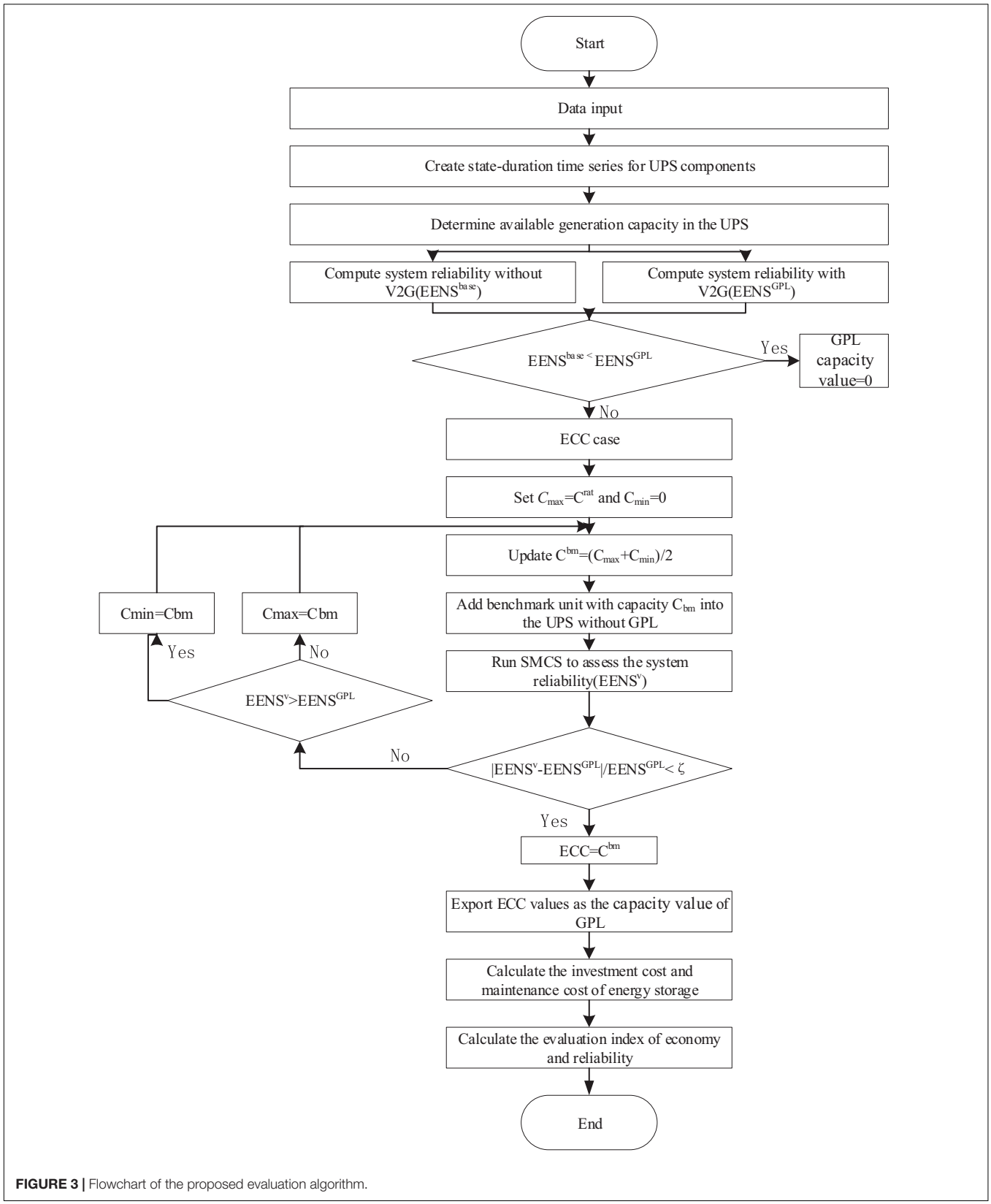

FIGURE 3 | Flowchart of the proposed evaluation algorithm.

network with GPLs participating in V2G to obtain the reliability index of the system:

6-1: According to Eqs. (3.2) - (3.4), randomly extract the behavior patterns of each PEV user from the means of the vector $\{t^{Ar}, Soc^{\mathrm{Ini}}, t^{\mathrm{De}}, \alpha^{\mathrm{E}}_{\mathrm{n}}\}$.

6-2: Determine the total available power generation ($\mathrm{P}^{\mathrm{TG}}_{\mathrm{t}}$) and system load demand ($\mathrm{P}^{\mathrm{TG}}_{\mathrm{t}}$) for each period t based on:

$$P_t^{\mathrm{TG}} = P_t^{\mathrm{DG}} + P_t^{\mathrm{T}} + P_t^{\mathrm{AG}} \tag{5.1}$$

$$P_t^{\mathrm{TD}} = \sum_{i\in\Omega_D} P_{i,t}^{l} + \sum_{n\in\Omega_{EV}} P^{\mathrm{C}}\alpha_{n,t}^{\mathrm{P}}\gamma_{n,t}^{\mathrm{G2V}} \tag{5.2}$$

where $P^{\mathrm{l}}_{i,t}$ represents the regular load demand of the i-th node in period t; $\gamma^{\mathrm{G2V}}_{n,t}$ is a 0/1 variable indicating whether the n-th charging pile is in the charging state during period t. According to the service selection method for the PEV users, the value of $\gamma^{\mathrm{G2V}}_{n,t}$ can be determined by the following formula:

$$\gamma_{n,t}^{\mathrm{G2V}} = \begin{cases} 1, & t \le \left[t_n^{\mathrm{Ar}} + E^{\mathrm{EV}}\left(Soc^{\mathrm{Tar}} - Soc_n^{\mathrm{Ar}}\right)/\left(P^{\mathrm{C}}\eta^{\mathrm{BC}}\right)\right] \\ 0, & \text{other} \end{cases} \tag{5.3}$$

6-3: By calculating the power flow, determine whether the distribution network fails to meet the constraints during t (i.e., there is load loss).

6-4: If no constraint violation is found, it means that the system is operating normally, so the energy-not-supplied (ENS) is zero; otherwise, the smart distribution network is in an emergency state. Therefore, the analysis will be based on optimal power flow to obtain the ENS indicators.

$ENS_t = \sum_{i\in\Omega_D} P^{\mathrm{Ls}}_{i,t}$, where $P^{\mathrm{Ls}}_{i,t}$ represents the unmet load demand of the i-th node in the corresponding period t.

6-5: Repeat steps 5-3–5-4 for each time period t.

6-6: Update and export the system reliability index result as $\mathrm{EENS} = (\sum_{\mathrm{t}=1}^{8760\times \mathrm{N}'} \mathrm{ENS_t})/\mathrm{N}'$, where N' represents the number of simulation years.

6-7: Repeat the sequential Monte Carlo method until the convergence condition $\sigma(\mathrm{EENS})/[\mathrm{E}(\mathrm{EENS})] \le 0.05$ is met, where E(EENS) and σ(EENS) represent the average expected value and standard deviation of the EENS value in the simulation year, respectively.

6-8: Record the EENS calculation in this scenario as $\mathrm{EENS}^{\mathrm{GPL}}$.

Step 7: Compare the obtained values of $\mathrm{EENS}^{\mathrm{B}}$ and $\mathrm{EENS}^{\mathrm{GPL}}$. If $\mathrm{EENS}^{\mathrm{B}} < \mathrm{EENS}^{\mathrm{GPL}}$, set the capacity value of the GPL to zero; otherwise, perform the following steps:

7-1: Define $\mathrm{C_{max}}$ and $\mathrm{C_{min}}$, and set $\mathrm{C_{max}} = \mathrm{C}^{\mathrm{Ra}}$ and $\mathrm{C_{min}} = 0$, where C^{Ra} is a positive value chosen artificially.

7-2: Add the generator set of the reference unit to the system without GPLs, where the installed capacity is $\mathrm{C}^{\mathrm{E}} = (\mathrm{C_{max}}+\mathrm{C_{min}})/2$.

7-3: Perform the sequential Monte Carlo method to evaluate the EENS index of the smart distribution network and record it as $\mathrm{EENS}^{\mathrm{V}}$.

7-4: According to the obtained $\mathrm{EENS}^{\mathrm{V}}$ and $\mathrm{EENS}^{\mathrm{GPL}}$ values, adjust the unit capacity of the reference unit in the distribution network. Specifically, if $\mathrm{EENS}^{\mathrm{V}} = \mathrm{EENS}^{\mathrm{GPL}}$, then $\mathrm{C_{min}} = \mathrm{C}^{\mathrm{E}}$, and $\mathrm{C_{max}}$ keeps its value from the previous iteration; otherwise, set $\mathrm{C_{max}} = \mathrm{C}^{\mathrm{E}}$ and keep $\mathrm{C_{min}}$ equal to its value in the previous iteration.

7-5: Update the result of C^{E} to $\mathrm{C}^{\mathrm{E}} = (\mathrm{C_{max}}+\mathrm{C_{min}})/2$ and recalculate the EENS Value ($\mathrm{EENS}^{\mathrm{V}}$).

7-6: Check whether the following convergence criterion is met: $|\mathrm{EENS}^{\mathrm{V}} - \mathrm{EENS}^{\mathrm{B}}|/\mathrm{EENS}^{\mathrm{B}} \le \zeta$ (this article sets ζ to 1%). If so, skip to step 8; otherwise, return to step 7-2.

Step 8: Set $\mathrm{ECC} = \mathrm{C}^{\mathrm{E}}$ to terminate the algorithm.

Step 9: According to Eqs. (4.1) - (4.4), calculate the economic index of the GPL based on the capacity value.

CASE STUDY

System Under Study

The capacity value evaluation framework of this paper is analyzed for the existing power supply system in Beijing. The network structure is shown in **Figure 4**. This system has a typical radial topology that is representative and universal in China. However, it should be noted that although our discussions are mainly based on this specific case, the findings of this research can be highly generalized and can be adapted to other UPSs that may have different topologies (such as mesh networks) and distributions.

The concerned system is connected to the outside through a 10 MVA 35 kV/10 kV substation and consists of 32 feeders and 33 load buses with a rated voltage of 10 kV. Node-1 is the balancing node, and node-15 is allocated 2 MW gas turbines. Node-10 is allocated 1.5 MW wind turbines. Node-27 is the location for the discussed GPL. The GPL contains 300 bilateral chargers with a rated capacity (Ai-Power Co Ltd, 2019). In this study, it is assumed that the wind speed in the system follows a Weibull distribution (Beijing Statistical Yearbook, 2011-2015). Additionally, the power supply available from the external grid follows a uniform distribution (Zeng et al., 2020a). The ramping constraints of the substation (Zeng et al., 2021b) are neglected. In addition, the chronological load curve used in this numerical study is determined based on the long-term statistics of a simple distribution system in Beijing, as shown in **Figure 5**.

In addition, the reliability parameters of the system components are summarized in **Table 3**.

For simplicity, it is assumed that all the PEVs in the system correspond to the BAIC-EC200 PEV, which has a rated battery capacity of 20.5 kWh (Beijing Automotive Group Co Ltd., 2019). Therefore, the parameter E^{EV} in Eq. (3.9) is set to 20.5 kWh.

Results

To determine the economics of the GPL capacity value and its impact mechanism, a series of comparative analyses were carried out. These analyses are introduced in the next subsections.

Impact of V2G Program

This subsection compares the impact of V2G on the reliability and economy of the power grid depending on whether the GPL participates. For this purpose, we assume that the discharge rate of the bilateral charger is 3.5 kW, the Soc threshold for the initiation of V2G operation is 90%, and the incentive payment for V2G participation is ¥1.50/kWh. On this basis, we compare

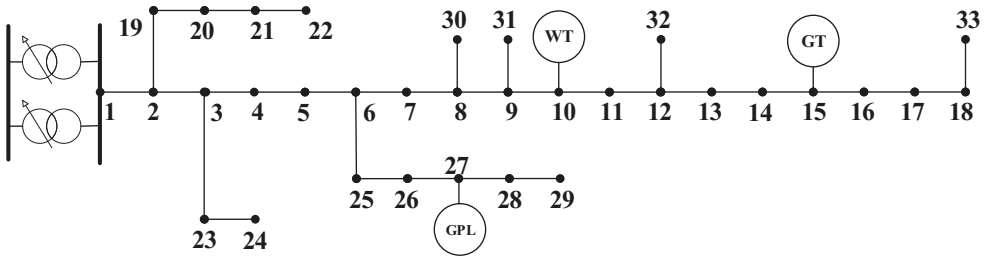

FIGURE 4 | Test system.

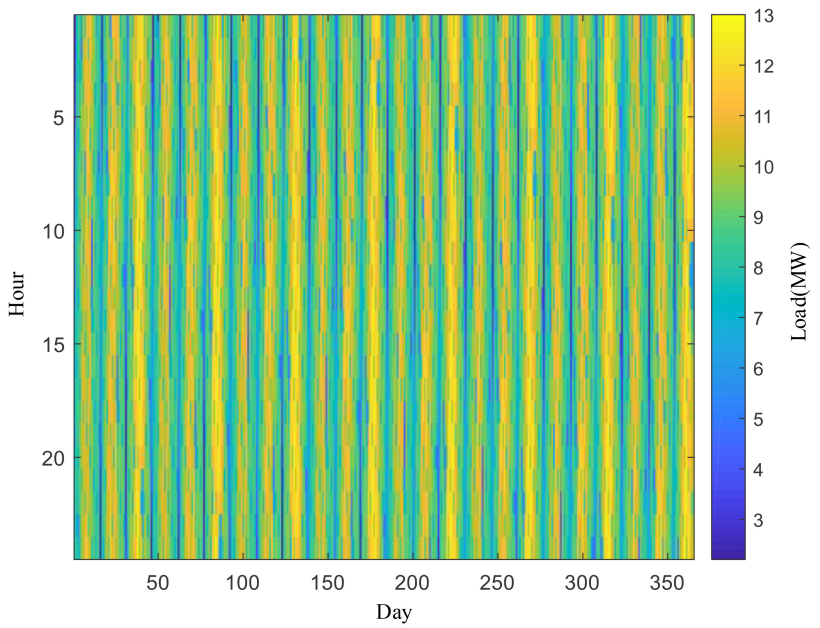

FIGURE 5 | Chronological load profile.

TABLE 3 | Reliability data of the system components.

Component	Bilateral charger	Transformer	Gas turbine	Wind turbine
MTTF (h)	4250	3500	1250	1920
MTTR (h)	5	7	60	80

TABLE 4 | Comparison of the reliability and economy of the GPL.

Operation strategy	EENS (kW·h)	Economic benefit (¥)
No V2G	259.8	0
V2G	223.4	312,000

the reliability and economic performance of the grid when the GPL participates in the V2G programme and when it does not participate.

The result is shown in **Table 4** the EENS drops from 259.8 to 223.4 when the GPL participates in V2G, indicating that the GPL can increase the reliability of the power system and therefore has a beneficial impact on the power system. When the GPL participates in V2G, it can provide the power grid with an economic benefit of ¥312,000.

TABLE 5 | Capacity value of GPL under different discharge rates.

Bilateral charger discharge rate (kW)	2	2.5	3	3.5	4	4.5	5
ECC (kW)	59.3	87.7	121.5	154.0	167.7	188.1	191.7

Influence of Bilateral Charger Discharge Rate

In this section, the primary object of analysis is the impact of the bilateral charger's discharge power on the GPL's capacity value. Because GPLs are equipped with different types of bilateral chargers, they may have different effects. Considering that the discharge capacity of most existing bilateral charger models on the market is the same (Ai-Power Co Ltd, 2019), we assume that the discharge rate P^{DC} of the bilateral charger varies from 2 kW to 5 kW. In addition, in this test, the incentive grade is set as ¥1.50/kWh. The other parameter settings are assumed to be the same as in the previous study. **Table 5** shows the

relationship between the capacity value of the GPL based on the ECC measurement and the discharge rate.

The results show that the technical specifications of bilateral charger equipment have a strong correlation with the capacity value of the GPL. When the GPL is installed with a bilateral charger with a higher discharge efficiency, it can provide greater capacity support for the power grid, reducing the time of power supply system failure. However, it is not necessary that a higher discharge rate of the bilateral chargers always leads to improved system performance. Due to the limitation of the battery capacity of PEVs, the benefits of utilizing GPLs as virtual energy storage tend to become saturated with the continuous increase of the discharging rate.

Influence of Operation Strategy

In the above tests, it was assumed that a PEV in a GPL can be used for V2G only after the Soc of its battery has been charged to 90%. However, in real-world implementations, the GPL operator determines the operation rule of the GPL. In other words, the GPL operator may decide when and how to implement the V2G according to his or her own interests. To investigate how the selection of the operation strategy influences the contribution of GPLs, further study is conducted in this section.

For this purpose, we define several scenarios by setting different values of 80, 82, 85, 87, and 90% to represent the V2G operation strategy of the GPL based on different starting Soc thresholds. Note that these scenarios are selected arbitrarily and are used here only for illustration and comparison purposes. In practice, the GPL operator should carefully determine the V2G operation scheme by comprehensively considering various issues, e.g., the target Soc of the PEVs, batter degradation, hardware compatibility, etc. However, detailed discussions of this topic are beyond the scope of this study.

In this test, we set the incentive grade as ¥1.50/kWh, and the other parameter settings remain the same as in the previous study in Section "Impact of V2G Program." The ECC of the GPL is evaluated under each of the considered scenarios, and **Table 6** illustrates the corresponding results derived.

The results show that choosing different V2G control strategies causes the capacity value of GPL exploitation to differ considerably. The maximum capacity value occurs when the Soc threshold is 90%, and the minimum capacity value occurs when this value is 80%. This shows that the capacity value that the GPL can generate is closely related to its adopted V2G control strategies. Specifically, the larger the Soc threshold used by the GPL is, the larger the expected capacity value. This is in line with our expectations. In actual situations, the possibility of a failure in the power supply system is far lower than that of regular operation. Hence, the power supply system works in a normal state most of the time. The PEVs in the GPL can be charged when the power supply system is operating in the normal state. A higher Soc setting means that the GPL has plentiful energy available for grid support purposes. More energy can participate in V2G when the power supply system fails, thereby improving the reliability benefits of GPL exploitation.

TABLE 6 | Capacity value of the GPL under various threshold Soc values.

Threshold Soc (%)	80	83	85	87	90
ECC (kW)	77.9	103.2	141.5	175.3	181.9

Analysis of Economic Implications

In this study, an incentive scheme was used to motivate PEV users to participate in the V2G programme. However, in practice, the inappropriate selection of the incentive scheme degrades the economics of system operation. Therefore, this section conducts a further analysis to investigate the impact of external stimuli, i.e., incentive signals on PEV participation as well as the economics of GPL exploitation. To do so, in this test, we consider the reward rates paid for V2G participants to be 1.0, 1.25, 1.5, 1.75, and 2.0 ¥/kWh. According to the behavior model of PEV users, different incentive grades result in different participation levels of PEVs in V2G, which can be concluded from **Figure 2**. Then, a comparison can be made for the resulting capacity value of the GPLs and their economic costs under different incentive grades. To clearly show the relationship between the reliability value and economic costs produced by GPL exploitation, the economic cost data are presented in terms of the per kW value, which is denoted as E^{G}. The results are illustrated in **Figure 6**.

As shown above, when the imposed incentive reward is increased, the ECC of the GPL grows sustainably; however, the economic cost of the system tends to first increase and then decrease. This implies that the increase in the incentive grade could encourage PEV users to participate in the V2G programme first; however, with the continuous growth of this rate, its marginal contribution would decrease, which results in the growth rate of the ECC becoming less significant. Additionally, we can observe the economic implications of GPL exploitation from **Figure 6**. Specifically, the grid utility needs to bear a higher economic cost to invoke V2G with the increase in the incentive grades. The cost-benefit efficiency is highest when the incentive grade reaches ¥1.5/kWh. This indicates that the design of an incentive scheme has a significant impact on the economic efficiency for GPL exploitation. Although imposing a higher reward could help to achieve a greater capacity value from the GPL, in the real world, this is not necessarily sensible and efficient from an economic perspective. As such, the grid utility or decision-makers need to pay close attention to the design of such incentive grades when evaluating the potential contribution of GPLs to the sustainability of power systems in order to take advantage of GPL benefits under an acceptable economic budget.

Policy Suggestions

It can be clearly seen from the calculation example in Section "Influence of Bilateral Charger Discharge Rate" that using a GPL as a virtual energy storage unit can improve the reliability of the power system and simultaneously improve the economy of the power system. The results in Sections "Influence of Bilateral Charger Discharge Rate and Influence of Operation Strategy" indicate that the GPL's use of higher-specification charging piles and a larger Soc threshold are conducive to improving reliability. Section "Analysis of Economic Implications" shows

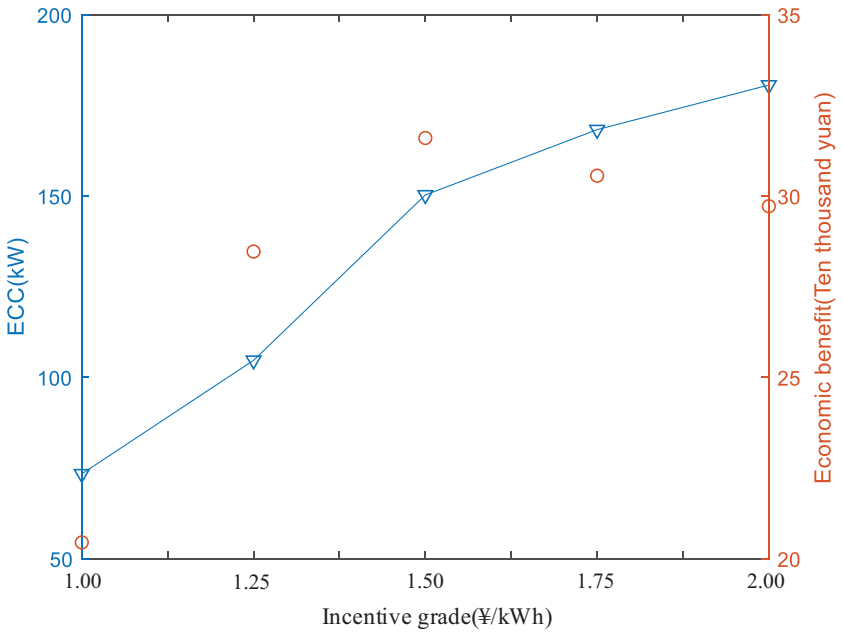

FIGURE 6 | Capacity value of GPLs and its economic benefit under different incentive grades.

that the impact of different incentive grades on user participation and capacity value is one of the most important factors. When the incentive grade reaches ¥1.5/kWh, as it increases, it can bring higher capacity value, but the economic value will decrease accordingly.

Therefore, to improve the sustainability of GPL power supply for future smart cities, it is recommended that the government take the following measures:

(1) It is recommended to incorporate PEV charging infrastructures into urban energy planning as energy storage resources and implement a comprehensive "source-network-load-storage" resource plan to effectively reduce the planned capacity of flexible resources such as electricity storage and natural gas power generation.
(2) It is recommended to improve the peak-valley price formation mechanism, establish a dynamic peak-valley price adjustment mechanism under the premise that the overall sales price level remains unchanged, increase the implementation of the peak-valley price, and use price signals to guide PEV users to participate in peak shaving and valley filling.
(3) It is recommended to improve the auxiliary service compensation mechanism, accelerate the construction of the auxiliary service market, and provide reasonable economic compensation for auxiliary services such as the frequency modulation and backup provided by PEVs in order to encourage PEV users to participate in V2G programs.

CONCLUSION

The method proposed in this paper is based on an integrated capacity-value and economic analysis procedure, which aims to quantify the potential benefits for exploiting GPLs as virtual energy storage resources to the reliability of power supply and its associated economic costs collectively under the same framework. To accurately describe the characteristics of GPLs during operation, this paper introduces a probabilistic approach to simulate the uncertainty of PEV users' behaviors and the sequential Monte Carlo method is also used to simulate the operation states of system equipment. The simulation results from the case study show that efficient utilization of GPLs would be helpful to improve the reliability of power supply at a lower economic expense than the conventional physical energy storage option. However, the capacity value of GPLs is highly dependent on the operating characteristics of its constituent facilities. The research results show that a higher charging rate of the bilateral chargers or larger battery capacity will increase the reliability benefits of the GPLs. Finally, in a liberalized market, the participation of PEV users for V2G is strongly influenced by the reward scheme that adopted. Higher incentive rates can encourage PEV users to participate in V2G and make greater contribution to the improvement of power grid performance. However, excessively high incentive rates will improve system reliability but decrease the economy of power system operation. This proves the necessity of conducting a comprehensive reliability-economic analysis for GPL exploitation in real-world implementations. Finally, we put forward a series of policy recommendations based on the results of the case study. Hopefully, the evaluation framework proposed in this study can help public utilities and government administrative departments better understand the potential of GPLs to be utilized and its associated costs on the development of smart cities at the present stage.

NOMENCLATURE

Acronyms

ECC	Equivalent conventional capacity
EENS	Expected energy not supplied
G2V	Grid-to-vehicle
GPL	Grid-connected parking lot
PEV	Plug-in electric vehicle
UPS	Urban power system
DG	distributed generation
Soc	State of charge
V2G	Vehicle-to-grid

Parameters and Variables

C^{T}	Total generation capacity installation (kW)
C^{E}	Capacity of energy storage that added (kW)
C^{PL}	Total installed capacity of bilateral chargers (kW)
γ^{C}	Binary variable indicating whether the user allows PEV to participate in V2G
γ^{OP}	Binary variable indicating whether GPL operator allows PEV to participate in V2G
γ^{V2G}	Binary variable indicating PEV participation in V2G
n^{Ch}	Binary variable indicating PEV charging
P^{AG}	GPL available power (kW)
P^{C}	Rated charging power of bilateral chargers (kW)
P^{DC}	Rated discharging power of bilateral chargers (kW)
P^{DG}	Available power of DG equipment (kW)
P^{DGN}	DG output power in non-fault state (kW)
P^{T}	Available power of transformer (kW)
P^{TN}	Transformer output power in non-fault state (kW)
P^{M}	Maximum output power of PEV parking lot (kW)
Soc^{Ini}	The initial Soc for PEV (%)
$\mathrm{Soc}^{\mathrm{Tar}}$	Soc threshold (%)
μ^{Soc}	Expected value of initial Soc for PEV (%)
σ^{Soc}	Variance of the initial Soc of the PEV (%)
$Soc^{\mathrm{PEV,min}}$	Minimum value of the initial Soc for PEV (%)
$Soc^{\mathrm{PEV,max}}$	Maximum value of the initial Soc of PEV (%)
t^{Ar}	PEV arrival time
μ^{Ar}	Expectation of PEV arrival time
σ^{Ar}	Variance of PEV arrival time
$t^{\mathrm{Ar,min}}$	Minimum PEV arrival time
$t^{\mathrm{Ar,max}}$	Maximum PEV arrival time
t^{De}	PEV departure time
μ^{De}	Expectation of PEV departure time
σ^{De}	Variance of PEV departure time
$t^{\mathrm{De,min}}$	Minimum PEV departure time
$t^{\mathrm{De,max}}$	Maximum PEV departure time
P^{TD}	Load demand (kW)
P^{TG}	Total available generation capacity (kW)
t^{Ar}	PEV arrival time
t^{De}	PEV departure time

Parameters and Variables

t^{Ch}	PEV charging time
Δt	Time duration of each period in hours
α^{P}	Binary variable indicating whether PEV is in GPL
$\beta^{\mathrm{DG}}/\beta^{\mathrm{T}}/\beta^{\mathrm{C}}$	Binary variable indicating whether generator set/transformer/bilateral chargers are available
ω^{V2G}	Parking lot participates in V2G electricity selling price
ω^{Pay}	Whether the parking lot participates in the boundary of V2G electricity selling price
$S^{\mathrm{P,E}}$	Energy storage investment cost
S^{m}	Energy storage operating cost
E^{V2G}	Cost of the power grid when the parking lot participates in V2G
C^{P}	Power cost of the energy storage device
P^{St}	Power of the energy storage device
C^{E}	Capacity cost of the energy storage device
E^{St}	Capacity of the energy storage device
C^{m}	Annual operation and maintenance cost per unit capacity
E^{EV}	Electric vehicle battery capacity (kWh)
λ_t^{V2G}	Price of V2G called from the parking lot
P_t^{V2G}	Power of the parking lot participating in V2G
η^{BC}	Charging/discharging efficiency of bilateral chargers (%)

Indices (Sets)

$i(\Omega_D)$	Load busel
$k\ (\Omega_{CP})$	Bilateral chargers
$n\ (\Omega_{EV})$	PEV users
t	Time

DATA AVAILABILITY STATEMENT

The original contributions presented in the study are included in the article/supplementary material, further inquiries can be directed to the corresponding author/s.

AUTHOR CONTRIBUTIONS

BZ, BS, and HM contributed to conception and design of the study. HM organized the database. XW performed the statistical analysis. BS wrote the first draft of the manuscript. BS, HM, and YW wrote sections of the manuscript. LW provided suggestions for amendments. All authors contributed to manuscript revision, read, and approved the submitted version.

FUNDING

This study is supported by the State Key Laboratory of Alternate Electrical Power System with Renewable Energy Sources (Grant No. LAPS19018) and the National Social Science Fund of China (Grant No. 19ZDA081).

REFERENCES

Ai-Power Co., Ltd (2019). *AC Charging Pile Products*. Available online at: http://aipower.com.cn/cn/service/005003.html (accessed May 12, 2019)

Al-Rubaye, S., Al-Dulaimi, A., and Ni, Q. (2019). Power interchange analysis for reliable vehicle-to-grid connectivity. *IEEE Commun. Mag.* 57, 105–111. doi: 10.1109/MCOM.2019.1800657

Beijing Automotive Group Co., Ltd *Vehicle Configuration of BAIC-EC200*. Available online at: http://www.bjev.com.cn/models/detile.htm?oid=9&name=ec200 (accessed May 12, 2019)

Beijing Statistical Yearbook (2011-2015). *Wind Speed Data*. Available online at: http://nj.tjj.beijing.gov.cn/nj/main/2015-tjnj/zk/indexch.htm (accessed October 01, 2020)

Billinton, R., and Allan, R. (1996). *Reliability Evaluation of Power Systems*. New York, NY: Plenum Press.

Bozic, D., and Pantos, M. (2015). Impact of electric-drive vehicles on power system reliability. *Energy* 83, 511–520. doi: 10.1016/j.energy.2015.02.055

Dent, C. J., Hernandez-Ortiz, A., Blake, S. R., Miller, D., and Roberts, D. (2015). Defining and evaluating the capacity value of distributed generation. *IEEE Trans. Power Syst.* 30, 2329–2337. doi: 10.1109/TPWRS.2014.2363142

Ding, M., and Xu, Z. (2017). Empirical model for capacity credit evaluation of utility-scale PV plant. *IEEE Trans. Sustain. Energy* 8, 94–103. doi: 10.1109/TSTE.2016.2584119

Du, Z., Lin, B., and Guan, C. (2019). Development path of electric vehicles in China under environmental and energy security constraints. *Resour. Conserv. Recycl.* 143, 17–26. doi: 10.1016/j.resconrec.2018.12.007

Farzin, H., Fotuhi-Firuzabad, M., and Moeini-Aghtaie, M. (2017). Reliability studies of modern distribution systems integrated with renewable generation and parking lots. *IEEE Tran. Sustain. Energy* 8, 431–440. doi: 10.1109/TSTE.2016.2598365

Farzin, H., and Monadi, M. (2019). Reliability enhancement of active distribution grids via emergency V2G programs: an analytical cost/worth evaluation framework. *Sci. Iran.* 26, 3635–3645. doi: 10.24200/sci.2019.54158.3624

Guner, S., and Ozdemir, A. (2020). Reliability improvement of distribution system considering EV parking lots. *Electr. Power Syst. Res.* 185:106353. doi: 10.1016/j.epsr.2020.106353

Heydarian-Forushani, E., Golshan, M. E. H., and Shafie-Khah, M. (2016). Flexible interaction of plug-in electric vehicle parking lots for efficient wind integration. *Appl. Energy* 179, 338–349. doi: 10.1016/j.apenergy.2016.06.145

Irshad, U. B., Rafique, S., and Town, G. (2020). "Reliability assessment considering intermittent usage of electric vehicles in parking lots," in *Proceedings of the 2020 IEEE 29th International Symposium on Industrial Electronics (ISIE)*, Delft, 965–970. doi: 10.1109/ISIE45063.2020.9152560

Keane, A., Milligan, M., Dent, C. J., Hasche, B., D' Annunzio, C., Dragoon, K., et al. (2011). Capacity value of wind power. *IEEE Trans. Power Syst.* 26, 564–572. doi: 10.1109/TPWRS.2010.2062543

Mohammadi-Hosseininejad, S. M., Fereidunian, A., and Lesani, H. (2018). Reliability improvement considering plug-in hybrid electric vehicles parking-lots ancillary services: a stochastic multi-criteria approach. *IET Gener. Trans. Distribut.* 12, 824–833. doi: 10.1049/iet-gtd.2017.0657

Momen, H., Abessi, A., and Jadid, S. (2020). Using EVs as distributed energy resources for critical load restoration in resilient power distribution systems. *IET Gener. Trans. Distribut.* 14, 3750–3761. doi: 10.1049/iet-gtd.2019.1561

Moradijoz, M., Heidari, J., Moghaddam, M. P., and Haghifam, M. R. (2020). Electric vehicle parking lots as a capacity expansion option in distribution systems: a mixed-integer linear programing-based model. *IET Electr. Syst. Transp.* 10, 13–22. doi: 10.1049/iet-est.2018.5062

Neyestani, N., Damavandi, M. Y., Shafie-Khah, M., Contreras, J., and Catalao, J. P. S. (2015). Allocation of plug-in vehicles' parking lots in distribution systems considering network-constrained objectives. *IEEE Trans. Power Syst.* 30, 2643–2656. doi: 10.1109/TPWRS.2014.2359919

Onishi, V. C., Antunes, C. H., and Fernandes Trovao, J. P. (2020). Optimal energy and reserve market management in renewable microgrid-PEVs parking lot systems: V2G, demand response and sustainability costs. *Energies* 13:1884. doi: 10.3390/en13081884

Shafie-Khah, M., Heydarian-Forushani, E., Osorio, G. J., Gil, F. A. S., Aghaei, J., Barani, M., et al. (2015). Optimal behavior of electric vehicle parking lots as demand response aggregation agents. *IEEE Trans. Smart Grid* 7, 2654–2665. doi: 10.1109/TSG.2015.2496796

Shaukat, N., Khan, B., Ali, S. M., Mehmood, C. A., Khan, J., Farid, U., et al. (2018). A survey on electric vehicle transportation within smart grid system. *Renew. Sustain. Energy Rev.* 81, 1329–1349. doi: 10.1016/j.rser.2017.05.092

Silva, B. N., Khan, M., and Han, K. (2018). Towards sustainable smart cities: a review of trends, architectures, components, and open challenges in smart cities. *Sustain. Cities Soc.* 38, 697–713. doi: 10.1016/j.scs.2018.01.053

Singh, S., Jagota, S., and Singh, M. (2018). Energy management and voltage stabilization in an islanded microgrid through an electric vehicle charging station. *Sustain. Cities Soc.* 41, 679–694. doi: 10.1016/j.scs.2018.05.055

Xu, N. Z., and Chung, C. Y. (2016). Reliability evaluation of distribution systems including vehicle-to-home and vehicle-to-grid. *IEEE Trans. Power Syst.* 31, 759–768. doi: 10.1109/TPWRS.2015.2396524

Yilmaz, M., and Krein, P. T. (2013). Review of battery charger topologies, charging power levels, and infrastructure for plug-in electric and hybrid vehicles. *IEEE Trans. Power Electron.* 28, 2151–2169. doi: 10.1109/TPEL.2012.2212917

Zaisen, Q. (2018). *Energy Storage Planning and Economic Research under Different Operating Modes*. Ph. D. thesis. Zhengzhou: Zhengzhou University.

Zeng, B., Dong, H., Sioshansi, R., Xu, F., and Zeng, M. (2020a). Bilevel robust optimization of electric vehicle charging stations with distributed energy resources. *IEEE Trans. Ind. Appl.* 56, 5836–5847. doi: 10.1109/TIA.2020.2984741

Zeng, B., Feng, J., Liu, N., and Liu, Y. (2021a). Co-optimized parking lot placement and incentive design for promoting PEV integration considering decision-dependent uncertainties. *IEEE Trans. Indus. Inform.* 17, 1863–1872. doi: 10.1109/TII.2020.2993815

Zeng, B., Liu, Y., Xu, F., Liu, Y., Sun, X., and Ye, X. (2021b). Optimal demand response resource exploitation for efficient accommodation of renewable energy sources in multi-energy systems considering correlated uncertainties. *J. Clean. Prod.* 288:125666. doi: 10.1016/j.jclepro.2020.125666

Zeng, B., Wei, X., Sun, B., Qiu, F., Zhang, J., and Quan, X. (2020a). Assessing capacity credit of demand response in smart distribution grids with behavior-driven modeling framework. *Int. J. Electr. Power Energy Syst.* 118:105745. doi: 10.1016/j.ijepes.2019.105745

Zeng, B., Zhu, Z., Xu, H., and Dong, H. (2020b). Optimal public parking lot allocation and management for efficient PEV accommodation in distribution systems. *IEEE Trans. Indus. Appl.* 56, 5984–5994. doi: 10.1109/TIA.2020.2986980

Conflict of Interest: LW was employed by company Shanxi Electrical Power Company of SGCC.

The remaining authors declare that the research was conducted in the absence of any commercial or financial relationships that could be construed as a potential conflict of interest.

frontiers in Energy Research

ORIGINAL RESEARCH
published: 28 May 2021
doi: 10.3389/fenrg.2021.700069

Automatic Generation Control for Distributed Multi-Region Interconnected Power System with Function Approximation

Yuchen Liu[1], *Le Zhang*[2,3]*, *Lei Xi*[3], *Qiuye Sun*[4] *and Jizhong Zhu*[5]

[1]School of Information Engineering, Nanchang University, Nanchang, China, [2]Zigong Power Supply Company, State Grid Sichuan Electric Power Corporation, Zigong, China, [3]College of Electrical Engineering and New Energy, China Three Gorges University, Yichang, China, [4]School of Information Science and Engineering, Northeastern University, Shenyang, China, [5]School of Electric Power Engineering, South China University of Technology, Guangzhou, China

Solving the energy crisis and environmental pollution requires large-scale access to distributed energy and the popularization of electric vehicles. However, distributed energy sources and loads are characterized by randomness, intermittence and difficulty in accurate prediction, which bring great challenges to the security, stability and economic operation of power system. Therefore, this paper explores an integrated energy system model that contains a large amount of new energy and combined cooling heating and power (CCHP) from the perspective of automatic generation control (AGC). Then, a gradient Q(σ,λ) [GQ (σ,λ)] algorithm for distributed multi-region interconnected power system is proposed to solve it. The proposed algorithm integrates unified mixed sampling parameter and linear function approximation on the basis of the Q(λ) algorithm with characteristics of interactive collaboration and self-learning. The GQ (σ,λ) algorithm avoids the disadvantages of large action spaces required by traditional reinforcement learning, so as to obtain multi-region optimal cooperative control. Under such control, the energy autonomy of each region can be achieved, and the strong stochastic disturbance caused by the large-scale access of distributed energy to grid can be resolved. In this paper, the improved IEEE two-area load frequency control (LFC) model and the integrated energy system model incorporating a large amount of new energy and CCHP are used for simulation analysis. Results show that compared with other algorithms, the proposed algorithm has optimal cooperative control performance, fast convergence speed and good robustness, which can solve the strong stochastic disturbance caused by the large-scale grid connection of distributed energy.

Keywords: automatic generation control, distributed multi-region, integrated energy system, function approximation, mixed sampling parameter

OPEN ACCESS

Edited by:
Yingjun Wu,
Hohai University, China

Reviewed by:
Xiaoshun Zhang,
Shantou University, China
Huaizhi Wang,
Shenzhen University, China

***Correspondence:**
Le Zhang
zhangle_unique@163.com

Specialty section:
This article was submitted to Smart Grids, a section of the journal Frontiers in Energy Research

Received: *25 April 2021*
Accepted: *12 May 2021*
Published: *28 May 2021*

Citation:
Liu Y, Zhang L, Xi L, Sun Q and Zhu J (2021) Automatic Generation Control for Distributed Multi-Region Interconnected Power System with Function Approximation. Front. Energy Res. 9:700069. doi: 10.3389/fenrg.2021.700069

INTRODUCTION

To cope with the fossil energy crisis and environmental pollution, many countries around the world are vigorously developing distributed energy, which can promote the transformation of low-carbon and intelligent power system (Xu et al., 2020; Kumar et al., 2020; An et al., 2020; Suh et al., 2017). However, the distributed energy and loads, such as wind power, photovoltaic and electric vehicles,

are intermittent and stochastic (Solanki et al., 2017; Xi et al., 2015; Zhang et al., 2021; Mukherjee and Gupta, 2016; Wang, 2020). The rapid growth of their installed capacity poses a huge challenge to power system. The traditional centralized automatic generation control (AGC) cannot easily meet the development requirements and operating conditions for smart grid (Jaleeli et al., 1992). Therefore, solving the strong stochastic disturbance caused by large-scale grid connections of distributed energy from the perspective of AGC, has become an urgent challenge in the field of power system.

Nowadays, the AGC control methods can be divided into two categories: conventional analytic and machine learning. The proportional-integral-derivative (PID) control, optimal control and robust control are representations of conventional analytical control methods (Yan et al., 2013). Based on a fuzzy logic approach, the fractional-order PID controller uses a genetic algorithm to change the controller parameters accurately and improve the dynamic response of AGC for two-region interconnected power system significantly (Ismayil et al., 2015). An optimal PI/PID method based on the social learning adaptive bacterial foraging algorithm was proposed in (Xie et al., 2016) to improve the convergence speed and merit-seeking accuracy of the algorithm. To obtain the dynamic control performance, the study adopted a PI-structured optimal controller based on a full state feedback strategy in the application of optimal control methods to AGC (Yamashita and Taniguchi, 2016). To overcome system perturbations, the study introduced robust control into complex power systems with large-scale access to renewable energy (Sharma et al., 2017). Thus, the dynamic performance and control stability of AGC can be improved. As another aspect of AGC control methods, reinforcement learning algorithms are representative of machine learning methods. The Q-learning algorithm based on the Markov decision process relies on a closed-loop feedback structure formed by the value function and control action under the control performance standard (CPS). This algorithm can improve the robustness and adaptability of the whole AGC system significantly (Yu et al., 2011). Based on multi-step backward Q (λ) learning, the optimal power allocation algorithm for AGC commands introduces a multi-step foresight capability to solve the delayed return problem caused by large time lag links in thermal power units (Yu et al., 2011). Based on the average payoff model, the full-process R (λ) learning controller can be directly introduced to the practical power grid to learn to imitate the output of other controllers online (Yu and Yuan, 2010). Hence, without building an accurate simulation model for offline prelearning, the controller can also improve the learning efficiency and applicability in practical power system (Xi et al., 2020; Zhang et al., 2020).

However, with the increasing access to a high proportion of new energy resources, grid patterns shift, thereby resulting in increased stochastic disturbances (Hou et al., 2021; Fu et al., 2021; Dehnavi and Ginn, 2019). The aforementioned methods cannot meet the optimal frequency control requirements of smart grid. Hence, scholars have proposed a series of distributed intelligent AGC methods. The forecasting model control, hierarchical recursive, adaptive control, reinforcement learning, and deep learning have been introduced into the distributed AGC controller. In particular, the wolf pack hunting (WPH) strategy based on the multi-agent systems-stochastic consensus game framework, which considers the integrated objectives of frequency deviation and short-term economic dispatch, can achieve the optimal power dispatch of AGC so as to solve coordinated control and power autonomy problems effectively (Xi et al., 2016). In order to promote the intelligence of AGC systems through the combination of reinforcement learning and artificial emotion, an artificial emotion reinforcement learning controller for AGC can generate different control strategies according to the environment of power system (Yin et al., 2017). As for realizing the optimal coordinated control of power systems, the DPDPN algorithm combines the decision mechanism of reinforcement learning with the prediction mechanism of a deep neural network to allocate power order among the various generators (Xi et al., 2020). Meanwhile, the distributed energy and loads, such as wind power, photovoltaic, biomass power and electric vehicles, continue to increase at a massive scale (Wang et al., 2015). This trend causes strong stochastic disturbances in the power grid and leads to a dramatic increase in the difficulty of a frequency control for the power grid. Therefore, a new AGC method must be investigated to address the problem of strong stochastic perturbations.

For the situation of low-dimensional state-action pairs, the reinforcement learning method uses a table to record value functions, with each state or state-action pair allocated storage space to record function values (Zhang et al., 2018; Sun and Yang, 2019; Xi et al., 2021). However, the increased access to distributed energy and the expansion of the installed capacity of generators cause the state-action pair storage space to expand geometrically. This drawback limits the dynamic optimization speed of reinforcement learning algorithms. Thus, the optimal control efficiency of AGC is reduced greatly. To solve the problem of storage space for state-action pairs, this study proposes a gradient Q(σ,λ) [GQ (σ,λ)] algorithm for distributed multi-region cooperative control. Linear function approximation with mixed sampling parameter is adopted to combine the full sampling algorithm with the pure expectation algorithm judiciously. Through the GQ (σ,λ) algorithm, the power allocation commands of each region for distributed AGC can be obtained. Thus, the stochastic disturbances caused by large-scale new energy access to the grid can be solved. The improved IEEE two-area load frequency control (LFC) model and integrated energy system model incorporating a large amount of new energy and combined cooling heating and power (CCHP) are simulated, and the results verify the effectiveness of the GQ (σ,λ) algorithm. Compared with other reinforcement learning algorithms, GQ (σ,λ) has better learning ability, better cooperative control performance, faster convergence and better robustness.

GQ(σ,λ) ALGORITHM

Q(λ) Algorithm

As one of the classical reinforcement learning algorithms, Q-learning is based on the discrete-time Markov decision process, which is a value function iteration rooted in online learning and dynamic optimization technology (Watkins and Dayan, 1992). Based on Q-learning, the Q (λ) algorithm integrates eligibility trace with the characteristics of multi-step backtracking update to improve the convergence speed. The Q (λ)

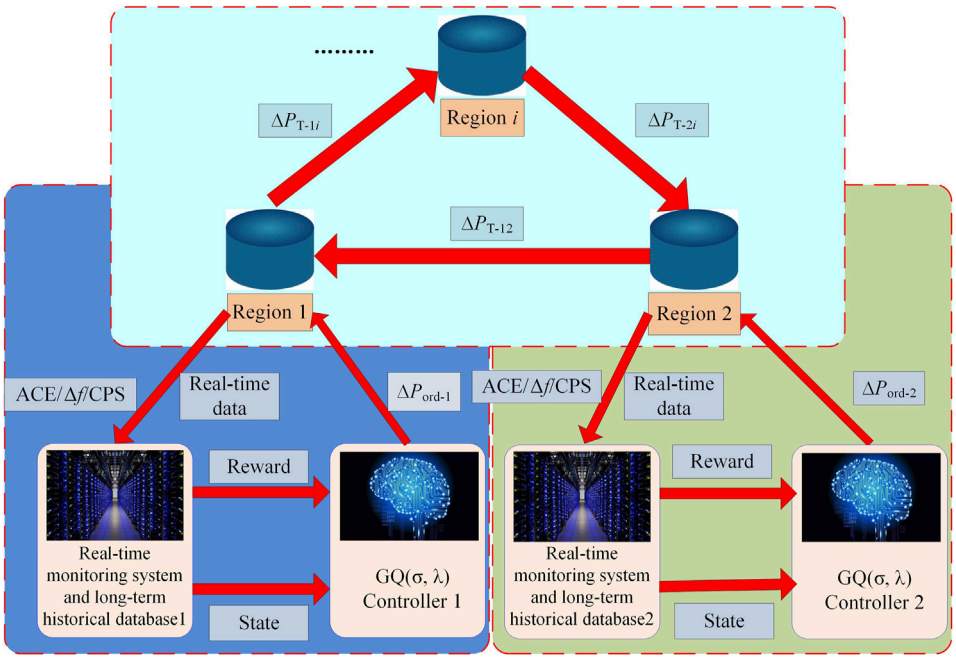

FIGURE 1 | Control framework of AGC system based on GQ (σ,λ).

algorithm uses eligibility trace to obtain two types of heuristic information, namely, frequency and gradual reliability of controller behavior (Barto and Sutton, 1998). This information can accurately and effectively reflect the influence of previous multi-step state-action pairs on subsequent decisions. Eligibility trace is mainly used to solve the problem of time reliability allocation in delayed reinforcement learning. It is a temporary record of previous state tracks and action information. For any state-action pair, eligibility trace is attenuated with timeliness (Xi et al., 2018). The iterative updating formula of eligibility trace is as follows:

$$e_{k+1}(s,a) = \begin{cases} \gamma\lambda e_k(s,a) + 1, & (s,a) = (s_k,a_k) \\ \gamma\lambda e_k(s,a), & \text{otherwise} \end{cases} \quad (1)$$

where $e_k(s,a)$ is the eligibility trace of the kth iteration under state s and action a, γ is the discount factor, and λ is the attenuation factor of eligibility trace.

According to the reward value obtained by the agent through the current exploration, the error of the Q value function and its evaluation are calculated as follows:

$$\rho_k = R_k + \gamma Q_k\left(s_{k+1}, a_g\right) - Q_k(s_k, a_k) \quad (2)$$

$$\delta_k = R_k + \gamma Q_k\left(s_{k+1}, a_g\right) - Q_k\left(s_k, a_g\right) \quad (3)$$

where R_k is the reward function of the kth iteration, a_g is the action of the greedy policy, ρ_k is the Q value function error of the agent at the kth iteration, and δ_k is the evaluation of the function error.

The iterative update process of the Q(λ) algorithm is as follows:

$$Q_{k+1}(s,a) = Q_k(s,a) + \alpha\delta_k e_k(s,a) \quad (4)$$

$$Q_{k+1}(s_k,a_k) = Q_{k+1}(s_k,a_k) + \alpha\rho_k \quad (5)$$

where α is the value function learning factor. When the value of α is large, it can accelerate the iterative updating and learning speed of the Q value function. While the value of α is small, the stability of the control system is improved.

Q(σ,λ) Algorithm

On the basis of the Q (λ) algorithm, this study proposes the Q (σ,λ) algorithm, which combines on-policy learning and off-policy learning. The mixed sampling parameter σ is introduced to unify the Sarsa algorithm (full sampling) and Expected-sarsa algorithm (pure expectation) (Long et al., 2018). As one of the classic algorithms in on-policy learning, the Sarsa algorithm uses a greedy policy to update the target strategy synchronously while evaluating the Q value function through the current target action strategy (Rummery and Niranjan, 1994). The Expected-sarsa algorithm, as an off-policy learning algorithm, uses the function expectation value of the next state-action pair to evaluate the Q value function (Seijen et al., 2009). Although the Expected-sarsa algorithm is computationally more complex than Sarsa, it eliminates the variance caused by the random selection of the next action. Given the same exploration path, Expected-sarsa performs significantly better than Sarsa.

Therefore, the mixed sampling parameter σ is introduced to integrate the Expected-sarsa algorithm and Sarsa algorithm and unify the advantages and disadvantages of on-policy and off-policy learning. The range of the mixed sampling parameter is (0,1). Although $0 < \sigma < 1$, the control

TABLE 1 | Parameters setting.

Parameters		Value
α	Learning factor of the decision-making strategy	0.1
β	Learning factor of the value function	0.3
γ	Discount factor of the value function	0.9
λ	Attenuation factor of the eligibility trace	0.95
σ	Mixed sampling parameter	0.5

performance of the algorithm is better than that at $\sigma = 0$ or 1. The iterative update of the Q (σ,λ) algorithm is obtained by linear weighting between the update of the full sampling Sarsa algorithm ($\sigma = 1$) and the update of the pure expectation Expected-sarsa algorithm ($\sigma = 0$).

$$\delta_k^{\sigma} = R_k + \gamma\left[\sigma Q_k(s_{k+1}, a_{k+1}) + (1-\sigma)\sum_{a\in A}\pi(s_{k+1}, a)Q_k(s_{k+1}, a)\right] - Q_k(s_k, a_k) \tag{6}$$

$$Q_k(s_k, a_k) = Q_k(s_k, a_k) + \alpha\delta_k^{\sigma} e_k(s, a) \tag{7}$$

where π (s_{k+1},a) is the value function of the decision-making strategy under state s_{k+1} and action a and $\delta_k{}^{\sigma}$ is the evaluation of the function error at the kth iteration.

The eligibility trace is also updated iteratively as follows:

$$e_{k+1}(s, a) = \begin{cases} \gamma\lambda e_k(s, a)[\sigma + (1-\sigma)\pi(a_k|s_k)] + 1, & Q_k(s_k, a_k) = \max\limits_{a\in A} Q_k(s_k, a) \\ \gamma\lambda e_k(s, a)[\sigma + (1-\sigma)\pi(a_k|s_k)], & \text{otherwise} \end{cases} \tag{8}$$

GQ(σ,λ) Algorithm

In this paper, the linear function approximation and mixed sampling parameter are combined to solve the problem of insufficient storage space in traditional reinforcement learning algorithms. The sampling problem is also solved using random approximation under double time scales (Yang et al., 2019). Moreover, the GQ (σ,λ) algorithm, which combines mixed sampling with function approximation, is proposed. The algorithm is oriented to a multi-agent system, which reduces the time needed for an intelligent algorithm to explore the path of multi-agent state-action pairs. Meanwhile, the optimal decision-making strategy can be obtained quickly. This strategy can solve the optimal cooperative control problem and promote the stochastic complex dynamic characteristics of multi-agent system (Sun et al., 2016).

The agent calculates the value function error of the decision-making strategy through the reward value R obtained from the current exploration, which is expressed as shown:

$$\delta_k^{\sigma} = R_k + \gamma\left[\sigma Q(s_{k+1}, a_{k+1})\pi(s_{k+1}, a_{k+1}) + (1-\sigma)V_k^{\pi}(s_{k+1})\right] - Q(s_k, a_k)\pi(s_k, a_k) \tag{9}$$

where $V_k{}^{\pi}(s_{k+1})$ is the function expectation value of the decision-making strategy under state s_{k+1}.

The decision-making strategy of the GQ (σ,λ) algorithm is updated iteratively as follows:

Initialize $Q(s,a)$, $\pi(s,a)$, R, $e(s,a)$, $\upsilon(s,a)$, $\omega(s,a)$, for all $s\in S$, $a\in A$.
Set parameters α, β, γ, λ, and σ.
Give the initial state s_0, k=0.
Repeat
(1) Choose and execute an exploration action a_k based on the decision-making strategy $\pi_k(s,a)$ under state s_k.
(2) Observe the state of the next moment, and record the observation value.
(3) Obtain the current reward R via (14).
(4) Calculate the value function error $\delta_k{}^{\sigma}$ according to (9).
(5) Calculate the function approximation value $\nabla_{\pi(sk,ak)}$ according to (11).
(6) Update the decision-making strategy $\pi_{k+1}(s_k,a_k)$ via (10).
(7) Calculate the value function error υ_k by (12) and evaluation of value function error ω_k by (13).
(8) Update the value function $Q_{k+1}(s_k,a_k)$ via (7).
(9) Update the eligibility trace element $e_{k+1}(s,a)$ via (8).
(10)Obtain the total power command ΔP_{Σ}.
(11)Set $k = k + 1$, and return to step 1.
End

FIGURE 2 | Execution procedure of the GQ (σ,λ) algorithm.

$$\pi_{k+1}(s_k, a_k) = \pi_k(s_k, a_k) + \alpha\frac{1}{2}\nabla_{\pi(s_k,a_k)} \tag{10}$$

where $\nabla_{\pi\ (sk,ak)}$ is the gradient of the decision-making strategy under state s_k and action a_k, that is, the optimal function approximation value of the decision-making strategy at (s_k,a_k), which can be calculated as follows:

$$\nabla_{\pi(s_k,a_k)} = 2\left[\delta_k^{\sigma} e_k(s, a) - \gamma\upsilon_k(s_k, a_k)\omega_k(s_k, a_k)\right] \tag{11}$$

where $e_k(s, a)$ is the eligibility trace of the kth iteration under state s and action a, it can be calculated by **Eq. 8**. υ_k (s_k,a_k) and ω_k (s_k,a_k) are the Q value function error and evaluation of the kth iteration under state s_k and action a_k, respectively. The iterative updates of υ_k (s_k,a_k) and ω_k (s_k,a_k) are as follows:

$$\upsilon_{k+1}(s_k, a_k) = \sigma(1-\lambda)Q(s_k, a_k)e_k(s, a) + (1-\sigma)\left[V_k^{\pi}(s_k) - \lambda Q(s_k, a_k)\right]e_k(s, a) \tag{12}$$

$$\omega_{k+1}(s_k, a_k) = \omega_k(s_k, a_k) + \beta\left[\delta_k^{\sigma} e_k(s, a) - Q(s_k, a_k)\omega_k(s_k, a_k)\right] \tag{13}$$

where β is the learning factor of the Q value function.

After several trial-error iterations, the decision-making strategy π (s,a) converges to a relatively fixed optimal action strategy, which speeds up the convergence of reinforcement learning, so as to obtain the optimal cooperative control strategy.

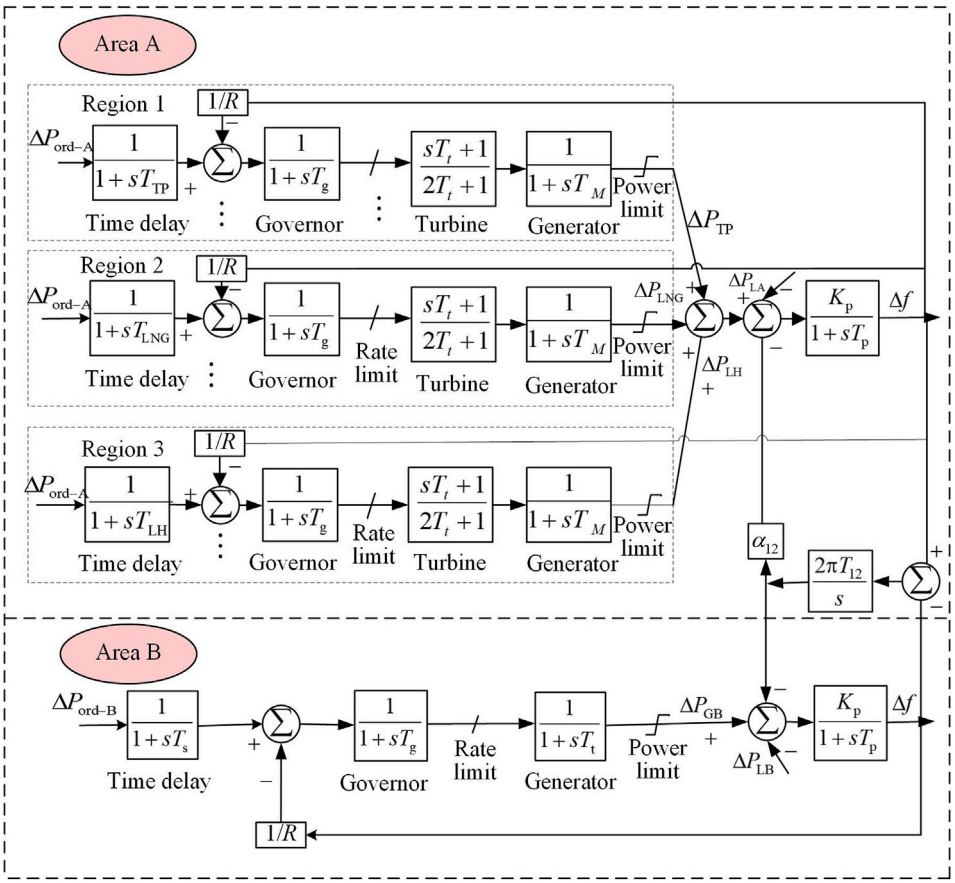

FIGURE 3 | Improved model of IEEE two-area LFC power system.

DESIGN OF AGC CONTROLLER

Control Framework of AGC System Based on GQ (σ,λ)

The control framework of AGC system based on GQ (σ,λ) is shown in **Figure 1**. The input of the GQ (σ,λ) controller of the *i*th regional power grid is the state under the current environment and the calculated reward value from the "real-time monitoring system and long-term historical database". The GQ (σ,λ) controller can realize online learning and give control signals. The control action is the general AGC regulation command $\Delta P_{\text{ord-}i}$ of dispatching the terminal of *i*th regional power grid.

Construction of Reward Function

Considering the problem of environmental pollution, this paper takes the linear weighting of ACE and carbon emission (CE) as the comprehensive, objective function. The CE value of the regional power grid is equal to the product of the unit output power and unit CE intensity coefficient. The reward function of each regional power grid is constructed as follows:

$$R = -\eta[\mathrm{ACE}(t)]^2 - (1-\eta)\left(\sum_{k=1}^{m} B_k[\Delta P_k(t)]\right) \Big/ 1000, \Delta P_k^{\min} \le \Delta P_k(t) \le \Delta P_k^{\max} \quad (14)$$

where ACE (*t*) is the instantaneous value of ACE, ΔP_k (*t*) is the actual output power of the *k*th unit, and η and 1-η are the weights of ACE and CE, respectively. The η value of each area is the same, and thus, the η value is set to 0.5.

Parameter Setting

In the design of the AGC controller, five system parameters, namely, α, β, γ, λ and σ, are set. After numerous trial-error iterations, the best control performance can be obtained when the parameters shown in **Table 1** are set.

1) The learning factor of the decision-making strategy α ($0 < \alpha < 1$), measure the influence of action selection strategy on iterative updating of decision-making strategy. The larger α can accelerate the convergence speed of the decision-making strategy, while the smaller α can ensure that the system can fully search other actions in the space.
2) The learning factor of the value function β ($0 < \beta < 1$), weigh the stability of GQ (σ,λ) algorithm. Larger β can accelerate the iterative updating speed of the value function, and when β is smaller, the stability of the system will be greatly improved. The parameter setting of learning factor is to have fast learning speed as much as possible under the condition of ensuring stability.

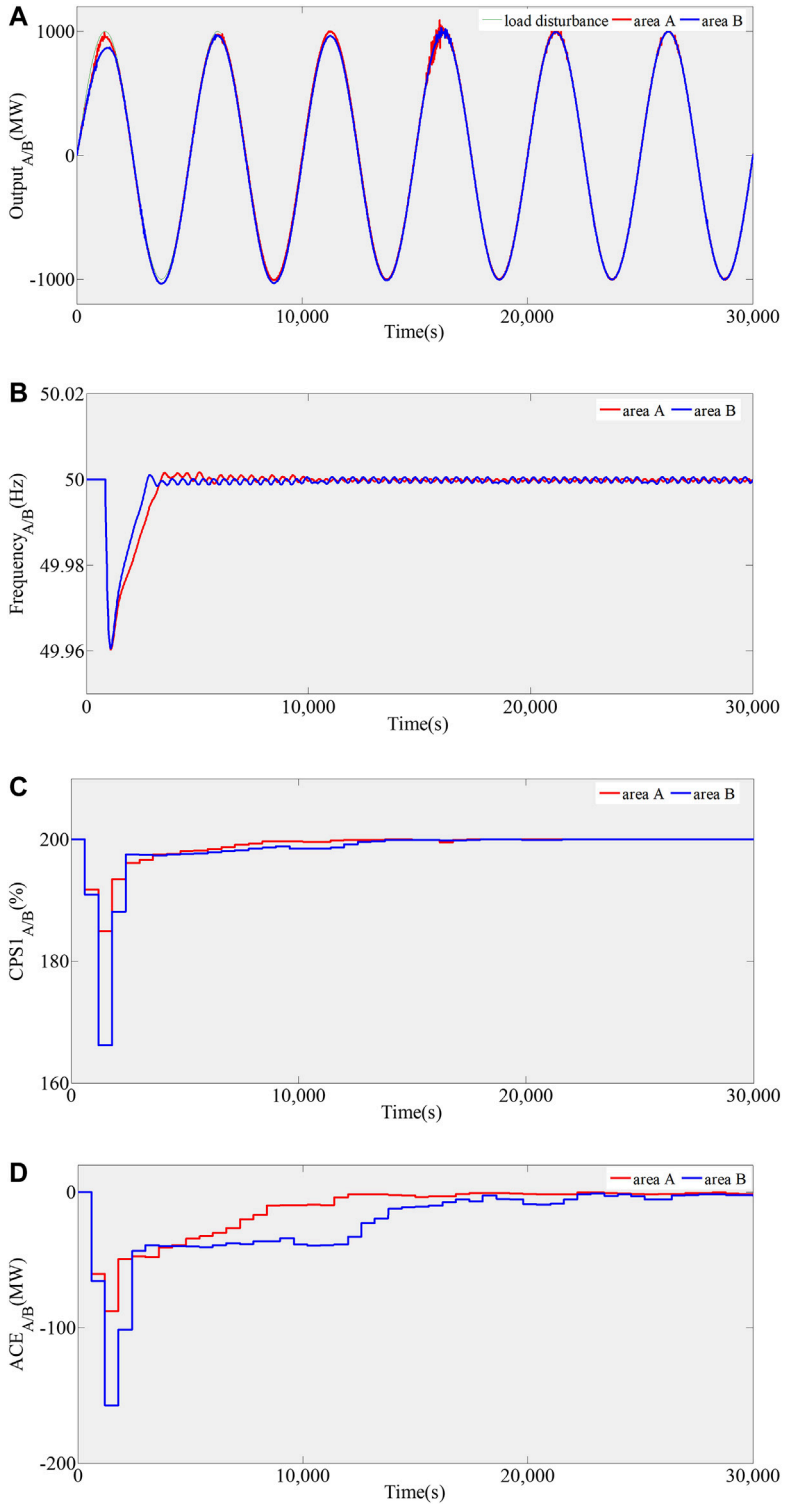

FIGURE 4 | Pre-learning of the GQ (σ,λ) algorithm in area A and B, 4 **(A)**, 4 **(B)**, 4 **(C)**, 4 **(D)**.

3) The discount factor of the value function γ $(0 < \gamma < 1)$, weigh the importance of current and future reward. The closer the value is to 1, the more emphasis is placed on long-term rewards; otherwise, more emphasis is on immediate rewards. Considering that the agent pursues long-term returns, the value close to one should be adopted.

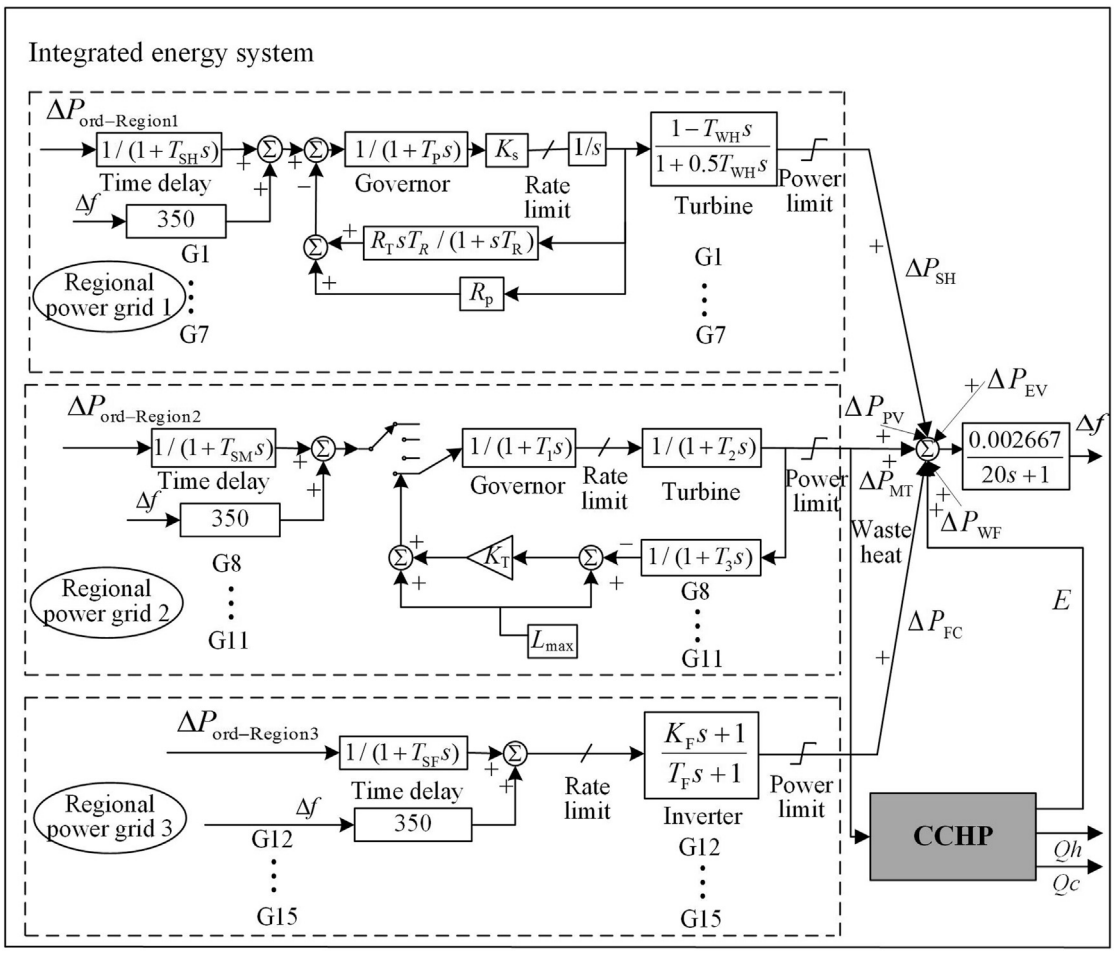

FIGURE 5 | The model of integrated energy system.

4) The attenuation factor of the eligibility trace λ ($0 < \lambda < 1$), reflect the degree of influence on convergence rate and non Markov effect. The larger λ is, the slower the eligibility trace of the previous historical state-action pair will decay, and the more reputation will be allocated. The smaller λ is, the less reputation will be allocated.
5) The mixed sampling parameter σ ($0 \le \sigma \le 1$), unify on-policy and off-policy learning. With different values, the linear weighting between full sampling algorithm and pure expectation algorithm will be different. The smaller σ is, the more full sampling is preferred in the process of strategy optimization, that is, the iterative update is carried out through the value function.

GQ(σ,λ) Procedure

The execution procedure of the AGC system based on the GQ (σ,λ) algorithm is shown in **Figure 2**. Before the controller runs online, extensive prelearning is needed to achieve the optimal action set and thereby obtain the optimal coordination control of online system operations.

EXAMPLE ANALYSIS

Improved IEEE Two-Area LFC Power System

Based on the IEEE standard two-area LFC model (Ray et al., 1999), the improved model replaces one equivalent unit in area A with three area power grids to analyze the control performance of the GQ (σ,λ)algorithm. The frame structure is shown in **Figure 3**, and the system parameters are selected from the model parameters in reference (Xi et al., 2020). Area A has 20 generating units, including thermal power (TP), liquefied natural gas (LNG) and large hydropower (LH). The specific parameters of the units are taken from reference (Zhang and Yu, 2015).

Before online operations, numerous offline trials and errors are needed to explore the CPS state and to obtain the optimal action strategy, optimize the Q function, and then introduce it into the integrated energy system model for online optimization operation.

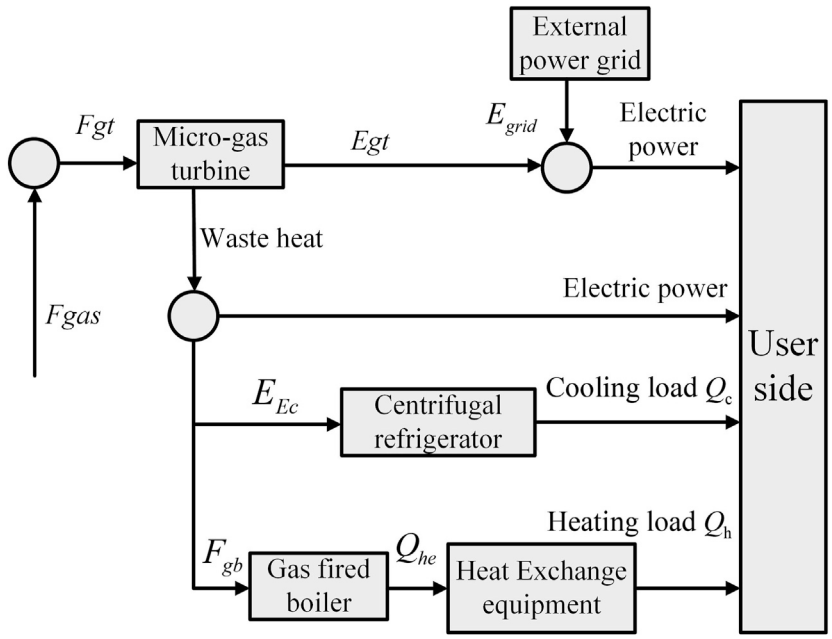

FIGURE 6 | The structure of CCHP system.

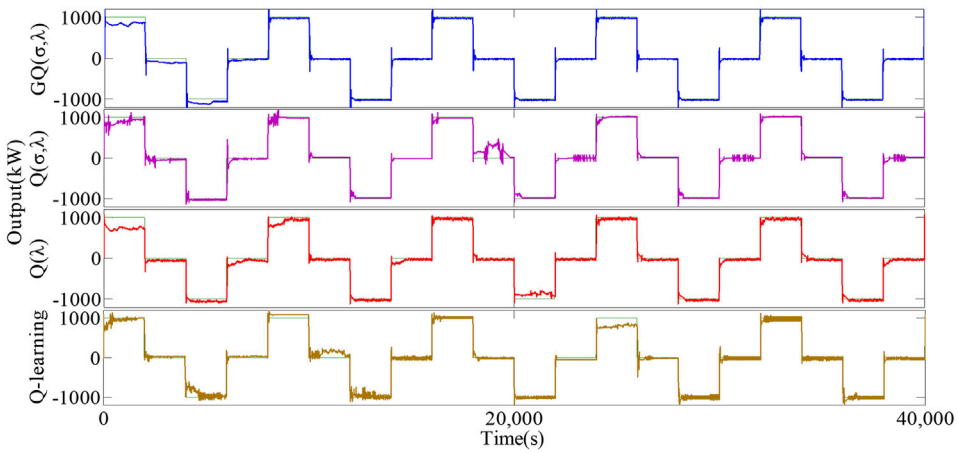

FIGURE 7 | Controller outputs of different algorithms under impulsive disturbance.

A continuous sinusoidal load disturbance with a period of 5,000 s and an amplitude of 1,000 MW is introduced into the two-area LFC model. **Figure 4** shows the prelearning process of the two areas generated by the continuous sinusoidal load disturbance. As shown in **Figures 4A,B**, the GQ (σ,λ) algorithm can track the load disturbance quickly in two areas, and the frequency deviation is far less than the standard value and is relatively stable. The control performance of AGC is evaluated by the average value of CPS1 ($CPS1_{AVE\text{-}10\text{-}min}$) and ACE ($ACE_{AVE\text{-}10\text{-}min}$) every 10 min. As shown in **Figures 4C,D**, the index value of CPS1 in area A is kept in the qualified range of 180–200%, and the value of ACE is kept in the range of -100-0 MW until a stable value is reached. Meanwhile, the index value of CPS1 in area B is kept in the qualified range of 165–200%, and the value of ACE is kept in the range of −160-0 MW until a stable value is reached.

Integrated Energy System

This paper establishes a small-scale integrated energy system model incorporating a large amount of new energy and CCHP, including photovoltaic (PV), wind farm (WF), electric vehicle (EV), small hydropower (SH), micro gas turbine (MT), fuel cell (FC) units. Given the randomness and uncontrollability of PV, WF, and EV, the output models of the three new energy are

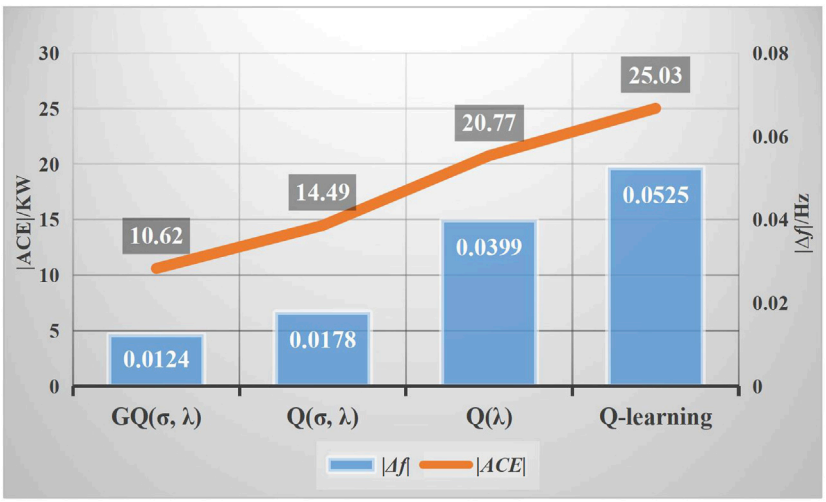

FIGURE 8 | Control performance of different algorithms under impulsive disturbance.

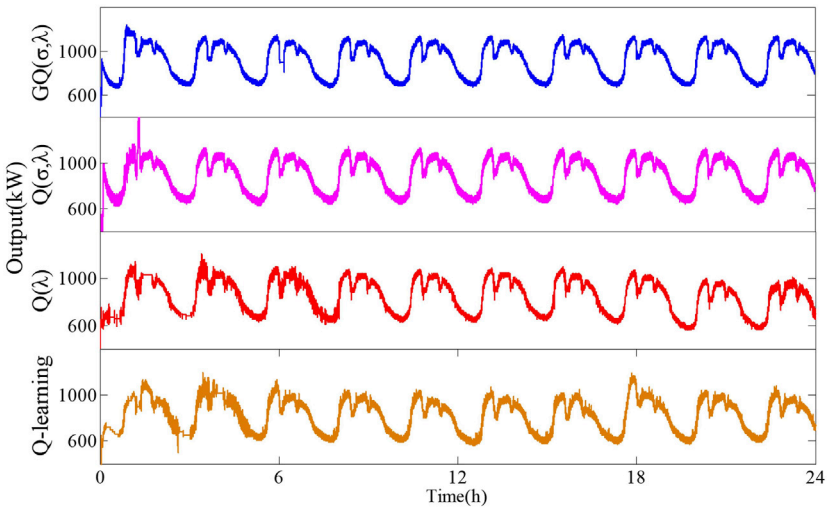

FIGURE 9 | Controller outputs of different algorithms under random white noise disturbance.

TABLE 2 | The data statistics under random white noise disturbance.

Region	Algorithm	|ACE|(kW)	$\|\Delta f\|$(Hz)	CPS1(%)	CE (t/h)
Regional power grid 1	GQ (σ,λ)	16.49	0.0204	196.99	648.8416
	Q (σ,λ)	18.51	0.0313	196.04	674.6462
	Q(λ)	31.83	0.0525	195.28	691.1481
	Q-learning	36.81	0.0819	195.01	703.3316
Regional power grid 2	GQ (σ,λ)	16.72	0.0198	198.73	639.9874
	Q (σ,λ)	20.18	0.0320	197.59	667.6710
	Q(λ)	29.95	0.0571	196.92	682.1672
	Q-learning	39.28	0.0759	196.17	700.7562
Regional power grid 3	GQ (σ,λ)	18.17	0.0215	198.24	651.9782
	Q (σ,λ)	19.94	0.0342	196.12	673.2178
	Q(λ)	28.54	0.0507	195.97	689.7916
	Q-learning	38.07	0.0794	194.18	705.9582

simplified. That is, they are treated as a random disturbance of the AGC system, and do not participate in system frequency regulation. The model structure of the built integrated energy system is shown in **Figure 5**, and the system parameters are selected from the reference (Xi et al., 2020). The total regulated power is 2,350 kW, and each adjustable unit (SH, MT, and FC) is regarded as a different agent. The relevant parameters of each unit in the integrated energy system model are taken from reference (Saha et al., 2008).

The introduced CCHP system is shown in **Figure 6**. This system can realize the complementary and collaborative optimal operation of multiple energy sources (Fang et al., 2012). It uses the waste heat of MT to produce electric energy and meet heating and cooling requirements. The structure of the CCHP system is mainly composed of MT, centrifugal refrigerator device and heat exchange equipment, which is a multi generation energy system integrating heating, cooling and power generation. The purpose is to reduce the emissions of carbides and harmful gases and thereby greatly improve energy efficiency.

Periodic Impulse Load Disturbance

After adequate prelearning, a periodic impulse load disturbance is introduced into the integrated energy system model to simulate the random load disturbance (i.e., regular sudden increase and decrease) in the random environment of power system, so as to analyze the performance of the proposed algorithm. The period of periodic impulse disturbance is 8,000 s, and the amplitude is 1,000 kW.

Under the given impulse load disturbance, the long-term control performance of the GQ (σ,λ) algorithm is evaluated by statistical experimental results within 24 h. At the same time, Q (σ,λ), Q(λ), and Q-learning are introduced to test the control performance of the four control algorithms. **Figures 7**, **8** respectively show the output power curve and control performance of different algorithms under periodic pulse load disturbance. **Figure 7** shows that under the four control algorithms, the actual output of the unit can effectively track the load disturbance. Meanwhile, the GQ (σ,λ) algorithm has a relatively fast convergence speed, and the output power curve is relatively smooth and can thus suitably fit the load disturbance curve. As shown in **Figure 8**, GQ (σ,λ), relative to other control algorithms, can reduce |ACE| by 26.71–57.57% and $|\Delta f|$ by 30.34–76.38%. The result further proves that GQ (σ,λ) has optimal control performance, fast dynamic optimization speed, and strong robustness under load disturbance.

AGC Control Performance Under Random White Noise Disturbance

The random white noise load disturbance is applied to the integrated energy system model to simulate the complex condition in which the power system load changes randomly at every moment in the large-scale grid-connected environment of unknown new energy. The results are expected to verify the application effect of the GQ (σ,λ) algorithm in the strong random grid environment. Similarly, the long-term performance of GQ (σ,λ), Q (σ,λ), Q(λ), and Q-learning algorithms are tested by random white noise disturbance within 24 h.

The controller outputs of the different algorithms under random white noise are shown in **Figure 9**. The GQ (σ,λ) algorithm can follow the load disturbance faster and more accurately than the other three algorithms. The statistical results of the simulation experiments are shown in **Table 2**. Relative to the other algorithms, GQ (σ,λ) can reduce |ACE| by 17.15–57.43%, and $|\Delta f|$ by 38.13–73.91%, CPS1 by 1.14–2.56%, and CE by 4.15–8.67% in regional power grid 2. Moreover, the data analysis reveals that GQ (σ,λ) has the better adaptive ability, better coordinated and optimized control performance, and less carbon emission than the other algorithms.

CONCLUSION

A control framework of an integrated energy system incorporating a large amount of distributed energy and CCHP is built in this paper. A novel GQ (σ,λ) algorithm for a distributed multi-region interconnected power system is also proposed to find the equilibrium solution so as to obtain the optimal cooperative control and solve the problem of strong random disturbances caused by the large-scale grid connection of distributed energy.

The proposed algorithm, which is based on the Q (λ) algorithm and features interactive collaboration and self-learning, adopts linear function approximation and mixed sampling parameter to organically unify full sampling and pure expectation. The GQ (σ,λ) algorithm can reduce the storage space of state-action pairs required by the control algorithm, so as to obtain the distributed multi-region optimal cooperative control quickly.

The improved IEEE two-area LFC model and integrated energy system model with CCHP are used for example analysis. The results show that compared with other algorithms, GQ (σ,λ) has better cooperative control performance and less carbon emission. Moreover, it can solve the random disturbance problem caused by the large-scale access of distributed energy in integrated energy system.

DATA AVAILABILITY STATEMENT

The original contributions presented in the study are included in the article/Supplementary Material, further inquiries can be directed to the corresponding author.

AUTHOR CONTRIBUTIONS

YL: literature review, writing, language editing and proofreading. LZ: mathematical analysis, writing, and simulation. LX: framework formation, and writing. QS: analysis and revised the manuscript. JZ: analysis with constructive discussions.

FUNDING

This work was supported by the National Natural Science Foundation of China (No. 51707102).

REFERENCES

An, Y., Zhao, Z. H. H., Wang, S. K., et al. (2020). Coordinative Optimization of Hydro-Photovoltaic-Wind-Battery Complementary Power Stations. *CSEE J. Power Energ. Syst.* 6 (2), 410–418. doi:10.17775/CSEEJPES.2019.00330

Barto, A. G., and Sutton, R. S. (1998). Reinforcement Learning: An Introduction. *IEEE Trans. Neural Networks* 9 (5), 1054.

Dehnavi, G., and Ginn, H. L. (2019). Distributed Load Sharing Among Converters in an Autonomous Microgrid Including PV and Wind Power Units. *IEEE Trans. Smart Grid* 10 (4), 4289–4298. doi:10.1109/tsg.2018.2856480

Fang, F., Wang, Q. H., and Shi, Y. (2012). A Novel Optimal Operational Strategy for the CCHP System Based on Two Operating Modes. *IEEE Trans. Power Syst.* 27 (2), 1032–1041. doi:10.1109/tpwrs.2011.2175490

Fu, W., Zhang, K., Wang, K., Wen, B., Fang, P., and Zou, F. (2021). A Hybrid Approach for Multi-step Wind Speed Forecasting Based on Two-Layer Decomposition, Improved Hybrid DE-HHO Optimization and KELM. *Renew. Energ.* 164, 211–229. doi:10.1016/j.renene.2020.09.078

Hou, K., Tang, P., Liu, Z., et al. (2021). Reliability Assessment of Power Systems with High Renewable Energy Penetration Using Shadow price and Impact Increment Methods. *Front. Energ. Res.* 9. Article ID 635071. doi:10.3389/fenrg.2021.635071

Ismayil, C., Kumar, R. S., and Sindhu, T. K. (2015). Optimal Fractional Order PID Controller for Automatic Generation Control of Two-Area Power Systems. *Int. Trans. Electr. Energ. Syst.* 25, 3329–3348. doi:10.1002/etep.2038

Jaleeli, N., VanSlyck, L. S., Ewart, D. N., Fink, L. H., and Hoffmann, A. G. (1992). Understanding Automatic Generation Control. *IEEE Trans. Power Syst.* 7 (3), 1106–1122. doi:10.1109/59.207324

Kumar, S., Saket, R. K., Dheer, D. K., Holm-Nielsen, J. B., and Sanjeevikumar, P. (2020). "Reliability Enhancement of Electrical Power System Including Impacts of Renewable Energy Sources: a Comprehensive Review. *IET Generation, Transm. Distribution* 14 10, 1799–1815. doi:10.1049/iet-gtd.2019.1402

Long, Y., Shi, M., Qian, Z., Meng, W., and Pan, G. (2018). "A Unified Approach for Multi-step Temporal-Difference Learning with Eligibility Traces in Reinforcement Learning," in Proceedings of the 27th International Joint Conference on Artificial Intelligence (IJCAI-18), Stockholm, Sweden.

Mukherjee, J. C., and Gupta, A. (2016). Distributed Charge Scheduling of Plug-In Electric Vehicles Using Inter-aggregator Collaboration. *IEEE Trans. Smart Grid* 8 (1), 331–341. doi:10.1109/TSG.2016.2515849

Ray, G., Prasad, A. N., and Prasad, G. D. (1999). A New Approach to the Design of Robust Load-Frequency Controller for Large Scale Power Systems. *Electric Power Syst. Res.* 51 (1), 13–22. doi:10.1016/s0378-7796(98)00125-4

Rummery, G. A., and Niranjan, M. (1994). *On-line Q-Learning Using Connectionist Systems*. Technical Report.

Saha, A. K., Chowdhury, S., and Chowdhury, S. P. (2008). "Modelling and Simulation of Microturbine in Islanded and Grid-Connected Mode as Distributed Energy Resource," in Power & Energy Society General Meeting-conversion & Delivery of Electrical Energy in the Century, Pittsburgh, USA. doi:10.1109/pes.2008.4596532

Seijen, H. V., Hasselt, H. V., Whiteson, S., and Wiering, M. (2009). "A Theoretical and Empirical Analysis of Expected Sarsa," in 2009 IEEE Symposium on Adaptive Dynamic Programming and Reinforcement Learning, Nashville, USA.

Sharma, G., Ibraheem, and Bansal, R. C. (2017). DFIG Based AGC of Power System Using Robust Methodology. *Energ. Proced.* 105, 590–595. doi:10.1016/j.egypro.2017.03.360

Solanki, B. V., Raghurajan, A., Bhattacharya, K., and Canizares, C. A. (2017). Including Smart Loads for Optimal Demand Response in Integrated Energy Management Systems for Isolated Microgrids. *IEEE Trans. Smart Grid* 8 (4), 1739–1748. doi:10.1109/tsg.2015.2506152

Suh, J., Yoon, D.-H., Cho, Y.-S., and Jang, G. (2017). Flexible Frequency Operation Strategy of Power System with High Renewable Penetration. *IEEE Trans. Sustain. Energ.* 8 (1), 192–199. doi:10.1109/tste.2016.2590939

Sun, Q. Y., and Yang, L. X. (2019). From independence to Interconnection-A Review of AI Technology Applied in Energy Systems. *CSEE J. Power Energ. Syst.* 5 (1), 21–34. doi:10.17775/CSEEJPES.2018.00830

Sun, L., Yao, F., and Chai, S. (2016). "Leader-following Consensus for High-Order Multi-Agent Systems with Measurement Noises," in 2016 8th International Conference on Intelligent Human-Machine Systems and Cybernetics, Hangzhou, China (IHMSC). doi:10.1109/ihmsc.2016.175

Wang, T., O'Neill, D., and Kamath, H. (2015). Dynamic Control and Optimization of Distributed Energy Resources in a Microgrid. *IEEE Trans. Smart Grid* 6 (6), 2884–2894. doi:10.1109/tsg.2015.2430286

Wang, S. C. (2020). Current Status of PV in China and its Future Forecast. *CSEE J. Power Energ. Syst.* 6 (1), 72–82. doi:10.17775/CSEEJPES.2019.03170

Watkins, C. J. C. H., and Dayan, P. (1992). Q-learning. *Machine Learn.* 8 (3), 279–292. doi:10.1023/a:1022676722315

Xi, L., Yu, T., Yang, B., and Zhang, X. (2015). A Novel Multi-Agent Decentralized Win or Learn Fast Policy hill-climbing with Eligibility Trace Algorithm for Smart Generation Control of Interconnected Complex Power Grids. *Energ. Convers. Manag.* 103 (10), 82–93. doi:10.1016/j.enconman.2015.06.030

Xi, L., Yu, T., Yang, B., Zhang, X., and Qiu, X. (2016). A Wolf Pack Hunting Strategy Based Virtual Tribes Control for Automatic Generation Control of Smart Grid. *Appl. Energ.* 178, 198–211. doi:10.1016/j.apenergy.2016.06.041

Xi, L., Chen, J., Huang, Y., Xu, Y., Liu, L., Zhou, Y., et al. (2018). Smart Generation Control Based on Multi-Agent Reinforcement Learning with the Idea of the Time Tunnel. *Energy* 153, 977–987. doi:10.1016/j.energy.2018.04.042

Xi, L., Wu, J., Xu, Y., and Sun, H. (2020). Automatic Generation Control Based on Multiple Neural Networks with Actor-Critic Strategy. *IEEE Trans. Neural Netw. Learn. Syst.*, 1–11. in press. doi:10.1109/TNNLS.2020.3006080

Xi, L., Yu, L., Xu, Y., Wang, S., and Chen, X. (2020). A Novel Multi-Agent DDQN-AD Method-Based Distributed Strategy for Automatic Generation Control of Integrated Energy Systems. *IEEE Trans. Sustain. Energ.* 11 (4), 2417–2426. doi:10.1109/tste.2019.2958361

Xi, L., Zhang, L., Liu, J., Li, Y., Chen, X., Yang, L., et al. (2020). A Virtual Generation Ecosystem Control Strategy for Automatic Generation Control of Interconnected Microgrids. *IEEE Access* 8, 94165–94175. doi:10.1109/access.2020.2995614

Xi, L., Zhou, L., Liu, L., et al. (2020). A Deep Reinforcement Learning Algorithm for the Power Order Optimization Allocation of AGC in Interconnected Power Grids. *CSEE J. Power Energ. Syst.* 6 (3), 712–723. doi:10.17775/CSEEJPES.2019.01840

Xi, L., Zhou, L., Xu, Y., and Chen, X. (2021). A Multi-step Unified Reinforcement Learning Method for Automatic Generation Control in Multi-Area Interconnected Power Grid. *IEEE Trans. Sustain. Energ.* 12 (2), 1406–1415. doi:10.1109/tste.2020.3047137

Xie, P., Li, Y. H., Liu, X. J., et al. (2016). Optimal PI/PID Controller Design of AGC Based on Social Learning Adaptive Bacteria Foraging Algorithm for Interconnected Power Grids. *Proc. CSEE* 36 (20), 5440–5448. doi:10.13334/j.0258-8013.pcsee.152424

Xu, D., Zhou, B., Wu, Q., Chung, C. Y., Li, C., Huang, S., et al. (2020). Integrated Modelling and Enhanced Utilization of Power-To-Ammonia for High Renewable Penetrated Multi-Energy Systems. *IEEE Trans. Power Syst.* 35 (6), 4769–4780. doi:10.1109/tpwrs.2020.2989533

Yamashita, K., and Taniguchi, T. (2016). Optimal Observer Design for Load-Frequency Control. *Int. J. Electr. Power Energ. Syst.* 8 (2), 93–100. doi:10.1016/0142-0615(86)90003-7

Yan, W., Zhao, R., and Zhao, X. (2013). Review on Control Strategies in Automatic Generation Control. *Power Syst. Prot. Control.* 41 (8), 149–155.

Yang, L., Zhang, Y., Zheng, Q., et al. (2019). *Gradient Q(σ,λ): A Unified Algorithm with Function Approximation for Reinforcement Learning*. arXiv, 02877.

Yin, L., Yu, T., Zhou, L., Huang, L., Zhang, X., and Zheng, B. (2017). *Transm. Distribution* 11 (9), 2305–2313. doi:10.1049/iet-gtd.2016.1734

Yu, T., and Yuan, Y. (2010). Optimal Control of Interconnected Power Grid CPS Based on R(λ) Learning of the Whole Process of Average Compensation Model. *Automation Electric Power Syst.* 34, 27–33.

Yu, T., Wang, Y., Zhen, W., et al. (2011). Multi-step Backtrack Q-Learning Based Dynamic Optimal Algorithm for Auto Generation Control Order Dispatch. *Control. Theor. Appl.* 28 (1), 58–64.

Yu, T., Zhou, B., Chan, K. W., and Lu, E. (2011). Stochastic Optimal CPS Relaxed Control Methodology for Interconnected Power Systems Using Q-Learning Method. *J. Energ. Eng.* 137 (3), 116–129. doi:10.1061/(asce)ey.1943-7897.0000017

Zhang, X., and Yu, T. (2015). Virtual Generation Tribe Based Collaborative Consensus Algorithm for Dynamic Generation Dispatch of AGC in Interconnected Power Grids. *Proc. CSEE* 35 (15), 3750–3759. doi:10.13334/j.0258-8013.pcsee.2015.15.002

Zhang, D., Han, X. Q., Han, X., and Deng, C. (2018). Review on the Research and Practice of Deep Learning and Reinforcement Learning in Smart Grids. *Csee Jpes* 4 (3), 362–370. doi:10.17775/cseejpes.2018.00520

Zhang, X., Xu, Z., Yu, T., Yang, B., and Wang, H. (2020). Optimal Mileage Based AGC Dispatch of a GenCo. *IEEE Trans. Power Syst.* 35 (4), 2516–2526. doi:10.1109/tpwrs.2020.2966509

Zhang, X., Tan, T., Zhou, B., Yu, T., Yang, B., and Huang, X. (2021). Adaptive Distributed Auction-Based Algorithm for Optimal Mileage Based AGC Dispatch with High Participation of Renewable Energy. *Int. J. Electr. Power Energ. Syst.* 124, 106371. doi:10.1016/j.ijepes.2020.106371

Conflict of Interest: LZ was employed by the company Zigong Power Supply Company, State Grid Sichuan Electric Power Corporation.

The remaining authors declare that the research was conducted in the absence of any commercial or financial relationships that could be construed as a potential conflict of interest.

frontiers in Energy Research

ORIGINAL RESEARCH
published: 17 June 2021
doi: 10.3389/fenrg.2021.688034

Impact of Large-Scale Mobile Electric Vehicle Charging in Smart Grids: A Reliability Perspective

Ping Xue[1], Yue Xiang[1], Jing Gou[2], Weiting Xu[2], Wei Sun[3], Zhuozhen Jiang[4], Shafqat Jawad[1], Huangjiang Zhao[1] and Junyong Liu[1]*

[1]College of Electrical Engineering, Sichuan University, Chengdu, China, [2]State Grid Sichuan Economic Research Institute, Chengdu, China, [3]School of Engineering, University of Edinburgh, Edinburgh, United Kingdom, [4]State Grid Chongqing Shiqu Power Supply Company, Chongqing, China

The charging load of electric vehicles (EVs) is characterized by uncertainty and flexibility, which burdens the distribution network, especially when there is a high penetration of distributed generation (DG) in smart grids. Large-scale EV mobility integration not only affects smart grid operation reliability but also the reliability of EV charging services. This paper aims at estimating the comprehensive impacts caused by spatial-temporal EV charging from the perspective of both electricity system reliability and EV charging service reliability. First, a comprehensive reliability index system, including two novel indexes quantifying EV charging service reliability, is proposed. Then, considering traffic constraints and users' charging willingness, a spatial-temporal charging load model is introduced. In the coupled transportation and grid framework, the reliability impacts from plenty of operation factors are analyzed. Moreover, the electricity system reliability and EV charging service reliability correlated with DG integration are discussed. A coupled transportation grid system is adopted to demonstrate the effectiveness and practicability of the proposed method. The numerical results analyze reliability impacts from EV penetration level, trip chain, EV battery capacity, DG installation location, and capacity. The proposed studies reveal that when the EV capacity ratio to DG capacity is 3:1, the system reliability reaches the maximum level.

Keywords: electric vehicle integration, electricity system reliability, transportation network, distributed generation, electric vehicle charging service reliability

OPEN ACCESS

Edited by:
Chenghong Gu,
University of Bath, United Kingdom

Reviewed by:
Feifei Bai,
The University of Queensland, Australia
Xiaohe Yan,
North China Electric Power University, China
Shenxi Zhang,
Shanghai Jiao Tong University, China

****Correspondence:***
Yue Xiang
xiang@scu.edu.cn

Specialty section:
This article was submitted to Smart Grids, a section of the journal Frontiers in Energy Research

Received: *30 March 2021*
Accepted: *06 May 2021*
Published: *17 June 2021*

Citation:
Xue P, Xiang Y, Gou J, Xu W, Sun W, Jiang Z, Jawad S, Zhao H and Liu J (2021) Impact of Large-Scale Mobile Electric Vehicle Charging in Smart Grids: A Reliability Perspective. Front. Energy Res. 9:688034. doi: 10.3389/fenrg.2021.688034

HIGHLIGHTS

1) Impacts on reliability are studied from the perspective of both electricity system and EV charging service.
2) A spatial-temporal simulation strategy for mobile EV charging load is proposed.
3) A coupled transportation and grid framework is used for reliability assessment.
4) Reliability impacts from EV penetration level, trip chain, EV battery capacity, DG installation location and capacity are quantified.

INTRODUCTION

The problems of carbon emissions and energy shortage have been increasingly serious nowadays, which has captured people's attention on sustainable and clean energy. Thus, the application of

electric vehicles (EVs) has attracted much attention recently (Shafiee et al., 2013; Veldman and Verzijlbergh, 2015; Patil and NagoKalkhambkar, 2021). According to an industry report forecast, sales for EVs in 2021 will be between 1.8 and 2 million, of which more than 80% will be private cars. Moreover, several countries, such as China, Japan, America, Germany, etc., provide lavish subsidies to EV users to promote the development of electric vehicles. For instance, Germany provided up to 1.2 billion euros of subsidies to individual EV users. In addition, the construction of charging infrastructure has also caused broad concern. It is predicted that, in China, by the end of 2021, the number of public charging piles will exceed 1.15 million, while the number for the private will be close to 1.5 million. And for battery swapping stations, the number will approach 1,000. Hence, EV penetration in smart grids is increased significantly. However, while environmental stress is relieved due to EV high penetration in smart grids, the potential risk of electricity system operation is also increased as EVs are charged stochastically based on traffic constraints and users' subjective willingness. This problem will be even more serious with the increasing penetration of distributed generation (DG) whose output power is also uncertain. On the other hand, with the large scale of EV integration, the reliability of EV charging services cannot be ignored as well. For EV users, the purpose of their charging behavior is to guarantee their own demand, while they are also an important part of electricity load. Hence, electricity system reliability and EV charging service reliability may conflict sometimes. However, there is still relatively little research on this field. As a result, impacts of EV integration on the coupled system considering EV spatial-temporal mobile charging should be investigated to make a trade-off between electricity system reliability and charging service reliability and to obtain a strategy for EV and DG coordination operation.

The transportation network and distribution network are closely coupled and interacted due to EV charging and movement. An integrated traffic-power framework proposed in Xiang et al. (2018) described the interactions between the evolution coherence of EV charging load and traffic flow. Reference Acha et al. (2010) discussed the impacts of different EV charging strategies on distribution system energy losses, which showed that distribution system operation can be optimized by EV coordination. Reference Sun et al. (2020) proposed a day-ahead robust, cost-minimizing scheduling strategy for EV overnight charging in low voltage distribution networks. In Hoog et al. (2015), EV charging was formulated as a linear optimization problem considering distribution network constraints, such as transformer capacity, voltage, and current magnitude limits. A mixed-integer linear programming model for EV coordinate charging in unbalanced distribution networks was presented in Franco et al. (2015), considering loads imbalance and three-phase circuits. However, traffic characteristics were not considered in the process of EV charging load modeling in these works, which was not in accordance with the load characteristics of EVs.

As participants in both urban transportation networks and distribution networks, characteristics of EV mobile charging load are closely associated with users' travel habits and traffic constraints. Furthermore, the larger the scale of EV integration, the tighter the correlation among different participants. On this basis, some scholars have studied how to model transportation characteristics accurately. In Xiang et al. (2016), the siting and sizing of EV charging stations were discussed considering traffic constraints. In Luo et al. (2020a), an EV charging strategy was proposed considering traffic speed and EV numbers in charging stations. A mathematical model of EV charging demand was introduced in Xia et al. (2019), where some important factors were considered, such as seasons, travel patterns, and traffic congestion. In Su et al. (2020), a novel control method was proposed to control imbalanced feeder power on EV flexible charging. In Xiang et al. (2019), existing EV charging modeling methods were summarized from the temporal and spatial dimension perspectives. On this basis, a scale EV evolution model of charging load was introduced in Xiang et al. (2019). In Ding et al. (2020), a multiperiod restoration model for distribution networks considering the coordination of mobile EVs, routing repair crews, and microgrids was proposed, which showed that EV could help with restoration during a system outage. Reference Su et al. (2019) investigated distribution network planning problems with aggregated EV charging, which took into account EV charging behavior and driving patterns. In Manbachi et al. (2016), impacts of EV integration with different penetration on quasi Volt-VAR Optimization in distribution networks were evaluated, where EV types, mixes, and ZIP modeling were illustrated to model EV and loads. But it was ignored in these studies that EV charging was stochastic, being based on users' own charging willingness to a great extent.

The existing research evaluates the impacts of electric vehicle integration on system reliability which is generally analyzed in terms of electricity system reliability. In contrast, the reliability of EV charging services is rarely discussed. In Cheng et al. (2020), considering spatial-temporal EV charging load predicting, the reliability of the distribution network was evaluated with large-scale electric vehicle integration. In Xu and Chung (2016), evaluation of the distribution network reliability was extended considering EVs' operation in different modes, including vehicle-to-home and vehicle-to-grid. Reference Sadeghian et al. (2019) analyzed the reliability impact of radial distribution systems considering demand response and EVs' flexible charging and discharging. A probabilistic reliability assessment method was introduced in Anand et al. (2020) to evaluate the effect of stochastic EV charging power on distribution network reliability. In Guner and Ozdemir (2020), reliability enhancement of distribution network was analyzed considering storage capacity of electric vehicles parking lots. The potential of battery-exchange stations in improving distribution system reliability was investigated in Farzin et al. (2016), where the conclusion that system reliability could be notably improved based on the location of the battery-exchange station was obtained. In Huang et al. (2020), a data-driven reliability evaluation method was proposed to quantify EV penetrated system reliability employing slice sampling and diffusion estimator. However, in these studies the reliability of the electricity system was studied while EV charging service

reliability was ignored, which is impractical since the basic purpose of EV charging is to ensure users' own charging demand. In Meng et al. (2021), optimal planning for EV charging infrastructure was introduced to maximize both distribution network and EV charging service reliability. Although EV charging service reliability was considered in Meng et al. (2021), it was based on EV users' traveling reliability rather than considering the reliability of EV charging power.

The impacts of distributed generation (DG) integration on urban distribution networks cannot be ignored for its intermittent and uncertain power characteristics Xiang et al. (2020). When DG penetration in the grid reaches a certain level, conventional generator capacity will be less than the total load capacity (Ge and Wang, 2013). In this case, the uncertainty of DG output may lead to a system outage, particularly when large-scale electric vehicle charging has occurred in the system. A DG planning model taking into account network reconfiguration and demand-side management was proposed in Zhang et al. (2018). In Cui et al. (2019), collaborative planning of distribution network and distributed generation was introduced, considering the flexible operation of heat pump load. Reference Das et al. (2020) analyzed the impacts of DG integration on optimal reactive power dispatch. In Luo et al. (2020b), an optimization model to determine the coordinated allocation of EV charging stations and DG was proposed. In Colmenar-Santos et al. (2019), a charging strategy was designed to increase DG penetration in the electricity system by electric vehicle dispatching. Impacts of EV integration on wind-thermal electricity systems were explored in Göransson et al. (2010) to reduce carbon emissions. An optimal bidding strategy considering plug-in EVs and DG was proposed to maximize microgrids and distribution system profits in Bostan et al. (2020), where coordination of energy resources was also optimized for system contingency. In Luo et al. (2019), an optimization model for joint locating and sizing of EV charging infrastructure and DG was presented taking into account real-time charging navigation. But it cannot be ignored that the coordination operation of EV and DG may lead to system instability since the power was stochastic for both. Reliability impacts of DG and EV operation in coordination on smart grids should be analyzed.

Considering insufficiency in these studies, the reliability impacts of large-scale mobile EV integration on electricity system-based sequential Monte Carlo method are discussed in this paper. The main contributions of this paper are as follows:

1) A comprehensive reliability assessment method that quantifies both electricity system reliability and EV charging service reliability is proposed. Two novel indexes aiming to quantify EV charging power reliability are put forward to evaluate the curtailing extent of charging energy in each bus and analyze the charging energy not supplied from a holistic perspective.
2) A spatial-temporal mobile EV charging load model based on the vehicle-transportation-grid trajectory is proposed considering EV traffic characteristics and users' charging willingness. In the coupled transportation and grid framework, reliability impacts considering plenty of operation factors are comprehensively analyzed.
3) Reliability impacts of DG integration on the grid with large-scale mobile EV deployment are quantified. The coordinated operation strategy of EVs and DG is discussed as well. DG installation locations can be selected to coordinate the reliability level of the distribution system and EV charging service. Moreover, the optimal DG capacity configuration, which brings the highest system reliability level, is provided.

The rest of this paper is organized as follows: in *Mobile Electric vehicle Charging Load Modeling*, spatial-temporal mobile EV charging load modeling is introduced; the reliability evaluation method for both system and EV charging service-based sequential Monte Carlo is proposed in *Reliability Assessment*; *Framework* provides a detailed description of the research framework employed in this paper; Numerical simulations about coupled system reliability with EV mobility and DG integration are performed in *Case Study*; and *Conclusion* draws some conclusions.

MOBILE ELECTRIC VEHICLE CHARGING LOAD MODELING

As an uncertain load coupling transportation system and distribution system, EVs should be modeled spatially and temporally. In this section, EV mobile trajectory is formulated first based on a trip chain and Dijkstra algorithm. Then flexible charging of EV is modeled, including EV trip time, SOC consumption, charging mode selection, and users' charging willingness.

Electric Vehicle Mobile Trajectory Modeling

EV charging load is different from conventional load due to its traffic characteristics. EV traveling starting point, destination, traveling distance, and users' habits will influence the charging behavior. Considering transportation constraints, EV state of charge (SOC) is determined through its travel trajectory. As a result, transportation topology should be modeled first. In this paper, graph theory is employed for bidirectional transportation network modeling (Tang and Wang, 2016). In graph theory, a set of vertices are linked by the corresponding disjoint edges, while the roads are modeled by the edges, and transportation system nodes are modeled via the set of vertices.

After transportation topology is obtained, EV mobile behavior should be modeled. The mobile behavior of EV users can be understood as a spatial and temporal interacting process, normally starting from one certain point and finally arriving at the destination, which can be simply categorized into three basic aspects: work, entertainment, and residence. A trip chain is usually utilized to reflect EV dynamic travel characteristics (Liang et al., 2020) and is therefore employed in this paper to provide a better description of user's travel patterns.

Assuming every trip starts at home, and after staying in several places, i.e., workplaces, EV users eventually return to home. Then trip chains are obtained to simulate EV users traveling behaviors depicted in **Figure 1**. The set of trip chains are described in **Table 1** as follows:

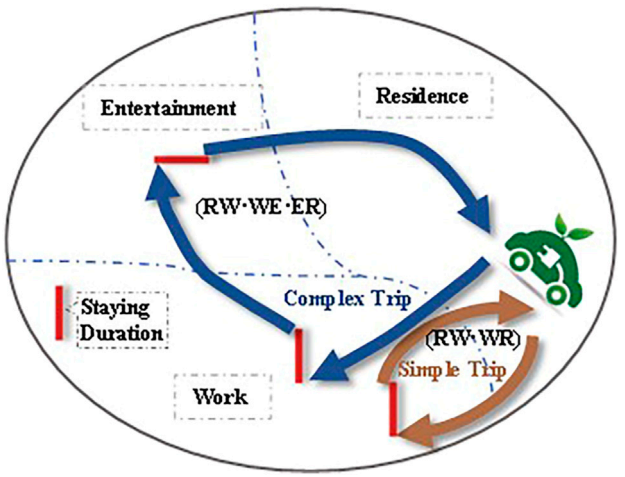

FIGURE 1 | EV traveling trajectory with two types of trip chains.

TABLE 1 | Trip chain of EVs.

C	C_1	C_2		
	RW•WR	RW•WE•ER	RE•EW•WR	RR•RW•WR
	RR•RR	RW•WR•RR	RE•ER•RR	RR•RE•ER
	RE•ER	RW•WW•WR	RW•EE•ER	RR•RR•RR

$$C = \{C_1, C_2\} \tag{1}$$

where C represents the whole set of trip chains; C_1 represents the simple chain which means there is only one activity during the trip; accordingly, C_2 represents the complex chain, which means that more than one activity has occurred during the trip; R represents the residence area; W is the work area, and E is for an entertainment area.

The Dijkstra algorithm proposed by Dijkstra in 1959 is a common algorithm to find the shortest path from a point to any other point in graph theory (Dijkstra, 1959). Assuming EV users will travel in the shortest path to save time and energy. Then specific traveling path is obtained based Dijkstra algorithm when the trip starting point and destination are determined.

Electric Vehicle Charging Load Predicting

In this section, EV traveling state, including traveling time and SOC consumption is modeled. As a flexible charging load, users' charging willingness and charging pattern are also discussed.

Electric Vehicle Traveling State Modeling

According to the statistics of the UK Ministry of Transport in 2016 (Li et al., 2019), the traveling time can be fitted to a normal distribution, which can be seen as follows:

$$f(t;\mu,\sigma) = \frac{1}{\sigma\sqrt{2\pi}}\exp\left(-\frac{(t-\mu)^2}{2\sigma^2}\right) \tag{2}$$

where μ is the expected value of EV traveling time; σ is the standard deviation; and μ and σ are trip chain type and traveling points respectively.

Then EV parking time and restarting time can be calculated based on EV traveling speed:

$$T^i_{Road} = \sum_{road=1}^{W} \frac{S_{road}}{V_{E_{road}}} \tag{3}$$

$$T^i_{park} = T^i_{start} + T^i_{Road} \tag{4}$$

$$T^{i+1}_{start} = T^i_{park} + T^i_{stay} \tag{5}$$

where T_{Road} is the traveling duration in the ith trip; W is the nodes number that the ith trip includes; $Sroad$ is the road length; $V_{E_{road}}$ represents the traveling speed; T_{park} is the point of parking time; T_{start} is the point of starting time of next trip; T_{stay} is the staying duration in the destination of the ith trip.

If EV is charged during the trip, then **Eq 4** can be corrected:

$$T^i_{park} = T^i_{start} + T^i_{Road} + T^i_{mid} \tag{6}$$

where T_{mid} is the midway charging duration in the ith trip.

SOC of EV is dependent on users driving length. If SOC is lower than its threshold value after a driving distance, then EV should be charged to ensure the next trip ends successfully. Thus, making sure SOC be able to support the next trip for each period is essential. Assuming that SOC is decreased linearly with the increase of traveling distance, SOC at one certain point during the trip can be calculated as follows:

$$SOC^i_{T_{park}} = SOC^i_{T_{start}} - \frac{\sum_{Road=1}^{W} S_{Road} \times b}{Cap} \tag{7}$$

where $SOC^i_{T_{park}}$ is the SOC after arriving at a destination; $SOC^i_{T_{start}}$ is the initial SOC during the trip; b is the power consumption per mileage; Cap is the EV battery capacity.

User Charging Pattern Modeling

Before EV charging mode selection, users should decide whether EV should be charged first. Based on the current SOC, the EV traveling distance that can be supported before reaching the threshold is formulated as follows:

$$S^{SOC_m} = \frac{\left(SOC^i_{T_{start}} - SOC_m\right) \times Cap}{b} \tag{8}$$

where SOC_m is the SOC threshold value.

If the following formula is met, then the n_f th node is the midway charging node:

$$0 < S^{SOC_m} - \sum_{road=1}^{W} S_{road} < \xi \tag{9}$$

where ξ is a prespecified value.

Naturally, the duration for midway charging can be calculated as follows:

$$T_{mid} = \frac{1 - SOC^{i}_{T_{start}} + b \times \left(\sum_{road=1}^{n_f} S_{road} \right) \Big/ Cap}{Power} Cap \tag{10}$$

where *Power* is the charging power based on the charging pattern.

However, considering users charging willingness, sometimes EV will still be charged even though the current SOC can support the next trip. In this case, users will choose to charge or not based on business urgency, or their behavioral habits, etc. Consequently, a user charging demand model is adopted in this paper to describe the charging probability based on fuzzy theory (Liu et al., 2018a). Define DEG_{SOC} as the index to measure the sufficiency extent of SOC for the next trip:

$$DEG_{SOC} = \frac{SOC^{i}_{T_{park}} \times Cap}{b \times S^{i+1}} \tag{11}$$

where S^{i+1} is the traveling distance for the next trip.

Then, the membership function $M(DEG_{SOC})$ representing the fuzzy set of charging willingness is formulated as follows:

$$M(DEG_{SOC}) = \begin{cases} 0, & DEG_{SOC} \geq X \\ 1, & DEG_{SOC} \leq Y \\ \frac{1}{2}\left\{1 + \sin\left[\frac{\pi}{X - Y}\left(\frac{X + Y}{2} - DEG_{SOC}\right)\right]\right\}, & Y < DEG_{SOC} < X \end{cases} \tag{12}$$

where X is the fuzzy coefficient. When the value of DEG_{SOC} is bigger than X, it means that SOC is adequate, and there is no need for charging; Y is the elastic coefficient. If DEG_{SOC} is smaller than Y, the next trip cannot be supported based on the current SOC. As a result, when DEG_{SOC} is between X and Y, users have the willingness to charge. The closer to X the value is, the weaker the charging demand is, and vice versa. The value of M ranges from 0 to 1.

After users decide to charge for EV, then the charging pattern should be discussed. EV users usually charge for EV at night when a full-day trip ended, as they should be prepared for the next day's trip, and electricity price in the evening is generally lower than during the day. For the charging mode, a slow-charging mode is preferred at night when there is enough time for the charging since frequent fast charging may accelerate battery aging. For other situations, the charging pattern should be analyzed. If SOC cannot be charged to the full state through slow-charging mode during the parking time, the fast-charge mode should be adopted, which can be expressed as follows:

$$\frac{Power_{slow} \times T^{i}_{stay}}{Cap} < 1 - SOC^{i}_{T_{park}} \tag{13}$$

where $Power_{slow}$ is the slow-charging power.

RELIABILITY ASSESSMENT

As the mobile EV charging load model proposed is time-dependent and the system state is continuously changed, the sequential Monte Carlo simulation is adopted in this paper to evaluate electricity system reliability (Sankarakrishnan and Billinton, 1995). In the process of composite reliability evaluation, the optimization with the objective of minimum load curtailment is performed:

$$Load_{shed} = \min \sum_{j=1}^{N_L} E_j \tag{14}$$

subject to

$$\begin{gathered} P_{inj} + E - P_{LD} = 0 \\ Q_{inj} + E_Q - Q_{LD} = 0 \\ \underline{P_G} \leq P_G \leq \overline{P_G} \\ \underline{Q_G} \leq Q_G \leq \overline{Q_G} \\ \underline{V} \leq V \leq \overline{V} \end{gathered} \tag{15}$$

where E_j is the load shedding in bus j; N_L is the number of distribution system load buses; P_{inj} and Q_{inj} are the vectors of active and reactive power injections respectively; E and E_Q are the vectors of corresponding active and reactive load curtailment; P_{LD} and Q_{LD} are the vectors of active and reactive power loads; P_G and Q_G are the vectors of active and reactive generating power and $\underline{P_G}$, $\overline{P_G}$, $\underline{Q_G}$, and $\overline{Q_G}$ are the vectors of their power limits respectively; V is the vector of bus voltage magnitude; and $\underline{V}$ and $\overline{V}$ are the vectors of corresponding limits.

In this part, three common reliability indexes to capture interruption duration, frequency, and load curtailment are introduced. In addition, two novel indexes aiming at EV charging service reliability are proposed to complement the existing indexes. All indexes are calculated based on sequential Monte Carlo simulation.

Reliability Indexes Calculation

For the distribution system, reliability indexes of SAIFI (system average interruption frequency index), SAIDI (system average interruption duration index), and EENS (expected energy not supplied) are adopted to perform reliability assessment, which can be calculated as **Eqs 16–18**. Additionally, two reliability indexes aiming at describing EV stochastic characteristics, i.e., POCCE (percentage of curtailed charging energy) and CENS (charging energy not supplied), are proposed to quantify EV charging service reliability. The two indexes are proposed from the perspective of EV charging power reliability. For POCCE, it is put forward to evaluate the curtailing extent of charging energy in each bus, which shows weaknesses of the charging service system. It should be noticed that in some charging points the value of POCCE is quite large while the total charging power is low. However, it still should be valued as EV charging service reliability is aimed at every EV user charging satisfaction not the charging reliability in society. For CENS, similar to distribution system index EENS, it is proposed to analyze the charging energy not supplied as a whole. It is assumed that when a system outage has occurred, EV charging load is considered to be curtailed first. Consequently, CENS can be regarded as a part of EENS. The calculation formulas are presented as follows:

$$SAIFI = \frac{\sum_{i_c=1}^{N_c} \sum_{j=1}^{N_L} f^{j}_{i_c} u_j}{N_Y \sum_{j=1}^{L} u_j} \tag{16}$$

$$SAIDI = \frac{\sum_{i_c=1}^{N_c}\sum_{j=1}^{N_L} T^j_{down\_i_c} u_j}{N_Y \sum_{j=1}^{N_L} u_j} \tag{17}$$

$$EENS = \frac{\sum_{i_c=1}^{N_c}\sum_{j=1}^{N_L} E^j_{i_c} \times T^j_{down\_i_c}}{N_Y} \tag{18}$$

$$POCCE = \frac{\sum_{i_c=1}^{N_c} EV^j_{i_c}}{\sum_{i_f=1}^{N_f} EVload^j_{i_c}} \times 100\% \tag{19}$$

$$CENS = \frac{\sum_{i_c=1}^{N_c}\sum_{j=1}^{N_L} EV^j_{i_c} \times T^j_{down\_i_c}}{N_Y} \tag{20}$$

where N_c is the number of simulated cycles, where each cycle including an outage period $T^j_{down\_i_c}$ and a working period $T^j_{up\_i_c}$; N_f is the number of the outage periods; N_Y is the simulation year; u_j is the number of users in load bus j; $f^j_{i_c}$ is the interruption frequency in bus j; $E^j_{i_c}$ is the load curtailment; $EVload^j_{i_c}$ is the EV charging load; $EV^j_{i_c}$ is the curtailment of EV charging load. It should be noticed that $EV^j_{i_c}$, which refers to EV charging load shedding, is included in $E^j_{i_c}$.

Reliability Evaluation Based Sequential Monte Carlo Simulation

Components faults in the distribution network are relevant to environmental and operational factors. Different factors, such as service time, production defects, temperature, etc., can lead to component fault with a specified probability (Spinato et al., 2009). The faults can be considered an independent component to be modeled as a Markovian component with two states, up and down (Sulaeman et al., 2017).

Assuming that the duration of components in each state obeys an exponential distribution, the random state of the system is obtained by combining the operation states of components. Additionally, the electricity system reliability index is calculated based on the optimal power flow (OPF) solved by MATPOWER. Specific steps of the reliability assessment based on sequential Monte Carlo are as follows:

1) Set up the initial system state and input the original data, including grid topology, power load, charging load, power generation, etc.
2) According to the failure rate and repair rate of components, the time series state of components is extracted, and the component state matrix is generated. The duration of down and upstate is obtained as follows:

$$T^j_{down\_i_c} = -\frac{1}{\mu_j}\ln N_{rand} \tag{21}$$

$$T^j_{up\_i_c} = -\frac{1}{\lambda_j}\ln N_{rand} \tag{22}$$

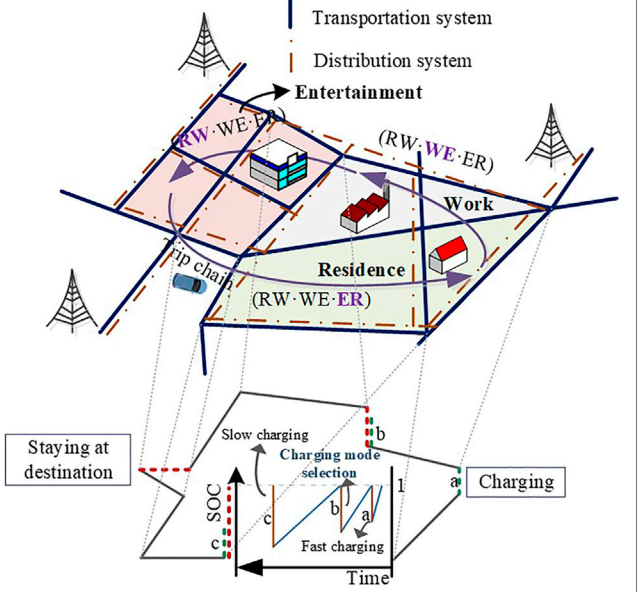

FIGURE 2 | Coupled system framework based spatial-temporal mobile EV charging.

where μ_j and λ_j are the repair state and failure state respectively; N_{rand} is a random number evenly distributed between 0 and 1.

3) According to the component state matrix, the optimal power flow is calculated when a component failure occurred. If part of the load is curtailed, the system is considered in a failure state. Based on the simulation results, the reliability indexes are calculated based on **Eqs 16–20**.
4) In the process of sequential Monte Carlo evaluation, a stopping criterion is adopted when calculated parameters during the simulation are tended to be stable, which can be seen as **Eq 23**. If the inequation is met, the simulation stops.

$$\beta = \frac{\sqrt{V\left(\beta_{n_{MC}}\right)}}{E\left[\beta_{n_{MC}}\right]} \le \varepsilon \tag{23}$$

where β is the variation coefficient; E[·] is the expectation function; $\beta_{n_{MC}}$ is the reliability index (such as EENS) after n_{MC} simulation cycles; V(·) is the variance function; ε is a predetermined tolerance.

FRAMEWORK

In this section, the overall framework of the proposed method is introduced. The coupled system framework-based spatial-temporal EV charging mobility is shown in **Figure 2**. The upper half part of the figure is the coupled transportation and distribution system, while the lower half is EV mobile trajectory-based "RW•WE•ER" trip chain and its corresponding SOC variation. Letter "a" represents the fast-charging mode adopted for midway charging during the trip in

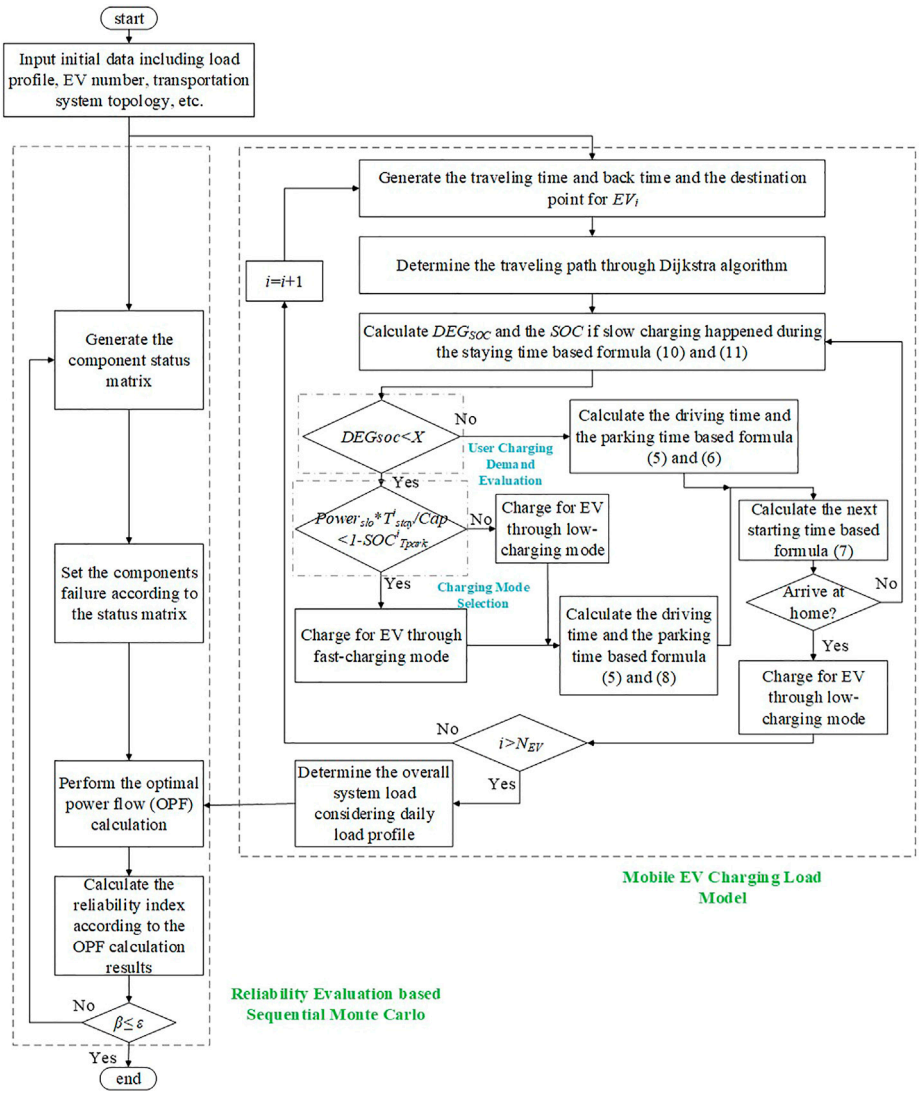

FIGURE 3 | Flowchart of reliability evaluation considering spatial-temporal EV charging load.

Figure 2. After the EV user gets home (the destination of the third trip), the EV is charged through low-charging mode as the letter "c" shows. Letter "b" means charging mode should be determined based on **Eqs 12**, **13**. As can be seen, the users prefer to charge for EV at the destination of the first trip rather than the second trip.

Solution steps of the proposed method are shown in **Figure 3**, which are divided into two parts: the mobile EV charging load modeling and the reliability evaluation based on sequential Monte Carlo.

For the first part, the spatial-temporal EV charging load is modeled. Firstly, EV traveling starting time and back time are obtained according to a normal distribution. Then, the EV traveling path is obtained through the trip chain and Dijkstra path search algorithm. Considering EV users' charging willingness, **Eqs 12**, **13** are calculated to decide whether to charge for EV or not during the trip. If EV users choose to charge, the slow-charging mode is preferred first. However, the fast-charging mode is chosen if SOC cannot be charged to the full state through slow charging mode during the staying time. When EV users get home, EVs will be charged through low-charging mode due to factors such as preparation for the next trip, lower electricity price, etc. The spatial-temporal EV charging load can be obtained when the whole EV time-space trajectory simulation is accomplished.

After EV charging load modeling, the total system load can be determined by combining the initial system load and EV charging load. The components are modeled as the Markovian components with two states, up and down. The optimal power flow (OPF) calculation is performed to obtain the system state with the minimum load shedding. If load curtailment occurs, the system state is identified as a failure. According to the OPF results, the reliability indexes are calculated. Repeat these steps until solutions are converged.

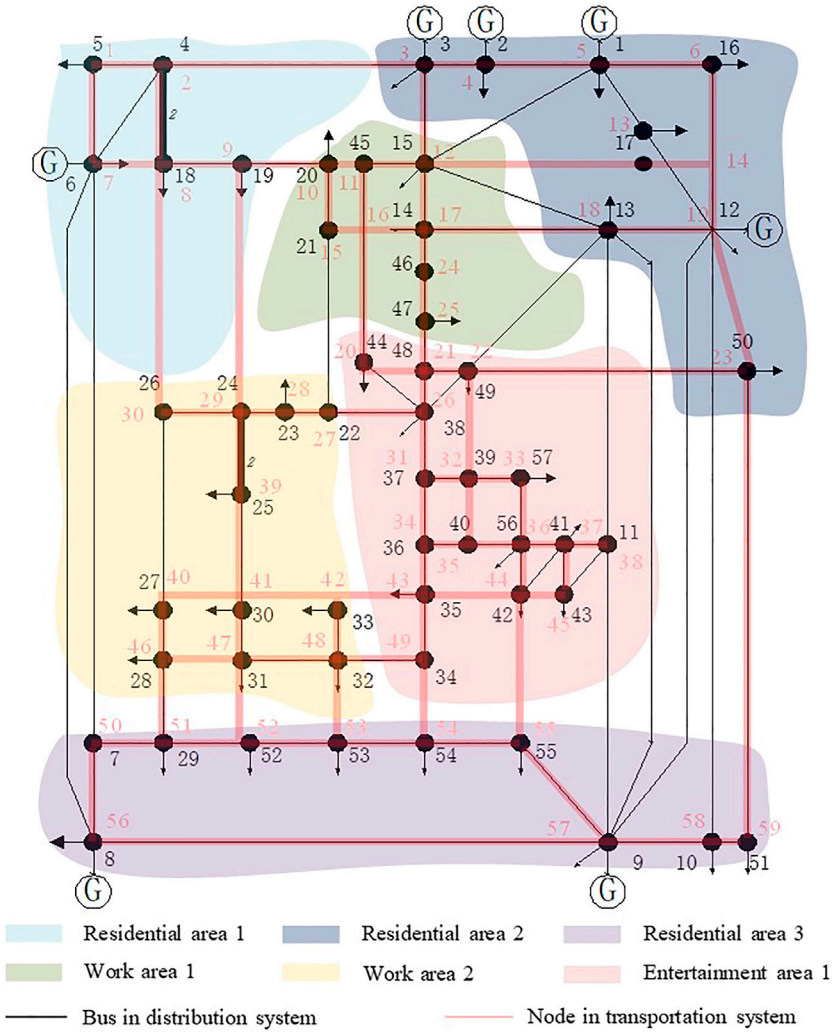

FIGURE 4 | Coupled system of distribution and transportation network.

CASE STUDY

In this section, simulations based on the IEEE 57-node test system and a coupled transportation system are performed. EV spatial and temporal characteristics are analyzed first. Then system reliability is deeply evaluated based on different EV penetration levels, trip chain, EV battery capacity, DG integrating location, and capacity.

Simulation Settings

The topology of coupled IEEE 57-bus system and 59-node transportation system is depicted in **Figure 4**. In the distribution system, there are 80 branches, seven generators, and 57 buses containing 42 load buses. The number of total users is 932. As for the transportation system, it is divided into six areas: three residential areas, two work areas, and one entertainment area. The matching nodes of the transportation system and the distribution system buses are shown in **Supplementary Appendix Tables A–C**. Moreover, the length of each road is illustrated in **Supplementary Appendix Table D**.

For the parameters of EVs, the battery capacity of each EV is set to be 30 kWh, and the fast-charging power and low-charging power are 20 and 6 kW, respectively. The whole generator capacity is 1976 MW in the 57-bus system. It is defined that the penetration level of EV is the ratio of the fast charging power of the whole fleet to the total generator capacity. For example, a 10% penetration level means there are 9800 EVs in the coupled system (Cheng et al., 2013). Private EV is adopted as the analysis object in this paper as the traveling mode of private cars is more flexible. The parameters of X and Y are set to 2 and 1.2 respectively.

The sequential Monte Carlo method is adopted in this paper, and the step size of the sequential simulation is set to 15 min. The failure rate of the feeder is set to 0.002, and the repair rate is 0.25. The failure of the generator is not considered. Virtual generators that have high generating and operation costs are connected to load buses to calculate load curtailment. The daily load profile data is obtained from Ge et al. (2014).

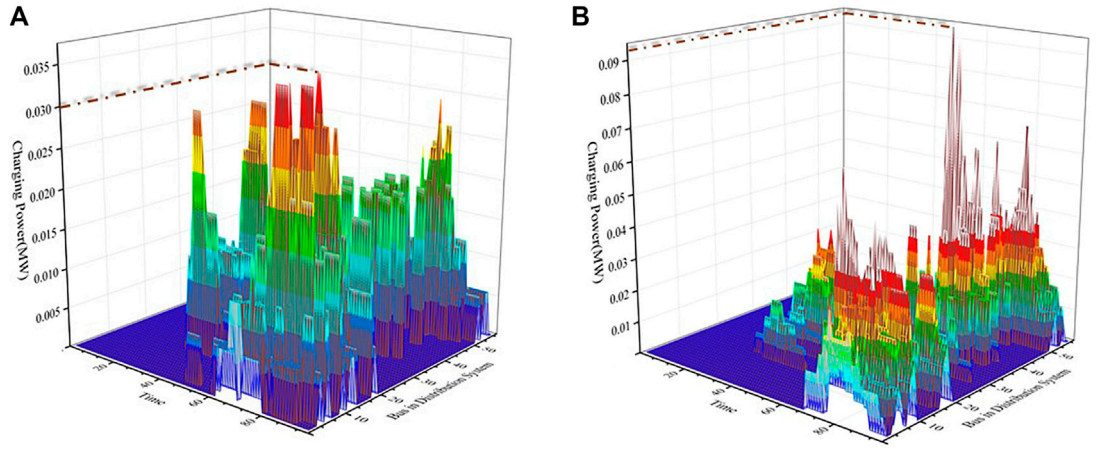

FIGURE 5 | Daily EV charging load in resting and working day.

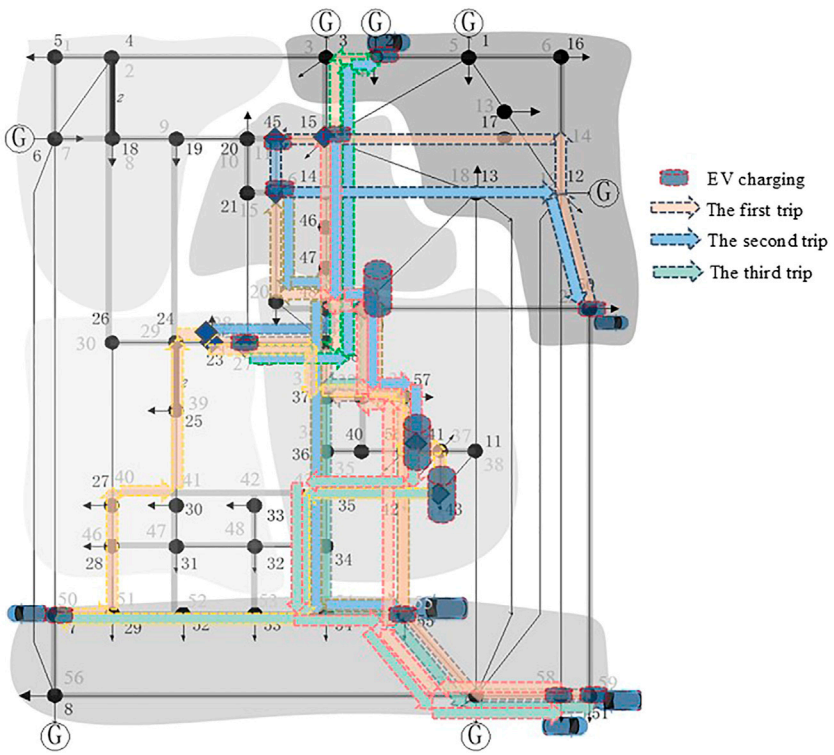

FIGURE 6 | Description of EVs' traveling trajectory and charging demand.

Electric Vehicle Spatial-Temporal Simulations

Charging load simulation for a working day and a resting day is performed in this section to evaluate the difference of charging load in different typical days. Assuming in a working day, simple trip chain accounts for 40%, and complex trip chain accounts for 60%. For resting day, 40% of people will choose to rest at home, and the complex and straightforward trip chain accounts for 50 and 10%, respectively. The charging load of 200 electric vehicles in working day and resting day are simulated, respectively, as shown in **Figure 5**.

It can be seen in **Figure 5** that the EV charging load on the working day is much bigger than the one on the resting day, where the peak value of working-day charging power is triple that of the resting day. In addition, for both resting and working days, the time from 7:30 to 10:30 and 16:00 to 23:00 are high-demand charging periods. Moreover, different from the resting days, the charging demand is heavy in the evening, as people will often

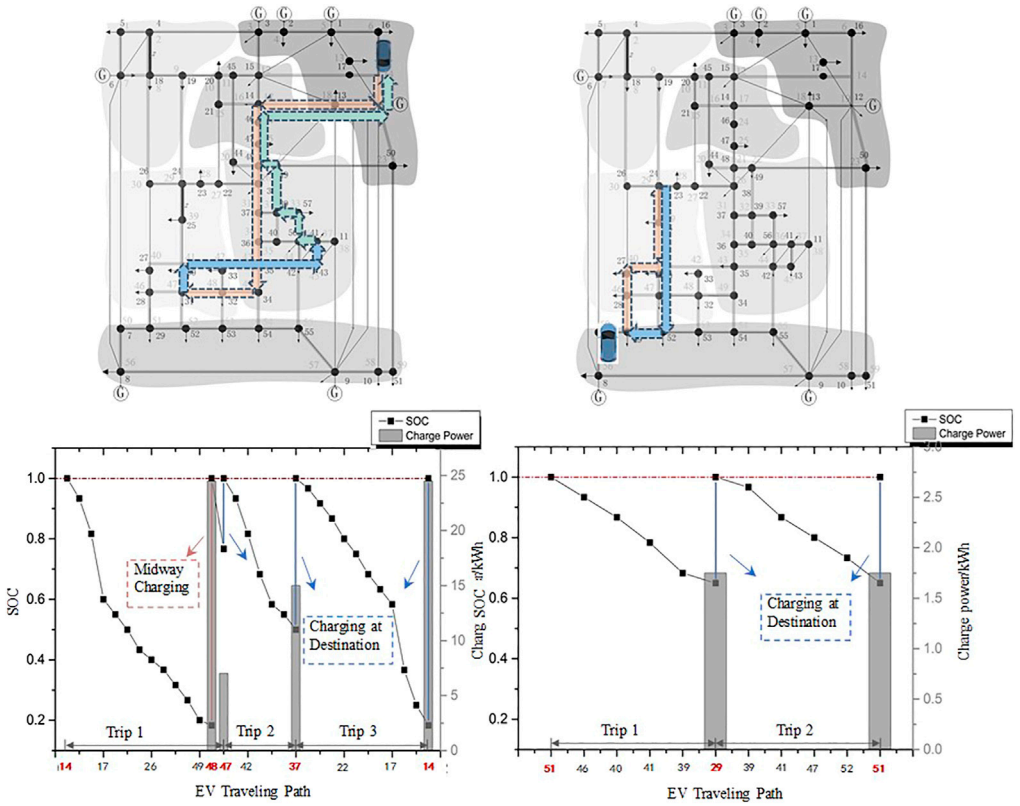

FIGURE 7 | The spatial-temporal EV mobile trajectory and corresponding SOC variation.

choose to charge for EV after work. As for the charging location, it can be seen that charging demand at the entertainment area on a resting day is more distinct than that on a working day. In contrast, the charging power on a working day is much higher than that on a resting day in a residential area.

EV is charged movably and indeterminately due to its traffic characteristics. Six electric vehicles' traveling trajectories and charging power are presented in **Figure 6**. Overall, the distribution of EV trajectory is mainly distributed at the central road of the transportation network. Compared to the upper part of the network depicted in **Figure 6**, EV charging in the lower part is more centralized. It can be noticed that the Entertainment area is located in the lower part of the transportation network, and so is Work area 2, which both lead to a high traffic density there. Consequently, the charging demand in these places is larger than the one in upper part of the system. As a result, EV charging in the lower part is more concentrated.

To draw EV spatial-temporal characteristics more clearly, a complex trip chain and a simple trip chain are extracted to be compared, as shown in **Figure 7**.

From **Figure 7**, we can see the first trajectory is presented as a complex trip train that passes through residential area 2 (the start point), work area 1, entertainment area 1, work area 2 (the destination 1), entertainment area 1 (the destination 2), work area 1 and residential area 2 (destination 3, i.e., home). As the first trip (from residential area 2 to work area 2) is a long trip, EV is charged midway at node 48 to support the next trip. For the second simple trip chain, it can be noticed that SOC is dropped to the same value at both two destinations (node 29 and node 51). This is because the two trips have the same distance according to the Dijkstra path search algorithm.

TABLE 2 | Reliability indexes based on different EV penetration.

Reliability index	EV penetration			
	10%	20%	30%	40%
SAIDI (h/year)	0.3050	0.3685	0.5633	0.7741
SAIFI (f/year)	0.6415	0.7631	1.0508	1.3006
EENS (MWh/year)	97.4986	119.7360	138.5801	191.2316
CENS (MWh/year)	5.2232	12.1849	24.8158	56.0833

Reliability Evaluation Based Sequential Monte Carlo

In this section, reliability indexes based on different EV penetration and trip chains are simulated. Besides, effects on the coupled system reliability due to EV charging based on different EV battery capacities are also discussed. Reliability indexes are shown in **Table 2** and **Figure 8** are based on EV penetration from 10 to 40%. The ratio of simple trip chain to complex trip chain is 1:9.

From the data above, it is not difficult to find that all reliability indexes, including CENS and POCCE, worsen with EV

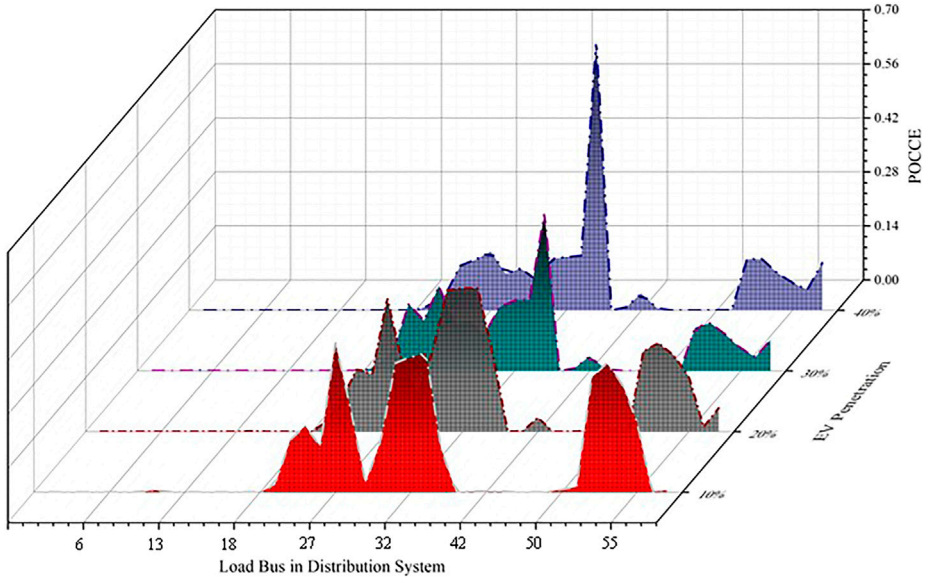

FIGURE 8 | Reliability index POCCE based different EV penetration.

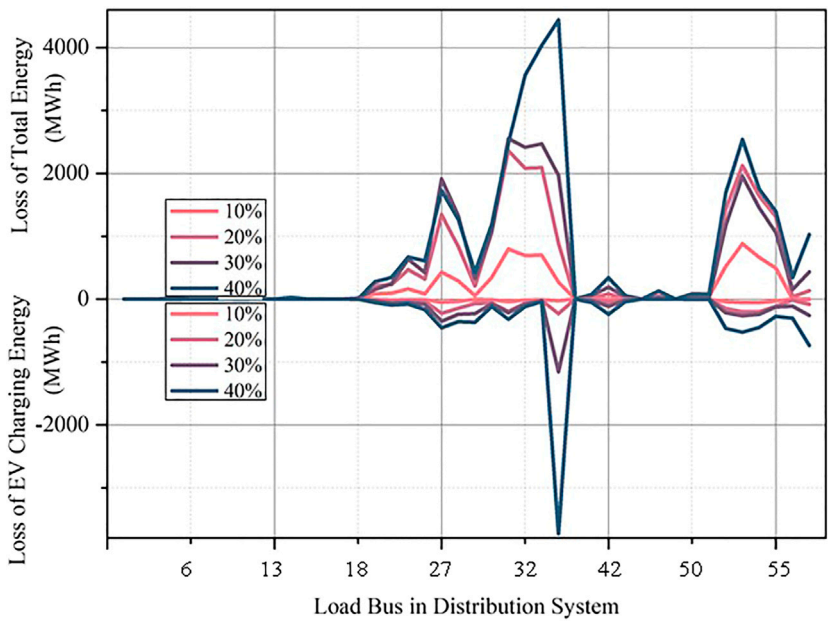

FIGURE 9 | Loss of total energy and EV charging energy at each load bus in a year based on different EV penetration.

penetration increasing. Moreover, it is noteworthy that there is a trend towards worsening POCCE value, which means that although the total EV charging power has been increased, the growth rate of curtailed charging power is more significant than before. As a result, a conclusion can be drawn that EV charging service reliability will be more seriously influenced by the growth of charging demand. Besides, there is a large capacity of charging power curtailment in buses 27, 32, 33, 35, 52, 53, and 54, which shows that the EV charging demand in the lower part of the network is more robust than the results obtained from *Electric Vehicle Spatial-Temporal Simulations*. To analyze the reliability level of different load buses, the loss of energy and charging energy in each load bus are compared in **Figure 9**.

By comparing the two kinds of curves of "Loss of Total Energy" and "Loss of EV Charging Energy" in **Figure 9**, it is easy to realize that the buses with poor reliability level are consistent with the results

TABLE 3 | Reliability indexes based on a different ratio of trip chain.

Reliability index	Ratio of simple trip chain to complex trip chain				
	1:9	3:7	5:5	7:3	9:1
SAIDI (h/year)	0.5596	0.4245	0.3926	0.3635	0.3543
SAIFI (f/year)	1.0611	0.8594	0.7550	0.7592	0.7208
EENS (MWh/year)	142.6823	138.8306	125.3006	119.4343	108.0768
CENS (MWh/year)	25.1174	23.6312	23.4708	23.0626	22.4251

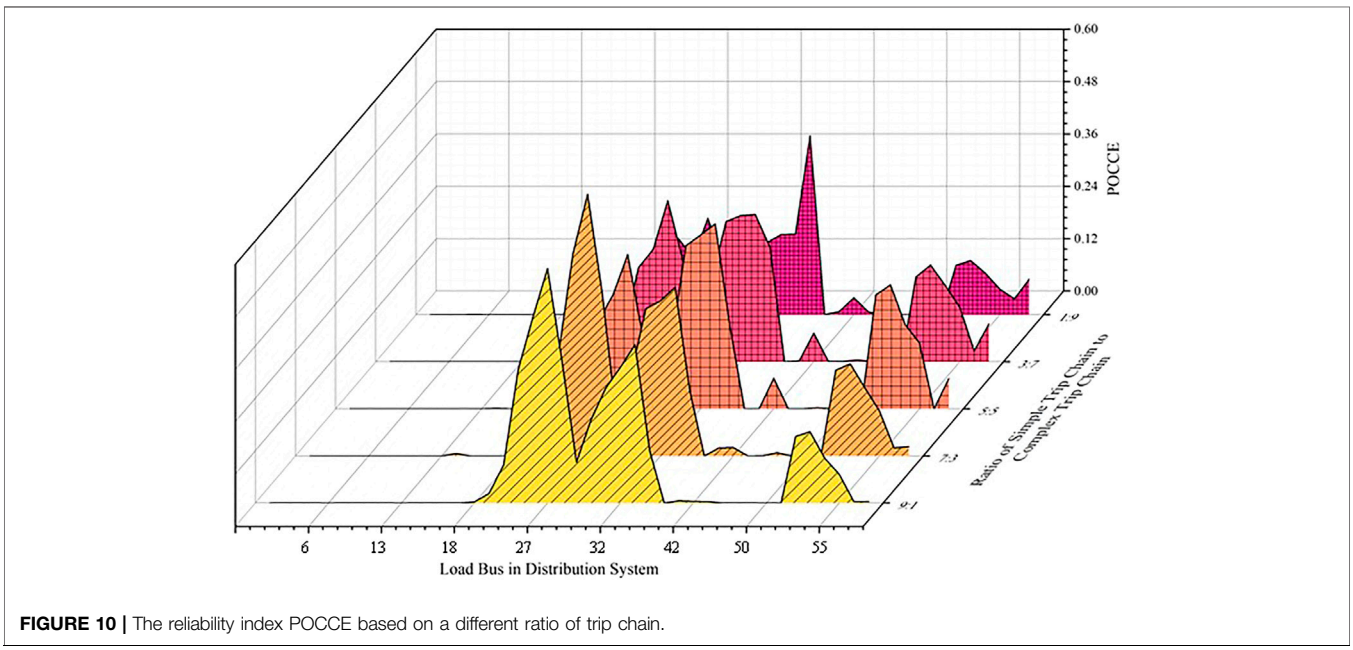

FIGURE 10 | The reliability index POCCE based on a different ratio of trip chain.

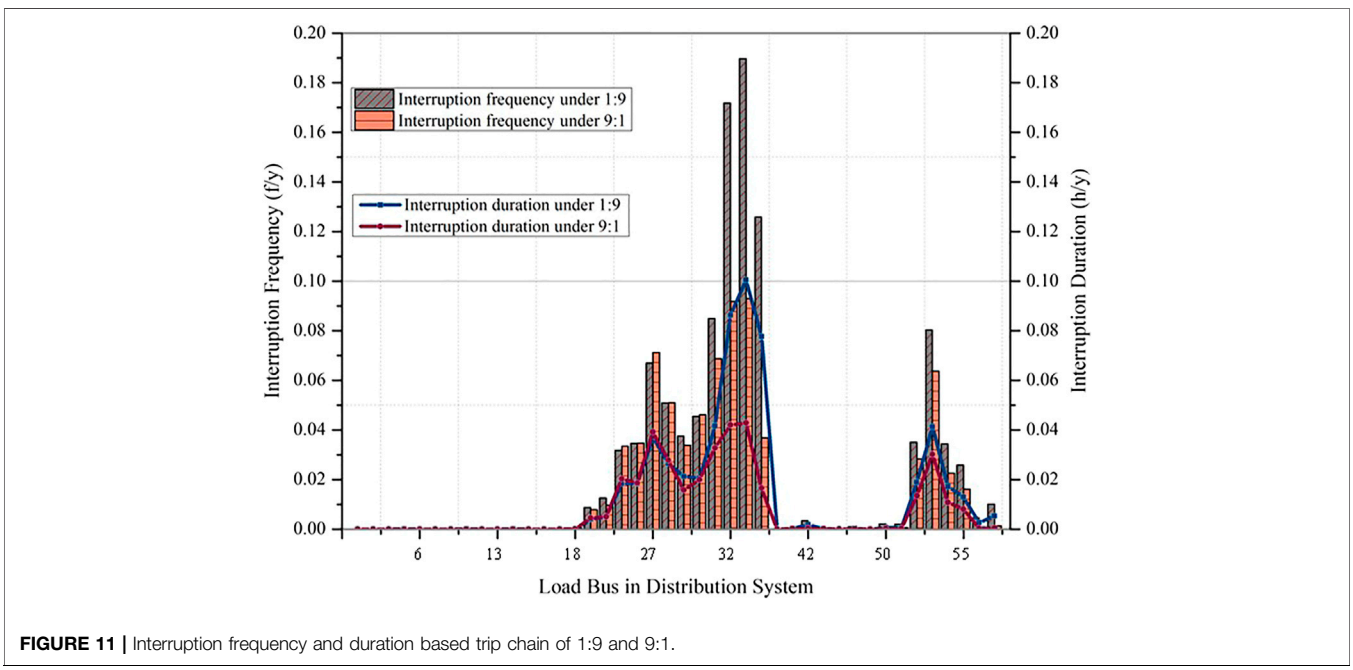

FIGURE 11 | Interruption frequency and duration based trip chain of 1:9 and 9:1.

TABLE 4 | Reliability indexes with increased battery EV capacity based on different EV penetration.

Reliability index	EV penetration			
	10%	20%	30%	40%
SAIDI (h/year)	0.3157	0.4927	0.8462	1.5880
SAIFI (f/year)	0.6329	0.7454	0.9752	1.1992
EENS (MWh/year)	96.0692	113.0622	122.7943	148.2297
CENS (MWh/year)	5.3000	15.9867	37.2476	109.8706

in **Figure 8** as well, which verifies the validity of the comprehensive reliability assessment method proposed in this paper. There may be three explanations for the phenomenon. First, the generators are mostly located at the upper part of the system, where the reliability level of buses is much higher. Besides, the lower part structure of the network is sparse; if there is a branch breaking down, nearby buses will severely be affected. Furthermore, high traffic density leads to a heavier load in the lower part.

EV traffic characteristics are much correlated to users' behaviors. The reliability indexes based on different ratios of the trip chains are shown in **Table 3** and **Figure 10**. The penetration level of EV is set to be 30% uniformly.

It can be noticed that with the decreasing of the complex trip chain proportion, the value of all reliability indexes is basically on a downward trend, which means system reliability has been improved. This is because, for the complex trip chain, the EV traveling trajectory is more complex. Therefore, the charging demand becomes more robust. As the proportion of the complex trip chain decreased, the system is less burdensome, and the reliability level is significantly improved. To see the difference further intuitively, the interruption frequency and duration in each load bus-based trip chain of 1:9 and 9:1 are shown in **Figure 11**.

From **Figure 11**, we can observe that the buses with high-reliability levels are basically in line with the previous results. And the interruption frequency and duration with the trip chain ratio of 1:9 is larger than the one with a ratio of 5:5, which is also consistent with the data in **Table 3**.

However, the above simulations are based on the constant capacity of each electric vehicle. In reality, different EV models may have various battery capacities. Thus, analyzing the effect of EV operation with different capacities is mandatory and practical. Keep the total EV capacity constant, i.e., the penetration level is the same as the data in **Table 3**. Increase the battery capacities of each EV to 30 kWh and the fast-charging power and low-charging power to 20 and 6 kW, respectively. The results are shown in **Table 4**.

To compare the data in **Tables 2**, **4** more intuitively, the corresponding change rate of the reliability index is calculated. The results are shown in **Figure 12**.

It can be seen that the change rates of index "SAIDI" and "CENS" are greater than zero with penetration 10–40%, while the change rates of index "SAIFI" and "EENS" are less than zero. It means that after increasing EV battery capacity, "SAIDI" and "CENS" are increased and "SAIFI" and "EENS" are decreased, and as EV penetration increases, the change becomes more

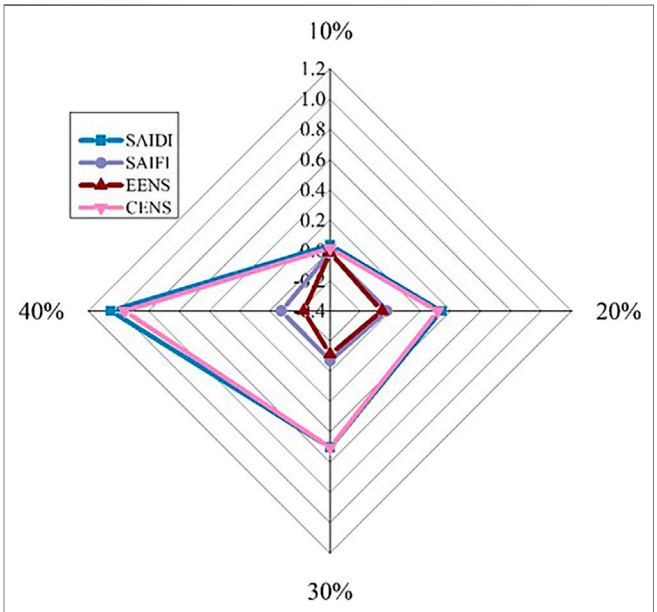

FIGURE 12 | Change rate of reliability index with increased EV battery capacity based on different EV penetration.

obvious. It may because EV users will have more unsatisfactory charging requirements in the event of a power outage when the capacity of the EV battery increases. Additionally, it may lead to a large amount of charging load at a certain moment, making the system burden much heavier. Consequently, the system becomes more complex to maintain steady-state operation. Hence, the Index "SAIDI" is increased. Since the total EV capacity is constant, the increase of EV charging power at certain moments leads to the charging power decrease at other moments. As a result, the frequency failure of the system and the amount of load curtailment are diminished.

Reliability evaluation With Electric Vehicle and Distributed Generation Integration

Due to the development of green energy and the requirements of national policies, the amount of DG in smart grids has been considerably increased. EV and DG are both characterized by their power uncertainty. Hence, system operation will be significantly influenced when they are jointly integrated into grids. This part describes the effect of DG integration on both EV charging service and distribution system reliability considering EV charging. Among all types of uncertain resources, the photovoltaic (PV) power characteristics differ greatly from charging load characteristics, as its power supply is cut off at night while EV is mainly charged at that time. In this case, PV is chosen to represent the uncertainty of DG.

In this section, two PVs with different capacities are integrated into the coupled system to evaluate its operation on system reliability. Considering the topology of the distribution system and traffic density, different PV installation locations may result

TABLE 5 | Reliability indexes with PV integration.

Reliability index	Total PV capacity							
	100 MW		200 MW		300 MW		400 MW	
Bus with PV integration	27.35	31.33	27.35	31.33	27.35	31.33	27.35	31.33
SAIDI (h/year)	0.2106	0.1564	0.1972	0.1589	0.3722	0.2459	0.7849	0.6005
SAIFI (f/year)	0.4320	0.3292	0.4395	0.3775	0.6320	0.4839	1.4952	1.2065
EENS (MWh/year)	70.4218	48.5267	55.2075	41.7842	72.0103	47.5085	171.1702	114.5682
CENS (MWh/year)	7.7053	7.7334	6.4259	6.4825	12.7411	10.8313	50.3606	38.3109
CENS/EENS	0.1094	0.1594	0.1164	0.1551	0.1769	0.2280	0.2942	0.3344

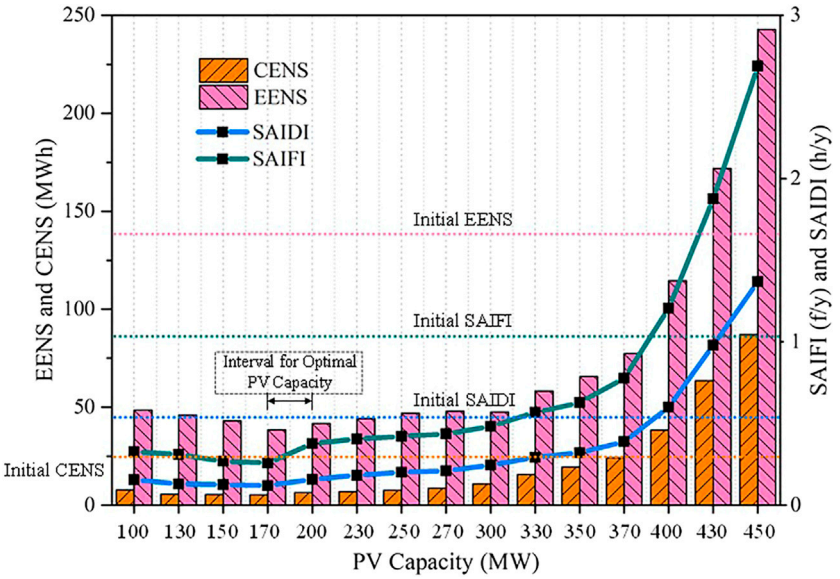

FIGURE 13 | Reliability indexes with PV integration-based capacity from 100 to 450 MW.

in different reliability impacts. The PV installation location is determined based on the coupled system reliability. Aiming at improving EV charging service reliability, locations can be obtained by selecting buses with the two most considerable values based on **Eq 24**. And for distribution network reliability, it is determined based on **Eq 25**.

$$\alpha_j = \sum_{\ell}\left(\frac{POCCE_j}{\sum_{j}^{N_L} POCCE_j} + \frac{\sum_{i_c=1}^{N_c} EV_{i_c}^{j} \times T_{down\_i_c}^{j}}{\sum_{j}^{N_L}\sum_{i_c=1}^{N_c} EV_{i_c}^{j} \times T_{down\_i_c}^{j}}\right) \tag{24}$$

$$\beta_j = \sum_{\ell}\frac{\sum_{i_c=1}^{N_c} E_{i_c}^{j} \times T_{down\_i_c}^{j}}{\sum_{j}^{N_L}\sum_{i_c=1}^{N_c} E_{i_c}^{j} \times T_{down\_i_c}^{j}} \tag{25}$$

where ℓ represents the set of EV penetration from 10 to 40%.

Based on the two formulas above, bus 27 and bus 35 are selected for PV installation locations based on EV charging service reliability, and bus 31 and bus 33 for distribution system reliability. The daily time-varying output of PV can be seen from Liu et al. (2018b); however, the failure of PV is not considered. Keep the total system generation capacity constant and increase the total PV capacity from 100 to 400 MW, respectively, i.e., the capacity of a single PV cluster is from 50 to 200 MW. The penetration of EV is set to be 30%. The calculated reliability indexes are shown in **Table 5**.

Table 5 shows that by selecting PV to installation location based on electricity system reliability, the overall reliability level of the system is much better. However, it can be noticed that the value of "CENS/EENS" with PV location in bus 31 and 33 is higher than the one with PV location in bus 27 and 35. It means that although the overall reliability level is improved by selecting PV location bus-based electricity system reliability, EV charging service reliability will be more obviously enhanced if PV is integrated into bus 27 and 35, which gives further verification on the validity of the novel reliability indexes.

Besides, it can be noticed that with the increase of PV integration capacity, both distribution system reliability and EV charging reliability are improved first and then decreased. To see trends more visually, select bus 31 and 33 as the integration locations, and the reliability indexes with PV capacity from 100 to 450 MW are shown in **Figure 13**.

When PV capacity is from 100 to 170 MW, the indexes are all on a downward trend, which means as PV penetration increases,

the electricity system reliability level is improved. Consequently, the optimal PV capacity leading to the highest reliability is about 170 MW. As PV is integrated into the system, the operation of the distribution network is changed from a single power supply mode by the main power grid to a more flexible multi-terminal power supply mode by both the power main grid and PV. EV can be supplied by DG, which alleviates the system burden to a great extent. Besides, the basic power supply can be ensured by PV output in some areas when there is a system failure occurred. It means that when the ratio of EV capacity to DG capacity is 3:1, the coordinated optimal operation strategy is obtained. However, when PV capacity exceeds 200MW, the electricity system reliability level starts to decline. It is noteworthy that when PV capacity is increased by more than 370 MW, the reliability index starts to keep proliferating. Furthermore, when PV capacity reaches 400 MW, the system reliability level is even lower than the initial reliability level without PV integration. PV cannot undertake the main load for its intermittency and uncertainty, especially when there are numerous flexible EV charging loads.

CONCLUSION

Reliability impacts of large-scale mobile EV integration on both electricity system and EV charging service system in a coupled transportation and grid framework are explored in this paper. The case study results indicate the following:

- With the increase in EV penetration level and proportion of the complex trip chain, the reliability level for both the electricity system and EV charging service shows a downward trend. EV charging service reliability will be more severely affected by the growth of charging demand.
- Through increasing EV battery capacity, indexes "SAIDI" and "CENS" are increased while "SAIFI" and "EENS" are decreased. As EV penetration increases, the change becomes more obvious. The results implicate that both distribution network reliability and EV charging service reliability can be improved significantly by increasing EV battery capacity if there is enough backup power during the peak period.
- DG installation locations can be determined to coordinate the reliability level of the distribution system and EV charging service. Appropriate DG capacity can improve system reliability, but once a certain threshold is exceeded, the system will rapidly collapse. When DG capacity is about 170 MW, i.e., the ratio of EV capacity to DG capacity is 3:1, the highest system reliability level is reached. However, when DG capacity exceeds 370 MW, system reliability starts to deteriorate rapidly.

DATA AVAILABILITY STATEMENT

The original contributions presented in the study are included in the article/**Supplementary Appendix Material**, further inquiries can be directed to the corresponding author.

AUTHOR CONTRIBUTIONS

PX, YX: Conceptualization, methodology; PX: Writing—original draft preparation; YX, JL: Supervision; JG, WX, WS, ZJ, SJ, HZ: Writing—reviewing and editing.

FUNDING

This work was supported by the National Natural Science Foundation of China (51807127, 52111530067), the Sichuan Science and Technology Program (2020YFSY0037).

SUPPLEMENTARY MATERIAL

The Supplementary Material for this article can be found online at: https://www.frontiersin.org/articles/10.3389/fenrg.2021.688034/full#supplementary-material

REFERENCES

Acha, S., Green, T. C., and Shah, N. (2010). *Effects of Optimised Plug-In Hybrid Vehicle Charging Strategies on Electric Distribution Network Losses*. New Orleans, LA, USA: IEEE PES T&D, 1–6.

Anand, M. P., Bagen, B., and Rajapakse, A. (2020). Probabilistic Reliability Evaluation of Distribution Systems Considering the Spatial and Temporal Distribution of Electric Vehicles. *Int. J. Electr. Power Energ. Syst.* 117, 105609. doi:10.1016/j.ijepes.2019.105609

Bostan, A., Nazar, M. S., Shafie-khah, M., and Catalão, J. P. S. (2020). An Integrated Optimization Framework for Combined Heat and Power Units, Distributed Generation and Plug-In Electric Vehicles. *Energy* 202, 117789. doi:10.1016/j.energy.2020.117789

Cheng, L., Chang, Y., Lin, J., and Singh, C. (2013). Power System Reliability Assessment with Electric Vehicle Integration Using Battery Exchange Mode. *IEEE Trans. Sustain. Energ.* 4 (4), 1034–1042. doi:10.1109/tste.2013.2265703

Cheng, S., Wei, Z., Shang, D., Zhao, Z., and Chen, H. (2020). Charging Load Prediction and Distribution Network Reliability Evaluation Considering Electric Vehicles' Spatial-Temporal Transfer Randomness. *IEEE Access* 8, 124084–124096.

Colmenar-Santos, A., Muñoz-Gómez, A.-M., Rosales-Asensio, E., and López-Rey, Á. (2019). Electric Vehicle Charging Strategy to Support Renewable Energy Sources in Europe 2050 Low-Carbon Scenario. *Energy* 183, 61–74. doi:10.1016/j.energy.2019.06.118

Cui, Q., Bai, X., and Dong, W. (2019). Collaborative Planning of Distributed Wind Power Generation and Distribution Network with Large-Scale Heat Pumps. *CSEE J. Power Energ. Syst.* 5 (3), 335–347.

Das, T., Roy, R., and Mandal, K. K. (2020). Impact of the Penetration of Distributed Generation on Optimal Reactive Power Dispatch. *Prot. Control. Mod. Power Syst.* 5 (1), 31. doi:10.1186/s41601-020-00177-5

Dijkstra, E. W. (1959). A Note on Two Problems in Connexion with Graphs. *Numer. Math.* 1, 269–271. doi:10.1007/bf01386390

Ding, T., Wang, Z., Jia, W., Chen, B., Chen, C., and Shahidehpour, M. (2020). Multiperiod Distribution System Restoration with Routing Repair Crews, mobile Electric Vehicles, and Soft-Open-point Networked Microgrids. *IEEE Trans. Smart Grid* 11 (6), 4795–4808. doi:10.1109/tsg.2020.3001952

Farzin, H., Moeini-Aghtaie, M., and Fotuhi-Firuzabad, M. (2016). Reliability Studies of Distribution Systems Integrated with Electric Vehicles under

Battery-Exchange Mode. *IEEE Trans. Power Deliv.* 31 (6), 2473–2482. doi:10.1109/tpwrd.2015.2497219

Franco, J. F., Rider, M. J., and Romero, R. (2015). A Mixed-Integer Linear Programming Model for the Electric Vehicle Charging Coordination Problem in Unbalanced Electrical Distribution Systems. *IEEE Trans. Smart Grid* 6 (5), 2200–2210. doi:10.1109/tsg.2015.2394489

Ge, S., Guo, J., Liu, H., and Zeng, P. (2014). Impacts of Electric Vehicle's Ordered Charging on Power Grid Load Curve Considering Demand Side Response and Output of Regional Wind Farm and Photovoltaic Generation. *Power Syst. Tech.* 38 (07), 1806–1811.

Ge, S., and Wang, H. (2013). Reliability Evaluation of Distribution Networks Including Distributed Generations Based on System State Transition Sampling. *Automation Electric Power Syst.* 37 (02), 28–35.

Göransson, L., Karlsson, S., and Johnsson, F. (2010). Integration of Plug-In Hybrid Electric Vehicles in a Regional Wind-thermal Power System. *Energy Policy* 38 (10), 5482–5492. doi:10.1016/j.enpol.2010.04.001

Guner, S., and Ozdemir, A. (2020). Reliability Improvement of Distribution System Considering EV Parking Lots. *Electric Power Syst. Res.* 185, 106353. doi:10.1016/j.epsr.2020.106353

Hoog, J. d., Alpcan, T., Brazil, M., Thomas, D. A., and Mareels, I. (2015). Optimal Charging of Electric Vehicles Taking Distribution Network Constraints into Account. *IEEE Trans. Power Syst.* 30 (1), 365–375.

Huang, S., Ye, C., Liu, S., Zhang, W., Ding, Y., Hu, R., et al. (2020). Data-driven Reliability Assessment of an Electric Vehicle Penetrated Grid Utilizing the Diffusion Estimator and Slice Sampling. *CSEE J. Power Energ. Syst.*, 1–9.

Li, H., Du, Z., Chen, L., Guan, L., and Zhou, B. (2019). Trip Simulation Based Load Forecasting Model and Vehicle-To-Grid Evaluation of Electric Vehicles. *Automation Electric Power Syst.* 43 (21), 88–96.

Liang, H., Lee, Z., and Li, G. (2020). A Calculation Model of Charge and Discharge Capacity of Electric Vehicle Cluster Based on Trip Chain. *IEEE Access* 8, 142026–142042. doi:10.1109/access.2020.3014160

Liu, D., Lv, L., Liu, J., Gao, H., and Zhou, C. (2018). Coordinated Planning of Capacity of DG and TOU price Considering Time-Varying Characteristics of DG and Types of Load in Micro-grid. *Electr. Meas. Instrumentation* 55 (12), 45–53.

Liu, H., Zhang, X., Liu, C., Zhang, J., and Ge, S. (2018). Timing Interactive Analysis of Electric Private Vehicle Traveling and Charging Demand Considering the Sufficiency of Charging Facilities. *Proc. CSEE* 38 (18), 5469–5478.

Luo, L., Gu, W., Wu, Z., and Zhou, S. (2019). Joint Planning of Distributed Generation and Electric Vehicle Charging Stations Considering Real-Time Charging Navigation. *Appl. Energ.* 242, 1274–1284. doi:10.1016/j.apenergy.2019.03.162

Luo, L., Wu, Z., Gu, W., Huang, H., Gao, S., and Han, J. (2020). Coordinated Allocation of Distributed Generation Resources and Electric Vehicle Charging Stations in Distribution Systems with Vehicle-To-Grid Interaction. *Energy* 192, 116631. doi:10.1016/j.energy.2019.116631

Luo, Y., Feng, G., Wan, S., Zhang, S., Li, V., and Kong, W. (2020). Charging Scheduling Strategy for Different Electric Vehicles with Optimization for Convenience of Drivers, Performance of Transport System and Distribution Network. *Energy* 194, 116807. doi:10.1016/j.energy.2019.116807

Manbachi, M., Sadu, A., Farhangi, H., Monti, A., Palizban, A., Ponci, F., et al. (2016). Impact of EV Penetration on Volt-VAR Optimization of Distribution Networks Using Real-Time Co-simulation Monitoring Platform. *Appl. Energ.* 169, 28–39. doi:10.1016/j.apenergy.2016.01.084

Meng, J., Xiang, Y., Gu, C., Chen, S., and Liu, J. (2021). Collaborative Optimization Planning of Electric Vehicle Charging Infrastructure for Reliability Improvement. *Electric Power Automation Equipment*, 1–9.

Patil, H., and Nago Kalkhambkar, V. (2021). Grid Integration of Electric Vehicles for Economic Benefits: a Review. *J. Mod. Power Syst. Clean Energ.* 9 (1), 13–26. doi:10.35833/mpce.2019.000326

Sadeghian, O., Nazari-Heris, M., Abapour, M., Taheri, S. S., and Zare, K. (2019). Improving Reliability of Distribution Networks Using Plug-In Electric Vehicles and Demand Response. *J. Mod. Power Syst. Clean. Energ.* 7 (5), 1189–1199. doi:10.1007/s40565-019-0523-8

Sankarakrishnan, A., and Billinton, R. (1995). Sequential Monte Carlo Simulation for Composite Power System Reliability Analysis with Time Varying Loads. *IEEE Trans. Power Syst.* 10 (3), 1540–1545. doi:10.1109/59.466491

Shafiee, S., Fotuhi-Firuzabad, M., and Rastegar, M. (2013). Investigating the Impacts of Plug-In Hybrid Electric Vehicles on Power Distribution Systems. *IEEE Trans. Smart Grid* 4 (3), 1351–1360. doi:10.1109/tsg.2013.2251483

Spinato, F., Tavner, P. J., van Bussel, G. J. W., and Koutoulakos, E. (2009). Reliability of Wind Turbine Subassemblies. *IET Renew. Power Gener.* 3, 387–401. doi:10.1049/iet-rpg.2008.0060

Su, J., Lie, T. T., and Zamora, R. (2020). Integration of Electric Vehicles in Distribution Network Considering Dynamic Power Imbalance Issue. *IEEE Trans. Ind. Applicat.* 56 (5), 5913–5923. doi:10.1109/tia.2020.2990106

Su, J., Lie, T. T., and Zamora, R. (2019). Modelling of Large-Scale Electric Vehicles Charging Demand: A New Zealand Case Study. *Electric Power Syst. Res.* 167, 171–182. doi:10.1016/j.epsr.2018.10.030

Sulaeman, S., Tian, Y., Benidris, M., and Mitra, J. (2017). Quantification of Storage Necessary to Firm up Wind Generation. *IEEE Trans. Ind. Applicat.* 53 (4), 3228–3236. doi:10.1109/tia.2017.2685362

Sun, W., Neumann, F., and Harrison, G. P. (2020). Robust Scheduling of Electric Vehicle Charging in LV Distribution Networks under Uncertainty. *IEEE Trans. Ind. Applicat.* 56 (5), 5785–5795. doi:10.1109/tia.2020.2983906

Tang, D., and Wang, P. (2016). Probabilistic Modeling of Nodal Charging Demand Based on Spatial-Temporal Dynamics of Moving Electric Vehicles. *IEEE Trans. Smart Grid* 7 (2), 627–636.

Veldman, E., and Verzijlbergh, R. A. (2015). Distribution Grid Impacts of Smart Electric Vehicle Charging from Different Perspectives. *IEEE Trans. Smart Grid* 6 (1), 333–342. doi:10.1109/tsg.2014.2355494

Xia, Y., Hu, B., Xie, K., Tang, J., and Tai, H.-M. (2019). An EV Charging Demand Model for the Distribution System Using Traffic Property. *IEEE Access* 7, 28089–28099. doi:10.1109/access.2019.2901857

Xiang, Y., Hu, S., Liu, Y., Zhang, X., and Liu, J. (2019). Electric Vehicles in Smart Grid: a Survey on Charging Load Modelling. *IET Smart Grid* 2, 25–33. doi:10.1049/iet-stg.2018.0053

Xiang, Y., Liu, J., Li, R., Li, F., Gu, C., and Tang, S. (2016). Economic Planning of Electric Vehicle Charging Stations Considering Traffic Constraints and Load Profile Templates. *Appl. Energ.* 178, 647–659. doi:10.1016/j.apenergy.2016.06.021

Xiang, Y., Liu, Z., Liu, J., Liu, Y., and Gu, C. (2018). Integrated Traffic-Power Simulation Framework for Electric Vehicle Charging Stations Based on Cellular Automaton. *J. Mod. Power Syst. Clean. Energ.* 6 (4), 816–820. doi:10.1007/s40565-018-0379-3

Xiang, Y., Wang, Y., Su, Y., Sun, W., Huang, Y., and Liu, J. (2020). Reliability Correlated Optimal Planning of Distribution Network with Distributed Generation. *Electric Power Syst. Res.* 186, 106391. doi:10.1016/j.epsr.2020.106391

Xu, N. Z., and Chung, C. Y. (2016). Reliability Evaluation of Distribution Systems Including Vehicle-To-home and Vehicle-To-Grid. *IEEE Trans. Power Syst.* 31 (1), 759–768. doi:10.1109/tpwrs.2015.2396524

Zhang, S., Cheng, H., Wang, D., Zhang, L., Li, F., and Yao, L. (2018). Distributed Generation Planning in Active Distribution Network Considering Demand Side Management and Network Reconfiguration. *Appl. Energ.* 228, 1921–1936. doi:10.1016/j.apenergy.2018.07.054

Conflict of Interest: Authors JG and WX were employed by company State Grid Sichuan Economic Research Institute. Author ZJ was employed by company State Grid Chongqing Shiqu Power Supply Company.

The remaining authors declare that the research was conducted in the absence of any commercial or financial relationships that could be construed as a potential conflict of interest.

GLOSSARY

$\boldsymbol{T_{Road}}$ traveling duration in a trip

$\boldsymbol{W}$ nodes number that a trip includes

$\boldsymbol{Sroad}$ road length

$V_{E_{road}}$ traveling speed

$\boldsymbol{T_{park}}$ point of parking time

$\boldsymbol{T_{start}}$ point of traveling starting time

$\boldsymbol{T_{stay}}$ staying duration in the destination

$\boldsymbol{T_{mid}}$ midway charging duration

$SOC_{T_{park}}$ SOC after arriving at a destination

$SOC_{T_{start}}$ initial SOC

S traveling distance

$\boldsymbol{b}$ power consumption per mileage

$\boldsymbol{Cap}$ EV battery capacity

$Power_{slow}$ slow-charging power

$\boldsymbol{X}$ fuzzy coefficient

$\boldsymbol{Y}$ elastic coefficient

S^{SOC_m} traveling distance before reaching SOC threshold

SOC_m SOC threshold value

$\boldsymbol{N_L}$ number of distribution system load buses

$\boldsymbol{Power}$ charging power based charging mode selection

$\boldsymbol{E_j}$ load shedding in bus j

$\boldsymbol{P_{inj}}$, $\boldsymbol{Q_{inj}}$ vectors of active and reactive power injections

$\boldsymbol{E}$, $\boldsymbol{E_Q}$ vectors of corresponding active and reactive load curtailment

$\boldsymbol{P_{LD}}$ **and** $\boldsymbol{Q_{LD}}$ vectors of active and reactive power loads

$\boldsymbol{P_G}$, $\boldsymbol{Q_G}$ vectors of active and reactive generating power

$\underline{P_G}$, $\overline{P_G}$ vectors of active power limits

$\underline{Q_G}$, $\overline{Q_G}$ vectors of reactive power limits

$\boldsymbol{V}$ vector of bus voltage magnitude

$\underline{V}$, $\overline{V}$ vectors of bus voltage limits

$\boldsymbol{N_c}$ number of simulated cycles

$T^j_{down\_i_c}$ outage period

$\boldsymbol{N_f}$ number of the outage periods

$\boldsymbol{N_Y}$ simulation year

$\boldsymbol{u_j}$ number of users in load bus j

$f^j_{i_c}$ interruption frequency of bus j

$E^j_{i_c}$ load curtailment of node j

$EVload^j_{i_c}$ EV charging load in bus j

$EV^j_{i_c}$ curtailment of EV charging load in node j

μ_j repair state

λ_j failure state

$\boldsymbol{N_{rand}}$ a random number evenly distributed between 0 and 1

β variation coefficient

frontiers in Energy Research

ORIGINAL RESEARCH
published: 15 July 2021
doi: 10.3389/fenrg.2021.719419

Increasing Renewable Energy Consumption Coordination With the Monthly Interprovincial Transaction Market

Ye Cai[1], *Ying Liu*[1], *Xiafei Tang*[1]*, *Yudong Tan*[2] *and Yijia Cao*[1]

[1]School of Electrical and Information Engineering, Changsha University of Science and Technology, Changsha, China, [2]State Grid Hunan Electric Power Company Limited Economic and Technical Research Institute, Changsha, China

The limited regulation capacity of the power grid, coupled with the imperfect market mechanism, has squeezed the space for renewable energy consumption in China. This article proposes a renewable energy consumption mechanism through the monthly interprovincial transaction market, to balance the revenue of each market participant and improve the consumption of renewable energy. A new player named "interprovincial traders" is introduced to serve as the middleman for the renewable generation, users, and the power grid company. The main function of "interprovincial traders" is to coordinate and match the user load with the output of renewable energy. In such a market mechanism, the social factors, influenced by the revenue of each trading cycle, are considered in the user responding model from the perspective of consumer psychology. Finally, a two-phase optimization model is proposed to promote renewable energy consumption coordination with the monthly interprovincial market. The optimization model is simulated in a provincial power grid example. The results show that the model can effectively increase the consumption of renewable energy as well as improve the profit of power grid companies and users.

Keywords: renewable energy consumption, uncertainty, interprovincial transactions, demand response, source–load interaction

OPEN ACCESS

Edited by:
Yingjun Wu,
Hohai University, China

Reviewed by:
Xiaoguang Wei,
Southwest Jiaotong University, China
Bin Zhou,
Hunan University, China

***Correspondence:**
Xiafei Tang
xiafei.tang@qq.com

Specialty section:
This article was submitted to Smart Grids, a section of the journal Frontiers in Energy Research

Received: *02 June 2021*
Accepted: *21 June 2021*
Published: *15 July 2021*

Citation:
Cai Y, Liu Y, Tang X, Tan Y and Cao Y (2021) Increasing Renewable Energy Consumption Coordination With the Monthly Interprovincial Transaction Market. Front. Energy Res. 9:719419. doi: 10.3389/fenrg.2021.719419

INTRODUCTION

Serious environmental problems affect sustainable development in China (Yang et al., 2010). To reduce their impact on the society, vigorous development of renewable energy sources, such as wind power and photovoltaic (PV), is one of the ambitious goals in China. At present, renewable energy installed capacity in China ranks the first in the world (Li J. et al., 2019). However, a series of difficulties, such as irrational energy structure, the mismatched spatial distribution of supply and demand, limited flexible regulation of power grids, and imperfect market mechanisms, have severely restricted the elevation of the renewable energy consumption ratio.

Several scholars make efforts to improve the renewable energy consumption through better generating forecast, joint scheduling, and electricity market. Improving the accuracy of generating estimation is important for dispatching and optimization in the short-time scale. Several methods are proposed and implied in renewable energy forecast through machine learning algorithm (Quan et al., 2014; Razavi et al., 2020) and the big data-driven method (Zhou et al., 2017). In terms of joint scheduling, it is mainly to use energy storage equipment to track and synchronize renewable energy

generation Shim et al. (2018) and Latifi et al. (2019) to alleviate the abandonment problem caused by the volatility of renewable energy. It is also an effective approach to improve renewable energy consumption through the electricity market transaction in the long-time scale. By providing ancillary services Melo et al. (2018) or making renewable portfolio standards Kroposki et al. (2013), users and the power grid company can be incentivized to participate in demand response to increase the consumption of renewable energy. However, these methods do not consider the impact of social factors on demand response in the long-time scales.

Power grid operation in China is security-oriented; thus, some different ideas for resolving the conflict between security and cleanliness are proposed through the demand response Xu et al. (2020) and interprovincial transactions (Wen et al., 2020). Under the organization of the national development and reform commission, the pilot construction work of demand response has been implemented in Jiangsu, Shanghai, and Beijing in China (Li B. et al., 2019). But it is difficult to take effect, for users who are not price-sensitive. The power grid company needs to start from interprovincial medium and long-term transactions, to achieve the purpose of renewable energy consumption.

In this article, a framework of increasing the renewable energy consumption through the interprovincial transactions is proposed. The transaction process involves day-ahead scheduling, intraday execution, and transaction settlement. A new player of "Interprovincial Traders" has been proposed as a middleman to coordinate and match the user load with the output of renewable energy. Social factors, such as the sensitivity to policy publicity and interactions among group behavior, are considered in the long-time scale, which are used to describe the impact of the phased revenue in the monthly interprovincial transaction process on user demand responsiveness. A two-phase optimization model is proposed to optimize the revenues of each market participant and to maximize the consumption of renewable energy.

The remainder of the article is organized as follows. The framework of interprovincial transactions is proposed in *Renewable Energy Consumption Mechanism in the Interprovincial Transaction*. *User Demand Response Model Considering Social Factors* introduces the user demand response model considering social factors. In *Medium- and Long-Term Source–Load Interactive Optimization Model to Promote Renewable Energy Consumption*, a two-phase optimization model is introduced in detail. Case studies are performed in *Case Studies*, where the results are discussed thereafter. Finally, the conclusions are presented in *Conclusion*.

RENEWABLE ENERGY CONSUMPTION MECHANISM IN THE INTERPROVINCIAL TRANSACTION

Interprovincial Transaction Mechanism with Interprovincial Traders

The interprovincial transaction market is one of the main electricity markets in the Chinese market. China has built the world's largest and most complex ultrahigh-voltage AC/DC power grid Li et al. (2018), which provides the possibility for the implementation of interprovincial transactions. The main function of interprovincial transactions is as follows.

Interprovincial transactions mainly use the surplus transmission capacity of trans-provincial tie-line to organize power trading, transmitting surplus power from renewable energy-rich areas to the areas on the demand side, and realizing the cross-regional consumption of renewable energy. It mainly adopts the daily clearing and the monthly settlement trading method.

Considering that most users cannot directly participate in electricity market transactions, the interprovincial traders (IPTs) play the role of the middleman for interprovincial transactions. As it is in the early stage of interprovincial transaction market construction, the power grid company participates in interprovincial transactions as IPTs (Guo et al., 2019). The framework of the interprovincial transaction mechanism is shown in **Figure 1**.

In **Figure 1**, the transaction mechanism is divided into two phases, short-time scales and long-term scales.

The short-time scale consists of three components: day-ahead scheduling, intraday execution, and transaction settlement. First, in the day-ahead scheduling, users report relevant information to IPTs, including load information, demand responsiveness, and demand response costs. Renewable generators report output information to IPTs. Based on the above information, IPTs determine the scheduling plan of each market participant on the next day and send the plan to them. Then, in the intraday execution, each market participant executes the corresponding day-ahead scheduling plan and reports the day execution to IPTs. Finally, in the transaction settlement, IPTs conduct trade settlements, including revenue calculations and cost allocations, based on the executions reported by each market player.

The long-term scale is mainly to carry out monthly continuous interprovincial transactions, based on daily settlement results. In the process of transaction, it is necessary to report the periodic revenue results to users, to further motivate users to participate in demand response and improve user demand responsiveness. Transactions are at last cleared at the end of the month.

Day-Ahead Scheduling

In the day-ahead scheduling, the information interaction among users, IPTs, and power company is shown in **Figure 1**. In **Figure 1**, the users need to report individual information of peak shaving power to IPTs, according to their electricity plan, including corresponding compensation cost, which reflects the loss caused by changing their electricity habits to participate in demand response.

Renewable generators forecast renewable energy output information for the next day based on historical weather data and report the output information to IPTs.

IPTs provide the service for users and renewable generators. They also collect the forecasted renewable energy output and load information. Based on the information provided by users and renewable generators, IPTs calculate the matching degree

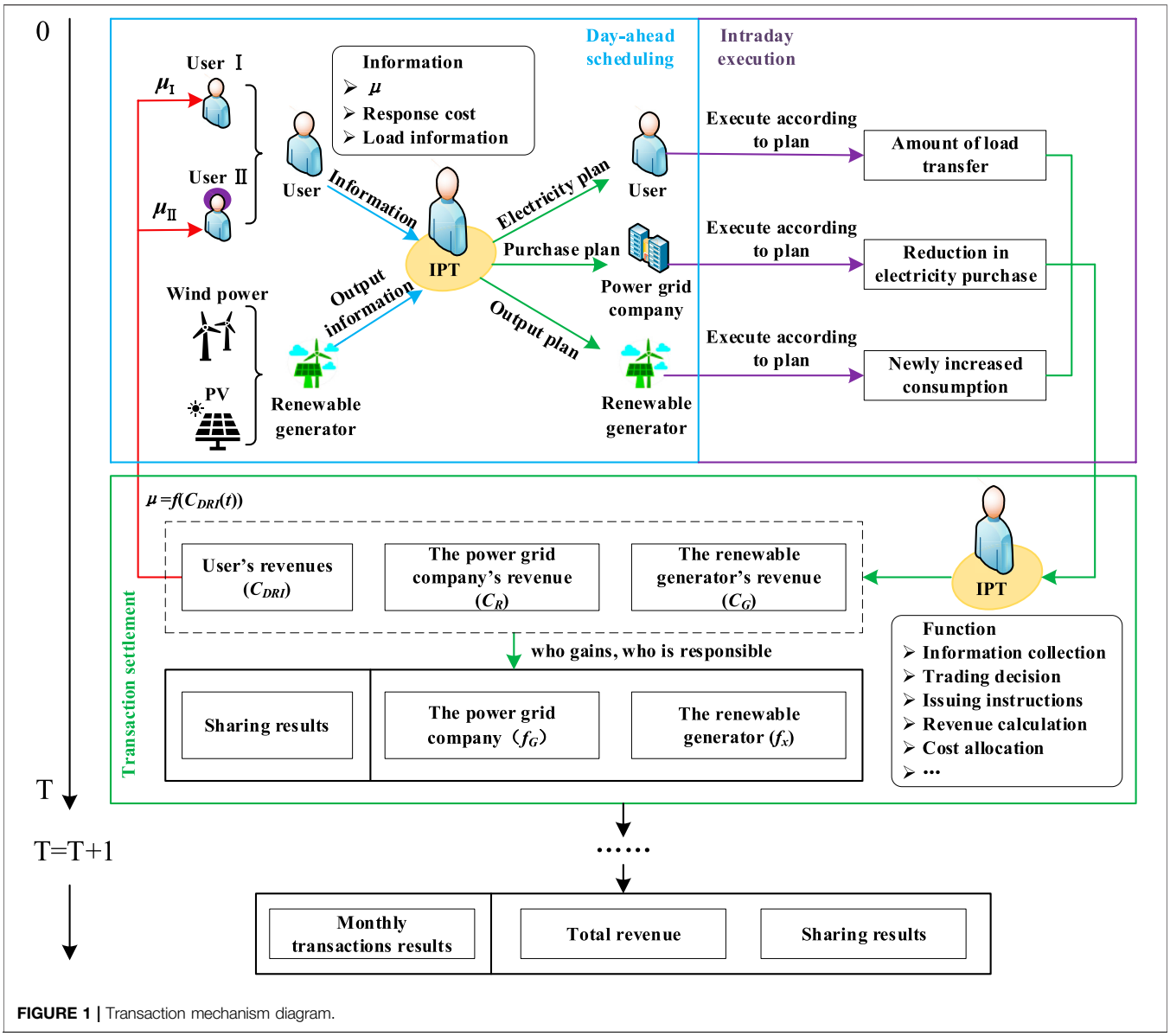

FIGURE 1 | Transaction mechanism diagram.

between user load and renewable energy output, and determine whether to activate users to participate in demand response according to the matching degree. From the relevant information, IPTs determine the out-purchased electricity information, the day-ahead scheduling plan, and report the day-ahead scheduling plan to the market participants.

Intraday Execution

During the intraday execution phase, users are required to consume electricity according to the scheduling plan, likewise renewable generators to generate power and power grid companies to purchase electricity. Errors between the forecasted and actual output of renewable energy can be adjusted by the thermal power units.

Transaction Settlement

At the end of the intraday execution, IPTs calculate the revenue of each market participants on that day, and settle the transactions according to the following mechanism.

After the user participates in the demand response, renewable generators receive renewable energy power generation revenue due to the increasing on-grid electricity. The power grid company can reduce power purchase expenditures due to the reduction of out-purchased electricity. The revenue of each market participants is as follows:

1) Revenues from user participation in demand response through load shifting

$$C_{DRI,t} = x_t * L_t^+, \tag{1}$$

$$L_t = L_{0,t} + L_t^+ - L_t^-, \tag{2}$$

$$L_t^+ - L_t^- \le \tau_{max} L_{0,t}, \tag{3}$$

where x_t is the subsidized price. $L_{0,t}$ and L_t represent the user load at time t before and after the response, respectively. L_t^+ and L_t^- are the load transferred in and out at time t. τ_{max} is the maximum proportion of load change at a certain moment.

2) Revenues of increased on-grid electricity from renewable generators

$$C_{R,t} = \left(C_{f,t} + C_{g,t}\right), \tag{4}$$

$$C_{f,t} = \left(L_t^f - L_{0,t}^f\right) * p_1, \tag{5}$$

$$C_{g,t} = \left(L_t^g - L_{0,t}^g\right) * p_2, \tag{6}$$

where $C_{R,t}$ is the renewable generators revenue at time t. $C_{f,t}$ and $C_{g,t}$ represent the newly added revenue of wind power and PV, respectively. $L_{0,t}^f$, L_t^f, $L_{0,t}^g$, and L_t^g represent the consumption of wind power and PV before and after the transaction, respectively. p_1 and p_2 denote the benchmark on-grid price of wind power and PV.

3) The revenue of power grid company by reducing power purchase expenditures

$$C_{G,t} = \left(L_{0,t}^G - L_t^G\right) * p_3, \tag{7}$$

where $L_{0,t}^G$ and L_t^G represent the out-purchased electricity before and after the transaction, respectively. p_3 is the contract price of the out-purchased electricity.

A transaction settlement method is designed based on the fairness criterion of "who gains, who is responsible" (Zhang and Zhou, 2018). The power grid company and renewable generators have profited after users participated in the demand response. Therefore, both sides have to share the compensation costs of the users. The sharing ratio is determined according to the proportion of the reduction in out-purchased power and the increase in renewable energy consumption. The specific calculation formula is as follows:

$$w_1 = \frac{Q_G}{Q_G + Q_x}, \tag{8}$$

$$w_2 = \frac{Q_x}{Q_G + Q_x}, \tag{9}$$

$$f_G = \varphi w_1, \tag{10}$$

$$f_x = \varphi w_2, \tag{11}$$

where w_1 and w_2 represent the sharing ratio of the power grid company and the renewable generators, respectively. φ is the user compensation cost to be paid. Q_G and Q_x represent the reduction in out-purchased power and the increase of renewable energy consumption, respectively. f_G and f_x are the compensation cost to be shared by the power grid company and the renewable generators, respectively.

Finally, the daily settlement results are accumulated to generate the monthly transaction results.

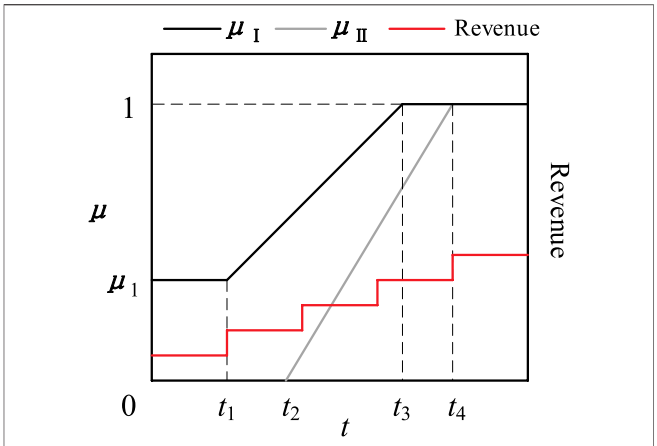

FIGURE 2 | Piecewise linear function of demand responsiveness.

USER DEMAND RESPONSE MODEL CONSIDERING SOCIAL FACTORS

Effects of Consumer Psychology on Demand Response

User electricity demand is influenced not only by the price of electricity but also by social factors. Changes in electricity prices can cause users to shift their electricity demand from peak period to valley period, thus increasing the consumption of renewable energy in the valley period. Due to individual difference to the incentives of users, social factors such as the sensitivity to policy publicity and interactions among group behavior, all of them, will also affect user electricity consumption behavior, so as to affect the consumption of renewable energy.

Based on consumer psychology (Rogers, 1995; Haws et al., 2017), this article establishes a response model to express the influence of social factors on the user's behavior.

In the early stages of monthly interprovincial transactions, because of low publicity and ignorance of new policy by users, there were two ways of participating in demand response. One is not to participate in demand response. The other is to participate in demand response but with little willingness to participate. Then, as the publicity increased, when those nonresponsive users in the early stage observed the considerable economic benefits of those participating in the demand response, the demand responsiveness of both ways increased. Until the end, most of users participated in the demand response. The demand responsiveness can be approximated as a piecewise-linear function, as shown in **Figure 2**.

In **Figure 2**, the x-axis represents time, the left side of the y-axis is the demand responsiveness, and the right side of the y-axis is the user's revenues.

The demand responsiveness of the above two ways can be described as follows:

$$\mu_1 = \begin{cases} \mu_1 & 0 < t \le t_1 \\ \dfrac{1-\mu_1}{t_3 - t_1} t + \dfrac{t_3 \mu_1 - t_1}{t_3 - t_1} & t_1 < t \le t_3 \\ 1 & t > t_3 \end{cases}, \tag{12}$$

$$\mu_{II} = \begin{cases} 0 & 0 < t \le t_2 \\ \dfrac{1}{t_4 - t_2} t - \dfrac{t_2}{t_4 - t_2} & t_2 < t \le t_4 \\ 1 & t > t_4 \end{cases}, \quad (13)$$

where μ_I and μ_{II} represent the demand responsiveness of the two ways, respectively.

The demand response model considers both the social and economic factors.

At time t, based on **Eq. 11** and **Eq. 12**, the electricity consumption under user participation response can be designed as follows:

$$\begin{bmatrix} L_1 \\ L_2 \\ \cdots \\ L_{24} \end{bmatrix} = \begin{bmatrix} L_{0,1} \\ L_{0,2} \\ \cdots \\ L_{0,24} \end{bmatrix} + \mu_i * \begin{bmatrix} L_{0,1} & 0 & \cdots & 0 \\ 0 & L_{0,2} & \cdots & 0 \\ \vdots & \vdots & \ddots & \vdots \\ 0 & 0 & \cdots & L_{0,24} \end{bmatrix} * E * \begin{bmatrix} \Delta P_1 / P_1 \\ \Delta P_2 / P_2 \\ \cdots \\ \Delta P_{24} / P_{24} \end{bmatrix}, \quad (14)$$

where $L_{0,t}$ and L_t represent the user load at time t before and after the response, respectively. E is the price elasticity matrix (Kirschen et al., 2000). ΔP is the change in the electrovalence. P_t is the electrovalence at time t. μ_i is the demand responsiveness, and i is I or II.

A MEDIUM- AND LONG-TERM SOURCE–LOAD INTERACTIVE OPTIMIZATION MODEL TO PROMOTE THE RENEWABLE ENERGY CONSUMPTION

Model Framework

The medium- and long-term source–load interactive optimization model framework to promote the renewable energy consumption includes two stages: short-time scale and monthly interprovincial transactions.

On a short-time scale with the day as the trading cycle, the user demand response model is used to reflect the user demand response-ability under the consideration of social environmental factors. Since most of the wind and PV power is abandoned during the flat and valley periods, users are guided to shift their load from peak periods to valley periods by implementing peak-cutting and valley-filling subsidies. Under such circumstances, the user load demand and wind/PV generation curves are close to each other, as well as the possible consumption of renewable energy.

Based on the short-time scale clearing results, monthly interprovincial transactions on the medium- and long-term scale are carried out. A monthly interprovincial transaction optimization model that promotes the consumption of renewable energy is established. The model takes the interests of the power grid company and renewable generators jointly as the objective function. Then, after the transaction is cleared, the user subsidy cost is reasonably allocated according to the settlement rules designed in *Transaction Settlement*.

Objective Function

Based on the safe and stable operation of the grid, the business goal of the power grid company and renewable generators is to maximize their economic benefits. Therefore, considering the economics of the power grid company and the capacity of renewable energy consumption, to promote the consumption of renewable energy and maximize the benefit of the power grid company, the objective function of this article is given as follows:

$$maxQ = \max\left(\sum_{1}^{T} \sum_{t=1}^{24} \left(C_{R,t} + C_{G,t} - C_{DRI,t} \right) \right), \quad (15)$$

where Q is the total revenue. The time period $T = 31$ in this article.

Constraints

1) Output constraints of thermal power units

$$P_{i,min}^{g} < P_{i,t}^{g} < P_{i,max}^{g}, \quad (16)$$

where $P_{i,t}^{g}$ is the power output of thermal power unit i at time t. $P_{i,max}^{g}$ and $P_{i,min}^{g}$ represent the upper and lower limits of the output of the thermal power unit, respectively.

2) Uncertainty constraints of wind power and PV output:

Errors affected by natural conditions and other unknown external factors occur between the results of the existing forecast methods and the actual output. When wind power and PV are connected to the grid on a large scale, the forecast errors cannot be ignored. In this article, the output uncertainty using the method is expressed as follows: (Yi et al., 2018)

$$L_{f,t}^{re} - L_{f,t}^{er} < L_{f,t} < L_{f,t}^{re} + L_{f,t}^{er}, \quad (17)$$

$$L_{g,t}^{re} - L_{g,t}^{er} < L_{g,t} < L_{g,t}^{re} + L_{g,t}^{er}, \quad (18)$$

$$L_{f,t}^{er} = \gamma_1 * L_{f,t}^{re}, \quad (19)$$

$$L_{g,t}^{er} = \gamma_2 * L_{g,t}^{re}, \quad (20)$$

where $L_{f,t}^{re}$, $L_{g,t}^{re}$, $L_{f,t}$, and $L_{g,t}$ represent the predicted and actual output of wind power and PV, respectively. $L_{f,t}^{er}$ and $L_{g,t}^{er}$ denote the forecast error of wind power and PV output, respectively. γ_1 and γ_2 denote the forecast error coefficient of wind power and PV output, respectively.

3) Wind power and PV output limit constraints are denoted as follows:

$$L_t^f \le L_{f,t}, \; L_t^g \le L_{g,t}. \quad (21)$$

4) Operating time constraints of thermal power units are obtained as follows:

$$\begin{cases} T_i^{on} \ge T_i^{MR} \\ T_i^{off} \ge T_i^{MS} \end{cases}, \quad (22)$$

where T_i^{on} and T_i^{off} represent the continuous start-up time and continuous shutdown time of the unit, respectively. T_i^{MR} and T_i^{MS} are the minimum start-up time and minimum shutdown time of the unit, respectively.

5) Ramp rate constraints of thermal power units are obtained as follows:

$$\begin{cases} P_{i,t}^{g} - P_{i,t-1}^{g} \le r_{i,up} \\ P_{i,t-1}^{g} - P_{i,t}^{g} \le r_{i,down} \end{cases}, \tag{23}$$

where $r_{i,up}$ and $r_{i,down}$ represent the upper and lower limits of the unit ramp rate, respectively.

6) Power balance constraints are obtained as follows:

$$L_t = P_{g,t} + L_t^f + L_t^g + L_t^G + L_t^s, \tag{24}$$

$$P_{g,t} = \sum_{i=1}^{I} \mu_{i,t} P_{i,t}^{g}, \tag{25}$$

where $P_{g,t}$ is the total output of thermal units. $\mu_{i,t}$ represents the operating state of thermal unit i at time t, $\mu_{i,t} = 0$ indicates that the unit is in the shutdown state, and $\mu_{i,t} = 1$ indicates that the unit is in operation. I is the number of thermal power units. L_t^s is the output of hydropower units. It is worthwhile to point out this article attaches great importance to hydropower. Therefore, hydropower is assumed to be fully consumed before and after the transaction.

7) Out-purchased electricity power constraints are obtained as follows:

$$0 \le L_t^G \le L_{t,max}^G, \tag{26}$$

where $L_{t,max}^G$ is the maximum value of the out-purchased electricity.

The model in this article is a mixed-integer nonlinear programming problem, which can be optimally solved by using an improved particle swarm optimization algorithm (Lee et al., 2016). The particle repair strategy (Lee et al., 2016) is used to repair the particle encoding matrix that does not meet the constraints until the conditions are fulfilled. Meanwhile, a penalty function is added in the iterative solution process, and a larger threshold is set for particles that do not meet the constraints, to make the search jump out of the infeasible region.

CASE STUDIES

Simulation Model of Renewable Energy Consumption Mechanism Considering the Monthly Interprovincial Transaction

In this section, monthly interprovincial transactions are carried out with data from the Hunan Province power grid in China, of which the structure is shown in **Figure 3**. In this case, due to the presence of renewable energy abandonment at the beginning of the month, only the user demand response scenario of way I is considered. The peak-valley time-of-use (TOU) price and time period data are shown in **table 1**. $t_1 = 10$, $t_3 = 20$, and $\mu_1 = 0.3$ in the piecewise linear function of demand responsiveness. $\tau_{max} = 0.4$, $p_1 = 0.47 RMB/(KW.h)$, $p_2 = 0.49 RMB/(KW.h)$, and $p_3 = 0.31345 RMB/(KW.h)$ in transaction settlement. The forecast error coefficient γ_1 of wind power and the forecast error coefficient γ_2 of PV are sampled from $[-0.2, 0.2]$ and $[-0.1, 0.1]$, respectively. The price elasticity coefficients described in the study by Gao et al. (2014) are used, the specific data are as follows:

$$E = \begin{bmatrix} -0.4546 & 0.2241 & 0.2305 \\ 0.2153 & -0.4459 & 0.2306 \\ 0.2151 & 0.2241 & -0.4392 \end{bmatrix}.$$

Analysis of Monthly Trading Results

Revenue of all Participators in the Monthly Interprovincial Transaction Market

The revenue results for each market participant are shown in **Figure 4**. From day 0 to day 10, as the initial stage of the monthly transaction, the user's willingness to participate in the demand response is not high when the revenue is less. The revenue of power grid company remains at around 4.5 million RMB during this period. Due to the volatility of the renewable energy output, the revenue of the renewable generators shows a fluctuating state, especially on day 2 and day 8, when the renewable energy output increases sharply. The revenue of the renewable generators then increases, leading to a decrease in the power purchased by the power grid company, and a slight decrease is observed in the revenue of the power grid company compared to the other time of the period.

From day 10 to day 20, as users gain revenue, the demand responsiveness increases. With the rise of the amount of load shifted by users, user revenue gradually increases, showing a ladder growth trend. Then the power grid company revenue continues to increase along with the reduction of out-purchased electricity demand.

From day 20 to day 30, the user demand response capacity reaches saturation. Compared with the previous 10 days, the total load of each day during this period has been reduced. Therefore, the user revenue is reduced. The grid company revenue also drops correspondingly.

Analysis of Monthly Trading Results

Table 2 shows the changes of renewable energy consumption and out-purchased electricity, and the sharing results of each beneficiary body after monthly interprovincial transaction. By guiding users to participate in demand response, the monthly consumption of renewable energy increases from 597,625.5 to 680,910.7 MW h, which is an increase of 13.9%. Monthly out-purchased electricity decreases from 3621429.1 to 2910808.1 MW h, which is a decrease of 19.6%. In this month, users need to be compensated with 43.47 million RMB. According to the settlement mechanism, renewable generators need to share 4.58 million RMB. The power grid company needs to share 38.89 million RMB. From the above analysis, the optimization model proposed in this article can not only effectively enhance the consumption of renewable energy but also effectively optimize the demand for out-purchased electricity and realize the optimal allocation of resources in different provinces.

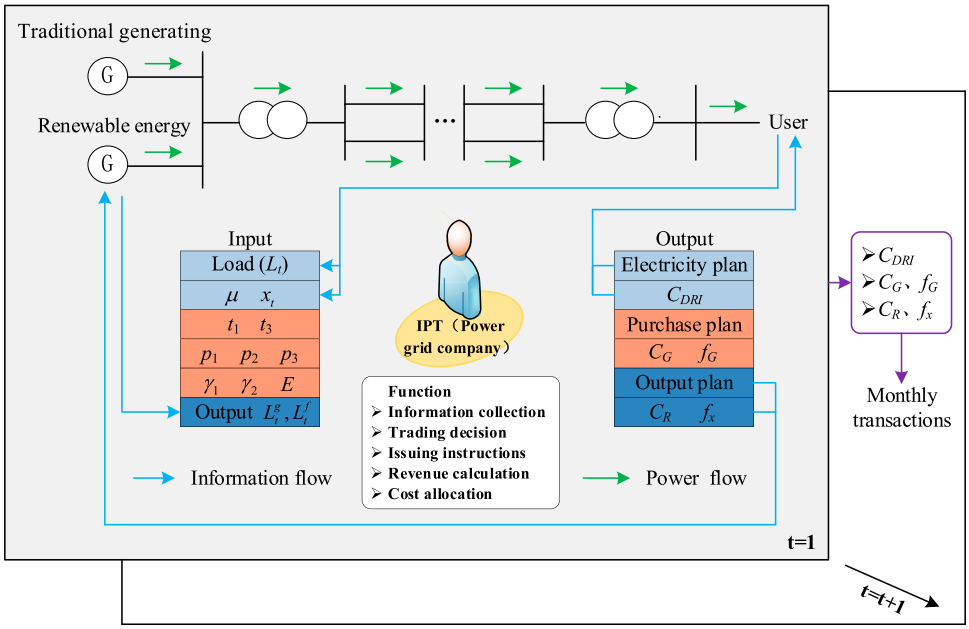

FIGURE 3 | Structure of monthly interprovincial transactions.

TABLE 1 | Peak-valley TOU price and time period.

Parameter	Time period	Electrovalence
Peak period	9:00–11:00; 15:00–22:00	0.7647
Flat period	7:00–9:00; 11:00–15:00; 22:00–23:00	0.6147
Valley period	23:00–7:00	0.4147

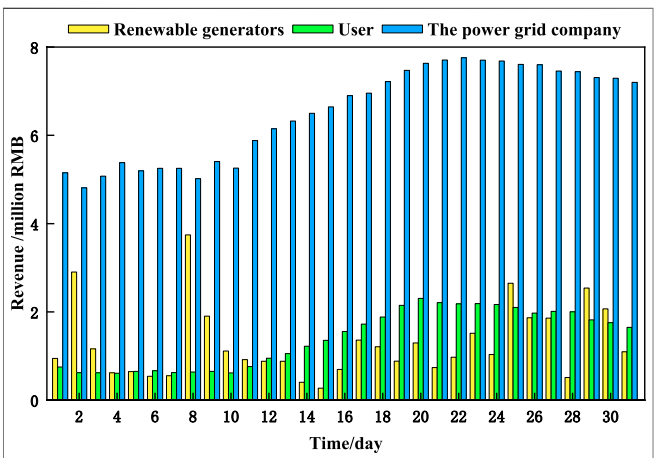

FIGURE 4 | Revenue results for each market participant.

Analysis of Typical Day Results

To further discuss the rationality and validity of the model, a typical day of the month is used as an example for specific analysis. The results of the analysis are as follows:

1) Unit scheduling results

By implementing price subsidies, the dispatch results of each unit are shown in **Figure 5** after users are guided to participate in the demand response. The total output situation of each unit is consistent with the change in load demand, in which the output of thermal power units is the largest, accounting for 40–55% of the user load demand. The output of hydropower units is relatively stable. At the same time, the load in the flat-valley period increases with the decrease of the load in the peak period after users participated in demand response. The system load peak-valley difference decreases by 4.6%.

2) Renewable energy consumption results

Figure 6 shows the consumption and output of wind power and PV before optimization. Wind power is abandoned the most in the early morning. The cumulative abandoned wind power is 3,668.73 MW h throughout the day, accounting for 11.37% of the total wind power output. The PV is abandoned the most at noon. The accumulative abandoned PV is 1,191.68 MW h throughout the day, accounting for 20.02% of the total PV output. Combined with **Figure 5**, it can be seen by guiding users that to participate in the demand response, their load demand has to be shift and electricity consumption during the flat-valley period has to be increased, and the wind power consumption rises by 4.5% and PV consumption by 9.1%. The problem of wind and PV abandonment is effectively alleviated.

3) Situation of out-purchased electricity

TABLE 2 | Allocation results of user compensation costs for each beneficiary body.

Parameter	Renewable generators	Power grid company
Power before optimization	597,625.5 MW h	3621429.1 MW h
Power after optimization	680,910.7 MW h (+ 13.9%)	2910808.1 MW h (–19.6%)
Income	39.78 million RMB	222.74 million RMB
Cost allocation	4.58 million RMB	38.89 million RMB

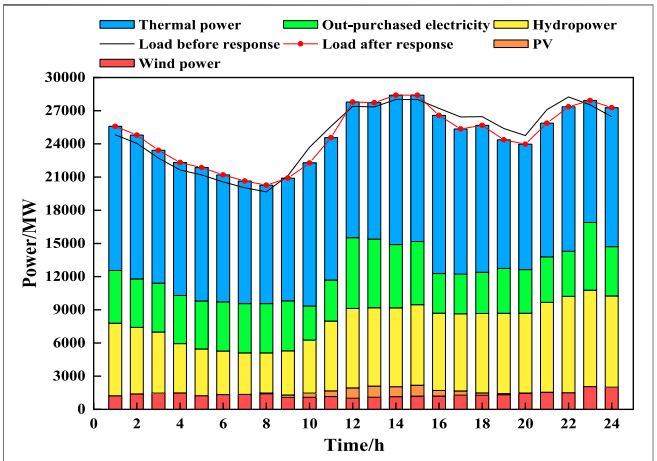

FIGURE 5 | Output diagram of various units after optimization.

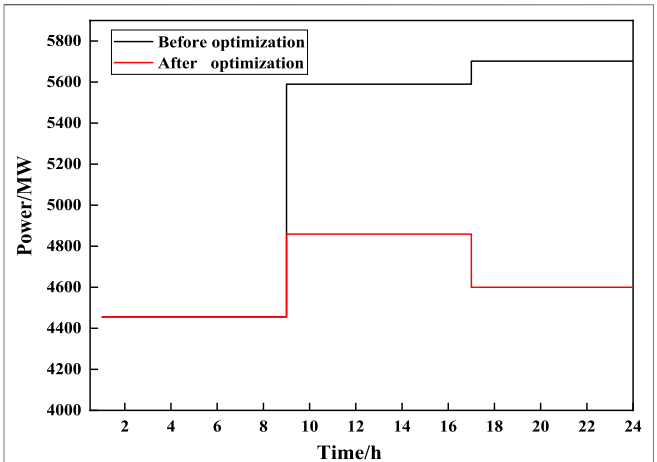

FIGURE 7 | Transmission power curve of the trans-provincial tie-line.

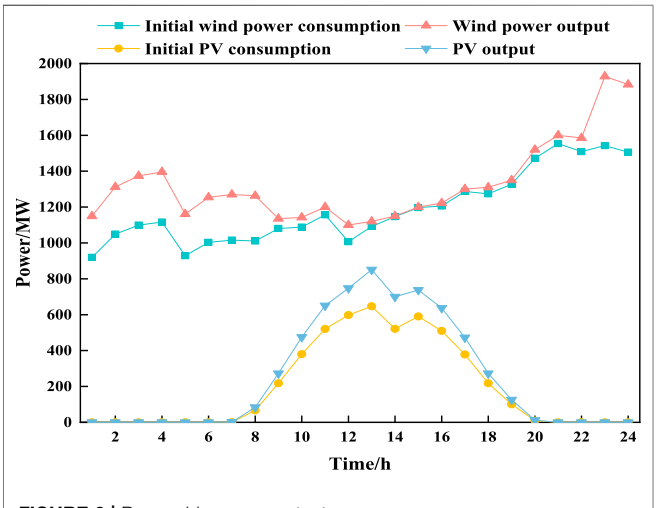

FIGURE 6 | Renewable energy output.

According to the actual operation mode, a three-step segmented operation mode is used for interprovincial power transmission. **Figure 7** shows the transmission power curve of the trans-provincial tie-line before and after optimization. Compared with the power transmission curve before optimization, the optimized out-purchased power is significantly reduced from 9:00 to 24:00. Since the peak periods are at this period, by guiding users to participate in the demand response and shifting a load of peak periods to the valley periods, the electricity demand of users is significantly reduced at this time. Therefore, the demand of inner-provincial out-purchased power drops accordingly.

TABLE 3 | Allocation results of user compensation costs for each beneficiary body.

Parameter	Renewable generators	Power grid company
Increase/decrease power	1988.38 MW h	15,316.19 MW h
Income	945,300 RMB	4,800,900 RMB
Cost allocation	86,200 RMB	663,900 RMB

4) Allocation situation of user compensation cost

The allocation results for each beneficiary body are shown in **table 3**. The typical daily renewable energy consumption increases by 1988.38 MW h, and it is calculated that the renewable generator new income is 945,300 RMB. Meanwhile, the out-purchased electricity decreases by 15,316.19 MW h; after calculating, the cost of the power grid company for out-purchased electricity decreases by 4,800,900 RMB. According to the cost-sharing rules, renewable generators need to share 86,200 RMB, while the reduction of out-purchased power is more reduced, and the benefits are greater. Therefore, the power grid company needs to share 663,900 RMB, which bears about 88.5% of user compensation costs. By reasonably sharing user compensation costs, while incentivizing the power grid companies to rationally use demand-side resources to reduce out-purchased electricity, it

also provides an effective market settlement method for further consumption of renewable energy.

CONCLUSION

With the increasing penetration of renewable energy, the problem of renewable energy consumption is standing out, especially in China, in which operational reliability is a priority. From the perspective of existing Chinese interprovincial transactions, this article proposes a medium- and long-term transaction mechanism that promotes the consumption of renewable energy and realizes the interaction among renewable generators, users, and power grids by setting a new player. The main contributions are as follows:

1) Through the implementation of price subsidies, innerprovincial users are guided to change their electricity consumption habits. Therefore, the closeness between user load demand and wind power/PV power output curves is maximized. The renewable energy consumption increases by 13.9%. Purchased power decreases by 27.9%. Common profit of grid companies, renewable generators, and users are realized.
2) According to the fairness principle of "who gains, who is responsible," the user compensation cost is reasonably shared among the beneficiaries. The fact provides an effective market settlement model for further promoting the consumption of renewable energy.
3) Interprovincial transaction can not only increase the consumption of inner-provincial renewable energy but also realize the optimal allocation of resources in different provinces.

In this article, the impact of user participation in interprovincial transactions on the consumption of renewable energy is studied. In the future, considering the different sensitivity of different industries to electricity prices, the renewable energy consumption measures under interprovincial transactions involving different types of users can be studied.

DATA AVAILABILITY STATEMENT

The original contributions presented in the study are included in the article/Supplementary Material; further inquiries can be directed to the corresponding author.

AUTHOR CONTRIBUTIONS

YeC and YL conceptualized the study. YeC and YL performed the analysis. XT and YT acquired resources. YeC, XT, and YiC acquired funding. YL wrote the original draft. YeC, XT, and YT reviewed and edited the manuscript. All authors agreed to be accountable for the content ofthe work.

FUNDING

This work is supported by the Joint Funds of the National Natural Science Foundation of China (No. U1966207), the Hunan Natural Science Foundation (No. 2020JJ5573), and the National Natural Science Foundation of China (No. 51807010).

ACKNOWLEDGMENTS

The authors gratefully acknowledge the support of the Joint Funds of the National Natural Science Foundation of China (No. U1966207), the Hunan Natural Science Foundation (No. 2020JJ5573), and the National Natural Science Foundation of China (No. 51807010).

REFERENCES

Gao, Y., Lv, M., Liang, H., and Zhang, J. (2014). Power Demand Price Elasticity Matrix Based on Discrete Attraction Model. *Automation Electric Power Syst.* 38 (13), 103–107+144. doi:10.7500/AEPS20131015003

Guo, L., Ding, Y., Bao, M., and Zeng, D. (2019). An Optimal Power Purchase Model of Inter-provincial Traders in Two-Level Electricity Market Considering Risk Management, *Power Syst. Tech.* 43, 2726–2734. doi:10.13335/j.1000-3673.pst.2019.0668

Haws, K. L., Mcferran, B., and Redden, J. P. (2017). The Satiating Effect of Pricing: The Influence of price on Enjoyment over Time. *J. Consumer Psychol.* 27, 341–346. doi:10.1016/j.jcps.2017.03.001

Kirschen, D. S., Strbac, G., Cumperayot, P., and de Paiva Mendes, D. (2000). Factoring the Elasticity of Demand in Electricity Prices. *IEEE Trans. Power Syst.* 15 (2), 612–617. doi:10.1109/59.867149

Kroposki, B., Sen, P. K., and Malmedal, K. (2013). Selection of Distribution Feeders for Implementing Distributed Generation and Renewable Energy Applications. *IEEE Trans. Ind. Applicat.* 49 (6), 2825–2834. doi:10.1109/TIA.2013.2262091

Latifi, M., Khalili, A., Rastegarnia, A., and Sanei, S. (2019). A Bayesian Real-Time Electric Vehicle Charging Strategy for Mitigating Renewable Energy Fluctuations. *IEEE Trans. Ind. Inf.* 15 (5), 2555–2568. doi:10.1109/TII.2018.2866267

Lee, J. H., Kim, J.-W., Song, J.-Y., Kim, Y.-J., and Jung, S.-Y. (2016). A Novel Memetic Algorithm Using Modified Particle Swarm Optimization and Mesh Adaptive Direct Search for PMSM Design. *IEEE Trans. Magn.* 52 (3), 1–4. doi:10.1109/TMAG.2015.2482975

Li, B., Chen, J., Li, D., Shi, K., Yang, B., Qi, B., et al. (2019a). Analysis and Prospect of Key Issues in China's Demand Response for Further Large Scale Implementation. *Power Syst. Tech.* 43 (02), 694–704. doi:10.13335/j.1000-3673.pst.2018.0737

Li, J., Fu, Y., Xing, Z., Zhang, X., Zhang, Z., and Fan, X. (2019b). Coordination Scheduling Model of Multi-type Flexible Load for Increasing Wind Power Utilization. *IEEE Access* 7, 105840–105850. doi:10.1109/ACCESS.2019.2932141

Li, Y., Yuan, S., Liu, W., Zhang, G., Teng, Y., and Chen, X. (2018). A Fast Method for Reliability Evaluation of Ultra High Voltage AC/DC System Based on Hybrid Simulation. *IEEE Access* 6, 19151–19160. doi:10.1109/ACCESS.2018.2817247

Quan, H., Srinivasan, D., and Khosravi, A. (2014). Short-Term Load and Wind Power Forecasting Using Neural Network-Based Prediction Intervals. *IEEE Trans. Neural Netw. Learn. Syst.* 25 (2), 303–315. doi:10.1109/TNNLS.2013.2276053

Razavi, S. E., Arefi, A., Ledwich, G., Nourbakhsh, G., Smith, D. B., and Minakshi, M. (2020). From Load to Net Energy Forecasting: Short-Term Residential Forecasting for the Blend of Load and PV behind the Meter. *IEEE Access* 8, 224343–224353. doi:10.1109/ACCESS.2020.3044307

Recalde Melo, D. F., Trippe, A., Gooi, H. B., and Massier, T. (2018). Robust Electric Vehicle Aggregation for Ancillary Service Provision Considering Battery Aging. *IEEE Trans. Smart Grid* 9 (3), 1728–1738. doi:10.1109/TSG.2016.2598851

Rogers, E. M. (1995). "Diffusion of Innovations, Fourth Edition," in *Ordinary Nonlinear Differential Equations in Engineering and Physical Sciences*.

Shim, J. W., Verbic, G., Zhang, N., and Hur, K. (2018). Harmonious Integration of Faster-Acting Energy Storage Systems into Frequency Control Reserves in Power Grid with High Renewable Generation. *IEEE Trans. Power Syst.* 33 (6), 6193–6205. doi:10.1109/TPWRS.2018.2836157

Wen, M., Li, Y., Xie, X., Cao, Y., Wu, Y., Wang, W., et al. (2019). Discussion on Key Factors for Efficient Consumption of Renewable Energy in Provincial Power Grid at Southern China. *Csee Jpes* 6 (3), 554–562. doi:10.17775/CSEEJPES.2019.01970

Xu, H., Jin, X., Kong, F., and Deng, Q. (2020). Two Level Colocation Demand Response with Renewable Energy. *IEEE Trans. Sustain. Comput.* 5 (1), 147–159. doi:10.1109/TSUSC.2019.2904867

Yang, X., Song, Y., Wang, G., and Wang, W. (2010). A Comprehensive Review on the Development of Sustainable Energy Strategy and Implementation in China. *IEEE Trans. Sustain. Energ.* 1 (2), 57–65. doi:10.1109/TSTE.2010.2051464

Yi, W., Zhang, Y., Zhao, Z., and Huang, Y. (2018). Multiobjective Robust Scheduling for Smart Distribution Grids: Considering Renewable Energy and Demand Response Uncertainty. *IEEE Access* 6, 45715–45724. doi:10.1109/ACCESS.2018.2865598

Zhang, H., and Zhou (2018). "The Application of Electricity-sale in Operation Mode of Pumped Storage Power Station," in 2018 International Conference on Power System Technology. (POWERCON), 869–872.

Zhou, Z., Xiong, F., Huang, B., Xu, C., Jiao, R., Liao, B., et al. (2017). Game-Theoretical Energy Management for Energy Internet with Big Data-Based Renewable Power Forecasting. *IEEE Access* 5, 5731–5746. doi:10.1109/ACCESS.2017.2658952

Conflict of Interest: Author YT was employed by the State Grid Hunan Electric Power Company Limited Economic and Technical Research Institute.

The remaining authors declare that the research was conducted in the absence of any commercial or financial relationships that could be construed as a potential conflict of interest.

frontiers in Energy Research

ORIGINAL RESEARCH
published: 23 July 2021
doi: 10.3389/fenrg.2021.707183

Event-Triggered Forecasting-Aided State Estimation for Active Distribution System With Distributed Generations

Xingzhen Bai[1], *Xinlei Zheng*[1], *Leijiao Ge*[2]*, *Feiyu Qin*[1] *and Yuanliang Li*[2]

[1]College of Electrical Engineering and Automation, Shandong University of Science and Technology, Qingdao, China, [2]Key Laboratory of Smart Grid of Ministry of Education, Tianjin University, Tianjin, China

In this study, the forecasting-aided state estimation (FASE) problem for the active distribution system (ADS) with distributed generations (DGs) is investigated, considering the constraint of data transmission. First of all, the system model of the ADS with DGs is established, which expands the scope of the ADS state estimation from the power network to the DGs. Moreover, in order to improve the efficiency of data transmission under the limited communication bandwidth, a component-based event-triggered mechanism is employed to schedule the data transmission from the measurement terminals to the estimator. It can efficiently reduce the amount of data transmission while guaranteeing the performance of system state estimation. Second, an event-triggered unscented Kalman filter (ET-UKF) algorithm is proposed to conduct the state estimation of the ADS with mixed measurements. To this end, the unscented transform (UT) technique is employed to approximate the probability distribution of the state variable after nonlinear transformation, which can reach more than second order, and then, an upper bound of the filtering error covariance is derived and subsequently minimized at each iteration. The gain of the desired filter is obtained recursively by following a certain set of recursions. Finally, the effectiveness of the proposed method is demonstrated by using the IEEE-34 distribution test system.

Keywords: active distribution system, forecasting-aided state estimation, event-triggered scheme, unscented Kalman filter, distribution generations

OPEN ACCESS

Edited by:
Yingjun Wu,
Hohai University, China

Reviewed by:
Yanbo Chen,
North China Electric Power University, China
Qiang Yang,
College of Electrical Engineering, Zhejiang University, China

***Correspondence:**
Leijiao Ge
legendglj99@tju.edu.cn

Specialty section:
This article was submitted to Smart Grids, a section of the journal Frontiers in Energy Research

Received: *09 May 2021*
Accepted: *08 June 2021*
Published: *23 July 2021*

Citation:
Bai X, Zheng X, Ge L, Qin F and Li Y (2021) Event-Triggered Forecasting-Aided State Estimation for Active Distribution System With Distributed Generations. Front. Energy Res. 9:707183. doi: 10.3389/fenrg.2021.707183

1 INTRODUCTION

With the widespread integration of distributed generations (DGs) in the power system, the conventional passive distribution system is being transformed into the active distribution system (ADS) (Ehsan and Yang, 2018; Ge et al., 2020a; Li et al., 2020; Luo et al., 2020). It is common that the inherent intermittence and variability of DG generation increase the complexity and uncertainty of the operation state for the ADS (Ge et al., 2021b; 2020b). In this regard, it is necessary to ensure the accuracy and efficiency of state estimation for the ADSs, which is prerequisite for the safe and reliable operation of the power distribution system (Chen Y. et al., 2017; Zhang et al., 2020; Ge et al., 2021a). In general, the traditional static state estimation (SSE) methods are mainly based on the weighted least square (WLS) that cannot meet the estimation requirements of ADSs, because it ignores the dynamics of the system. For this reason, the forecasting-aided state estimation (FASE) is proposed to

improve the accuracy and speed of the estimator effectively for the ADSs (Do Coutto Filho and Stacchini de Souza, 2009; Wang et al., 2020). The FASE method takes into consideration the time evolution of the ADS states that can make the state prediction of the next time instant, so as to provide the information required for a security analysis and preventive control functions. Moreover, when the measurement data of ADS are flawed or even unavailable due to certain reasons, the state prediction values can be used to provide a set of pseudo states of the ADS, thus improving the robustness of the estimator to external interference.

Due to the advantages of the FASE method and its promising prospect of practical application, it has attracted increasing attention for research, and there have been plenty of remarkable achievements made in addressing FASE problems for the ADS (Ćetenović and Ranković, 2018; Macii et al., 2020; Cheng and Bai, 2021; Geetha et al., 2021). For instance, a novel approach in assessing the process noise covariance matrix for FASE in ADS has been proposed by Ćetenović and Ranković (2018), which contributes in improving the accuracy of estimation. The asynchronous hierarchical FASE method has been proposed by Geetha et al. (2021). According to this method, the global estimation values are calculated by collating the estimates of smaller reduced order subsystems to reduce the overall level of computational complexity. Cheng and Bai (2021) put forward the robust FASE for ADSs by using a strict linearization method for the purpose of dealing with the nonlinear measurements, which can reduce the nonlinear error for the state estimation. However, in the prior literature, the monitoring scope of the state estimation system is often limited to the power network part of the ADS. In general, the DGs are modeled as equivalent power injection, but they are not monitored and modeled in detail. In fact, when there are a large number of DGs connected to the distribution network, the accurate estimation of real-time DG states plays a crucial role in the flexible control and dispatch of the ADS (Yang et al., 2018). Meanwhile, with the development of smart sensor, more information of the DG system is allowed to be collected to the monitoring center (Fang et al., 2020). The information redundancy can be improved by considering the measurement of DG system in the context of ADS state estimation, thereby facilitating to enhance the estimation performance. Therefore, it is of much practical significance to construct an adequate model of the ADSs with DGs for expanding the scope of state estimation and improving the estimation performance of ADSs.

In addition, due to economic constraint and the complexity of reconstruction, it is impractical to replace all distribution remote terminal units (DRTUs) with phasor measurement units (PMUs) within a short period of time (Yang et al., 2017). In the foreseeable future, both PMUs and DRTUs will provide measurement data for the FASE of the ADSs collectively (Dobakhshari et al., 2021). Therefore, the FASE algorithm is based on PMU/DRTU mixed nonlinear measurements. In practice, it is significant to deal with nonlinear measurement, which would seriously affect the performance of FASE for the ADSs. In this regard, there are various nonlinear filtering algorithms developed to handle the nonlinear system state estimation, such as the particle filter (PF), the extended Kalman filter (EKF), and the unscented Kalman filter (UKF). The PF algorithm can carry out the recursive Bayesian estimation using the nonparametric Monte Carlo simulation method. Due to the high dimension of the distribution system, however, a considerable amount of particles are required, which would give rise to a huge computational workload. The EKF algorithm linearizes the nonlinear system through the Taylor series expansion but ignores the higher order terms (Sun et al., 2017, 2018), which cannot guarantee the high estimation accuracy. As for the UKF algorithm, the unscented transform (UT) technique is applied to approximate the probability distribution of the state variable after nonlinear transformation (Zhao and Mili, 2019; Dang et al., 2020). The UKF algorithm produces better estimation performance than the EKF algorithm, and it is more suitable to realize the online application of estimation.

Furthermore, with the rapid increase in the number of power users and the extensive connection of DGs, the scale of the ADS is also expanding. In order to meet the monitoring requirements of the ADS, it is necessary to install more measurement devices. As a result, a considerable amount of measurement data would be transmitted to the estimator. Due to the limited network communication resources, the transmission of numerous data may contribute to the network-induced phenomena, for example, data loss and transmission delay, which makes it likely to lose useful information, thus affecting the estimation performance of the ADS (Ding et al., 2017; Cheng et al., 2018; Xing et al., 2018). In order to reduce the transmission of redundant data, the communication strategy based on the event-triggered mechanism has been proposed. According to this strategy, the measurement will be transmitted to the data center for processing only when the preset event-triggering conditions are satisfied. Compared with the traditional time-triggered one, the event-triggered mechanism has the advantage in alleviating the communication burden with ensuring the expected estimation performance. Therefore, the estimation problem based on the event-triggered mechanism has recently attracted much attention (Liu et al., 2018; Li et al., 2019; Kooshkbaghi et al., 2020; Shanmugam et al., 2020; Zhu et al., 2020). For instance, an event-triggered PF algorithm has been proposed by Liu et al. (2018) to estimate the state of the synchronous generator in real time, and the UKF algorithm has been used as the local estimator to provide trigger information in the study by Li et al. (2019), which reduces the computational burden of the intelligent terminal. So far, to our knowledge, the FASE of the ADS based on the event-triggered mechanism has not been considered as carefully as required.

As motivated by the above discussion, this study is purposed to address the FASE problem for the ADS with DGs under the constraints of communication resource, and the main contributions of it are detailed as follows.

1) The system model of the ADSs with DGs is established by considering the state variables and measurements of DGs in detail, which expands the estimation scope of the ADS and facilitates the accurate FASE of the ADS.
2) An appropriate component-based event-triggered mechanism is adopted to reduce "unnecessary" data transmissions from the measuring terminals to the monitoring center, thus alleviating the burden placed on the network transmission.
3) Given the nonlinear mixed measurement of the ADS and the intermittent observation attributed to the event-triggered mechanism, the event-triggered UKF (ET-UKF) algorithm is proposed to ensure the performance of the state estimation.

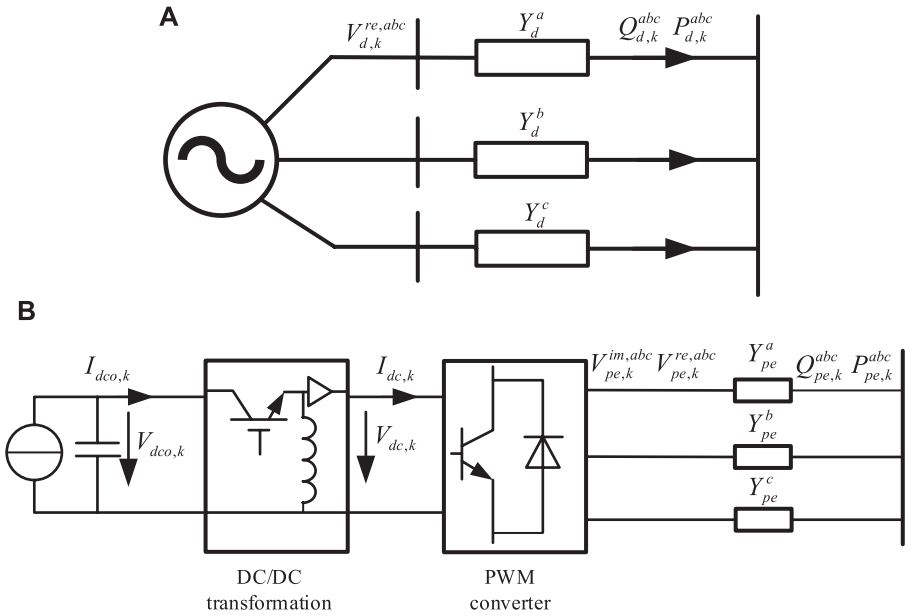

FIGURE 1 | The models of the two most commonly used DGs: **(A)** model of DGs connected to the grid directly and **(B)** model of direct current type DGs connected to grid *via* a chopper-inverter device.

The rest of this article is organized as follows. The state and measurement models of the ADS are built by incorporating the state and measurement information of DGs into the distribution system in **System Model of ADS with DGs** section. In **FASE with Component-Based Event-Triggered Mechanism** section, the component-based event-triggered mechanism is introduced, and the ET-UKF algorithm is designed. In **Simulation Results and Analysis** section, the IEEE-34 distribution test system is taken as an example to verify the effectiveness of the proposed method.

2 SYSTEM MODEL OF THE ACTIVE DISTRIBUTION SYSTEM WITH DISTRIBUTED GENERATIONS

For the FASE of ADSs, the system model is composed of the state model and the measurement model. The state model is linear, which represents the transition trajectory between consecutive states (Zhao et al., 2019). The measurement model expresses the functional relationship between measurements and state variables. In this study, considering the widespread connection of DGs in the ADS, the system model is built by combining the state and measurement variables of power networks and DGs.

2.1 State Model

The system state $x_k \in \mathbb{R}^n$ is composed of the state of the network part of the ADS and the DGs connected to the distribution system, and $x_k = [x_{DG,k}^T, x_{DN,k}^T]^T$. In reality, there are many types of DGs, including DGs that are directly connected to the distribution network such as synchronous generators and asynchronous generators (as shown in **Figure 1A**), and DGs that are connected to the grid through power electronic converters, such as photovoltaic cells and energy storage batteries (Chen S. et al., 2017). The most common DGs connected to the grid *via* power electronic devices are the direct current DGs, which are connected to the grid *via* a chopper-inverter device (as shown in **Figure 1B**).

For the DGs connected to the grid directly, the state variables are selected as $x_{d,k} = [V_{d,k}^{re,a}, V_{d,k}^{re,b}, V_{d,k}^{re,c}, V_{d,k}^{im,a}, V_{d,k}^{im,b}, V_{d,k}^{im,c}]^T$, where $V_{d,k}^{re,p}$ and $V_{d,k}^{im,p}$ $(p \in \{a, b, c\})$ represent the real and imaginary parts of the alternating current voltage output by the DGs, respectively. For the direct current–type DGs connected to grid *via* a chopper-inverter device, the state variables are set as $x_{pe,k} = [V_{dco,k}, I_{dco,k}, V_{dc,k}, V_{pe,k}^{re,a}, V_{pe,k}^{re,b}, V_{pe,k}^{re,c}, V_{pe,k}^{im,a}, V_{pe,k}^{im,b}, V_{pe,k}^{im,c}]^T$, where $V_{dco,k}$ and $I_{dco,k}$ are the voltage and current output by the direct current–type DGs, respectively, and $V_{dc,k}$ represents the direct current voltage output by the DC/DC transformation. Therefore, $x_{DG,k} = [x_{d,1,k}^T, \ldots, x_{d,n_d,k}^T, x_{pe,1,k}^T, \ldots, x_{pe,n_{pe},k}^T]^T \in \mathbb{R}^{n_{DG}}$. In addition, the state vector of the distribution network part $x_{DN,k} = [V_{1,k}^T, \ldots, V_{\iota,k}^T, \ldots, V_{n_{DN},k}^T]^T \in \mathbb{R}^{n_{DN}}$ is consisted of the real and imaginary parts of bus voltage in the distribution network, where $V_{\iota,k} = [V_{\iota,k}^{re,a}, V_{\iota,k}^{re,b}, V_{\iota,k}^{re,c}, V_{\iota,k}^{im,a}, V_{\iota,k}^{im,b}, V_{\iota,k}^{im,c}]^T$ is a vector representing the state of the ι – th bus.

Then, the state model of the ADS with DGs can be described as

$$x_k = F_{k-1}x_{k-1} + g_{k-1} + w_{k-1}, \tag{1}$$

where F_{k-1} is the transition matrix that represents the speed of the state transition process, and vector g_{k-1} is associated with the trend behavior of the state trajectory. $w_{k-1} \in \mathbb{R}^n$ represents the process noise that obeys Gaussian distribution, which satisfies $\mathbb{E}\{w_{k-1}\} = 0$ and $\mathbb{E}\{w_{k-1}w_{k-1}^T\} = Q_{k-1}$. In this study, with the consideration of the adequacy and parsimony of the state

model, we adopt the Holt–Winters double exponential smoothing method in **Eq. 1** to update F_{k-1} and g_{k-1} as follows:

$$F_{k-1} = \alpha_H(1+\beta_H)I, \tag{2}$$

$$g_{k-1} = (1+\beta_H)(1-\alpha_H)\widehat{x}_{k-1|k-2} - \beta_H a_{k-2} + (1-\beta_H)b_{k-2}, \tag{3}$$

where I is the identity matrix; α_H and β_H are smoothing parameters, which are commonly in the range from 0 to 1; $\widehat{x}_{k-1|k-2}$ is the predicted state at instant $k-1$; and a_k and b_k are recursively defined as

$$a_k = \alpha_H \widehat{x}_{k|k} + (1-\alpha_H)\widehat{x}_{k|k-1}, \tag{4}$$

$$b_k = \beta_H(a_k - a_{k-1}) + (1-\beta_H)b_{k-1}, \tag{5}$$

2.2 Measurement Model

The measured data of the ADS primarily originate from alternating current voltage, power, other measurement information of the network part, and the measurement information provided by sensors in DGs.

In general, the measurements obtained from different types of DGs are different. For the DGs directly connected to the grid, the measurement information is $y_{d,k} = [P^a_{d,k}, P^b_{d,k}, P^c_{d,k}, Q^a_{d,k}, Q^b_{d,k}, Q^c_{d,k}, \mathrm{V}^a_{d,k}, \mathrm{V}^b_{d,k}, \mathrm{V}^c_{d,k}]^T$. Assuming the DG is connected to the $\iota-$th bus in the ADS, according to the equivalent model shown in **Figure 1A**, the measurement equation can be obtained as

$$\begin{cases} P^p_{d,k} = -V^{re,p}_{d,k}\left(G^p_d \overrightarrow{V}^{re,p}_{d-\iota,k} - B^p_d \overrightarrow{V}^{im,p}_{d-\iota,k}\right) + V^{im,p}_{d,k}\left(G^p_d \overrightarrow{V}^{im,p}_{d-\iota,k} + B^p_d \overrightarrow{V}^{re,p}_{d-\iota,k}\right) \\ Q^p_{d,k} = -V^{re,p}_{d,k}\left(G^p_d \overrightarrow{V}^{im,p}_{d-\iota,k} + B^p_d \overrightarrow{V}^{re,p}_{d-\iota,k}\right) + V^{im,p}_{d,k}\left(G^p_d \overrightarrow{V}^{re,p}_{d-\iota,k} - B^p_d \overrightarrow{V}^{im,p}_{d-\iota,k}\right) \end{cases}, \tag{6}$$

$$\mathrm{V}^p_{d,k} = \sqrt{\left(V^{re,p}_{d,k}\right)^2 + \left(V^{im,p}_{d,k}\right)^2}, \tag{7}$$

where $\overrightarrow{V}^{re,p}_{d-\iota,k} = V^{re,p}_{d,k} - V^{re,p}_{\iota,k}$, $\overrightarrow{V}^{im,p}_{d-\iota,k} = V^{im,p}_{d,k} - V^{im,p}_{\iota,k}$. G^p_d and B^p_d are the real and imaginary parts of equivalent admittance Y^p_d, respectively. $P^p_{d,k}$ and $Q^p_{d,k}$ represent the active and reactive power outputs by the DGs, and $\mathrm{V}^p_{d,k}$ is the voltage amplitude of the DGs.

For the direct current DGs connected to the grid by the chopper-inverter device, according to the data that can be measured by the chopper-inverter device sensors, the measurement is $y_{pe,k} = [V_{dco,k}, I_{dco,k}, V_{dc,k}, I_{dc,k}, \mathrm{V}^a_{pe,k}, \mathrm{V}^b_{pe,k}, \mathrm{V}^c_{pe,k}, P^a_{pe,k}, P^b_{pe,k}, P^c_{pe,k}, Q^a_{pe,k}, Q^b_{pe,k}, Q^c_{pe,k}]^T$. From the equivalent model shown in **Figure 1B**, the measurement equation can be expressed as

$$\begin{cases} V_{dco,k} = V_{dco,k} \\ I_{dco,k} = I_{dco,k} \\ V_{dc,k} = V_{dc,k} \\ I_{dc,k} = \dfrac{I_{dco,k}V_{dco,k}\eta_{dc}}{V_{dc,k}} \end{cases} \tag{8}$$

$$\mathrm{V}^p_{pe,k} = \sqrt{\left(V^{re,p}_{pe,k}\right)^2 + \left(V^{im,p}_{pe,k}\right)^2}, \tag{9}$$

$$\begin{cases} P^p_{pe,k} = -V^{re,p}_{pe,k}\left(G^p_{pe}\overrightarrow{V}^{re,p}_{pe-\iota,k} - B^p_{pe}\overrightarrow{V}^{im,p}_{pe-\iota,k}\right) + V^{im,p}_{pe,k}\left(G^p_{pe}\overrightarrow{V}^{im,p}_{pe-\iota,k} + B^p_{pe}\overrightarrow{V}^{re,p}_{pe-\iota,k}\right) \\ Q^p_{pe,k} = -V^{re,p}_{pe,k}\left(G^p_{pe}\overrightarrow{V}^{im,p}_{pe-\iota,k} + B^p_{pe}\overrightarrow{V}^{re,p}_{pe-\iota,k}\right) + V^{im,p}_{pe,k}\left(G^p_{pe}\overrightarrow{V}^{re,p}_{pe-\iota,k} - B^p_{pe}\overrightarrow{V}^{im,p}_{pe-\iota,k}\right) \end{cases}, \tag{10}$$

where $\overrightarrow{V}^{re,p}_{pe-\iota,k} = V^{re,p}_{pe,k} - V^{re,p}_{\iota,k}$, $\overrightarrow{V}^{im,p}_{pe-\iota,k} = V^{im,p}_{pe,k} - V^{im,p}_{\iota,k}$. $I_{dc,k}$ is the DC/DC converter output current, η_{dc} is the efficiency of the DC/DC converter, and $\mathrm{V}^p_{pe,k}$ represents the voltage amplitude at the ports of power electronic grid–connected devices. G^p_{pe} and B^p_{pe} are the real and imaginary parts of equivalent admittance Y^p_{pe}, respectively.

The measurement information of the network part is mainly provided by the PMUs and the DRTUs. The PMU can measure the real and imaginary parts of bus voltage and branch current, respectively. Moreover, the DRTU can measure the voltage amplitude, injected power of the bus, and the power flow of the branch. **Figure 2** shows the three-phase line model of the distribution system. Combined with the circuit theorem, the functional relationship between measurement variable and state variable can be calculated.

Then, the PMU measurements are expressed as

$$\begin{cases} V^{re,p}_{\iota,k} = V^{re,p}_{\iota,k} \\ V^{im,p}_{\iota,k} = V^{im,p}_{\iota,k} \end{cases}, \tag{11}$$

$$\begin{cases} I^{re,p}_{\iota-\iota',k} = \dfrac{1}{2}b^p_{\iota-\iota'}V^{im,p}_{\iota,k} + \sum\limits_{q\in\{a,b,c\}} G^{pq}_{\iota-\iota'}\overrightarrow{V}^{re,q}_{\iota-\iota',k} - B^{pq}_{\iota-\iota'}\overrightarrow{V}^{im,q}_{\iota-\iota',k} \\ I^{im,p}_{\iota-\iota',k} = \dfrac{1}{2}b^p_{\iota-\iota'}V^{re,p}_{\iota,k} + \sum\limits_{q\in\{a,b,c\}} G^{pq}_{\iota-\iota'}\overrightarrow{V}^{im,q}_{\iota-\iota',k} - B^{pq}_{\iota-\iota'}\overrightarrow{V}^{re,q}_{\iota-\iota',k} \end{cases}, \tag{12}$$

and the DRTU measurements are expressed as

$$\mathrm{V}^p_{\iota,k} = \sqrt{\left(V^{re,p}_{\iota,k}\right)^2 + \left(V^{im,p}_{\iota,k}\right)^2}, \tag{13}$$

$$\begin{cases} P^p_{\iota,k} = V^{re,p}_{\iota,k}\sum\limits_{\iota'\in N_\iota}\sum\limits_{q\in\{a,b,c\}} G^{pq}_{\iota-\iota'}\overrightarrow{V}^{re,q}_{\iota-\iota',k} - B^{pq}_{\iota-\iota'}\overrightarrow{V}^{im,q}_{\iota-\iota',k} \\ \qquad + V^{im,p}_{\iota,k}\sum\limits_{\iota'\in N_\iota}\sum\limits_{q\in\{a,b,c\}} G^{pq}_{\iota-\iota'}\overrightarrow{V}^{im,q}_{\iota-\iota',k} + B^{pq}_{\iota-\iota'}\overrightarrow{V}^{re,q}_{\iota-\iota',k} \\ Q^p_{\iota,k} = -\dfrac{1}{2}\sum\limits_{\iota'\in N_\iota} b^p_{\iota-\iota'}\left[\left(V^{re,p}_{\iota,k}\right)^2 + \left(V^{im,p}_{\iota,k}\right)^2\right] \\ \qquad - V^{re,p}_{\iota,k}\sum\limits_{\iota'\in N_\iota}\sum\limits_{q\in\{a,b,c\}} G^{pq}_{\iota-\iota'}\overrightarrow{V}^{im,q}_{\iota-\iota',k} + B^{pq}_{\iota-\iota'}\overrightarrow{V}^{re,q}_{\iota-\iota',k} \\ \qquad + V^{im,p}_{\iota,k}\sum\limits_{\iota'\in N_\iota}\sum\limits_{q\in\{a,b,c\}} G^{pq}_{\iota-\iota'}\overrightarrow{V}^{re,q}_{\iota-\iota',k} - B^{pq}_{\iota-\iota'}\overrightarrow{V}^{im,q}_{\iota-\iota',k} \end{cases}, \tag{14}$$

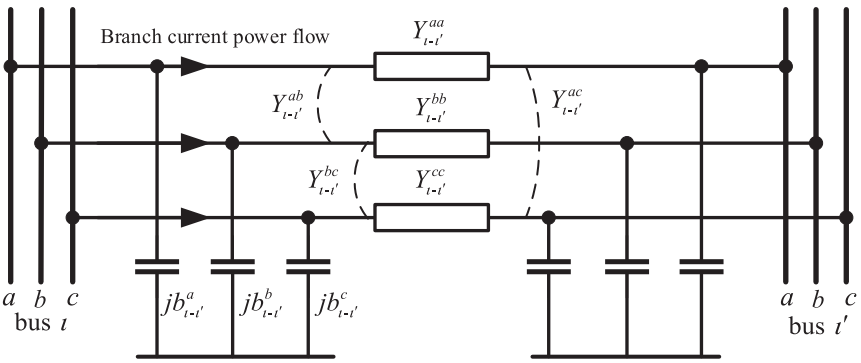

FIGURE 2 | Three-phase line model of the distribution system.

$$\begin{cases} P^{p}_{\iota-\iota',k} = -V^{re,p}_{\iota,k}\sum\limits_{q\in\{a,b,c\}} G^{pq}_{\iota-\iota'}\overrightarrow{V}^{re,q}_{\iota-\iota',k} - B^{pq}_{\iota-\iota'}\overrightarrow{V}^{im,q}_{\iota-\iota',k} \\ \qquad\quad +V^{im,p}_{\iota,k}\sum\limits_{q\in\{a,b,c\}} G^{pq}_{\iota-\iota'}\overrightarrow{V}^{im,q}_{\iota-\iota',k} + B^{pq}_{\iota-\iota'}\overrightarrow{V}^{re,q}_{\iota-\iota',k} \\ Q^{p}_{\iota-\iota',k} = -\dfrac{1}{2}b^{p}_{\iota-\iota'}\left[\left(V^{re,p}_{\iota,k}\right)^2 + \left(V^{im,p}_{\iota,k}\right)^2\right] \\ \qquad\quad -V^{re,p}_{\iota,k}\sum\limits_{q\in\{a,b,c\}} G^{pq}_{\iota-\iota'}\overrightarrow{V}^{im,q}_{\iota-\iota',k} + B^{pq}_{\iota-\iota'}\overrightarrow{V}^{re,q}_{\iota-\iota',k} \\ \qquad\quad +V^{im,p}_{\iota,k}\sum\limits_{q\in\{a,b,c\}} G^{pq}_{\iota-\iota'}\overrightarrow{V}^{re,q}_{\iota-\iota',k} - B^{pq}_{\iota-\iota'}\overrightarrow{V}^{im,q}_{\iota-\iota',k} \end{cases}, \tag{15}$$

where $V^{p}_{\iota,k}$ represents the p-phase voltage amplitude at the $\iota-$th bus. $P^{p}_{\iota,k}$ and $Q^{p}_{\iota,k}$ represent the p-phase–injected active power and reactive power at the $\iota-$th bus, respectively. $P^{p}_{\iota-\iota'}$ and $Q^{p}_{\iota-\iota'}$ represent the p-phase active power and reactive power flow at the $\iota-\iota'$ branch, respectively. N_ι represents the set of bus directly connected to the $\iota-$th bus.

Combining all measurements of PMUs, DRTUs, and DGs' sensors, the measurement output $y_k \in \mathbb{R}^m$ is composed as follows:

$$y_k = h(x_k) + v_k, \tag{16}$$

where $y_k = [y^T_{DG,k}, y^T_{DN,k}]^T$, and $y_{DG,k} = [y^T_{d,1,k},\ldots,y^T_{d,m_d,k}, y^T_{pe,1,k},\ldots,y^T_{pe,m_{pe},k}]^T$ is the measurement vector of DGs, $y_{DN,k} = [y^T_{DRTU,k}, y^T_{PMU,k}]^T$ represents the measurement vector of the network part, $h(\cdot)$ is a high-order nonlinear function, and $v_k \in \mathbb{R}^m$ is the measurement noise subject to the Gaussian distribution, which satisfies $\mathbb{E}\{v_k\} = 0$ and $\mathbb{E}\{v_k v_k^T\} = R_k$.

Remark 1: In this study, the system model of ADS with DGs is established by considering the state variables and measurements of DGs in detail, which expands the scope of ADS state estimation from the network to the DGs and improves estimated accuracy. It should be noted that the two most commonly used DGs are taken as examples for modeling in this study. The modeling methods of other DGs are similar to it. In practical applications, the models can be established according to the specific structure of the DGs.

Remark 2: According to the IEEE standard c37.118–2005, the PMUs ought to provide data in both the angular form (i.e., the phasor angles and magnitudes) and the rectangular form (i.e., the real and imaginary parts of voltages of the buses) (Martin et al., 2008). In this study, both the state and measured variables are presented in the rectangular form to build a linear PMU measurement model. In doing so, the complexity of the estimator is reduced, and the estimation performance is improved.

3 FASE WITH THE COMPONENT-BASED EVENT-TRIGGERED MECHANISM

3.1 Component-Based Event-Triggered Mechanism

With the event-triggered mechanism, the event generator determines whether the newly obtained measurement is sent to the estimator or not, which is based on the difference between the previously transmitted measurement and the latest measurement. To reduce the amount of data transmissions from measurement terminals to the estimator and ensure the desired estimation performance, each measurement terminal examines the event generator independently, and the consistency with other measurement terminals in the ADS is not required. As such, the component-based event-triggered mechanism is adopted in the data transmission of the ADS (**Figure 3**). The measured data are obtained by the measurement terminals (e.g., the DRTUs, the PMUs, and the DGs' sensors) and screened by the event generator with the triggering condition. Then, the measured data meeting the triggering conditions are transited to the communication system. Moreover, the trigger detector determines which terminals have triggered and which terminals have not, and then the "zero-order hold" strategy is adopted to update the measurement data in the detector. Last, the data are passed into the estimator for processing.

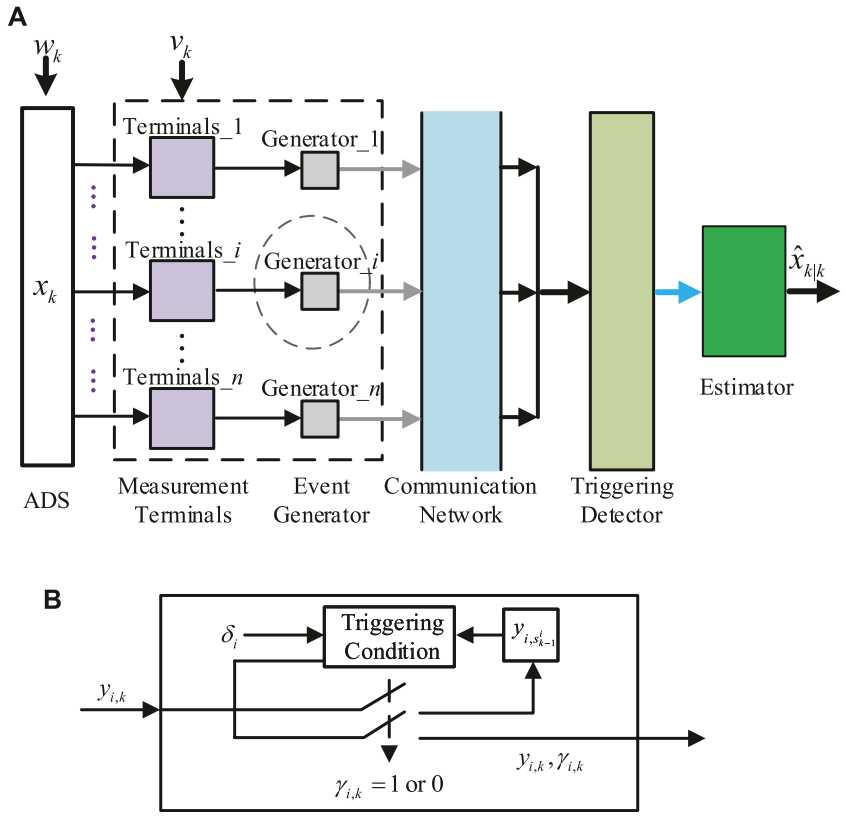

FIGURE 3 | State estimation with the event-triggered mechanism in the ADS: **(A)** flow of the event-triggered mechanism and **(B)** event generator.

The event-triggered condition is described as

$$\gamma_{i,k} = \begin{cases} 1, \ l_i\left(y_{i,s^i_{k-1}}, y_{i,k}\right) > 0 \\ 0, \ l_i\left(y_{i,s^i_{k-1}}, y_{i,k}\right) \le 0 \end{cases}, \tag{17}$$

where $l_i(y_{i,s^i_{k-1}}, y_{i,k}) = \left\| y_{i,s^i_{k-1}} - y_{i,k} \right\| - \delta_i$, $\{s^i_k\}$ represents the triggering instants sequence, $s^i_0 = 0$ and $s^i_k = \min_{k \ge s^i_{k-1}} \{k \in N^+ \left| l_i(y_{i,s^i_{k-1}}, y_{i,k}) > 0\right.\}$.

In this study, the "zero-order hold" strategy is used to update the measurement $\breve{y}_k$ received by the estimator subject to the component-based event-triggered mechanism, where $\breve{y}_k = [\breve{y}^T_{1,k}, \cdots, \breve{y}^T_{i,k}, \cdots, \breve{y}^T_{m_1,k}]^T$ and $\breve{y}_{i,k}$ is the received measurement data associated with the ith measuring device.

$$\breve{y}_{i,k} = \begin{cases} y_{i,k}, \gamma_{i,k} = 1 \\ \breve{y}_{i,k-1}, \gamma_{i,k} = 0 \end{cases}. \tag{18}$$

Based on the above analysis, we can get $\breve{y}_{i,k-1} = y_{s^i_{k-1}}$. $y_{s_k} = [y^T_{1,s^1_k}, y^T_{2,s^2_k}, \cdots, \breve{y}^T_{m_1,s^{m_1}_k}]^T$ is defined to the measurement transmitted under the event-triggered mechanism, and the matrix $\phi_k = diag\{\gamma_{1,k} I_1, \ldots, \gamma_{i,k} I_i, \ldots \gamma_{m_1,k} I_{m_1}\}$ is defined, where I_i is an identity matrix. Then, the measurement received by the estimator at instant k can be expressed as

$$\breve{y}_k = \phi_k y_k + (I - \phi_k) y_{s_{k-1}}. \tag{19}$$

It is possible for the component-based event-triggered mechanism to make the measurement information transmitted in the communication network incomplete. Despite the "zero-order hold" strategy being used to update the measurement in the triggering detector, the non-triggering error would bring about serious effect on the estimation performance of the ADS. As such, it is necessary to design a suitable filter algorithm for reducing the impact of the non-triggering error. Fortunately, with the component-based event-triggered mechanism, the estimator can acquire some valuable information that will facilitate the effective design of the filter. On the one hand, the triggering sequence of the triggering generator is known. On the other hand, the non-triggering error would fall into a certain range.

Remark 3: In order to save network communication resources of the ADS, the component-based event-triggered mechanism is employed, with which the measurement transmission of each component is scheduled individually according to its own triggering condition. The component-based event-triggered mechanism pays attention on the individual change of each component of the system output, while the usual one

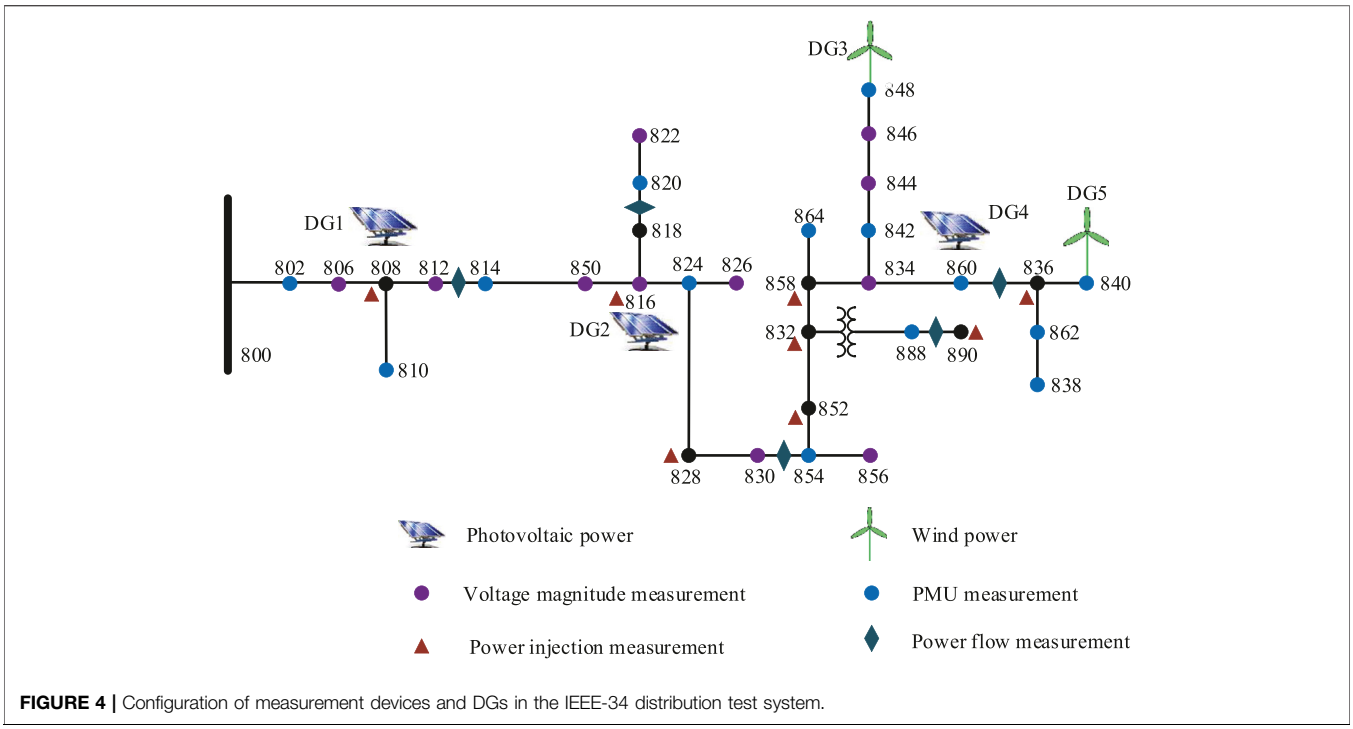

FIGURE 4 | Configuration of measurement devices and DGs in the IEEE-34 distribution test system.

TABLE 1 | Measurement noise in different scenarios.

Parameters	$R_{PMU,k}$	$R_{DRTU,k}$	$R_{DG,k}$
Scenario 1	$8 \times 10^{-6}I$	$8 \times 10^{-4}I$	$8 \times 10^{-6}I$
Scenario 2	$6 \times 10^{-6}I$	$6 \times 10^{-4}I$	$6 \times 10^{-6}I$
Scenario 3	$4 \times 10^{-6}I$	$4 \times 10^{-4}I$	$4 \times 10^{-6}I$
Scenario 4	$2 \times 10^{-6}I$	$2 \times 10^{-4}I$	$2 \times 10^{-6}I$

focuses on the output vector. Considering that there are the characteristics of extremely different operating states between the busses, complex structure, and wide distribution in the ADS, the component-based event-triggered mechanism is more suitable for the ADS.

3.2 Event-Triggered UKF Algorithm

In order to ensure the state estimation performance of the ADS with DGs under the event-triggered mechanism, a filter is designed based on the framework of the UKF algorithm. First, the one-step prediction and filtering error covariances are calculated. Second, some parameters were adjusted by using some lemmas to find the upper bound of the covariance. Last, such an upper bound is minimized by designing an appropriate filter gain.

For the state model **Eq. 1** and event-triggered measurement model **Eq. 19**, the filter is designed as follows:

$$\hat{x}_{k|k-1} = F_{k-1}\hat{x}_{k-1|k-1} + g_{k-1}, \tag{20}$$

$$\hat{x}_{k|k} = \hat{x}_{k|k-1} + K_k\left(\breve{y}_k - \hat{y}_{k|k-1}\right), \tag{21}$$

where $\hat{x}_{k-1|k-1}$ denotes the estimation of the state x_{k-1}, $\hat{x}_{k|k-1}$ is the one-step state prediction at time instant k, K_k is the filter gain to be deigned, and $\hat{y}_{k|k-1}$ is the predicted value of the measurement. Then we define $\tilde{e}_{k|k-1} = x_k - \hat{x}_{k|k-1}$ and $\tilde{e}_{k|k} = x_k - \hat{x}_{k|k}$ that represent the one-step prediction and filtering error, respectively, and the corresponding covariance matrices are defined as $P_{k|k-1} = \mathbb{E}\{\tilde{e}_{k|k-1}\tilde{e}_{k|k-1}^T\}$ and $P_{k|k} = \mathbb{E}\{\tilde{e}_{k|k}\tilde{e}_{k|k}^T\}$.

Before proceeding, the following lemma is recalled, which will be used in later developments.

Lemma 1 (Cheng and Bai, 2021): For any two vectors $X, Y \in \mathbb{R}^n$, the following inequality holds:

$$XY^T + YX^T \leq aXX^T + a^{-1}YY^T, \tag{22}$$

where a is a positive scalar.Combining **Eqs 19**, **21**, we can get the state estimation at instant k:

$$\hat{x}_{k|k} = \hat{x}_{k|k-1} + K_k\left(y_k - \hat{y}_{k|k-1}\right) + K_k\varepsilon_k, \tag{23}$$

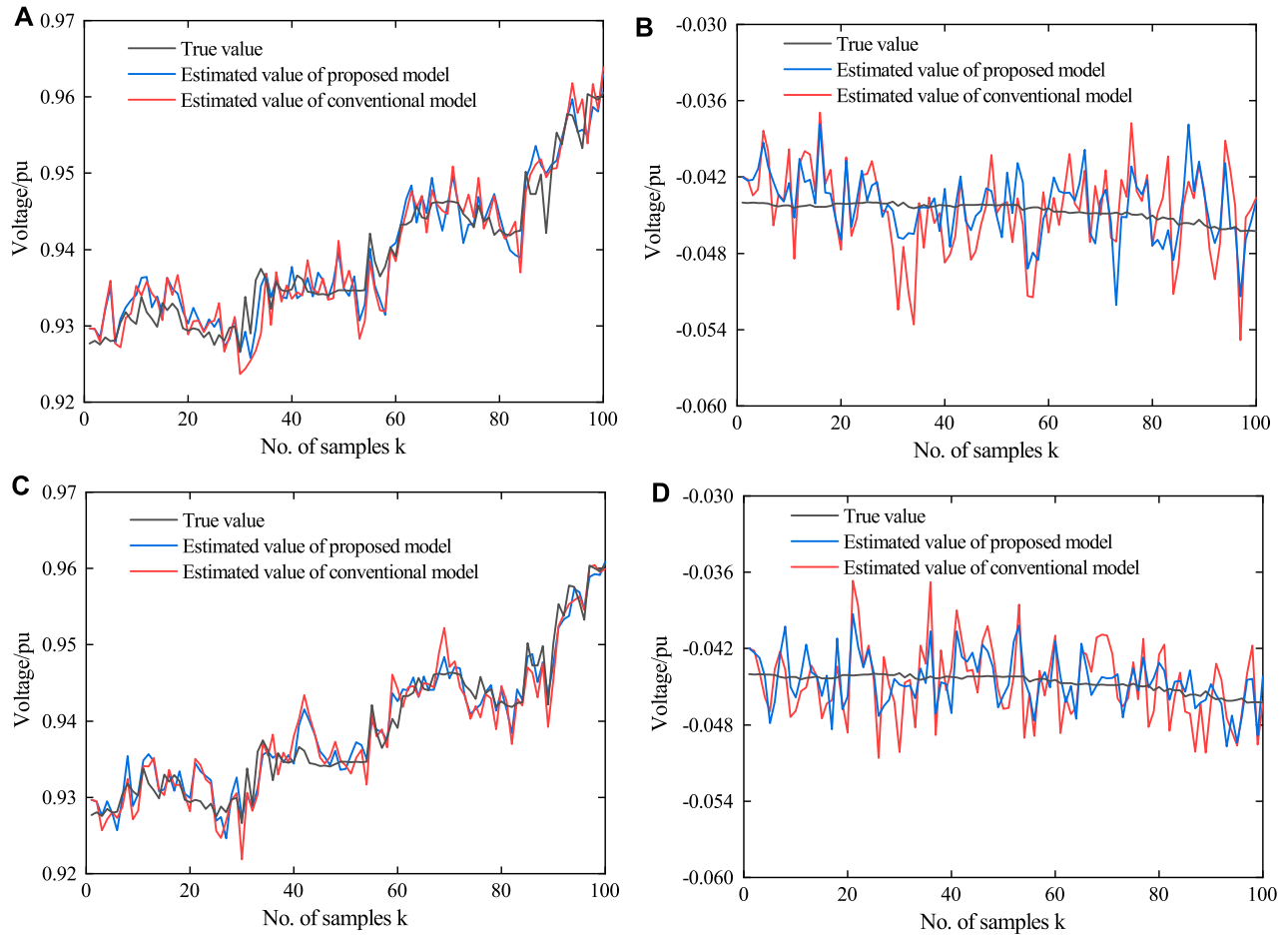

FIGURE 5 | Actual state and its estimation of *a*-phase voltage at the 816 bus. **(A)** Real part of bus voltage in the case of Scenario 1, **(B)** imaginary part of bus voltage in the case of Scenario 1, **(C)** real part of bus voltage in the case of Scenario 2, and **(D)** imaginary part of bus voltage in the case of Scenario two.

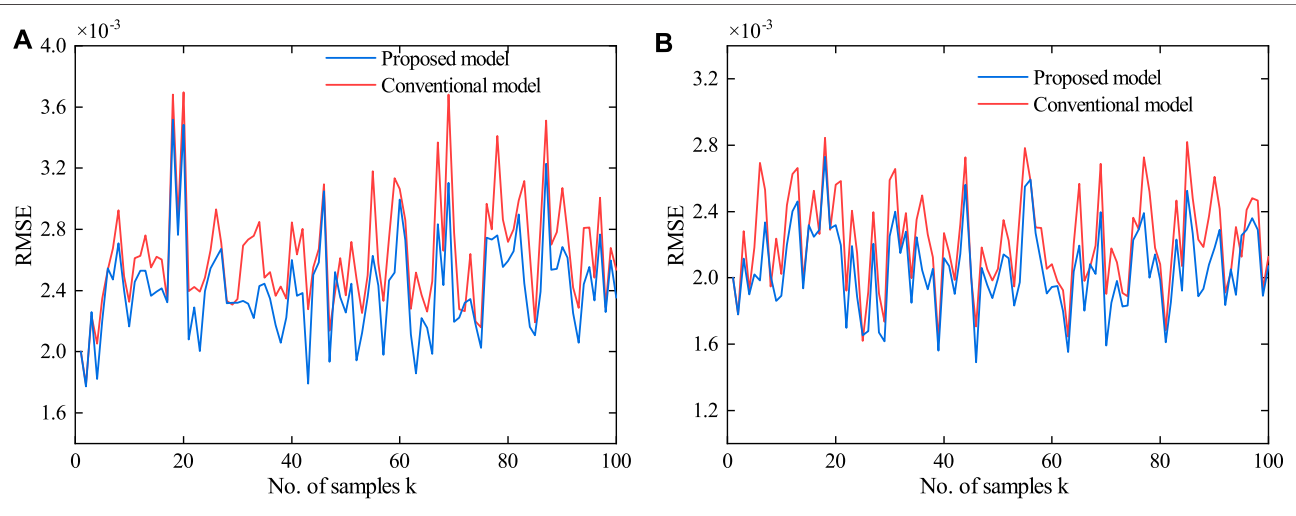

FIGURE 6 | RMSE between the estimation and true values under the proposed and conventional models. **(A)** Scenario 1 and **(B)** Scenario 2.

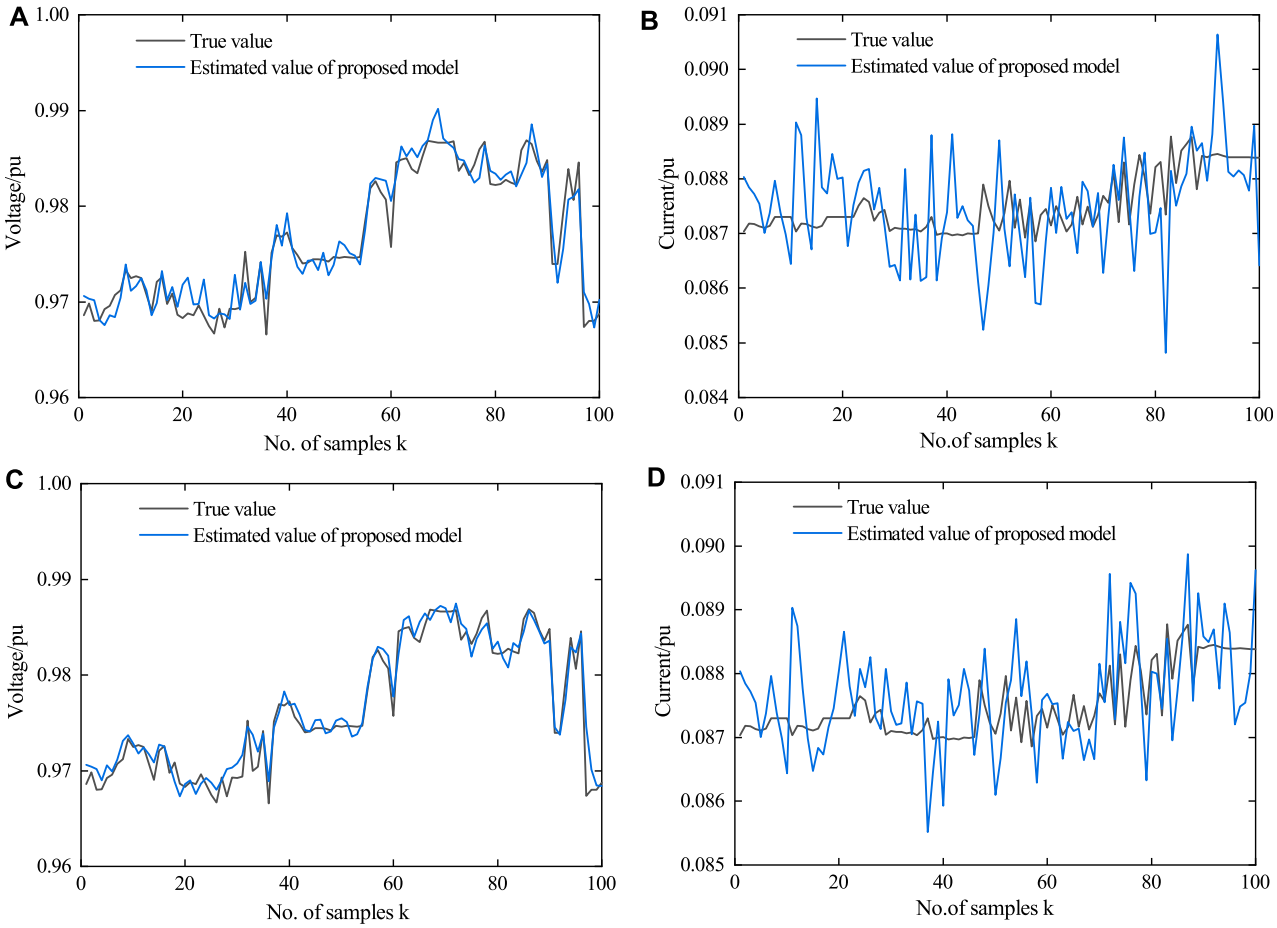

FIGURE 7 | Actual state and its estimation of DG2. **(A)** Voltage output by the DG2 in the case of Scenario 1, **(B)** current output by the DG2 in the case of Scenario 1, **(C)** voltage output by the DG2 in the case of Scenario 2, and **(D)** current output by the DG2 in the case of Scenario 2

where $\varepsilon_k = (I - \phi_k)(y_{s_{k-1}} - y_k)$ represents the non-triggered error. The estimation error at instant k can be expressed as

$$\tilde{e}_{k|k} = \tilde{e}_{k|k-1} - K_k\left(y_k - \hat{y}_{k|k-1}\right) - K_k\varepsilon_k. \tag{24}$$

Then, covariance of the filtering error can be calculated as following:

$$\begin{aligned} P_{k|k} &= \mathbb{E}\left\{\tilde{e}_{k|k}\tilde{e}_{k|k}^T\right\} \\ &= \mathbb{E}\left\{\tilde{e}_{k|k-1}\tilde{e}_{k|k-1}^T\right\} \\ &-\mathbb{E}\left\{\tilde{e}_{k|k-1}\left(y_k - \hat{y}_{k|k-1}\right)^T\right\}K_k^T - K_k\mathbb{E}\left\{\left(y_k - \hat{y}_{k|k-1}\right)\tilde{e}_{k|k-1}^T\right\} \\ &+K_k\mathbb{E}\left\{\left(y_k - \hat{y}_{k|k-1}\right)\left(y_k - \hat{y}_{k|k-1}\right)^T\right\}K_k^T \\ &-\mathbb{E}\left\{\tilde{e}_{k|k-1}\varepsilon_k^T\right\}K_k^T - K_k\mathbb{E}\left\{\varepsilon_k\tilde{e}_{k|k-1}^T\right\} \\ &+K_k\mathbb{E}\left\{\left(y_k - \hat{y}_{k|k-1}\right)\varepsilon_k^T\right\}K_k^T + K_k\mathbb{E}\left\{\varepsilon_k\left(y_k - \hat{y}_{k|k-1}\right)^T\right\}K_k^T \\ &+K_k\mathbb{E}\left\{\varepsilon_k\varepsilon_k^T\right\}K_k^T. \end{aligned} \tag{25}$$

Theorem 1: Consider the system described by **Eqs 1**, **19** with filter **Eqs 20**, **21** and define the following two Riccati-like different equations.

$$\overline{P}_{k|k-1} = F_{k-1}\overline{P}_{k-1|k-1}F_{k-1} + Q_{k-1}, \tag{26}$$

$$\begin{aligned} \overline{P}_{k|k} &= \mu_{1,k}\overline{P}_{k|k-1} - \mathbb{E}\left\{\tilde{e}_{k|k-1}\left(y_k - \hat{y}_{k|k-1}\right)^T\right\}K_k^T \\ &-K_k\mathbb{E}\left\{\left(y_k - \hat{y}_{k|k-1}\right)\tilde{e}_{k|k-1}^T\right\} + \mu_{2,k}K_k\mathbb{E}\left\{\left(y_k - \hat{y}_{k|k-1}\right)\left(y_k - \hat{y}_{k|k-1}\right)^T\right\}K_k^T \\ &+\mu_{3,k}K_k\left(\sum_{i\in N_{y=0}}\delta_i^2 I\right)K_k^T, \end{aligned} \tag{27}$$

where $\mu_{1,k} = 1 + a_{1,k}$, $\mu_{2,k} = 1 + a_{2,k}$, and $\mu_{3,k} = 1 + a_{1,k}^{-1} + a_{2,k}^{-1}$, $a_{1,k}$, and $a_{2,k}$ are positive scalar. If there exist positive-definite solutions $\overline{P}_{k|k-1}$ and $\overline{P}_{k|k}$ with initial conditions $\overline{P}_{0|0} = P_{0|0}$, the matrix $\overline{P}_{k|k}$ is the upper bound of covariance matrix $P_{k|k}$, namely, $\overline{P}_{k|k} \geq P_{k|k}$.

Proof: According to Lemma 1, the following inequalities are obtained:

$$-\mathbb{E}\left\{\tilde{e}_{k|k-1}\varepsilon_k^T\right\}K_k^T - K_k\mathbb{E}\left\{\varepsilon_k\tilde{e}_{k|k-1}^T\right\} \leq a_{1,k}P_{k|k-1} + a_{1,k}^{-1}K_k\mathbb{E}\left\{\varepsilon_k\varepsilon_k^T\right\}K_k^T, \tag{28}$$

$$\begin{aligned} &K_k\mathbb{E}\left\{\left(y_k - \hat{y}_{k|k-1}\right)\varepsilon_k^T\right\}K_k^T + K_k\mathbb{E}\left\{\varepsilon_k\left(y_k - \hat{y}_{k|k-1}\right)^T\right\}K_k^T \\ &\leq a_{2,k}K_k\mathbb{E}\left\{\left(y_k - \hat{y}_{k|k-1}\right)\left(y_k - \hat{y}_{k|k-1}\right)^T\right\}K_k^T + a_{2,k}^{-1}K_k\mathbb{E}\left\{\varepsilon_k\varepsilon_k^T\right\}K_k^T. \end{aligned} \tag{29}$$

According to the event-triggered condition **Eq. 17**, we can obtained

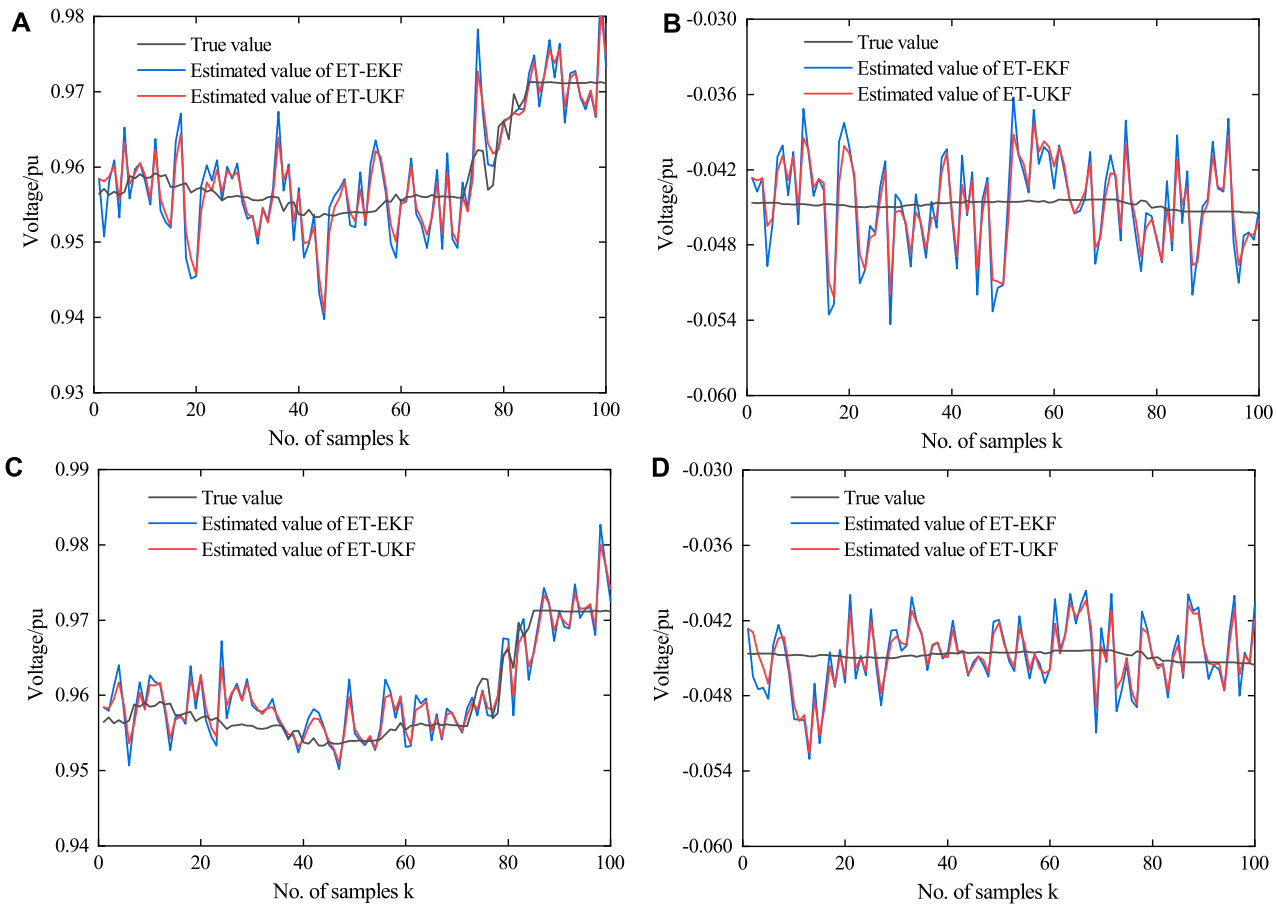

FIGURE 8 | Actual state and its estimation of *a*-phase voltage at 864 bus. **(A)** Real part of bus voltage in the case of Scenario 3, **(B)** imaginary part of the bus voltage in the case of Scenario 3, **(C)** real part of bus voltage in the case of Scenario 4, and **(D)** imaginary part of bus voltage in the case of Scenario 4.

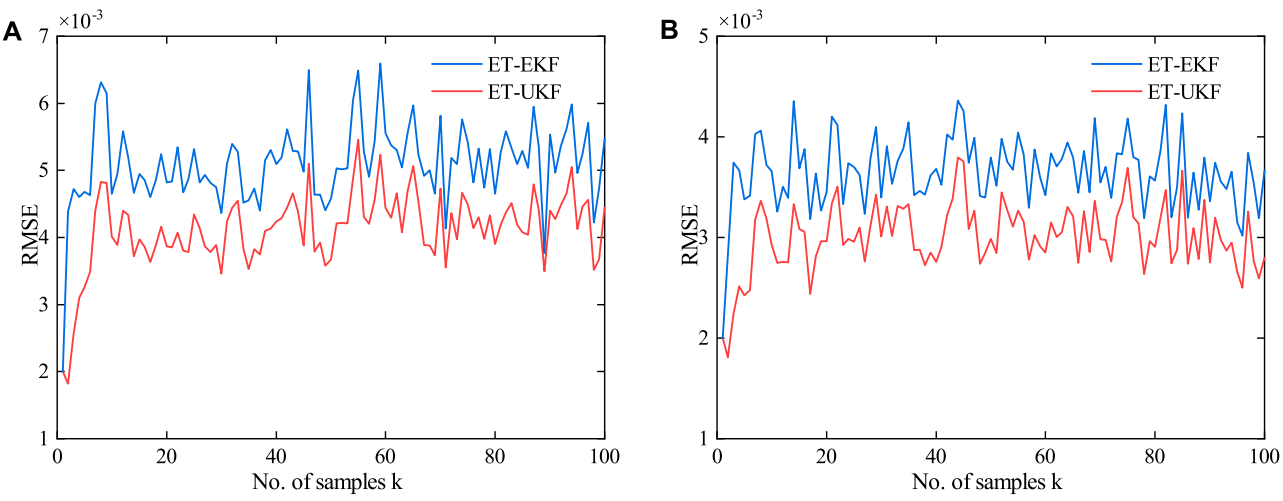

FIGURE 9 | RMSE between the estimated and true values for ET-UKF and ET-EKF algorithms. **(A)** Scenario 3 and **(B)** Scenario 4.

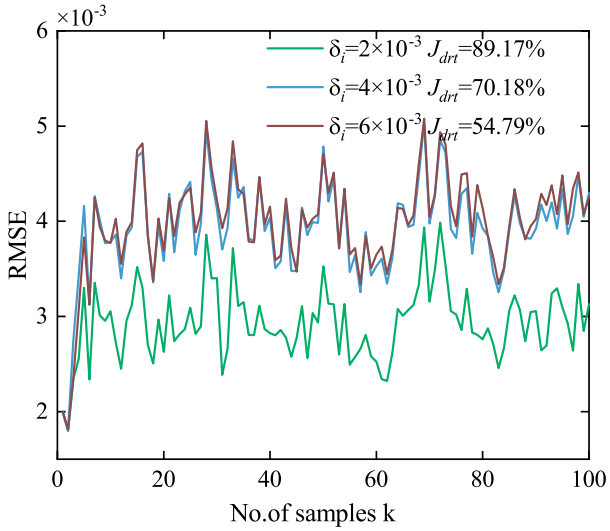

FIGURE 10 | Variation of the RMSE and J_{drt} with the trigger threshold (in the case of Scenario 3).

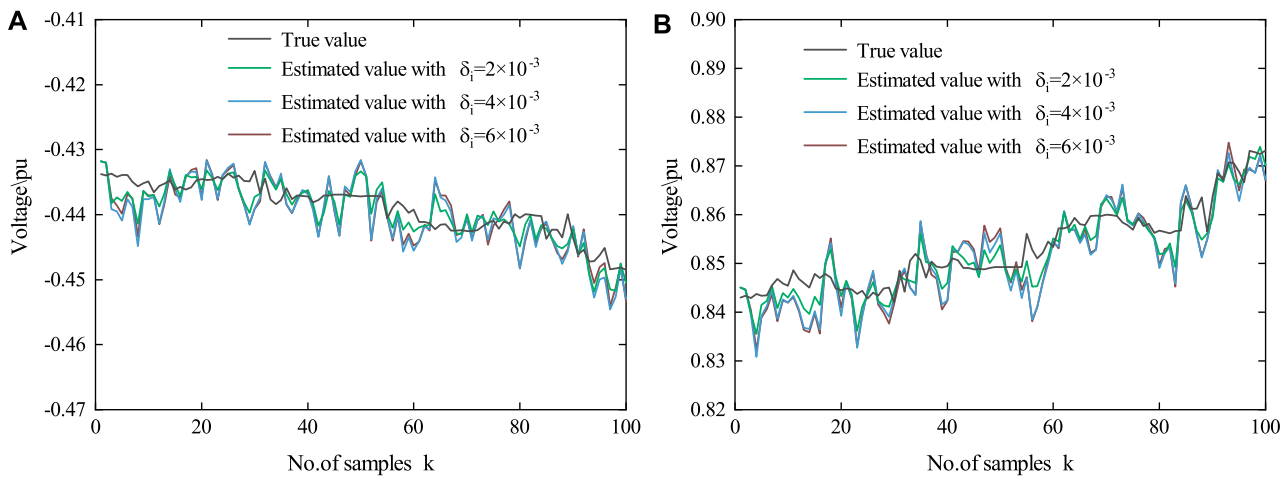

FIGURE 11 | Actual state and its estimation of *c*-phase voltage at the 814 bus (in the case of Scenario 3). **(A)** Real part of bus voltage and **(B)** imaginary part of bus voltage.

$$\varepsilon_k \varepsilon_k^T \le \varepsilon_k^T \varepsilon_k I \le \sum_{i \in N_{\gamma=0}} \delta_i^2 I, \tag{30}$$

where $N_{\gamma=0}$ represents a set of measurement devices that are not triggered by an event.Then

$$-\mathbb{E}\{\tilde{e}_{k|k-1}\varepsilon_k^T\}K_k^T - K_k\mathbb{E}\{\varepsilon_k \tilde{e}_{k|k-1}^T\} \le a_{1,k}P_{k|k-1} + a_{1,k}^{-1}K_k\left(\sum_{i \in N_{\gamma=0}} \delta_i^2 I\right)K_k^T, \tag{31}$$

$$K_k\mathbb{E}\{(y_k - \hat{y}_{k|k-1})\varepsilon_k^T\}K_k^T + K_k\mathbb{E}\{\varepsilon_k(y_k - \hat{y}_{k|k-1})^T\}K_k^T \le a_{2,k}K_k\mathbb{E}\{(y_k - \hat{y}_{k|k-1})(y_k - \hat{y}_{k|k-1})^T\}K_k^T + a_{2,k}^{-1}K_k\left(\sum_{i \in N_{\gamma=0}} \delta_i^2 I\right)K_k^T. \tag{32}$$

This completes the proof.After that, the filter gain K_k can be obtained by the $\overline{P}_{k|k}$.

$$\frac{\partial tr(\overline{P}_{k|k})}{\partial K_k} = -2\mathbb{E}\{\tilde{e}_{k|k-1}(y_k - \hat{y}_{k|k-1})^T\} + 2\mu_{2,k}K_k\mathbb{E}\{(y_k - \hat{y}_{k|k-1})(y_k - \hat{y}_{k|k-1})^T\} + 2\mu_{3,k}K_k\sum_{i \in N_{\gamma=0}} \delta_i^2 I. \tag{33}$$

Let $\partial tr(\overline{P}_{k|k})/\partial K_k = 0$, and through some algebraic operations, the filter gain can be obtained.

subject to

$$K_k = P_{xy,k|k-1}P_{\delta,k|k-1}^{-1}, \tag{34}$$

$$P_{\delta,k|k-1} = \mu_{2,k}P_{yy,k|k-1} + \mu_{3,k}\sum_{i \in N_{\gamma=0}} \delta_i^2 I, \tag{35}$$

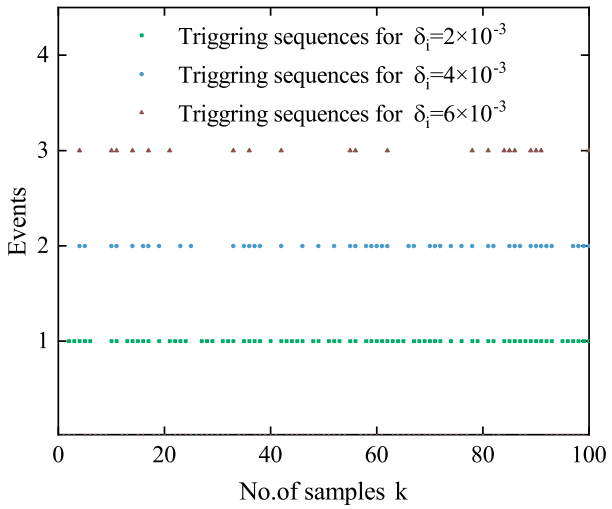

FIGURE 12 | Triggering sequences of the measurement device installed at the 814 bus (in the case of Scenario 3).

where $P_{yy,k|k-1} = \mathbb{E}\{(y_k - \hat{y}_{k|k-1})(y_k - \hat{y}_{k|k-1})^T\}$ and $P_{xy,k|k-1} = \mathbb{E}\{\tilde{e}_{k|k-1}(y_k - \hat{y}_{k|k-1})^T\}$ represent the predicted measurement covariance matrix and state-measurement cross-covariance matrix, respectively. Then the upper bound of the covariance matrix can be expressed as

$$\overline{P}_{k|k} = \mu_{1,k}\overline{P}_{k|k-1} - K_k P_{\delta,k|k-1} K_k. \tag{36}$$

Next, the UT technology is employed to calculate the prediction of measurement and predicted measurement covariance matrix and state-measurement cross-covariance matrix. Considering the high-dimensional nonlinearity of the ADS, in order to ensure the accuracy of the algorithm, while avoiding non-local effects and high-order term errors, in this study, the proportional symmetric sampling strategy is selected as the sigma point sampling strategy of the UT (Wang et al., 2019). The calculation method of the sigma points and its weight is as follows:

$$\chi_{j,k|k-1} = \begin{cases} \hat{x}_{k|k-1}, j = 0 \\ \hat{x}_{k|k-1} + \psi_{j,k|k-1}, j = 1, \ldots, n \\ \hat{x}_{k|k-1} - \psi_{j-n,k|k-1}, j = n+1, \ldots, 2n \end{cases}, \tag{37}$$

where $\psi_{j,k|k-1} = (\sqrt{(n+\lambda)\overline{P}_{k|k-1}})_j$ represents the jth column of the square root of the positive definite matrix $(n+\lambda)\overline{P}_{k|k-1}$. In order to obtain the prediction of measurement and covariance matrix, we define two set weighted coefficient θ_j^m and θ_j^c as follows:

$$\begin{cases} \theta_j^{\mathrm{m}} = \dfrac{\lambda}{n+\lambda}, j = 0 \\ \theta_j^{\mathrm{c}} = \dfrac{\lambda}{n+\lambda} + (1 - a^2 + \beta), j = 0 \\ \theta_j^{\mathrm{m}} = \theta_j^{\mathrm{c}} = \dfrac{1}{2(n+\lambda)}, j = 1, 2, \cdots, 2n \end{cases}, \tag{38}$$

where $\lambda = \alpha^2(n+\kappa) - n$. κ is used to capture the information of higher-order moments of a given probability distribution, and the value of κ is usually 0 or $3 - n$. α is the scale correction factor to determine the distribution range of sigma points, and for the Gaussian distribution, commonly $\alpha \in [10^{-4}, 1]$. β is a parameter related to the prior distribution of the state vector, and for the Gaussian distribution, $\beta = 2$ is optimal.The prediction of measurement and covariance matrix can be calculated as follows:

$$\hat{y}_{j,k|k-1} = h\left(\chi_{j,k|k-1}\right), j = 0, 1, \ldots, 2n, \tag{39}$$

$$\hat{y}_{k|k-1} = \sum_{j=0}^{2n} \theta_j^m \hat{y}_{j,k|k-1}, \tag{40}$$

$$P_{xy,k|k-1} = \sum_{j=0}^{2n} \theta_j^c \left(\chi_{j,k|k-1} - \hat{x}_{k|k-1}\right)\left(\hat{y}_{j,k|k-1} - \hat{y}_{k|k-1}\right)^T, \tag{41}$$

$$P_{yy,k|k-1} = \sum_{j=0}^{2n} \theta_j^c \left(\hat{y}_{j,k|k-1} - \hat{y}_{k|k-1}\right)\left(\hat{y}_{j,k|k-1} - \hat{y}_{k|k-1}\right)^T + R_k. \tag{42}$$

In order to show the proposed filtering algorithm more clearly, the ET-UKF algorithm is summarized as in **Algorithm 1**.

Algorithm 1ET-UKF Algorithm.

1: Initialization: select the initial values of $\hat{x}_{0|0}$ and $P_{0|0}$, set $k = 0$ and the maximum computation step k_{max}, and set $a_{1,0}$, $a_{2,0}$, and δ_i.
2: At time k, compute the state prediction value $\hat{x}_{k|k-1}$ and the upper bound of state prediction error covariance matrix $\overline{P}_{k|k-1}$ by **Eqs 20**, **26**.
3: Compute $2n + 1$ sigma points and weigh coefficients by using **Eqs 37**, **38**. Then compute the prediction of measurement $\hat{y}_{k|k-1}$ and the covariances $P_{xy,k|k-1}$ and $P_{yy,k|k-1}$ by using **Eqs 39–42**.
4: Calculate filter gain K_k by using **Eq. 34**.
5: With the obtained K_k, compute $\hat{x}_{k|k}$ and $\overline{P}_{k|k}$ by using **Eqs 21**, **36**.
6: Set $k = k + 1$, if $k > k_{max}$, exit. Otherwise, go to step 2.

Remark 4: In this study, for the purpose of saving network communication resources of the ADS, the component-based

event-triggered transmission mechanism is adopted to reduce the unnecessary data transmission. However, this method makes it difficult to calculate the error covariance matrix recursively. To this issue, an alternative approach is proposed to introduce some adjustable parameters (e.g., $a_{1,k}$ and $a_{2,k}$) through some lemmas to obtain the upper bound of the covariance matrix. Next, the upper bound is minimized by designing appropriate filtering gain, and the minimized bound of the covariance matrix is closely related to the parameters. For this reason, with these parameters selected appropriately, the possible conservatism of the upper bound can be reduced. Fortunately, the research on optimization is a significantly active field of applied mathematics, which helps determine the optimal parameters.

4 SIMULATION RESULTS AND ANALYSIS

4.1 Simulation Settings

In this section, the IEEE-34 distribution test system is adopted to simulate and verify the effectiveness of the proposed state estimation algorithm. The topology structure and line parameters of the IEEE-34 distribution test system are originated from the study by Kersting (1991). The simulation is implemented in MATLAB R2019b. The dynamic variation of the ADS is simulated by changing the load dynamically. The law of load change is assumed to be $S_{L,k+1} = (1 + 0.1\text{rands}(\cdot))S_{L,k}$, and $S_{L,0}$ represents the initial load provided in the study by Kersting (1991). The measuring devices consist of the DRTUs, the PMUs, and the DGs' sensors. **Figure 4** illustrates the installation positions of the measuring devices and DGs in the test system.

In the simulation, the parameters are set to $a_{1,k} = a_{2,k} = 0.5$. The process noise parameter is expressed as $Q_k = 4 \times 10^{-3} I$. In the Holt–Winters double exponential smoothing method, the parameters α_H and β_H are selected as $\alpha_H = 0.9$ and $\beta_H = 0.1$. The initial value of the covariance matrix is set to $P_{0|0} = 4 \times 10^{-6} I$. Moreover, in order to further evaluate the effectiveness of the proposed state estimation method under different scenarios, four measurement noise scenarios are set in the simulation, and their noise parameters are shown in **Table 1**.

4.2 Result Analysis

1) Verification of the proposed ADS system model.

In this section, the ET-UKF algorithm ($\delta_i = 0$) is applied for state estimation under different scenarios, so as to validate the system model proposed in this study. The estimation results will be compared between the model proposed and the conventional model where DGs are not modeled in detail. **Figure 5** shows the root-mean-square error (RMSE) of state variables associated with the network obtained by the two models under different noise scenarios, where $\text{RMSE}(k) = \sqrt{\frac{1}{n}\sum_{j=1}^{n}(\tilde{e}_{j,k|k})^2}$. It can be found out that the estimated result produced by the proposed model is more accurate than the conventional model in all scenarios. To make the estimation results more intuitive, **Figure 6** plots the state tracking curves of the *a*-phase voltage at the 816 bus. **Figure 7** presents the state tracking curves of the DG2. Obviously, the proposed model can not only improve the accuracy of the state estimation but also expand the scope of state estimation, which is effective in monitoring the operation states of the IEEE-34 distribution test system and the DGs.

2) Verification of the ET-UKF algorithm.

In order to demonstrate the performance of the event-triggered mechanism, a data transmission ratio (DTR) is defined as a transmission performance index by $J_{drt} = \frac{1}{mk_{\max}}\sum_{j=1}^{m}\sum_{k=1}^{k_{\max}}\gamma_{j,k} \times 100\%$. In particular, to demonstrate the superior performance of the ET-UKF algorithm, simulation is performed with the event-triggered threshold $\delta_i = 5 \times 10^{-3}$ under the two noise scenarios. In the case of scenarios 3 and 4, the DTRs are $J_{drt} = 61.60\%$ and $J_{drt} = 55.81\%$, respectively. **Figure 8** shows the state tracking curves of the *a*-phase voltage at the 816 bus. From this figure, it can be seen that the ET-UKF algorithm is capable to track the changes in the system state in real time and make accurate estimates even if only a part of the measurement data is received, which is attributed to the non-triggering error getting well handled by the ET-UKF algorithm. In **Figure 9**, the RMSE of estimated results is compared between the ET-UKF algorithm and the ET-EKF algorithm. It is evident that the estimation accuracy of the ET-UKF algorithm is higher than that of the ET-EKF algorithm under any situation, which is because the UT technology is advantageous over the linearization method applied by the EKF algorithm.

3) The impact from the different triggering thresholds on estimation performance.

In order to figure out the impact of various triggering thresholds on estimation performance, simulations are conducted with $\delta_i = 2 \times 10^{-3}$, $\delta_i = 4 \times 10^{-3}$, and $\delta_i = 6 \times 10^{-3}$, respectively. **Figure 10** shows the RMSE of estimation results and DTR with different triggering thresholds. In order to view the estimation results more intuitively, **Figures 11**, **12** show the state tracking curve and measuring device trigger sequence of the 814 bus *c*-phase with different event-triggering thresholds, respectively. It can be found out from these figures that the DTR decreases sharply with the increase in the triggering threshold, which is because the large triggering threshold prevented more measurement data from being transmitted to the remote estimation center, suggesting that the event-triggered mechanism contributes to reducing data transmission in the communication network and alleviating the communication pressure. With the increase in the threshold, however, the RMSE for the estimation results of the ET-UKF algorithm would also rise. Therefore, choosing an appropriate threshold in the practical ADS is effective in relieving the communication pressure and ensuring the performance of state estimation.

5 CONCLUSION

In this study, a FASE method for the ADS with DGs has been developed under the condition of limited communication resources. First, the system model of the ADS has been built to improve the accuracy and extend the scope of state estimation. Moreover, in order to solve the network-induced phenomena attributed to considerable data transmission in ADS, the component-based event-triggered mechanism has been adopted to reduce the amount of data transmitted through communication network and save the communication resources. Besides, the ET-UKF algorithm has been designed to guarantee the estimation performance of the system. Finally, the effectiveness of the proposed method has been verified by the simulation. In view of the importance of the integrated energy system as a development trend in the energy field, the development

of high-performance state estimation algorithms for the integrated energy system has become a top priority. Future study will consider the dynamic characteristics and time scales of different systems in the integrated energy system (Chen et al., 2020; Chen et al., 2021) and apply the algorithm proposed in this study to integrated energy systems.

DATA AVAILABILITY STATEMENT

The original contributions presented in the study are included in the article/Supplementary Material; further inquiries can be directed to the corresponding author.

AUTHOR CONTRIBUTIONS

XB designed the component-based event-triggered mechanism. XZ designed the ET-UKF algorithm for the FASE of the ADSs. LG proposed the state space model of ADS with DGs. FQ and YL conducted the simulation verification.

FUNDING

This research was supported by the National Natural Science Foundation of China (Grant No. 51807134) and the Shandong Provincial Natural Science Foundation, China (Grant No. ZR2020MF071).

ACKNOWLEDGMENTS

We would like to thank the project team members of the National Natural Science Foundation of China and the Shandong Provincial Natural Science Foundation who encouraged this research.

REFERENCES

Ćetenović, D. N., and Ranković, A. M. (2018). Optimal Parameterization of Kalman Filter Based Three-phase Dynamic State Estimator for Active Distribution Networks. *Int. J. Electr. Power Energ. Syst.* 101, 472–481. doi:10.1016/j.ijepes.2018.04.008

Chen, S., Wei, Z., Sun, G., Lu, N., Sun, Y., and Zhu, Y. (2017a). Multi-area Distributed Three-phase State Estimation for Unbalanced Active Distribution Networks. *J. Mod. Power Syst. Clean Energ.* 5, 767–776. doi:10.1007/s40565-016-0237-0

Chen, Y., Ma, J., Zhang, P., Liu, F., and Mei, S. (2017b). Robust State Estimator Based on Maximum Exponential Absolute Value. *IEEE Trans. Smart Grid* 8, 1537–1544. doi:10.1109/TSG.2015.2485280

Chen, Y., Yao, Y., Lin, Y., and Yang, X. (2020). Dynamic State Estimation for Integrated Electricity-Gas Systems Based on Kalman Filter. *CSEE J. Power Energ. Syst.*, 1–11. doi:10.17775/CSEEJPES.2020.02050

Chen, Y., Yao, Y., and Zhang, Y. (2021). A Robust State Estimation Method Based on Socp for Integrated Electricity-Heat System. *IEEE Trans. Smart Grid* 12, 810–820. doi:10.1109/TSG.2020.3022563

Cheng, C., and Bai, X. (2021). Robust Forecasting-Aided State Estimation in Power Distribution Systems with Event-Triggered Transmission and Reduced Mixed Measurements. *IEEE Trans. Power Syst.*, 1. doi:10.1109/TPWRS.2021.3062386

Cheng, C., Bai, X., Zhang, Q., and Huang, C. (2018). Set-membership Filtering for Generator Dynamic State Estimation with Delayed Measurements. *Syst. Sci. Control. Eng.* 6, 35–43. doi:10.1080/21642583.2018.1531794

Dang, L., Chen, B., Wang, S., Ma, W., and Ren, P. (2020). Robust Power System State Estimation with Minimum Error Entropy Unscented Kalman Filter. *IEEE Trans. Instrumentation Meas.* 69, 8797–8808. doi:10.1109/TIM.2020.2999757

Ding, F., Wang, X., Mao, L., and Xu, L. (2017). Joint State and Multi-Innovation Parameter Estimation for Time-Delay Linear Systems and its Convergence Based on the Kalman Filtering. *Digital Signal. Process.* 62, 211–223. doi:10.1016/j.dsp.2016.11.010

Do Coutto Filho, M. B., and Stacchini de Souza, J. C. (2009). Forecasting-aided State Estimation––part i: Panorama. *IEEE Trans. Power Syst.* 24, 1667–1677. doi:10.1109/TPWRS.2009.2030295

Dobakhshari, A. S., Abdolmaleki, M., Terzija, V., and Azizi, S. (2021). Robust hybrid linear state estimator utilizing scada and pmu measurements. *IEEE Trans. Power Syst.* 36, 1264–1273. doi:10.1109/TPWRS.2020.3013677

Ehsan, A., and Yang, Q. (2018). Optimal integration and planning of renewable distributed generation in the power distribution networks: A review of analytical techniques. *Appl. Energ.* 210, 44–59. doi:10.1016/j.apenergy.2017.10.106

Fang, Z., Lin, Y., Song, S., Song, C., Lin, X., and Cheng, G. (2020). Active distribution system state estimation incorporating photovoltaic generation system model. *Electric Power Syst. Res.* 182, 106247. doi:10.1016/j.epsr.2020.106247

Ge, L., Li, Y., Li, S., Zhu, J., and Yan, J. (2021a). Evaluation of the situational awareness effects for smart distribution networks under the novel design of indicator framework and hybrid weighting method. *Front. Energ.* 15, 143–158. doi:10.1007/s11708-020-0703-2

Ge, L., Song, Z., Xu, X., Bai, X., and Yan, J. (2021b). Dynamic networking of islanded regional multi-microgrid networks based on graph theory and multi-objective evolutionary optimization. *Int. Trans. Electr. Energ. Syst.* 35, e12687. doi:10.1002/2050-7038.12687

Ge, L., Xian, Y., Yan, J., Wang, B., and Wang, Z. (2020a). A hybrid model for short-term pv output forecasting based on pca-gwo-grnn. *J. Mod. Power Syst. Clean Energ.* 8, 1268–1275. doi:10.35833/MPCE.2020.000004

Ge, L., Zhang, S., Bai, X., Yan, J., Shi, C., and Wei, T. (2020b). Optimal capacity allocation of energy storage system considering uncertainty of load and wind generation. *Math. Probl. Eng.* 2020, 2609674. doi:10.1155/2020/2609674

Geetha, S. J., Chakrabarti, S., and Rajawat, K. (2021). Asynchronous hierarchical forecasting-aided state estimator with sub-area data validation for power systems. *IEEE Sensors J.* 21, 2124–2133. doi:10.1109/JSEN.2020.3017920

Kersting, W. (1991). Radial distribution test feeders. *IEEE Trans. Power Syst.* 6, 975–985. doi:10.1109/59.119237

Kooshkbaghi, M., Marquez, H. J., and Xu, W. (2020). Event-triggered approach to dynamic state estimation of a synchronous machine using cubature kalman filter. *IEEE Trans. Control. Syst. Tech.* 28, 2013–2020. doi:10.1109/TCST.2019.2923374

Li, S., Li, L., Li, Z., Chen, X., Fernando, T., Iu, H. H.-C., et al. (2019). Event-trigger heterogeneous nonlinear filter for wide-area measurement systems in power grid. *IEEE Trans. Smart Grid* 10, 2752–2764. doi:10.1109/TSG.2018.2810224

Li, Y., Wang, C., and Li, G. (2020). A mini-review on high-penetration renewable integration into a smarter grid. *Front. Energ. Res.* 8, 84. doi:10.3389/fenrg.2020.00084

Liu, X., Li, L., Li, Z., Chen, X., Fernando, T., Iu, H. H.-C., et al. (2018). Event-trigger particle filter for smart grids with limited communication bandwidth infrastructure. *IEEE Trans. Smart Grid* 9, 6918–6928. doi:10.1109/TSG.2017.2728687

Luo, F., Yang, X., Wei, W., Zhang, T., Yao, L., Zhu, L., et al. (2020). Bi-level load peak shifting and valley filling dispatch model of distribution systems with virtual power plants. *Front. Energ. Res.* 8, 305. doi:10.3389/fenrg.2020.596817

Macii, D., Fontanelli, D., and Barchi, G. (2020). A distribution system state estimator based on an extended kalman filter enhanced with a prior evaluation of power injections at unmonitored buses. *Energies* 13, 6054. doi:10.3390/en13226054

Martin, K. E., Hamai, D., Adamiak, M. G., Anderson, S., Begovic, M., Benmouyal, G., et al. (2008). Exploring the ieee standard c37.118–2005 synchrophasors for power systems. *IEEE Trans. Power Deliv.* 23, 1805–1811. doi:10.1109/TPWRD.2007.916092

Shanmugam, L., Mani, P., and Joo, Y. H. (2020). Stabilisation of event-triggered-based neural network control system and its application to wind power generation systems. *IET Control. Theor. Appl.* 14, 1321–1333. doi:10.1049/iet-cta.2019.0246

Sun, Y., Wang, Y., Wu, X., and Hu, Y. (2018). Robust extended fractional kalman filter for nonlinear fractional system with missing measurements. *J. Franklin Inst.* 355, 361–380. doi:10.1016/j.jfranklin.2017.10.030

Sun, Y., Wu, X., Cao, J., Wei, Z., and Sun, G. (2017). Fractional extended kalman filtering for non-linear fractional system with lévy noises. *IET Control. Theor. Appl.* 11, 349–358. doi:10.1049/iet-cta.2016.1041

Wang, S., Lyu, Y., and Ren, W. (2019). Unscented-transformation-based distributed nonlinear state estimation: Algorithm, analysis, and experiments. *IEEE Trans. Control. Syst. Tech.* 27, 2016–2029. doi:10.1109/TCST.2018.2847290

Wang, Y., Sun, Y., and Dinavahi, V. (2020). Robust forecasting-aided state estimation for power system against uncertainties. *IEEE Trans. Power Syst.* 35, 691–702. doi:10.1109/TPWRS.2019.2936141

Xing, Z., Xia, Y., Yan, L., Lu, K., and Gong, Q. (2018). Multisensor distributed weighted kalman filter fusion with network delays, stochastic uncertainties, autocorrelated, and cross-correlated noises. *IEEE Trans. Syst. Man, Cybernetics: Syst.* 48, 716–726. doi:10.1109/TSMC.2016.2633283

Yang, Q., Jiang, L., Ehsan, A., Gao, Y., and Guo, S. (2018). Robust power supply restoration for self-healing active distribution networks considering the availability of distributed generation. *Energies* 11, 210. doi:10.3390/en11010210

Yang, Q., Jiang, L., Hao, W., Zhou, B., Yang, P., and Lv, Z. (2017). Pmu placement in electric transmission networks for reliable state estimation against false data injection attacks. *IEEE Internet Things J.* 4, 1978–1986. doi:10.1109/JIOT.2017.2769134

Zhang, Y., Wang, J., and Li, Z. (2020). Interval state estimation with uncertainty of distributed generation and line parameters in unbalanced distribution systems. *IEEE Trans. Power Syst.* 35, 762–772. doi:10.1109/TPWRS.2019.2926445

Zhao, J., Gómez-Expósito, A., Netto, M., Mili, L., Abur, A., Terzija, V., et al. (2019). Power system dynamic state estimation: Motivations, definitions, methodologies, and future work. *IEEE Trans. Power Syst.* 34, 3188–3198. doi:10.1109/TPWRS.2019.2894769

Zhao, J., and Mili, L. (2019). A theoretical framework of robust h-infinity unscented kalman filter and its application to power system dynamic state estimation. *IEEE Trans. Signal Process.* 67, 2734–2746. doi:10.1109/TSP.2019.2908910

Zhu, C., Su, Z., Xia, Y., Li, L., and Dai, J. (2020). Event-triggered state estimation for networked systems with correlated noises and packet losses. *ISA Trans.* 104, 36–43. doi:10.1016/j.isatra.2019.11.038

Conflict of Interest: The authors declare that the research was conducted in the absence of any commercial or financial relationships that could be construed as a potential conflict of interest.

Publisher's Note: All claims expressed in this article are solely those of the authors and do not necessarily represent those of their affiliated organizations, or those of the publisher, the editors and the reviewers. Any product that may be evaluated in this article, or claim that may be made by its manufacturer, is not guaranteed or endorsed by the publisher.

frontiers in Energy Research

ORIGINAL RESEARCH
published: 30 July 2021
doi: 10.3389/fenrg.2021.728834

Optimal Investment Decision of Distribution Network With Investment Ability and Project Correlation Constraints

Jianping Yang, Yue Xiang, Zeqi Wang, Jiakun Dai and Yanliang Wang*

College of Electrical Engineering, Sichuan University, Chengdu, China

Power grid enterprises are faced with a serious mismatch between limited investment capacity and numerous investment projects. How to accurately match the weak links with investment projects according to the power system diagnosis is the key to improve investment accuracy. On the basis of an investment-oriented label, a project portfolio optimization framework with coherent diagnosis–evaluation–optimization is proposed in this study. First, a two-layer index system for investment benefit evaluation is established, which considers unit investment efficiency and macroinvestment benefit. Second, by weighing the diagnosis results of power grid and the biased investment environment, the benefit evaluation of the project is implemented as the basis of project portfolio optimization. To meet different investment demands, two combination optimization models of maximizing investment benefit and minimizing investment cost are established considering the coupling benefit relationship and time series relationship between projects. Finally, a case study is conducted for a regional distribution network. The proposed framework has been proven to be able to effectively cope with different investment needs and realize the dynamic adjustment of the scheme in the whole investment cycle.

Keywords: investment decision, distribution network, power system diagnosis, project portfolio, evaluation

OPEN ACCESS

Edited by:
Chenghong Gu,
University of Bath, United Kingdom

Reviewed by:
Feifei Bai,
The University of Queensland, Australia
Bin Zhou,
Hunan University, China

****Correspondence:***
Yue Xiang
xiang@scu.edu.cn

Specialty section:
This article was submitted to Smart Grids, a section of the journal Frontiers in Energy Research

Received: *22 June 2021*
Accepted: *30 June 2021*
Published: *30 July 2021*

Citation:
Yang J, Xiang Y, Wang Z, Dai J and Wang Y (2021) Optimal Investment Decision of Distribution Network With Investment Ability and Project Correlation Constraints. Front. Energy Res. 9:728834. doi: 10.3389/fenrg.2021.728834

INTRODUCTION

As a significant part to ensure safe and stable operation of power grids and improve power supply quality, the distribution network planning has become the focus of medium- and long-term investment of power enterprises. Taking China as an example, the scale of power grid investment has increased continuously from 344.8 billion yuan in 2010 to 460 billion yuan in 2020. At the same time, with the access to a high proportion of clean energy and the deepening of the interaction between supply and demand, the investment decision of distribution network involves new elements, such as clean energy (Telukunta et al., 2017; Erdiwansyah and Husin, 2021) installation and automation equipment so that grid investment faces a large number of investment projects of various types. In addition to the basic power supply level and quality, the unbalanced economic development between regions and the policy changes are also within the planning scope of the decision-making level. The traditional rough attribute association system is not conducive to quantifying the investment benefit of the project. Therefore, realizing fine fund allocation and accurate project investment by selecting targeted construction projects from planning projects for efficient investment is of great significance for decision-making departments.

A great deal of research has been conducted in establishing an index evaluation system to optimize distribution network projects. By sorting the investment scale and investment direction of distribution network, an accurate investment project was realized by Wang et al. (2019a). In a study by Liu et al. (2019a), on the basis of the historical power supply situation in a specific area, through the time series weight analysis of key indicators of the distribution network, the urgency consideration function of the feeder is established to optimize a reconstruction project. The entropy weight method is used to make up for the subjective defects in weighting, and the projects are evaluated on the basis of comprehensive quantitative indicators as given in Luo and Li (2013). On the basis of the ability of different attributes to improve existing problems of the distribution network, the optimization index of high- and medium-voltage distribution network is constructed in the study by Tang et al. (2018). The TOPSIS (Technique for Order Preference by Similarity to an Ideal Solution) method is introduced to sort the ideal solutions of the first- and second-level indicators of planning projects and guided the second ranking by project relevance and investment limit as given by Ye et al. (2019). However, the investment projects in the abovementioned models are mainly ranked by scores and lack specific optimization models. In this regard, predecessors have made progress in using optimization models to assist decision making. In the study by Li et al. (2018), a project optimization model combining investment quota and investment scale is constructed by associating the attributes of satisfying power supply demand, heavy load, and neck problem with a single planned project. By focusing on the spatial layout according to the impact of projects under construction on the whole or local distribution network, the dynamic planning of distribution network projects is realized by Fu et al. (2019). The investment efficiency of a single attribute is calculated through the historical investment effect, and the allocation iteration model is established to realize the investment management with different granularities in the work by Li et al. (2019). As given by Wang et al. (2019b), the quantitative and qualitative indexes of project evaluation are transformed into the numerical value of [−1, 1] interval, the subjective risk preference of decision makers is considered, and the maximum prospect optimization model is established. In the study by Huang et al. (2020), considering the random errors of distribution network indicators, a two-stage robust project optimization model under uncertain factors is constructed and the adaptability of the model is verified by the C&CG algorithm.

Besides, there are also studies conducting in-depth discussions based on data envelopment analysis (DEA) in project evaluation (Çelen and Yalçın, 2012; Gouveia et al., 2015; Oskuee et al., 2015; Arcos-Vargas et al., 2017; Mardani et al., 2017; Liu et al., 2019b). The above method builds the model according to the different project characteristics, but the whole system lacks the consideration of the coupling benefit relationship between the projects and fails to finely construct the necessary correlation constraints for the optimization of distribution network projects. In addition, the diagnosis–evaluation–optimization stages in the project optimization process are conducted independently, but a set of coherent project optimization methods is lacking.

In view of the above problems, the tool of investment-oriented label is introduced in this study. A two-layer index system for investment benefit evaluation of distribution network projects is first constructed to diagnose the development of power grids, which quantifies the efficiency of project funds based on the specific label. On the basis of constraints such as traditional total investment, power grid development demand, and portfolio return, combined with the project coupling benefit and timing correlation constraints in actual production, a distribution network portfolio optimization model aiming at maximizing comprehensive benefits and minimizing investment cost is established, respectively. Finally, with years of deduction and analysis of time series results, reference opinions can be provided for dynamic adjustment of investment schemes and improve the effectiveness of project construction.

The rest of the article is organized in the following manner. In the *Label-Based Investment Decision Framework* section, the investment decision-making framework based on project label is introduced. In the *Multistage Project Selection Method Considering Coupling Benefit and Time Series Correlation* section, the proposed project portfolio optimization method, considering the characteristics of coupling benefit and time series correlation, is described in detail. In the *Case Study* section, a case study is conducted for a regional distribution network. *Conclusion* section draws the conclusions.

LABEL-BASED INVESTMENT DECISION FRAMEWORK

China's power grid investment plan usually takes five years as a cycle. The label-based investment decision process can be summarized as follows:

① Before the investment period, each region reports the project according to the current situation of the local power grid and the expected state of power grids. Because of the difference in specific construction contents, various projects usually have different functional directions, such as meeting the new load demand and strengthening the grid structure to solve heavy overload equipment.

② According to the distribution network construction list and the unit project cost in previous years, the required investment amount in the next planning period is calculated. Then, the project investment effect is estimated; a project label system including different kinds of information (e.g., project basic information, project investment information, project scope information, and project progress information) is also formed.

③ According to the given investment budget and the list of future construction in each region, on the premise of ensuring that the total distribution network investment in each region does not exceed the total investment budget, each investment project is evaluated and screened. The project optimization process is shown in **Figure 1**.

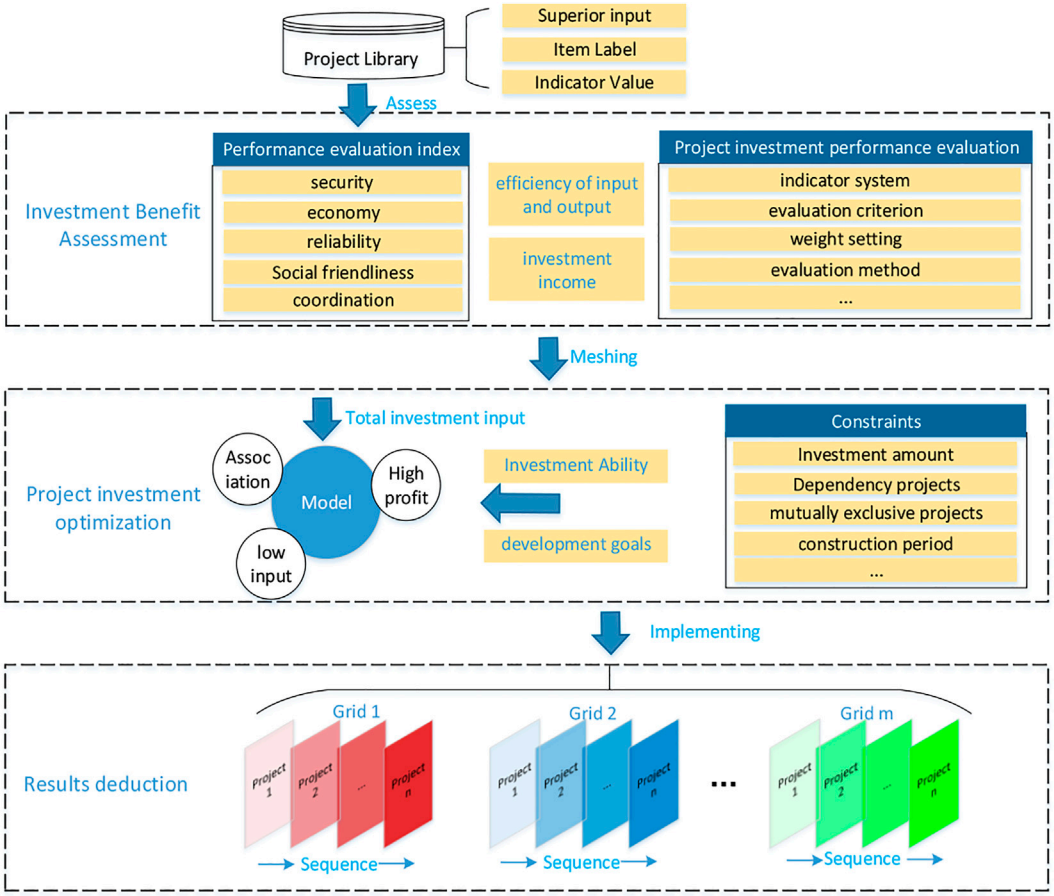

FIGURE 1 | Label-based project optimization.

④ In the five-year cycle, to prevent the expected amount of project investment from changing due to the change of project plan and price level, reviewing and adjusting the investment plans and budgets of each city every year are necessary to ensure that the total project investment in the planning cycle meets expectations.

MULTISTAGE PROJECT SELECTION METHOD CONSIDERING COUPLING BENEFIT AND TIME SERIES CORRELATION

The whole project optimization process can be divided into three main stages: project diagnosis and comprehensive benefit evaluation, project portfolio optimization, and portfolio deduction analysis.

Step 1: project diagnosis and comprehensive benefit evaluation

On the basis of the project label system of distribution network planning, this study investigates the weighting mode of project weight coefficient; considers the development demand, investment expectation, and investment ability as a whole; and establishes an intelligent evaluation model aimed at the optimal comprehensive benefit of technology, economy, and society.

Step 2: optimal selection of project portfolio

Under the given investment capacity or development demand, an intelligent optimal selection model aiming at the optimal comprehensive benefit of technology, economy, and society can be established. Here, the objective function considers the coupling benefit characteristics and the constraints involve time series correlation characteristics among the projects.

Step 3: Analysis of portfolio deduction

The results deduction analysis considers the investment preference in different time periods and flexibly selects the appropriate investment decision model according to different investment needs. Through time series analysis, the investment scheme can be dynamically adjusted in the whole life cycle.

The next section describes the details of each phase.

Project Diagnosis and Comprehensive Benefit Evaluation

The fundamental purpose of investment decision precision is to improve efficiency. A scientific and reasonable index evaluation system is the basis of analyzing the input and output of the distribution network. At present, relevant research (Mansor and Levi, 2017; Molina et al., 2017) has provided a comprehensive index evaluation system. To harmonize the results of portfolio investment benefit evaluation and power grid development diagnosis, the evaluation index system used in this study is divided into two layers which are shown in **Table 1**. The upper index is used to diagnose the current situation of power grid development to accurately sense the investment demand and determine the boundary conditions of the optimal selection model. The lower index is mainly used for the comprehensive benefit evaluation of the project through scoring to quantify the unit input–output benefits of different dimensions to provide a numerical basis for the optimal selection of project portfolio. In this research, considering the evaluation objectives, objectivity, and difficulty of data acquisition, the evaluation index system reference is given from five levels: grid strength, power supply safety quality, operation economy and efficiency, power supply coordination, and social friendliness. On the basis of the target layer index, according to the actual situation of the target distribution network, we can select the representative quite easily to quantify the index, such as voltage qualified rate and network loss rate. The index system includes the traditional dimensions of safety, economy, and reliability, considering the new characteristics of distributed energy and electric vehicles, focusing on the investment efficiency of the project.

Determination of Index Weight

The evaluation index of different dimensions is usually reflected by the way of empowerment. However, the power grid investment decision is a complex decision-making process affected by multidimensional factors such as investment capacity and policy orientation. Subjective weighting (Shen et al., 2018; Alvarado et al., 2019) ignores the natural physical relationship among indicators, whereas objective weighting (Muñoz-Delgado et al., 2019; Verástegui et al., 2019) based on the data itself cannot consider the external environmental impact dominated by human factors. In this study, the index weight and investment weight are used to quantitatively evaluate the impact of the internal development of the power grid and the external complex environment on the key investment direction of the power grid.

On the one hand, with the results of power system diagnosis, the index weight w_1 of different dimensions can be determined by the difference between the current development situation and the expected objectives, which can directly reflect the weak links of power grid development to screen the investment projects. **Eq. 1** is the formula used for calculating the index weight as follows:

$$w_{1,k} = \frac{s_k - s_k^{'}}{\sum_{m=1}^{M} s_m - s_m^{'}}, \tag{1}$$

where s_k and $s_k^{'}$, respectively, represent the status score and target score of the kth target layer indicators and M represents the total number of target layer indicators.

On the other hand, under the constraint of the total investment, the distribution network investment should also emphasize the investment bias and have a choice. In different periods, different regions may have different investment weights w_2. For example, high requirements for power supply quality are demanded during the Olympic Games. w_2 can be flexibly adjusted on the basis of w_1 to meet different investment needs. In general, w_2 is mainly given by experts' experience according to the actual situation in a certain period, considering factors such as natural climate and environment and policy support. w_2 can also be flexibly adjusted according to work priorities or experiences.

Finally, the comprehensive weight can be calculated as follows:

TABLE 1 | Benefit index system of distribution network portfolio investment.

Target layer	Diagnostic evaluation index system		Investment performance evaluation index system	
	Secondary evaluation index	Unit	Unit investment promotion	Unit
Strong structure	"N-1" pass rate	%	Number of new "N-1" pass lines	-
	Line connection rate	%	Number of new connection lines	-
	Qualified rate of line segment	%	Number of new line segment qualified lines	-
	Qualified rate of lines' power supply radius	%	Number of new supply radius qualified lines	-
Safety and quality	Qualified rate of comprehensive voltage	%	Expected improvement of qualified rate of local comprehensive voltage	%
	Insulation rate of lines	%	Added miles of insulation lines	km
	Power supply reliability	%	Expected improvement of local power supply reliability	%
	Distribution automation coverage	%	Number of new automation stations	-
Economy and efficiency	High loss ratio of distribution transformers	%	Decreased number of high loss distribution transformers	-
	Heavy load rate of lines	%	Decreased number of heavy load lines	-
	Heavy load rate of transformers	%	Decreased number of heavy load transformers	-
	Comprehensive line loss rate	%	Expected improvement of line loss rate	%
Power supply coordination	Capacity–load ratio	%	New power supply capacity	KW·h
		%	New load supply capacity	KW
Social friendliness	Grid-connected rate of distributed energy	%	New distributed power capacity	KW·h
	Electric vehicle ratio	%	Number of new charging piles	-

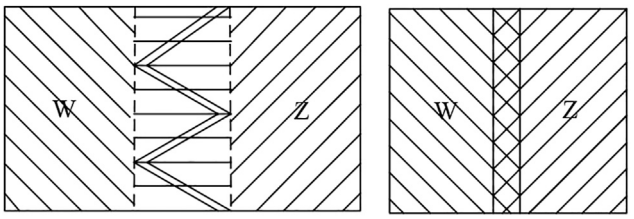

FIGURE 2 | Coupling benefit relationship of projects.

$$w_{c,k} = w_{1,k} * w_{2,k}. \tag{2}$$

Comprehensive Benefit Evaluation Model

Considering the different dimensions and attributes of each index, initializing the data is necessary before the comprehensive scoring of the project is performed. According to the principle of preferred investment, the larger the output value of unit investment is, the more ideal it will be. The maximum value of the index in all projects is set to 100 points, whereas the minimum value is 0 points. The scores of each index are calculated as follows:

$$s_{i,j} = \frac{l_{i,j} - l_j^{\min}}{l_j^{\max} - l_j^{\min}} \times 100, \tag{3}$$

where $s_{i,j}$ and $l_{i,j}$ are the jth index scores and data values of the ith project and $l_j^{\max}$ and $l_j^{\min}$ represent the maximum and minimum values of the jth index in all projects, respectively.

The investment benefit score of a single project can be calculated using the following formula:

$$S_i = \sum_{m=1}^{M} w_m \sum_{j=1}^{n} \frac{s_{i,j}}{n}, \tag{4}$$

where S_i is the comprehensive score of the ith investment project; $s_{i,j}$ are the scores of the jth index; w_m represents the weight of the kth objective criterion; and n represents the total number of indicators.

Project Optimization Model With the Goal of Maximizing Benefit

Benefit Coupling Characteristics

Some distribution network planning projects have the characteristics of matching and continuity (Shen et al., 2020). According to the benefit relationship from two projects or a single one, the project coupling benefit characteristics can be defined as compatibility and support. **Figure 2** illustrates the diagram of both coupling benefit characteristics.

Time Series Correlation Characteristics

In addition to the coupling benefit characteristics, time series correlation characteristics also exist among distribution network planning projects according to the construction requirements and time. Thus, some distribution network planning projects must be constructed according to certain timing construction, cannot be put into operation at the same time, or must be put into operation at the same time to be able to implement and play a role, respectively, defined as dependent, mutually exclusive, and complementary characteristics.

Objective Function

According to the difference in objective function, the investment decision problem in this study is divided into two categories: one is to improve the performance within a certain amount of investment, and the other is to minimize the total investment cost under certain security constraints. To improve the comprehensive investment benefit of distribution network and minimize the investment cost in the economic life cycle of equipment, the optimal selection model of the project is established.

Maximum Investment Benefit Model

$$f = \max I = \max\left[\sum_{k=1}^{M} S_k^{(P)} R_k S_k^{(P)}\right)^{\mathrm{T}}\Bigg]. \tag{5}$$

The optimal performance improvement model mainly solves the problem of how to improve the performance index of the distribution network as much as possible under the condition that the total investment is certain. In **Eq. 4**, $S_k^{(P)}$ is the present value of the investment benefit converted to the first year and R_k represents the coupling characteristic matrix considering the efficiency coupling characteristics of each project, which can be expressed as follows:

$$R_k = \begin{bmatrix} r_{1,1} & r_{1,2} & \cdots & r_{1,n} \\ r_{2,1} & r_{2,2} & \cdots & r_{2,n} \\ \cdots & \cdots & \cdots & \cdots \\ r_{n,1} & r_{n,1} & \cdots & r_{n,n} \end{bmatrix}, \tag{6}$$

where $r_{i,j}$ represents the coupling coefficient between projects i and j. When projects i and j are compatible, a promoting effect is observed between the two projects, which is manifested as $r_{i,j} > 0$; when i and j are supporting projects, an overlap is found between the two projects, which is manifested as $r_{i,j} < 0$; the total investment constraint is taken as an additional constraint as follows:

$$\sum_{i=1}^{n} c^t\left(y_i\right) \le c_{\max}^t, \tag{7}$$

where c represents the project investment cost and t represents the investment year.

Minimum Investment Cost Model

The minimum investment cost model considers the problem of how to find the technical path with the minimum investment under certain performance index requirements. At this time, the model takes the minimum total investment amount as the objective function as follows:

$$F_2 = \min \sum_{i=1}^{n} c(y_i), \tag{8}$$

where $c(x_i)$ represents the cost of the ith project and y_i represents the status variable of whether the ith project is selected. If $y_i = 0$, then it means that project i is eliminated. The performance index constraints are taken as additional constraints as follows:

$$\Phi_{\max}(\Omega) \geq \Phi(\Omega) \geq \Phi_{\min}(\Omega), \tag{9}$$

where Φ represents the performance index set and $\Phi_{\min}(\Omega)$ and $\Phi_{\max}(\Omega)$, respectively, represent the minimum and maximum values of corresponding indexes.

Base Constraints

In addition to the total investment constraints and performance constraints, the two models should meet other basic constraints, such as mutually exclusive and complementary project constraints.

Mutually Exclusive Project Constraints

Suppose Ω_e is the information set of mutually exclusive relationships of projects; if $\{P_i, P_j\} \in \Omega_e$, then it means that P_i and P_j are mutually exclusive projects. That is, projects i and j can only be put into operation at most, which can be expressed as follows:

$$y_i y_j \leq 0. \tag{10}$$

Dependent Project Constraints

Suppose Ω_d is the information set of dependent relationships of projects; if $\{P_i, P_j\} \in \Omega_d$, then it means that P_i can only be put into operation depending on P_j. That is, the selected year of project i must be after the selected year of project j, which can be expressed by the following formula:

$$x_{i,t} \leq x_{j,t-1}. \tag{11}$$

Complementary Project Constraints

Suppose Ω_b is the information set of dependent relationships of projects; if $\{P_i, P_j\} \in \Omega_b$, then it means that P_i and P_j are complementary projects and projects i and j must be put into operation at the same time, which can be expressed as follows:

$$x_{i,t} = x_{j,t}. \tag{12}$$

Radio Constraints

Given that the project selection process considers the multiyear timing relationship, to avoid the same project being selected multiple times in different years, the radio constraint should be added for each project and the function relationship can be expressed as follows:

$$\sum_{t=1}^{T} x_{i,t} \leq 1, \tag{13}$$

where $x_{i,t}$ represents the status of the first project in year t and T represents the investment cycle.

Logical Constraints

Some logical constraints exist between the one-year selected state and the final selected state. No matter which year of project i is selected in the investment cycle, the project will be reflected as the final selection. That is, the project selected in a single year must be selected in the final project, expressed in mathematical terms as follows:

$$\sum_{t=1}^{T} x_{i,t} = y_i. \tag{14}$$

CASE STUDY

Taking a batch of investment plans of a county-level company as an example, the proposed model is verified. The annual power supply capacity of the company's 35 kV and below distribution network is 2.101 billion kWh, the average annual load of the whole society is 119.92 MW, and 2,743 distribution transformers (including on-column transformers) and 180 medium-voltage distribution lines (35 and 10 kV) are installed. The electricity consumption of the secondary industry accounts for 60.13%, mainly textile and manufacturing industries, and the electricity consumption of the tertiary industry and residents accounts for 33.54%. In recent years, the electricity consumption of the service and commercial industries has increased rapidly and the annual load growth rate is expected to reach 5.3%. The electrification degree of terminal energy consumption in the county is high, and the proportion of electricity consumption in the tertiary industry is increasing year by year. The investment capital is planned to be 30 million yuan. Twenty key alternative projects exist in the project library, with a total capital demand of 52.6731 million yuan, far exceeding the existing investment capacity. This section assumes that the investment period is five years. First, the diagnosis and analysis process of power grid development is displayed on the basis of the project label, and the weights of various indicators are obtained by analyzing the weak links according to the diagnosis results. Second, taking the calculation of investment performance of a project as an example, the scoring method is expounded. Considering the coupling benefit and time series relationships of the project, the optimal multiyear portfolio investment scheme of the distribution network project in this region is also calculated. Last, to adapt to the changing investment demand in the whole life cycle, by setting different development scenarios, the project optimization scheme is extended and deduced on the basis of the proposed project optimization model for realizing the dynamic adjustment of the scheme.

Power System Diagnosis and Analysis

The statistics of power grid development indicators in this area are shown in **Table 2**, in which the current power grid index values and expected index values are given.

From the results of the diagnosis and analysis, all indicators meet the expected requirements; the qualified rate of line segmentation and line connection rate reach 97.56 and

TABLE 2 | Power system diagnosis results.

Target layer	Diagnostic evaluation index system (investment benefit) for distribution network development			
	Name	Unit	State	Target
Strong structure	"N-1" pass rate	%	87.12	85
	Qualified rate of lines' power supply radius	%	78.83	69
	Line connection rate	%	94.27	89
	Qualified rate of line segment	%	97.56	91
Safety and quality	Qualified rate of comprehensive voltage	%	99.11	99.5
	Distribution automation coverage	%	47.1	52
	Insulation rate of lines	%	40.73	47
	Power supply reliability	%	99.988	99.990
Economy and efficiency	High loss ratio of distribution transformers	%	5.83	4
	Comprehensive line loss rate	%	3.18	3
	Heavy load rate of lines	%	6.93	2.7
	Heavy load rate of transformers	%	5.33	3.1
Power supply coordination	Capacity–load ratio	%	1.99	1.85
Social friendliness	Grid connection rate of distributed energy	%	—	—
	Electric vehicle ratio	%	—	—

TABLE 3 | Setting of indicator weight.

	Strong structure	Safety and quality	Economy and efficiency	Power supply coordination	Social friendliness
Weight	0.1	0.4	0.3	0.1	0.1

94.27%, respectively, indicating that the network frame of the area is relatively strong. However, a huge gap is observed between the current and expected values of power supply safety and quality. For example, the coverage rate of distribution automation and the line insulation rate are only 47.1 and 40.73%, respectively, suggesting a gap with expectations. In addition, further optimization is needed for the equipment loss. Through the above analysis, the idea that the key points of regional investment should be concentrated on power safety and quality and on the economic and efficient operation can be concluded.

According to the method of determining the weight described in the *Project Diagnosis and Comprehensive Benefit Evaluation* section, the weight of the indicators shown in **Table 3** is obtained.

Label-Based Project Evaluation

Figure 3 shows the content and structure of the project label by taking Project 1 as an example. Four kinds of indicators, namely, project type, project correlation, project function, and project effectiveness, are distinguished by different colors. Reference information is also revealed by labels in different stages of project optimization.

Among them, the project type index describes the functional classification of the project; the project function index provides the estimated values of various diagnostic indicators after the implementation of the project; the project effectiveness index shows the unit investment return brought by construction project n on the basis of the project function index, which mainly provides data information for the evaluation and scoring of this project; the and project correlation index includes the construction urgency, mutually exclusive project, complementary project, and dependent project of Project 1, which provides constraint conditions for the combination optimization model. Based on the contents in the *Project Diagnosis and Comprehensive Benefit Evaluation* section, the scoring results of Project 1 are shown in **Table 4**.

The project properties of the label show that the project is mainly used to strengthen the grid structure, including the construction of new wells, underground cables, and new communication equipment. The qualified rate of subsection and the index of automatic distribution with per unit of line invested are excellent, the scores of which are 88.9 and 83.33, respectively. The underground cable laying not only effectively improves the poor insulation rate in the area but also further improves the power supply quality. Moreover, due to the implementation of the project, the comprehensive rate of voltage qualification in this area is expected to increase by 0.15% and the reliability of power supply will increase by 0.45%.

The five major categories of projects in the project library, namely, load-satisfaction, weakness-elimination, substation-supplementary, grid-enhancement, and overload-relief are evaluated in **Table 5**, where T1, T2, T3, T4, and T5 represent the five performance categories, namely, strong structure, safety and quality, economy and efficiency, power supply coordination, and social friendliness.

The evaluation results based on the scoring standard will be compared and indicate the benefit contribution from various projects intuitively. The load-satisfaction projects that meet the added demand load mainly improve the indicators of power supply coordination, power supply safety, and social friendliness,

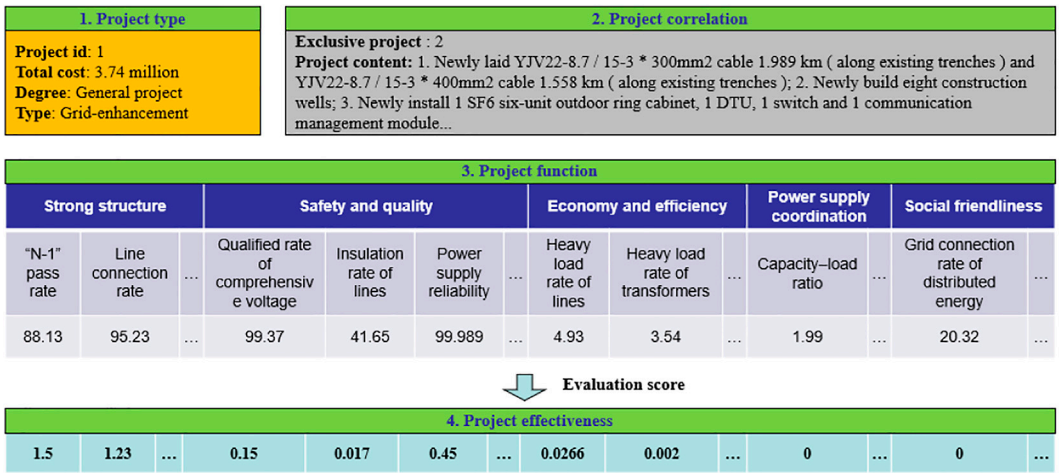

FIGURE 3 | Example of project label content display.

TABLE 4 | Investment benefit score of Project 1.

Target layer	Investment performance evaluation index system		Index calculation	Score
	Unit investment promotion	Unit		32.246
Strong structure	Number of new "N-1" pass lines	N/million yuan	1.5	77.78
	Number of new connection lines	N/million yuan	1.23	66.47
	Number of new line segment qualified lines	N/million yuan	0.8	50
	Number of new supply radius qualified lines	N/million yuan	1.7	88.90
Safety and quality	Expected improvement of qualified rate of local comprehensive voltage	%	0.15	34.23
	Added miles of insulation lines	km/million yuan	0.0166	44.03
	Expected improvement of local power supply reliability	%	0.45	70.77
	Number of new automation stations	One/million yuan	0.001	83.33
Economy and efficiency	Decreased number of high loss distribution transformers	One/million yuan	0.0000	0
	Decreased number of heavy load lines	One/million yuan	0.0266	3.71
	Decreased number of high loss distribution transformers	One/yuan	0.0020	0.05
	Expected improvement of line loss rate	%	0%	0
Power supply coordination	New power supply capacity	kWh/yuan	0	0
	New load supply capacity	kW/yuan	0.0266	3.71
Social friendliness	New distributed power capacity	kWh/yuan	0	0
	Number of new charging piles	One/yuan	0.12	29.27

TABLE 5 | Statistics of various projects.

Project category	Number	T1	T2	T3	T4	T5
Load-satisfication	6	17.85	46.18	21.54	74.26	48.49
Weakness-elimination	4	10.04	20.47	45.06	7.45	0
Substation-supplementary	4	5.67	26.48	3.21	1.51	41.77
Grid-enhancement	4	73.66	65.06	1.04	2.06	21.65
Overload-relief	2	5.74	13.34	45.79	54.08	0

and the average scores reach 74.26, 46.18, and 48.49, respectively. The weakness-elimination projects to eliminate hidden danger of equipment and overload-relief projects to solve line overload can significantly reduce the equipment loss and heavy load, and make great contributions to improve the economy and efficiency with the scores of 45.06 and 45.79, while the grid-enhancement projects is mainly conducive to the grid stability and power supply quality.

Considering the impact of uncertain load growth in the future, there is a preference in the setting of investment weights w_2 which is given as $w_2 = [1, 0.75, 0.67, 3, 1]$. Based on the weights w_1 shown in **Table 3**, the final comprehensive weight can be

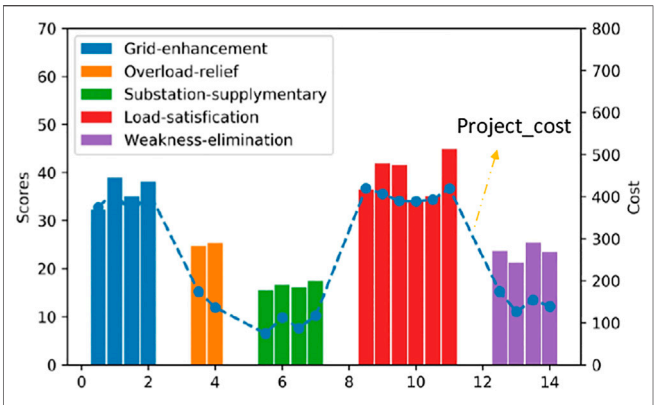

FIGURE 4 | Cost-benefit display of various projects.

obtained as follows: $w = [0.1, 0.3, 0.2, 0.3, 0.1]$. The total score of comprehensive benefits of each project is shown in **Figure 4**. As can be seen from the figure, load-satisfaction projects can generally obtain high scores, whose average score is 38.99. Grid-enhancement projects also obtain good scores because of their high contribution to power supply quality. Both types of projects in the case of only considering the benefit of investment have great advantages in the optimization, which is in line with the results of the diagnosis of the power grid. Along with good benefits, they are also accompanied by high construction costs. The average construction costs of load-satisfaction and grid-enhancement projects reach 4,027,700 yuan and 3,889,500 yuan, respectively, which are much higher than those of other projects.

Project Portfolio Optimization

During the actual project optimization process, apart from the investment cost constraint, the investment benefit should also consider the time series correlation constraints, such as mutually exclusive, dependent, and complementary projects. The optimal portfolio cannot be selected simply by the score. On the basis of the project labels shown in the *Power System Diagnosis and Analysis* section, the coupling benefit relationship among various projects is given. The basic information is presented in **Table 6**. In particular, Project 11←Project 3 indicates that Project 11 depends on Project 3 to be implemented.

According to the project optimization model proposed in this study, the optimization of the abovementioned project library is divided into the following three cases:

Case 1: given that the total investment limit of the region in the investment cycle is 30 million yuan, the goal is to maximize the investment benefit for five years in the whole investment cycle. The optimization process considers the project coupling benefit relationship and time series correlation relationship.

Case 2: Investment decisions are independent each year in the investment cycle, and investment optimization is performed on the basis of the previous year's investment portfolio with the maximization of investment benefit as the objective function. For the convenience of comparative analysis, the total investment limit in the investment cycle of this region is set to be the same as case 1, and the total investment in each year is six, seven, six, five, and six million.

Case 3: Given the constraints of (1) meeting the annual maximum load growth of 5.3%, (2) the N-1 pass rate being increased to 90%, and (3) maintaining the proportion of heavy overload equipment below 3%, the investment ability is unknown and the goal is to minimize the total investment cost while meeting the performance requirements.

GUROBI is used to solve the problem, and the optimal portfolio scheme is obtained, as illustrated in **Figure 5**.

Figure 5 displays the project portfolio schemes under different cases in which multiyear shows the total investment distribution and corresponding accumulated benefits as of each year, whereas single year shows the new projects and the investment proportion of various projects every year in the investment cycle. In addition, the single year in **case 2** gives the investment ability of each year additionally. Also, the single year in **case 3** indicates the index improvement value of each year. LR, TR, N-1, and LG, respectively, represent the heavy load rate of lines, the heavy load rate of transformers, the "N-1" pass rate, and the satisfied load growth rate.

As illustrated in **Figure 5**, **cases 1** and **2** use the maximum investment benefit model, whereas **case 3** uses the minimum investment cost model for project optimization. From the perspective of investment benefit, the benefits brought by **case 1** are obviously higher than those of the two other cases, thereby maximizing the benefits of all cases. However, **case 1** also has higher investment costs. As observed in the *f* in **Figure 5**, LR, TR, N-1, and LG of **case 3,** respectively, reached 0, 0, 95.7, and 45.45% in the fifth year, which met the performance requirements and ensured the economy well. This finding is consistent with the original intention of the model setting. By setting different models, the proposed model can flexibly meet different investment decision-making needs.

In addition, some details between cases 1 and 2 deserve further discussion. Although case 2 adopts the model of maximizing investment benefit, the ultimate benefit improvement is less than case 1. The reason is that the investment decision-making process is conducted every year, which is limited by the annual total investment. Moreover, the flexibility of the project portfolio

TABLE 6 | Statistics of project time series correlation constraints.

Project correlation type	Project number
Mutually exclusive	Projects 1 and 2
	Projects 3 and 4
Complementary	Projects 5 and 8
	Projects 6 and 7
Dependent	Project 11←Project 3
	Project 12←Project 2
	Project 13←Project 1
	Project 14←Project 1
	Project 15←Project 4
	Project 16←Project 4

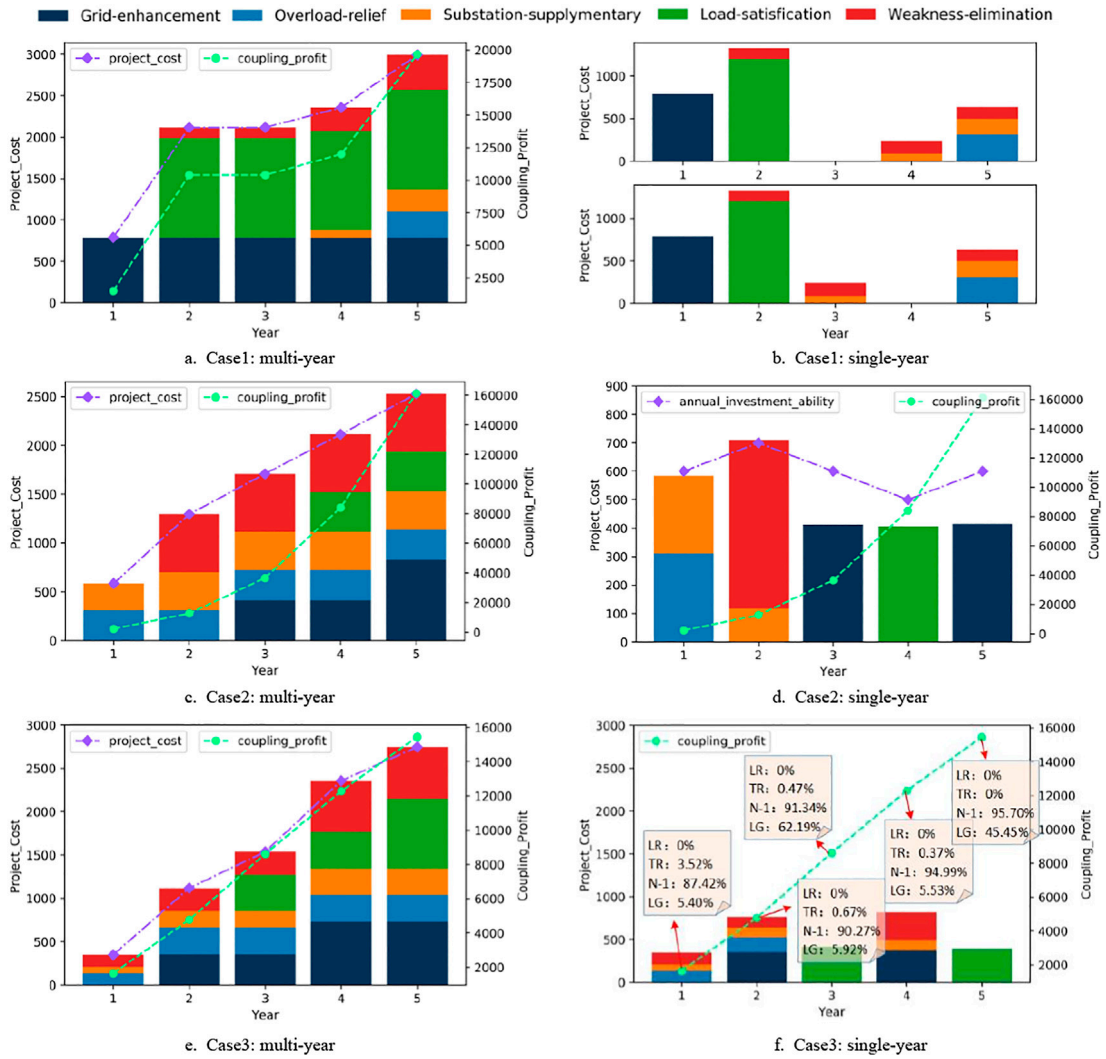

FIGURE 5 | Optimal portfolio scheme under different cases.

decreases to a certain extent; thus, the optimal project portfolio scheme cannot be obtained. From this perspective, we can see that case 1 can make more effective use of funds and achieve better investment benefits. However, due to the influence of geographical environments, natural disasters, and policy requirements, determining the load growth and various unexpected situations in advance for the actual investment decision-making process is often difficult. In addition, the optimal investment portfolio scheme in the whole multiyear investment cycle can only be determined on the basis of the investment background of the first year, which makes the investment scheme deviate greatly from reality. Considering that case 1 takes the total investment benefit in the investment cycle as the objective function and lacks specific constraints on a single-year investment, no project may be selected in nth year. In this scenario, no essential difference is observed when n takes 3 or 4, and the optimal portfolio scheme may not be unique. However, during the actual process, the uncertainty of the scheme may bring different risks and benefits, which are often difficult to quantify. Coincidentally, case 2 can only effectively make up for the poor flexibility by making investment decisions separately. Through the combination of cases 1 and 2, various complex investment scenarios can be considered comprehensively, thus providing reference opinions for the dynamic adjustment of optimized portfolio in the whole investment cycle.

CONCLUSION

In view of the problems of extensive investment and low investment efficiency in the current power grid investment, this study integrates the stages of diagnosis–evaluation–optimization by introducing investment-oriented label and puts forward a decision-making framework for an accurate investment in distribution network, considering the coupling relationship of project benefit and time series

correlation. The following conclusions are drawn through the case study:

1) The adoption of a two-layer index system can macroscopically analyze local investment demand and quantify the investment efficiency of a single project. By setting the two-layer weights of investment weight and index weight, the weak links of power grid development can be effectively matched with various investment projects. While considering the influence of external investment environment, the investment portfolio can also be targeted according to the actual situation which improves the investment accuracy.
2) By introducing the concept of investment-oriented label, the problems of inconsistent information and dimensions of various projects are solved; the coupling benefit relationship and time series relationship between various projects are also quantitatively considered during the project optimization process. The proposed method can well meet the investment demand under the two modes of maximizing investment benefit and minimizing investment cost.
3) By setting different cases, the advantages and disadvantages of two investment decision-making schemes based on single-year and multiyear investment are demonstrated. The results reveal that the multiyear investment scheme can make more effective use of funds and obtain better investment benefits, but it cannot cope with the investment capacity and the change of investment environment in the investment cycle. Moreover, a situation exists where the optimal scheme is not unique, which further brings different risks and benefits. The combination of the two schemes can consider various complex investment scenarios more comprehensively and realize the dynamic adjustment of the optimized portfolio in the whole investment cycle.

DATA AVAILABILITY STATEMENT

The original contributions presented in the study are included in the article/supplementary material; further inquiries can be directed to the corresponding author.

AUTHOR CONTRIBUTIONS

JY and YX: conceptualization and methodology; JY: writing—original draft preparation; YX: supervision; ZW, JD, and YW: writing—reviewing and editing.

FUNDING

This project was supported by the Young Elite Scientists Sponsorship Program by the Chinese Society of Electrical Engineering (CSEE-YESS-2018006) and the National Natural Science Foundation of China (U2066209).

REFERENCES

Alvarado, D., Moreira, A., Moreno, R., and Strbac, G. (2019). Transmission Network Investment with Distributed Energy Resources and Distributionally Robust Security. *IEEE Trans. Power Syst.* 34 (6), 5157–5168. doi:10.1109/tpwrs.2018.2867226

Arcos-Vargas, A., Núñez-Hernández, F., and Villa-Caro, G. (2017). A DEA Analysis of Electricity Distribution in Spain: an Industrial Policy Recommendation. *Energy Policy* 102, 583–592. doi:10.1016/j.enpol.2017.01.004

Çelen, A., and Yalçın, N. (2012). Performance Assessment of Turkish Electricity Distribution Utilities: an Application of Combined FAHP/TOPSIS/DEA Methodology to Incorporate Quality of Service. *Utilities Policy* 23 (4), 59–71. doi:10.1016/j.jup.2012.05.003

Erdiwansyah, Mahidin., and Husin, H. (2021). A Critical Review of the Integration of Renewable Energy Sources with Various Technologies. *Prot. Control. Mod. Power Syst.* V (1), 37–54.

Fu, G. H., Li, Q. Y., and Li, K. (2019). A Dynamic Project Selection Method Based on Network Analysis. *Comput. Tech. Automation* 38 (02), 51–57.

Gouveia, M. C., Dias, L. C., Antunes, C. H., Boucinha, J., and Inácio, C. F. (2015). Benchmarking of Maintenance and Outage Repair in an Electricity Distribution Company Using the Value-Based DEA Method. *Omega* 53, 104–114. doi:10.1016/j.omega.2014.12.003

Huang, J. Q., Zhang, Y. W., and He, J. F. (2020). A Robust Expansion Planning Method for Distribution Networks Considering Extreme Scenarios. *Electric Power Construction* 41 (07), 67–74.

Li, K., Fu, G. H., and Tian, C. Z. (2019). Distribution Network Investment Allocation and Project Optimization Method Considering the Historical Investment Effectiveness. *Comput. Tech. Automation* 38 (03), 33–38.

Li, w., Cui, W. T., and Feng, J. H. (2018). Investment Decision-Making Method of Medium Voltage Distribution Network Considering Project Attributes. *Proc. CSU-EPSA* 30 (05), 50–55+62.

Liu, H. F., Liu, H. P., and Zhang, Y. F. (2019). Auxiliary Decision-Making for Optimization of Distribution Network Reconstruction Projects. *Rural Electrification* 2019 (10), 14–16.

Liu, Y., Wang, M., Liu, X., and Xiang, Y. (2019). Evaluating Investment Strategies for Distribution Networks Based on Yardstick Competition and DEA. *Electric Power Syst. Res.* 174, 105868. doi:10.1016/j.epsr.2019.105868

Luo, Y., and Li, Y. L. (2013). Comprehensive Decision-Making of Transmission Network Planning Based on Entropy Weight and Grey Relational Analysis. *Power Syst. Tech.* 37 (01), 77–81.

Mansor, N. N., and Levi, V. (2017). Integrated Planning of Distribution Networks Considering Utility Planning Concepts. *IEEE Trans. Power Syst.* 32 (6), 4656–4672. doi:10.1109/tpwrs.2017.2687099

Mardani, A., Zavadskas, E. K., Streimikiene, D., Jusoh, A., and Khoshnoudi, M. (2017). A Comprehensive Review of Data Envelopment Analysis (DEA) Approach in Energy Efficiency. *Renew. Sust. Energ. Rev.* 70, 1298–1322. doi:10.1016/j.rser.2016.12.030

Molina, J. D., Contreras, J., and Rudnick, H. (2017). A Risk-Constrained Project Portfolio in Centralized Transmission Expansion Planning. *IEEE Syst. J.* 11 (3), 1653–1661. doi:10.1109/jsyst.2014.2345736

Muñoz-Delgado, G., Contreras, J., and Arroyo, J. M. (2019). Distribution System Expansion Planning Considering Non-Utility-Owned DG and an Independent Distribution System Operator. *IEEE Trans. Power Syst.* 34 (4), 2588–2597. doi:10.1109/tpwrs.2019.2897869

Oskuee, M. R. J., Babazadeh, E., and Najafi-Ravadanegh, S. (2015). Multi-Stage Planning of Distribution Networks with Application of Multi-Objective Algorithm Accompanied by DEA Considering Economical, Environmental and Technical Improvements. *J. Circuits Syst. Comput.* 25 (04), 1650025, 2015 . Article 1650025.

Shen, M. Y., Hu, Z. S., Liu, Z. Y., Dai, P., Huang, J. J., and Yang, L. (2020). Optimal Multi-Stage Dual-Q Selection for Distribution Network Planning Projects Considering Benefit Coupling and Timing Correlation Characteristics. *Electric Power Automation Equipment* 40 (06), 22–2933.

Shen, X., Shahidehpour, M., Zhu, S., Han, Y., and Zheng, J. (2018). Multi-Stage Planning of Active Distribution Networks Considering the Co-Optimization of Operation Strategies. *IEEE Trans. Smart Grid* 9 (2), 1425–1433. doi:10.1109/tsg.2016.2591586

Tang, W., Zhang, H. H., and Xiao, S. (2018). Research on Accurate Investment Strategy of Distribution Network Based on Attribute Classification of Planning Projects. *Sci. Tech. Industry* 18 (01), 63–67.

Telukunta, V., Pradhan, J., Pradhan, J., Agrawal, A., Singh, M., and Srivani, S. G. (2017). Protection Challenges under Bulk Penetration of Renewable Energy Resources in Power Systems: A Review. *Csee Jpes* 3 (04), 365–379. doi:10.17775/cseejpes.2017.00030

Verástegui, F., Lorca, A., Olivares, D. E., Negrete-Pincetic, M., and Gazmuri, P. (2019). An Adaptive Robust Optimization Model for Power Systems Planning with Operational Uncertainty. *IEEE Trans. Power Syst.* 34 (6), 4606–4616. doi:10.1109/tpwrs.2019.2917854

Wang, Y. X., Fang, R. C., Zhang, J., Ge, T., and Chen, Y. B. (2019). Research on Investment Decision System of Distribution Network. *distribution Netw. Technol.* 47 (02), 56–62.

Wang, Z. C., Pan, X. P., and Ma, Q. (2019). Multi-Attribute Investment Ranking Method for Power Grid Project Construction Based on Improved Prospect Theory of "Rewarding Good and Punishing Bad" Linear Transformation. *Power Syst. Tech.* 43 (06), 2154–2164.

Ye, X. D., Zhang, J. J., and Xu, Q. (2019). Medium-Voltage Distribution Network Planning Optimization by Improved. *TOPSIS* 38 (01), 92–97.

Conflict of Interest: The authors declare that the research was conducted in the absence of any commercial or financial relationships that could be construed as a potential conflict of interest.

frontiers in Energy Research

ORIGINAL RESEARCH
published: 05 August 2021
doi: 10.3389/fenrg.2021.723702

A Dynamic Multi-Stage Planning Method for Integrated Energy Systems considering Development Stages

Donglou Fan[1], Xun Dou[1], Yang Xu[2], Chen Wu[2], Guiyuan Xue[2] and Yunfan Shao[1]*

[1]College of Electrical Engineering and Control Science, Nanjing TECH University, Nanjing, China, [2]Economic Research Institute, State Grid Jiangsu Electric Power Co., Ltd., Nanjing, China

Integrated energy system (IES) planning is a long-term and rolling decision-making process. According to System Development Theory, the development-needs at different stages are different. Therefore, an IES dynamic multi-stage planning method considering different development stages is proposed. The first step of the method is putting forward a model based on the degree of system coupling, the reserve ratio, and the penetration rate of clean energy to divide dynamic development stages. Secondly, establishing a dynamic multi-stage planning model of the IES by combining the needs of different development stages through dynamic goals and constraints. Finally, the results given by the optimal configuration of critical IES equipment will be analysed in different scenarios. Following these steps, the result shows that the dynamic multi-stage planning method proposed is able to reduce the total planning cost of the system by 14% and reducing the clean energy penetration rate by 3%. Therefore, the proposed dynamic multi-stage planning scheme is effective and economical.

Keywords: multi-stage planning, integrated energy system, development stage, dynamic planning, configuration

OPEN ACCESS

Edited by:
Yingjun Wu,
Hohai University, China

Reviewed by:
Rui Bo,
Missouri University of Science and Technology, United States
Jun Liu,
Xi'an Jiaotong University, China

****Correspondence:***
Xun Dou
dxnjut@njtech.edu.cn

Specialty section:
This article was submitted to Smart Grids, a section of the journal Frontiers in Energy Research

Received: *11 June 2021*
Accepted: *23 July 2021*
Published: *05 August 2021*

Citation:
Fan D, Dou X, Xu Y, Wu C, Xue G and Shao Y (2021) A Dynamic Multi-Stage Planning Method for Integrated Energy Systems considering Development Stages. Front. Energy Res. 9:723702. doi: 10.3389/fenrg.2021.723702

INTRODUCTION

The issue of reducing the usage of fossil fuel is widely considered by the world. With the continuous progress of energy system development in low-carbon technology and sustainability (Liu et al., 2009), integrated energy systems (IES) can provide an organic energy supply and integrated system that coordinates energy production, transmission, distribution, conversion, storage, and consumption. IES can improve energy cleanliness through the conversion of multiple forms of energy, as well as coordinated operation and utilization (Wang et al., 2019). A suitable planning method is required to promote the efficient and stable development of IES and approach suitable resource allocation. This arrangement involves utilizing the complementary energy characteristics of IES, promoting cascaded energy usage, and reducing fossil fuel energy consumption. According to the system development theory, the development includes an initial stage, linear and nonlinear development stages, and a decline stage, and every stage has different characteristics (Zhong and Yihua, 2005). The initial stage is the initial stage of multi-stage planning. It is mainly to adjust the internal structure and external relations of the system. At this time, more investment and less income, is the preparation stage of rapid development of the system. The linear development stage corresponds to the medium stage of multi-stage planning, the development speed is fast and the structure changes less. The mature stage of the corresponding system in the nonlinear stage of development produces qualitative changes from the accumulation of linear development, and the IES adjusts the internal structure appropriately and coexists harmoniously with the equipment. Multi-stage planning must adapt

to these characteristics to ensure reasonable system development. Considering the development stage, the planning goals can be determined according to changes in the system. The planning stage can be dynamically adjusted to update the current plan. This method improves the system economy and energy cascade utilization. It can also adapt to ongoing developments.

Most integrated energy system planning is based on single-phase planning (Cheng et al., 2017; Zheng et al., 2017), which can lead to energy equipment lying idle at the beginning of planning. The single-phase planning also leads to the aging of equipment and insufficient capacity at the end of planning. Therefore, to achieve the timeliness of integrated energy system planning, the planning cycle needs to be divided into several stages to determine the different stages of planning objectives and the planning process (Ge and Jia, 2012). There is less research on multi-stage planning at present, and the focus of the research is on the planning objectives and objectives of IES based on different forms of energy coupling at different planning stages. Existing research has established the electric–gas coupling (Wu, 2016; Huang et al., 2019) and electric–heat–gas multi-energy coupling planning models (Unsihuay-Vila et al., 2010; Zhang et al., 2015; Gan et al., 2017). The annual operating cost (Yang et al., 2012; Salimi et al., 2015; Pazouki and Haghifam, 2016; Jiang et al., 2017), investment operating cost (Mago and Chamra, 2009; Wang et al., 2018; Bai et al., 2019), carbon transaction cost (Zeng et al., 2019a), and energy conversion efficiency (Jiang et al., 2004; Guo et al., 2013) of a system are important for energy station planning (Chen et al., 2018) and network reconstruction (Quan et al., 2018; Wu et al., 2019). The current multi-stage approach typically involves fixed-time dynamic planning. This method does not consider the needs of the different development stages of IES. Considering the characteristics of IES and the needs of objective low-carbon sustainable development, the basic energy supply capacity of the system should be considered in the initial stage of development, the system maturity should be examined in the medium stage, and the system energy cleanliness should be accounted for in the mature stage. Therefore, in a new multi-stage planning method, the planning goals of the different development stages should be determined according to the impact of system technology, policy, load, and other developments on the system economy, safety, and energy cleanliness. Additionally, the IES energy cascade capabilities should be fully utilized so system planning is aligned with the development needs of the system.

This paper proposes an innovative method of IES dynamic multi-stage planning focusing on the development stage. This method divides the development phase of IES into different parts in order to make sure that the plan can satisfy the requirements of system's phased development and can enhance the economics of the system. The conclusions of this paper are:

1) This paper proposes a more reasonable IES development stage division method considering the energy cascade utilization demand, basic load supply demand, energy cleanliness demand, and economic development demand in the development process of IES.

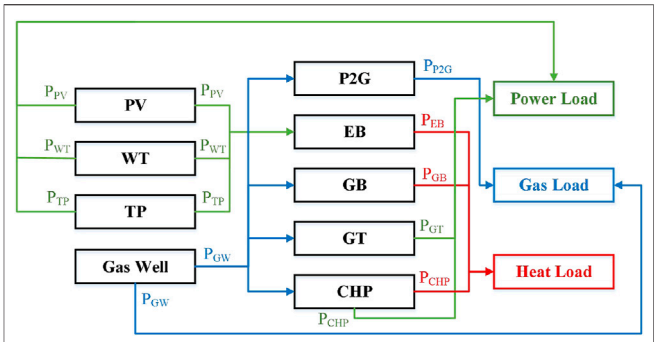

FIGURE 1 | Structure of the IES.

2) Based on the proposed IES development stage division method, a dynamic multi-stage planning model that focuses on the IES development stage is built. Unlike dynamic planning with one fixed time step, the approach improves the level of energy cascade utilization of the system and aligns the system development goals with the system development needs.

This paper is aimed to design a dynamic multi-stage planning considering the development stage to improve the economy of the system. Section *Modeling of the IES Structure and Key Equipment* builds a basic model of the key IES equipment. Section *Model of IES Planning Considering Development Stages* describes the division of the IES development stages and establishes a dynamic multi-stage IES planning model that focuses on the development stages. Section *Results Development Stages* verifies the economy of the proposed method through a comparative analysis of multiple scenarios. Finally, the paper's conclusion is presented in section Conclusion.

MODELING OF THE INTEGRATED ENERGY SYSTEM STRUCTURE AND KEY EQUIPMENT

Integrated Energy System Structure

The structure of the IES considered in this paper is illustrated in **Figure 1** (Zeng et al., 2019b). The IES includes wind turbines (WT), photovoltaics (PV), combined heat and power (CHP), gas turbines (GT), electricity-to-gas equipment (P2G), gas boilers (GB), and heat pumps (HPs). The load includes three types of heat, electricity, and gas. The heat load is supplied by CHP, GB, or HP, and the associated energy supply equipment operate as standbys for each other. It is assumed that CHP works by generating power in heat mode. The gas load is supplied by the P2G and gas source. The electric loads are supplied by the thermal power units, PV, WT, CHP, and GT.

The following section introduces the physical model of the coupled equipment in the IES based on a previous study (Jiang et al., 2004).

Modeling of Coupled Physical Equipment

Physical models of the coupled IES equipment introduced above are built as follow (Jiang et al., 2004).

Combined Heat and Power Unit Physical Model

$$P_{\mathrm{CHP,P},t} = P_{\mathrm{CHP,G},t} \cdot \eta_{\mathrm{CHP,P}} \tag{1}$$

$$P_{\mathrm{CHP,H},t} = P_{\mathrm{CHP,G},t} \cdot \eta_{\mathrm{CHP},H} \tag{2}$$

where $\eta_{\mathrm{CHP},P}$ and $\eta_{\mathrm{CHP},H}$ are the power generation efficiency and heating efficiency of the CHP unit, respectively. $P_{\mathrm{CHP},P,t}$, $P_{\mathrm{CHP},H,t}$, and $P_{\mathrm{CHP,G},t}$ are the output power, output heat, and input power of the CHP unit at time t, respectively.

Gas Boilers Physical Model

$$P_{\mathrm{GB},t} = v_{\mathrm{GB},t} L_{\mathrm{NG}} \eta_{\mathrm{GB}} \tag{3}$$

where P_{GB} is the heating output power of the GB at time t, $v_{\mathrm{GB},t}$ is the natural gas consumption of the GB at time t, L_{NG} is the low-level heating value of natural gas, and η_{GB} is the heating efficiency of the GB.

Heat Pump Physical Model

$$P_{\mathrm{HP},t} = P_{\mathrm{P,HP},t} \eta_{\mathrm{H,HP}} \tag{4}$$

where $P_{\mathrm{HP},t}$ is the heating power of the HP at time t, $P_{\mathrm{P,HP},t}$ is the input power of the HP at time t, and $\eta_{\mathrm{H,HP}}$ is the heating energy efficiency of the HP.

Gas Turbines Physical Model

$$P_{\mathrm{GT},t} = v_{\mathrm{GT},t} L_{\mathrm{NG}} \eta_{\mathrm{GT}} \tag{5}$$

where $P_{\mathrm{GT},t}$ is the electrical output power of the GT at time t, $v_{\mathrm{GT},t}$ is the natural gas consumption of the GT at time t, and η_{GT} is the power generation efficiency of the GT.

Electricity-to-Gas Equipment Physical Model

A typical physical model of a P2G unit can be expressed as:

$$P_{\mathrm{P2G},\mathrm{H}_2,t} = P_{\mathrm{P2G},t} \eta_{\mathrm{P2G},\mathrm{H}_2} \tag{6}$$

$$P_{\mathrm{P2G},\mathrm{CH}_4,t} = P_{\mathrm{P2G},t} \eta_{\mathrm{P2G},\mathrm{CH}_4} \tag{7}$$

where $\eta_{\mathrm{P2G,H2}}$ and $\eta_{\mathrm{P2G,CH2}}$ are the H_2 efficiency and CH_4 efficiency. $p_{\mathrm{P2G,H2},t}$ and $p_{\mathrm{P2G,CH4},t}$ are the output H_2 and output CH_4 at time t. $p_{\mathrm{P2G},t}$ is the input gas at time t.

Modeling of Source–Load Interaction Behavior

This paper considers the electricity price in comparison with the gas price. The supply–demand relationship of the IES is constructed based on the high flexibility of the electricity price. Accordingly, considering the impact of external policies and scientific and technological signals, the source–load supply and demand of the IES is established using the following model:

$$C_{\mathrm{P}} = C_{p,\mathrm{re}}\left(1 + \alpha_{\mathrm{GOV}} + \alpha_{\mathrm{g}}\right) \tag{8}$$

$$C_{\mathrm{H}} = C_{\mathrm{H,re}}\left(1 + \alpha_{\mathrm{GOV}} + \alpha_{\mathrm{g}}\right) \tag{9}$$

$$P_{LD,P} = A_P C_P + B_P \tag{10}$$

$$P_{LD,H} = A_H C_H + B_H \tag{11}$$

$$P_{\mathrm{LD,G}} = P_{\mathrm{ALL}} - P_{\mathrm{LD,P}} - P_{\mathrm{LD,H}} \tag{12}$$

where C_{P} is the electricity price in the process of source–load interaction; $C_{\mathrm{p.re}}$ is the predicted electricity price; $C_{\mathrm{H}}$is the heating price associated with the source–load interaction behavior; $C_{\mathrm{H.re}}$ is the predicted heating price; $\alpha_{\mathrm{GOV}}$is the policy impact factor; $\alpha_{\mathrm{g}}$is the technology impact factor; $P_{\mathrm{LD,P}}$ is the demand for electrical load in the process of source–load interaction; $A_{\mathrm{p}}$is the electricity price fluctuation coefficient; $B_P$is the basic electricity price; $A_{\mathrm{H}}$is the heat price fluctuation coefficient; B_H is the basic heat price; $P_{\mathrm{LD,G}}$ is the demand for natural gas during source–load interactions; P_{ALL} is the normalized total electrical and gas load.

MODEL OF INTEGRATED ENERGY SYSTEM PLANNING CONSIDERING DEVELOPMENT STAGES

Development Stage Division of the Integrated Energy System

For an IES, the system configuration in the decline stage no longer fulfils the production and living needs, and a new planning scheme must be launched. Therefore, the system is divided into initial, medium, and mature stages based on the characteristics of the system's initial stage, linear development stage, and nonlinear development stage (Zhong and Yihua, 2005). The development of the IES is affected by external factors such as policies, science, and technology, and has a phased nature (Chen et al., 2018). Apparently, changes in equipment input costs and the energy supply-demand will cause changes in the development stage related to the degree of system coupling, economic benefits, and clean energy penetration. Therefore, the system development process can include initial stage, medium stage, and mature stage.

In the initial stage of the IES, the system is generally weak and incomplete, and usually only fulfils the basic needs of the environment (Zhong and Yihua, 2005). Thus, only the system's reserve requirements are considered in the initial stage. Due to the limited science and technology levels in the initial stage of the system, the construction cost of coupling equipment is high, this stage only requires a system reserve rate. This paper defines this stage as the initial stage of the IES.

In the linear development stage of the system, the development speed is fast and there are few structural changes (Zhong and Yihua, 2005). Thus, there are not too many requirements on the function of the system, only considering the initial requirements of the coupling degree. When the load increases to a certain extent, the original energy supply level can no longer meet the system load demand. Therefore, the supply

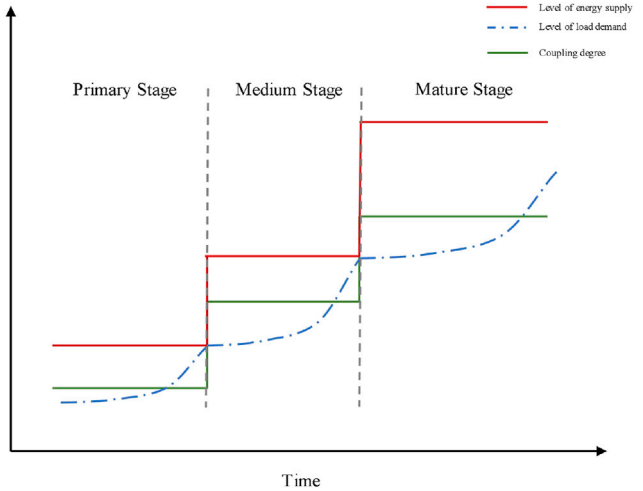

FIGURE 2 | Schematic diagram of the development stages of the IES.

capacity of the system should be enhanced by equipment expansion at specific time points. As shown in **Figure 2**, the energy supply level of the system rises in a stepwise manner, and the system is coupled at this time. The capacity improvements enabled by the coupling devices increase the system energy cascade utilization (Quan et al., 2018). This paper defines this stage as the medium stage of the IES.

In the nonlinear development stage of the system, the IES adaptively adjusts its internal structure and coexists harmoniously with other developments (Zhong and Yihua, 2005). Therefore, in the nonlinear development stage, the IES needs to further emphasize its own development goals while taking into account the needs of sustainable environmental development. When the technology level of the equipment matures and the degree of coupling of the system increases, the ratio of production and the penetration of clean energy must be considered. This paper defines this stage as the mature stage of the IES.

According to the relevant economic and security requirements, energy cascade utilization requirements, and cleaning requirements of the above IES stages, several development indicators for IES are proposed. These indicators include the degree of coupling, the ratio of input to output, the reserve ratio, and the clean energy penetration rate. The development requirements of each stage are also quantified and divided into different development stages. The calculation formulas are:

$$\eta_C = \sum_{i=1}^{N_C} Q_i \Big/ \sum_{j=1}^{N} Q_j \times 100\% \tag{13}$$

$$\eta_{CB} = C_I / C_O \times 100\% \tag{14}$$

$$\eta_R = \sum_{i=1}^{N} Q_{B,i} \Big/ \sum_{j=1}^{N} Q_j \times 100\% \tag{15}$$

$$\eta_{\mathrm{Re}} = \sum_{i=1}^{N_{re}} Q_{RE,i} \Big/ \sum_{j=1}^{N} Q_j \times 100\% \tag{16}$$

where η_C is the degree of IES coupling; Q_i is the installed capacity of the ith coupled device in the system; N_C is the total number of coupled devices in the system; Q_j is the installed capacity of the jth device in the system; C_I is the total system revenue; C_O is the total system cost; η_R is the IES reserve rate; $Q_{R,i}$ is the reserve capacity of the ith device; η_{Re} is the renewable energy penetration rate of the IES; N_{Re} is the amount of clean energy in the system; and $Q_{RE,i}$ is the capacity of the ith renewable energy device.

Planning Model in Each Stage

The IES optimal allocation problem considering the development stage is studied by minimizing the total cost of the whole IES planning cycle. The planning goals are divided into basic planning goals and periodic planning goals. The basic planning goals are an inherent part of the objective function, and the periodic planning goals are a unique part of each development stage. The objective functions are adjusted according to the development requirements of each stage.

Planning Model of the Initial Stage

1) Planning goals of the initial stage.

The basic planning goals of the system include the initial investment of the IES and the minimum operation and maintenance costs. The objective function is specifically shown in **Eqs. 17–20**.

$$\min C_{\mathrm{ALL}} = C_{\mathrm{S}} + C_{\mathrm{M}} \tag{17}$$

$$C_{\mathrm{S}} = \sum_{j=1}^{N} \frac{C_j Q_j}{(1+i)^n} (1 - t_{\mathrm{r}}) \tag{18}$$

$$C_{\mathrm{M}} = \sum_{n=1}^{L_{\mathrm{P}}} \frac{C_{\mathrm{MP}}}{(1+i)^n} (1 - t_{\mathrm{r}}) \alpha_n \tag{19}$$

$$C_{\mathrm{MP}} = r_{\mathrm{M}} \sum_{j=1}^{N} C_j Q_j \tag{20}$$

where C_{ALL} is the total cost of the IES; C_{S} is the initial input cost of the system; C_{M} is the total cost of system operation and maintenance; N is the total number of devices that require investment in the system; C_j is the initial investment cost per unit capacity of device j; Q_j is the capacity of device j; t_{r} is the tax rate; i is the interest rate; L_{p} is the number of system planning years; r_M is the equipment maintenance rate; C_{MP} is the equipment operation and maintenance costs in the first year; and α_n is the technology impact index in the nth year.

2) Constraints of the initial stage.

Equipment operating constraints.

Considering the actual interaction between the supply and demand entities, the optimization variables need to be kept within the following ranges:

$$\begin{cases} Q_{\mathrm{EX},k}^{\min} \le Q_{\mathrm{EX},k} \le Q_{\mathrm{EX},k}^{\max} \\ P_j^{\min} \le P_j \le P_j^{\max} \\ P_{\mathrm{u},j}^{\min} \le P_{\mathrm{u},j} \le P_{\mathrm{u},j}^{\max} \\ P_{\mathrm{d},j}^{\min} \le P_{\mathrm{d},j} \le P_{\mathrm{d},j}^{\max} \end{cases} \tag{21}$$

where $Q_{EX,k}^{\min}$ is the minimum reserve capacity for the kth energy source; $Q_{EX,k}$ is the actual reserve capacity for the kth energy source; $Q_{EX,k}^{\max}$ is the maximum reserve capacity for the kth energy source; P_j, $P_j^{\max}$, and $P_j^{\min}$ are the actual, maximum, and minimum output of the jth device; $P_{u,j}$, $P_{\mathrm{u},j}^{\max}$, $P_{\mathrm{u},j}^{\min}$ are the actual, maximum, and minimum upward climbing power of the jth device; $P_{d,j}$, $P_{\mathrm{d},j}^{\max}$, and $P_{\mathrm{d},j}^{\min}$ are the actual, maximum, and minimum downward climbing power of the jth device.

The output of each piece of equipment is subject to a corresponding physical model. Therefore, the equipment operation constraints are covered by **Eqs. 1–7**.

Energy Conservation Constraints

The power balance constraints of electricity, heat, and gas are considered respectively.

1) Electric power balance constraint

$$\begin{aligned} P_{\mathrm{LD,P}} = {} & P_{\mathrm{GEN}} + P_{\mathrm{PV}} + P_{\mathrm{WT}} + P_{\mathrm{GT}} + P_{\mathrm{CHP,P}} \\ & - P_{\mathrm{P,P2G}} - P_{\mathrm{P,HP}} \end{aligned} \tag{22}$$

where $P_{\mathrm{LD},p}$ is the electrical load in the system; P_{GEN} is the output power of the GEN; P_{PV} is the output power of PV; P_{WT} is the output power of WT; P_{GT} is the output power of GT; $P_{\mathrm{CHP},p}$ is the output electrical power of the CHP; $P_{\mathrm{P,P2G}}$ is the input power of the P2G; and $P_{\mathrm{P,HP}}$ is the input power of the HP.

2) Natural gas power balance constraint

$$P_{\mathrm{LD,G}} = P_{\mathrm{P2G,G}} - P_{\mathrm{CHP,G}} - P_{\mathrm{GT,G}} - P_{\mathrm{GB,G}} \tag{23}$$

where $P_{\mathrm{LD,G}}$ is the natural gas load; $p_{\mathrm{P2G,G}}$ is the output power of the P2G; $P_{\mathrm{CHP,G}}$ is the input power of the CHP; $P_{\mathrm{GT,G}}$ is the input power of the GT; and $P_{\mathrm{GB,G}}$ is the input power of the GB.

3) Thermal power balance constraint

$$P_{\mathrm{LD,H}} = P_{\mathrm{CHP,H}} + P_{\mathrm{GB,H}} + P_{\mathrm{HP,H}} \tag{24}$$

where $P_{\mathrm{LD,H}}$ is the thermal load; $P_{\mathrm{CHP,H}}$ is the output heating power of the CHP; $P_{\mathrm{GB,H}}$ is the output heating power of GB; and $P_{\mathrm{HP,H}}$ is the output heating power of HP.

Planning Model of Medium Stage

1) Planning goals of the medium stage.

In the medium stage, there is no obvious change in planning goals, and **Eqs. 17–20** are used as the planning goals.

2) Constraints of the medium stage.

In the medium stage, the coupling capacity of the IES is improved, and the requirements for the cascade utilization of the system are considered. Therefore, the following constraints are added on the basis of the constraints in the initial stage:

$$\eta_{R,y} \ge P_{\mathrm{R}} \tag{25}$$

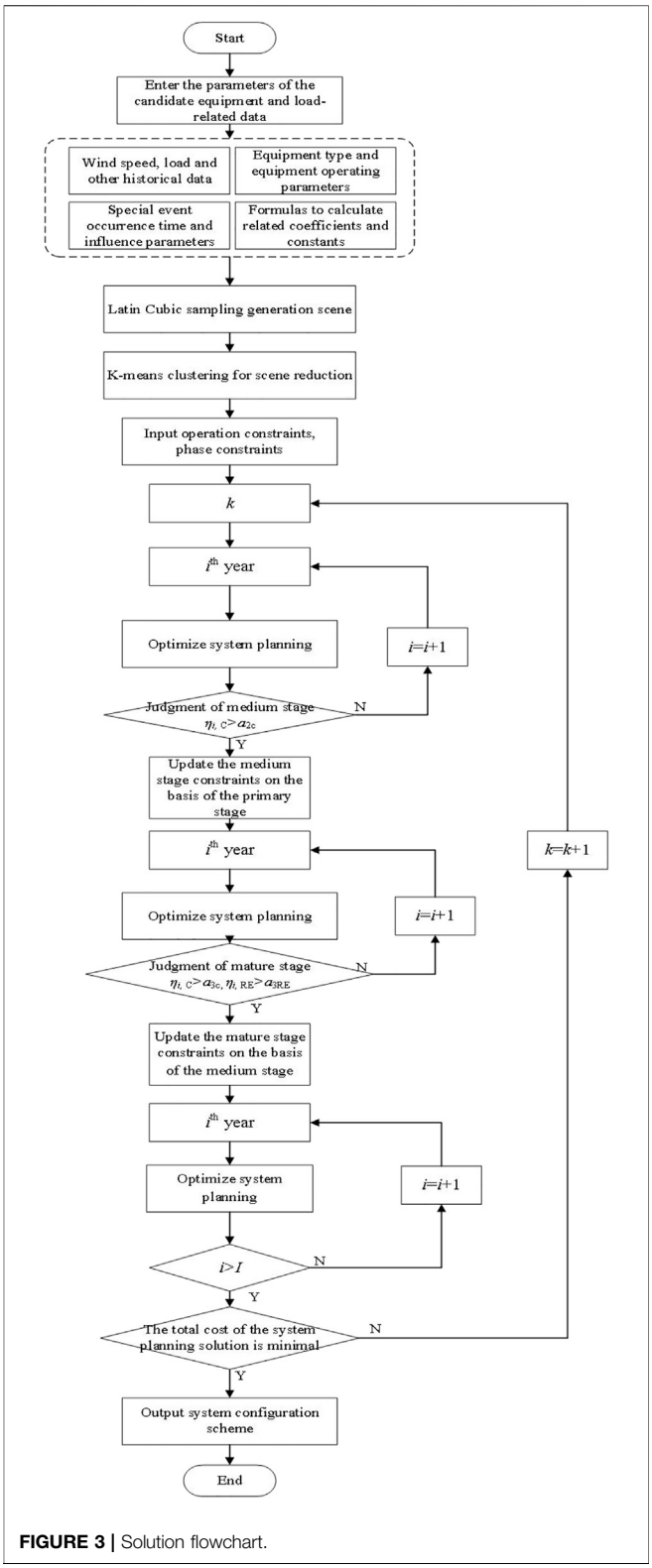

FIGURE 3 | Solution flowchart.

$$\eta_{C,y} \geq a_{2c} \tag{26}$$

where a_{1c} is the requirement for determining the coupling degree of the IES in the medium stage.

Planning Model of the Mature Stage

1) Planning goals of the mature stage.

In the mature stage, the main coupling equipment in the IES should be relatively mature. Thus, the initial input costs of major equipment are low and the mature equipment can be used to improve the system's clean energy consumption level. Therefore, based on the planning goals in the initial stage, the planning goals are updated to:

$$\min C_{ALL} = C_S + C_M + C_Q \tag{27}$$

$$C_Q = \sum_{n=1}^{L_P} \frac{C_{QP}}{(1-i)^n} (1 - t_r) \tag{28}$$

$$C_{QP} = C_r P_r \tag{29}$$

where C_Q is the cost of abandoning wind and light in the system, C_{QP} is the cost of abandoning wind and light in the first year of the system, C_r is the penalty coefficient for abandoning wind and light, and P_r is the amount of abandoned wind and light.

2) Constraints of the mature stage.

In the mature stage, there are no obvious changes in the constraints. **Eqs 1–7** and **21–24** again provide the constraints in this stage.

Optimization Solution

Based on the above model, the mixed-integer linear programming method of the GAMS platform is used to obtain a solution. The algorithm flowchart is shown in **Figure 3**.

Considering the development stage, an optimized configuration model of energy supply equipment is established to allow the IES to optimize the selection of GT, GB, CHP, and other equipments. The solution process is shown in **Figure 3**. The first step is to enter wind power, photovoltaic information, load data, equipment parameters, and other basic data. Random scenarios are then generated by Latin cube sampling, with K-means clustering used to reduce the total number of scenarios. The second step is to use the GAMS software to run the planning model, with the minimum annual cost of the system as the target. For this, a tree structure is used to code a one-parent genetic algorithm, and the original dual interior point method is applied to obtain the system operation strategy. The third step involves determining the index value of the development stage of the system, updating the planning goals and constraints, and determining whether it is necessary to expand the capacity. In the fourth step, a model with the minimum integrated cost in the planning cycle is developed as the optimization goal. The GAMS software is used to solve the problem and obtain the optimal configuration plan for the IES.

RESULTS

Basic Data

MATLAB and GAMS were used to execute a series of simulations and optimization analysis. This example selects data from an industrial park for analysis. This paper is based on the data of the literature (Wang et al., 2017; Liu et al., 2018), and some modifications have been made (DIW Berlin, 2021). Wind and photovoltaic outputs from a typical day in each of the four seasons were used (Liu et al., 2018). In the example, the multi-demand factor and the supply factor interact through coupling equipment. The equipment used in the IES includes GT, HP, P2G units, GB, CHP, thermal power units, PV, and WT. The specific equipment parameters (Wang et al., 2017) are listed in **Table 1**. To achieve effective cascade utilization of multiple sources of electrical heat, each subsystem in the IES should have a certain degree of coupling. This paper assumes that the required degree of coupling eventually reaches 40%.

Load forecasting was performed based on historical load data (Hong et al., 2018), which are shown in **Figure 4**.

Based on typical load scenarios, the models established in Sections 2 and 3 were then applied under the assumption of a system planning period of 20 years. A new steel plant and a textile mill are to be built in the park in the 6th year, with an impact factor of 0.4 for the electricity and heat loads. In the 15th year, a major breakthrough occurs in the CHP and GB manufacturing process, for which the impact factor of the construction cost is 0.4. The resulting load curve is shown in **Figure 5**.

Analysis of Results

In this paper, three scenarios are set up for dynamic multi-stage IES planning to consider the development stage.

Case 1: Dynamic multi-stage IES planning that takes into account the development needs of different stages of development.

Case 2: Multi-stage IES planning considering a fixed stage of development.

Case 3: Dynamic multi-stage IES planning without considering the development needs of different stages of development.

Analysis of Dynamic Multi-Stage IES Planning Considering Development Stage

Case 1: This case considers the basic energy supply demand in the initial stage of IES, with a limited reserve ratio. In the medium stage, we further consider the maturity of the system and increase the degree of coupling. In the mature stage, the system energy utilization cleanliness is also considered, and a clean energy penalty cost is added to the planning goals. The results for this configuration are shown in **Figure 6**.

As shown in **Figure 6**, in the first 5 years, the system is in the initial stage. The system is mainly equipped with renewable energy and thermal power units, with little coupling. At this time, the electricity, gas, and heat loads steadily increase, and the electric load is greater than the gas and heat loads. The cost of renewable energy generation is low, and the degree of system

TABLE 1 | Parameter list of equipment to be selected.

Candidate equipment	Number	Amount	Capacity/MW	Energy conversion efficiency	Construction cost/× 10 3 $
GT	A1	3	200	0.40	2,500
	A2	3	150	0.45	2,250
GB	B1	4	100	0.90	1,400
EB	C1	2	150	0.95	900
	C2	2	100	0.97	750
P2G	D1	1	100	0.76	1,500
	D2	1	100	0.76	1,500
CHP	E1	3	50	0.79	2,750
	E2	3	100	0.79	2,750
	E3	2	200	0.82	3,000
TP	F1	1	200	0.70	2,250
	F2	1	200	0.72	2,500
	F3	2	200	0.72	2,500
	F4	2	200	0.70	2,250
PV	G1	1	200	—	1,500
	G2	2	150	—	1,500
WT	H1	1	200	—	1,500
	H2	2	150	—	1,500

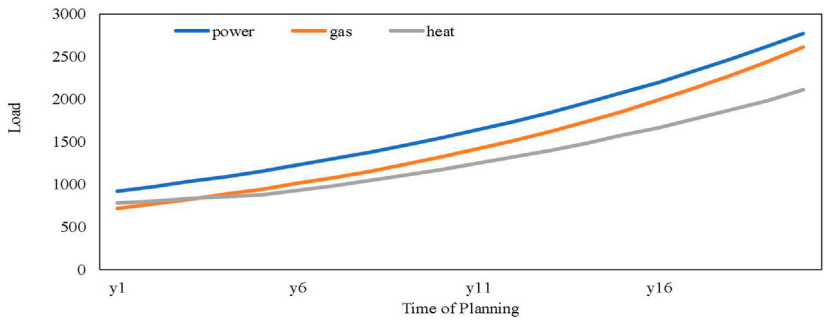

FIGURE 4 | Typical annual load forecasting curve.

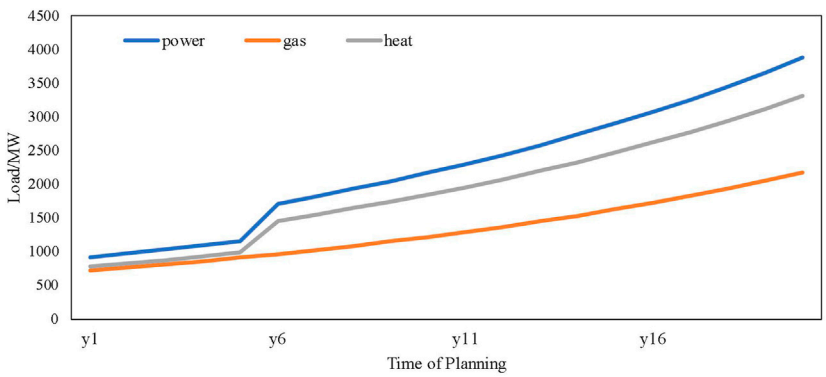

FIGURE 5 | Load curve considering special events.

coupling is low. There are no requirements for the installed capacity of the coupled equipment in the initial stage.

In the 6th year, the IES of the park is expanded and some coupled equipment is added, allowing the system to enter the medium stage. To cope with the surge in electrical and thermal loads and meet the new system development constraints, the park adds thermal power units, CHP, and GB. As shown in **Figure 5**, in the 6th year of the planning cycle, the park

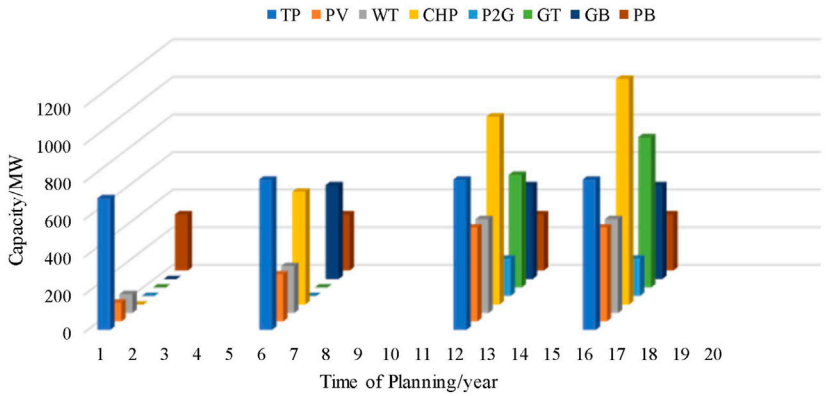

FIGURE 6 | Planning and configuration results in case 1.

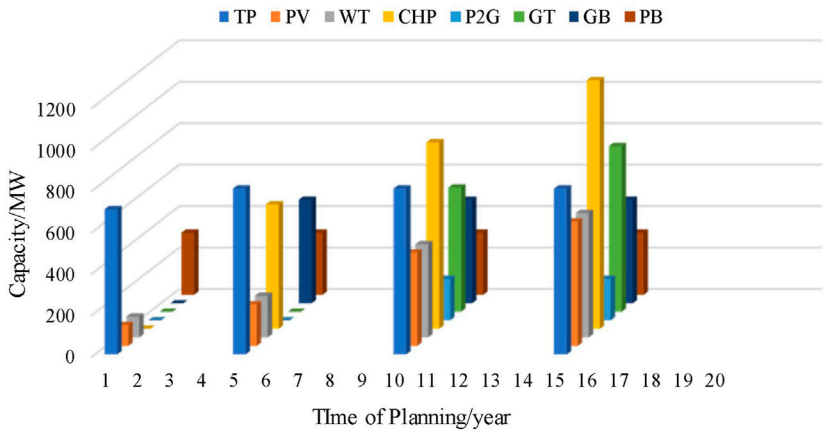

FIGURE 7 | Planning and configuration results of case 2.

undergoes industrial expansion, with the addition of a steel plant and a textile mill. Both industries cause large increases in the electrical and thermal loads of the park.

In the 12th year, the second expansion is carried out, and the system enters the mature stage. The costs of wind and light are added to the objective function, and the clean energy consumption capacity of the system is considered without further increasing the installed capacity of clean energy.

In the 15th year, the reserve is sufficient until the third expansion in the 16th year. At this point the system is still in the mature stage, and so gas coupling equipment is added to replace the electrical coupling equipment and a CHP unit and a GT are added. The impact of scientific and technological progress reduces the initial investment cost of new equipment, resulting in an increase in the power supply and heating capacity of the system. As shown in **Figure 5**, the reductions in gas-to-electricity and gas-to-heat costs increase the demand for gas loads, and the growth rate of the electrical load slows.

Analysis of the Impact of Dynamic Division of Development Stages

Case 2: To study the impact of the dynamic division of development stages on the planning results, the results for case 1 were trimmed to provide a basis for the stage division in case 2. In this case, we assume that IES enters the medium stage in the 5th year and the mature stage in the 10th year. Dynamic planning considers a fixed development stage. The configuration results are shown in **Figure 7**.

It can be seen that the planning results in case 1 and case 2 are similar. This is because the development requirements in each stage of case 2 are the same as for case 1. However, the first and second expansion time nodes of case 1 are the 6th and 12th years, whereas the first and second expansion time nodes of case 2 are the 5th, and 10th years. It can be seen from this analysis that the system has a fixed development stage, so the system enters the medium stage in the 5th year and the mature stage in the 10th year. To meet the needs of system development, capacity expansion is required. By comparing case1 and case 2, it can be

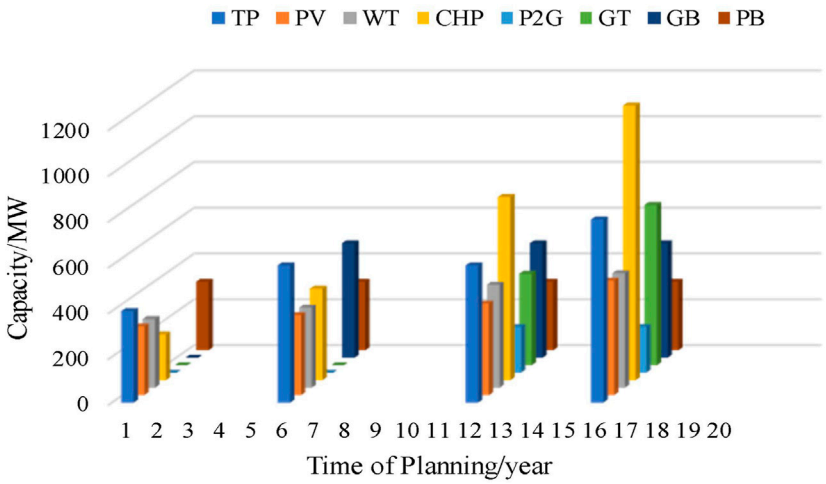

FIGURE 8 | Planning and configuration results of case 3.

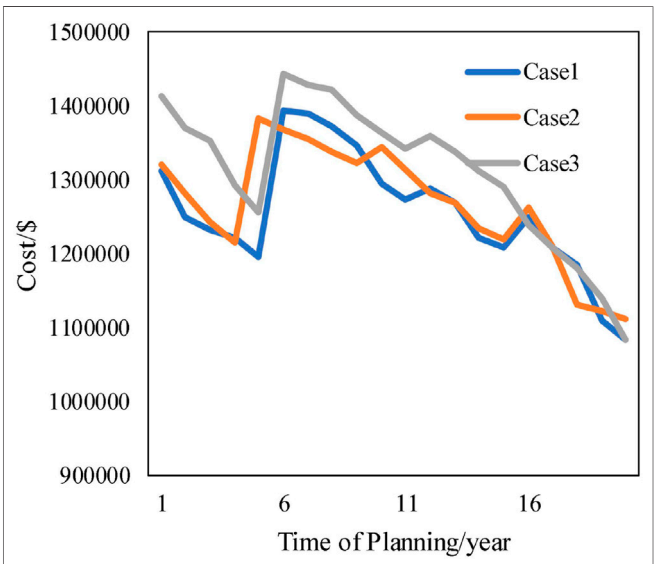

FIGURE 9 | Comparison of planning costs for each scenario.

found that, compared with fixed stage IES planning, dynamic multi-stage IES planning can delay the system expansion time by about 1–2 years, saving system expansion costs.

Analysis of the Impact of Development Stage Changes

Case 3: To compare and analyze the impact of the development stage changes on the planning results, case 3 does not consider the impact of different development needs. This case is based on case 1, assuming that the initial development requirements of IES are the same as the development requirements in the mature stage of case 1. The planning results are shown in **Figure 8**.

As shown in **Figure 8**, the system expansion time points are the 6th, 12th, and 16th years, as for case 1. This is because case 3 also uses dynamic planning and has the same load changes as case 1. To face these load changes, the system must be expanded at these moments. The planning result for case 3 in the 16th year is similar to that of case 1. Analysis suggests that the development needs considered in case 3 are similar to those considered in the mature stage of case 1. In case 1 and case 2, the initial stage costs are 6.22 × 106 $ and 6.23 × 106 $, respectively, whereas case 3 requires 6.69 × 106 $ in the first stage. This is because the entire planning cycle of the system places high requirements on the clean energy penetration and energy cascade utilization performance of the system. Initially, 150 MW CHP was selected, and 300 MW PV and WT were configured. Compared to case 1, 2 and case 3, dynamic IES planning that takes into account the needs of different stages of development can save about 7.5% of system construction costs compared to unconsidered, which shows that ignoring the development needs of the system results in larger investment in the initial stage.

Effectiveness Analysis

Analysis of the System Economy

To verify the effectiveness of the proposed method, the costs, capacity expansion results, coupling degree, and clean energy penetration rate in Cases 1, 2, and 3 are compared in **Figures 9**, **10** and **Table 2**.

Figure 9 shows the annual cost changes during the planning process in the three scenarios. The overall cost is on a downward trend from case 1 to case 3. The main reason for this is that the cost of equipment changes in line with the development law of the life cycle, so the initial input cost decreases year by year. Case 2 has higher costs than case 1 in the 5th year. As shown in **Figure 2**, case 1 is still in the initial stage in the 5th year, whereas case 2 has entered the medium stage, whereby the system must satisfy the demand for energy cascade utilization. That is, the system has been expanded. This can delay the system investment. The overall system cost of case 3 is higher than both case 1 and case 2. Analysis shows that case 3 has only a single development stage, and its development needs are the same as the mature stage of case 1. The development requirements are high and more

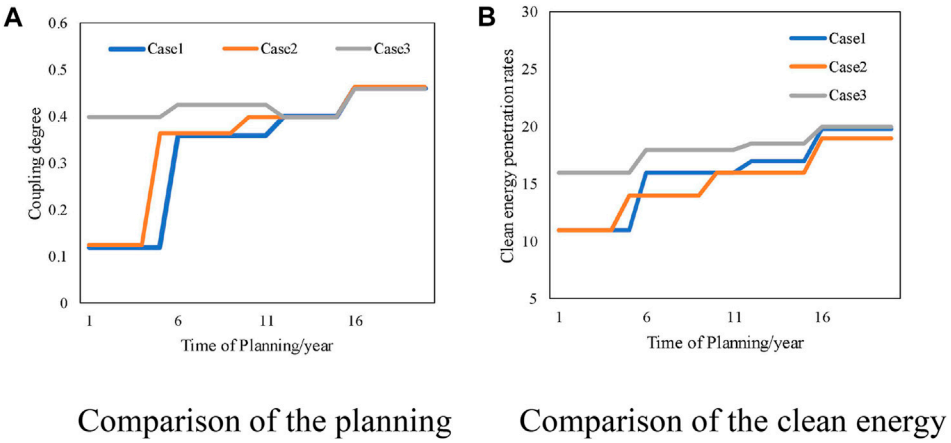

FIGURE 10 | Comparison of the planning performance.

Table 2 | Comparison of the expansion results for each configuration.

Planning results	Case1	Case2	Case3
First expansion time (y)	6	5	6
Second expansion time (y)	12	10	12
Third expansion time (y)	16	16	16
Total cost ($)	2.511 × 107	2.534 × 107	2.623 × 107

Indicates that case 1 has the lowest cost, followed by case 2 and then case 3. The total investment cost of case 1 is approximately 0.9% lower than case 2 and approximately 4.4% lower than case 3. Analysis shows that case 1 and case 2 both consider different development requirements in three different development stages. However, case 2 enters the mature stage earlier than case 1, and case 1 delays the need to increase the degree of coupling, which can delay investment.

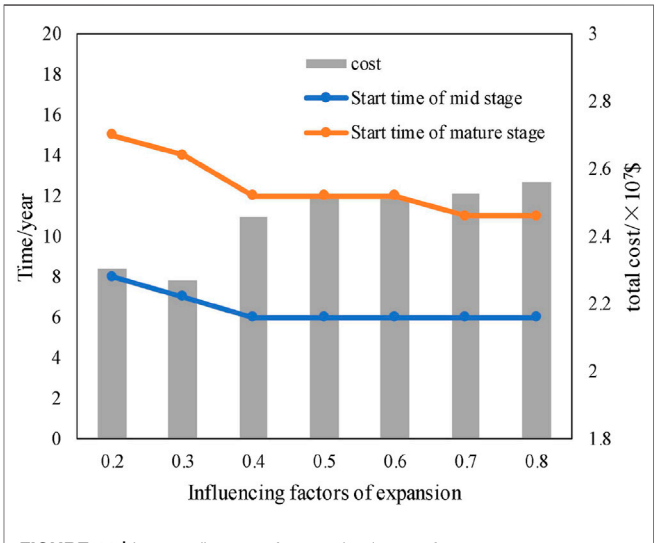

FIGURE 11 | Impact diagram of expansion impact factors.

coupling equipment needs to be configured, making the overall cost higher.

Hence, the IES planning scheme considering dynamic stages can rationally manage and improve economic benefits according to the development requirements of each stage of the system.

Analysis of System Performance

Figure 10 shows the changes in the coupling degree during the three scenarios. **Figure 10A** shows that the coupling degree rises in steps, because the energy cascade utilization demand in each stage of the system changes with the development stage. The coupling degree and clean energy penetration rate of case 2 are higher than those of case 1 in both the initial and medium stages. This is because the fixed development requirements mean that the system enters the medium and mature stages earlier than case 1, and pushes forward the requirements for the coupling degree of the system. From **Figure 10B**, we see that the expansion of case 1 occurred in the 6th, 12th, and 16th years, whereas the expansion of case 2 occurred in the 5th, 10th, and 16th years. The expansion occurred later in case 1 than in case 2. Over time, the reduction in the cost of new energy allocation has made the system lean towards more renewable energy installations. Furthermore, the increase in the load gives the system greater capacity to absorb the renewable energy, so the overall clean energy penetration is better in case 1 than in case 2.

The coupling degree and clean energy penetration rate of case 3 is higher than that of both case 1 and case 2, but the coupling degree decreases slightly in the 12th year. This is because case 3 does not consider the changes in the development stage, and the coupling degree and clean energy penetration rate requirements are higher than the other cases before Cases 1 and 2 enter the mature stage. In years 1–11, there has been more investment in coupling equipment. However, from the 12th to the 16th years, 350 MW of coupling equipment and 600 MW of other equipment have been added. The additional coupling equipment has less capacity than the other equipment, reducing the overall coupling degree.

Hence, the IES dynamic stage planning method can satisfy the development goals of cascade utilization and effectively improve

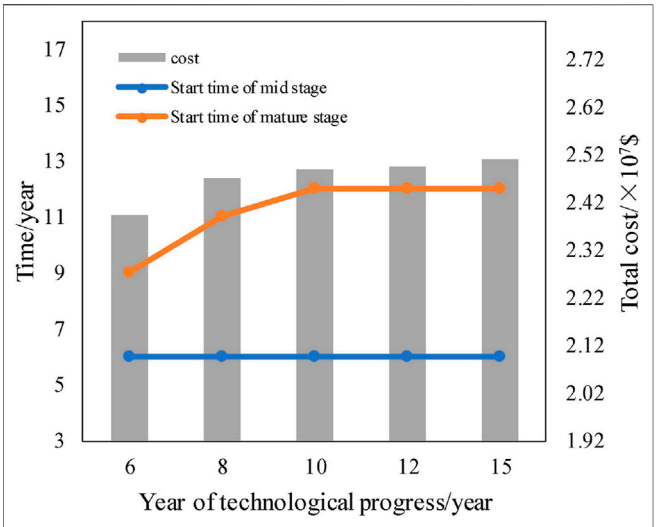

FIGURE 12 | Impact diagram of technological impact factors.

the clean energy penetration rate of the system in different stages while retaining the economic benefits of the system.

Sensitivity Analysis

The effects of different expansion impact factors and technology impact factors on the configuration results are now analyzed.

Sensitivity Analysis of Expansion Impact Factors

Figure 11 compares the configuration results for various expansion factors. The initial and development stages of the system advance with the expansion factor. In the 5th year, the system load surges at higher expansion factors. To meet the load demand, some equipment must be configured in advance, which causes the system to enter the medium and mature stages earlier.

The cost of each case first decreases and then increases as the expansion factor increases. This is because the minimum reserve rate is 0.25. When the expansion impact factor is 0.3, the average annual reserve rate of the system is 0.254. Expansion impact factors of 0.2 and 0.4 produce average annual reserve rates are 0.283 and 0.294 in the system. This shows that increasing the electric and thermal loads brings them more in line with the operating characteristics of the source-side equipment, thus reducing additional equipment investment. When the expansion impact factor is 0.3, the investment cost is lower than when the expansion factor is 0.2 or 0.4. However, as the expansion impact factor further increases, the total amount of electric and thermal load also increases, and larger-capacity equipment is required to handle the supply, resulting in a gradual increase in costs.

Therefore, the IES planning model established in this paper is suitable because it takes into account dynamic planning and can cope with regional expansion.

Sensitivity Analysis of Technological Impact Factors

Figure 12 compares the configuration results under different technology impact factors. The initial stage of the system is always in the 6th year. Technological progress means that the mature stage is eventually reached after the 9th year, rather than the 12th year. As shown by the costs in Figure 14, advances in science and technology reduce the equipment investment cost. The earlier these advances occur, the earlier the larger-capacity and more efficient equipment can be configured, which results in better energy cascade utilization capability. Therefore, scientific and technological progress will accelerate the development of IES to the mature stage.

CONCLUSION

Based on system development theory, this paper has identified the characteristics of the different development stages of an IES, and divided the development process into initial, medium, and mature stages. A dynamic multi-stage planning model, focusing specifically on the development stage, has been established. The following conclusions can be drawn from the case study:

1) In this study, compared with multi-stage planning method without considering the development stage, the proposed dynamic planning approach reduces the total system planning costs by 14% and increases the average clean energy penetration rate by 3%.
2) Considering the different requirements of the various development stages of the IES, this proposed approach can ensure that the system plan matches the technological and economic levels and that the system develops in a reasonable manner.

DATA AVAILABILITY STATEMENT

The original contributions presented in the study are included in the article/Supplementary Material, further inquiries can be directed to the corresponding author.

AUTHOR CONTRIBUTIONS

DF: Methodology, Software, Writing. XD: Methodology, Software, Validation, Reviewing and editing. YX: Data curation, Validation, Reviewing and editing. CW: Validation, Reviewing and editing. GX: Data curation, Conceptualization. YS: Conceptualization, Methodology.

FUNDING

This paper is supported by Science and Technology Foundation of SGCC "Research on energy trading mechanism and simulation based on multi-energy collaborative optimization" (No. 1400-202118231A-0-0-00).

ACKNOWLEDGMENTS

We thank the Economic Research Institute, State Grid Jiangsu Electric Power Co., Ltd. and Nanjing TECH University for their funding, knowledge and development contributions in the study.

REFERENCES

Bai, H., Yin, S., and Li, H. (2019). Optional Planning of Multi-Energy Stations Considering Carbon-Trading Cost. *J. Electron. Power Sci. Technology.* 34 (1), 11–19. doi:10.19781/j.issn.1673-9140.2019.01.002

Chen, B., Liao, Q., and Liu, D. (2018). Comprehensive Evaluation Indices and Methods for Regional Integrated Energy System. *Automation of Electric Power Systems.* 42, (4), pp.174–182.

Cheng, L., Zhang, J., and Huang, R. (2017). Case Analysis of Multi-Scenario Planning Based on Multi-Energy Complementation for Integrated Energy System [J]. *Electric Power Automation Equipment.* 37 (6), 282–287. doi:10.16081/j.issn.1006-6047.2017.06.037

DIW Berlin (2021). DIETER. [Online]. Available at: https://www.diw.de/de/diw_01.c.508843.de/forschung_beratung/nachhaltigkeit/umwelt/verkehr/energie/modelle/dieter/dieter.html. (Accessed May 17, 2019).

Gan, L., Chen, Y., and Liu, Y. (2017). Coordinative Optimization of Multiple Energy Flows for Microgrid with Renewable Energy Resources and Case Study. *Electric Power Automation Equipment.* 37 (6), 275–281. doi:10.16081/j.issn.1006-6047.2017.06.036

Ge, S., and Jia, O. (2012). Multi-Stage Model for Optimal Distribution Substation Planning[J]. *Power Syst. Technology.* 36 (10), 113–118. doi:10.13335/j.1000-3673.pst.2012.10.024

Guo, L., Liu, W., and Cai, J. (2013). A Two-Stage Optimal Planning and Design Method for Combined Cooling, Heat and Power Microgrid System. *Energ. Convers. Management.* 74, 433–445. doi:10.1016/j.enconman.2013.06.051

Hong, B., Chen, J., and Zhang, W. (2018). Integrated Energy System Planning at Modular Regional-User Level Base on a Two-Layer Bus Structure[J]. *CSEE J. Power Energ. Syst.* 4 (2), 188–196. doi:10.17775/cseejpes.2018.00110

Huang, C., Wang, C., and Ning, X. (2019). Distribution Expansion Planning Based on Strong Coupling of Operation and Spot Market. *Proceeding of the CSEE.* 39 (16), 4716–4731. doi:10.13334/j.0258-8013.pcsee.180685

Jiang, H., Wang, K., and Wang, Y. (2017). Energy Big Data: A Survey. *IEEE Access.* 4, 3844–3861.

Jiang, Y., Liu, X., and Xue, Z. (2004). Research on Evaluation Index of Energy Conversion System. *Res. Approach.* 26 (3), 27–31. doi:10.1016/j.eneco.2004.02.002

Liu, W., Wang, D., Yu, X., Ma, L., Xue, S., and Wu, Z. (2018). Multi-objective Planning of Micro Energy Network Considering P2G-Based Storage System and Renewable Energy Integration. *Automation Electric Power Syst.* 42 (16), 11–20. doi:10.7500/AEPS20180228003

Liu, Y., Ming, Z., and Lin, X. (2009). Generation Capacity Investmen Dynamics Based on Price Elasticity of Demand Side. *Automation Electric Power Syst.* 33 (01), 22–26.

Mago, P.J., and Chamra, L.M. (2009). Analysis and Optimization of CHP Systems Based on Energy, Economical, and Environmental Considerations. *Energy and Buildings.* 41 (10), 1099–1106. doi:10.1016/j.enbuild.2009.05.014

Pazouki, S., and Haghifam, R. (2016). Optimal Planning and Scheduling of Energy Hub in Presence of Wind, Storage and Demand Response under Uncertainty. *Int. J. Electr. Power Energ. Syst.* 80 (9), 219–239. doi:10.1016/j.ijepes.2016.01.044

Quan, C., Dong, X., and Jiang, T. (2018). Optimization Planning of Integrated Electricity-Gase Community Energy System Based on Couple CCHP. *Power Syst. Technology.* 42 (08), 2456–2466.

Salimi, M., Ghasemi, H., and Adelpour, M. (2015). Optimal Planning of Energy Hubs in Interconnected Energy Systems: a Case Study for Natural Gas and Electricity. *IET Generation Transm. Distribution.* 9 (8), 695–707. doi:10.1049/iet-gtd.2014.0607

Unsihuay-Vila, C., Marangon-Lima, J. W., Zambroni de Souza, A. C., Perez-Arriag, I. J., Balestrassi, P. P., et al. (2010). A Model to Long-Term, Multiarea, Multistage, and Integrated Expansion Planning of Electricity and Natural Gas Systems. *IEEE Trans. Power Syst.* 25 (2), 1154–1168. doi:10.1109/tpwrs.2009.2036797

Wang, D., Hu, Q., Jia, H., Hou, K., Du, W., Chen, N., et al. (2019). Integrated Demand Response in District Electricity-Heating Network Considering Double Auction Retail Energy Market Based on Demand-Side Energy Stations. *Appl. Energ.* 248, 656–678. doi:10.1016/j.apenergy.2019.04.050

Wang, W., Wang, D., and Jia, H. (2017). Steady State Analysis of Electricity-Gas Regional Integrated Energy System with Consideration of NGS Network Status. *Proc. CSEE.* 37 (5), 1293–1304. doi:10.13334/j.0258-8013.pcsee.160250

Wang, Z., Tang, Y., and Qiao, B. (2018). Research on Integrated Natural Gas and Electric Power System Optimal Power Flow and its Environmental Synergy. *Proc. CSEE.* 38, 111–120. doi:10.13334/j.0258-8013.pcsee.180068

Wu, J. (2016). Drivers and State-Of-The-Art of Integrated Energy Systems in Europe. *Automation Electric Power Syst.* 40 (5), 1–7. doi:10.7500/AEPS20150512001

Wu, Z., Liu, Y., and Gu, W. (2019). A Modified Decomposition Method for Multistage Planning of Energy Storage, Distributed Generation and Distribution Network. *Proc. CSEE.* 39 (16), 4705–4714. doi:10.13334/j.0258-8013.pcsee.180668

Yang, Y., Pei, W., and Qi, Z. (2012). Planning Method for Hybrid Energy Microgrid Based on Dynamic Operation Strategy. *Automation Electric Power Syst.* 36 (19), 30–36. doi:10.3969/j.issn.1000-1026.2012.19.006

Zeng, H., Liu, T., and He, C. (2019a). Multi-objective Optimization for Integrated Natural-Gas and Electricity Energy System Considering Power-To-Gas. *Electr. Meas. Instrumentation.* 56 (8), 99–107. doi:10.19753/j.issn1001-1390.2019.08.016

Zeng, M., Liu, Y., and Zhou, P. (2019b). Review and Prospects of Integrated Energy System Modeling and Benefit Evaluation. *Power Syst. Technology.* 42 (6), 1697–1708. doi:10.13335/j.1000-3673.pst.2018.0150

Zhang, X., Shahidehpour, M., and Alabdulwahab, A. (2015). Optimal Expansion Planning of Energy Hub with Multiple Energy Infrastructures. *IEEE Trans. Smart Grid.* 6 (5), 2302–2311. doi:10.1109/tsg.2015.2390640

Zheng, X., Qiu, Y., Zhan, X., Zhu, X., Keirstead, J., Shah, N., et al. (2017). Optimization Based Planning of Urban Energy Systems: Retrofitting a Chinese Industrial Park as a case-Study[J]. *Energy.* 139, 31–41. doi:10.1016/j.energy.2017.07.139

Zhong, C., and Yihua, S. (2005). *Modern Systems Science [M]*. Shanghai: Shanghai Science and Technological Litetature Press

Conflict of Interest: YX, CW, and GX were employed by the company State Grid Jiangsu Electric Power Co., Ltd.

The remaining authors declare that the research was conducted in the absence of any commercial or financial relationships that could be construed as a potential conflict of interest.

frontiers in Energy Research

ORIGINAL RESEARCH
published: 18 August 2021
doi: 10.3389/fenrg.2021.723370

Charging Strategy for Electric Vehicles Considering Consumer Psychology and Trip Chain

Jiwei Gou[1], Changsheng Lin[1], Jun Li[1], Bo Geng[1], Zhi Li[1], Yang Cao[2], Yang Li[2] and Yuqing Bao[2]*

[1]Shenzhen Power Supply Bureau Co., Ltd., Shenzhen, China, [2]School of Electrical Engineering, Southeast University, Nanjing, China

As a kind of movable storage device, the electrical vehicles (EVs) are able to support load shaving through orderly charging. The existing researches mostly focus on the design of EVs charging control technology with little consideration of trip-chain-based consumer psychology of EV owners. To fill this gap, this article proposes a price-based orderly charging strategy for EVs considering both consumer psychology and trip chain. Then, the load shaving problem is transformed into a multiobjective optimization problem, to minimize peak-to-valley difference and network loss. A time-of-use price optimization model based on consumer psychology is established to describe the charging behavior of EV owners influenced by electricity price. Finally, the examples verify the feasibility of the proposed strategy by comparing the impact of EVs connected to grid under different ratios, different load transfer rates, and different scenarios.

Keywords: electrical vehicles, consumer psychology, trip chain, time-of-use price, peak shaving and valley filling

OPEN ACCESS

Edited by:
Yingjun Wu,
Hohai University, China

Reviewed by:
Lei Xi,
China Three Gorges University, China
Fu Rong,
Nanjing University of Posts and Telecommunications, China

****Correspondence:***
Yang Cao
220192779@seu.edu.cn

Specialty section:
This article was submitted to Smart Grids, a section of the journal Frontiers in Energy Research

Received: *10 June 2021*
Accepted: *19 July 2021*
Published: *18 August 2021*

Citation:
Gou J, Lin C, Li J, Geng B, Li Z, Cao Y, Li Y and Bao Y (2021) Charging Strategy for Electric Vehicles Considering Consumer Psychology and Trip Chain. Front. Energy Res. 9:723370. doi: 10.3389/fenrg.2021.723370

INTRODUCTION

Electric vehicle (EV) is a zero-emission and low-emission green transportation tool, whose large-scale promotion can effectively alleviate the increasingly severe social problems such as energy crisis and environmental pollution today. Therefore, it has received extensive attention from all walks of life. Monte Carlo (MC) simulation is a stochastic simulation method based on probability and statistical theory. It is a method that uses random numbers to solve many calculation problems, which connects the problem to be solved with a certain probability model, and realizes statistical simulation or sampling with an electronic computer to obtain an approximate solution.

The development of vehicle-to-grid (V2G) technology has made EVs a mobile energy storage device with functions including "peak shaving and valley filling," frequency modulation, and increasing reserve capacity (Cheng et al., 2014; Shafie-khah et al., 2016; Tang and Wang, 2015). Meanwhile, through proper scheduling of EVs charging and discharging, the ability of power system to absorb wind power, photovoltaic power, and other intermittent renewable energy can be enhanced (Ashtari et al., 2012; Li and Zhang, 2012; Xing et al., 2021).

As for the EVs charging and discharging control strategy in distribution network, there have been discussions in various directions at home and abroad. The trip data of household vehicles in the United States are analyzed by Rautiainen et al. (2012), where it is assumed that EVs and fuel vehicles have the same trip rules. Probabilistic models of trip start and end time, daily mileage, and charging characteristics are established through distribution fitting, and MC sampling is adopted to estimate EVs charging load distribution. Under the premise of considering constraints of EVs charging demand, a charging and discharging control strategy for EVs participating in power system

frequency modulation services is proposed by Liu et al. (2013). For a three-phase unbalanced power distribution system, a mixed-integer linear programming model for orderly charging of EVs with the goal of minimizing power generation costs is established by Franco et al. (2015). A mixed integer programming model for EVs charging and discharging based on distributed control is established by Xing et al. (2016), where an efficient solution method for the characteristics of typical load curves is proposed. An optimal charging model with the minimum network loss within a given period as the objective function is established by Clement-Nyns et al. (2010), where impact of a large number of EVs on distribution system is analyzed from the perspective of network loss and voltage offset. The theory of traffic trip chain is introduced into the study of EVs load forecasting by Guo et al. (2014), Tang and Wang (2016), where a dynamic trip chain is assigned to each EV in the area. It characterizes the all-weather trip trajectory and driving law of EVs, and simulates the trip and charging behavior of EVs.

In the above-mentioned references, the main focus is on the design of EVs charging control technology with little consideration of trip-chain-based consumer psychology of EV owners. This article creatively considers both consumer psychology and trip chain, and proposes a price-based orderly charging strategy for EVs. First, based on the trip characteristics and charging behavior of EVs, the two characteristic variables of EV's daily mileage and daily return time are modeled. Second, the load shaving problem is transformed into a multiobjective optimization problem, to minimize peak-to-valley difference and network loss. Then, a time-of-use price optimization model based on consumer psychology is established to describe the charging behavior of EV owners influenced by electricity price. Finally, the examples are provided to compare the impact of EVs connected to grid under different ratios, different load transfer rates, and different scenarios, whose results verify the feasibility of the proposed strategy.

ESTABLISHMENT OF EVS LOAD MODEL

Classification of EVs

The EVs load model is closely related to the type, charging characteristics, and trip demand of EVs; meanwhile, the type of EVs directly determines the required charging characteristics and trip demand. According to different uses, EVs can be divided into different types such as electric buses, electric cars, and electric taxis. Electric taxis need to change shifts frequently, whose daily mileage, charging time, and location are relatively random, so their charging controllability is relatively weak. Therefore, this article mainly investigates two types of EVs, electric buses and electric cars.

Trip Chain and its Characteristic Variables

The trip chain refers to the connection form of different trip purposes in a certain time sequence to complete one or several activities. It is generally described as the process of a user starting from home and returning home during a scheduling period. During the process, the user will trip several times, and each time includes driving process and destination stopping process, which is the ith drive and the ith stop ($i = 1,2, \ldots ,n$) in **Figure 1**.

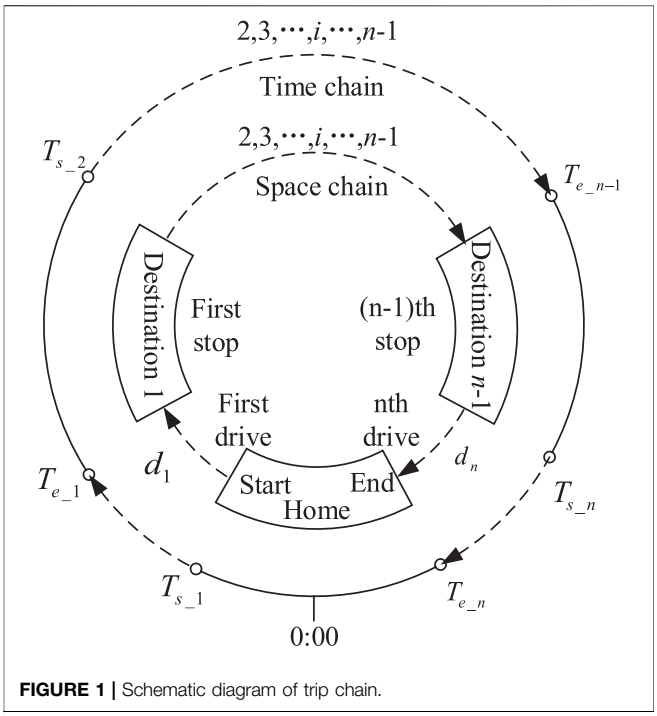

FIGURE 1 | Schematic diagram of trip chain.

The trip chain includes time chain and space chain. Similarly, its characteristic variables can also be divided into two categories.

1) Space chain characteristic variables, which describe the transfer of user trip in the space during scheduling period, including daily mileage, daily parking times, etc. This article mainly considers the daily mileage D_{dr} of EVs, as shown in **Figure 1**, $D_{\mathrm{dr}} = \sum_{i=1}^{n} d_i$.

According to reference (Sun et al., 2020; Heinisch et al., 2021), the daily mileage of buses conforms to normal distribution, and its probability density function is

$$f_D\left(D_{\mathrm{dr}}^{\mathrm{b}}\right) = \frac{1}{\sqrt{2\pi}\sigma_{\mathrm{b}}} \exp\left[-\frac{\left(D_{\mathrm{dr}}^{\mathrm{b}} - \mu_{\mathrm{b}}\right)^2}{2\sigma_b^2} \right] \tag{1}$$

where $D_{\mathrm{dr}}^{\mathrm{b}}$ is the daily mileage of buses, μ_{b} is the expected value of the daily mileage of buses, and σ_{b} is their standard deviation.

According to reference (Sun et al., 2020; Heinisch et al., 2021), the daily mileage of cars conforms to log-normal distribution, and its probability density function is

$$f_D\left(D_{\mathrm{dr}}^{\mathrm{c}}\right) = \frac{1}{\sqrt{2\pi}\sigma_{\mathrm{c}} D_{\mathrm{c}}} \exp\left[-\frac{\left(\ln D_{\mathrm{dr}}^{\mathrm{c}} - \mu_{\mathrm{c}}\right)^2}{2\sigma_c^2} \right] \tag{2}$$

where $D_{\mathrm{dr}}^{\mathrm{c}}$ is the daily mileage of cars, μ_{c} is the expected natural logarithm value of the daily mileage of cars, and σ_{c} is their standard deviation.

2) Time chain characteristic variables, which describe the patterns of user trip in the time during scheduling period, including daily return time, daily trip time, etc. This article

mainly considers the daily return time T_{re} of EVs, as shown in **Figure 1**, $T_{re} = T_{e\_n}$.

According to reference (Muratori et al., 2018; Dagdougui et al., 2020), the daily return time of buses and cars both conform to normal distribution, and their probability density functions are

$$f_T(T_{re}) = \begin{cases} \frac{1}{\sqrt{2\pi}\sigma_T} \exp\left[-\frac{(T_{re}+24-\mu_T)^2}{2\sigma_T^2} \right] 0 < T_{re} \le \mu_T - 12 \\ \frac{1}{\sqrt{2\pi}\sigma_T} \exp\left[-\frac{(T_{re}-\mu_T)^2}{2\sigma_T^2} \right] \mu_T - 12 < T_{re} \le 24 \end{cases} \tag{3}$$

where T_{re} is the daily return time of EVs, μ_T is the expected value of the daily return time of EVs, and σ_T is their standard deviation.

The probability density functions of characteristic variables of EVs' daily mileage and daily return time are taken to carry out MC simulation. Then the distribution of the above random variables is taken as input. Starting from the time of first trip, data are extracted sequentially based on the mutual determination of each variable, to generate a complete trip chain.

In the trip chain, under the condition that some variables are known, the remaining variables can be calculated. It is assumed that EV is fully charged before first trip during the scheduling period, that is the state of charge (SOC) is 1, so its SOC at the beginning of charging is

$$S_{start} = 1 - \frac{D_{dr} \cdot E_{100}}{100 \cdot C_{battery}} \tag{4}$$

where D_{dr} is the daily mileage of EV, E_{100} is its energy consumption per 100 km, and $C_{battery}$ is its battery capacity.

It is assumed that EV has enough time to fully charge at night, and its charging speed can also meet the above requirements, so its charging duration is

$$T_{ch} = \frac{D_{dr} \cdot E_{100}}{100 \cdot P_{ch} \cdot \eta_{ch}} \tag{5}$$

where P_{ch} is the charging power of EV and η_{ch} is its charging efficiency.

ESTABLISHMENT OF CONSUMER PSYCHOLOGY MODEL

Price Response Model Based on Consumer Psychology

The user's response to electricity prices is embodied in adjusting own electricity usage periods according to price signals, changing electricity usage patterns by time periods, and so on. The price elasticity of electricity demand is the relative change in electricity consumption caused by the relative change in electricity price, which is

$$e = \frac{\Delta q}{q} \left(\frac{\Delta \rho}{\rho} \right)^{-1} \tag{6}$$

where Δq and $\Delta \rho$ are the increment of electricity consumption and price respectively; q and ρ are the electricity consumption and price respectively before the electricity price change.

However, the user response model based on the electricity demand price elasticity matrix cannot reflect consumer psychology. There is a minimum noticeable difference in the stimulus of selling electricity price to users. When electricity price is less than the minimum noticeable difference, users basically have no response, and when selling electricity price is greater than an upper limit, users will no longer provide more transferable loads, whose response capacity is approaching saturation (Zhou et al., 2016). Therefore, this section builds a demand response (DR) model for electricity prices based on consumer psychology, and the load transfer rate from the peak to valley period is shown in **Figure 2**.

For a certain user, the EV load transfer rate from the peak to valley period is

$$\lambda_{EV} = \begin{cases} 0 & 0 \le \Delta\rho_{pv} \le a_{EV} \\ K_{EV}\left(\Delta\rho_{pv} - a_{EV}\right) & a_{EV} \le \Delta\rho_{pv} \le \frac{\lambda_{EV,max}}{K_{EV}} + a_{EV} \\ \lambda_{EV,max} & \Delta\rho_{pv} \ge \frac{\lambda_{EV,max}}{K_{EV}} + a_{EV} \end{cases} \tag{7}$$

where $\Delta\rho_{pv} = \rho_p - \rho_v$ is the peak-to-valley price difference; $\lambda_{EV,max}$ is the upper limit of EV load transfer rate; a_{EV} is the upper limit of dead zone of EV load transfer rate to peak-to-valley price difference; K_{EV} is the slope of its linear zone. Since buses are more sensitive to load changes than cars, K_{EV} of buses is greater than that of cars.

Under the influence of time-of-use price, EV load will shift from peak to valley period. Given the value of λ_{EV}, the EV load in each period is

$$P_t^{EV} = (1 - \lambda_{EV}) P_t^{EV,base} + \lambda_{EV} P_t^{EV,optimal} \qquad t \in T \tag{8}$$

where $P_t^{EV,base}$ is the baseline load at time t when EVs do not adopt any orderly charging control strategy; $P_t^{EV,optimal}$ is the optimal load at time t after load is completely transferred when the orderly charging control strategy is adopted; T is the scheduling period.

Except for EVs, other loads will also respond to changes in electricity prices. Similarly, the other load transfer rate from peak to valley period is

$$\lambda_{else} = \begin{cases} 0 & 0 \le \Delta\rho_{pv} \le a_{else} \\ K_{else}\left(\Delta\rho_{pv} - a_{else}\right) & a_{else} \le \Delta\rho_{pv} \le \frac{\lambda_{EV,max}}{K_{else}} + a_{else} \\ \lambda_{else,max} & \Delta\rho_{pv} \ge \frac{\lambda_{else,max}}{K_{else}} + a_{else} \end{cases} \tag{9}$$

where $\lambda_{else,max}$ is the upper limit of other load transfer rate; a_{else} is the upper limit of dead zone of other load transfer rates to peak-to-valley price difference; K_{else} is the slope of its linear zone. Then the other load in each period is

$$P_t^{else} = \begin{cases} P_t^{else,base} - \lambda_{else} P_t^{else,ave} & t \in T_p \\ P_t^{else,base} + \lambda_{else} P_t^{else,ave} & t \in T_v \end{cases} \tag{10}$$

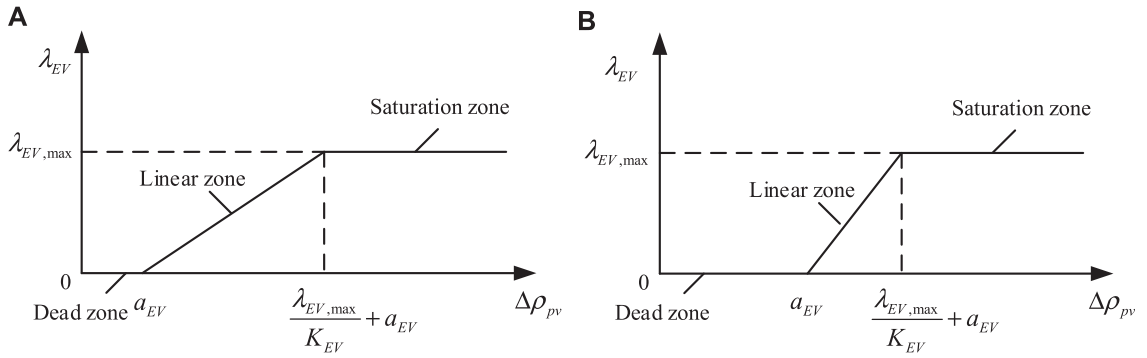

FIGURE 2 | Load transfer rate from peak to valley period. **(A)** Electric buses. **(B)** Electric cars.

where $P_t^{\text{else,base}}$ is the baseline of other load at time t; $P_t^{\text{else,ave}}$ is the average of other load in the period of time t; T_{p} is the peak period; T_{v} is the valley period, $T = T_p + T_v$.

In summary, the baseline load of distribution network at each period without considering consumer psychology is

$$P_t^{\text{base}} = P_t^{\text{EV,base}} + P_t^{\text{else,base}} \qquad t \in T \tag{11}$$

Considering consumer psychology, the total load of distribution network at each period is

$$P_t = P_t^{\text{EV}} + P_t^{\text{else}} \qquad t \in T \tag{12}$$

Time-of-Use Price Optimization Model

Objective Function

Taking peak price ρ_{p} and valley price ρ_{v} as decision variables, the problem of EVs charging with consumer psychology is transformed into an optimization problem. As a control variable, time-of-use price will directly determine the performance of peak shaving and valley filling, and then affect peak-to-valley difference, network loss, voltage deviation, and other indicators. By minimizing such indicators, the optimal peak-valley price for distribution network can be determined. The weighted sum of peak-to-valley difference rate and network loss rate of total distribution network load is selected as the multiobjective function, which is

$$\min \ F_{\text{total}} = \omega_1 F_1 + \omega_2 F_2 \tag{13}$$

where $\omega_i (i = 1, 2)$ is weight coefficients, which can be set according to actual needs, $\omega_1 + \omega_2 = 1$; F_i is indicators, as follows:

1) F_1: Peak-to-valley difference rate, used to measure the improvement of orderly charging and discharging of EVs on load curve, which is

$$F_1 = \frac{P_{\max} - P_{\min}}{P_{\max}} \tag{14}$$

where $P_{\max}$ and $P_{\min}$ are the maximum and minimum loads of the distribution network during scheduling period, respectively.

2) F_2: Network loss rate, used to measure the improvement of orderly charging and discharging of EVs on electricity utilization, which is

$$F_2 = \frac{\sum_{t \in T} P_t^{\text{loss}} \cdot \Delta t}{\sum_{t \in T} P_t \cdot \Delta t} \tag{15}$$

where P_t^{loss} is the network loss at time t; Δt is the time interval.

Constraints

The model needs to meet five types of constraints. Constraints (1)–(2) ensure the operation requirements of distribution network, and constraints (3)–(5) maintain the benefits of EVs' users to encourage users to follow the strategy to orderly charge.

1) Load change speed constraint

To prevent transferred load from exceeding the regulating capacity of generators, load change at adjacent moments needs to meet

$$-R_{\text{D}} \le P_t - P_{t-1} \le R_{\text{U}} \qquad t \in T \tag{16}$$

where R_{U} and R_{D} are the upper and lower limits of load change at adjacent moments, respectively.

2) Load transfer rate constraint

$$\begin{cases} 0 \le \lambda_{\text{EV}} \le \lambda_{\text{EV,max}} \\ 0 \le \lambda_{\text{else}} \le \lambda_{\text{else,max}} \end{cases} \tag{17}$$

3) Average price constraint

The average price after implementation of time-of-use price is

$$\overline{\rho_{\text{pv}}} = \frac{\rho_{\text{p}} \sum_{t \in T_{\text{p}}} P_t \Delta t + \rho_{\text{v}} \sum_{t \in T_{\text{v}}} P_t \Delta t}{\sum_{t \in T} P_t \Delta t} \tag{18}$$

The average price before and after implementation of time-of-use price is required to remain unchanged, which is

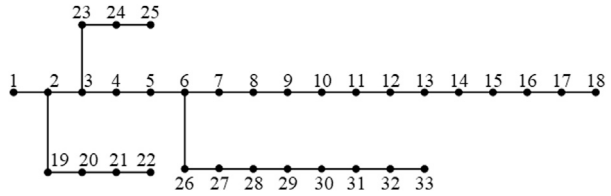

FIGURE 3 | IEEE-33 node distribution network (node-numbering diagram).

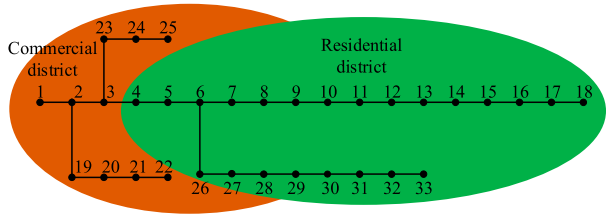

FIGURE 4 | Schematic diagram of distribution network functional districts.

$$\rho_0 = \overline{\rho_{pv}} \tag{19}$$

where ρ_0 is the constant price before implementation of time-of-use price.

4) Users charging cost constraint

The charging cost of users before and after implementation of time-of-use price are respectively

$$\begin{cases} M_0 = \rho_0 \sum_{t\in T} P_t^{base} \Delta t \\ M_{pv} = \rho_p \sum_{t\in T_p} P_t \Delta t + \rho_v \sum_{t\in T_v} P_t \Delta t \end{cases} \tag{20}$$

Users respond to time-of-use price by changing original electricity consumption habits, whose purpose is to make charging cost not higher than the original one after implementation of time-of-use price, which is

$$M_0 \geq M_{pv} \tag{21}$$

5) Users satisfaction constraint

Generally, the less the load changes, the higher the user satisfaction, so users satisfaction is defined as

$$S_{user} = \sum_{t\in T} \varepsilon(t) \left[1 - \frac{|P_t - P_t^{base}|}{P_t} \right] \tag{22}$$

$$S_{user} \geq S_{user}^{min} \tag{23}$$

where S_{user}^{min} is the minimum value of users satisfaction; $\varepsilon(t)$ is the satisfaction coefficient of users responding to time-of-use price at time t, which depends on the impact degree of load transfer on users, and satisfies

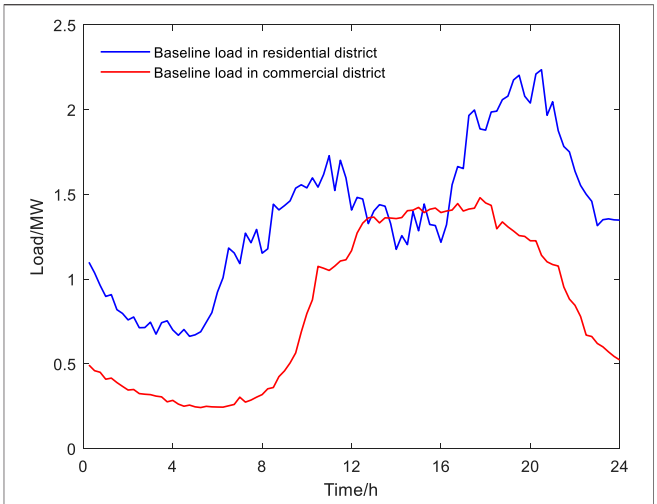

FIGURE 5 | Baseline load curve.

$$\sum_{t\in T} \varepsilon(t) = 1 \tag{24}$$

MODEL SOLVING METHOD

The price response model based on consumer psychology is solved by matlab with MC simulation. The time-of-use price optimization model is solved by matlab with yalmip/gurobi toolboxes, which transforms the original load distribution problem into a large-scale mixed integer programming (MIP) problem. Specifically, on the basis of branch and bound method, outer approximation method and tangent secant method are introduced, which reduces invalid branches in the optimization of binary tree, and finally the optimal solution within tolerance range is obtained.

The power flow and node voltage of distribution network containing EVs are solved by matlab with matpower toolbox, specifically using the standard Newton-Raphson method. The testing process in this article is carried out on Gurobi 9.1.1 and Matpower 7.1.

CASE STUDY

Basic Data and Parameter Settings

In this article, the IEEE-33 node distribution network with buses and cars is used for simulation verification, whose topology is shown in **Figure 3**.

According to the structure of trip chain and function of plot, the IEEE-33 node distribution network is divided into two functional districts, a residential district and a commercial district. Nodes 1–3, 19–25 are divided into

TABLE 1 | Parameters of EVs.

Parameters	Buses (commercial district)	Cars (residential district)	Parameters	Buses (commercial district)	Cars (residential district)
u_b、u_c	10	500	μ_T/h	21	19
$C_{battery}$/kWh	324	60	σ_T/h	1	1
E_{100}/kWh	140	20	$t_{vs} \sim t_{ve}$	23:00–9:00 + 1	21:00–7:00 + 1
P_{ch}/kW	45	14	a_{EV}/¥	0.05	0.05
η_{ch}	0.9	0.9	K_{EV}/¥$^{-1}$	2.5	1.5
u_b、u_c/km	170	2.98	$\lambda_{EV,max}$	1.0	0.8
σ_b、σ_c/km	20	1.14	ρ_0/(¥·kWh^{-1})	0.6715	0.5483

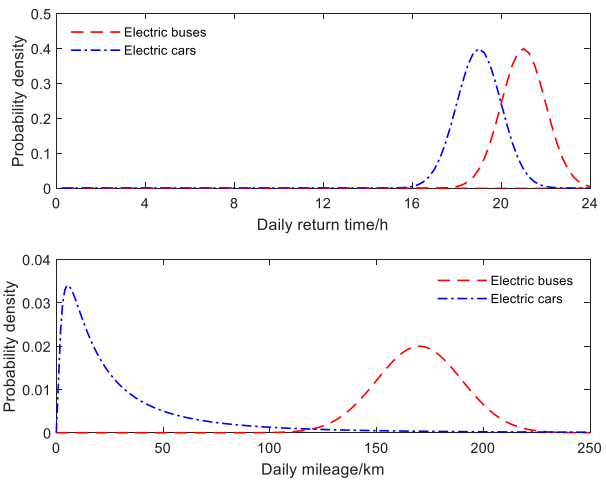

FIGURE 6 | Probability distribution. **(A)** Daily return time. **(B)** Daily mileage.

commercial district, and nodes 4–18, 26–33 are divided into residential one, as shown in **Figure 4**. It is assumed that the final arrival of buses during scheduling period are all in commercial district, similarly, that of cars are all in residential district. EVs are only charged after daily returning, which has no effect on distribution network load during the driving process. It is assumed that each plot contains sufficient charging piles. The influence of location distribution of charging piles on charging behavior and route selection of EVs is not considered.

Based on actual situation, the day-ahead scheduling period with a time interval of 1 h is adopted. The baseline load curves of residential and commercial districts on a typical day in Shenzhen city are selected, as shown in **Figure 5**. The total load of two functional districts is distributed to each node in proportion.

The parameters of EVs are set as listed in **Table 1**. Users' parameters are set as $\frac{R_D}{P_{max}} = \frac{R_U}{P_{max}} = 0.05$, $S_{user}^{min} = 0.6$, $\varepsilon(t) = \frac{1}{40}$, $\varepsilon(t) = \frac{1}{25}$. Relevant parameters of other load transfer rate are $K_{else} = 1.2¥^{-1}$, $a_{else} = 0.15¥$, $\lambda_{else,max} = 0.39$, respectively.

According to formula **Equations 1–3** and the parameters in **Table 1**, the probability distributions of daily return time and daily mileage of buses and cars are shown in **Figure 6**.

Performance of EVs Charging Under Different Proportions

According to the probability density function of EVs' daily return time and daily mileage, the situation of EVs connected to grid is simulated by MC simulation. It is assumed that EV starts charging immediately when it returns, until its battery is fully charged, which is a kind of disorderly charging strategy. The characteristic variables data of n_b buses and n_c cars are obtained by simulation, then the situations when EVs account for 25, 50, and 100% of total number of vehicles are considered respectively. The results are shown in **Figure 7**.

Enlarging the nonoverlapping part of curves corresponding to different proportions of EVs, it can be seen that: 1) Compared with buses, cars have a greater impact on the load of their district due to their larger number. 2) Since daily return times of buses are already in valley period of commercial district load, if buses start charging immediately when they return, their charging period will coincide with valley period, which has certain "valley filling" effect. 3) Since daily return times of cars are just close to starting time of evening peak period of residential district load, if cars do that, their charging period will coincide with evening peak period, resulting in "peak plus peak" situation.

Performance of EVs Charging Under Different Load Transfer Rates

Taking the load transfer rate as a control variable, simulations are performed on n_b buses and n_c cars. Since K_{EV} of buses is greater than that of cars, it is assumed that K_{EV} of commercial district is increased from 0 to 1 with a step of 0.25, and that of residential district is increased from 0 to 0.8 with a step of 0.2.

The results are shown in **Figure 8**. It can be seen that: 1) The greater the load transfer rate, the smaller the peak-to-valley difference, and the more obvious the effect of peak shaving and valley filling. 2) Since buses' charging period coincides with valley period, and cars' charging period coincides with evening peak period, impact of changes in load transfer rate on the load in commercial district is mainly reflected in "valley filling," while that in residential district is mainly reflected in "peak shaving."

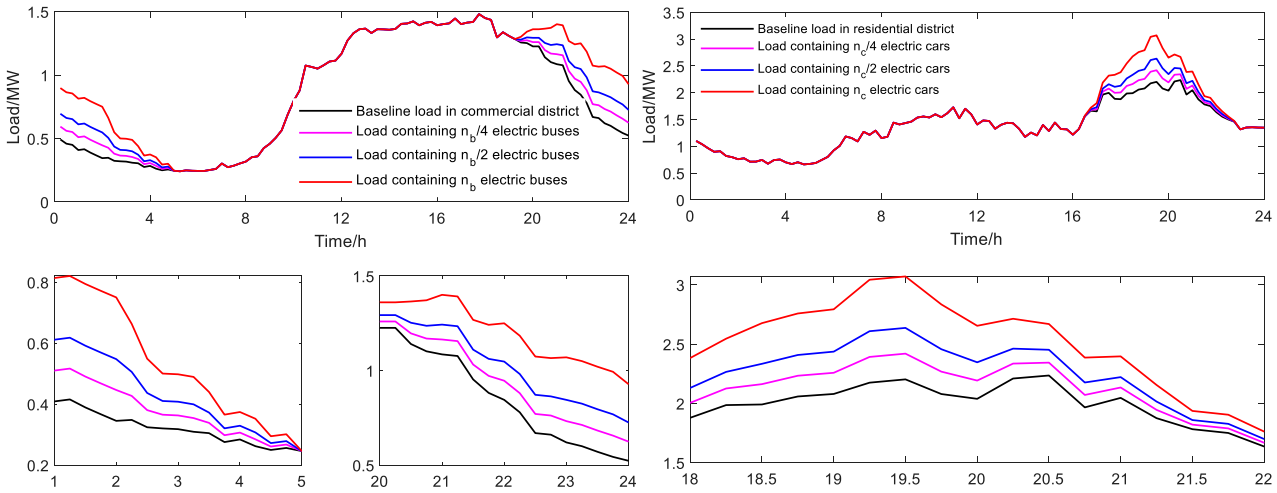

FIGURE 7 | Disorderly charging load of different EVs proportions. **(A)** Electric buses. **(B)** Electric cars.

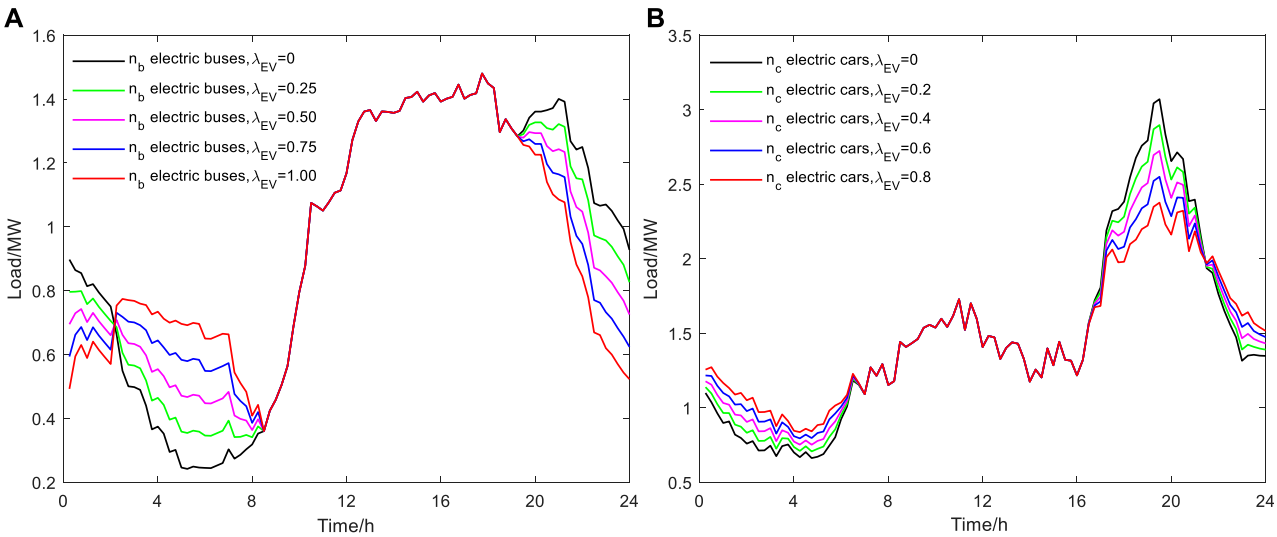

FIGURE 8 | Disorderly charging load of different load transfer rates of EVs. **(A)** Electric buses. **(B)** Electric cars.

Comparison of Different Charging Strategies of EVs

The following 3 scenarios are considered:

Scenario 1: The disorderly charging strategy for EVs is adopted. EVs start charging immediately when they return.

Scenario 2: The traditional orderly charging strategy for EVs is adopted. It is assumed that EV users are completely rational. Under the influence of time-of-use price (the whole day only includes peak and valley periods), EVs start charging at the beginning of valley period.

Scenario 3: The orderly charging strategy considering consumer psychology and trip chain is adopted. It is assumed that charging time of EVs is evenly distributed in valley period through the intelligent charging control technology. The probability density function of EVs charging starting time is

$$f_T(T_{\text{start}}) = \begin{cases} \dfrac{1}{t_{\text{ve}} - t_{\text{vs}} - T_{\text{ch}}} & t_{\text{vs}} \le T_{\text{start}} < t_{\text{ve}} - T_{\text{ch}} \\ 0 & \text{else} \end{cases} \tag{25}$$

where T_{start} is the charging starting time of EVs; t_{vs} and t_{ve} are the start and end time of valley period respectively.

In each scenario, simulations are performed on n_{b} buses and n_{c} cars. The results are shown in **Figure 9**. It can be seen that: 1) Due to the unreasonable control of charging load in scenario 1, charging of EVs at night is mostly concentrated before 24:00, which makes load distribution at night more uneven and increases local peak-to-valley difference. 2) Compared with

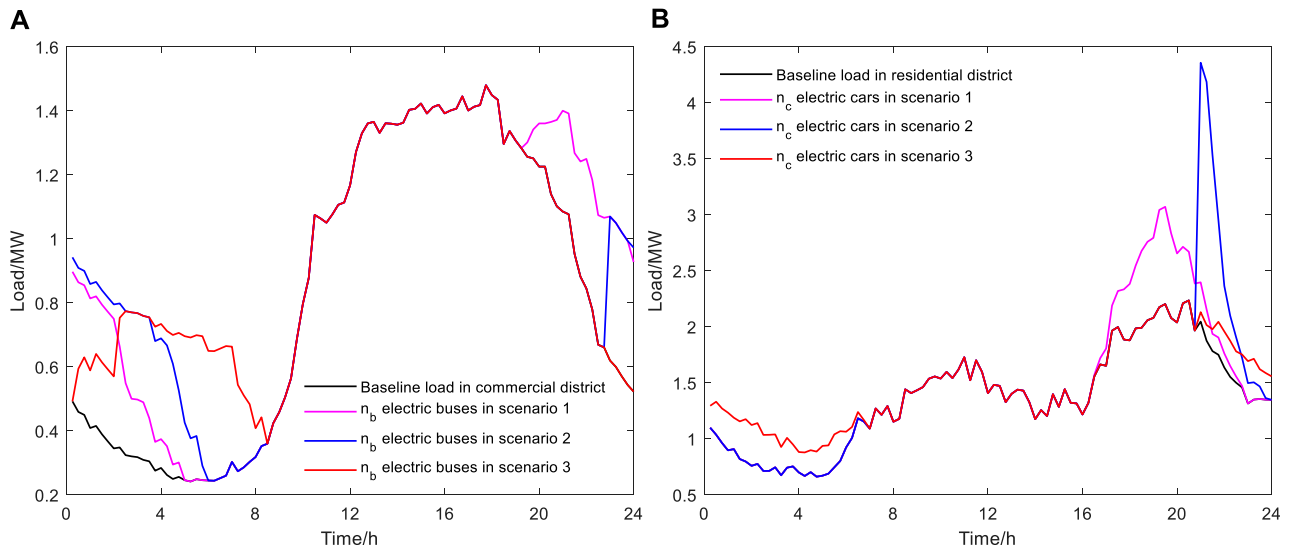

FIGURE 9 | Charging load of different scenarios of EVs. **(A)** Electric buses. **(B)** Electric cars.

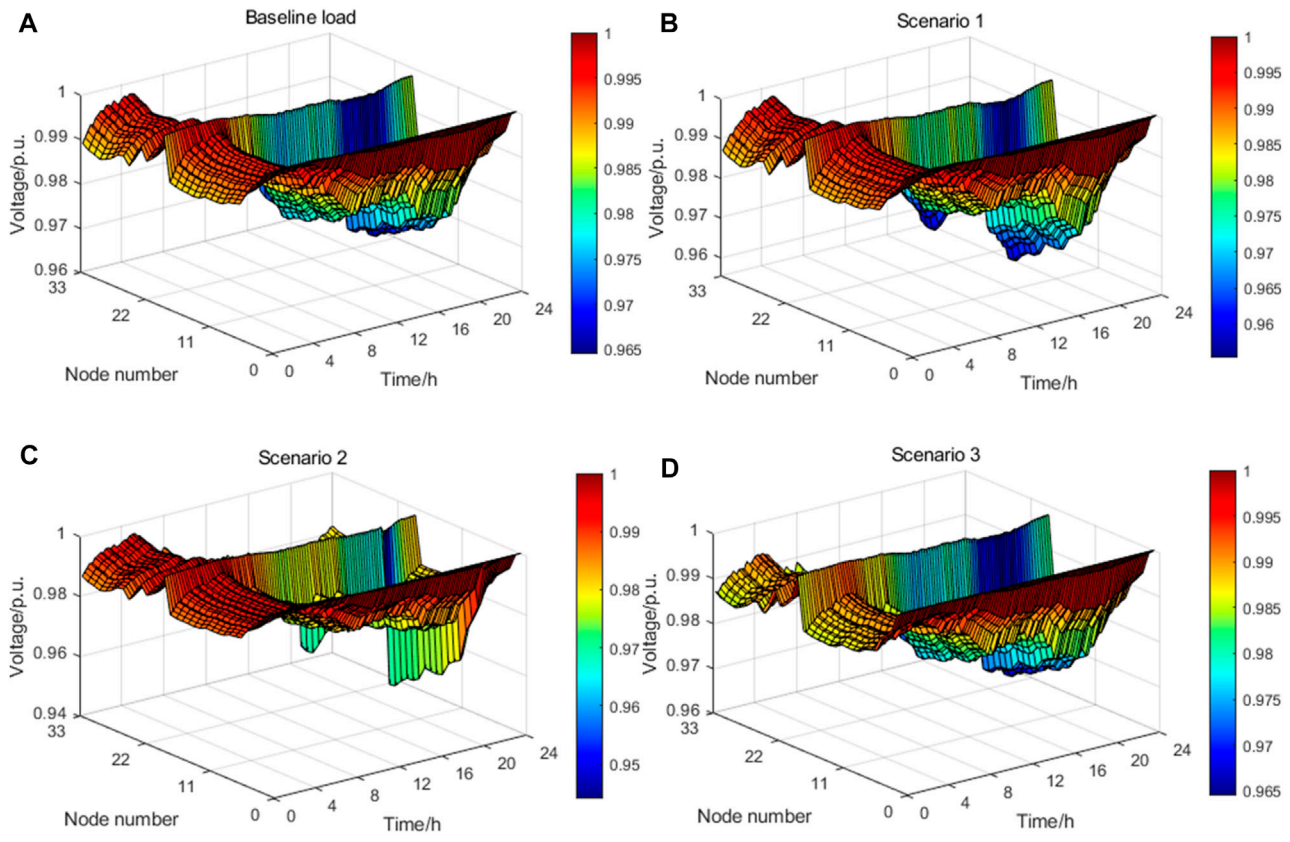

FIGURE 10 | Nodal voltage surface diagram. **(A)** Baseline load. **(B)** Scenario 1. **(C)** Scenario 2. **(D)** Scenario 3.

TABLE 2 | Total load indicators in different scenarios.

Scenario	Peak-to-valley difference rate	Network loss rate
Baseline load	0.7568	0.0968
Scenario 1	0.7008	0.0833
Scenario 2	0.8416	0.0901
Scenario 3	0.6451	0.0735

Scenario 1, Scenarios 2 and 3 can transfer charging load under the influence of time-of-use price. However, Scenario 2 still lacks sufficient control of charging load, so a large number of EVs are integrated into grid for charging at the same time, causing a sudden load change at the beginning of valley period. 3) Since cars have a more obvious impact on load than buses, the sudden load change is also more obvious in Scenario 2, which has reached the level of impacting grid. 4) Scenario 3 evenly distributes charging time of EVs in valley period, which makes full use of power generation potential of valley period. It has the least impact on grid without generating new load peaks, and truly realizes "valley filling."

In each scenario, voltage of each node when n_b buses and n_c cars trip in the distribution network is calculated. The results are shown in **Figure 10**. It can be seen that: 1) Since the access of EVs will increase total load of distribution network, voltage per unit values of three scenarios are all slightly lower than that of baseline load. 2) It is generally required that safety voltage per unit value is between 0.95 and 1.05. Owing to the sudden load change at the beginning of valley period in Scenario 2, the voltage drops below the lower limit. 3) The charging process in Scenario 3 has the least impact on grid, whose voltage deviation is smaller than Scenarios 1 and 2.

The calculation results of total load indicators in different scenarios are shown in **Table 2**. It can be seen that: 1) Scenarios 1 and 2 have no obvious improvement effect on peak-to-valley difference and network loss. Even due to the sudden load change in Scenario 2, the peak-to-valley difference rate slightly increases. 2) Scenario 3, where the orderly charging strategy considering consumer psychology and trip chain is adopted, can greatly reduce peak-to-valley rate and network loss rate, and play a role in fully improving load curve.

Optimization Results of Time-of-Use Price

The function surface diagrams of peak-to-valley difference rate and network loss rate with respect to load transfer rate in residential district and commercial district are drawn respectively, as shown in **Figure 11**. It can be seen that: the greater the two load transfer rates, the peak-to-valley difference rate generally tends to decrease, and the network loss rate shows a slower growth trend.

To solve the optimization problem established in Trip Chain and its Characteristic Variables, the relative MIP gap tolerance in gurobi is set to 0.01%. Considering that peak-to-valley difference rate and network loss rate are both dimensionless physical quantities, and the two have little difference in their status when measuring the qualities of load curve, so the weight coefficients of multiobjective function are selected as $\omega_1 = \omega_2 = 0.5$. Total load curve before and after optimization is shown in **Figure 12**, and optimization results of time-of-use price in commercial and residential district are listed in **Table 3**.

It can be seen that: 1) The optimal load curve considering consumer psychology is relatively stable on the whole, showing an obvious effect of "peak shaving and valley filling." 2) The load during peak and valley periods both have a certain amount of transfer. Moreover, EVs load transfer rate in residential and commercial district and other load transfer rate are all in linear region. In summary, by establishing the time-of-use price optimization model, EVs can be guided to charge orderly, which can reduce peak-to-valley difference and network loss, and provide a theoretical basis for system operators to determine time-of-use price.

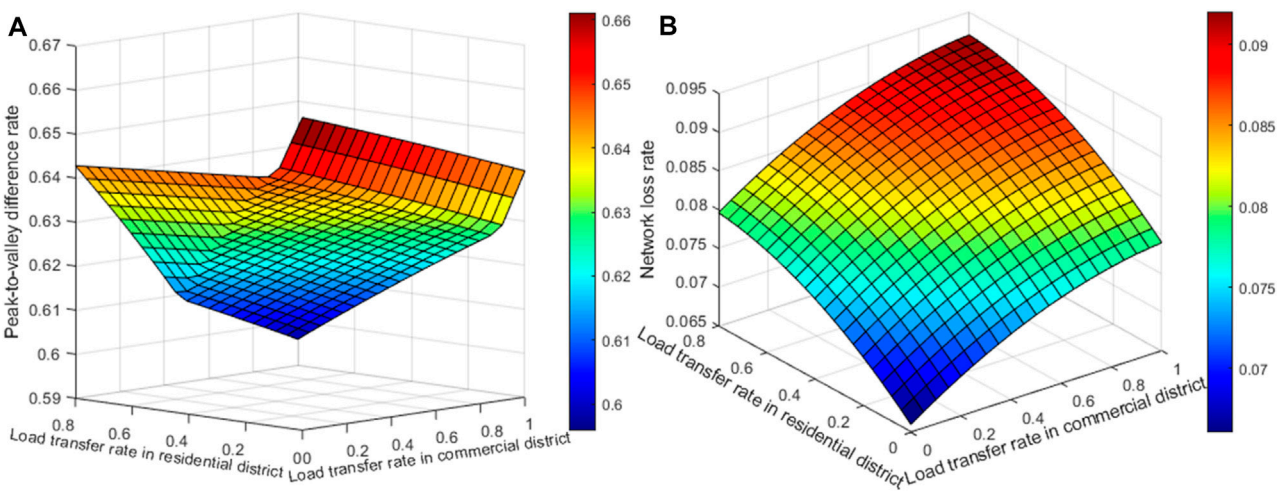

FIGURE 11 | Function surface diagram of indicators. **(A)** Peak-to-valley difference rate. **(B)** Network loss rate.

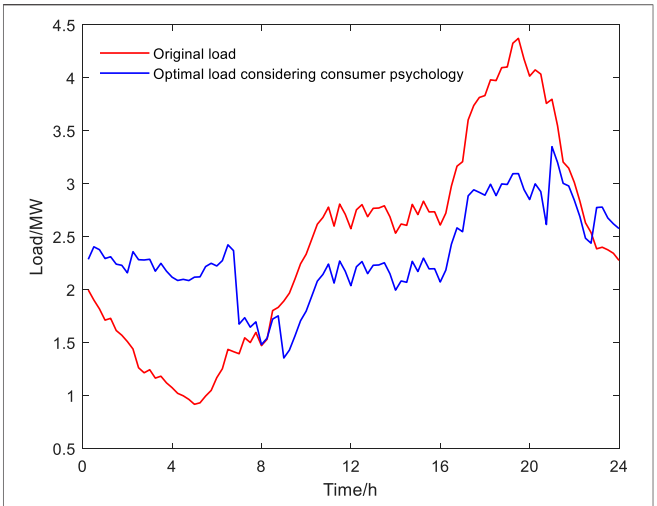

FIGURE 12 | Total load before and after time-of-use price optimization.

TABLE 3 | Optimization results of time-of-use price. Unit: ¥/kWh.

	Commercial district	Residential district
ρ_p	0.8974	0.7383
ρ_v	0.4133	0.2905

CONCLUSION

Aiming at the hot issue of impact of large-scale EVs connected to grid on distribution network load, this article proposes a price-based orderly charging strategy for EVs considering both consumer psychology and trip chain. A time-of-use price optimization model based on consumer psychology is established to describe the charging behavior of EV owners influenced by electricity price. The examples are provided to compare the impact of EVs connected to grid under different ratios, different load transfer rates, and different scenarios. The conclusions are as follows:

1) The impact of disorderly charging for EVs without considering consumer psychology on distribution network is related to their daily return time. Disorderly charging of buses can achieve a certain "valley filling" effect; that of cars can result in "peak plus peak" situation.
2) When considering consumer psychology, the greater the load transfer rate, the smaller the peak-to-valley difference, and the more obvious the effect of peak shaving and valley filling. Impact of changes in load transfer rate on the load in commercial district is mainly reflected in "valley filling," while that in residential district is mainly reflected in "peak shaving."
3) Among a variety of charging strategies, the orderly charging strategy considering consumer psychology and trip chain can greatly reduce peak-to-valley difference and network loss, and make voltage deviation smaller.
4) Time-of-use price optimization model, established based on consumer psychology and trip chain, can guide EVs to charge orderly, and provide a theoretical basis to determine time-of-use price.

In the future work, the uncertainty of renewable energy power will be considered, combined with the SOC transition probability of EVs based on Markov Chain, to further investigate impact of the SOC of EVs on distribution network load in different scenarios.

DATA AVAILABILITY STATEMENT

The original contributions presented in the study are included in the article/Supplementary Material, further inquiries can be directed to the corresponding author.

AUTHOR CONTRIBUTIONS

JG and CL proposed the methodology. JL, BG, and ZL conducted the theoretical analysis as well as the simulation verification. YC wrote the original draft which was reviewed and edited by YL and YB. All authors agree to be accountable for the content of the work.

FUNDING

This research was supported by the Science and Technology Project of China Southern Power Grid Corporation (Research on key technologies of flexible load participation in regional power grid dispatching in megalopolis 090000KK52190230).

REFERENCES

Ashtari, A., Bibeau, E., Shahidinejad, S., and Molinski, T. (2012). PEV Charging Profile Prediction and Analysis Based on Vehicle Usage Data. *IEEE Trans. Smart Grid.* 3, 341–350. doi:10.1109/TSG.2011.2162009

Cheng, X., Hu, X., Yang, L., Husain, I., Inoue, K., Krein, P., et al. (2014). Electrified Vehicles and the Smart Grid: the ITS Perspective. *IEEE Trans. Intell. Transport. Syst.* 15, 1388–1404. doi:10.1109/TITS.2014.2332472

Clement-Nyns, K., Haesen, E., and Driesen, J. (2010). The Impact of Charging Plug-In Hybrid Electric Vehicles on a Residential Distribution Grid. *IEEE Trans. Power Syst.* 25, 371–380. doi:10.1109/TPWRS.2009.2036481

Dagdougui, Y., Ouammi, A., and Benchrifa, R. (2020). High Level Controller-Based Energy Management for a Smart Building Integrated Microgrid with Electric Vehicle. *Front. Energ. Res.* 8, 248. doi:10.3389/FENRG.2020.535535

Franco, J. F., Rider, M. J., and Romero, R. (2015). A Mixed-Integer Linear Programming Model for the Electric Vehicle Charging Coordination Problem in Unbalanced Electrical Distribution Systems. *IEEE Trans. Smart Grid.* 6, 2200–2210. doi:10.1109/TSG.2015.2394489

Guo, Q., Xin, S., Sun, H., Li, Z., and Zhang, B. (2014). Rapid-Charging Navigation of Electric Vehicles Based on Real-Time Power Systems and Traffic Data. *IEEE Trans. Smart Grid.* 5, 1969–1979. doi:10.1109/TSG.2014.2309961

Heinisch, V., Göransson, L., Erlandsson, R., Hodel, H., Johnsson, F., and Odenberger, M. (2021). Smart Electric Vehicle Charging Strategies for

Sectoral Coupling in a City Energy System. *Appl. Energ.* 288, 116640. doi:10.1016/j.apenergy.2021.116640

Li, G., and Zhang, X.-P. (2012). Modeling of Plug-in Hybrid Electric Vehicle Charging Demand in Probabilistic Power Flow Calculations. *IEEE Trans. Smart Grid.* 3, 492–499. doi:10.1109/TSG.2011.2172643

Liu, H., Hu, Z., Song, Y., and Lin, J. (2013). Decentralized Vehicle-to-Grid Control for Primary Frequency Regulation Considering Charging Demands. *IEEE Trans. Power Syst.* 28, 3480–3489. doi:10.1109/TPWRS.2013.2252029

Muratori, M. (2018). Impact of Uncoordinated Plug-in Electric Vehicle Charging on Residential Power Demand. *Nat. Energ.* 3, 193–201. doi:10.1038/s41560-017-0074-z

Rautiainen, A., Repo, S., Jarventausta, P., Mutanen, A., Vuorilehto, K., and Jalkanen, K. (2012). Statistical Charging Load Modeling of PHEVs in Electricity Distribution Networks Using National Travel Survey Data. *IEEE Trans. Smart Grid.* 3, 1650–1659. doi:10.1109/TSG.2012.2206411

Shafie-khah, M., Heydarian-Forushani, E., Osório, G. J., Gil, F. A. S., Aghaei, J., Barani, M., et al. (2016). Optimal Behavior of Electric Vehicle Parking Lots as Demand Response Aggregation Agents. *IEEE Trans. Smart Grid.* 7, 2654–2665. doi:10.1109/TSG.2015.2496796

Sun, Q., Xu, S., and Zhu, S. (2020). Distribution Network Planning Considering DG Timing Characteristics and EV Spatiotemporal Characteristics. *Electric Power Automation Equipment.* 40, 30–38. doi:10.16081/j.epae.202008010

Tang, D., and Wang, P. (2015). Probabilistic Modeling of Nodal Charging Demand Based on Spatial-Temporal Dynamics of Moving Electric Vehicles. *IEEE Trans. Smart Grid.* 7, 1. doi:10.1109/TSG.2015.2437415

Tang, D., and Wang, P. (2016). Nodal Impact Assessment and Alleviation of Moving Electric Vehicle Loads: From Traffic Flow to Power Flow. *IEEE Trans. Power Syst.* 31, 4231–4242. doi:10.1109/TPWRS.2015.2495254

Xing, H., Fu, M., Lin, Z., and Mou, Y. (2016). Decentralized Optimal Scheduling for Charging and Discharging of Plug-in Electric Vehicles in Smart Grids. *IEEE Trans. Power Syst.* 31, 4118–4127. doi:10.1109/TPWRS.2015.2507179

Xing, Q., Cheng, M., Liu, S., Xiang, Q., Xie, H., and Chen, T. (2021). Multi-Objective Optimization and Dispatch of Distributed Energy Resources for Renewable Power Utilization Considering Time-Of-Use Tariff. *Front. Energ. Res.* 9, 68. doi:10.3389/FENRG.2021.647199

Zhou, M., Yin, Y., and Huang, Y. (2016). Dynamic Critical Peak price and its Gaming Approach Considering Customers' Response. *Power Syst. Tech.* 40, 3348–3354. doi:10.13335/j.1000-3673.pst.2016.11.011

Conflict of Interest: Authors JG, CL, JL, BG, and ZL were employed by the Shenzhen Power Supply Bureau Co., Ltd. The remaining authors declare that the research was conducted in the absence of any commercial or financial relationships that could be construed as a potential conflict of interest.

The authors declare that this study received funding from the Science and Technology Project of China Southern Power Grid Corporation. The funder had the following involvement with the study: provide practical application scenario for the case study.

Publisher's Note: All claims expressed in this article are solely those of the authors and do not necessarily represent those of their affiliated organizations, or those of the publisher, the editors and the reviewers. Any product that may be evaluated in this article, or claim that may be made by its manufacturer, is not guaranteed or endorsed by the publisher.

frontiers in Energy Research

ORIGINAL RESEARCH
published: 20 August 2021
doi: 10.3389/fenrg.2021.723647

An Energy Efficiency Index Formation and Analysis of Integrated Energy System Based on Exergy Efficiency

Huiling Su, Qifeng Huang and Zhongdong Wang*

Marketing Service Center, State Grid Jiangsu Electric Power Co., Ltd., Nanjing, China

In the context of the energy crisis and environmental deterioration, the integrated energy system (IES) based on multi-energy complementarity and cascaded utilization of energy is considered as an effective way to solve these problems. Due to the different energy forms and the various characteristics in the IES, the coupling relationships among various energy forms are complicated which enlarges the difficulty of energy efficiency evaluation of the IES. In order to flexibly analyze the energy efficiency of the IES, an operation efficiency evaluation model for the IES is established. First, energy utilization efficiency (EUE) and exergy efficiency (EXE) are proposed based on the first/second law of thermodynamics. Second, the energy efficiency models for five processes and four subsystems of the IES are formed. Lastly, an actual commercial-industrial park with integrated energy is employed to validate the proposed method.

Keywords: integrated energy system, multi-energy complementarity, energy efficiency, energy utilization efficiency, exergy efficiency

OPEN ACCESS

Edited by:
Yingjun Wu,
Hohai University, China

Reviewed by:
Tao Chen,
Southeast University, China
Fei Xue,
Xi'an Jiaotong-Liverpool University, China

****Correspondence:***
Qifeng Huang
hqfyqhqy@126.com

Specialty section:
This article was submitted to Smart Grids, a section of the journal Frontiers in Energy Research

Received: *11 June 2021*
Accepted: *19 July 2021*
Published: *20 August 2021*

Citation:
Su H, Huang Q and Wang Z (2021) An Energy Efficiency Index Formation and Analysis of Integrated Energy System Based on Exergy Efficiency. Front. Energy Res. 9:723647. doi: 10.3389/fenrg.2021.723647

INTRODUCTION

The high-efficient utilization of clean energy received widespread attention and the energy internet and the IES has set off a wave of global energy systems reform (Meibom et al., 2013; Mancarella, 2014). In order to improve the economy and environmental protection of systems, IES can coordinate the multi-energy allocation, improve energy efficiency, and offer high-quality energy services by energy cascaded utilization. Because of the complicated structure, various equipment, and the utilization of and terminal energy, it is of great significance to study the optimal operation for the realization of multi-energy complementarity and energy efficiency promotion (OMalley and Kroposki, 2013; Chen et al., 2019). IES is made up of energy production process (EPP), energy transmission process (ETP), energy conversion process (ECP), energy storage process (ESP), and energy utilization process (EUP). These processes can affect the energy efficiency and function of the IES. Therefore, it is necessary to propose a rational energy efficiency evaluation model for elaborating the relationship between those processes and IES.

At present, much valuable research about the energy efficiency evaluation of IES had been done from various points of view. And the result of those researches provides experience for reference. However, due to the various kinds of IES and new techniques applied in IES, a universally applicable energy efficiency evaluation method of IES is still unformed. The main problems of existing research are as follows: 1) much research mainly focused on the modeling, evaluating, and analysis of the entire systems; it is not practical to apply the energy efficiency evaluation of the practical IES. 2) These researches works put much attention on the energy efficiency evaluation of power systems but neglect the natural gas equipment and the cooling and heating equipment.

There are mainly two energy efficiency indices for IES. One is the "energy utilization efficiency" based on the first law of thermodynamics. The first law of thermodynamics mainly studies the

quantity relationship between energy input and output. The relevant research of EUE mainly focuses on the energy efficiency of heat pumps (Willem et al., 2017), combined cooling, heating, and power (CCHP) (Wang et al., 2015), and heating ventilation air conditioning (Alves et al., 2016) in the IES. However, the references above ignore the effect of energy quality when evaluating the efficiency of IES *via* the EUE index.

The other index is the "exergy efficiency" based on the second law of thermodynamics. The second law of thermodynamics puts emphasis on energy quality. The energy efficiency evaluation based on the second law of thermodynamics is concentrated on the field of thermodynamic engineering such as thermal power plants (Ibrahim et al., 2017) and heating ventilation air conditioning, but there is little research on the efficiency analysis of IES via the EXE index. Wang et al. (2015) analyzed and calculated the EUE and the EXE of renewable energy without adequate consideration of the energy coupling relationship in the IES. Huang et al. (2017) summarized four factors affecting the energy efficiency of the IES based on the parametric method. The efficiency analysis emphasizes the equipment but neglects the comprehensive analysis of energy supply subsystems.

In addition to the problems mentioned above, the current references mainly focus on the planning and operation mode optimization of the IES (Li et al., 2018; Qin et al., 2021; Li and Wang, 2021; Li et al., 2021), but they pay less attention to its performance. Besides, there is most literature only considering an independent energy system (Zhang et al., 2021; Ding et al., 2021) but they neglect the complementary coupling between different energy subsystems in the IES. It results in the inadequate efficiency analysis of the IES and the interrelationship among EPP, ETP, ECP, ESP, and EUP. Moreover, making a single analysis for a subsystem or a process cannot completely reflect the energy efficiency of the IES due to the lack of overall evaluation.

The energy efficiency analysis aims to find out the shortcomings of the processes in the IES and then to improve the utilization of non-renewable energy. In this study, the ratio of the total energy consumption on the demand side and the total energy input on the supply side is defined as the EUE index of the IES. Under the different energy quality of multi-energy, this article utilizes the energy quality coefficient to convert distinct energy levels of multi-energy into the same energy level (Hu et al., 2020; Abu-Rayash and Dincer, 2020), and the ratio of the exporting and the inputting amount after conversion is defined as the EXE index.

Based on the definition above, the energy efficiency index evaluation models are established for EPP, ETP, ECP, ESP, and EUP. In this study, it is assumed that the IES can be decomposed into an electric subsystem (ESS), heat subsystem (HSS), cooling subsystem (CSS), and gas subsystem (GSS). The energy efficiency models corresponding to each subsystem are established for elaborating their influence on the IES. This study has two main contributions:

1) Formed the energy efficiency index evaluation models for investigating the relation among EPP, ETP, ECP, ESP, EUP, and the IES.
2) Constructed the energy efficiency models of ESS, HSS, CSS, and GSS based on the energy coupling relationship in each subsystem.

The remainder of this study is organized as follows: *Basic Indices for Energy Efficiency* established the universal energy efficiency calculation model of this study such as EUE and EXE. Based on the universal energy efficiency calculation model, the energy efficiency model of each process in IES is formed in *Energy Efficiency Analysis of the Five Processes in the Integrated Energy System*. *Energy Efficiency Analysis of Subsystem of Integrated Energy System* proposed the energy efficiency model of subsystems. Then, the case study of a typical IES based on the AHP-entropy weight method is provided in *Case Study*. Some conclusions are finally drawn in *Conclusion*.

BASIC INDICES FOR ENERGY EFFICIENCY

Energy Utilization Efficiency

The EUE index η, the first law efficiency, refers to the ratio of total output energy to total input energy in each process and it can be calculated by (**Eq. 1**).

$$\eta = \frac{\sum\limits_{i\in I} P_d^{i,out}\delta_i}{\sum\limits_{i\in I} P_d^{i,in}\delta_i} \tag{1}$$

where $i \in I$ represents the type of energy; d represents the equipment in the IES; $P_d^{i,in}$ and $P_d^{i,out}$ are the amount of energy i input and output of equipment d in each process; and δ_i is the conversion coefficient of energy i.

Exergy Efficiency

The EXE index η', known as the second law efficiency, is the ratio of the output exergy to the input exergy in each process. It can be represented as follows:

$$\eta' = \frac{\sum\limits_{i\in I} \lambda_i P_d^{i,out}\delta_i}{\sum\limits_{i\in I} \lambda_i P_d^{i,in}\delta_i}. \tag{2}$$

The energy quality coefficient λ_i is defined as follows: the ratio of the work of different energy to the total energy, which means the amount of exergy contained in each unit of energy. It is worth pointing out that the surrounding temperature has a strong influence on the energy quality coefficient. The energy quality coefficient of different energy considering the ambient temperature is as follows:

1) Coal

$$\lambda_{coal} = 1 - \frac{T_0}{T_{burn}^{coal} - T_0}\ln\frac{T_{burn}^{coal}}{T_0}, \tag{3}$$

where λ_{coal} is the energy quality coefficient of coal; T_{burn}^{coal} is the theoretical combustion temperature of coal; T_0 indicates the ambient temperature; and the theoretical combustion gas

temperature of coal is about 1,600°C (1,873.15 K). As the ambient temperature changes, the energy quality coefficient of coal fluctuates between 0.65 and 0.68.

2) Gas

$$\lambda_g = 1 - \frac{T_0}{T_{burn}^{gas} - T_0} \ln \frac{T_{burn}^{gas}}{T_0}, \tag{4}$$

where λ_g is the energy quality coefficient of gas. T_{burn}^{gas} is the theoretical combustion temperature of the gas. The theoretical combustion temperature of the gas in the gas equipment is generally 1,300°C (1,573.15 K), so the theoretical combustion temperature of the gas in this article is 1,300°C, which accord with the reality and technical level of China. With the change of seasons, the energy quality coefficient of gas is between 0.60 and 0.64.

3) Power

Power has the highest level of energy quality in various types of energy. Therefore, the energy coefficient of power hardly changes with the temperature, so its energy quality coefficient can be defined as one. It elaborates that all the external electric energy input can be converted to active power. Therefore, power can be considered as a benchmark for various energy conversions.

4) Thermal energy

$$\lambda_h = 1 - \frac{T_0}{T_g - T_h} \ln \frac{T_g}{T_h}, \tag{5}$$

where λ_h is the energy quality coefficient of thermal energy. T_g and T_h are the heating temperature and regenerative temperature of thermal energy(K). For the primary energy such as coal and natural gas, it cannot exist after utilization. However, thermal and cooling energy are usually represented by the energy carriers selected by human beings, such as water and steam. For the use of secondary energy, part of the energy can be recycled after utilization. Taking the thermal energy transmitted by water, for example, the supply temperature of the water when supplying heat to various equipment and loads is generally 90°C (363.15 K). After passing through the equipment, the return temperature is generally 70°C (343.15 K). Therefore, it should be necessary to concentrate on the consumption of thermal energy during the water temperature from 90 to 70°C. So when calculating the energy quality coefficient of thermal energy carried by the water, both the supply temperature and the return temperature after energy consumption should be taken into consideration. Therefore, this study assumes water as the carrier of thermal energy supply. When the supply temperature is 90°C and the return temperature is 70°C, the energy quality coefficient of the thermal energy varies between 0.14 and 0.25 with the ambient temperature changes.

5) Cooling energy

$$\lambda_c = \frac{T_0}{T_p - T_b} \ln \frac{T_p}{T_b} - 1, \tag{6}$$

where λ_c is the energy quality coefficient of cooling energy. T_p and T_b are the cooling temperature and return temperature of cooling energy (K). Cooling energy is the same as heat energy, and most of it uses water as a carrier for transmission. The cooling temperature is generally 7°C (280.15 K), and the return temperature is 12°C (285.15 K). In this case, the energy quality coefficient of the cooling energy varies between 0.0026 and 0.0566 with the ambient temperature changes.

ENERGY EFFICIENCY ANALYSIS OF THE FIVE PROCESSES IN THE INTEGRATED ENERGY SYSTEM

The energy efficiency analysis should consider the energy efficiency of both the five processes and the entire IES so that it can find out the deficient process in time when the energy efficiency varies low. It also makes the IES a safe, stable, and effective operation mode. Therefore, in this section, the energy efficiency evaluation models of five processes are established, respectively, for making a comprehensive analysis of the influence of each process on the whole energy efficiency of the IES.

Energy Production Process

The research objects of EPP are the production equipment, the purchased power, and interior energy. As shown in **Figure 1**, there is various interior energy such as coal and gas. There are multiple ways to utilize these centralized resources, such as power generation by coal-fired power generation (CFPG) and producing thermal energy by electrical heating. The EUE and the EXE of EPP are calculated by the primary energy consumption and the energy production.

The EUE of EPP η_{epp} can be calculated by

$$\eta_{epp} = \frac{P_{e,h}^1 + P_{co,e}^1 + P_{co,h}^1 + P_{co,g,e,h}^1 + P_{co,g,e,h}^2 + P_{g,h}^1}{P_{ele}^1 + P_{coal}^1 + P_{coal}^2 + P_{coal}^3 + P_{gas}^1 + P_{gas}^2}. \tag{7}$$

The EXE of EPP $\eta'_{production}$ can be calculated by

$$\eta'_{epp} = \frac{P_{co,e}^1 + P_{co,g,e,h}^1 + \lambda_h\left(P_{e,h}^1 + P_{co,h}^1 + P_{co,g,e,h}^2 + P_{g,h}^1\right)}{P_{ele}^1 + \lambda_{co}\left(P_{coal}^1 + P_{coal}^2 + P_{coal}^3\right) + \lambda_g\left(P_{gas}^1 + P_{gas}^2\right)}. \tag{8}$$

$P_{coal}^1$is the coal consumption of CFPG equipment; P_{coal}^2stands for the coal consumption of the coal-fired thermal generation (CFTG) equipment; $P_{coal}^3$and P_{gas}^1 represent the coal consumption and gas consumption of the combined heat and power (CHP); P_{gas}^2 is the gas consumption of gas-fired thermal generation (GFTG) equipment; $P_{co,e}^1$ represents the output power of CFPG equipment; $P_{e,h}^1$, $P_{co,h}^1$, $P_{g,h}^1$, respectively, stands for the thermal energy produced by electrical-thermal coupling equipment (ETCE), CFTG equipment, and GFTG equipment; and $P_{co,g,e,h}^1$ and $P_{co,g,e,h}^2$ stand for the power and thermal energy produced by the combined heat and power.

Energy Transmission Process

The ETP mainly considers the transmission loss of multi-energy. In the ETP, the energy input is composed of two parts:

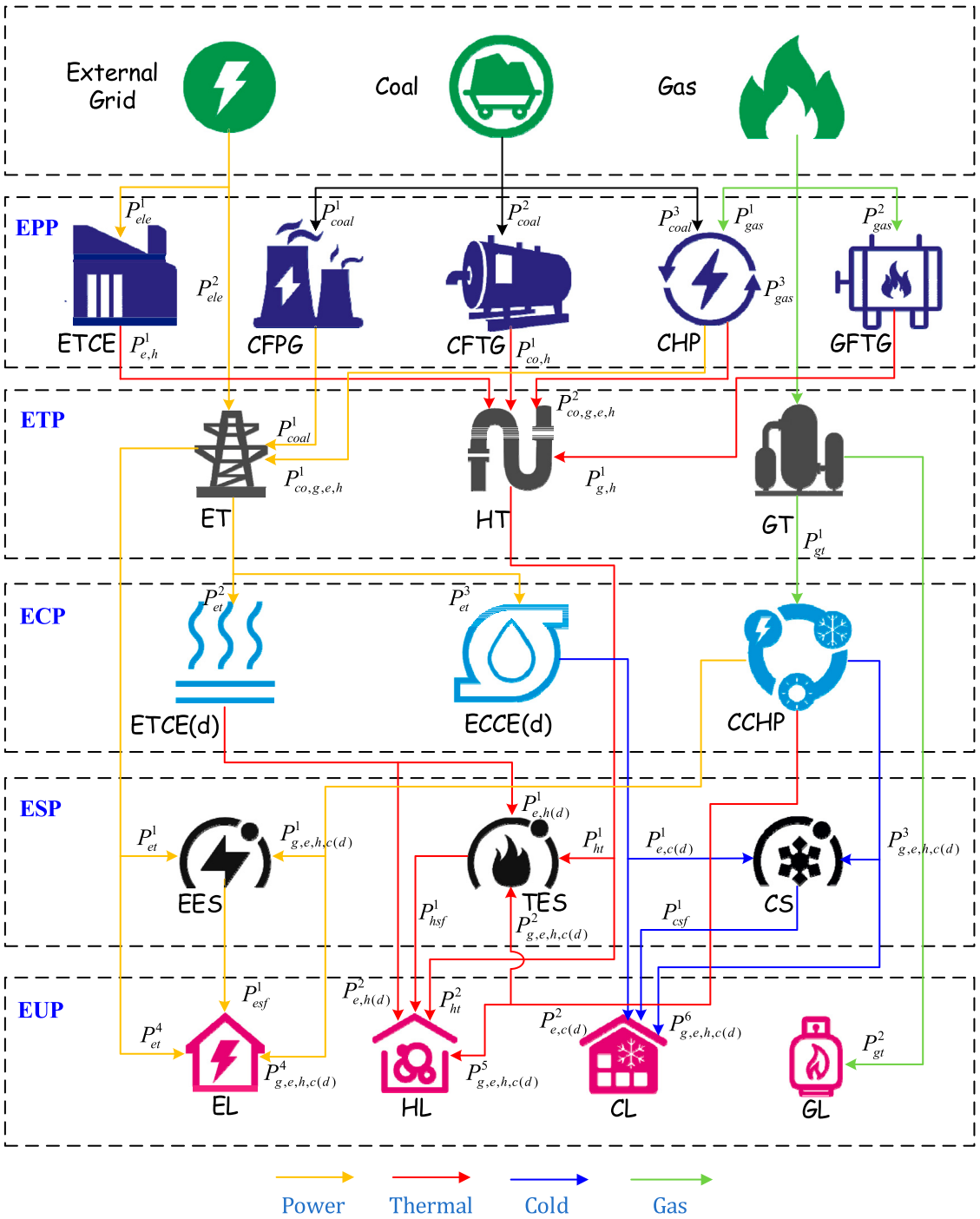

FIGURE 1 | Schematic diagram of the district multi-energy system.

one comes from the external energy source network, the other is the energy export from EPP. The influencing factors of electricity transmission (ET) loss include loads, the length, material, and rated voltage of the transmission line. Heat transmission (HT) loss is generated by heat radiation and heat convection. The gas transmission (GT) loss is caused by pressure differences. Taking these factors into consideration, the "EUE" and the "EXE" of ETP can be calculated by

$$\eta_{etp} = \frac{P^1_{et} + P^2_{et} + P^3_{et} + P^4_{et} + P^1_{ht} + P^2_{ht} + P^1_{gt} + P^2_{gt}}{P^2_{ele} + P^1_{co,e} + P^1_{co,g,e,h} + P^1_{e,h} + P^2_{co,g,e,h} + P^1_{g,h} + P^3_{gas}}, \quad (9)$$

$$\eta'_{etp} = \frac{P^1_{et} + P^2_{et} + P^3_{et} + P^4_{et} + \lambda_h\left(P^1_{ht} + P^2_{ht}\right) + \lambda_g P^1_{gt} + \lambda_g P^2_{gt}}{P^2_{ele} + P^1_{co,e} + \lambda_h\left(P^1_{co,g,e,h} + P^1_{e,h} + P^2_{co,g,e,h} + P^1_{g,h}\right) + \lambda_g P^3_{gas}}, \tag{10}$$

where P^2_{ete}stands for the power from the external grid in the ETP; P^3_{gas} represents the gas from external gas pipe network;P^1_{et} and P^2_{et} stand for the electricity supplied to distributed electrical-heat coupling equipment and distributed electric refrigeration equipment of the ECP; and P^3_{et} and P^4_{et} are the electricity stored by energy storage equipment and supplied directly to electric loads *via* the grid.P^1_{ht} represents the thermal energy stored by energy storage equipment. P^2_{ht} is the thermal energy supplied directly to heat loads through the gas pipeline; P^1_{gt} and P^2_{gt} represent the gas supplied to the CCHP and the gas load *via* gas pipeline, respectively.

Based on the above models, the primary energy consumption can be calculated by

$$P_{electricity} = P^1_{ele} + P^2_{ele}, \tag{11}$$

$$P_{coal} = P^1_{coal} + P^2_{coal} + P^3_{coal}, \tag{12}$$

$$P_{gas} = P^1_{gas} + P^2_{gas} + P^3_{gas}, \tag{13}$$

where $P_{electricity}$ represents the total amount of electricity bought from the external grid; P_{coal} is the coal consumption; and P_{gas} stands for the gas consumption.

Energy Conversion Process

Similar to the EPP, the ECP also concerns the change of type of energy. The ECP emphasizes multi-energy coupling and multi-agent interaction. The main differences between these two processes are the type of equipment they used. The EPP mostly adopts centralized equipment such as the thermal plant and centralized electrical heating equipment. But the ECP mainly adopts the distributed equipment, such as combined cooling, heating, and power (CCHP); distributed electric-thermal coupling equipment (*ETCE*(d)); and so on. CCHP is a typical equipment of multi-energy coupling which has a great influence on the energy efficiency of the IES. The EUE and the EXE of ECP are as follows:

$$\eta_{ecp} = \left(P^1_{e,h(d)} + P^2_{e,h(d)} + P^1_{e,c(d)} + P^2_{e,c(d)} + P^1_{g,e,h,c(d)} + P^2_{g,e,h,c(d)} + P^3_{g,e,h,c(d)} + P^4_{g,e,h,c(d)} + P^5_{g,e,h,c(d)} + P^6_{g,e,h,c(d)}\right)/P^1_{et} + P^2_{et} + P^1_{gt}, \tag{14}$$

$$\eta'_{ecp} = \left(P^1_{g,e,h,c(d)} + P^4_{g,e,h,c(d)} + \lambda_h\left(P^1_{e,h(d)} + P^2_{e,h(d)} + P^2_{g,e,h,c(d)} + P^5_{g,e,h,c(d)}\right) + \lambda_c\left(P^1_{e,c(d)} + P^2_{e,c(d)} + P^3_{g,e,h,c(d)} + P^6_{g,e,h,c(d)}\right)\right)/P^1_{et} + P^2_{et} + \lambda_g P^1_{gt}, \tag{15}$$

where the thermal energy supplied to the thermal storage equipment (TES) which is generated by the *ETCE*(d) is represented by $P^1_{e,h(d)}$; $P^2_{e,h(d)}$ is the thermal energy produced by the distributed ETCE which supplied directly to the heat loads; $P^1_{e,c(d)}$ is the cooling energy supplied to the cooling storage equipment (CS) which is produced by the distributed electrical-cooling coupling equipment (*EECE*(d)); $P^2_{e,c(d)}$ is the cooling energy produced by *EECE*(d) which is directly supplied to the cooling loads. The electricity, thermal energy, and cooling energy that CCHP supplies to the corresponding storage equipment for storage are represented by $P^1_{g,e,h,c(d)}$, $P^2_{g,e,h,c(d)}$, and $P^3_{g,e,h,c(d)}$, respectively. $P^4_{g,e,h,c(d)}$, $P^5_{g,e,h,c(d)}$, and $P^6_{g,e,h,c(d)}$ stand, respectively, for the electricity, thermal energy, and cooling energy produced by CCHP which are supplied directly to the corresponding load.

Energy Storage Process

The ESP is an indispensable process for IES. The improvement of energy storage not only deepens the degree of multi-energy coupling but also promotes the energy efficiency level of IES. Besides, it is helpful to the power peak load shifting, improves the stable operation of IES, and reduces the running cost of the system. The storage equipment has two working modes: energy storage mode and energy discharge mode. One storage equipment cannot perform both modes at the same time, so a coefficient that represents the working mode of the storage equipment should be considered. The EUE and the EXE can be written as

$$\eta_{esp} = \frac{\begin{array}{c}\sum_f \varepsilon_{esf}P^s_{esf} + \left(1-\varepsilon_{esf}\right)P^1_{esf} + \varepsilon_{hsf}P^s_{hsf} \\ +\left(1-\varepsilon_{hsf}\right)P^1_{hsf} + \varepsilon_{csf}P^s_{csf} + \left(1-\varepsilon_{csf}\right)P^1_{csf}\end{array}}{\begin{array}{c}\varepsilon_{esf}\left(P^3_{et} + P^1_{g,e,h,c(d)}\right) + \left(1-\varepsilon_{esf}\right)D_{esf} \\ \sum_f +\varepsilon_{hsf}\left(P^1_{ht} + P^1_{e,h(d)} + P^2_{g,e,h,c(d)}\right) + \left(1-\varepsilon_{hsf}\right)D_{hsf} \\ +\varepsilon_{csf}\left(P^2_{e,c(d)} + P^3_{g,e,h,c(d)}\right) + \left(1-\varepsilon_{csf}\right)D_{csf}\end{array}}, \tag{16}$$

$$\eta'_{esp} = \frac{\begin{array}{c}\varepsilon_{esf}P^s_{esf} + \left(1-\varepsilon_{esf}\right)P^1_{esf} \\ \sum_f +\lambda_h\left(\varepsilon_{hsf}P^s_{hsf} + \left(1-\varepsilon_{hsf}\right)P^1_{hsf}\right) \\ +\lambda_c\left(\varepsilon_{csf}P^s_{csf} + \left(1-\varepsilon_{csf}\right)P^1_{csf}\right)\end{array}}{\begin{array}{c}\varepsilon_{esf}\left(P^3_{et} + P^1_{g,e,h,c(d)}\right) + \left(1-\varepsilon_{esf}\right)D_{esf} \\ \sum_f +\lambda_h\left(\varepsilon_{hsf}\left(P^1_{ht} + P^1_{e,h(d)} + P^2_{g,e,h,c(d)}\right) + \left(1-\varepsilon_{hsf}\right)D_{hsf}\right) \\ +\lambda_c\left(\varepsilon_{csf}\left(P^2_{e,c(d)} + P^3_{g,e,h,c(d)}\right) + \left(1-\varepsilon_{csf}\right)D_{csf}\right)\end{array}}, \tag{17}$$

where ε_{esf}, ε_{hsf}, and ε_{csf} are the coefficients, respectively, representing the working mode of electrical energy storage (EES), TES, and CS. Storage equipment is in energy storage mode when the coefficient is 1. P^s_{esf}, P^s_{hsf}, and P^s_{csf}, respectively, stand for the amount of practical energy storage of EES, TES, and CS. D_{esf}, D_{hsf}, and D_{csf} represent the reduced energy in storage equipment during the energy discharge mode; P^1_{esf}, P^1_{hsf}, and P^1_{csf} are the practical amount of energy discharge of EES, TES, and CS.

Energy Utilization Process

Comprehensively considering the ETP, ECP, and ESP shown in **Figure 1**, the EUE and the EXE of the EUP can be, respectively, written as

$$\eta_{eup} = \frac{P^{e,out}_{EL} + P^{h,out}_{HL} + P^{c,out}_{CL} + P^{g,out}_{GL}}{P^4_{et} + P^1_{esf} + P^4_{g,e,h,c(d)} + P^2_{ht} + P^2_{e,h(d)} + P^1_{hsf} + P^5_{g,e,h,c(d)} + P^2_{e,c(d)} + P^1_{csf} + P^6_{g,e,h,c(d)} + P^2_{gt}}, \tag{18}$$

$$\eta'_{eup} = \frac{P^{e,out}_{EL} + \lambda_h P^{h,out}_{HL} + \lambda_c P^{c,out}_{CL} + \lambda_g P^{g,out}_{GL}}{P^4_{et} + P^1_{esf} + P^4_{g,e,h,c(d)} + \lambda_h\left(P^2_{ht} + P^2_{e,h(d)} + P^1_{hsf} + P^5_{g,e,h,c(d)}\right) + \lambda_c\left(P^2_{e,c(d)} + P^1_{csf} + P^6_{g,e,h,c(d)}\right) + \lambda_g P^2_{gt}}, \tag{19}$$

where η_{eup} is the EUE of EUP; η'_{eup} is the EXE of ESP; and $P_{EL}^{e,out}$, $P_{HL}^{h.out}$, $P_{CL}^{c,out}$, and $P_{GL}^{g,out}$, respectively, represent the practical demand of electric load (EL), heat load (HL), cooling load (CL), and gas load (GL).

Energy Efficiency of Entire Integrated Energy System

With the energy efficiency analysis of the five processes, the EUE and the EXE of the entire IES can be obtained:

$$\eta_{all} = \frac{P_{EL}^{e,out} + P_{HL}^{h.out} + P_{CL}^{c,out} + \sum_f \left(\varepsilon_{esf} P_{esf}^{s} + \varepsilon_{hsf} P_{hsf}^{s} + \varepsilon_{csf} P_{csf}^{s}\right)}{P_{electricity} + P_{coal} + P_{gas} + \sum_f \left(\left(1-\varepsilon_{esf}\right)D_{esf} + \left(1-\varepsilon_{hsf}\right)D_{hsf} + \left(1-\varepsilon_{csf}\right)D_{csf}\right)}, \quad (20)$$

$$\eta'_{all} = \frac{P_{EL}^{e,out} + \lambda_h P_{HL}^{h.out} + \lambda_c P_{CL}^{c,out} + \sum_f \left(\varepsilon_{esf} P_{esf}^{s} + \varepsilon_{hsf}\lambda_h P_{hsf}^{s} + \varepsilon_{csf}\lambda_c P_{csf}^{s}\right)}{P_{electricity} + \lambda_{co} P_{coal} + \lambda_g P_{gas} + \sum_f \left(\left(1-\varepsilon_{esf}\right)D_{esf} + \left(1-\varepsilon_{hsf}\right)\lambda_h D_{hsf} + \left(1-\varepsilon_{csf}\right)\lambda_c D_{csf}\right)}, \quad (21)$$

where η_{all} is the EUE of the entire IES and η'_{all} is the EXE of the entire IES.

ENERGY EFFICIENCY ANALYSIS OF SUBSYSTEM OF INTEGRATED ENERGY SYSTEM

IES is mainly represented by ESS, HSS, CSS, and GSS. The coupling and interaction of the subsystems mentioned above is not only a typical physical phenomenon in the IES but also a key part of IES. The analysis of each subsystem helps to further clarify the internal relationship of the energy system. In this section, this study analyzes the energy flow relationship of each piece of equipment in the IES. After that, we decouple the energy flow in each process based on the different types of loads to obtain the internal energy flow relationship of each subsystem. Finally, the energy efficiency calculation models of each subsystem are established according to the internal energy flow relationships of each subsystem. During the energy efficiency analysis of each subsystem, the energy flow in one transmission line might participate in different subsystems. Hence, the distribution coefficient is proposed to determine the amount of different energy in each subsystem. The distribution coefficients and energy flow in their corresponding subsystem are given in **Table 1**.

Electric Subsystem

As pictured in **Figure 2**, the EL can be satisfied through four ways: 1) the electric energy produced by CFPG equipment and CHP and then supplied to the EL by transmission network; 2) the output power of CCHP in ECP; 3) the power discharged by TES; and 4) the electricity bought from the external grid.

According to **Figure 2**, the EUE and the EXE of the electric subsystem can be, respectively, written as

$$\eta_{all(e)} = \frac{P_{EL}^{e,out} + \sum_f \varepsilon_{esf} P_{esf}^{s}}{\omega_{ele}^{e,1} P_{ele}^{2} + \omega_{coal}^{e,1} P_{coal}^{1} + \omega_{coal}^{e,2} P_{coal}^{3} + \omega_{gas}^{e,1} P_{gas}^{1} + \omega_{gas}^{e,1} P_{gas}^{3} + \sum_f \left(1-\varepsilon_{esf}\right)D_{esf}}, \quad (22)$$

$$\eta'_{all(e)} = \frac{P_{EL}^{e,out} + \sum_f \varepsilon_{esf} P_{esf}^{s}}{\omega_{ele}^{e,1} P_{ele}^{2} + \lambda_{coal}\left(\omega_{coal}^{e,1} P_{coal}^{1} + \omega_{coal}^{e,2} P_{coal}^{3}\right) + \lambda_g\left(\omega_{gas}^{e,1} P_{gas}^{1} + \omega_{gas}^{e,1} P_{gas}^{3}\right) + \sum_f \left(1-\varepsilon_{esf}\right)D_{esf}}, \quad (23)$$

where $\eta_{all(e)}$ is the EUE of the electric subsystem and $\eta'_{all(e)}$ is the EXE of the electric subsystem.

Heat Subsystem

As can be seen in **Figure 2** the structure of HSS is more complicated compared to the structure of ESS. The source of thermal energy supply consists of three parts: 1) the thermal energy produced by the electrical-heat coupling equipment, CFTG equipment, CHP, and GFTG equipment; 2) the output thermal energy of distributed electrical-heat coupling equipment and CCHP in ECP; and 3) the thermal energy discharged by TES.

According to **Figure 2**, the energy efficiency models of HSS can be expressed as

$$\eta_{all(h)} = \frac{P_{HL}^{h,out} + \sum_f \varepsilon_{hsf} P_{hsf}^{s}}{\begin{array}{l} P_{ele}^{1} + \omega_{ele}^{h,1} P_{ele}^{2} + \omega_{coal}^{h,1} P_{coal}^{1} + P_{coal}^{2} + \omega_{coal}^{h,2} P_{coal}^{3} \\ + \omega_{gas}^{h,1} P_{gas}^{1} + P_{gas}^{2} + \omega_{gas}^{e,1} P_{gas}^{3} + \sum_f \left(1-\varepsilon_{hsf}\right)D_{hsf} \end{array}}, \quad (24)$$

$$\eta'_{all(h)} = \frac{\lambda_h\left(P_{HL}^{h,out} + \sum_f \varepsilon_{hsf} P_{hsf}^{s}\right)}{\begin{array}{l} P_{ele}^{1} + \omega_{ele}^{h,1} P_{ele}^{2} + \lambda_{coal}\left(\omega_{coal}^{h,1} P_{coal}^{1} + P_{coal}^{2} + \omega_{coal}^{h,2} P_{coal}^{3}\right) \\ + \lambda_g\left(\omega_{gas}^{h,1} P_{gas}^{1} + P_{gas}^{2} + \omega_{gas}^{e,1} P_{gas}^{3}\right) + \sum_f \left(1-\varepsilon_{hsf}\right)\lambda_h D_{hsf} \end{array}}, \quad (25)$$

where $\eta_{all(h)}$ is the EUE of the heat subsystem and $\eta'_{all(e)}$ is the EXE of the heat subsystem.

Cooling Subsystem

As can be seen in **Figure 2**, there is no cooling energy generated in the EPP of CSS. The source of cooling energy supply consists of two parts: 1) the output cooling energy of CCHP in ECP and 2) the cooling energy discharged by CS. The EUE and the EXE of the CSS can be calculated by

$$\eta_{all(c)} = \frac{P_{CL}^{c,out} + \sum_f \varepsilon_{csf} P_{csf}^{s}}{\omega_{ele}^{c,1} P_{ele}^{2} + \omega_{coal}^{c,1} P_{coal}^{1} + \omega_{coal}^{c,2} P_{coal}^{3} + \omega_{gas}^{c,1} P_{gas}^{1} + \omega_{gas}^{e,1} P_{gas}^{3} + \sum_f \left(1-\varepsilon_{csf}\right)D_{csf}}, \quad (26)$$

$$\eta'_{all(c)} = \frac{\lambda_c\left(P_{CL}^{c,out} + \sum_f \varepsilon_{csf} P_{csf}^{s}\right)}{\begin{array}{l} \omega_{ele}^{c,1} P_{ele}^{2} + \lambda_{coal}\left(\omega_{coal}^{c,1} P_{coal}^{1} + \omega_{coal}^{c,2} P_{coal}^{3}\right) \\ + \lambda_g\left(\omega_{gas}^{c,1} P_{gas}^{1} + \omega_{gas}^{e,1} P_{gas}^{3}\right) + \sum_f \left(1-\varepsilon_{csf}\right)\lambda_c D_{csf} \end{array}}, \quad (27)$$

where $\eta_{all(c)}$ is the EUE of the cooling subsystem and $\eta'_{all(c)}$ is the EXE of the cooling subsystem.

Gas Subsystem

The structure of the GSS is depicted in **Figure 2**. The research on the GSS is mainly around the modeling of the gas supply system which is composed of the ETP and EUP. The structure of GSS is simpler compared with other subsystems. The gas demand is satisfied with the gas bought from the external gas pipe network. The EUE and the EXE are equal because there is no multi-energy involved in GSS. The energy efficiency indices of this subsystem are as follows:

TABLE 1 | The distribution coefficient of each energy flow.

Energy flow	Subsystem	Distribution coefficient
Coal consumption of CFPG equipment	ESS	$\omega_{coal}^{e,1}$
Coal consumption of CHP		$\omega_{coal}^{e,2}$
Gas consumption of CHP		$\omega_{gas}^{e,1}$
Electricity from the external grid		$\omega_{ele}^{e,1}$
Power produced by CFPG equipment		$\omega_{co,e}^{e,1}$
Power produced by CHP		$\omega_{co,g,e,h}^{e,1}$
Gas transmitted by GT equipment		$\omega_{gas}^{e,2}$
Coal consumption of CFPG equipment	HSS	$\omega_{coal}^{h,1}$
Coal consumption of CHP		$\omega_{coal}^{h,2}$
Gas consumption of CFPG equipment		$\omega_{gas}^{h,1}$
Gas transmitted by GT equipment		$\omega_{gas}^{h,2}$
Electricity from the external grid		$\omega_{ele}^{h,1}$
Power produced by CFPG equipment		$\omega_{co,e}^{h,1}$
Power produced by CHP		$\omega_{co,g,e,h}^{h,1}$
Coal consumption of CFPG equipment	CSS	$\omega_{coal}^{c,1}$
Coal consumption of CHP		$\omega_{coal}^{c,2}$
Gas consumption of CHP		$\omega_{gas}^{c,1}$
Electricity from the external grid		$\omega_{ele}^{c,1}$
Power produced by CFPG equipment		$\omega_{co,e}^{c,1}$
Power produced by CHP		$\omega_{co,g,e,h}^{c,1}$
Gas transmitted by GT equipment		$\omega_{gas}^{c,2}$
Gas transmitted by GT equipment	GSS	$\omega_{gas}^{g,1}$

$$\eta_{all(g)} = \eta'_{all(g)} = \frac{P_{GL}^{g,out}}{\omega_{gas}^{g,1} P_{gas}^{3}}, \tag{28}$$

where $\eta_{all(g)}$ is the EUE of the cooling subsystem and $\eta'_{all(g)}$ is the EXE of the cooling subsystem.

CASE STUDY

Case Background

1) System Description

Taking actual data of an actual commercial-industrial park to analyze. The main load area of this park is composed of the business district, industrial district, and residential district. Each district has the load demand of electricity, heating, cooling, and gas. Due to the long heating periods and high heat load level, the installation rate of the heat supply unit accounts for a large proportion. The output of the IES involves power, gas, 9°C chilled medium water, and 90°C heating medium water. The energy equipment mainly includes centralized electric heating (CEH), thermal power (TP), coal-fired boiler (CFB), combined heat and power (CHP), and gas boiler (GB) in EPP; power grid (PG), heating supply pipeline (HSP), and gas supply pipeline (GSP) in ETP; and distributed electrical-heat transfer (DEHT), distributed electric cooling (DEC), and combined cooling heating and power (CCHP) in ECP; EES, TES, and CS in ESP. The GB uses natural gas as the input energy to produce the 1 MPa 180°C steam, which is supplied to the heat load *via* water. CCHP consists of a gas engine and absorption water heating and chilling unit. The absorption water heating and chilling unit has two working modes: one is the cooling mode (produce cooling water at 9°C) and the other is the heating mode (produce hot water at 90°C). The heat generated by the gas engine during the power generation is utilized by absorption water heating and chilling unit to produce cooling or thermal energy. The energy conversion efficiency models and parameters of the typical equipment in this paper can be found in (Liu et al., 2016; Abeysekera et al., 2016; Huang et al., 2018; Li et al., 2018; Wang et al., 2020; Xi et al., 2021). Particularly, the equivalent models mentioned above are not the actual physical equipment but the equivalence and abstraction of each piece of equipment in the IES according to the energy conversion relationship.

2) Energy Quality Coefficient

The energy quality coefficient varies with the temperature variety of the environment so that taking the variation of energy quality coefficient under different seasons into consideration is very important. The summer average temperature and winter average temperature in the IES region is 27.6°C (300.75 K) and 7.9°C (281.05 K), respectively. The energy quality coefficients of various energy sources in different seasons are shown in **Table 2**.

Figure 3 shows the load curves of electrical, thermal, cooling, and gas on a typical day in winter and summer. The IES has a high demand for EL in winter and summer, but the demand for HL, CL, and GL varies greatly with the season due to the variation of temperature and sunshine time.

3) Energy Demand Situation

Energy Efficiency Evaluation Analysis

Using the energy efficiency indices calculation equation of the IES proposed in this study, we can get the energy efficiency indices

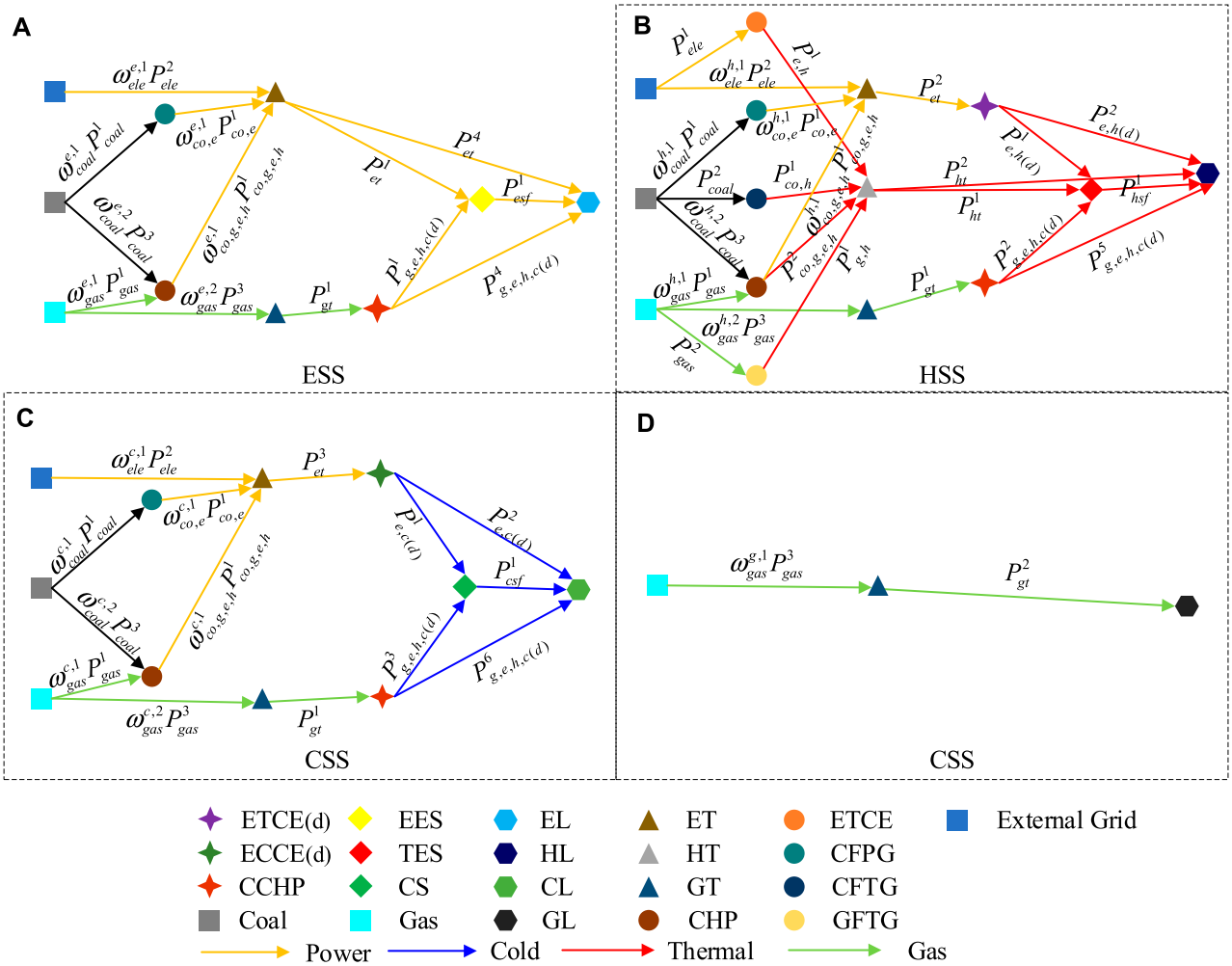

FIGURE 2 | Schematic diagram of subsystems.

value of the typical day in winter and summer (24 h) and count the maximum and the minimum value of the indices. Then, we do a comprehensive analysis and comparison to the energy efficiency differences of IES, each subsystem, and each process. **Table 3**, **Table 4**, **Table 5**, **Table 6**, **Table 7**, and **Table 8** show the highest and lowest value of energy efficiency indices for IES and each subsystem in EPP.

Energy Efficiency Evaluation Analysis on the Integrated Energy System

The size relationship between the EUE and the EXE is related to the quality of energy. It can be seen from **Table 3** that the EXE of the ESS is higher than its EUE. It is because electricity, as the highest quality energy, is obtained through the conversion of lower quality primary energy sources. The energy quality of thermal and cooling energy is low and is generally generated by consuming high-quality energy, so the EXE of HSS and CSS are less than the EUE of them. The EUE and EXE of the IES are both higher in summer than those in winter. The reason is that more heat-generating units are involved in the operation of the IES in winter than that in summer, resulting in lower energy efficiency levels in the system.

TABLE 2 | The energy quality coefficient of common energy resources.

Energy resources	Energy quality coefficient		Note
	Summer (27.6°C)	Winter (7.9°C)	
Electricity	1	1	—
Coal	0.6502	0.6652	T = 1,600°C
Gas	0.6089	0.6254	T = 1,300°C
Heating medium water	0.1482	0.2039	90–70°C
Chilled water	0.0566	0.0026	9–14°C

Energy Efficiency Evaluation Analysis on Different Processes

a) Energy Efficiency of EPP

Table 4 shows that the EUE of HSS in summer is 0.459 but the EXE of HSS is significantly lower than that of ESS and the CSS, with

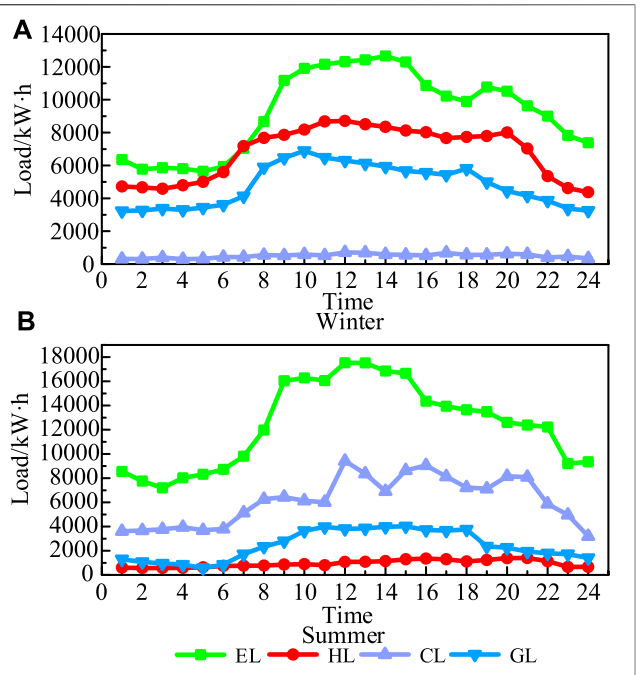

FIGURE 3 | The load data of IES in winter and summer.

TABLE 3 | The energy efficiency of IES.

Index	Season		ESS	HSS	CSS	GSS	Entire
EUE	Winter	Max	0.674	0.497	0.099	0.533	0.597
		Min	0.492	0.376	0.054	0.456	0.456
	Summer	Max	0.817	0.242	0.373	0.514	0.749
		Min	0.551	0.137	0.296	0.450	0.484
EXE	Winter	Max	0.903	0.125	0.003	0.533	0.573
		Min	0.673	0.090	0.001	0.456	0.315
	Summer	Max	0.973	0.059	0.026	0.514	0.718
		Min	0.787	0.033	0.018	0.450	0.342

TABLE 4 | The energy efficiency of EPP.

Index	Season		ESS	HSS	CSS	Entire
EUE	Winter	Max	0.757	0.815	0.744	0.777
		Min	0.680	0.708	0.657	0.683
	Summer	Max	0.806	0.509	0.824	0.802
		Min	0.754	0.459	0.677	0.705
EXE	Winter	Max	0.978	0.643	0.931	0.798
		Min	0.843	0.291	0.811	0.575
	Summer	Max	0.985	0.131	0.980	0.977
		Min	0.848	0.111	0.771	0.801

TABLE 5 | The energy efficiency of ETP.

Index	Season		ESS	HSS	CSS	GSS	Entire
EUE	Winter	Max	0.934	0.951	0.934	0.979	0.938
		Min	0.929	0.935	0.928	0.956	0.932
	Summer	Max	0.931	0.974	0.932	0.987	0.931
		Min	0.928	0.955	0.927	0.97	0.929
EXE	Winter	Max	0.930	0.941	0.932	0.977	0.934
		Min	0.928	0.932	0.928	0.952	0.929
	Summer	Max	0.929	0.973	0.929	0.985	0.930
		Min	0.927	0.955	0.927	0.969	0.927

TABLE 6 | The energy efficiency of ECP.

Index	Season		ESS	HSS	CSS	Entire
EUE	Winter	Max	0.395	0.506	0.261	0.397
		Min	0.372	0.436	0.260	0.372
	Summer	Max	0.375	0.432	0.260	0.297
		Min	0.342	0.430	0.258	0.263
EXE	Winter	Max	0.652	0.105	0.008	0.093
		Min	0.615	0.098	0.006	0.058
	Summer	Max	0.671	0.126	0.015	0.035
		Min	0.638	0.105	0.014	0.016

TABLE 7 | The energy efficiency of ESP.

Index	Season		ESS	HSS	CSS	Entire
EUE	Winter	Max	0.743	0.863	0.976	0.911
		Min	0.712	0.825	0.969	0.835
	Summer	Max	0.739	0.889	0.954	0.862
		Min	0.701	0.875	0.942	0.834
EXE	Winter	Max	0.748	0.824	0.972	0.845
		Min	0.714	0.795	0.963	0.815
	Summer	Max	0.735	0.878	0.952	0.858
		Min	0.689	0.869	0.925	0.824

TABLE 8 | The energy efficiency of EUP.

Index	Season		ESS	HSS	CSS	GSS	Entire
EUE	Winter	Max	0.899	0.432	0.421	0.589	0.705
		Min	0.757	0.422	0.398	0.504	0.638
	Summer	Max	0.906	0.425	0.410	0.517	0.764
		Min	0.768	0.421	0.385	0.457	0.727
EXE	Winter	Max	0.899	0.432	0.421	0.589	0.705
		Min	0.757	0.422	0.398	0.504	0.638
	Summer	Max	0.906	0.425	0.410	0.517	0.764
		Min	0.768	0.421	0.385	0.457	0.727

only 0.111. It is caused by the high temperature in summer compared to that in winter which leads to the low energy quality coefficient of thermal energy. HSS provides low-quality energy production at the cost of high-quality energy consumption so that the degree of energy utilization of this subsystem is not satisfactory. Since the CSS of this IES produces only electricity in the EPP and does not produce cooling energy with a lower energy quality coefficient, the EUE and EXE of ESS and CSS are similar in this process. The EUE and the EXE of the IES in winter are lower than those in summer in EPP because the heat load demand is higher in winter but the overall efficiency of the main heat production equipment is lower compared to that of the power generation equipment, resulting in lower overall energy efficiency.

TABLE 9 | The information entropy results in winter.

	EUE				EXE			
	ESS	HSS	CSS	GSS	ESS	HSS	CSS	GSS
Entire	0.936	0.960	0.887	0.904	0.925	0.960	0.916	0.904
EPP	0.877	0.923	0.88	0	0.919	0.917	0.976	0
ETP	0.884	0.918	0.876	0.892	0.882	0.898	0.902	0.892
ECP	0.945	0.898	0.876	0	0.948	0.902	0.862	0
ESP	0.952	0.944	0.930	0	0.971	0.954	0.933	0
EUP	0.905	0.935	0.920	0.912	0.905	0.935	0.920	0.912

TABLE 10 | The information entropy results in summer.

	EUE				EXE			
	ESS	HSS	CSS	GSS	ESS	HSS	CSS	GSS
Entire	0.904	0.952	0.921	0.912	0.937	0.952	0.905	0.912
EPP	0.968	0.935	0.939	0	0.964	0.945	0.937	0
ETP	0.936	0.951	0.939	0.921	0.936	0.959	0.939	0.921
ECP	0.9428	0.896	0.939	0	0.941	0.882	0.939	0
ESP	0.938	0.922	0.941	0	0.962	0.936	0.944	0
EUP	0.922	0.939	0.904	0.901	0.922	0.939	0.904	0.901

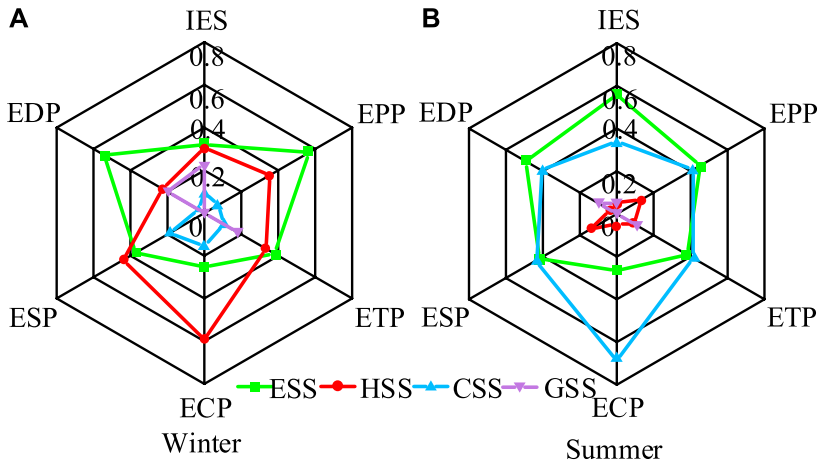

FIGURE 4 | The weight of each subsystem in winter and summer.

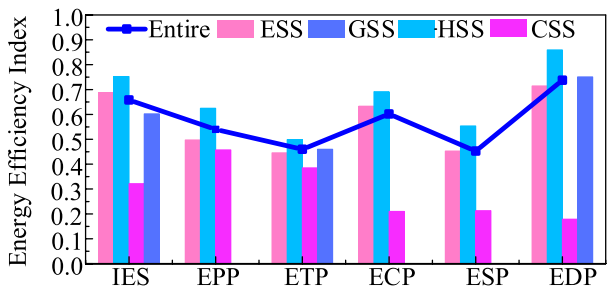

FIGURE 5 | The energy efficiency evaluation results of the IES in winter.

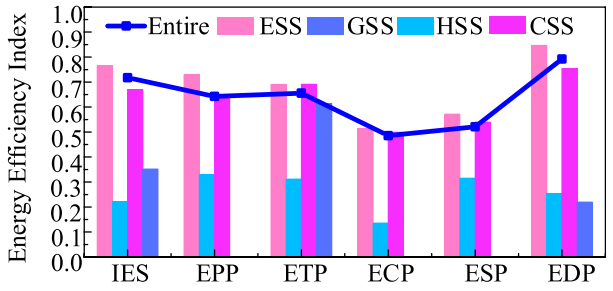

FIGURE 6 | The energy efficiency evaluation results of the IES in summer.

b) Energy Efficiency of ETP

The energy efficiency of the ETP is related to the quantity of energy transmission. **Table 5** shows that the EUE and EXE of HSS and GSS in winter is lower than that in summer due to the high demand for thermal energy and gas in winter. It also can be seen that the EUE and EXE of ESS and CSS are higher in summer than those in winter. This is because there has been an increase in the amount of electricity delivered by transmission lines. On the whole, the EUE and EXE of ETP in winter is higher than those in summer. The reason is that the share of electrical energy in the ETP in winter is less than that in summer.

c) Energy Efficiency of ECP

Table 6 shows that, in ECP, the EXE of CSS is very low in winter and summer which leads to the low EXE of IES. There are two reasons: one is that the energy level of thermal and cooling energy is very low and both are generated by consuming high energy at high energy levels, so the EXE is low. The other is that the electric energy output accounts for a very small proportion of the output of ECP, so although the EXE of the ESS is much higher in this process than that of the HSS and CSS, the EXE of IES in this process is still low.

d) Energy Efficiency of ESP

The energy efficiency of the ESP mainly depends on the storage and discharge energy of energy storage equipment. As it can be seen from **Table 7**, the energy efficiency of the ESP of HDD is higher in winter than in summer, because the storage and discharge energy of thermal energy are larger in winter. Due to the higher storage and discharge energy in summer than that in winter, the overall energy efficiency of the ESP in winter is higher than that in summer.

e) Energy Efficiency of EUP

As can be seen in **Table 8**, the energy efficiency of EUP in summer is higher than that in winter. This is because the efficiency of the electric energy consumption is much higher than that of the thermal, gas, and cooling energy consumption, and the proportion of the electric to total load is higher than that in winter. Therefore, the overall efficiency in EUP in summer is improved compared to winter.

Evaluation of Energy Efficiency Indices

In the previous section, the energy efficiency indices of the whole system, each subsystem, and each process are calculated considering a typical winter and summer day. In order to make good use of these data to evaluate the energy efficiency of each subsystem and each process, the AHP-entropy weight method (Yang et al., 2020) is introduced to process the results of these indices. The AHP-entropy method is an index calculation method that combines subjective weight and objective weight. First, the subjective weight based on the AHP is obtained from the following steps: 1) determining the hierarchy structure of each index; 2) forming the judgment matrix; and 3) consistency check of subjective weight. Second, the objective weight determined by the entropy weight method is obtained from the following three steps: 1) normalization processing of each index; 2) calculating the entropy value of each index; and 3) calculating the entropy weight of each index. At last, the general weight of each index which reflects the actual situation is calculated by integrating the subjective and objective weight. The information entropy results in winter and summer are shown in **Table 9** and **Table 10**.

Calculate the weight of each subsystem in each process according to the information entropy, and then combine them with the weights calculated by the AHP method for calculation. The results are the weights used in this study for the energy efficiency evaluation, as shown in **Figure 4**.

It can be seen from **Figure 4** that the weights of HSS and CSS vary greatly under different seasons. The main cause of that is the less demand for the heat and gas load in summer which leads to the less weight of HSS and GSS in summer.

From the aforementioned analysis, it is clear that the amount of energy efficiency of each subsystem depends on the amount of the various loads and the equipment involved in the operation of each subsystem. Based on the weights and the normalized data of each index, the evaluation results of each subsystem in the integrated energy system can be obtained.

As we can see in **Figure 5**, in winter, the HSS has the best energy efficiency level, the ESS and the GSS took second place, and the CSS is the worst. The evaluation results in production and ETP of CSS are very close to that of ESS. It is because the CSS only considers the production of electricity and the transmission of electricity and gas involved just like the ESS so that the efficiency levels of these two subsystems EPP and ETP are very similar. However, the overall evaluation results of these two subsystems are quite different. The causes are included: 1) the energy quality coefficient is very low due to the low temperature in winter and 2) the demand for cooling energy is less, resulting in lower weights of CSS in each process. The energy efficiency level of GSS is high because the demand for gas is high in winter and the transmission loss is low.

From the evaluation results of this park in summer shown in **Figure 6**, it can be seen that, unlike the evaluation results of the cooling system in winter, the energy efficiency level of the HSS always keeps at a low level. This is because the energy quality of thermal energy and the demand for thermal energy in summer is much lower than that in winter. And then the biggest difference between the thermal energy supply in summer and the cooling energy supply in winter is that the thermal energy is present in all processes of the IES which leads to the low energy efficiency level in each process of the HSS. The ESS and the CSS have high energy efficiency levels because the coupling degree and the demand for cooling energy and gas are high. The GSS has a significant decrease in energy efficiency level compared to winter because the gas load demand is lower in summer and the overall efficiency of the EUP is lower than that in winter.

CONCLUSION

In this study, the calculation models of EUE and EXE for the IES are constructed. The energy efficiency of each process (including EPP, ETP, ECP, ESP, and EUP) and each subsystem (including ESS, HSS, CSS, and GSS) can be obtained through the proposed models. Based on the example of an IES park, the validity of these models is verified. By comparing the energy efficiency of IES in winter and summer, it can be seen that the energy efficiency in summer is better than that in winter because of the higher energy efficiency level of EPP and ETP in summer. In addition, it was found after analysis that there is a relationship between the EUE and the EXE. The calculation of EXE is based on the EUE, and they are positively correlated. Therefore, it is of great significance for the improvement of the energy efficiency of the IES.

The proposed models provide a novel idea and direction for the energy efficiency evaluation of the IES. They can provide the tool for the energy efficiency improvement of processes, subsystems, and the IES. These models can guide the IES operator to make the scientific and practical dispatch planning and operation management strategy.

For further study, future work can form the energy efficiency in more detail. For EPP, we will consider the uncertainty of distributed energy resources. For energy resources supply, we will take the energy price and cost of each subsystem into consideration to establish a more comprehensive model.

DATA AVAILABILITY STATEMENT

The original contributions presented in the study are included in the article/Supplementary Material; further inquiries can be directed to the corresponding author.

AUTHOR CONTRIBUTIONS

HS and QH designed the model and the computational framework and analyzed the data. HS and ZW carried out the implementation and performed the calculations. HS and QH wrote the manuscript with input from all authors. QH conceived the study and was in charge of overall direction and planning.

FUNDING

The authors declare that this study received funding from the Project of State Grid Jiangsu Electric Power Co., Ltd (No. J2020115). The funder was not involved in the study design, collection, analysis, interpretation of data, the writing of this article or the decision to submit it for publication.

REFERENCES

Abeysekera, M., Wu, J., Jenkins, N., and Rees, M. (2016). Steady state analysis of gas networks with distributed injection of alternative gas. *Appl. Energ.* 164, 991–1002. doi:10.1016/j.apenergy.2015.05.099

Abu-Rayash, A., and Dincer, I. (2020). Development of an integrated energy system for smart communities. *Energy* 202, 117683. doi:10.1016/j.energy.2020.117683

Alves, O., Monteiro, E., Brito, P., and Romano, P. (2016). Measurement and classification of energy efficiency in HVAC systems. *Energy and Buildings* 130, 408–419. doi:10.1016/j.enbuild.2016.08.070

Chen, S., Wei, Z., Sun, G., Cheung, K. W., Wang, D., and Zang, H. (2019). Adaptive Robust Day-Ahead Dispatch for Urban Energy Systems. *IEEE Trans. Ind. Electron.* 66 (2), 1379–1390. doi:10.1109/TIE.2017.2787605

Ding, H., Li, J., and Heydarian, D. (2021). Energy, exergy, exergoeconomic, and environmental analysis of a new biomass-driven cogeneration system. *Sustainable Energ. Tech. Assessments* 45, 101044. doi:10.1016/j.seta.2021.101044

Hu, X., Zhang, H., Chen, D., Li, Y., Wang, L., Zhang, F., et al. (2020). Multi-objective planning for integrated energy systems considering both exergy efficiency and economy. *Energy* 197, 117155. doi:10.1016/j.energy.2020.117155

Huang, X., Xu, Z., Sun, Y., Xue, Y., Wang, Z., Liu, Z., et al. (2018). Heat and power load dispatching considering energy storage of district heating system and electric boilers. *J. Mod. Power Syst. Clean. Energ.* 6 (5), 992–1003. doi:10.1007/s40565-017-0352-6

Huang, Z., Yu, H., Chu, X., and Peng, Z. (2017). Energetic and exergetic analysis of integrated energy system based on parametric method. *Energ. Convers. Manag.* 150, 588–598. doi:10.1016/j.enconman.2017.08.026

Ibrahim, T. K., Basrawi, F., Awad, O. I., Abdullah, A. N., Najafi, G., Mamat, R., et al. (2017). Thermal performance of gas turbine power plant based on exergy analysis. *Appl. Therm. Eng.* 115, 977–985. doi:10.1016/j.applthermaleng.2017.01.032

Li, M., and Wang, Z. (2021). Modeling and Optimization of Integrated Energy System Based on Energy Circuit Theory. *IEEJ Trans. Elec Electron. Eng.* 16 (5), 696–703. doi:10.1002/tee.23349

Li, P., Wang, Z., Wang, N., Yang, W., Li, M., Zhou, X., et al. (2021). Stochastic robust optimal operation of community integrated energy system based on integrated demand response. *Int. J. Electr. Power Energ. Syst.* 128, 106735. doi:10.1016/j.ijepes.2020.106735

Li, S., Guo, L., Zhang, P., Wang, H., Cai, Z., Zhu, X., et al. "Modeling and Optimization on Energy Efficiency of Urban Integrated Energy System," 2018. 2nd IEEE Conference on Energy Internet and Energy System Integration (EI2), Beijing, China. IEEE, pp. 1–6. doi:10.1109/EI2.2018.8582411

Liu, X., Wu, J., Jenkins, N., and Bagdanavicius, A. (2016). Combined analysis of electricity and heat networks. *Appl. Energ.* 162, 1238–1250. doi:10.1016/j.apenergy.2015.01.102

Mancarella, P. (2014). MES (multi-energy systems): An overview of concepts and evaluation models. *Energy* 65, 1–17. doi:10.1016/j.energy.2013.10.041

Meibom, P., Hilger, K. B., Madsen, H., and Vinther, D. (2013). Energy Comes Together in Denmark: The Key to a Future Fossil-free Danish Power System. *IEEE Power Energ. Mag.* 11 (5), 46–55. doi:10.1109/MPE.2013.2268751

OMalley, M., and Kroposki, B. (2013). Energy Comes Together: The Integration of All Systems [Guest Editorial]. *IEEE Power Energ. Mag.* 11 (5), 18–23. doi:10.1109/MPE.2013.2266594

Qin, C., Wang, L., Han, Z., Zhao, J., and Liu, Q. (2021). Weighted directed graph based matrix modeling of integrated energy systems. *Energy* 214, 118886. doi:10.1016/j.energy.2020.118886

Wang, J.-J., Yang, K., Xu, Z.-L., and Fu, C. (2015). Energy and exergy analyses of an integrated CCHP system with biomass air gasification. *Appl. Energ.* 142, 317–327. doi:10.1016/j.apenergy.2014.12.085

Wang, J., Zhong, H., Yang, Z., Wang, M., Kammen, D. M., Liu, Z., et al. (2020). Exploring the trade-offs between electric heating policy and carbon mitigation in China. *Nat. Commun.* 11(1), 6054. doi:10.1038/s41467-020-19854-y

Willem, H., Lin, Y., and Lekov, A. (2017). Review of energy efficiency and system performance of residential heat pump water heaters. *Energy and Buildings* 143, 191–201. doi:10.1016/j.enbuild.2017.02.023

Xi, L., Wu, J., Xu, Y., and Sun, H. (2021). Automatic generation control based on multiple neural networks with actor-critic strategy. *IEEE Trans. Neural Networks Learn. Syst.* 32(6), 2483–2493. doi:10.1109/TNNLS.2020.3006080

Yang, G., Sun, J., and Xiao, H. (2020). *Research on Testability Allocation Method Based on AHP-Entropy Weight Combination*. IEEE International Conference on Information Technology. Chongqing: Big Data and Artificial Intelligence (ICIBA), 49–53. doi:10.1109/ICIBA50161.2020.9276984

Zhang, H., Liu, X., Liu, Y., Duan, C., Dou, Z., and Qin, J. (2021). Energy and exergy analyses of a novel cogeneration system coupled with absorption heat pump and organic Rankine cycle based on a direct air cooling coal-fired power plant. *Energy* 229, 120641. doi:10.1016/j.energy.2021.120641

Conflict of Interest: HS, QH, and ZW were employed by the company State Grid Jiangsu Electric Power Co., Ltd.

Publisher's Note: All claims expressed in this article are solely those of the authors and do not necessarily represent those of their affiliated organizations, or those of the publisher, the editors, and the reviewers. Any product that may be evaluated in this article, or claim that may be made by its manufacturer, is not guaranteed or endorsed by the publisher.

frontiers in Energy Research

ORIGINAL RESEARCH
published: 23 August 2021
doi: 10.3389/fenrg.2021.711716

Research on Dynamic Equivalent SOC Estimation of Hybrid Energy Storage System Based on Sliding Mode Observer

Yifei Wang[1,2]*, *Wei Jiang*[1], *Chengwei Zhu*[3], *Zhiqi Xu*[1] and *Yifan Deng*[1]

[1]School of Electrical Engineering, Southeast University, Nanjing, China, [2]Jiangsu Provincial Key Laboratory of Smart Grid Technology and Equipment, Southeast University, Nanjing, China, [3]State Grid Anhui Electric Power Co. Ltd., Tongling Power Supply Company, Tongling, China

This article proposes a sliding mode observer based dynamic equivalent state of charge (ESOC) estimation method for hybrid energy storage system (HESS). Since different types of energy storage components and power electronics circuit are coupled in the HESS, the traditional SOC estimation method cannot reflect the real-time operation characteristics of the HESS. To tackle this problem, a sliding mode observer based on the model of the HESS is built in this article. By collecting the corresponding voltage and current signals, the internal parameters of energy storage elements can be observed accurately in real time. The dynamic ESOC is further defined with the idea of real-time charge balance to reflect the accurate available capacity of the HESS. Finally, the simulation results based on MATLAB/Simulink model are given to verify the feasibility of the proposed dynamic ESOC.

Keywords: hybrid energy storage system, sliding mode observer, dynamic ESOC, SOC estimation, real-time charge balance

OPEN ACCESS

Edited by:
Yingjun Wu,
Hohai University, China

Reviewed by:
Xu Wang,
Shanghai Jiao Tong University, China
Zhiyi Li,
Zhejiang University, China

***Correspondence:**
Yifei Wang
wyf@seu.edu.cn

Specialty section:
This article was submitted to Smart Grids, a section of the journal Frontiers in Energy Research

Received: *19 May 2021*
Accepted: *23 July 2021*
Published: *23 August 2021*

Citation:
Wang Y, Jiang W, Zhu C, Xu Z and Deng Y (2021) Research on Dynamic Equivalent SOC Estimation of Hybrid Energy Storage System Based on Sliding Mode Observer. Front. Energy Res. 9:711716. doi: 10.3389/fenrg.2021.711716

INTRODUCTION

Because of the high performance and flexibility of the hybrid energy storage system (HESS), HESS has been widely concerned and studied (Choi et al., 2012; Kim et al., 2015; Akar et al., 2017). The HESS can be applied to applications like motor driving, distributed generation, and backup power (Hammond, 1995; Franquelo et al., 2008; Kouro et al., 2010). The HESS usually consists of two or more types of energy storage components. Battery and supercapacitors are a classic combination. With the high energy density of the battery and the high power density of the supercapacitors, the battery/supercapacitor HESS can provide instantaneous high power output while meeting the capacity demand of the system.

Since the characteristics and parameters of different types of energy storage components vary greatly, power electronic circuits are required in the HESS to couple these components. DC bus-based structure is a common solution (Wang et al., 2014). As a result, unlike the single energy storage technology system, the state of charge (SOC) evaluation of HESS is tricky. The operation mode and power allocation ratio between the components change in real-time according to the need of loads; thus, the dc source of the HESS can be included with either or both of the components. Therefore, neither the SOC of single type of components nor their summation can be simply used as the residual capacity evaluation result of the system.

On the other hand, the SOC is an important factor to be used in the control of the HESS (Xie et al., 2018). Without the accurate estimation of the capacity, the remaining operation time, the power output capability, and the safety of the system cannot be determined.

The SOC evaluation technologies for traditional energy storages have been studied for many years and can be classified into four categories: the open-circuit voltage method, the ampere hour integration method, the neural network method, and the state observation method (He et al., 2012; Lu et al., 2013; Kang et al., 2014).

The open-circuit voltage method is one of the earliest approaches for battery SOC evaluation, which requires experiments' results to generate the SOC curve. The preparation of open-circuit voltage measurement is tedious. The ampere hour integration method is simple and easy to implant, but the disadvantage is obvious: it needs the accurate initial SOC value of the battery. At present, the open-circuit voltage method and the ampere hour integration method are frequently used in combination due to their complementary functions in practical battery SOC evaluation applications. The neural network method is a novel approach that has received more and more attention in recent years. As a data-driven technology, its parameters can be automatically updated. However, its drawbacks include the overreliance on historical data and computation complexity.

Overall, the above SOC estimation methods mainly aim at the single energy storage technology system. For the HESS, the SOC estimation method must consider not only the nature of the energy storage component, but also the overall operating characteristics of the system. The estimation method requires high real-time performance and accuracy. The state observation method is the method to estimate SOC by establishing a state space model, which has a clear physical meaning, as well as outstanding dynamic performance. The current commonly used methods include the Kalman filter method and the sliding mode observation method. The sliding mode observation method is based on the state space model of the energy storage component. It directly uses the control theory to make the SOC estimation results gradually converge to a specific value. It has the advantages of small calculation, good convergence property, and robustness in the interference environment (Il-Song, 2008; Il-Song, 2010; Li et al., 2017). The application of sliding mode observation method in SOC estimation has been more and more widely studied. In Gong et al. (2016), the sliding mode observation method is used to estimate the SOC of the battery, and the equivalent circuit model including the uncertain disturbance is established. The reliability of the observer is verified by simulating the constant current discharge and the operation of the electric vehicle. In Chen et al. (2016), a robust sliding mode observer for power battery is built and studied. The radial basis function (RBF) neural network is used to adjust the switch gain of the sliding mode observer, and the target factor recursive least square algorithm is used to identify the parameters of the equivalent model in real time. According to the electrochemical and thermal characteristics of the battery/supercapacitor, a real-time estimation scheme of the state parameters of the energy storage element composed of multiple sliding mode observers is designed in reference Dey et al. (2015). This scheme simulates the internal characteristics of the energy storage element and verifies the convergence of the overall estimation scheme.

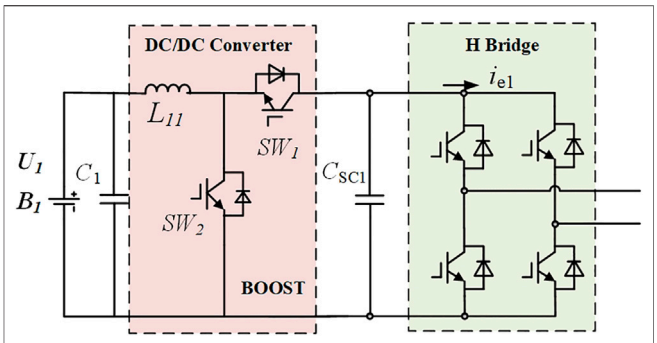

FIGURE 1 | The topology of hybrid energy storage system.

To summarize, the sliding mode observation method is more suitable for SOC estimation in HESS, because of its robustness and simple control algorithm. However, it has not been applied on the estimation of SOC of the HESS. The difficulty lies in the coupling between the energy storage components and the power electronics' circuit in the HESS. Traditionally, the remaining energy of the energy-density component is the basis of the SOC in the HESS. However, the restrictions in the discharging ability and dynamic performance of the energy-density component cannot be reflected in these models, resulting in the overrated SOC.

In this article, a dynamic equivalent SOC (ESOC) index of the HESS is proposed. With the established index, the equivalent SOC can be well reflected. Moreover, the estimation algorithm of the dynamic equivalent index is proposed based on the sliding mode observer. In addition, the models of battery, the supercapacitor, and the DC-DC converter are established to build the observer. The principle of the ESOC is introduced, and an overall dynamic ESOC estimation system is given and verified.

MATHEMATICAL MODEL OF THE HYBRID ENERGY STORAGE SYSTEM

Battery Cascaded Supercapacitors Hybrid Energy Storage System

Battery cascaded supercapacitors structure is one of the most common topologies for HESS. As shown in **Figure 1**, the battery bank and the supercapacitors module are coupled with a DC-DC converter. Since the focus of this work is to illustrate the ESOC evaluation principle, the Boost circuit is used in the following analysis. In microgrid related applications, the HESS needs to interface AC bus. Therefore, a DC-AC inverter is connected to the terminal of the supercapacitor.

In this design, the supercapacitors operate as an energy buffer. It is charged by the battery through DC-DC converter to maintain the DC side voltage of the inverter. In a normal operation, the SOC and the terminal voltage of the supercapacitors keep constant, because their energy can be recovered by the battery in real-time. When high power demand occurs, the supercapacitor can respond quickly and provide an

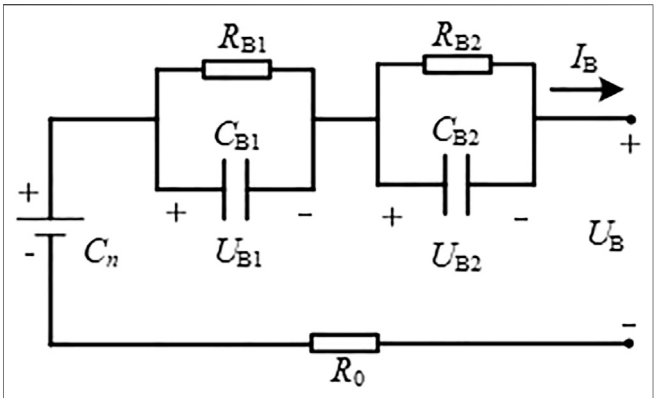

FIGURE 2 | The equivalent circuit model of battery.

instantaneous output with high climbing rate (Ben et al., 2014; Golchoubian and Azad, 2017). Due to the terminal voltage decline of supercapacitors in high power mode, the operation duration is restrained. When the voltage reaches the lower threshold, the HESS needs to quit the high power mode to recover the energy of the supercapacitors module from battery.

According to the operation principle of the battery cascaded supercapacitors HESS, the working energy storage components in different modes are as follows:

1) Normal operation mode. In this mode, it can be considered that only the battery provides power to the system. The supercapacitor acts as the DC bus buffer. The operation duration in this mode mainly depends on the capacity of the battery.
2) High power mode. In this mode, the battery and the supercapacitor respond to the output at the same time. The power allocation ratio between them usually depends on the frequency characteristics and the peak value of the output. Since the energy is extracted from the supercapacitor faster than that in the normal operation mode, there is not sufficeint time for its terminal voltage to recover from the battery. Therefore, the operation duration in this mode mainly relies on the residual energy of the supercapacitor and the output power it shares.
3) Extreme high power mode. In this mode, the output power share of the supercapacitor is much larger than that of the battery. Since the battery cannot maintain the output of the supercapacitor, the operation duration of the HESS completely depends on the SOC of the supercapacitor.

Thus, at different moment, the energy can be extracted from the HESS, which is determined by the SOC of the battery or/and the supercapacitors, as well as the output power of the system. Meanwhile, the energy recovery speed of the supercapacitors relies on the discharge speed of the battery and the rated power of the DC-DC converter. Therefore, the equivalent models of the two types of energy storage components and the DC-DC converter need to be built and integrated.

Model of the Energy Storage Components

In the HESS studied in this article, the energy-density and power-density energy storage components are the battery and the supercapacitor, respectively. In order to establish the comprehensive model of the HESS for ESOC estimation, the equivalent circuit model of the battery and the supercapacitor should be analyzed first.

As shown in **Figure 1**, the battery model used in this article is the second-order Thevenin equivalent circuit model, which has been proved to be effective in the static and dynamic characteristics simulation of the battery (Chen and Rincon-Mora, 2006).

In **Figure 2**, C_n represents the rated capacity of the battery, I_B and U_B, respectively, represent the terminal voltage and operating current of the battery, U_{ocv} is the ideal open-circuit voltage source, and R_0 represents the internal resistance. The parallel *RC* network is composed of electrochemical polarization capacitor C_{B1} and resistor R_{B1}, concentration capacitor C_{B1} and resistor R_{B1}, and concentration polarization capacitor C_{B2} and resistor R_{B2}, which are used to reflect the short-term and long-term dynamic characteristics of the battery. U_{B1} and U_{B2} represent the terminal voltages of the two RC branches.

According to the circuit theory, there are

$$\dot{U}_{ocv} = -\frac{\eta I_B}{C_n} \tag{1}$$

$$\dot{U}_{ocv} = -\frac{\eta I_B}{C_n} \tag{2}$$

$$\dot{U}_{B2} = \frac{1}{R_{B2}C_{sc2}}U_B + \frac{1}{C_{sc2}}I_B \tag{3}$$

As a power-density energy storage component, the supercapacitor belongs to the double electric layer capacitor family, whose electrode surfaces are coated with the activated carbon. In this article, an improved second-order *RC* equivalent circuit model is adopted, which is shown in **Figure 2**.

The improved second-order *RC* model simulates the effect of supercapacitor leakage current by adding parallel resistance on the basis of the traditional *RC* model and reflects the dynamic characteristics of the supercapacitor while ensuring a simple structure (Solano et al., 2013; Graydon et al., 2014). It includes three branches as follows:

1) The branch where R_{C1} and C_{sc1} are located is an instantaneous branch, which is used to simulate the instantaneous external characteristics of supercapacitor under the state of charging and discharging, and its time constant is small. U_{sc1} is its terminal voltage.
2) The branch where R_{C2} and C_{sc2} are located is the self-adjusting branch, which reflects the internal of the supercapacitor charging redistribution. U_{sc2} is its terminal voltage.
3) The branch where R_L is located is the self-discharge branch, which is used to represent the self-discharge phenomenon of the supercapacitor. R_P is the additional internal resistance. I_C and U_{out} represent the operating current and output voltage during the charging and discharging of the supercapacitor, respectively.

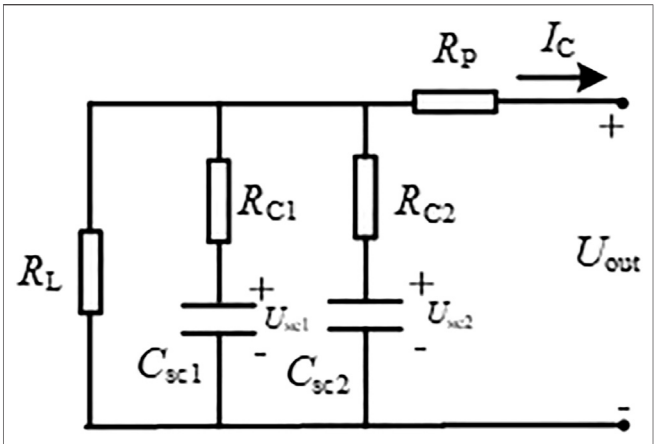

FIGURE 3 | The equivalent circuit model of Supercapacitor.

According to the **Figure 3**, there are

$$\dot{U}_{C1} = -\frac{1}{R_{C1}C_{sc1}}U_{out} + \frac{1}{R_{C1}C_{sc1}}U_{C1} + \frac{R_p}{R_{C1}C_{sc1}}I_C \tag{4}$$

$$\dot{U}_{C2} = -\frac{1}{R_{C2}C_{sc2}}U_{out} + \frac{1}{R_{C1}C_{sc2}}U_{C2} + \frac{R_p}{R_{C1}C_{sc2}}I_C \tag{5}$$

$$\begin{aligned}\dot{U}_{out} =& \left[\left(-\frac{1}{R_{C1}C_{sc1}}\right)\frac{1}{R_{C1}\left(\frac{1}{R_L}+\frac{1}{R_{C1}}+\frac{1}{R_{C2}}\right)}\right.\\ &\left.+\left(-\frac{1}{R_{C1}C_{sc1}}\right)\frac{1}{R_{C2}\left(\frac{1}{R_L}+\frac{1}{R_{C1}}+\frac{1}{R_{C2}}\right)}\right]U_{out}\\ &+\frac{1}{R_{C1}\left(\frac{1}{R_L}+\frac{1}{R_{C1}}+\frac{1}{R_{C2}}\right)}\left(\frac{1}{R_{C1}C_{sc1}}\right)U_{C1}\\ &+\frac{1}{R_{C2}\left(\frac{1}{R_L}+\frac{1}{R_{C1}}+\frac{1}{R_{C2}}\right)}\left(\frac{1}{R_{C2}C_{sc2}}\right)U_{C2}\\ &+\left[\frac{R_P}{R_{C1}^2C_{sc1}\left(\frac{1}{R_L}+\frac{1}{R_{C1}}+\frac{1}{R_{C2}}\right)}+\frac{R_P}{R_{C2}^2C_{sc2}\left(\frac{1}{R_L}+\frac{1}{R_{C1}}+\frac{1}{R_{C2}}\right)}\right]I_C\\ &= M_1U_{out} + M_2U_{C1} + M_3U_{C2} + M_4I_C\end{aligned} \tag{6}$$

The above models will be integrated into the comprehensive model of the HESS. Meanwhile, their internal components will be selected as the state variables of the sliding mode observer to estimate the remaining energy of the battery and the supercapacitor.

Equivalent Model of the Hybrid Energy Storage System

According to the equivalent circuit model of the energy storage components and the Boost converter, the comprehensive model of the battery cascaded supercapacitors HESS is established as shown in **Figure 4**.

The large signal circuit model consists of controlled voltage and current sources used to represent the dynamic characteristics of the boost converter. (Chen et al., 2004). In **Figure 4**, D represents the duty cycle of the switching device, so the input and output voltage of the converter are as follows:

$$\begin{cases} U_B = (1-D)U_{out} \\ I_B = \dfrac{1}{1-D}(I_{out} - I_C) \end{cases} \tag{7}$$

The state space model of the HESS reflects the relationship of the internal voltage and current signals, which is the basis for the sliding mode observer. Based on the internal structure diagram of the HESS, the output voltage of the energy storage system U_{out}, the terminal voltages of the ideal voltage source and two polarization capacitances of the battery model U_{ocv}, U_{B1} and U_{B2}, and the terminal voltages of the two branch capacitances of the supercapacitor model U_{sc1} and U_{sc2} are taken as the state variables x. There is

$$x = [U_{out} \quad U_{B1} \quad U_{B2} \quad U_{ocv} \quad U_{sc1} \quad U_{sc2}]^T \tag{8}$$

The sampled output currents of the system and the supercapacitor compose the input vector $u = [I_{out} \quad I_C]^T$. The output voltage of the system is selected as the output vector $y = U_{out}$.

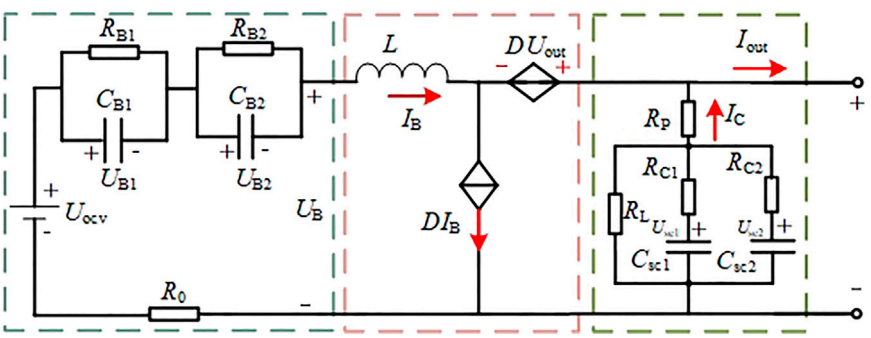

FIGURE 4 | The internal structure diagram of the HESS.

Based on **Eqs. 1–3**, **Eqs. 4–6** and **Eq. 7**), the state space model of hybrid energy storage system is given as follows:

$$\begin{bmatrix} \dot{U}_{out} \\ \dot{U}_{B1} \\ \dot{U}_{B2} \\ \dot{U}_{ocv} \\ \dot{U}_{C1} \\ \dot{U}_{C2} \end{bmatrix} = \begin{bmatrix} 0 & \frac{M_1}{1-D} & \frac{M_1}{1-D} & \frac{M_1}{1-D} & M_2 & M_3 \\ a_{11}(1-D) & a_{12} & a_{11} & -a_{11} & 0 & 0 \\ a_{21}(1-D) & a_{22} & a_{21} & -a_{21} & 0 & 0 \\ 0 & 0 & 0 & 0 & 0 & 0 \\ a_{31} & 0 & 0 & 0 & -a_{31} & 0 \\ a_{41} & 0 & 0 & 0 & 0 & -a_{41} \end{bmatrix} \begin{bmatrix} U_{out} \\ U_{B1} \\ U_{B2} \\ U_{ocv} \\ U_{C1} \\ U_{C2} \end{bmatrix} + \begin{bmatrix} -\frac{M_1}{(1-D)R_0} & \frac{M_1}{(1-D)R_0} + M_4 \\ 0 & 0 \\ 0 & 0 \\ -\frac{\eta}{C_n(1-D)} & -\frac{\eta}{C_n(1-D)} \\ 0 & \frac{R_p}{R_{C1}C_{SC1}} \\ 0 & \frac{R_p}{R_{C2}C_{SC2}} \end{bmatrix} \begin{bmatrix} I_{out} \\ I_C \end{bmatrix} \tag{9}$$

$$y = \begin{bmatrix} 1 & 0 & 0 & 0 & 0 & 0 \end{bmatrix} \cdot x \tag{10}$$

where $a_{11} = -1/R_{B0}C_{B1}$, $a_{12} = -(1/R_{B1}C_{B1}+1/R_0C_{B1})$, $a_{21} = -1/R_{B0}C_{B2}$, $a_{22} = -(1/R_{B2}C_{B2} + 1/R_0C_{B2})$, $a_{31} = -1/R_{C1}Csc_1$, $a_{41} = -1/R_{C2}Csc_2$.

When the state space model is given, the ESOC estimator needs the accurate voltage and current signals in the equivalent circuit model of energy storage elements, which will be achieved with the sliding mode observer.

DESIGN OF SLIDING MODE OBSERVER

The sliding mode observer is a nonlinear observer that obtains the estimated values of the state variables through the measured input and output values of the system. The sum of the input and the negative feedback of the output can force the system to move along a specific state curve with small and high frequency steps, which is defined as the sliding motion. Finally, the state estimation value will approach a hyperplane. Therefore, the error between the estimated output and the actual value approaches zero, so as to realize the accurate estimation of the state variables.

The sliding mode observer is based on the Luenberger observer. Its structure can be expressed as follows:

$$\dot{\hat{x}} = A\hat{x} + K(y - \hat{y}) + Bu + M(e, \rho) \tag{11}$$

where x is the state variable, u is the input variable, and y is the output variable. A and B are the system matrix and input matrix, respectively. K is the constant of the feedback correction, which is used to make the system stable, and e is the error between the observed value and the actual measured value of the state. The function M is the control variable of the sliding mode observer. When the output error is not zero, the variable is used to make the system move along the sliding mode surface at a high frequency.

The premise that the sliding mode observer can estimate the internal energy storage elements of the energy storage system is that the matrix system is observable (Gong et al., 2016). The observability matrix of the nonlinear system is expressed as

$$O_b = \begin{bmatrix} C \\ CA \\ \cdots \\ CA^{n-1} \end{bmatrix} \tag{12}$$

According to **Eq. 9** and **Eq. 10**, it can be easily proven that O_b is full rank. Therefore, the system is observable; that is, the observer can be used to observe the parameters of the HESS.

By adapting the Walcott–Zak observer (Chang and Zheng, 2015), the sliding mode observer of the HESS is established:

$$\begin{cases} \dot{\hat{U}}_{out} = \frac{M_1}{1-D}\hat{U}_{B1} + \frac{M_1}{1-D}\hat{U}_{B2} + \frac{M1}{1-D}\hat{U}_{ocv} + M_2\hat{U}_{C1} \\ \qquad + M_3\hat{U}_{C2} - \frac{M_1}{(1-D)R_0}I_{out} + \left(\frac{M_1}{(1-D)R_0} + M_4\right)I_C \\ \qquad + L_{out}sgn(e_{out}) \\ \dot{\hat{U}}_{B1} = a_{11}(1-D)\hat{U}_{out} + a_{12}\hat{U}_{B1} + a_{11}\hat{U}_{B2} - a_{11}\hat{U}_{ocv} \\ \qquad + L_{B1}\mathrm{sgn}(e_{B1}) \\ \dot{\hat{U}}_{B2} = a_{21}(1-D)\hat{U}_{out} + a_{22}\hat{U}_{B1} + a_{21}\hat{U}_{B2} - a_{21}\hat{U}_{ocv} \\ \qquad + L_{B2}\mathrm{sgn}(e_{B1}) \\ \dot{\hat{U}}_{ocv} = -\frac{\eta}{C_n(1-D)}I_{out} - \frac{\eta}{C_n(1-D)}I_B + L_{ocv}\mathrm{sgn}(e_{ocv}) \\ \dot{\hat{U}}_{C1} = a_{31}\hat{U}_{out} - a_{31}\hat{U}_{C1} + \frac{R_p}{R_{C1}C_{sc1}}I_C + L_{C1}\mathrm{sgn}(e_{C1}) \\ \dot{\hat{U}}_{C2} = a_{41}\hat{U}_{out} - a_{41}\hat{U}_{C2} + \frac{R_p}{R_{C2}C_{sc2}}I_C + L_{C2}\mathrm{sgn}(e_{C2}) \end{cases} \tag{13}$$

where $\hat{U}_{out}$, $\hat{U}_{B1}$, $\hat{U}_{B2}$, $\hat{U}_{ocv}$, $\hat{U}_{C1}$, $\hat{U}_{C2}$, respectively, represent the estimated values of U_{out}、U_{B1}、U_{B2}、U_{ocv}、U_{C1}、U_{C2} and define e_{out}、e_{B1}、e_{B2}、e_{ocv}、e_{C1}、e_{C2} as the errors between the estimated value and the actual value. L_{out}、L_{B1}、L_{B2}、L_{ocv}、L_{C1} and L_{C2} are the feedback gains. The function sgn is defined as

$$sgn(e) = \begin{cases} 1 & e > 0 \\ -1 & e < 0 \end{cases} \tag{14}$$

If the sliding surface $s = e_B$ is defined, the state equation of error is

$$\begin{cases} \dot{e}_{out} = \dfrac{M_1}{1-D}e_{B1} + \dfrac{M_1}{1-D}e_{B2} + \dfrac{M_1}{1-D}e_{ocv} + M_2 e_{C1} \\ \quad +M_3 e_{C2} - L_{out}sgn(e_{out})I_C + |d_1| \\ \dot{e}_{B1} = a_{11}(1-D)e_{out} + a_{12}e_{B1} + a_{11}e_{B2} - a_{11}e_{ocv} \\ \quad -L_{B1}sgn(e_{B1}) + |d_2| \\ \dot{e}_{B2} = a_{21}(1-D)e_{out} + a_{22}e_{B1} + a_{21}e_{B2} - a_{21}e_{ocv} \\ \quad -L_{B2}sgn(e_{B2}) + |d_3| \\ \dot{e}_{ocv} = -L_{ocv}sgn(e_{ocv}) + |d_4| \\ \dot{e}_{C1} = a_{31}e_{out} - a_{31}e_{C1} + L_{C1}sgn(e_{C1}) + |d_5| \\ \dot{e}_{C2} = a_{41}e_{out} - a_{41}e_{C2} + L_{C2}sgn(e_{C2}) + |d_6| \end{cases} \tag{15}$$

where d_1–d_6 is used to simulate the influence of system noise.

According to the requirements of Lyapunov stability function, it is necessary to ensure that the difference value of each voltage of the state variable approaches 0. Take U_{out} as an example. If the system is stable on the sliding surface, it needs to meet the following requirements:

$$V_{out} = e_{out} \cdot \dot{e}_{out} < 0 \tag{16}$$

According to **Eq. 15**, if **Eq. 16** stands, the feedback gain L_{out} should satisfy

$$L_{out} > \left|\frac{M_1}{1-D}e_{B1}\right| + \left|\frac{M_1}{1-D}e_{B2}\right| + \left|\frac{M_1}{1-D}e_{ocv}\right| + |M_2 e_{C1}| + |M_2 e_{C1}| + |d_1| \tag{17}$$

Assuming that the estimated terminal voltage gradually stabilizes in a certain period of time and finally reaches the sliding mode surface, that is, $e_{out} = \dot{e}_{out} = 0$, at this time, the observation of U_{B1} in the battery equivalent model is considered first. If it can still meet the requirements of Lyapunov stability function, $e_{B1} = \dot{e}_{B1} = 0$ in the stable state, then there is

$$L_{B1} > |a_{12}e_{B1}| + |a_{11}e_{B2}| + |b_{11}e_{ocv}| + |d_2| \tag{18}$$

Considering the observation of U_{B2} and U_{ocv}, the following formula stands:

$$L_{B2} > |a_{12}e_{B2}| + |a_{21}e_{ocv}| + |d_3| \tag{19}$$

$$L_{ocv} > |d_4| \tag{20}$$

Then, the observation of U_{C1} and U_{C2} inside the supercapacitor is analyzed. According to the requirements of Lyapunov stability function, its feedback gain meets the following formulas:

$$L_{C1} > |a_{31}e_{C1}| + |d_5| \tag{21}$$

$$L_{C2} > |a_{41}e_{C2}| + |d_6| \tag{22}$$

According to the above analysis, if the designed sliding mode observer can realize the accurate estimation of relevant parameters, and L_{out}、L_{B1}、L_{B2}、L_{ocv}、L_{C1} and L_{C2} need to meet the requirements of **Eqs. 17–22**. In the practical design, because the above feedback gains are only constrained by the minimum value, the error value in the formula can be considered as the extreme value. Through the reasonable selection of L_{out}、L_{B1}、L_{B2}、L_{ocv}、L_{C1} and L_{C2}, the state variables in the HESS can be accurately estimated by using the sliding mode observer.

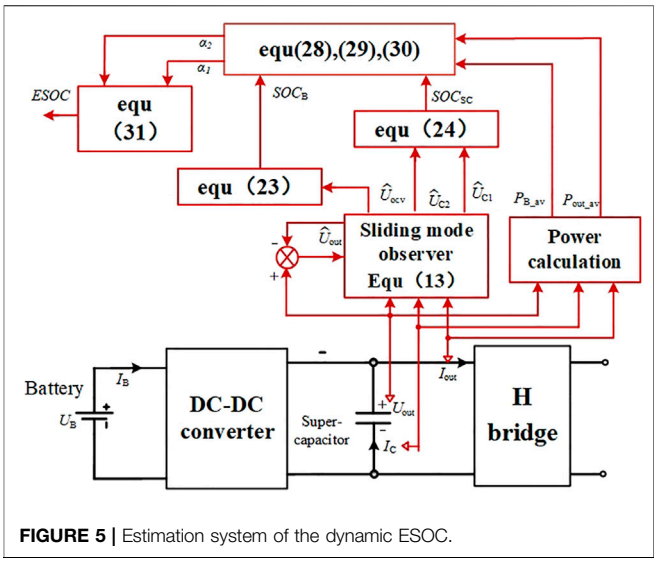

FIGURE 5 | Estimation system of the dynamic ESOC.

THE ESTIMATION OF DYNAMIC EQUIVALENT STATE OF CHARGE

First, we introduce the proposed estimation System of the dynamic ESOC. The complete estimation system of the $ESOC_D$ is based on sliding mode observer and shown in **Figure 5**. The output voltage U_{out}, current I_{out} and supercapacitor branch current I_C of the DC side are collected in each T_{SOC}. Based on the sliding mode observer defined in **Eq. 13**, the observed values of $\hat{U}_{ocv}$, $\hat{U}_{C1}$ and $\hat{U}_{C2}$ can be obtained. Through **Eq. 23** and **Eq. 24**, the SOCs of the battery and supercapacitor can be obtained.

At the same time, the average values of P_{B_av} and P_{out_av} are generated from the collected voltage and current. Consequently, **Eq. 28**, **Eq. 29**, and **Eq. 30** are used to obtain the weighting coefficients α_1 and α_2 for **Eq. 31** to finally calculate the $ESOC_D$. With this design, the estimation of the dynamic $ESOC_D$ can be realized with the available voltage and current signals.

According to the above analysis, the voltage of ideal voltage source U_{OCV} and the capacitance voltages U_{C1} and U_{C2} of the two branches of the supercapacitor in the state space equation of the HESS can be accurately estimated with the sliding mode observer. Considering that the observed value of U_{OCV} has a nonlinear function relationship with the SOC of battery, which can be obtained through experiments, the specific method is to measure the U_{OCV} of the battery after a period of continuous discharge with a fixed current value. The SOC at the corresponding time can be obtained by simple integral calculation. After several experiments, U_{OCV} and SOC value data can be synthesized into a curve by the least square method. In this article, they can be calculated by the following **Eq. 25**:

$$U_{ocv} = K_0 + K_1 In(SOC_B) + K_2 In(1 - SOC_B) \quad (23)$$

where K_0–K_2 are the experimental constants.

According to the definition of SOC, that is, the ratio of residual capacity to rated capacity, the SOC of supercapacitor can be defined as

$$SOC_{SC} = \frac{C_{SC1}U_{C1} + C_{SC2}U_{C2}}{C_{SC1}U_{C1N} + C_{SC2}U_{C2N}} \times 100\% \quad (24)$$

where U_{C1N} and U_{C2N} are rated voltages of capacitors C_{SC1} and C_{SC2}.

As aforementioned, for the HESS, which is composed of battery and supercapacitor, its SOC cannot be defined as the sum of the remaining capacity of the two energy storage components and the total capacity of the system. Since the energy-density of the battery is far larger than that of the supercapacitors, the sum of their remaining capacity will mainly represent the SOC of the battery. However, in high power and extreme high power operation modes, the capacity of the battery cannot be utilized because of its discharge speed. In these modes, the SOC of the HESS is determined by the supercapacitors.

Therefore, the ESOC of the HESS needs to be evaluated dynamically according to the real-time operation mode of the system. In this work, the dynamic ESOC $ESOC_D$ is defined with two weighting coefficients α_1 and α_2, which change with the real-time operation mode:

$$ESOC_D = \frac{\alpha_1 SOC_B + \alpha_2 SOC_{SC}}{\alpha_1 + \alpha_2} \quad (25)$$

$ESOC_D$ is estimated in every time period T_{SOC}. With the proposed sliding mode observer, the average output powers P_{B_av} and P_{out_av} of the battery and the system can be obtained based on the real-time detected U_{out}, I_C and I_{out} in T_{SOC}:

$$P_{out\_av} = U_{out} \cdot I_{out} \cdot T_{SOC} \quad (26)$$

$$P_{B\_av} = P_{out\_av} - U_{out} \cdot I_C \quad (27)$$

The SOC lower and upper thresholds of battery and supercapacitor are defined as (SOC_{Bmin}, SOC_{Bmax}) and (SOC_{SCmin}, SOC_{SCmax}), respectively. N_{t1} and N_{t2} are defined as the number of time periods that two kinds of energy storage components can continue to operate with the current output power:

$$N_{t1} = \frac{E_{BN}(SOC_B - SOC_{Bmin})}{P_{B\_av}T_{SOC}} \quad (28)$$

$$N_{t2} = \frac{E_{SCN}(SOC_{SC} - SOC_{SCmin})}{(P_{out\_av} - P_{B\_av})T_{SOC}} \quad (29)$$

where E_{BN} and E_{SCN}, respectively, represent the rated capacity of battery and supercapacitor.

Therefore, N_{t1} and N_{t2} dynamically change with time and reflect the duration of continuous operation of the two kinds of energy storage components in real time. In order to ensure that the SOCs of energy storage components are restricted within the threshold range, the weighting coefficients are further designed as the reciprocal value of N_{t1} and N_{t2}:

TABLE 1 | Simulation parameters.

Parameters	Symbol	Value
Battery		
Electrochemical polarization capacitor	C_{B1}	2000 F
Resistance 1	R_{B1}	0.007 Ω
Concentration polarization capacitance	C_{B2}	200 F
Resistance 2	R_{B2}	0.05 Ω
Internal resistance	R_0	0.027 Ω
Supercapacitor		
Instantaneous branch resistance	R_{C1}	0.0025 Ω
Instantaneous branch capacitance	C_{sc1}	1.01 F
Self-adjusting branch resistance	R_{C2}	13364 Ω
Self-adjusting branch capacitance	C_{SC2}	0.1 F
Self-discharge branch resistance	R_L	12000 Ω
Additional internal resistance	R_P	0.001 Ω
Boost Converter		
Capacitance	C_1	5e-5 F
Inductance	L_{11}	0.01 H

$$\alpha_1 = \frac{1}{N_{t1}}, \ \alpha_2 = \frac{1}{N_{t2}} \quad (30)$$

The physical meaning of α_1 and α_2 is the ratio of the energy consumed by the battery and supercapacitor to their respective residual capacity in the current time of T_{SOC}. With this design, the corresponding weighting coefficient of the energy storage component with long operation duration will be relatively small, and that of the one with short duration will be relatively large. The greater the operation duration difference, the greater the weight coefficient difference, so that $ESOC_D$ can reflect the residual operation duration of the HESS according to its operation mode. For example, with extreme high power output mode, although the SOC_B is high, since P_{B_av} is low, α_1 will be a small number. Therefore, the effective proportion of SOC_B in $ESOC_D$ will be small.

Denote $m = \alpha_2/\alpha_1$, and then the dynamic $ESOC_D$ can be expressed as

$$ESOC_D = \frac{SOC_B + mSOC_{SC}}{1 + m} \quad (31)$$

In **Equation 31**, since both values of the SOC_B and $SOCsc$ are between 0 and 1, the calculated $ESOC_D$ value will be between 0 and 1. According to **Eq. 31**, there is

$$\min(SOC_B, SOC_{SC}) < ESOC_D < \max(SOC_B, SOC_{SC}) \quad (32)$$

It can be seen from **Eq. 32** that the upper and lower limits of $ESOC_D$ will not exceed those of the battery and supercapacitor. By defining the $ESOC_D$, the real-time estimation of output power and SOCs of the battery and supercapacitors can be used to accurately determine the residual operation duration of the HESS in the current conditions.

SIMULATION RESULTS

In order to verify the effectiveness of the designed sliding mode observer in SOC estimation, a simulation model is built based on

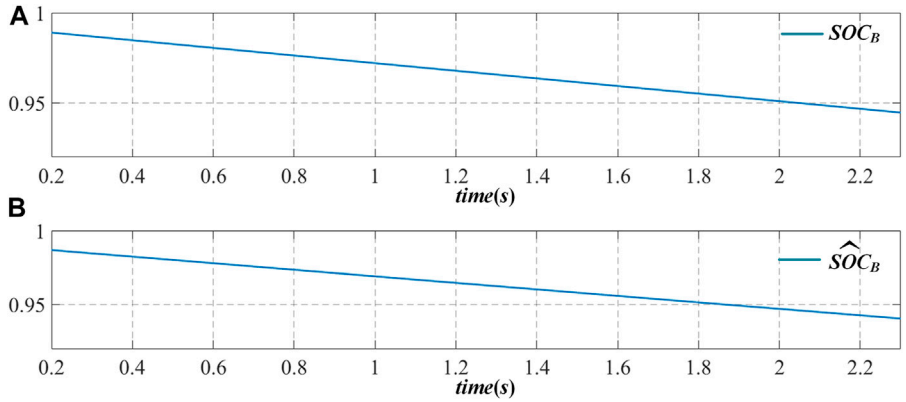

FIGURE 6 | Schematic diagram of SOC actual value and estimated value change of battery in high power mode.

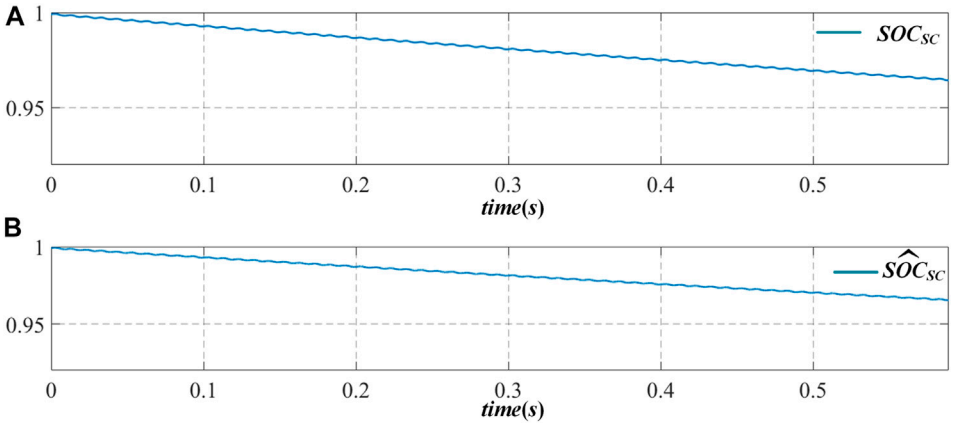

FIGURE 7 | Schematic diagram of SOC actual value and estimated value change of supercapacitor in high power mode.

the MATLAB/Simulink platform. The model is based on the HESS model in **Figure 1**, while an adjustable resistive load is connected to the output of the DC-AC inverter to change the output power of the system. The simulation parameters are shown in **Table 1**.

According to the simulation model, considering the corresponding accuracy requirements of the sliding mode observer, the parameters are selected as follows: L_{out} = 100, L_{B1} = 21, L_{B2} = 12, L_{ocv} = 0.01, L_{C1} = 1 and L_{C2} = 1. In order to intuitively reflect the real-time observation effect of sliding mode observer on the battery and supercapacitor, the HESS is considered in the high-power working mode. For comparison, when the basic output characteristics are the same, the existing battery and supercapacitor models in Simulink are also used at the same time, and the value of SOC, which is measured directly, is taken as the actual value.

In the high-power operation mode, the battery and the supercapacitor provide power to the load at the same time, and the SOC of the two energy storage components changes in real-time according to their outputs. **Figures 6A,B** are the actual and estimated values of the SOC of the battery in operation, while **Figures 7A,B** show those of the supercapacitor. From **Figures 6**,**7**, it can be seen that the actual value is basically consistent with the estimated value.

The error between them is within 0.02, which proves the accuracy of SOC estimation based on sliding mode observer proposed in this article.

According to the definition of $ESOC_D$ in **Eq. 31**, the simulation model is established to analyze its effectiveness. The max–min ranges of the energy storage components are, respectively, set as (SOC_{Bmin}, SOC_{Bmax}) = (0.4, 1), (SOC_{SCmin}, SOC_{SCmax}) = (0.6, 1), P_{Bmax} = 324 w, P_{SCmax} = 3 KW, E_B = 1 Ah. The initial SOC of the battery is set to 0.69. The supercapacitor capacity C_{SC} is 3 F. The experiments are designed in three modes.

In the normal operation mode, the supercapacitor is not involved in providing energy and the output power of the battery P_{B1} = 240 W. In the high power mode, the battery and the supercapacitor supply power to the system at the same time. The output power of the battery P_{B2} = 300 W, and the output power of the supercapacitor P_{SC1} = 1100 W. In the extreme high power mode, the output of the supercapacitor occupies the main power output, and P_{SC2} = 2000 W.

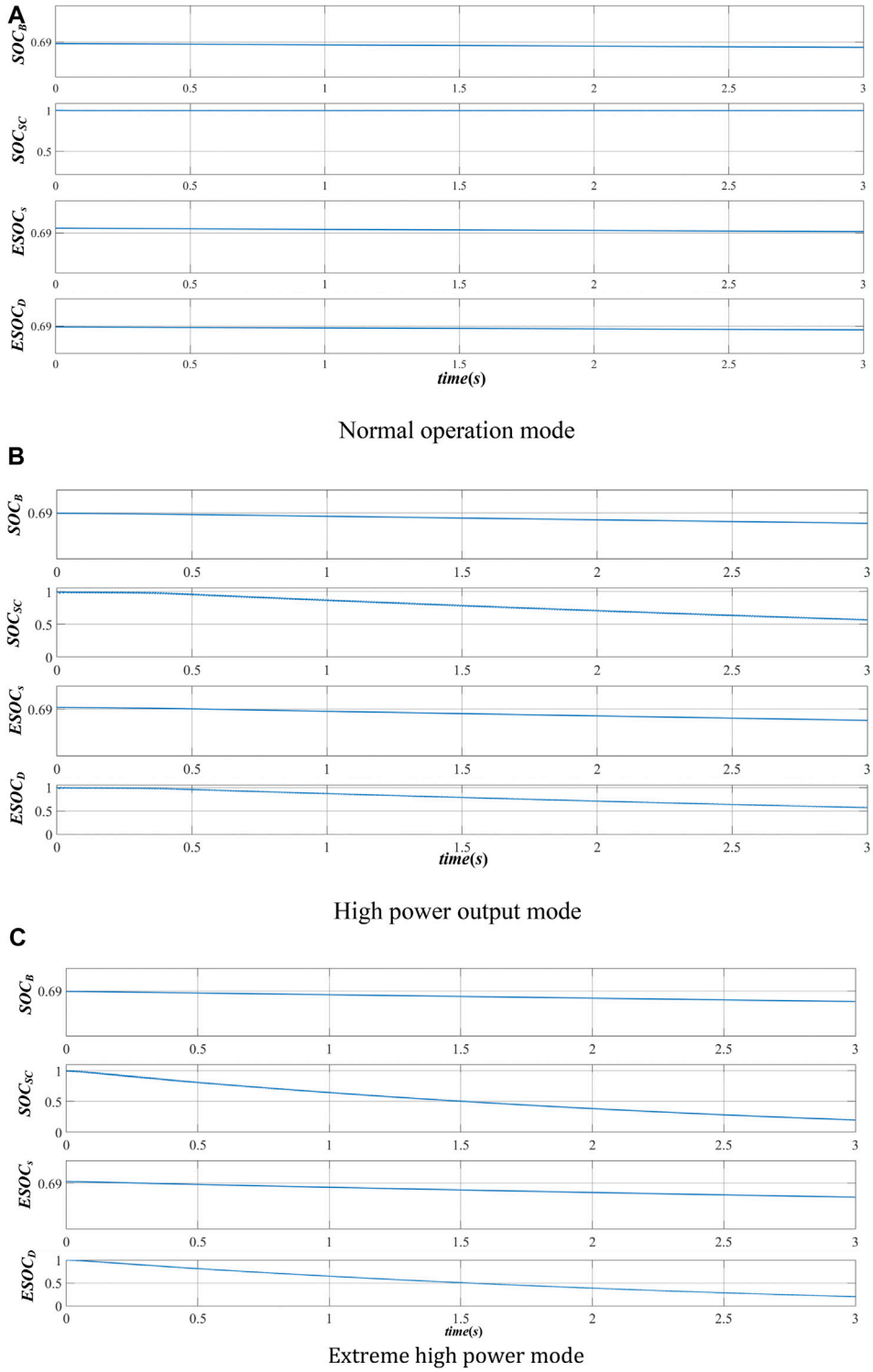

FIGURE 8 | Schematic diagram of SOCB, SOCSC, ESOCs, and ESOCD changes.

Figure 8 shows the changes of the SOC of the battery SOC_B, the SOC of the supercapacitor SOC_{SC}, and two sets of *ESOC* values in different mode. Except the proposed $ESOC_D$, the $EOSC_s$ is defined as

$$ESOC_S = \frac{E_{BN}SOC_B + E_{SCN}SOC_{SC}}{E_{BN} + E_{SCN}} \quad (33)$$

$EOSC_s$ mainly reflects the direct definition of the ESOC of HESS by calculating the residual capacity of all energy storage elements. In this work, $EOSC_s$ is used for comparison.

Figure 8A shows that, in the normal operation mode, SOC_{SC} keeps constant. The $ESOC_D$ follows SOC_B. **Figure 8B** shows that, in the high power mode, the SOC_{SC} starts to decline from the initial time, since its power cannot be recovered from the battery. Therefore, the change trend of $ESOC_D$ is consistent with that of the supercapacitor. In this process, although the SOC_B of the battery drops faster than that in **Figure 8A**, $ESOC_D$ is mainly affected by the supercapacitor. **Figure 8C** shows the change of SOCs in the extreme high power mode. It can be seen that the SOC_{SC} drops more rapidly, which drops to about 0.3 within 3S. At this time, the change trend of $ESOC_D$ is almost the same as SOC_{SC}. The influence of SOC_B on $ESOC_D$ can be ignored.

As the $ESOC_s$ reflects the residual capacity of the HESS, it can be seen from **Figure 8** that the change of $ESOC_s$ in the three modes is consistent with SOC_B. It is obvious that the residual energy of the HESS cannot reflect the remaining operation duration. If the real-time equivalent *SOC* index is not properly defined and used, the overcharge and overdischarge of energy storage components will occur, which will reduce the safety and reliability of the system.

CONCLUSION

A sliding mode observer based dynamic ESOC estimation method for HESS is proposed in this article. By analyzing the topological structure of the HESS and the equivalent circuit model of the energy storage elements, the corresponding sliding mode observer is established by using the state space model. The parameters of the sliding mode observer are designed to realize the real-time and accurate estimation of the internal parameters of the HESS. In view of the high coupling of different types of energy storage elements, the concept of dynamic ESOC is proposed. Using the real-time acquisition value and estimation value, the remaining working time of energy storage elements is taken as the comparison way, so that ESOC can evaluate the working state of the whole energy storage system. The simulation results further verify the accuracy and real-time performance of SOC estimation based on sliding mode observer, as well as the effectiveness of dynamic ESOC evaluation.

DATA AVAILABILITY STATEMENT

The original contributions presented in the study are included in the article/Supplementary Material. Further inquiries can be directed to the corresponding author.

AUTHORS' CONTRIBUTIONS

YW did the modeling and writing. WJ provided the technical support. CZ performed running case studies. ZX and YD helped modify the article.

FUNDING

This paper is supported by National Natural Science Foundation of China (51877041), Basic Research Program of Jiangsu Province (BK20200385), Guangdong Basic and Applied Basic Research Foundation (2020A1515011160) and the foundation of Jiangsu Provincial Key Laboratory of Smart Grid Technology and Equipment, Southeast University.

REFERENCES

Akar, F., Tavlasoglu, Y., and Vural, B. (2017). An Energy Management Strategy for a Concept Battery/Ultracapacitor Electric Vehicle with Improved Battery Life. *IEEE Trans. Transp. Electrific.* 3 (1), 191–200. doi:10.1109/tte.2016.2638640

Ben, I. S., Bayoudhi, B., and Diallo, D. (2014). *EV energy management strategy based on a single converter fed by a hybrid battery/supercapacitor power source*. Tunisia: Sfax, 246–250.2014 First International Conference on Green Energy ICGE 2014

Chang, F., and Zheng, Z. (2015). *An SOC estimation method based on sliding mode observer and the Nernst Equation*. Montreal: IEEE Energy Conversion Congress and Exposition (ECCE), 6187–6190. QC, 2015.

Chen, M., and Rincon-Mora, G. A. (2006). Accurate electrical battery model capable of predicting runtime and I-V performance. *IEEE Trans. Energ. Convers.* 21 (2), 504–511. doi:10.1109/tec.2006.874229

Chen, X., Shen, W., Dai, M., Cao, Z., Jin, J., and Kapoor, A. (2016). Robust Adaptive Sliding-Mode Observer Using RBF Neural Network for Lithium-Ion Battery State of Charge Estimation in Electric Vehicles. *IEEE Trans. Veh. Technol.* 65 (4), 1936–1947. doi:10.1109/tvt.2015.2427659

Chen, Y. F., Qiu, S. S., and Long, M. (2004). *Nonlinear large-signal modeling of PWM DC-DC switching power converters, 2004 International Conference on Communications*, 2. Chengdu: Circuits and Systems (IEEE Cat. No.04EX914), 1507–1510.

Choi, M.-E., Kim, S.-W., and Seo, S.-W. (2012). Energy Management Optimization in a Battery/Supercapacitor Hybrid Energy Storage System. *IEEE Trans. Smart Grid* 3 (1), 463–472. doi:10.1109/tsg.2011.2164816

Dey, S., Mohon, S., Pisu, P., Ayalew, B., and Onori, S. (2015). *Online state and parameter estimation of Battery-Double Layer Capacitor Hybrid Energy Storage System, 2015 54th IEEE Conference on Decision and Control*. Osaka: CDC, 676–681.

Franquelo, L., Rodriguez, J., Leon, J., Kouro, S., Portillo, R., and Prats, M. (2008). The age of multilevel converters arrives. *EEE Ind. Electron. Mag.* 2 (2), 28–39. doi:10.1109/mie.2008.923519

Golchoubian, P., and Azad, N. L. (2017). Real-Time Nonlinear Model Predictive Control of a Battery-Supercapacitor Hybrid Energy Storage System in Electric Vehicles. *IEEE Trans. Veh. Technol.* 66 (11), 9678–9688. doi:10.1109/tvt.2017.2725307

Gong, X., Huang, Z., Li, L., Lu, H., Liu, S., and Wu, Z. (2016). *A new state of charge estimation for lithium-ion battery based on sliding-mode observer and battery status, 2016 35th Chinese Control Conference*. Chengdu: CCC, 8693–8697.

Graydon, J. W., Panjehshahi, M., and Kirk, D. W. (2014). Charge redistribution and ionic mobility in the micropores of supercapacitors. *J. Power Sourc.* 245, 822–829. doi:10.1016/j.jpowsour.2013.07.036

Hammond, P. W. (1995). *A new approach to enhance power quality for medium voltage drives*. Denver, CO, USA: Industry Applications Society 42nd Annual Petroleum and Chemical Industry Conference, 231–235.

He, H., Zhang, X., Xiong, R., Xu, Y., and Guo, H. (2012). Online model-based estimation of state-of-charge and open-circuit voltage of lithium-ion batteries in electric vehicles. *Energy* 39 (1), 310–318. doi:10.1016/j.energy.2012.01.009

II-Song, K. (2010). A Technique for Estimating the State of Health of Lithium Batteries through a Dual-Sliding-Mode Observer. *IEEE Trans. Power Elect.* 25 (4), 1013–1022.

II-Song, K. (2008). Nonlinear State of Charge Estimator for Hybrid Electric Vehicle Battery. *IEEE Trans. Power Elect.* 23 (4), 2027–2034.

Kang, L., Zhao, X., and Ma, J. (2014). A new neural network model for the state-of-charge estimation in the battery degradation process. *Appl. Energ.* 121 (5), 20–27. doi:10.1016/j.apenergy.2014.01.066

Kim, S.-T., Bae, S., Kang, Y. C., and Park, J.-W. (2015). Energy Management Based on the Photovoltaic HPCS with an Energy Storage Device. *IEEE Trans. Ind. Electron.* 62 (7), 4608–4617. doi:10.1109/tie.2014.2370941

Kouro, S., Malinowski, M., Gopakumar, K., Pou, J., Franquelo, L. G., Bin Wu, B., et al. (2010). Recent advances and industrial applications of multilevel converters. *IEEE Trans. Ind. Electron.* 57 (8), 2553–2580. doi:10.1109/tie.2010.2049719

Li, W., Liang, L., Liu, W., and Wu, X. (2017). State of Charge Estimation of Lithium-Ion Batteries Using a Discrete-Time Nonlinear Observer. *IEEE Trans. Ind. Electron.* 64 (11), 8557–8565. doi:10.1109/tie.2017.2703685

Lu, L., Han, X., Li, J., Hua, J., and Ouyang, M. (2013). A review on the key issues for lithium-ion battery management in electric vehicles. *J. Power Sourc.* 226 (3), 272–288. doi:10.1016/j.jpowsour.2012.10.060

Solano, J., Hissel, D., and P'era, M. C. (2013). Modeling and parameter identification of ultracapacitors for hybrid electrical vehicles. *Proc. IEEE 9th Veh. Power Propul. Conf.*, 1–4.

Wang, C., Li, X., Guo, L., and Li, Y. W. (2014). A Nonlinear-Disturbance-Observer-Based DC-Bus Voltage Control for a Hybrid AC/DC Microgrid. *IEEE Trans. Power Elect.* 29 (1), 6162–6177. doi:10.1109/tpel.2013.2297376

Xie, B., Liu, Y., Ji, Y., and Wang, J. (2018). Two-Stage Battery Energy Storage System (BESS) in AC Microgrids with Balanced State-of-Charge and Guaranteed Small-Signal Stability. *Energies* 11, 322. doi:10.3390/en11020322

Conflict of Interest: Author CZ was employed by Tongling Power Supply Company.

The remaining authors declare that the research was conducted in the absence of any commercial or financial relationships that could be construed as a potential conflict of interest.

Publisher's Note: All claims expressed in this article are solely those of the authors and do not necessarily represent those of their affiliated organizations, or those of the publisher, the editors, and the reviewers. Any product that may be evaluated in this article, or claim that may be made by its manufacturer, is not guaranteed or endorsed by the publisher.

frontiers in Energy Research

ORIGINAL RESEARCH
published: 25 August 2021
doi: 10.3389/fenrg.2021.723665

A Marginal Contribution Theory-Based Energy Efficiency Contribution Analysis for Integrated Energy System

Shihai Yang[1,2,3], *Mingming Chen*[1,3]* *and Qiang Zuo*[1,3]

[1]State Grid Jiangsu Electric Power Co. LTD., Nanjing, China, [2]College of Energy and Electrical Engineering, Hohai University, Nanjing, China, [3]State Grid Electric Power Demand Side Coordinated Control Technology Joint Laboratory, Nanjing, China

The energy efficiency analysis is a prerequisite for the construction of the integrated energy system (IES). In this study, a novel energy efficiency analysis method is proposed considering different energy subsystems in the IES. First, the energy efficiency index of the subsystems and conversion devices is formed for elaborating their influence on the IES. The IES is composed of four energy subsystems, i.e., power/gas/heat/cooling subsystems, and six energy conversion devices. Next, the energy efficiency contribution models of energy subsystems and conversion devices are proposed based on their energy efficiency index, respectively. Then, in order to calculate the energy flow in the IES, an equivalent topological model of the IES weighted directed graph is proposed to calculate the energy efficiency contribution. Finally, an actual park is employed to illustrate the validity of the proposed analysis method.

Keywords: integrated energy system, weighted directed graph, energy efficiency contribution, energy efficiency, energy quality coefficient

OPEN ACCESS

Edited by:
Yingjun Wu,
Hohai University, China

Reviewed by:
Bei Han,
Shanghai Jiao Tong University, China
Yujian Ye,
Southeast University, China

***Correspondence:**
Mingming Chen
rd1228@163.com

Specialty section:
This article was submitted to Smart Grids, a section of the journal Frontiers in Energy Research

Received: *11 June 2021*
Accepted: *21 July 2021*
Published: *25 August 2021*

Citation:
Yang S, Chen M and Zuo Q (2021) A Marginal Contribution Theory-Based Energy Efficiency Contribution Analysis for Integrated Energy System. Front. Energy Res. 9:723665. doi: 10.3389/fenrg.2021.723665

INTRODUCTION

Energy is the fundamental and motivation of society development. With the rapid growth of the economy, the energy demand has a sharp increase. In the past, the main source for the energy demand is the traditional fossil energy sources, such as coal and oil. However, these fossil energy sources caused a huge concern on the environment pollution.

Therefore, in order to cope with the challenges of environmental pollution and shortage of conventional energy (Zhang et al., 2020), the concept of IES has gained widespread attention (Wang et al., 2017) because it can realize the various energy complementarity (Xue, 2015). In order to achieve the purpose of the IES, it is important to improve the energy utilization efficiency of IES(Abu-Rayash and Dincer, 2020).

The global renewable and sustainable energy industry has witnessed a rapid development over the past decades (Wang et al., 2020). Energy efficiency is a generic index to measure the relationship between the input and output of the energy. There are many energy efficiency assessment methods being proposed and are mainly based on the first law of thermodynamics and the second law of thermodynamics. The first law of thermodynamics focuses on the "quantity" of energy and is mainly studied in the content of heat pumps (Willem et al., 2017), combining cooling, heat, and power (CCHP) units (Wang et al., 2015), HVAC (Alves et al., 2016), and the IES. The second law of thermodynamics focuses on the "quality" of energy. It uses the size of the exergy to evaluate differences in the ability of doing work. The assessment method based on the second law of thermodynamics is frequently utilized in the field of thermodynamic engineering. The first law of thermodynamics ignores the difference of energy grade and the loss of "quality" of the energy in the

system. While the second law of thermodynamics considers these problems. Therefore, the energy efficiency assessment method used in this paper adopts the second law of thermodynamics.

There are many researches using the assessment method based on thermodynamics to analyze energy systems' energy efficiency. Birol and Keppler (2000) propose that the energy efficiency of the system can be improved from two aspects. The first one introduces new technologies that can increase the productivity of each energy unit, and the second one adjusts the price of energy through economic instruments, but they ignore the reasonable utilization of energy devices which can improve the energy efficiency economically. In Miao et al. (2020), the layering approach has been applied to evaluate the energy efficiency of the IES, and the energy utilization structure of the IES is proposed. While this work does not consider the influence of energy types in the layering approach, Filippini and Hunt (2016); Zou et al. (2013); and Kavousian and Rajagopal (2014) propose a new indicator to evaluate the energy efficiency of the system named energy intensity. The energy efficiency evaluation models considering energy intensity can eliminate the bad factors like unnecessary energy consumption from all production sections of the system. Torres et al. (2018) and Choi et al. (2018) investigate effective ways to improve the energy efficiency of energy storage devices, and the results show that improvements in the energy efficiency of energy storage devices contribute to the availability of the system. Nevertheless, this research ignores the analysis of the operation cost of the energy storage device, which may reduce the energy efficiency of the IES. Liu et al. (2020) propose an improved dynamic energy grading system to evaluate energy in the building. However, this study ignores the analysis of multienergy coupling in the building. Elmirghani et al. (2018) propose some techniques to improve the energy efficiency in general, while this measure ignores the internal energy flow relationship of the evaluation object. Obviously, many studies concentrate on the analysis of system energy efficiency, but paying little attention to the energy grade and difference.

To address these problems, this work proposes the definition of energy efficiency contribution based on the marginal contribution. Actually, "marginal contribution" means "marginal utility". It is a terminology of finance. In microeconomics, the marginal utility means when adding (or removing) a unit of goods or service, the utility increasing (or decreasing) the income of the goods or service. This definition reflects the derivative of the utility to the goods or service. According to this concept, the energy efficiency contribution is represented when the energy efficiency of the energy subsystem or device adds (or removes) a unit, the utility increasing (or decreasing) the energy efficiency of the integrated energy system. Therefore, this article utilizes the partial derivative to define the energy efficiency contribution. First, the structure of the IES is described detailedly and the energy efficiency model of the IES is obtained. Next, according to the definition of energy efficiency, the energy efficiency index of energy subsystems and conversion devices can be obtained. Then, according to the content above, the energy efficiency contribution models of the energy subsystems and devices can be deduced. Finally, this study adopts a weighted directed graph modeling the IES to handle the energy efficiency contribution models. Compared with traditional energy efficiency assessment methods, this method is innovative in that it proposes the concept of energy efficiency contribution according to the different contribution degree of energy subsystems to the energy efficiency of the IES, which reasonably reveals the hierarchy of energy efficiency of energy subsystem.

The rest of this study is structured as follows. *Description About Energy Efficiency Indexes of the IES* introduces the energy efficiency expression of the IES in detail. In *Energy Efficiency Index of Subsystems and Energy Conversion Devices*, energy efficiency models of subsystems and energy conversion devices are proposed and illustrated. Then the energy efficiency contribution models of each subsystem and energy conversion devices are provided in *Energy Efficiency Contribution Models for Energy Subsystems* and *Impact of Energy Conversion Devices on the IES*. *Energy Efficiency Contribution Method Based on Weighted Directed Graph* provides a feasible-solution method to the energy efficiency contribution models. Then its simulation analysis on the energy efficiency contribution of each subsystem is provided in *Case Study*. Some conclusions are finally drawn in *Conclusion*.

DESCRIPTION OF ENERGY EFFICIENCY INDEXES OF THE IES

The Structure of the IES

This article considers four types of energy, i.e., power, heat, cooling, and natural gas. The IES can be divided into the power subsystem, the heat subsystem, the cooling subsystem, the natural gas subsystem, and the energy conversion devices like power boiler, combined heat and power (CHP) unit, power to gas (P2G), gas boiler, and absorption chiller, as shown in **Figure 1**. Each energy subsystem includes energy transmission, storage, and load. These energy conversion devices include the conversion and transmission of energy, and the loss of transmission is not considered. The natural gas can be converted into heat by the gas boiler. The waste heat recovery boiler in the CHP converts the natural gas into heat, and the gas turbine in the CHP converts the natural gas into power. P2G can convert the off-peak power into natural gas which is easy to store. In addition, refrigeration equipment can convert the power into cooling or into heat by the power boiler. The absorption chiller can convert the heat into cooling, and it is one of the energy inputs of the cooling subsystem.

This section mainly analyzes the energy efficiency assessment model of the IES, making preparation for the analysis of the energy efficiency of energy subsystems and energy conversion devices.

Energy Efficiency Assessment Model of the IES

The energy efficiency of the IES can be defined as the ratio of the energy demand to the energy input from the external system. It can reflect the energy loss in the IES. When the system contains energy storage device, it needs to be considered in the process of energy transmission.

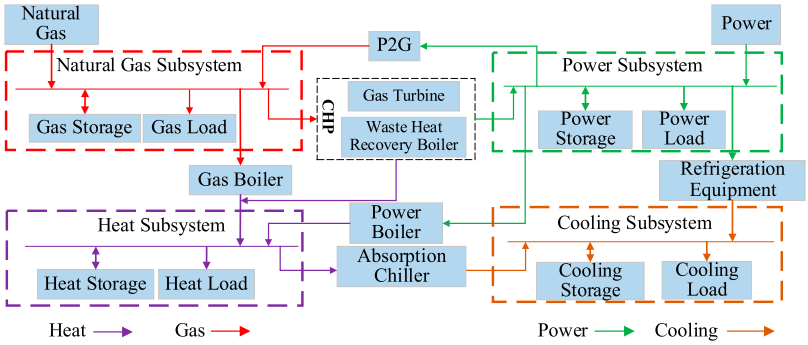

FIGURE 1 | The structure of the integrated energy system.

The traditional calculation method of energy efficiency only considers the quantity superposition of energy. However, the energy system has another important attribute like quality, which has been ignored. The quality of energy means the degree of the energy level. If the energy system ignores the difference in energy level, it cannot represent the degree of energy utilization accurately. As a result, the energy quality loss in the IES cannot be revealed. Therefore, in this research, an energy efficiency assessment model considering the energy quality coefficient is established.

The energy quality coefficient is defined as the ratio of the work did by different energy system to their total energy, which can be shown as

$$\omega_e = \frac{W_{dw}}{W_t}, \tag{1}$$

where W_{dw} is the work did by one of the energy systems and W_t is the total energy.

The energy quality coefficient reflects the ability of the energy which does work. This ability is usually a fixed value in a standard environment and never vary due to different conversion devices. The detailed formulas for calculating the energy quality coefficient can be found in some papers. Thus, the integrated energy efficiency can be expressed as

$$\eta'_{IES} = \frac{\sum_i l_i\lambda_i + \sum_i \varepsilon_i S_{s/i} C_i}{\sum_j P_j C_j + \sum_i (1-\varepsilon_i) S_{r/i} C_i} \tag{2}$$

where P_j denotes the energy input from the external network; l_i denotes the load demand for energy i; C_i, C_j denotes the energy quality coefficients of energy i and j; $S_{s/i}$, $S_{r/i}$ indicates the stored and discharged energy value of energy i; ε_i indicates the state of the energy storage device, which is 1 when storing energy and 0 when discharging energy.

The energy flow in each subsystem can be clearly seen in **Figure 1**. Based on the energy flow of all subsystems, the integrated energy efficiency η_{IES} can be expressed as

$$\eta_{IES} = \frac{\left(l_p + S_{s/p}\right)C_p + \left(l_h + S_{s/h}\right)C_h + \left(l_c + S_{s/c}\right)C_c + \left(l_g + S_{s/g}\right)C_g}{\left(P_p + S_{r/p}\right)C_E + \left(P_g + S_{r/g}\right)C_G + S_{r/h}C_H + S_{r/c}C_c} \tag{3}$$

where P_p, P_g represent the power and natural gas purchased from the external pipeline network, respectively; l_p, l_h, l_c, l_g indicate power, heat, cooling, and gas load, respectively; $S_{s/p}$, $S_{s/h}$, $S_{s/c}$, $S_{s/g}$ represent the actual energy stored after taking into account the storage loss of the power, heat, cooling, and gas storage device, respectively; $S_{r/p}$, $S_{r/g}$, $S_{r/h}$, $S_{r/c}$ represent the actual energy discharged after taking into account the energy loss of the power, gas, heat, and cooling storage device, respectively; C_E, C_G, C_H represent the energy quality coefficient for power, natural gas, and heat energy; C_p, C_h, C_c, C_g represent the energy quality coefficient for power, heat, cooling, and air load.

According to the energy flow, the load demand of each subsystem, i.e., l_p, l_h, l_c, l_g can be shown as

$$l_p = W_p - E_{p-c} - E_{p-h} - E_{p-g} - \gamma_p S_{s/p}/\eta_{s/p} \tag{4}$$

$$l_h = W_h - H_{h-c} - \gamma_h S_{s/h}/\eta_{s/h} \tag{5}$$

$$l_c = W_c - \gamma_c S_{s/c}/\eta_{s/c} \tag{6}$$

$$l_g = W_g - G_{g-h} - G_{chp} - \gamma_g S_{s/g}/\eta_{s/g} \tag{7}$$

where W_p, W_h, W_c, W_g denote the supply of power, heat, cooling, and gas; $E_{p\text{-}c}$, $E_{p\text{-}h}$, $E_{p\text{-}g}$ represent the power energy consumed to form cooling, heat, and gas, respectively; $H_{h\text{-}c}$ indicates the heat energy consumed to form cooling; $G_{g\text{-}h}$, G_{chp} represent the amount of natural gas supplied to the gas boiler, CHP by the natural gas subsystem, respectively; γ_p, γ_h , γ_c , γ_g indicate the state of the power, heat, cooling, and gas storage device, with 1 for storing and 0 for discharging; $\eta_{s/p}$, $\eta_{s/h}$, $\eta_{s/c}$, $\eta_{s/g}$ indicate the energy storage efficiency of power, heat, cooling, and gas storage device, respectively.

ENERGY EFFICIENCY INDEX OF SUBSYSTEMS AND ENERGY CONVERSION DEVICES

The energy efficiency represents the ratio of the demand to the supply of the power/natural gas/cooling/heat subsystem. It reflects the energy loss during the transmission and storage process of energy subsystem. Similarly, the efficiency of the energy conversion device reflects the utilization degree of energy. In this section, the energy efficiency model of each

energy subsystem is conducted according to the formula above. In addition, the efficiency model of the energy conversion device is established as well.

Energy Efficiency Index of Energy Subsystems

Power Subsystem

In the power subsystem, the energy efficiency can be expressed as

$$\eta_p = \frac{W_{p,out}}{W_{p,in}} \tag{8}$$

where η_p is the energy efficiency; $W_{p,out}$ and $W_{p,in}$ are the energy output and input of the subsystem, respectively.

The input power is mainly obtained in three ways: it can be purchased from the main grid, obtained by energy conversion device, and discharged by the storage battery:

$$W_{p,in} = P_p + E_{chp} + \left(1-\gamma_p\right)S_{r/p}/\eta_{r/p} \tag{9}$$

where $\eta_{r/p}$ is the discharging efficiency of the energy storage battery and E_{chp} is the power generated by the combined heat and power unit.

The output is usually provided for power load and storage battery; otherwise, it is converted into other energy, i.e., natural gas, heat, and cooling energy:

$$W_{p,out} = W_p - \gamma_p S_{s/p}\left(\frac{1}{\eta_{s/p}} - 1\right) \tag{10}$$

where W_p is the total power supply and $\eta_{s/p}$ is the charging efficiency of the battery.

In the power transmission process, it is worth pointing out the problem of the bus voltage level and the line transmission efficiency. Therefore, it needs to consider the bus voltage level and the power loss on the line. The power supply can be expressed in

$$W_p = \left[\left(P_p + E_{chp}\right)\eta_t + \left(1-\gamma_p\right)S_{r/p}\right]\eta_l \tag{11}$$

where η_t and η_l are the efficiency of the translator and power line, respectively.

Substituting **(9**, **10)** into **(8)**, the energy efficiency can be written as

$$\eta_p = \frac{W_p - \gamma_p S_{s/p}\left(\frac{1}{\eta_{s/p}} - 1\right)}{P_p + E_{chp} + \left(1-\gamma_p\right)S_{r/p}/\eta_{r/p}} \tag{12}$$

Natural Gas Subsystem

In the natural gas subsystem, the energy input is mainly from the purchased gas and the gas transferred from the energy conversion devices. The output is provided for gas load and gas storage device and converted into power or heat.

$$W_{g,in} = P_g + G_{p-g} + \left(1-\gamma_g\right)S_{r/g}/\eta_{r/g} \tag{13}$$

$$W_{g,out} = W_g - \gamma_g S_{s/g}\left(\frac{1}{\eta_{s/g}} - 1\right) \tag{14}$$

where $\eta_{s/g}$ and $\eta_{r/g}$ are the storage and discharge efficiency of the gas storage device.

The gas supply can be written as

$$W_g = P_g + G_{p-g} + \left(1-\gamma_g\right)S_{r/g} \tag{15}$$

where $G_{p\text{-}g}$ represents the natural gas generated by power energy through P2G.

Natural gas is a kind of gas energy; there could not be too much loss during the process of gas transmission and storage. The energy efficiency index of the natural gas subsystem is defined as

$$\eta_g = \frac{W_g - \gamma_g S_{s/g}\left(\frac{1}{\eta_{s/g}} - 1\right)}{P_g + G_{p-g} + \left(1-\gamma_g\right)S_{r/g}/\eta_{r/g}} \tag{16}$$

Heat Subsystem

In the heat subsystem, the input is mainly from the heat transferred from the energy conversion devices and the heat discharged by heat energy storage devices. The output is provided for heat load and heat storage device and converted into cooling energy.

$$W_{h,out} = W_h - \gamma_h S_{s/h}\left(\frac{1}{\eta_{s/h}} - 1\right) \tag{17}$$

$$W_{h,in} = H_{g-h} + H_{chp-h} + H_{g-h} + \left(1-\gamma_h\right)S_{r/h}/\eta_{r/h} \tag{18}$$

where $\eta_{s/h}$ and $\eta_{r/h}$indicate the efficiency of the heat storage device in storing and discharging heat, respectively.

During the process of heat transmission and storage, there may exist the loss of temperature, which should be taken into consideration. In this article, the energy consumption rate of pipelines is utilized to describe the loss of temperature (Kong et al., 2020). Hence, the heat supply can be expressed as

$$W_h = \left[H_{g-h} + H_{chp-h} + H_{p-h} + \left(1-\gamma_h\right)S_{r/h}\right]\left(1 - 0.01 l_h \sigma_h\right) \tag{19}$$

where $H_{g\text{-}h}$, $H_{chp\text{-}h}$ represent the heat energy produced by natural gas through gas boiler and waste heat recovery boiler, respectively; $H_{p\text{-}h}$ indicates the heat energy generated by power through power boiler; l_h indicates the length of the heat pipe network; σ_h represents the dissipation rate per 100 m of the heat pipe network.

The energy efficiency index of the heat subsystem is defined as

$$\eta_h = \frac{W_h - \gamma_h S_{s/h}\left(\frac{1}{\eta_{s/h}} - 1\right)}{H_{g-h} + H_{chp-h} + H_{p-h} + \left(1-\gamma_h\right)S_{r/h}/\eta_{r/h}} \tag{20}$$

Cooling Subsystem

In the cooling subsystem, the energy input is mainly from the cooling energy transferred from the energy conversion devices and the cooling energy discharged by the cooling storage device. The output is provided for the cooling load, cooling storage device.

$$W_{c,out} = W_c - \gamma_c S_{s/c}\left(\frac{1}{\eta_{s/c}} - 1\right) \tag{21}$$

$$W_{c,in} = C_{p-c} + C_{h-c} + \left(1-\gamma_c\right)S_{r/c}/\eta_{r/c} \tag{22}$$

where $\eta_{s/c}$ and $\eta_{r/c}$ indicate the efficiency of the storage and discharge of the cooling storage device.

Similar to the heat subsystem, there also exists the loss of temperature during the process of energy transmission and storage. The total supply quantity of cooling energy considering the energy consumption rate can be expressed as

$$W_c = \left[C_{p-c} + C_{h-c} + (1-\gamma_c)S_{r/c}\right](1 - 0.01 l_c \sigma_c) \tag{23}$$

where $C_{p\text{-}c}$ indicates the cooling energy converted by refrigeration equipment; $C_{h\text{-}c}$ indicates the cooling energy converted by absorption chiller; l_c is the length of the cool pipe network; σ_c indicates the dissipation rate per 100 m of the cool pipe network.

The energy efficiency index of the cooling subsystem is defined as

$$\eta_c = \frac{W_c - \gamma_c S_{s/c}\left(\frac{1}{\eta_{s/c}} - 1\right)}{C_{p-c} + C_{h-c} + (1-\gamma_c)S_{r/c}/\eta_{r/c}} \tag{24}$$

Efficiency Index of Energy Conversion Devices

In the IES, the energy conversion devices play a necessary role in making a close relationship among the subsystem above. Therefore, the efficiency index of the energy conversion devices should be considered to analyze the energy efficiency of the IES objectively. In this subsection, efficiency indexes of six energy conversion devices are given as follows.

1) Power-to-Heat Device

In this study, the power-to-heat device is considered as the power boiler. According to the concept of the energy quality coefficient in *Description About Energy Efficiency Indexes of the IES*, the efficiency index of the power boiler can be written as

$$\eta_{p-h} = \frac{C_h}{C_E}\lambda_{cop\,(p-h)} \tag{25}$$

where $\lambda_{cop(p-h)}$ is the heating coefficient.

2) Power-to-Cool Device

The power-to-cool device is usually considered as refrigeration equipment. The efficiency index of the refrigeration equipment is

$$\eta_{p-c} = \frac{C_c}{C_E}\lambda_{cop\,(p-c)} \tag{26}$$

where $\lambda_{cop(p-c)}$ is the cooling factor for the power-to-cool device.

3) Combined Heat and Power Unit

The combined heat and power unit is composed of the gas turbine and the waste heat recovery boiler. The gas turbine can convert the natural gas into power and heat, and the waste heat recovery boiler can reutilize the waste heat which is generated in the process of energy conversion. Hence, the efficiency index of the combined heat and power unit is

$$\eta_{chp} = \frac{C_E E_{chp} + C_s H_{chp-h}}{C_G G_{chp}} \tag{27}$$

where C_s is the energy quality coefficient of hot steam.

4) Device Converting Natural Gas to Heat

Besides the combined heat and power unit, the gas boiler is also an efficient device converting gas to heat and its efficiency index can be given as

$$\eta_{g-h} = \frac{C_h}{C_G}\lambda_{cop\,(g-h)} \tag{28}$$

where $\lambda_{cop(g-h)}$ is the heat production coefficient of the gas boiler.

5) Heat-to-Cool Device

The heat-to-cool device in the IES is usually considered as the absorption chiller. The efficiency index of the absorption chiller is

$$\eta_{h-c} = \frac{C_c}{C_H}\lambda_{cop\,(h-c)} \tag{29}$$

where $\lambda_{cop(h-c)}$ indicates the heat-to-cool coefficient of an absorption chiller.

6) P2G Device

The efficiency index of the P2G device is

$$\eta_{p-g} = \frac{C_g}{C_E}\lambda_{cop\,(p-g)} \tag{30}$$

where $\lambda_{cop(p-g)}$ denotes the coefficient of the power-to-gas of P2G.

ENERGY EFFICIENCY CONTRIBUTION MODELS FOR ENERGY SUBSYSTEMS

The energy efficiency of the IES is determined by that of each subsystem. However, due to the fact that each subsystem has different influence on the efficiency of IES, it is hard to measure the contribution of subsystems to the IES. Therefore, in this section, an energy efficiency contribution model for subsystem is proposed. The IES operator can classify the subsystems according to their contributions. When the energy efficiency of IES decreases, the IES operator should adjust the subsystem whose contribution is high to enhance the efficiency of the IES.

Actually, the contribution degree in this research means marginal utility. It reflects the variation degree of the energy efficiency at one point of time. Therefore, this study uses partial derivative to express the energy efficiency contribution. Thus, the contributions of subsystems can be defined as the partial derivatives demanded by η_{IES} on η_p, η_g, η_h, and η_c. We use ζ to represent the energy efficiency contribution. We use energy efficiency contribution to represent the energy efficiency contribution degree of the energy subsystems and

conversion devices to the integrated energy system, and the positive or negative of this value indicates whether the influence of the energy subsystem and the energy conversion devices to the integrated energy system is positive or negative. The positive correlation represents that the larger the energy efficiency contribution of the subsystems and devices is, the more obvious the integrated energy efficiency increases. The negative correlation represents that the larger the energy efficiency contribution of the subsystems and devices is, the more obvious the integrated energy efficiency decreases.

Energy Efficiency Contribution of the Power Subsystem

According to **Eqs 2**, **3**, **12**, the energy efficiency contribution of the power subsystem can be obtained as

$$\zeta_p = C_p\left(P_p + E_{chp} + \left(1-\gamma_p\right)S_{r/p}/\eta_{r/p}\right)\left[\left(P_p + S_{r/p}\right)C_E + \left(P_g + S_{r/g}\right)C_G + S_{r/h}C_H + S_{r/c}C_c\right]^{-1} \tag{31}$$

where is the partial derivative demanded by η_{IES} on η_p. γ_p indicates the operating state of the energy storage device, which is 1 when storing energy and 0 when discharging energy.

When the energy storage device is in the storage state, the energy efficiency contribution of the power subsystem is

$$\zeta_p = C_p\left(P_p + E_{chp}\right)\left[\left(P_p + S_{r/p}\right)C_E + \left(P_g + S_{r/g}\right)C_G + S_{r/h}C_H + S_{r/c}C_c\right]^{-1} \tag{32}$$

And when the energy storage device is in the discharge state, the energy efficiency contribution can be obtained as

$$\zeta_p = C_p\left(P_p + E_{chp} + S_{r/p}/\eta_{r/p}\right)\left[\left(P_p + S_{r/p}\right)C_E + \left(P_g + S_{r/g}\right)C_G + S_{r/h}C_H + S_{r/c}C_c\right]^{-1} \tag{33}$$

These formulas represent different expressions of the formula under different working conditions of the energy storage device.

Energy Efficiency Contribution of Natural Gas Subsystem

Similarly, the energy efficiency contribution of the natural gas subsystem can be shown as

$$\zeta_g = C_g\left(P_g + G_{p-g} + \left(1-\gamma_g\right)S_{r/g}/\eta_{r/g}\right)\left[\left(P_p + S_{r/p}\right)C_E + \left(P_g + S_{r/g}\right)C_G + S_{r/h}C_H + S_{r/c}C_c\right]^{-1} \tag{34}$$

where is the partial derivative demanded by η_{IES} on η_g. γ_g indicates the operating state of the energy storage device, which is 1 when storing energy and 0 when discharging energy.

When the energy storage device is in storing, i.e., $\gamma_g = 1$, the energy efficiency contribution is

$$\zeta_g = C_g\left(P_g + G_{p-g}\right)\left[\left(P_p + S_{r/p}\right)C_E + \left(P_g + S_{r/g}\right)C_G + S_{r/h}C_H + S_{r/c}C_c\right]^{-1} \tag{35}$$

When $\gamma_g = 0$, the energy efficiency contribution is

$$\zeta_g = C_g\left(P_g + G_{p-g} + S_{r/g}/\eta_{r/g}\right)\left[\left(P_p + S_{r/p}\right)C_E + \left(P_g + S_{r/g}\right)C_G + S_{r/h}C_H + S_{r/c}C_c\right]^{-1} \tag{36}$$

These formulas represent different expressions of the formula under different working conditions of the energy storage device.

Energy Efficiency Contribution of Heat Subsystem

The energy efficiency contribution of the heat subsystem can be obtained as

$$\zeta_h = C_h\left(H_{g-h} + H_{chp-h} + H_{p-h} + \left(1-\gamma_h\right)S_{r/h}/\eta_{r/h}\right)\left[\left(P_p + S_{r/p}\right)C_E + \left(P_g + S_{r/g}\right)C_G + S_{r/h}C_H + S_{r/c}C_c\right]^{-1} \tag{37}$$

where the partial derivative demanded by η_{IES} is on η_h. γ_h indicates the operating state of the energy storage device, which is 1 when storing energy and 0 when discharging energy.

When $\gamma_h = 1$, the energy efficiency contribution is

$$\zeta_h = C_h\left(H_{g-h} + H_{chp-h} + H_{p-h}\right)\left[\left(P_p + S_{r/p}\right)C_E + \left(P_g + S_{r/g}\right)C_G + S_{r/h}C_H + S_{r/c}C_c\right]^{-1} \tag{38}$$

When $\gamma_h = 0$, the energy efficiency contribution is

$$\zeta_h = C_h\left(H_{g-h} + H_{chp-h} + H_{p-h} + S_{r/h}/\eta_{r/h}\right)\left[\left(P_p + S_{r/p}\right)C_E + \left(P_g + S_{r/g}\right)C_G + S_{r/h}C_H + S_{r/c}C_c\right]^{-1} \tag{39}$$

These formulas represent different expressions of the formula under different working conditions of the energy storage device.

Energy Efficiency Contribution of Cooling Subsystem

The energy efficiency contribution of the cooling subsystem can be obtained as

$$\zeta_c = C_c\left(C_{p-c} + C_{h-c} + \left(1-\gamma_c\right)S_{r/c}/\eta_{r/c}\right)\left[\left(P_p + S_{r/p}\right)C_E + \left(P_g + S_{r/g}\right)C_G + S_{r/h}C_H + S_{r/c}C_c\right]^{-1} \tag{40}$$

where is the partial derivative demanded by η_{IES} on η_c. γ_c indicates the operating state of the energy storage device, which is 1 when storing energy and 0 when discharging energy.

When $\gamma_c = 1$, the energy efficiency contribution is

$$\zeta_c = C_c\left(C_{p-c} + C_{h-c}\right)\left[\left(P_p + S_{r/p}\right)C_E + \left(P_g + S_{r/g}\right)C_G + S_{r/h}C_H + S_{r/c}C_c\right]^{-1} \tag{41}$$

When $\gamma_c = 0$, the energy efficiency contribution is

$$\zeta_c = C_c\left(C_{p-c} + C_{h-c} + S_{r/c}/\eta_{r/c}\right)\left[\left(P_p + S_{r/p}\right)C_E + \left(P_g + S_{r/g}\right)C_G + S_{r/h}C_H + S_{r/c}C_c\right]^{-1} \tag{42}$$

In conclusion, the energy efficiency contributions above are positively correlated to the energy efficiency of the IES.

IMPACT OF ENERGY CONVERSION DEVICES ON THE IES

For the energy conversion devices among energy subsystems in this study, it is necessary to analyze the impact of energy conversion devices on the energy efficiency of the IES. The energy conversion devices influence the flexibility of the system and play a key role in the energy efficiency of the IES. In this article, the energy conversion devices include CHP unit, gas boiler, power boiler, absorption chiller, P2G device, and refrigeration equipment. Similar to the contribution of the subsystems in *Energy Efficiency Contribution Models for Energy Subsystems*, the contribution of each energy conversion device to the IES can be defined as the partial derivatives demanded by η_{IES} on η_{p-h}, η_{p-c}, η_{chp}, η_{g-h}, η_{h-c}, and η_{p-g}. We use ζ_{p-h}、ζ_{p-c}、ζ_{chp}、ζ_{g-h}、ζ_{h-c} and ζ_{p-g} to represent the energy efficiency contribution of the energy conversion devices.

1) Power-to-Heat Device

According to **Eqs 3**, **25**, the contribution of power boilers can be written as

$$\zeta_{p-h} = C_E\left(l_h + S_{s/h}\right)\left[\lambda_{cop\left(p-h\right)}\left(\left(P_p + S_{r/p}\right)C_E + \left(P_g + S_{r/g}\right)C_G + S_{r/h}\lambda_H + S_{r/c}C_c\right)\right]^{-1} \tag{43}$$

where the partial derivative is demanded by η_{IES} on η_{p-h}. We use this formula to represent the energy efficiency contribution degree of the power boiler.

2) Power-to-Cool Device

According to **Eqs 3**, **26**, the contribution of the refrigeration equipment is

$$\zeta_{p-c} = C_E\left(l_c + S_{s/c}\right)\left[\lambda_{cop\left(p-c\right)}\left(\left(P_p + S_{r/p}\right)C_E + \left(P_g + S_{r/g}\right)C_G + S_{r/h}\lambda_H + S_{r/c}C_c\right)\right]^{-1} \tag{44}$$

where the partial derivative is demanded by η_{IES} on η_{p-c}. We use this formula to represent the energy efficiency contribution degree of the refrigeration equipment.

3) Combined Heat and Power Unit

The CHP unit consists of a gas turbine and a waste heat recovery boiler, and its impact on energy efficiency is also determined by these devices. According to **Eqs 3**, **27**, the contribution of CHP unit can be obtained as

$$\zeta_{chp} = \frac{\left(l_p + S_{s/p}\right)C_p + \left(l_h + S_{s/h}\right)C_h + \left(l_c + S_{s/c}\right)C_c + \left(l_g + S_{s/g}\right)C_g}{\left(P_p + S_{r/p}\right)C_E + \left(P_g + S_{r/g}\right)\left(C_E E_{chp} + C_s H_{chp-h}\right) + S_{r/h}\lambda_H + S_{r/c}C_c} G_{chp} \tag{45}$$

where the partial derivative is demanded by η_{IES} on η_{chp}. We use this formula to represent the energy efficiency contribution degree of the combined heat and power unit.

4) Gas-to-Heat Device

According to **Eqs 3**, **28**, the contribution of gas boiler can be written as

$$\zeta_{g-h} = C_G \left(l_h + S_{s/h}\right)\left[\lambda_{cop\left(g-h\right)}\left(\left(P_p + S_{r/p}\right)C_E + \left(P_g + S_{r/g}\right)C_G + S_{r/h}\lambda_H + S_{r/c}C_c\right)\right]^{-1} \tag{46}$$

where the partial derivative is demanded by η_{IES} on η_{g-h}. We use this formula to represent the energy efficiency contribution degree of the gas boiler.

5) Heat-to-Cool Device

According to **Eqs 3**, **29**, the contribution of the absorption chiller is

$$\zeta_{h-c} = C_H\left(l_c + S_{s/c}\right)\left[\lambda_{cop\left(h-c\right)}\left(\left(P_p + S_{r/p}\right)C_E + \left(P_g + S_{r/g}\right)C_G + S_{r/h}\lambda_H + S_{r/c}C_c\right)\right]^{-1} \tag{47}$$

where the partial derivative is demanded by η_{IES} on η_{h-c}. We use this formula to represent the energy efficiency contribution degree of the absorption chiller.

6) Power-to-Gas Device

According to **Eqs 3**, **30**, the contribution of the P2G device can be written as

$$\zeta_{p-g} = C_E\left(l_g + S_{s/g}\right)\left[\lambda_{cop\left(p-g\right)}\left(\left(P_p + S_{r/p}\right)C_E + \left(P_g + S_{r/g}\right)C_G + S_{r/h}\lambda_H + S_{r/c}C_c\right)\right]^{-1} \tag{48}$$

where the partial derivative is demanded by η_{IES} on η_{p-g}. We use this formula to represent the energy efficiency contribution degree of the P2G.

ENERGY EFFICIENCY CONTRIBUTION METHOD BASED ON WEIGHTED DIRECTED GRAPH

This section proposes an energy efficiency contribution solution method based on a weighted directed graph (Qin et al., 2021). From the above equations, it can be seen that the solution of the model depends on the input and output energy flows, while the physical properties of the integrated energy flows can be simplified by means of a directed graph, establishing a description of the steady-state energy flow relationship of the system.

A directed graph includes the set of nodes T as well as the set of branches L; we represent it by $D(T, L)$. The node sets are used to describe the input, output, conversion, and storage nodes of energy within the system, while the branch set represents the connection between nodes. The direction from node i to node j is denoted by $e(i, j)$, and the energy transferred from node i to node j is denoted by e_{ij}. In addition, weights are assigned to the branches to characterize the energy loss between the nodes, and the size of the weights indirectly reflects the length of the branch. As shown

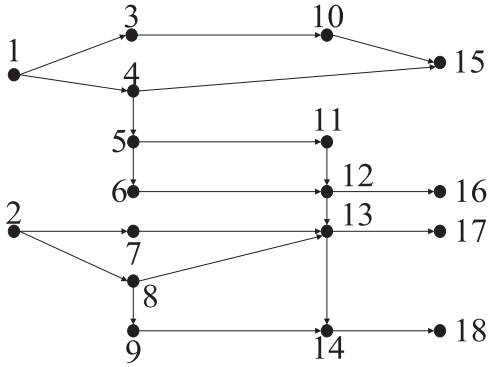

FIGURE 2 | The weighted directed graph of the IES.

in **Figure 2**, nodes 1 and 2 represent the purchased natural gas and power energy, respectively, and nodes 15, 16, 17, and 18 represent the energy demand side of the system.

According to the definition of a weighted directed graph, the system can be described in terms of a normalized node matrix (Wang et al., 2019). Supposing that there are N nodes and B branches organized, the node-branch incidence matrix (Li et al., 2019) $A=(a_{ik})_{N\times B}$ is a $N \times B$ matrix; i.e.,

$$a_{ik} = \begin{cases} 1, & \text{if branch } l_k \text{ starts from node } i \\ -1 & \text{if branch } l_k \text{ ends with node } i \\ 0, & \text{if branch } l_k \text{ is not connected with node } i \end{cases} \tag{49}$$

where l_k denotes the k-th edge, $k = 1, 2, \cdots, m$.

Considering the value of the weight on each branch, it is necessary to create the weight matrix and define the weight on the branch as

$$\eta_{ij} = \begin{cases} -\ln \mu_{ij}, e(i,j) \in L \\ 0, \qquad e(i,j) \notin L \end{cases} \tag{50}$$

where μ_{ij} is the energy conversion efficiency between the two nodes.

This article defines S as a path from an input node to an output node. $X = (x_1, x_2, \cdots, x_m)^T$ represents the connection relationship between nodes. The elements in X are all binary variables, as shown in

$$x_k = \begin{cases} 1, e_k \in S \\ 0, e_k \notin S \end{cases}, k = 1, 2, \cdots, m \tag{51}$$

where e_k denotes the k-th edge, and the length of the path S can be calculated as

$$d_s = \sum_k \eta_{ij} x_k \tag{52}$$

Based on the weighted directed graph, the energy flow value required from the starting point can be calculated by the length of the path considering the end node needs per unit of energy flow. It can also obtain the energy flow of all nodes in the path to calculate the energy efficiency of the system and the energy conversion devices and then analyze their contribution.

We use the path length of the weighted directed graph to calculate the energy flow from which the starting point needs supply, when the end exports unit energy flow. According to the weighted directed graph model, we can adopt a discretized energy flow calculation method to handle the energy efficiency model. The specific solution steps can be seen in **Figure 3**.

1) Initialize the energy flow value of each side in the system weighted directed graph model, and calculate the initial value of the input energy flow value and output energy flow value of the system. Meanwhile, initializing two weight matrices of the system. This step is used to handle some presets of the system.
2) Discretize the energy flow of each output node known by the system into a number of unit step lengths. If a certain energy flow value Δp is used as the step length, the output energy flow of the system shown in **Figure 2** is discretized, respectively.
3) Find a feasible path from each input node to each output node to form the path set of the system. In **Figure 2**, all available paths from input node 1 to output node 15 can be obtained by solving **Eq. 52**. After obtaining the path set of the system, the system paths will be sorted according to certain priority rules.
4) The priority path is selected according to the priority order, and the current path length d_l of the system is calculated using formula **(52)** to obtain the increment $e^{dl}\Delta p$ of the input node energy flow value of the system in the unit step length. At the same time, the energy flow value increment of each side in the path is traced. Based on the previous calculation of the energy flow value, superimpose the new calculated value and judge whether the capacity of the side is exceeded. If the capacity of the edge is exceeded, the path will be deleted from the path set.
5) Judge whether the output node of the system has reached the expected energy output demand. If the system demand has been met, all paths ending at the node will be deleted from the path set.
6) According to the calculation results of the energy flow value of each side, update the weight matrix and the path set in the system.
7) Circulate until the system path set is empty or the energy flow of each output node reaches the setting value and complete the energy flow calculation of the system.
8) According to the input and output energy flow values, the energy efficiency contribution models will be calculated.

CASE STUDY

System Description

The case study does not analyze the energy efficiency contribution of the energy conversion devices singly, because the content has included the study of the energy conversion devices efficiency in the process of simulating the energy efficiency contribution of the energy subsystem. And the energy flow in the energy subsystems can be calculated by the analysis of the energy conversion devices. As we all know, the energy efficiency contribution of the devices to the integrated energy system is very small. The energy loss of the energy transmission, storage, and supply in the energy subsystem is the main reason of influencing the system energy efficiency. Therefore, we simulate the energy efficiency contribution of the energy subsystem mainly and do not analyze the energy conversion devices.

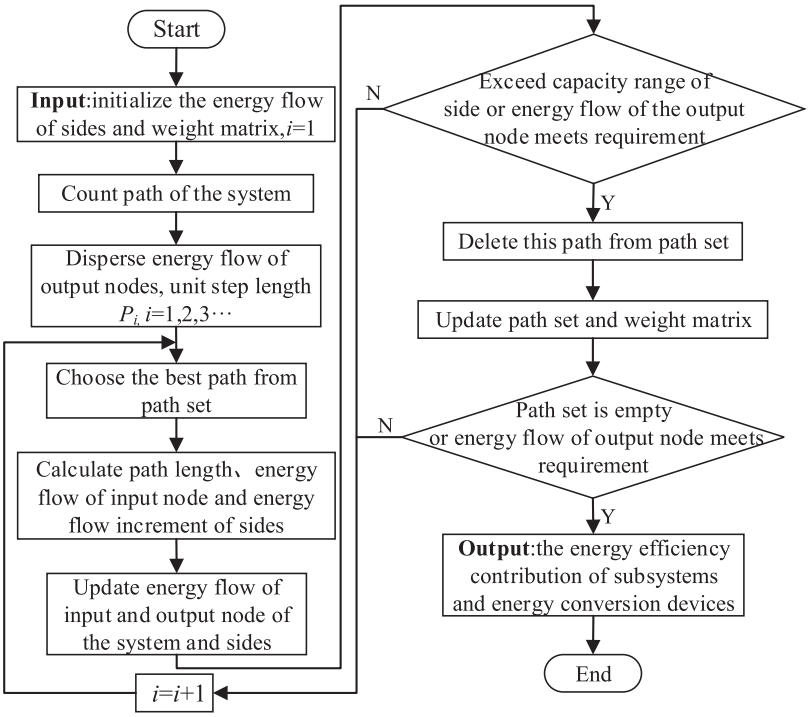

FIGURE 3 | Calculation steps based on the weighted directed graph.

Taking a demonstration park as an example, Phase I and Phase II projects are carried out gradually in temporal sequence, and every project has "cooling/heat/power/gas" load demand. Phase I was the first to be built, using the traditional energy supply method to meet the multiple loads demand in the area. The power load is supplied by purchased power and energy storage device like batteries, and the cooling load is supplied by refrigeration equipment and energy storage device, and the heat load is supplied by gas boiler and the gas load is provided by purchased natural gas. Phase II adopts multienergy complementarity of the IES to meet the load demand in the park. The installed capacity and efficiency of all equipment are shown in **Table 1**.

The data of cooling/heat/power/gas load in summer typical day are shown in **Figure 4**. The cooling load and natural gas load mainly come from appliance load. The heat load mainly includes drying technology load and appliance load. Power load includes production load and appliance load.

Results of the Energy Efficiency Contribution of the Park

Firstly, it is assumed that the configured capacity of the CHP unit is equal to its operating power, the energy efficiency contribution of the park is calculated by using the energy efficiency contribution equation, and the evaluation period is 24 h. The data of Phase II are shown in **Figure 5**.

As can be seen from **Figure 5**, the power subsystem has the highest energy efficiency contribution in the construction of the IES, followed by the natural gas subsystem. While the heat subsystem and the cooling subsystem have a relatively low energy efficiency contribution. The power subsystem has the highest energy efficiency contribution, because the park has very high load demand for power energy and needs to purchase power from the external grid. Moreover, the power subsystem contacts with other subsystems frequently. Otherwise, the energy efficiency contribution of the power subsystem is lower than that of the natural gas subsystem at points 9, 14, 15, 16, and 17. The decrease in purchased power and the increase in demand for natural gas during these time periods are the main reasons. This leads to the increase in the energy efficiency contribution of the natural gas subsystem. Natural gas, as a common primary energy source, has a low load demand, but it is an important input energy source for energy conversion equipment, which needs to be purchased from the external gas grid. Therefore, it has a high energy efficiency contribution. Although heat and cooling subsystems have a certain load demand, they are supplied by the park itself. Therefore, the energy efficiency contribution is relatively small. The heat subsystem interacts with the other subsystems frequently; therefore, the energy efficiency contribution is higher than that of the cooling subsystem.

Figures 6–9 give the energy efficiency contribution comparison of two construction areas. The energy efficiency contribution of the subsystems in Phase II is higher than that in Phase I. It shows that the manner of energy supply in the IES is superior to the traditional manner. The results also prove the validity of the calculation method of energy efficiency contribution.

TABLE 1 | Parameter of regional energy devices.

Device	Installed capacity of the energy equipment/MW		Equipment conversion efficiency
	Phase I	Phase II	
CHP unit	0	4.0	Power generation: 0.35 Thermal generation: 0.4
Gas boiler	12.5	5.5	0.905
Power boiler	0	5.7	$\lambda_{cop(e-h)} = 4$
Absorption chiller	0	4.0	1.28
Refrigeration equipment	21.0	16.5	$\lambda_{cop(e-c)} = 4.5$
P2G	0	3.0	0.56
Battery	5.0	5.0	0.9
Cooling storage device	12.0	12.0	0.98

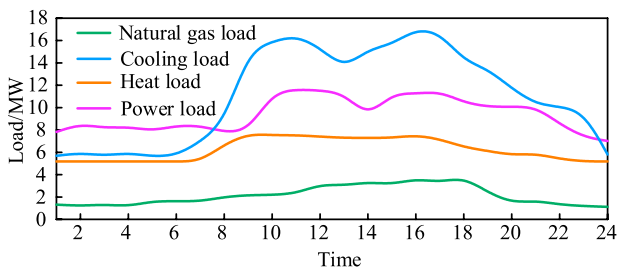

FIGURE 4 | Curves of power/heat/gas/cooling load in summer typical day.

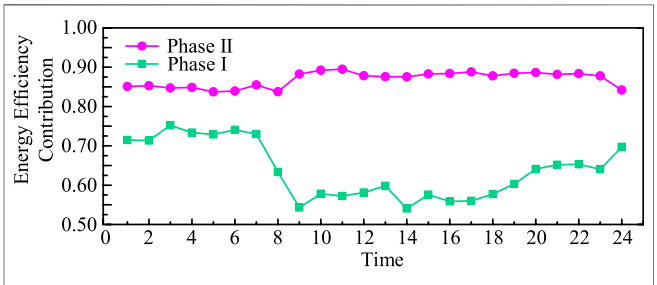

FIGURE 6 | The comparison of the power subsystem.

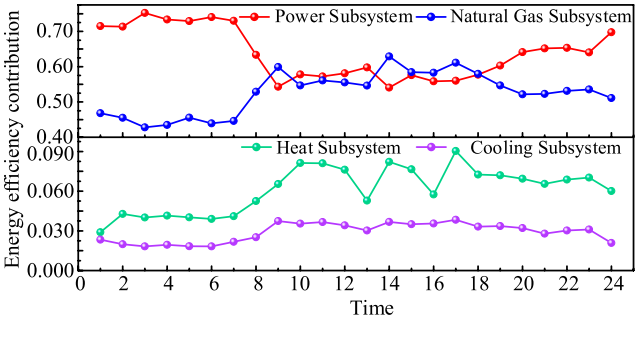

FIGURE 5 | Curves of energy efficiency contribution in Phase II.

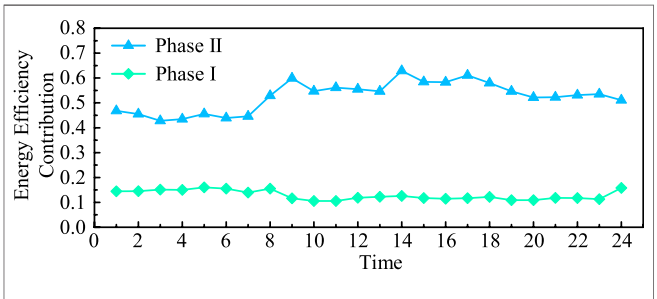

FIGURE 7 | The comparison of the natural gas subsystem.

Impact of the Energy Storage Scheme on the Energy Efficiency Contribution

Energy storage device is an important device in the energy subsystem, which can realize peak cutting and valley filling. Therefore, it plays an important role in the economic operation of the IES. However, there is energy loss in the operation process of the energy storage device, which will influence the energy efficiency contribution value of the energy subsystem. This subsection takes Phase II as an example and includes the battery and the cooling storage device. This content analyzes the energy efficiency contribution of different configuration schemes.

Four configuration schemes are developed according to the requirements, where scheme 1 indicates that the energy storage devices are all in operation, scheme 2 indicates that only the cooling storage device is in operation, scheme 3 indicates that only the battery is in operation, and scheme 4 indicates that none of the energy storage devices are in operation. The results are shown in **Figure 10**. Considering the energy loss of the energy storage devices, the introduction of energy storage devices will reduce the energy efficiency contribution of the energy subsystem in the park. While the operation cost of the system will decrease because of the reasonable invocation of energy storage devices. The cost of each configuration scheme is shown in **Table 2**.

Although the introduction of energy storage device will lead to energy loss and reduce the energy efficiency contribution of subsystems, they not only reduce the operation cost of the park, but also realize peak cutting, and valley filling and reduce the

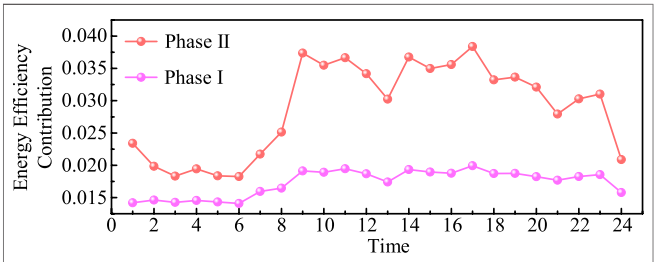

FIGURE 8 | The comparison of the cooling subsystem.

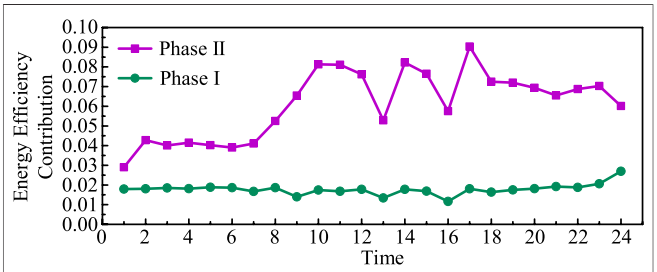

FIGURE 9 | The comparison of the heat subsystem.

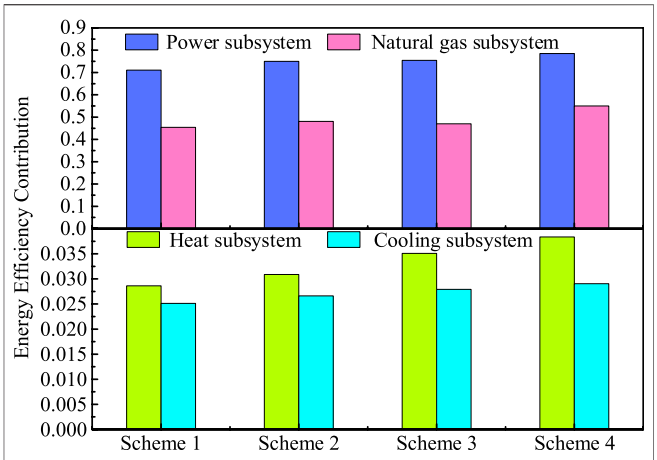

FIGURE 10 | The comparison of energy efficiency contribution under four configuration schemes.

TABLE 2 | Operation cost under different configuration schemes.

Scheme	1	2	3	4
Operation Cost/¥	24,924.4	27,672.6	24,925.4	30,427.44

frequent start-up and shut-down of units. Therefore, a comprehensive planning of the park construction is required.

CONCLUSION

In this study, a method for calculating the energy efficiency contribution of the IES is proposed and is simulated *via* the case study. Through the calculation and analysis of the energy efficiency contribution of energy subsystems and energy conversion devices, some conclusions can be drawn as follows:

1) Due to the complementarity of multiple energy sources, this article proposes the computational expressions of system energy efficiency and energy conversion device efficiency. According to these expressions, energy efficiency contribution models of the energy subsystems are inferred to analyze the influence of energy subsystem on the comprehensive energy efficiency. Hence, all subsystems can be classified as adjustment basis when system energy efficiency decreases.
2) The operation cost of the IES will increase when the energy storage device is put in operation, but it will improve the energy efficiency contribution of the system. Therefore, the construction of the park needs to be planned rationally and takes into account both the contribution index and the economic index.

The research results in this article present new content on the basis of traditional energy efficiency assessment. As an important index for the rational planning and operational adjustment of the IES, the energy efficiency contribution index can help system operator to choose a reasonable operation plan under different energy supply methods, configuration schemes and operation methods in the system, which has guiding significance for improving the comprehensive energy efficiency of the system.

DATA AVAILABILITY STATEMENT

The original contributions presented in the study are included in the article/supplementary material; further inquiries can be directed to the corresponding author.

AUTHOR CONTRIBUTIONS

SY and MC were responsible for the construction of the energy efficiency indexes. SY and QZ focused on deducing the energy efficiency contribution models, and SY searched for a reasonable method to handle the models. The case study of this research was conducted by SY and QZ. The article was written by SY.

FUNDING

This work was supported by the Project of State Grid Jiangsu Electric Power Co., Ltd. (J2020115).

REFERENCES

Abu-Rayash, A., and Dincer, I. (2020). Development of an Integrated Energy System for Smart Communities. *Energy* 202, 117683. doi:10.1016/j.energy.2020.117683

Alves, O., Monteiro, E., Brito, P., and Romano, P. (2016). Measurement and Classification of Energy Efficiency in HVAC Systems. *Energy and Buildings* 130, 408–419. doi:10.1016/j.enbuild.2016.08.070

Birol, F., and Keppler, J. H. (2000). Prices, Technology Development and the Rebound Effect. *Energy Policy* 28 (6), 457–469. doi:10.1016/S0301-4215(00)00020-3

Choi, J.-Y., Choi, I.-S., Ahn, G.-H., and Won, D.-J. (2018). Advanced Power Sharing Method to Improve the Energy Efficiency of Multiple Battery Energy Storages System. *IEEE Trans. Smart Grid* 9 (2), 1292–1300. doi:10.1109/TSG.2016.2582842

Elmirghani, J. M. H., Klein, T., Hinton, K., Nonde, L., Lawey, A. Q., El-Gorashi, T. E. H., et al. (2018). GreenTouch GreenMeter Core Network Energy-Efficiency Improvement Measures and Optimization. *J. Opt. Commun. Netw.* 10 (2), A250–A269. doi:10.1364/JOCN.10.00A250

Filippini, M., and Hunt, L. C. (2016). Measuring Persistent and Transient Energy Efficiency in the US. *Energy Efficiency* 9 (3), 663–675. doi:10.1007/s12053-015-9388-5

Kavousian, A., and Rajagopal, R. (2014). Data-Driven Benchmarking of Building Energy Efficiency Utilizing Statistical Frontier Models. *J. Comput. Civ. Eng.* 28 (1), 79–88. doi:10.1061/(ASCE)CP.1943-5487.0000327

Kong, X., Sun, F., Huo, X., Li, X., and Shen, Y. (2020). Hierarchical Optimal Scheduling Method of Heat-Electricity Integrated Energy System Based on Power Internet of Things. *Energy* 210, 118590. doi:10.1016/j.energy.2020.118590

Li, P., Dong, B., Yu, H., Wang, C., Huo, Y., Li, S., et al. (2019). A Unified Energy Bus Based Multi-Energy Flow Modeling Method of Integrated Energy System. *Energ. Proced.* 159, 418–423. doi:10.1016/j.egypro.2018.12.066

Liu, J., Li, K., Liu, B., and Li, G. (2020). Improvement of the Energy Evaluation Methodology of Individual Office Building with Dynamic Energy Grading System. *Sust. Cities Soc.* 58, 102133. doi:10.1016/j.scs.2020.102133

Miao, B., Lin, J., Li, H., Liu, C., Li, B., Zhu, X., et al. (2020). Day-Ahead Energy Trading Strategy of Regional Integrated Energy System Considering Energy Cascade Utilization. *IEEE Access* 8, 138021–138035. doi:10.1109/ACCESS.2020.3007224

Qin, C., Wang, L., Han, Z., Zhao, J., and Liu, Q. (2021). Weighted Directed Graph Based Matrix Modeling of Integrated Energy Systems. *Energy* 214, 118886. doi:10.1016/j.energy.2020.118886

Torres, J., Moreno-Torres, P., Navarro, G., Blanco, M., and Lafoz, M. (2018). Fast Energy Storage Systems Comparison in Terms of Energy Efficiency for a Specific Application. *IEEE Access* 6, 40656–40672. doi:10.1109/ACCESS.2018.2854915

Wang, H., Zhang, R., Peng, J., Wang, G., Liu, Y., Jiang, H., et al. (2017). GPNBI-inspired MOSFA for Pareto Operation Optimization of Integrated Energy System. *Energ. Convers. Manag.* 151, 524–537. doi:10.1016/j.enconman.2017.09.005

Wang, J.-J., Yang, K., Xu, Z.-L., and Fu, C. (2015). Energy and Exergy Analyses of an Integrated CCHP System with Biomass Air Gasification. *Appl. Energ.* 142, 317–327. doi:10.1016/j.apenergy.2014.12.085

Wang, Y., Zhang, N., Kang, C., Kirschen, D. S., Yang, J., and Xia, Q. (2019). Standardized Matrix Modeling of Multiple Energy Systems. *IEEE Trans. Smart Grid* 10 (1), 257–270. doi:10.1109/TSG.2017.2737662

Willem, H., Lin, Y., and Lekov, A. (2017). Review of Energy Efficiency and System Performance of Residential Heat Pump Water Heaters. *Energy and Buildings* 143, 191–201. doi:10.1016/j.enbuild.2017.02.023

Wang, J., Zhong, H., Yang, Z., Lai, X., Xia, Q., and Kang, C. (2020). Incentive Mechanism for Clearing Energy and Reserve Markets in Multi-Area Power Systems. In *IEEE Transactions on Sustainable Energy* 11 (4), 2470–2482. doi:10.1109/TSTE.2019.2961780

Xue, Y. (2015). Energy Internet or Comprehensive Energy Network?. *J. Mod. Power Syst. Clean. Energ.* 3 (3), 297–301. doi:10.1007/s40565-015-0111-5

Zhang, T., Wang, J., Zhong, H., Li, G., Zhou, M., and Zhao, D. (2020). Soft Open Point Planning in Renewable-Dominated Distribution Grids with Building Thermal Storage. In *CSEE Journal of Power and Energy Systems*. doi:10.17775/CSEEJPES.2020.03660

Zou, G., Chen, L., Liu, W., Hong, X., Zhang, G., and Zhang, Z. (2013). Measurement and Evaluation of Chinese Regional Energy Efficiency Based on Provincial Panel Data. *Math. Comp. Model.* 58 (5), 1000–1009. doi:10.1016/j.mcm.2012.09.020

Conflict of Interest: Authors SY, MC and QZ were employed by the company State Grid Jiangsu Electric Power Co. LTD.

frontiers in Energy Research

ORIGINAL RESEARCH
published: 03 September 2021
doi: 10.3389/fenrg.2021.713245

Integrated Energy System Planning Based on Life Cycle and Emergy Theory

Jun Wang[1,2]*, *Wei Du*[1,2] *and Dongmei Yang*[1,2]

[1]NARI Group Corporation (State Grid Electric Power Research Institute), Nanjing, China, [2]NARI Technology Co., Ltd., Nanjing, China

Integrated energy system (IES) is of great significance in the construction of the modern energy system. Reasonable planning is one of the important means to improve the economy of the IES and promote the consumption of renewable energy. However, the complex coupling characteristics between energy sources make it difficult to quantify the production efficiency of multi-energy heterogeneous resources uniformly in the economic benefit model during the planning cycle. Quantifying the production efficiency of the IES for planning is currently an urgent problem to be solved. This study proposes a planning method for the IES based on the life cycle and emergy theory. First, emergy theory is applied to quantify the production efficiency of the IES. A complete economic benefit model is established based on life cycle theory. Second, a bi-level planning model of the IES is established. The upper-level model aims at minimizing the whole life cycle cost of the IES to plan the capacity and location of the coupling equipment. The lower-level model aims at maximizing the emergy yield ratio of the IES to provide the operating data for the upper level. Finally, comparing experimental evaluations with traditional planning schemes considering annual average cost and energy quality coefficient, the method in this study reduces planning costs by 23.16% and increases the consumption rate of renewable energy by 4.26%. It can be seen that the planning method proposed in this study improves the planning economy and the level of renewable energy consumption of the IES.

Keywords: integrated energy system, planning, life cycle, emergy, bi-level programming

OPEN ACCESS

Edited by:
Yingjun Wu,
Hohai University, China

Reviewed by:
Lijuan Duan,
Tsinghua University, China
Hantao Cui,
The University of Tennessee, Knoxville, United States

***Correspondence:**
Jun Wang
wangjun18@sgepri.sgcc.com.cn

Specialty section:
This article was submitted to Smart Grids, a section of the journal Frontiers in Energy Research

Received: *22 May 2021*
Accepted: *19 July 2021*
Published: *03 September 2021*

Citation:
Wang J, Du W and Yang D (2021) Integrated Energy System Planning Based on Life Cycle and Emergy Theory. Front. Energy Res. 9:713245. doi: 10.3389/fenrg.2021.713245

INTRODUCTION

Integrated energy system (IES) is an effective way to centralized supply of multi-energy and improves the absorptive capacity of renewable energy. A large number of renewable energy access lead to increase in the uncertainty of energy supply and affect energy utilization (Li et al., 2021). A reasonable IES planning scheme is an effective way to realize energy cascade utilization and ensure system economy. However, there is a complex coupling relationship among energy production, transmission, and utilization in the IES (Dou et al., 2020). In the system long time scale, the planning, construction, production, and other economic activities increased the difficulty for reasonable quantitative system energy conversion efficiency and the system construction of the comprehensive assessment of the economic benefit. Multi-energy centralized planning faces huge challenges (Heleno and Ren, 2020). The emergy theory can unify the measurement methods of various energy forms in the IES (Wei et al., 2020). It is also conducive to realizing the unified quantification of heterogeneous energy. The life cycle (LC) theory can coordinate the economic benefits of each stage in the whole LC

of the IES (Harris et al., 2020). This is beneficial in obtaining the full LC assessment of economic benefits in the planning process based on the LC theory. Therefore, in the process of IES planning, facing the challenges of incomplete description of the economic behavior process in the LC of the system and difficulties in the unified quantification of multiple types of resources, it is urgent to carry out IES planning research based on LC and emergy theory. It is conducive to the rational allocation of resources and the improvement of energy utilization efficiency.

The IES couples each energy subsystem through the energy hub (EH). The site selection of EHs has significant influence on the system's economic efficiency and energy utilization efficiency. Therefore, at present, research studies on IES planning are mostly based on different coupling modes of different energies. The selection of EHs is based on economic benefits, energy utilization efficiency, and other factors. According to different coupling modes, some research studies established planning models of electric–gas coupling model (Xie et al., 2020) and electric–heat–gas coupling model (Zhang et al., 2015) based on the operation of typical scenarios. The advantages and disadvantages of planning schemes of different coupling modes have been compared and analyzed. In terms of planning objectives, based on the medium and long-term load forecasting (Gan et al., 2017; Jiang et al., 2017), operation cost (Salimi et al., 2015; Pazouki and Haghifam, 2016; Gao et al., 2018; Wang et al., 2019a), investment cost (Bai et al., 2019), carbon trading cost (Wang et al., 2018a), environmental pollution cost (Zhang and Gao, 2016), and energy conversion efficiency (Gao et al., 2017; Wang et al., 2019b; Zeng et al., 2019) have been set as the goals to establish the EH planning model of the IES. A multi-objective EH planning model (Garmabdari et al., 2020) and a multi-layer EH planning model (Zhang et al., 2017) based on typical operation scenarios and combined with a general performance flow model of the system have also been proposed. The objective of the current research on IES planning is mainly to determine the economic benefits of the system according to the market value of the equipment and energy in the system (Wang et al., 2018b) and to establish equipment selection and capacity allocation model of the EH. In this process, the energy quality coefficients based on the exergy theory are applied to uniformly quantify the energy values of different energy forms usually based on different energy coupling methods (Chen et al., 2018). The energy conversion efficiency is described by the quantified energy value (Tian et al., 2019). However, existing research studies rarely quantify the social resources involved in the LC of the system by considering the economic benefits of the whole LC of system planning, construction, operation, and scrapping, so that the composition of energy conversion efficiency is not comprehensive.

In this study, on the IES containing renewable energy, LC theory is introduced to quantify the economic benefits of the whole LC. The economic benefits of EH construction and scrapping stages are taken into account to improve the description of the whole life cycle cost (LCC) of the system. The emergy theory is used to take the input of social resources into account and refine energy conversion efficiency of the system. The main contributions of the study are as follows:

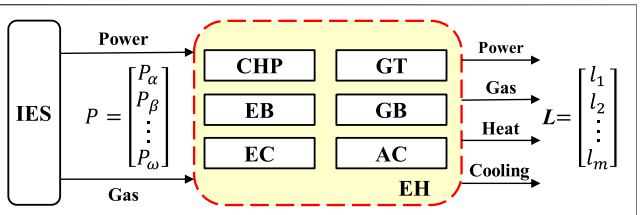

FIGURE 1 | IES structure based on EHs.

1) The energy conversion efficiency in the IES planning process is accurately quantified based on emergy theory. It is conducive to improving the energy efficiency of the system.
2) The LCC of the system planning, construction, operation, and scrapping in the process of siting and sizing the EH of the IES is calculated based on LC theory. It is conducive to improving the economic benefits of the whole LC of the system.
3) The IES planning method based on LC and emergy theory is proposed. It is conducive to ensuring the economic benefits of the system in the whole LC while improving energy efficiency.

The structure of this article is as follows. In the second section, the subsystem models and main energy equipment models of the IES are established. In the third section, emergy analysis of the IES is carried out to obtain the energy value model of the system output energy. In the fourth section, a bi-level IES planning model based on LC and emergy theory is established. In the fifth section, the effectiveness of different planning objectives on the planning result is analyzed using experimental evaluations. And the rationality and validity of the proposed method was also verified. The main achievements of this study are summarized in the sixth section.

INTEGRATED ENERGY SYSTEM MODEL

Energy Hub Model

A typical IES structure is shown in **Figure 1**. EH is an important hub of the IES in the process of energy conversion, transmission, and supply. An EH mainly includes combined heat and power (CHP), gas turbine (GT), electric boiler (EB), gas-fired boiler (GB), electric chiller (EC), and absorption chiller (AC).

The essence of an EH is to describe the function between the input and output pluripotent in the IES. Without considering the energy conversion process under the premise of transient conditions, we can use the EH model (Yao et al., 2018) to describe the ideal steady state of the EH:

$$\begin{bmatrix} L_1 \\ L_2 \\ \vdots \\ L_n \end{bmatrix} = \begin{bmatrix} c_{11} & c_{12} & \cdots & c_{1m} \\ c_{21} & c_{22} & \cdots & c_{2m} \\ \vdots & \vdots & \ddots & \vdots \\ c_{n1} & c_{n2} & \cdots & c_{nm} \end{bmatrix} \begin{bmatrix} P_1 \\ P_2 \\ \vdots \\ P_m \end{bmatrix}, \quad (1)$$

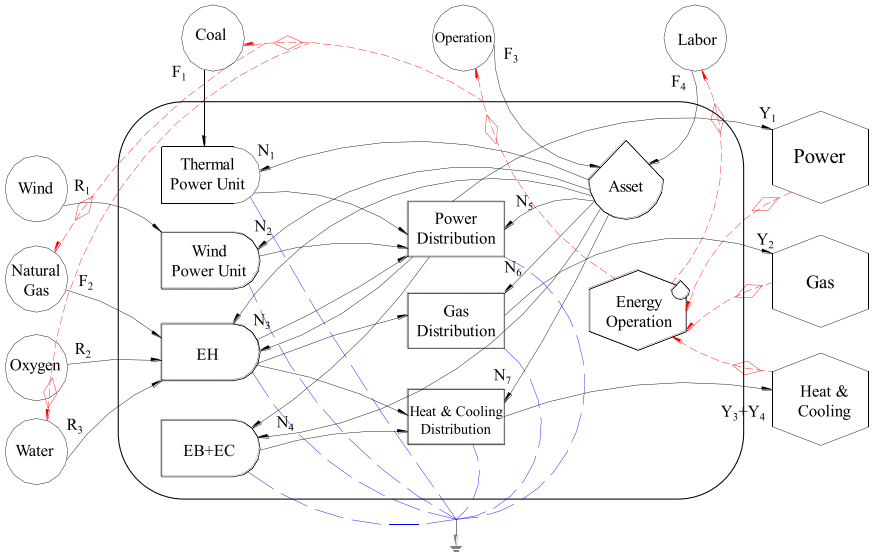

FIGURE 2 | IES emergy analytical structure.

where L_i (i = 1, 2, . . . , n) is the output of the ith energy form of the EH, P_j (j = 1, 2, . . . , m) is the input of the ith energy form of the EH, and c_{ij} is the conversion efficiency of i to j.

Energy Network Model

Energy network models mainly include the models of electrical power system (EPS), natural gas system (NGS), and district heat system (DHS). EPS mainly includes the constraints of three-phase power flow, power balance, generator output, node voltage, line power, and generator climbing (Correa-Posada and Sanchez-Martin, 2015; Eeea and Esa, 2019). NGS mainly includes the constraints of pipe flow, natural gas well, flow balance, compressor, pipe storage, and node pressure (Gao et al., 2017; Wei et al., 2017). DHS mainly considers the constraints of node flow balance, node power access feature fusion, load, and heat transfer characteristics (Dong et al., 2018).

EMERGY ANALYSIS OF THE INTEGRATED ENERGY SYSTEM

Emergy refers to the production of a product or service directly or indirectly by the consumption of the total available energy (Odum, 2012). It aims to convert different forms of energy into a unified value. The unit is solar emjoule, which is used to interpret a variety of social and natural value theory quantitative relations of energy and materials in the system. Through energy and material and economic flows, the IES links natural resources and human production activities closely together. It can be considered as a complete energy ecosystem. In this study, integrated analysis of the process of energy production, transportation, and supply of the IES is performed. Based on the general steps of emergy analysis (Zhang et al., 2016), the emergy analysis of the IES can be done and valued, as shown in **Figure 2**.

In this study, considering the power of the IES comes from thermal power, wind power generation, and power generation equipment in the EH, all power is sold to the system load demand. Certain energy loss occurs in the process of power transmission and supply, and **Figure 2** shows the economic flow between the system and user (a dotted line). Based on the way to value associated with the power of energy flow and computational algorithms, IES the can value Y_1 of the output power can be expressed as follows:

$$Y_1 = (R_1 + F_1 + F_2 + F_3 + F_4 + N_1 + N_2 + N_3 + N_5)\frac{E_{Y_1}}{E^{in}_{p,EH} + E_{Y_1}}, \tag{2}$$

where R_1 is the emergy of the loss of wind. F_1 is the thermal power unit generated electricity. F_2 is the emergy of the power consumption of natural gas. F_3 is the operation and maintenance costs of emergy consumption of the system. F_4 is the human resources value system consumption. N_1 is the asset's wreck value of power generation equipment. N_2 is the asset's wreck value of wind power equipment. N_3 is the asset's worth of the EH. N_5 is the asset's wreck value of power distribution facilities. E_{Y_1} is the electric power consumed by the user. $E^{in}_{p,EH}$ is the electricity consumed by the EH coupling equipment.

In the IES, the user's consumption of natural gas is mainly from gas wells, and the energy of the system output of natural gas Y_2 can be expressed as follows:

$$Y_2 = (F_2 + N_3 + N_6)\frac{E_{Y_2}}{E^{in}_{g,EH} + E_{Y_2}}, \tag{3}$$

where E_{Y_2} is the amount of gas consumed within the IES, $E^{in}_{g,EH}$ is the flow of gas consumption in the EH coupling device, and N_6 is the asset's wreck value of gas distribution device.

In the IES, heating and cooling needs hot/cold water from natural gas waste heat utilization, electric boiler, and electric machine. In this study, the unified value calculation for hot and cold water is carried out, and the system output of hot and cold water can be expressed as follows:

$$\begin{aligned} &Y_3 + Y_4 \\ &= (R_1 + F_1 + F_2 + F_3 + F_4 + N_1 + N_2 + N_3 + N_5)\frac{E_{p,EH}^{in}}{E_{p,EH}^{in} + E_{Y_1}} \\ &+ (F_2 + N_3 + N_6)\frac{E_{g,EH}^{in}}{E_{g,EH}^{in} + E_{Y_2}} + N_7 + N_4 + R_2 + R_3 + F_3 + F_4, \end{aligned} \quad (4)$$

where R_3 is the emergy of the oxygen the IES has used, R_4 is the emergy of the water the IES has used, N_4 is the asset's worth of the EC and EB, and N_7 is the asset's wreck value of heating and cooling distribution device.

The energy output is the ratio of the system output value and economic input values. The economy input values are derived from the human society economy. The primary energy is derived from a variety of means of production and labour services. The higher the emergy yield ratio, the higher the production efficiency of the system. The emergy yield ratio E_{YR} is as follows:

$$E_{YR} = Y/F. \quad (5)$$

BI-LEVEL PROGRAMMING MODEL FOR IES BASED ON THE THEORY OF LC AND EMERGY

Objective Function

This study considers IES system energy conversion efficiency and economical aspects and optimizes the IES configuration research. The optimization goal includes minimization of the LCC and maximization of the emergy yield ratio.

1) The objective function 1: minimization of the LCC.

Based on the LC theory, equipment purchase cost, replacement cost, material handling cost, annual maintenance cost, annual operation cost, residual value, and waste treatment equipment costs of the IES are considered synthetically. The LCC of the IES is calculated using the following equation:

$$\begin{aligned} &\min C_{LC} \\ &= \sum_{n=1}^{N} C_n P_n + \sum_{n=1}^{N}\sum_{j=1}^{R_n}\frac{C_n P_n}{(1+i)^{jt_n}}(1-r) + \sum_{n=1}^{L_p}\frac{M}{(1+i)^n}(1-t_r) \\ &+ \sum_{n=1}^{L_p}\frac{B}{(1+i)^n}(1-t_r) + \frac{S}{(1+i)^{L_p}}t_r - \sum_{n=1}^{L_p}\frac{D}{(1+i)^n}t_r, \end{aligned} \quad (6)$$

where N is the number of devices used in the IES. C_n is the initial investment cost of equipment n. P_n is the installed capacity of equipment n. R_n is the number of energy supplements of equipment n. i is the interest rate. t_r is the tax rate. L_p is the life of the design project. M is the system maintenance costs. B is the use of the energy cost in a year. S is the processing cost of abandoned equipment. D is the depreciation expense of equipment for a year.

The number of times rebuilding the equipment (R_n), the cost of equipment maintenance in a year (M), the use of the energy cost in a year (B), and the depreciation cost for a year (D) are as follows:

$$R_n = \mathrm{floor}\left(\frac{L_p}{L_n}\right) - 1, \quad (7)$$

$$M = r_M \sum_{n=1}^{N} C_n P_n, \quad (8)$$

$$B = \sum_{d=1}^{365}\sum_{t=1}^{24} E_{grid}^{d}(t)\pi_e(t) + F_{tot}^{d}(t)\pi_{gas}, \quad (9)$$

$$D = r_D \sum_{n=1}^{N} C_n P_n, \quad (10)$$

where floor(x) is a function that is used to calculate the biggest integer no greater than x. r_M is the equipment maintenance rate. $E_{grid}^{d}(t)$ is the thermal power unit capacity on day d in time t. $\pi_e(t)$ is the price of coal in time t. $F_{tot}^{d}(t)$ is the amount of gas use. π_{gas} is the price of gas. r_D is the allowance for depreciation of equipment. L_n is the service life of equipment n.

2) The objective function 2: maximization of the emergy yield ratio.

According to the definition of the emergy yield ratio in **Section 3**, it is expressed as follows:

$$\max E_{YR} = Y/F. \quad (11)$$

Constraints

The constraints mainly include equipment capacity, equipment operation, and energy balance. In this study, the unit to be selected for the EH includes the CHP, GT, EB, GB, EC, and AC. Considering the physical significance of optimized variables and the actual situation, equipment capacity needs to be maintained within a certain range, namely:

$$Q_{i,min} \le Q_i^r \le Q_{i,\max}, \quad (12)$$

where i = 1, 2, 3, 4, 5, and 6 represent the CHP, GT, EB, GB, EC, and AC. $Q_{i,\min}$ is the lowest installed capacity of the ith equipment. Q_i^r is the installed capacity of the ith equipment. $Q_{i,\max}$ is the highest installed capacity of the ith equipment.

The operation constraints of equipment are mainly rated power constraints of equipment. The operation constraints of the EH are as follows:

$$P_{i,\min} \le P_i^r \le P_{i,\max}, \quad (13)$$

where $P_{i,\min}$ is the lowest operating power of the ith equipment, P_i^r is the actual operating power of the ith equipment, and $P_{i,\max}$ is the rated power of the ith equipment.

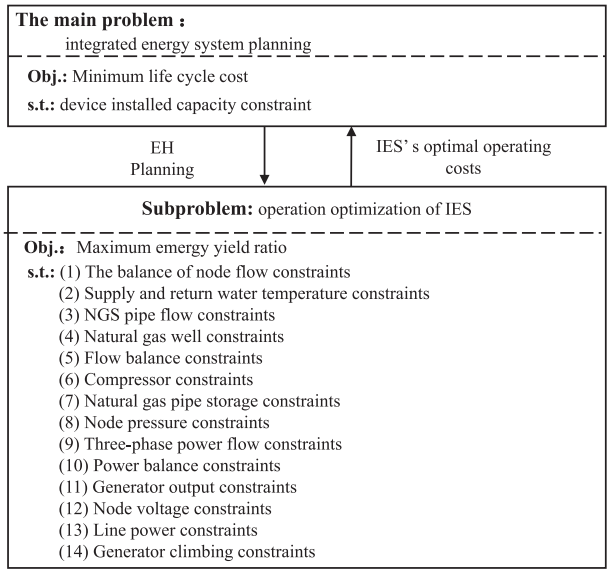

FIGURE 3 | EH bi-level programming model framework.

Model Transformation

It can be seen that the EH planning model in IES considering the whole LCC and emergy yield ratio is a very complex mixed integer nonlinear programming model. According to the multi-level optimization theory, based on the idea of decomposition coordination, the model is decomposed into the bi-level programming model, as shown in **Figure 3**.

In **Figure 3**, the first layer model is EH planning, which is the main problem in IES and is used to determine the installation type, location, and capacity of coupling equipment in the EH. The objective function is the system LCC minimization. The constraints include the installed capacity constraints and the discrete capacity constraints of the selected node. The second layer model is used to simulate the optimal operation mode of the IES in each scenario under the given EH site selection scheme. The objective function is to maximize the output rate of the system. Constraints include heat supply network node flow balance, change in the return water temperature and flow of natural gas pipeline network, air source, gas flow rate balance, air compressor, gas network management, gas network node pressure, trends in power system, power balance, generator output, node voltage, line power, and generating set climbing capacity. It is a typical optimal flow problem. This is a typical bi-level programming model; KKT conditions can be used to transform the lower targets into upper constraints and then into a mixed integer nonlinear programming model. The Lagrange multiplier method is used to solve the problem.

The parameter transfer relationship of the two-layer programming model is as follows: the first-layer planning model transfers the EH planning scheme (EH type, location, and capacity) to the operational sub-problem of the second layer, the second layer optimizes the running simulation for each scenario of the IES on this basis and returns the calculation result (the output of each unit in each scenario) to the first layer, and then the first layer plans to calculate the final objective function value (the system LCC).

Model Solving Process

The model solving process of this study is shown in **Figure 4**, which first generates a random run scenario, and then the selection of the EH site and optimization of the IES operation strategy including the EH are carried out considering the LCC of the system and the emergy output rate.

EXPERIMENTAL EVALUATIONS

Experiment Settings

The simulation and optimization analysis are based on MATLAB and GAMS platform in the win10 operating system, i7CPU, 2.20 GHz processor environment. The IES structure with renewable energy as an example is shown in **Figure 5**. The IES mainly consists of a modified IEEE 14-node EPS, an 11-node NGS (Abeysekera et al., 2016), and a DHS based on literature modification (Zhu et al., 2018). Heterogeneous energy flows through the EH to achieve coupling and complete energy type conversion. The equipment to be selected in the EH includes CHP, GT, EB, GB, EC, and AC. Based on the equipment parameter data in Wang et al. (2017), the specific parameter data in **Table 1** are formed after modification and supplementation. In the NGS, the minimum pressure is 22.5 mbar. The upper flow limit of the pipeline 12–14 is 150 m^3/h. The candidate nodes are 4, 11, and 9 of the EPS, 1 and 7 of the NGS, and 8 and 11 of the DHS.

After generating the scenario by Latin cube sampling according to the historical load data and minimizing it by the k-means clustering method, the load is divided into three categories: heating season, transition season, and cooling season. **Figure 6** shows the three types of IES load situations under different scenarios.

Then, based on the models in the typical load scenarios, a complex bi-level programming model is transformed into a general mixed-integer nonlinear model using STEP 2 in **Figure 4**. Finally, based on the model transformation results, STEP 3 in **Figure 4** is used to obtain the site selection of EHs, taking into account the 30-year service LC of the system.

For comparative analysis, the following four different programming target modes are set in the calculation example:

S1: the upper target is the lowest full LCC, and the lower target is the maximum energy yield.
S2: the upper target is the lowest LCC, and the lower target is the maximum energy conversion efficiency of the system based on energy and quality coefficient.
S3: the upper target is the lowest annual operating and construction cost of the system, and the lower target is the maximum output rate.
S4: the upper target is the lowest annual operating and construction cost of the system, and the lower target is the maximum energy conversion efficiency of the system based on energy and quality coefficient.

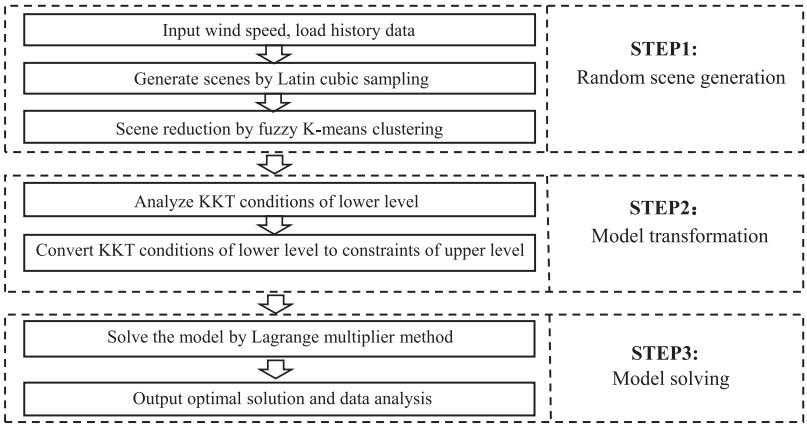

FIGURE 4 | Solving process.

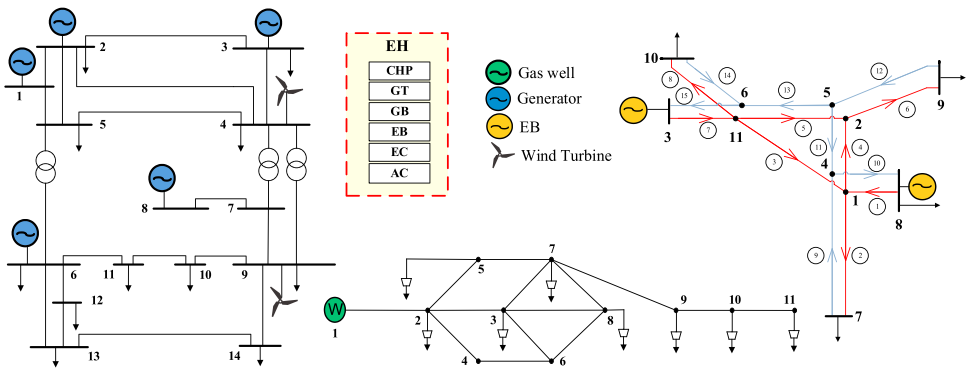

FIGURE 5 | IES test case.

TABLE 1 | EH equipment parameter.

Equipment to be selected	Number	Installed capacity (MW·h)	Energy conversion efficiency	Construction cost (×10^3$)
GT	A1	500	0.40	2,500
	A2	450	0.45	2,250
GB	B1	400	0.90	1,400
EB	C1	300	0.95	900
	C2	200	0.97	750
AC	D1	200	1.30	800
EC	E1	50	4.00	150
	E2	100	3.90	200
CHP	F1	200	0.70	30,000

Analysis of Results

1) Analysis of planning results of S1

The planning results of S1 are shown in **Table 2**. Due to large fluctuation of the electrical load, it needs to be balanced in time. Coupled with the power flow constraint, the node load far from the thermal power unit on the EPS still needs to be supplied by other equipment in time. Due to the uncertainty of renewable energy output, the load demand cannot be satisfied in time. The four nodes are connected with a typhoon power unit. When the output of renewable energy exceeds the load demand, the coupling equipment in the EH is used to absorb surplus power. When the output of renewable energy cannot meet the load demand, the electric energy supplied by other energy

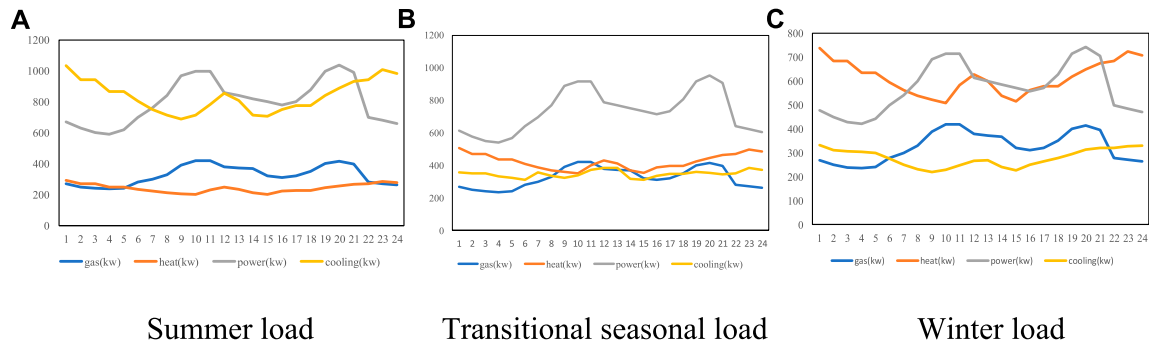

FIGURE 6 | Daily load of a typical scenario.

TABLE 2 | EH planning results under S1.

Equipment type	Number	Capacity (MW·h)	Construction cost ($\times 10^3$\$)	EH access node	EYR	LCC ($\times 10^9$\$)
GT	A2	450	2,500	4-1-8	9.74	2.19
GB	B1	400	1,400			
EB	C1	300	750			
AC	D1	200	800			
EC	E1	50	150			
CHP	F1	200	30,000			

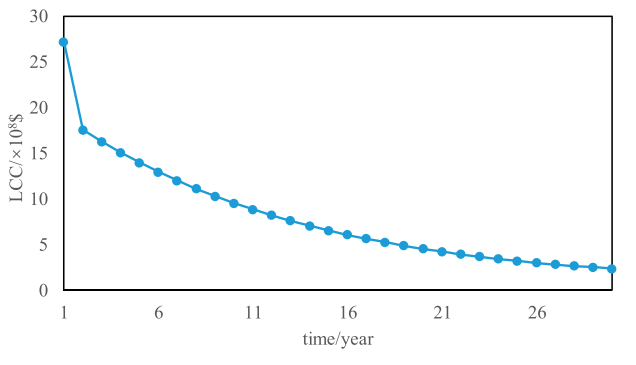

FIGURE 7 | Annual capital input in the whole LC of the IES.

networks is obtained through the EH. Due to the characteristics of high energy conversion efficiency and relatively low construction cost of electricity-cold coupling equipment and electricity-heat coupling equipment, it is more inclined to choose the coupling equipment that uses electric energy for energy conversion and supply when meeting the system load demand. As the coupling equipment to be selected in the EH is mainly used for energy conversion and supply of natural gas, the EH is connected to node 1 of the NGS. Despite the influence of seasonal factors, heat load demand is relatively stable; at the same time, since the DHS itself has certain energy storage ability, it can make full use of the tube. Hence, the EH is connected to the DHS to increase the ability of energy conversion. Therefore, large-capacity AC and GB are selected to connect to the 8 nodes of NGS in order to give priority to the use of excess heat energy in NGS and DHS for energy supply. The annual investment of the whole LC is shown in **Figure 7**.

2) Analysis of planning results of S2

The planning results of S2 are shown in **Table 3**. S2 aims at the lower level with the maximum energy conversion efficiency of the system based on energy and mass coefficient. Because the energy conversion efficiency based on energy and quality coefficient does not consider the economic factors of the system, the system does not consider the economic benefits during operation, which leads to the increase in the operation cost. However, the intermediate output rate of S1 is the energy conversion efficiency of the system that considers economic input and human resource input and can coordinate energy conversion efficiency and economic benefits. Since the four nodes in the EPS are connected to wind turbines with large capacity but small load, the EH of S2 is still connected to the four nodes in the EPS. Node 8 in the DHS is an important cold/hot load point. In order to ensure energy conversion efficiency and load demand, it is still connected to node 8 in the DHS. Therefore, in **Table 3**, the EH planning result of S2 is the same as that of S1 and the access location is the same as that of S1. Some equipment chooses models with large energy conversion efficiency, but the LCC increases.

3) Analysis of planning results of S3

The planning results of S3 are shown in **Table 4**. S3 takes the lowest annual operating and construction cost of the system as the upper target and the lower target with the maximum output

TABLE 3 | EH planning results under S2.

Equipment type	Number	Capacity (MW·h)	Construction cost ($\times10^3$$)	EH access node	Energy conversion efficiency	LCC ($\times10^9$$)
GT	A1	500	2,500	4-1-8	2.74	2.53
GB	B1	400	1,400			
EB	C2	200	750			
AC	D1	200	800			
EC	E2	100	200			
CHP	F1	200	30,000			

TABLE 4 | EH planning results under S3.

Equipment type	Number	Capacity (MW·h)	Construction cost ($\times10^3$$)	EH access node	EYR	Total cost ($\times10^9$$)
GT	A2	450	2,250	4-1–8	6.94	2.00
GB	B1	400	1,400			
EB	C2	200	750			
AC	D1	200	800			
EC	E1	50	200			
CHP	F1	200	30,000			

TABLE 5 | EH planning results under S4.

Equipment type	Number	Capacity (MW·h)	Construction cost ($\times10^3$$)	EH access node	Energy conversion efficiency	Total cost ($\times10^9$$)
GT	A2	450	2,500	6-1-11	2.46	2.19
GB	B1	400	1,400			
EB	C1	300	750			
AC	D1	200	800			
EC	E1	50	150			
CHP	F1	200	30,000			

rate, respectively. The lower level target of S3 is still the system emergy output rate, and some economic factors have been taken into account, leading to the same access location of the EH as S1. On the premise of meeting the load demand, in order to pursue a lower construction and operation cost, the construction cost of coupling equipment that uses electric energy for energy conversion and supply is relatively high and the equipment with relatively small capacity and low price is selected. Since the upper model does not consider the cost of the system in the construction and scrapping stages, the lower model puts forward certain requirements on most economic behaviors of the system through emergy utilization, thus ensuring the economic benefits of the system operation. Therefore, in **Table 4**, compared with the results of S1, the planning results in objective model 3 have the same access location as that of S1. However, as the economic behaviors considered in the upper goal are less than those in the lower model, the economic benefits of the part are better than S1 and the emergy output rate is lower than S1.

4) Analysis of planning results of S4

The planning results of S4 are shown in **Table 5**. The upper target of S4 is the lowest annual operating and construction cost of the system, and the lower target is the maximum energy conversion efficiency of the system based on energy and quality coefficient. Electric energy has the highest grade of energy, so the coupling conversion efficiency is relatively high when using electric energy for energy conversion. Since S4 considers the maximum energy conversion efficiency of the system, it will choose a larger capacity electrical coupling device. Therefore, EH is connected to the 6 nodes of the EPS with the thermal power unit. Node 11 is the connection hub of multiple water supply pipelines; since the pipeline diameter is large, transmission speed is fast, and it can effectively improve the heating efficiency, the EH is connected to node 11 of the NGS. This mode is the most traditional planning model, and the objective function lacks the planning of the economic behavior of the whole LC of the system, resulting in the neglect of part of the cost in the planning process of the EH. Therefore, in **Table 5**, the planning result of S4 is higher than that of S3, and the whole LCC is higher than that of S3. Meanwhile, the economic benefit of S3 is worse than that of S1, indicating that the economic benefit of S4's planning result is better than that of S1.

5) EH configuration schemes in different target modes consume renewable energy

The consumption of renewable energy under the configuration results of S1, S2, S3, and S4 in different scenarios is compared and analyzed, as shown in **Table 6**.

TABLE 6 | Comparison of planning results of different scenarios.

Scenarios	Wind power consumption rate (%)	LCC ($\times 10^{10}$\$)	Average daily operating cost ($\times 10^{5}$\$)
S1	44.82	2.19	1.51
S2	43.76	2.24	1.45
S3	43.65	2.53	1.38
S4	42.99	2.85	1.81

For EH planning based on emergy theory, the input of economic resources of the system is considered in the lower operating model. The system will have better economic benefits after two-layer economic benefit planning, and the wind abandoning cost has a great impact on the planning result, which improves the consumption of wind power and other renewable energy. As the social significance of environmental protection increases year by year, the unit price of environmental governance costs increases year by year, which leads to the increasing influence of the absorption rate of renewable energy on the annual cost of the system year by year and promotes the scheduling quantity of renewable energy in the planning process. Therefore, in **Table 6**, the S1 target mode has the highest absorption rate of wind power, S2 is similar to S3, and S4 is the smallest. Since the LCC not only includes the system operating cost, the LCC with the construction operating cost as the planning goal under the same lower planning goal is higher than the LCC considering the economic behavior in the system LC.

CONCLUSION

In this study, the whole LC theory and emergy theory are introduced, and the bi-level programming model of the IES is established to optimize the selection of the equipment in EHs. Among them, the upper-level model takes the cost of system planning, construction, operation, and scrapping into consideration, aiming at the minimum cost of the whole LC to provide the siting and sizing scheme for the lower level model. Considering the input of social resources, the lower level model of operation takes the maximum output rate of the system emergy into account to provide the optimal operation cost for the upper level of model. Finally, after transforming the complex bi-level model into a mixed-integer nonlinear model by KKT conditions, the Lagrange multiplier method is adopted to solve the model. The effectiveness of the IES programming method proposed in this paper is verified by experimental evaluations. The following conclusions are mainly drawn from the results of our experiment:

1) The introduction of the planning model of emergy theory can effectively unify and quantify heterogeneous energy sources in the IES, including social resources, which is conducive to coordinating the economic benefits of system investment and energy utilization. Compared with planning with energy quality coefficients, planning costs can be reduced by 11.43%.
2) The planning model with the introduction of LC theory can effectively integrate the costs of all stages of system planning, construction, operation and scrapping. The system cost description is improved. Compared with planning by considering the average annual cost, the planning cost can be reduced by 21.40%.
3) For the IES containing renewable energy, compared with the traditional planning scheme, the planning scheme of LC theory and emergy theory is beneficial to improve the absorption rate of wind power and other renewable energy, reduce the total cost of the system, and improve the utilization rate of resources. Compared with planning in consideration of the average annual cost and energy quality coefficient, the planning cost has been reduced by 23.16% and the renewable energy consumption rate has increased by 4.26%.
4) In the future research, the planning method of the energy network will be further studied on the basis of the article and the integrity of the theory and the method of IES planning will be improved.

DATA AVAILABILITY STATEMENT

The original contributions presented in the study are included in the article/Supplementary Material; further inquiries can be directed to the corresponding author.

AUTHOR CONTRIBUTIONS

JW: conceptualization, methodology, and writing. WD: data curation, software, validation, reviewing, and editing. DY: data curation, software, reviewing, and editing.

FUNDING

This study received funding from the Science and Technology Project of State Grid Corporation of China "Research on key technologies of planning and design of county energy Internet for energy transition" (5400-202119156A-0-0-00). The funder was not involved in the study design, collection, analysis, interpretation of data, the writing of this article, or the decision to submit it for publication. All authors declare no other competing interests.

ACKNOWLEDGMENTS

The content of this manuscript has been presented in part at the 8th Renewable Power Generation Conference (RPG 2019), Shao Y., Dou X., Wang J., et al. "Integrated energy system planning with distributed generation based on emergy theory", 8th Renewable Power Generation Conference (RPG 2019), 2019. The article has obtained the copyright to be reused for publication.

REFERENCES

Abeysekera, M., Wu, J., Jenkins, N., and Rees, M. (2016). Steady State analysis of gas networks with distributed injection of alternative gas. *Appl. Energ.* 164, 991–1002. doi:10.1016/j.apenergy.2015.05.099

Bai, H., Yin, S., and Li, H. (2019). Optional planning of multi-energy Stations considering Carbon-trading cost. *J. Electron. Power Sci. Tech.* 34 (1), 11–19.

Chen, B., Liao, Q., Liu, D., and Wang, W. (2018). Comprehensive Evaluation Indices and Methods for Regional Integrated Energy System. *Automation Electric Power Syst.* 42 (4), 174–182.

Correa-Posada, C. M., and Sanchez-Martin, P. (2015). Integrated power and natural gas model for energy adequacy in Short-term operation. *IEEE Trans. Power Syst.* 30 (6), 3347–3355. doi:10.1109/tpwrs.2014.2372013

Dong, S., Wang, C., and Xu, S. (2018). Day-ahead optimal Scheduling of electricity-gas-heat integrated energy System considering dynamic characteristics of network. *Automation Electric Power Syst.* 42 (13), 12–19.

Dou, X., Wang, J., Wang, Z., Li, L., Bai, L., Ren, S., et al. (2020). A dispatching method for integrated energy System based on dynamic time-interval of model predictive control. *J. Mod. Power Syst. Clean Energ.* 8 (5), 841–852. doi:10.35833/mpce.2019.000234

Eeea, B., and Esa, C. (2019). Modified JAYA algorithm for optimal power flow incorporating renewable energy Sources considering the cost, emission, power loss and voltage profile improvement. *Energy* 178, 598–609.

Gan, L., Chen, Y., Liu, Y., and Xiong, W. (2017). Coordinative optimization of multiple energy flows for microgrid with renewable energy resources and case Study. *Electric Power Automation Equipment* 37 (6), 275–281.

Gao, M., Wang, K., and He, L. (2018). Probabilistic Model Checking and Scheduling Implementation of an Energy Router System in Energy Internet for Green Cities. *IEEE Trans. Ind. Inf.* 14 (4), 1501–1510. doi:10.1109/tii.2018.2791537

Gao, M., Wang, K., and He, L. (2017). Probabilistic Model Checking for Green Energy Router System in Energy Internet. Proc. Int. Conf. 2017 IEEE Global Communications Conference. Singapore. doi:10.1109/glocom.2017.8254465

Garmabdari, R., Moghimi, M., and Yang, F. (2020). Multi-objective optimisation and planning of grid-connected cogeneration Systems in presence of grid power fluctuations and energy Storage dynamics. *Energy*, 212.

Harris, A., Soban, D., Smyth, B. M., and Best, R. (2020). A probabilistic fleet analysis for energy consumption, life cycle cost and greenhouse gas emissions modelling of bus technologies. *Appl. Energ.*, 261.

Heleno, M., and Ren, Z. (2020). Multi-energy microgrid planning considering heat flow dynamics. *IEEE Trans. Energ. Convers.* (99), 1, 2020 . 1. doi:10.1109/tec.2020.3041572

Jiang, H., Wang, K., Wang, Y., and Gao, M. (2017). Energy Big Data: A Survey. *IEEE Access* 4, 3844–3861.

Li, X., Wang, W., and Wang, H. (2021). A novel bi-level robust game model to optimize a regionally integrated energy System with large-Scale centralized renewable-energy Sources in Western China. *Energy* (10), 120513.

Odum, H., T. (2012). *Handbook of emergy evaluation*. . https://cep.ees.ufl.edu/emergy/publications/folios.shtml (accessed May 14, 2019).

Pazouki, S., and Haghifam, M.-R. (2016). Optimal planning and Scheduling of energy hub in presence of wind, Storage and demand response under uncertainty. *Int. J. Electr. Power Energ. Syst.* 80 (9), 219–239. doi:10.1016/j.ijepes.2016.01.044

Salimi, M., Ghasemi, H., Adelpour, M., and Vaez-ZAdeh, S. (2015). Optimal planning of energy hubs in interconnected energy Systems: a case Study for natural gas and electricity. *IET Generation, Transm. Distribution* 9 (8), 695–707. doi:10.1049/iet-gtd.2014.0607

Tian, L., Cheng, L., and Guo, J. (2019). Multi-energy System Valuation Method Based on Emergy Analysis. *Power Syst. Tech.* 43 (8), 2925–2934. doi:10.13335/j.1000-3673.pst.2018.2310

Wang, G., Yang, Y., Wang, S., Zhang, H., and Wang, Y. (2019). Efficiency analysis and experimental validation of the ocean thermal energy conversion with phase change material for underwater vehicle. *Appl. Energ.* 248 (AUG.15), 475–488. doi:10.1016/j.apenergy.2019.04.146

Wang, W., Wang, D., and Jia, H. (2017). Steady State analysis of electricity-gas regional integrated energy System with consideration of NGS network Status. *Proc. CSEE* 37 (5), 1293–1304.

Wang, Y., Wang, Y., Huang, Y., Li, F., Zeng, M., Li, J., et al. (2019). Planning and operation method of the regional integrated energy System considering economy and environment. *Energy* 171 (MAR.15), 731–750. doi:10.1016/j.energy.2019.01.036

Wang, Y., Zhang, N., Zhuo, Z., Kang, C., and Kirschen, D. (2018). Mixed-integer linear programming-based optimal configuration planning for energy hub: Starting from Scratch. *Appl. Energ.* 210 (jan.15), 1141–1150. doi:10.1016/j.apenergy.2017.08.114

Wang, Z., Tang, Y., and Qiao, B. (2018). Research on Integrated Natural Gas and Electric Power System Optimal Power Flow and its Environmental Synergy. *Proc. CSEE* 38, 111–120.

Wei, J., Zhang, Y., Wang, J., Cao, X., and Khan, M. A. (2020). Multi-period planning of multi-energy microgrid with multi-type uncertainties using chance constrained information gap decision method. *Appl. Energ.*, 260.

Wei, Z., Zhang, S., and Sun, G. (2017). Power-to-gas considered peak load Shifting research for integrated electricity and natural-gas energy Systems. *Proc. CSEE* 37 (16), 4601–4609.

Xie, S., Hu, Z., Wang, J., and Chen, Y. (2020). The optimal planning of Smart multi-energy Systems incorporating transportation, natural gas and active distribution networks. *Appl. Energ.* 269, 115006. doi:10.1016/j.apenergy.2020.115006

Yao, S., Gu, W., and Zhang, X. (2018). Effect of heating network characteristics on ultra-short-term Scheduling of integrated energy System. *Automation Electric Power Syst.* 42 (14), 89–96.

Zeng, H., Liu, T., and He, C. (2019). Multi-objective Optimization for Integrated Natural-gas and Electricity Energy System Considering Power-to-gas. *Electr. Meas. Instrumentation* 56 (8), 99–107.

Zhang, L., and Gao, J. (2016). Exploring the effects of international tourism on China's economic growth, energy consumption and environmental pollution: Evidence from a regional panel analysis. *Renew. Sust. Energ. Rev.* 53, 225–234. doi:10.1016/j.rser.2015.08.040

Zhang, S., Yuan, J., and Cheng, H. (2016). Optimal Distributed Generation Planning in Active Distrbution Network Considering Demand Side Management and Nerwork Reconfiguration. *Proceeding of the CSEE* 36, 1–9.

Zhang, X., Shahidehpour, M., Alabdulwahab, A., and Abusorrah, A. (2017). Optimal expansion planning of energy hub with multiple energy infrastructures. *IEEE Trans. Smart Grid* 6 (5), 2302–2311.

Zhang, X., Shahidehpour, M., Alabdulwahab, A., and Abusorrah, A. (2015). Optimal expansion planning of Energy hub with multiple energy infrastructures. *IEEE Trans. Smart Grid* 6 (5), 2302–2311. doi:10.1109/tsg.2015.2390640

Zhu, J., Ye, Q., and Zou, J. (2018). Short-term operation Service mechanism of ancillary Service in the UK electricity market and its enlightenment. *Automation Electric Power Syst.* 42 (17), 1–8.

Conflict of Interest: JW, WD, and DY were employed by the company NARI Group Corporation.

frontiers in Energy Research

ORIGINAL RESEARCH
published: 28 September 2021
doi: 10.3389/fenrg.2021.722606

Control of the Distributed Hybrid Energy Storage System Considering the Equivalent SOC

Wei Jiang[1]*, *Zhiqi Xu*[1], *Bin Yu*[1], *Ke Sun*[2], *Kai Ren*[1], *Yifan Deng*[1] and *Saifur Rahman*[3]

[1]School of Electrical Engineering, Southeast University, Nanjing, China, [2]Jiangsu Provincial Key Laboratory of Smart Grid Technology and Equipment, Southeast University, Nanjing, China, [3]Advanced Research Institute, Virginia Tech, Arlington, VA, United States

A hybrid energy storage system (HESS) consists of two or more types of energy storage components and the power electronics circuit to connect them. Therefore, the real-time capacity of this system highly depends on the state of the system and cannot be simply evaluated with traditional battery models. To tackle this challenge, an equivalent state of charge (ESOC) which reflects the remaining capacity of a HESS unit in a specific operation mode, is proposed in this paper. Furthermore, the proposed ESOC is applied to the control of the distributed HESS which contains several units with their own local targets. To optimally distribute the overall power target among these units, a sparse communication network-based hierarchical control framework is proposed. This framework considers the distributed control and optimal power distribution in the HESS from two aspects - the power output capability and the ESOC balance. Based on the primary droop control, the total power is allocated according to the maximum output capacity of each unit, and the secondary control is used to adjust the power from the perspective of ESOC balance. Therefore, each energy storage unit can be controlled to meet the local power demand of the microgrid. Simulation results based on MATLAB/Simulink verify the effectiveness of the application of the proposed equivalent SOC.

Keywords: consistency algorithm, variable droop coefficient, hybrid energy storage system, state of charge, hierarchical control structure

OPEN ACCESS

Edited by:
Yingjun Wu,
Hohai University, China

Reviewed by:
Kailong Liu,
University of Warwick,
United Kingdom
Wei Liu,
Nanjing University of Science and Technology, China

***Correspondence:**
Wei Jiang
jiangwei@seu.edu.cn

Specialty section:
This article was submitted to Smart Grids, a section of the journal Frontiers in Energy Research

Received: *09 June 2021*
Accepted: *09 August 2021*
Published: *28 September 2021*

Citation:
Jiang W, Xu Z, Yu B, Sun K, Ren K, Deng Y and Rahman S (2021) Control of the Distributed Hybrid Energy Storage System Considering the Equivalent SOC. Front. Energy Res. 9:722606. doi: 10.3389/fenrg.2021.722606

INTRODUCTION

Energy storage systems are widely deployed in microgrids to reduce the negative influences from the intermittency and stochasticity characteristics of distributed power sources and the load fluctuations (Rufer and Barrade, 2001; Hai Chen et al., 2010; Kim et al., 2015; Ma et al., 2015). From both economic and technical aspects, hybrid energy storage systems (HESSs) have several benefits compared to traditional battery-based energy storage systems. In a battery-supercapacitor HESS unit, the requirements for both the energy density and the power density can be satisfied (Zhou et al., 2011). With the help of supercapacitors, the peak power performance of the energy storage system can be enhanced, and thus, the stress on batteries can be reduced, and their lives are extended (Dougal et al., 2002; Gao et al., 2005).

Since a HESS unit usually consists of two or more types of energy storage components and a power electronic circuit to couple them, accurate evaluation of the remaining energy in the system is challenging. In (Mesbahi et al., 2017), an integrated model for energy storage components coupled with power electronic devices is built for an electrical vehicle simulator. In (Dey et al., 2019), an

online state and parameter estimation scheme in a battery-double-layer-capacitor system is proposed. However, since the two above approaches focus on specific applications, they cannot be used as comprehensive techniques to evaluate the remaining energy in hybrid energy storage systems.

Meanwhile, energy storage systems are usually widely invested and installed in power system. In a distributed HESS, the HESS units with relatively low power and energy capacities can be equipped where the distributed power sources are located and can be used to suppress local fluctuations and stabilize the node voltage. Through coordinated control of these distributed units, the units can cooperate to fulfill an overall goal in the microgrid, such as stabilizing the transmission line power and providing emergency frequency control, with proper energy evaluation, power allocation strategies and communication links (Zhao et al., 2011; Le Dinh and Hayashi, 2013; Arif and Aziz, 2017; Yongqiang and Tianjing, 2017).

The classical coordinated control methods can be classified into three categories: centralized control, distributed control and decentralized control. Centralized control methods require a high-speed high-throughput data processing center (Tsikalakis and Hatziargyriou, 2008; Tan et al., 2012) and reliable communication between the center and each unit, which results in higher costs and potential risk of failures (Chen and Wang, 2015). The distributed control methods, do not have these requirements (Chandorkar et al., 1993; Shu et al., 2018). However, directly using droop control in a distributed energy storage system without considering the state of charge (SOC) of the energy storage components may cause over-charging and over-discharging problems. To tackle this issue, in (Mokhtari et al., 2013), a distributed control strategy with limited communications between neighboring energy storage units is proposed. In (Li et al., 2014), the output power adjustment of each unit is based on the ratio determined by its SOC level. In (Li et al., 2017), both consistency control and droop control methods are used for frequency adjustment. However, considering the asymmetric characteristics of the energy storage components in a HESS unit, these approaches cannot be directly applied. Decentralized control also has its disadvantages. The local information collected by local controller is limited, so it is difficult to comprehensively consider the dynamic characteristics of all distributed generation and the whole microgrid system. Meanwhile, it is difficult to realize the frequency and voltage regulation of the distributed generation and as well as the economic dispatch of microgrid (Xin et al., 2011). Due to the absence of microgrid central controller (MGCC) and communication system, the recovery speed of voltage and frequency is relatively slow after interference.

In the isolated operation mode of microgrid, the energy storage device can be used to maintain the stability of system frequency and voltage with the distributed generations (Rodrigues et al., 2018). However, few literatures introduce how to utilize the features of the HESS to support the isolated microgrid with a distributed structure.

In this paper, a sparse communication network based hierarchical control structure with considering the equivalent SOC (ESOC) evaluation is proposed, in which the power demand is distributed according to two criteria: 1) the real-time power output ability of each HESS unit and 2) the control in state of charge of each HESS unit.

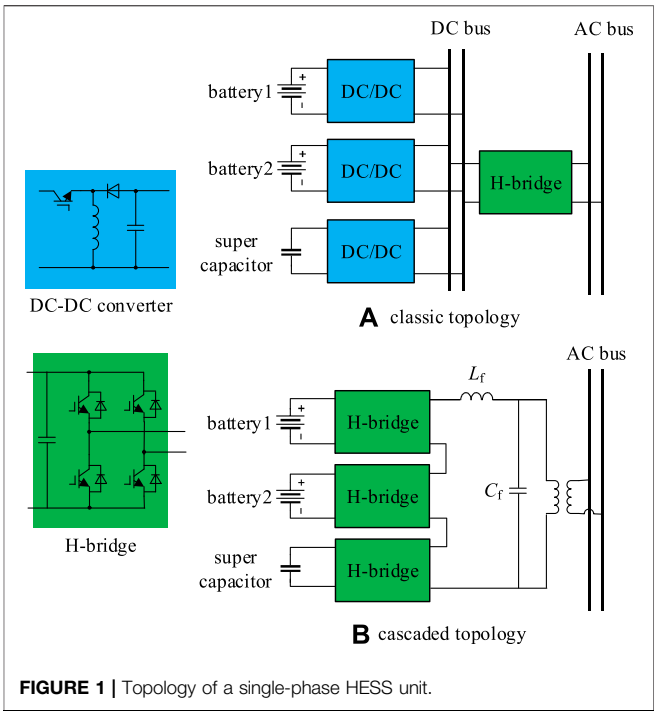

FIGURE 1 | Topology of a single-phase HESS unit.

The rest of this paper is organized as follows. In *Equivalent Circuit and SOC of HESS*, the generalized equivalent model of HESS and the method of evaluating the remaining energy in HESS is proposed. The power distribution method which considers the real-time power output ability and state of charge of each HESS units is described in *Hierarchical Control Structure For Distributed HESS*. Simulation results are presented in *Simulation Analysis* to verify the effectiveness of the proposed method. Conclusions are drawn in *Conclusion*.

EQUIVALENT CIRCUIT AND SOC OF HESS

The power conversion system (PCS) connecting the hybrid energy storage components and the AC/DC bus are variously studied (Ghazanfari et al., 2012; Hai-Feng et al., 2014; Kawakami et al., 2014; Tian et al., 2019). The most classic topology is shown in **Figure 1A**. The battery and the supercapacitor are individually regulated and inverted with DC/DC and DC/AC converters and eventually paralleled connected to the AC bus. To enhance the output voltage level and improve power quality, the cascaded HESS system has been investigated, as shown in **Figure 1B**, In this structure, each energy storage component is connected to an H-bridge, and multiple H-bridges are series-connected to form high-voltage output. The output power of the unit can be flexibly controlled by regulating the amplitude and phase of the output voltage.

In this paper, the cascaded structure is selected to be the PCS of HESS units since it is more complicated than the traditional

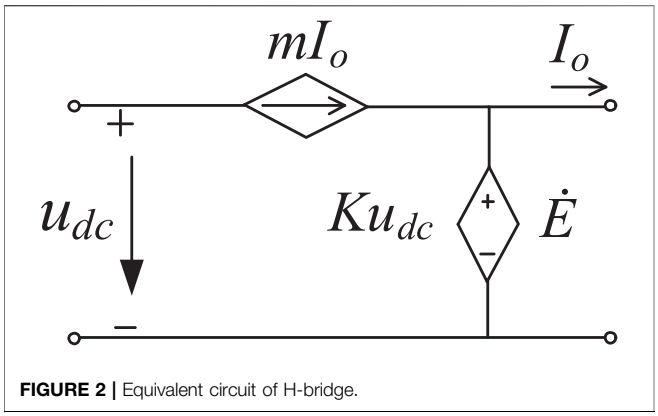

FIGURE 2 | Equivalent circuit of H-bridge.

parallel-connected converters. It should be noted that the proposed ESOC evaluation algorithm can also be applied to other HESS PCS topologies.

Operation Modes of the HESS Unit

Considering different levels of power demand, cascaded modules in **Figure 1B** usually operate in asymmetric states. For example, when high power surge emerges, the supercapacitor modules need to enhance power output by increasing their terminal voltages. In this case, the remaining operation duration highly depends on the SOC of the supercapacitor. In contrast, when the output power is relatively low, the operation duration is mainly related to the SOC of the battery since the supercapacitor modules are standby.

Therefore, the equivalent SOC of the HESS units hinges on its operation mode and the dominating energy storage component. There are totally four different modes:

1) Standby mode: The HESS unit does not inject or absorb active power.
2) Operation mode 1 (normal power): The active power injection or absorption requirement is within the ability of the batteries, so only batteries are injecting or absorbing power. The supercapacitors are used as an energy buffer.
3) Operation mode 2 (instantaneous peak power): When peak power requirement which lasts shorter than the dynamic response time constant of the batteries occurs, batteries are on standby, and only supercapacitors are injecting or absorbing power.
4) Operation mode 3 (continuous high power): To meet the continuous high power requirement, all the batteries and supercapacitors are injecting or absorbing power simultaneously.

Equivalent Circuit of a Cascaded HESS Unit

The equivalent circuit model of the HESS unit is the basis of the accurate evaluation of the SOCs of each component in and the equivalent SOC of a HESS unit. A HESS unit consists of batteries, supercapacitors and H-bridges.

The equivalent circuits of the battery and the supercapacitor are introduced in (Newman et al., 2003) and (Li et al., 2016) respectively. In addition to these components, the equivalent circuit of the H-bridge is proposed in this paper. The complete model, which is composed of the equivalent circuits of these three components, is further simplified as a generalized equivalent circuit for ESOC definition purposes.

The equivalent circuit of the H-bridge is shown in **Figure 2**. K is chosen from −1, 0 and 1, determined by the control signal of the PWM. I_o is the effective value of the output current. m is the equivalent modulation depth, which indicates the amount of power the DC source on the left side absorb or inject. It is defined as

$$m_* = \frac{P_* T}{u_* I_o T} = \frac{P_*}{u_* I_o} \tag{1}$$

where T is the sampling period; $*$ represents the type of the DC source (b-battery, c-supercapacitor); P_* is the active power injected into or absorbed by the DC-source, corresponding to positive and negative values respectively; u_* is the output voltage of the energy storage component at the end of last sampling period; and I_o is the effective value of the output current in last sampling period.

According to the equivalent circuits of the battery, the supercapacitor and the H-bridge, the equivalent circuit of a HESS unit is shown in **Figure 3**.

In **Figure 3**, the output voltage u_B of a battery can be calculated as

$$u_B = E_0 - K\frac{Q}{Q - \int_0^t i_b\,dt} + A \cdot exp\left(-B\int_0^t i_b dt\right) - i_b r \tag{2}$$

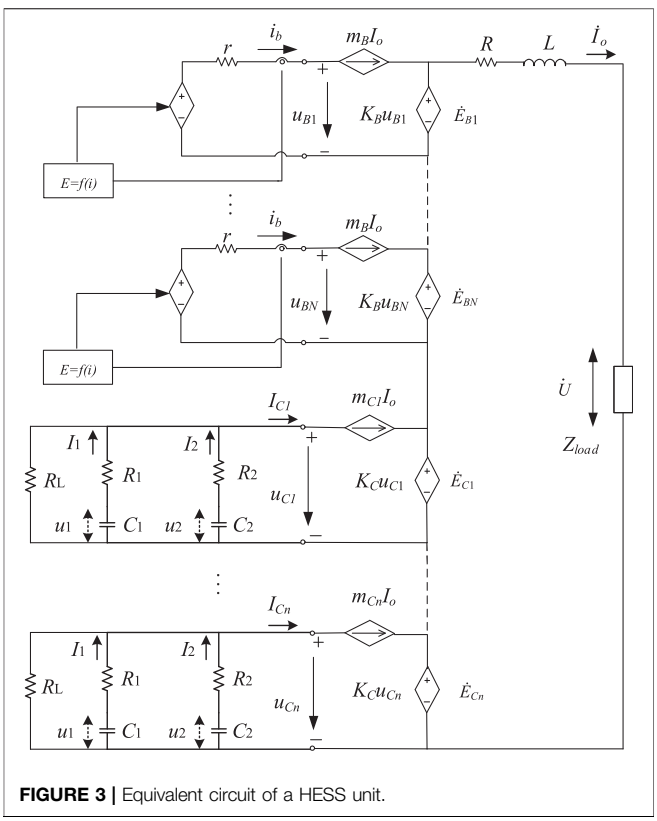

FIGURE 3 | Equivalent circuit of a HESS unit.

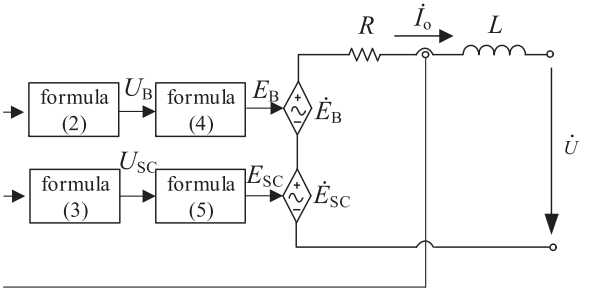

FIGURE 4 | Equivalent circuit of a HESS unit.

where r is the internal resistor of the battery and E_0, K, A and B are parameters obtained from the discharging curve.

The output voltage u_C of a supercapacitor can be calculated as

$$\begin{cases} \dfrac{du_1}{dt} = \dfrac{(I_C R_2 R_L + R_L u_2 - (R_2 + R_L)u_1)}{C_1 (R_1 R_2 + R_2 R_L + R_1 R_L)} \\ \dfrac{du_2}{dt} = \dfrac{(I_C R_1 R_L + R_L u_1 - (R_1 + R_L)u_2)}{C_2 (R_1 R_2 + R_2 R_L + R_1 R_L)} \\ u_C = R_L \left(I_C - C_1 \dfrac{du_1}{dt} - C_2 \dfrac{du_2}{dt} \right) \end{cases} \tag{3}$$

where the parameters R_1, C_1, R_2, C_2, and R_L can be obtained from the charging and discharging curve of the supercapacitor.

The complete model shown in **Figure 3** is too complex for analysis and thus needs further simplification. Based on the principle of combining the adjacent energy storage components of the same type without changing the output power, the model can be simplified as the generalized equivalent circuit, which is shown in **Figure 4**.

In **Figure 4**, two controlled voltage sources (CVSs) are used to represent two types of energy storage components (the battery and the supercapacitor). The resistor R and the inductor L are used to represent the loss and the inertial characteristics of the HESS unit. $\dot{U}$ and $\dot{I}_o$ are the output voltage and current of the HESS unit. $\dot{E}_B$ and $\dot{E}_{SC}$ are the output voltage of the equivalent CVS of the batteries and the supercapacitors. E_B and E_{SC}, the effective values of $\dot{E}_B$ and $\dot{E}_{SC}$, are determined by

$$E_B = m_B \cdot N \cdot u_B \tag{4}$$

$$E_{SC} = m_{SC} \cdot n \cdot u_{SC} \tag{5}$$

where m_B and m_{SC} are the equivalent modulation depth of the H-bridge connected with the battery(s) and the supercapacitor(s), respectively. N and n are the numbers of battery(s) and supercapacitor(s), respectively. u_B and u_{SC} are the voltages of a battery and a supercapacitor, which are explicated in **Eqs 2, 3**.

Definition of the Equivalent SOC and its Normalization

Based on the generalized equivalent circuit (**Figure 4**), the SOC of each energy storage component is defined as

$$SOC_{*j+1} = SOC_{*j} - \frac{1}{C_{*N}} \int_0^T \eta_* i_{o*j} E_{*j} dt \tag{6}$$

where * represents the type of energy storage component (*B*-battery, *SC*-supercapacitor) and SOC_{*j} is the SOC of the energy storage component in time period j. i_{o*j} and E_{*j} are the output current and output voltage in time period j, respectively. η_* is the efficiency of charging and discharging; C_{*N} is the rated capacity of this energy storage component; η_* and C_{*N} are parameters provided by the producer of the energy storage component.

Based on the SOCs of the energy storage components in a HESS unit, this paper proposes equivalent SOC (ESOC) to reflect the state of charge of a HESS unit by a comprehensive consideration of the operating conditions of all the energy storage components in the HESS unit. It is defined as

$$ESOC^j = \frac{\sum_{*=B,SC} \mathrm{sgn}(m_{*j}) \cdot SOC_{*j} C_{*N}}{\sum C_{*N}} \tag{7}$$

where $ESOC^j$ is the ESOC of a HESS unit in time period j; SOC_{*j} is the SOC of the specific type of energy storage components indicated by * (*B* -battery, *SC* -supercapacitor) in time period j; C_{*N} is the total rated capacity of this type of energy storage component(s); and $\mathrm{sgn}(m_{*j})$ is a sign function, the definition is as follows. The four categories in its definition correspond to the standby mode and three operation mode mentioned in *Operation Modes of the HESS Unit*.

$$\begin{cases} sgn(m_{*j}) = 0 & , if \ |m_{Bj}| < k \ and \ |m_{SCj}| < l \\ sgn(m_{Bj}) = 1, sgn(m_{SCj}) = 0, & if \ |m_{Bj}| \geq k \ and \ |m_{SCj}| < l \\ sgn(m_{Bj}) = 0, sgn(m_{SCj}) = 1, & if \ |m_{Bj}| < k \ and \ |m_{SCj}| \geq l \\ sgn(m_{*j}) = 1 & , if \ |m_{Bj}| \geq k \ and \ |m_{SCj}| \geq l \end{cases} \tag{8}$$

where k and l are small constants, which are used to judge the working states of the battery and the supercapacitor, respectively.

Considering the difference of the ESOC ranges of each energy storage unit under different modes, if we simply control the ESOC of all units to tend to a global average $ESOC^*$, it may cause that the ESOC of some units to exceed their limits. Therefore, this paper considers the standardization of the ESOC in different modes to the range of 0–1. The definition of the standardized ESOC of the unit $\langle \mathrm{ESOC}_i \rangle$ is as follows

$$\langle \mathrm{ESOC}_i \rangle = \frac{\mathrm{ESOC}_i - \mathrm{ESOC}_{i\_min}}{\mathrm{ESOC}_{i\_max} - \mathrm{ESOC}_{i\_min}} \tag{9}$$

where ESOC_{i_max}、ESOC_{i_min} is the upper and lower limits of the reasonable working range of ESOC of the i-th energy storage unit, and the specific calculation of the lower limits is given in the following formula.

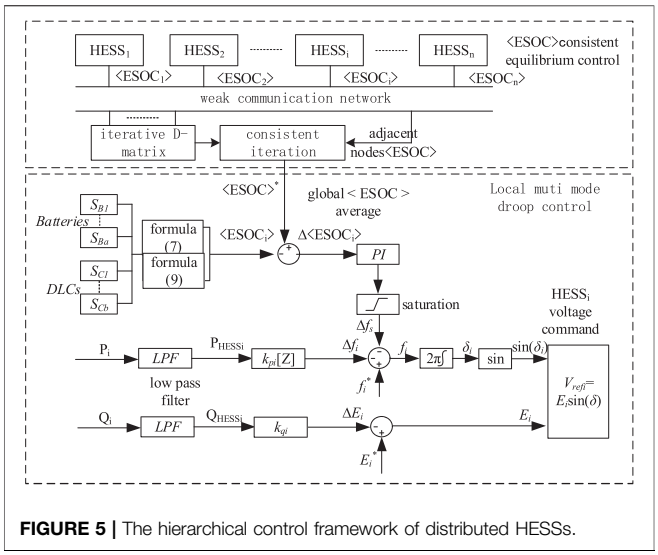

FIGURE 5 | The hierarchical control framework of distributed HESSs.

$$\begin{cases} ESOC_{min}^{\mathrm{I}} = \dfrac{\sum_{B1,B2\ldots Bn} S_{B\_\min} C_{BN}}{\sum C_{*N}} \\ ESOC_{min}^{\mathrm{II}} = \dfrac{\sum_{SC1,SC2\ldots SCn} S_{SC\_\min} C_{SCN}}{\sum C_{*N}} \\ ESOC_{min}^{\mathrm{III}} = \dfrac{\sum_{*=B,SC} S_{*\_\min} C_{*N}}{\sum C_{*N}} \end{cases} \tag{10}$$

The changes of ⟨ESOC⟩ when a HESS unit switches different operation modes is much smaller than that of ESOC. Thus, ⟨ESOC⟩ is a much better choice for the state of charge control for multiple HESS units.

HIERARCHICAL CONTROL STRUCTURE FOR DISTRIBUTED HESS

Sparse Communication Network Based Hierarchical Control

Figure 5 shows the hierarchical control framework of the distribute HESS proposed in this paper. The distributed control strategy is mainly divided into two levels: the primary control and the secondary control. The lower level is the local droop control. According to the maximum output power of the energy storage unit in different modes, the output power of each energy storage unit can be reasonably allocated by using the droop coefficient of different modes, and the power can be allocated once without the aid of communication. The upper level secondary control is a consistency control. In order to reduce the difference of ⟨ESOC⟩ in the working process of distributed energy storage system, the weak communication based consistency control is adapted to calculate $\langle ESOC \rangle^*$, As the ⟨ESOC⟩ follows the instruction of secondary control, the output frequency of each energy storage unit is dynamically adjusted. The energy storage units in different modes can operate in their respective reasonable working range to ensure their continuous operation.

The main control targets of this hierarchical framework include:

1) In order to respond to the power fluctuation of the system, it is necessary to determine the operation mode of each HESS unit according to the total power demand assessment results, so as to determine the P-F droop control coefficient. In this way, active power can be optimally distributed among all HESS units.
2) In order to share the control target among units, the distributed algorithm based on discrete consistency principle is used. The average value of each energy storage unit ⟨ESOC⟩ is calculated iteratively through the information achieved from adjacent units.
3) On the basis of variable droop coefficient control, the correction considering ⟨ESOC⟩ equalization is superimposed, so that the ESOC of each energy storage unit can be regulated within a reasonable range while the power of each unit is distributed once according to the proportion of the maximum output power of each unit, and the $\langle ESOC_i \rangle$ of each energy storage unit tends to be consistent.

Traditional droop control is difficult to comprehensively consider the above objectives.

Consistency Control Strategy Based on Equivalent SOC

Considering that the power distribution control of the distributed energy storage system is discontinuous, the first-order discrete-time consistency algorithm is utilized (Yinliang et al., 2011). For the distributed multi-agent control system with n agents, the discrete-time consistency algorithm can be expressed as:

$$x_i[k+1] = x_i[k] + \sum_{j=1}^{n} a_{ij}\left(x_j[k] - x_i[k]\right)(i = 1, 2, .., n) \tag{11}$$

where: $x_i[k]$ and $x_j[k]$ represent the state variables of nodes i and j in the kth iteration respectively; $x_i[k+1]$ is the updated value of $x_i[k]$ in the $(k+1)^{\text{th}}$ iteration; a_{ij} is the element of adjacency matrix A, which is used to describe the relationship between nodes. If there is no connection between nodes i and j or $i = j$, then $A_{ij} = 0$, otherwise $0 < A_{ij} < 1$. In the process of consistent iteration, A_{ij} has an important influence on the convergence rate and stability. A_{ij} is defined as:

$$a_{ij} = \begin{cases} 0 < a_{ij} < 1, \left(v_i, v_j\right) \in E \\ 0, others \end{cases} \tag{12}$$

Eq. 11 can also be written as a matrix:

$$X[k+1] = X[k] + A * X[k] = (I + A)X[k] = DX[k] \tag{13}$$

where, $X[k] = [x_1[k], \ldots, x_i[k], \ldots, x_i[k]]^T$, I is the identity matrix, and D is:

$$D = \begin{bmatrix} 1 - \sum_{j=1}^{n} a_{1j} & \cdots & a_{1n} \\ \vdots & \ddots & \vdots \\ a_{n1} & \cdots & 1 - \sum_{j=1}^{n} nj \end{bmatrix} \tag{14}$$

If all elements of matrix D are nonzero, and the sum of elements in each row and column is 1, then D is called a bi-random matrix (Alfred, 1954). According to Gerschgorin's disks theorem, all eigenvalues of matrix D are less than or equal to 1. In order to apply Perron Frobenius lemma:

$$\lim_{k\to\infty} D^k = \frac{ee^T}{n} \tag{15}$$

where $e = [1, 1, \ldots, 1]^T$, n are the dimensions of matrix D. Matrix D should satisfy two conditions of double random matrix. However, the diagonal element of matrix D given in **Eq.14** may be negative, so the matrix is not a bi-random matrix. However, it is easy to prove that the proof of Perron Frobenius lemma is also valid for the matrix D given by **Eq. 14**. Therefore, **Eq. 15** can still be used for the stability analysis of consistency algorithm (Yinliang et al., 2011).

According to the above lemma, a positive definite Lyapunov function is constructed to analyze the stability of the system. Finally, the following conclusion is obtained: if A_{ij} in D matrix satisfies the following equation, the designed system is stable:

$$0 < a_{ij} < \frac{2}{n_i + n_j} \tag{16}$$

where n_i and n_j are the number of adjacent nodes of node i and j respectively.

Therefore, in this paper, the D-matrix satisfying **Eq. 16** is constructed by means metropolis method (Xu and Liu, 2011), which has high convergence speed.

$$d_{ij} = \begin{cases} \dfrac{1}{n_i + n_j + \varepsilon}, j \epsilon N_j \\ 1 - \sum\limits_{j \epsilon N_j} \dfrac{1}{n_i + n_j + \varepsilon}, i = j \\ 0, others \end{cases} \tag{17}$$

where N_i is the set of nodes connected with node i, and ε is a very small number. When the number of system nodes is large and complex, it can be set to 0.

Improved Droop Control of HESS

Under the condition of inductive equivalent line impedance, the droop control equation of parallel Hess is as follows:

$$f_i = f_i^* - k_{pi} P_{HESSi} \tag{18}$$

$$E_i = E_i^* - k_{qi} Q_{HESSi} \tag{19}$$

where f_i and E_i are the frequency and amplitude of the output AC voltage of $HESS_i$ unit respectively; f_i^* and E_i^* are the rated value of frequency and amplitude respectively, which generally correspond to the frequency and voltage amplitude of inverter under no-load condition; P_{HESSi} and Q_{HESSi} are the active power and reactive power of $HESS_i$ unit respectively; k_{pi} and k_{qi} are the droop coefficient of active power and reactive power of $HESS_i$ unit respectively.

If the active droop coefficient is set according to the ratio of the maximum output power of each energy storage unit, the load power can be distributed in proportion among the energy storage units.

$$\frac{P_{HESS1}}{P_{max1}} = \frac{P_{HESS2}}{P_{max2}} = \ldots = \frac{P_{HESSn}}{P_{maxn}} \tag{20}$$

In addition, in order to avoid large frequency offset, the active power droop coefficient k_{pi} meets the following requirements:

$$k_{pi} \le \frac{\Delta F_{max}}{P_i^*} \tag{21}$$

where ΔF_{max} is the maximum allowable frequency change of the system, taking 0.5Hz, and P_i^* is the rated active power of hessi unit.

Similarly, the reactive power distribution in distributed energy storage system is related to the reactive power droop coefficient k_q. In this paper, the reactive power is divided equally, and each energy storage unit sets the same droop coefficient k_{qi} to achieve the average distribution of reactive power, so we do not do too much analysis. Similar to the active droop coefficient, the reactive droop coefficient k_{qi} satisfies:

$$k_{qi} \le \frac{\Delta E_{max}}{Q_i^*} \tag{22}$$

where ΔE_{max} is the maximum allowable voltage change of the system, not exceeding ±5%, and Q_i^* is the rated reactive power of $HESS_i$ unit.

Because the maximum output active power of Hess varies with different working modes, the traditional droop control method with fixed droop coefficient is not suitable for Hess application. Therefore, this paper considers the way of changing the droop coefficient in different modes, so that the local droop control of energy storage system can be adjusted according to the maximum output active power at any time and in any mode. The calculation formula of active power droop coefficient considering sub mode is as follows:

$$k_{pi}[Z] = \frac{\Delta f_{max}}{P_{i\_max}[Z]} \tag{23}$$

where Δf_{max} is the maximum allowable frequency change of the system, taking 0.5Hz, $P_{i\_max}[Z]$ is the maximum output active power of $HESS_i$ unit in Z mode, where Z represents three typical working modes of Hess.

In order to achieve the balance of each energy storage unit ⟨ESOC⟩, the traditional droop control can be improved and the control quantity related to the energy storage unit ⟨ESOC⟩ can be increased. Based on the droop control, the secondary power distribution is realized according to the ⟨ESOC⟩ index. Improved droop control based on ⟨ESOC⟩ regulation:

TABLE 1 | Parameters of the energy storage components.

Type	Rated capacity	Initial SOC (%)	Max SOC (%)	Min SOC (%)
battery	300 Wh	67	20	80
SC*2	31.2 Wh	75	10	95

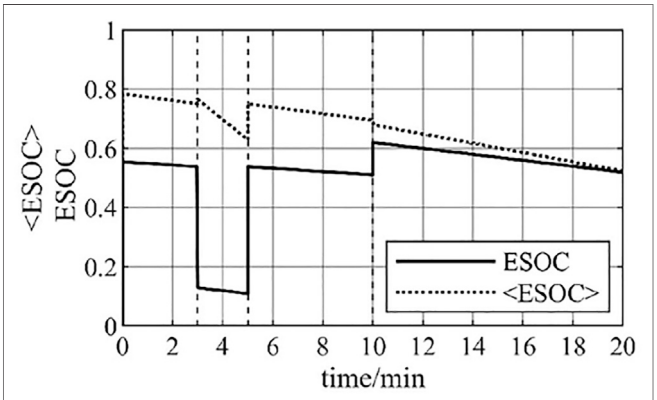

FIGURE 6 | ESOC and normalized ESOC.

$$f_i = f_i^* - k_{pi}[Z]P_{HESSi} - \left(N_{ip} + \frac{N_{ii}}{s}\right) \times \left(\langle ESOC\rangle^* - \langle \mathrm{ESOC}_i\rangle\right) \tag{24}$$

where: N_{ip} and N_{ii} are the PI parameters of the ⟨ESOC⟩ regulation term corresponding to the ith energy storage unit $HESS_i$, $ESOC^*$ is the average value of ⟨ESOC⟩ of the distributed energy storage system obtained by the consistent algorithm, and $k_{pi}[Z]$ represents the active power droop coefficient of the energy storage unit in Z mode.

SIMULATION ANALYSIS

Verification of the Proposed ESOC Evaluation Method

To verify the proposed ESOC evaluation method, a simplified model consists of a cascaded HESS unit connected to a load is built in the Matlab/Simulink platform. The HESS unit switches between different modes and the ESOC is calculated in real-time. The rated capacity and initial SOC condition of the battery and supercapacitor in this HESS unit is shown in **Table 1**.

The simulation was taken in four stages (0–3, 3–5, 5–10, 10–20 min), corresponding to operation mode 1, 2, 1 and 3 respectively. The details of the three operation modes are introduced in Section II (a). **Figure 6** shows the changes in ESOC and its normalized value < ESOC> during the four stages.

The HESS unit was operating in mode 1 from 0 to 3 min and from 5 to 10 min. In these time periods, only the batteries inject power to the load and the supercapacitor is standing by. That means that the remaining energy in the HESS unit totally depends on the remaining energy in the battery. Therefore, the remaining energy in the ESOC is completely determined by the SOC of the battery.

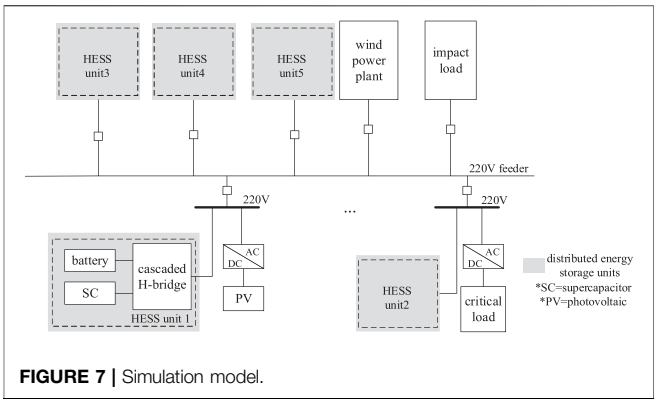

FIGURE 7 | Simulation model.

The HESS unit was operating in mode 2 from 3 to 5 min, in the time period when instantaneous extreme high power demand occurs. The provided power from HESS to the load almost all comes from the supercapacitors. Thus, the remaining energy in the HESS unit totally depends on the remaining energy in the supercapacitors. The capacity of the supercapacitors is much smaller than that of the battery, so there is a significant drop in ESOC.

The HESS unit was operating in mode three from 10 to 20 min. To meet the high power demand, both the battery and the supercapacitors provide power to the load, so there is an increase in ESOC when switching from operation mode 1. This increase in ESOC indicates that the remaining energy in the supercapacitors starts to be injected to the load in addition to the remaining energy in the battery.

Figure 6 also illustrates that while the <ESOC > has a linear relationship with the ESOC, the change in the ESOC when switching the operation mode is mitigated in the <ESOC>. This can avoid too acute changes in the power distribution, which may cause HESS units to go beyond their appropriate operation ranges.

Verification of the Hierarchical Control Structure of Distributed Hess

The model shown in **Figure 7** is used to verify the proposed control framework to support the isolated microgrid. The equivalent output impedance of the power network used in the voltage level 220 V is inductive.

The configurations of the five HESS units are shown in **Table 2**.

As the isolated microgrid, the simulation model contains wind power, photovoltaic and other renewable energy. These distributed generators usually use the algorithm to track the maximum power point for PQ control, and the output active power is intermittent and random. Meanwhile, the load also has the stochastic characteristics. Thus, the HESSs are used to meet the difference between generations and usage, as well as to suppress the power fluctuations.

Figure 8 shows overall generations, loads and their difference of the isolated microgrid. The HESSs unit is used to support the

TABLE 2 | Parameters and Initial SOCs of each HESS Unit.

HESS unit		1	2	3	4	5
capacity/Wh	battery SC*2	300 31.2	300 31.2	180 21	180 21	420 16.8
output impedance	L/mH	238.7	238.7	238.7	238.7	238.7
Communicable node		2,3	1,3,4	1,2,5	2	3
Pmax/W		500/750/1250	500/750/1250	300/500/800	300/500/800	700/400/1100
initial SOC	battery SC*2	0.67 0.75	0.75 0.72	0.71 0.67	0.69 0.57	0.78 0.63

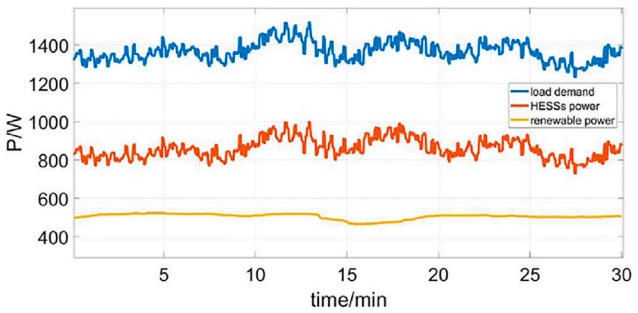

FIGURE 8 | The power demand of isolated microgrid.

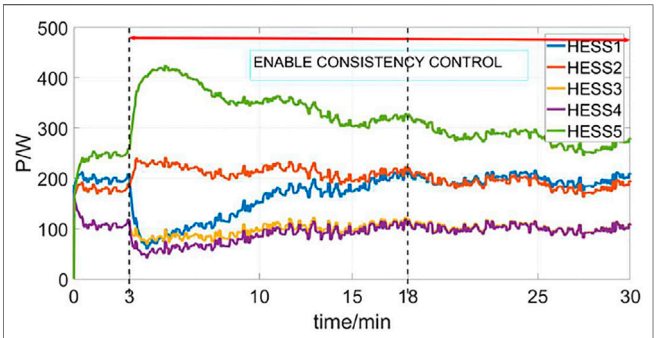

FIGURE 9 | Active power injection of each HESS unit in the initial 30 min.

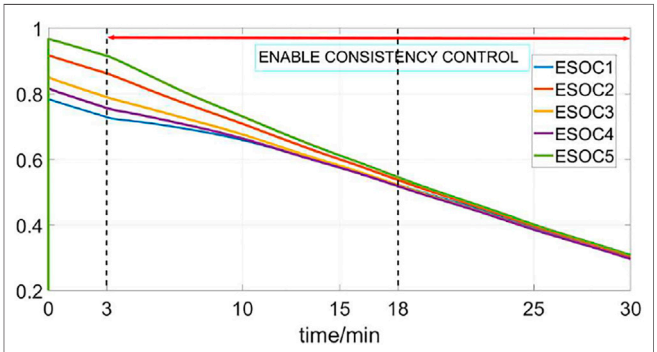

FIGURE 10 | Normalized ESOC of the five HESS units.

microgrid when severe failure occurs and the distributed generations cannot meet the load demand. In this situation, all HESS units will share the total difference.

The proposed hierarchical control framework is used to allocate power among HESS units. **Figure 9** shows the output power of these HESS units in the first 30 min. The simulation process is divided into three stages. From 0 to 3 min, the primary control is enabled, and each HESS unit contribute to the active power demand according to its own state. From 3 to 18 min, since the secondary control is activated, the output power of HESS5 with relatively large capacity and HESS2 with high initial SOC increases significantly. In 18–30 min, With the consistency process of the normalized ESOC of the five HESS units, the ESOC is gradually consistent.

Figure 10 shows the changes in <ESOC> of these HESS units in the first 30 min. In 0–3 min, the N_{ip} and N_{ii} in **Eq. 24** was set as 0, the power allocation is determined by the primary power allocation strategy, and the amount of injected active power of each HESS unit is proportional to respect $k_{pi}[Z]$. The decrease rate of ⟨ESOC⟩ was the same. In 3 min–18 min, the N_{ip} and N_{ii} in 24) was set as 1.5 and 0.005 so the secondary power adjustment was applied and the target ⟨ESOC⟩ was taken into consideration. Because of this, for each HESS unit, the drop speed of its ⟨ESOC⟩ was influenced by the gap between its actual ⟨ESOC⟩ and its reference. It can be seen that the ⟨ESOC⟩ values of all HESS units tend to converge after starting the consistency control. In 18–30 min, ⟨ESOC⟩ was consistent and decreased at almost the same rate.

CONCLUSION

In this paper, the equivalent SOC (ESOC) is proposed as an index to evaluate the state of charge of a HESS unit considering its operation mode. Based on this, a distributed control method is proposed that aims to optimize the power allocation among HESS units that are in the same microgrid. The main innovations are: consideration of the operation mode of a HESS unit while evaluating its state of charge, and determining the droop coefficient of primary control. Use the distributed algorithm and secondary control to balance the equivalent SOC among HESS units. Simulation results show that the proposed ESOC can reflect the actual condition of a HESS unit according to its operation mode. Meanwhile, with the proposed distributed control method, the power can be reasonably allocated among all HESS units considering their current states and their ESOC targets.

DATA AVAILABILITY STATEMENT

The raw data supporting the conclusions of this article will be made available by the authors, without undue reservation.

AUTHOR CONTRIBUTIONS

WJ: Conceptualization, Methodology, Funding acquisition, Investigation, Supervision, Validation, Visualization, Writing—original draft, Writing—review and editing. ZX: Data curation, Visualization, Writing—review and editing. BY: Validation, Visualization, Writing—review and editing. KS: Validation, Visualization, Writing—review and editing. KR: Validation, Visualization, Writing—review and editing. YD: Validation, Visualization, Writing—review and editing. SR: Validation, Visualization, Writing—review and editing.

FUNDING

This work was supported by the National Natural Science Foundation of China under Grant 51877041.

REFERENCES

Alfred, Horn. (1954). Doubly Stochastic Matrices and the Diagonal of a Rotation Matrix. *Am. J. Math.* 76 (3), 620–630.

Arif, S., and Aziz, T. (2017).Study of Frequency Response with Centralized vs. Distributed Placement of Battery Energy Storage Systems in Renewable Integrated Microgrid. 2017 IEEE International WIE Conference on Electrical and Computer Engineering. Dehradun: WIECON-ECE), 96–99. doi:10.1109/wiecon-ece.2017.8468928

Rufer, A., and Barrade, P., "A supercapacitor-based energy storage system for elevators with soft commutated interface," Conference Record of the 2001 IEEE Industry Applications Conference. 36th IAS Annual Meeting (Cat. No.01CH37248), Chicago, IL, USA, 2001, pp. 1413–1418 vol.2.

Chandorkar, M. C., Divan, D. M., and Adapa, R. (1993). Control of parallel connected inverters in standalone AC supply systems. *IEEE Trans. Industry Appl.* 29 (1), 136–143.

Chen, W., and Wang, G. (2015). Decentralized Voltage-Sharing Control Strategy for Fully Modular Input-Series-Output-Series System with Improved Voltage Regulation. *IEEE Trans. Ind. Electron.* 62 (5), 2777–2787. doi:10.1109/tie.2014.2365433

Li, Chendan., Dragicevic, T., Diaz, N. L., Vasquez, J. C., and Guerrero, J. M., "Voltage scheduling droop control for State-of-Charge balance of distributed energy storage in DC microgrids," IEEE International Energy Conference (ENERGYCON), Cavtat, 2014, pp. 1310–1314. doi:10.1109/energycon.2014.6850592

Dey, S., Mohon, S., Ayalew, B., Arunachalam, H., and Onori, S. (2019). A Novel Model-Based Estimation Scheme for Battery-Double-Layer Capacitor Hybrid Energy Storage Systems. *IEEE Trans. Contr. Syst. Technol.* 27 (2), 689–702. doi:10.1109/tcst.2017.2781650

Dougal, R. A., Liu, S., and White, R. E. (2002). Power and life extension of battery-ultracapacitor hybrids. *IEEE Trans. Comp. Packag. Technol.* 25 (1), 120–131. doi:10.1109/6144.991184

Gao, L., Dougal, R. A., and Liu, S. (2005). Power Enhancement of an Actively Controlled Battery/Ultracapacitor Hybrid. *IEEE Trans. Power Electron.* 20 (1), 236–243. doi:10.1109/tpel.2004.839784

Ghazanfari, A., Hamzeh, M., Mokhtari, H., and Karimi, H. (2012). Active Power Management of Multihybrid Fuel Cell/Supercapacitor Power Conversion System in a Medium Voltage Microgrid. *IEEE Trans. Smart Grid* 3 (4), 1903–1910. doi:10.1109/tsg.2012.2194169

Hai Chen, H., Dongsheng Ma, B., and Ma, D. (2010). Energy Storage and Management System with Carbon Nanotube Supercapacitor and Multidirectional Power Delivery Capability for Autonomous Wireless Sensor Nodes. *IEEE Trans. Power Electron.* 25 (12), 2897–2909. doi:10.1109/tpel.2010.2081380

Hai-Feng, G., Man, C., Yang, C., Qin-Dong, M., and Zhi-Bin, L. (2014).Design of 2MW/10kV cascaded H-bridge power conversion system. 2014 International Conference on Power System Technology. Chengdu, 3335–3340. doi:10.1109/powercon.2014.6993906

Kawakami, N., Iijima, Y., Li, H., and Ota, S. (2014).High efficiency power converters for battery energy storage systems. 2014 International Power Electronics Conference (IPEC-Hiroshima 2014 - ECCE ASIA). Hiroshima, 2095–2099. doi:10.1109/ipec.2014.6869877

Kim, S.-T., Bae, S., Kang, Y. C., and Park, J.-W. (2015). Energy Management Based on the Photovoltaic HPCS with an Energy Storage Device. *IEEE Trans. Ind. Electron.* 62 (7), 4608–4617. doi:10.1109/tie.2014.2370941

Le Dinh, K., and Hayashi, Y. (2013).Coordinated BESS control for improving voltage stability of a PV-supplied microgrid. 2013 48th International Universities' Power Engineering Conference. Dublin: UPEC), 1–6. doi:10.1109/upec.2013.6715027

Li, C., Coelho, E. A. A., Dragicevic, T., Guerrero, J. M., and Vasquez, J. C. (2017). Multiagent-Based Distributed State of Charge Balancing Control for Distributed Energy Storage Units in AC Microgrids. *IEEE Trans. Ind. Applicat.* 53 (3), 2369–2381. doi:10.1109/tia.2016.2645888

Li, X., Xu, T., Tan, S., Chen, X., and Zeng, X. (2016). Integrated dynamic equivalent model of super capacitor energy storage system. *in J. Syst. Simulation* 28 (04), 783–792+799. (in Chinese).

Ma, T., Yang, H., and Lu, L. (2015). Development of hybrid battery-supercapacitor energy storage for remote area renewable energy systems. *Appl. Energ.* 153, 56–62.

Mesbahi, T., Rizoug, N., Khenfri, F., Bartholomeüs, P., and Le Moigne, P. (2017). Dynamical modelling and emulation of Li-ion batteries–supercapacitors hybrid power supply for electric vehicle applications. *IET Electr. Syst. Transportation* 7 (2), 161–169.

Mokhtari, G., Nourbakhsh, G., and Ghosh, A. (2013). Smart Coordination of Energy Storage Units (ESUs) for Voltage and Loading Management in Distribution Networks. *IEEE Trans. Power Syst.* 28 (4), 4812–4820. doi:10.1109/tpwrs.2013.2272092

Newman, J., Thomas, K. E., Hafezi, H., and Wheeler, D. R. (2003). Modeling of lithium-ion batteries. *J. Power Sourc.* 119-121 (121), 838–843. doi:10.1016/s0378-7753(03)00282-9

Rodrigues, Y. R., Monteiro, M. R., Zambroni de Souza, A. C., Riberiro, P. F., Wang, L., and Eberle, W. (2018). "Adaptative Secondary Control for Energy Storage in Island Microgrids," in *IEEE Power & Energy Society General Meeting* (Portland, OR, USA: (PESGM), 1–5. doi:10.1109/PESGM.2018.8586228

Shu, L., Chen, W., and Jiang, X. (2018). Decentralized Control for Fully Modular Input-Series Output-Parallel (ISOP) Inverter System Based on the Active Power Inverse-Droop Method. *IEEE Trans. Power Electron.* 33 (9), 7521–7530. doi:10.1109/tpel.2017.2773559

Tan, K. T., Peng, X. Y., So, P. L., Chu, Y. C., and Chen, M. Z. Q. (2012). Centralized Control for Parallel Operation of Distributed Generation Inverters in Microgrids. *IEEE Trans. Smart Grid* 3 (4), 1977–1987. doi:10.1109/tsg.2012.2205952

Tian, K., Ali, S., Huang, Z., and Ling, Z. (2019).Power control and experiment of 2MW/10kV cascaded H-bridge power conversion system for battery energy storage system. 8th Renewable Power Generation Conference. Shanghai, China: RPG 2019, 1–7. doi:10.1049/cp.2019.0378

Tsikalakis, A. G., and Hatziargyriou, N. D. (2008). Centralized Control for Optimizing Microgrids Operation. *IEEE Trans. Energ. Convers.* 23 (1), 241–248. doi:10.1109/tec.2007.914686

Xin, H., Qu, Z., Seuss, J., and Maknouninejad, A. (2011). A Self-Organizing Strategy for Power low Control of Photovoltaic enerators in a Distribution Network [J]. *IEEE Trans. Power Syst.* 26 (3), 1462–1473.

Xu, Y., and Liu, W. (2011). Novel Multiagent Based Load Restoration Algorithm for Microgrids. *IEEE Trans. Smart Grid* 2 (1), 152–161. doi:10.1109/tsg.2010.2099675

Yinliang, Xu., Wenxin, Liu., and Jun, Gong. (2011). Stable Multi-Agent-Based Load Shedding Algorithm for Power Systems[J]. *IEEE Trans. Power Syst.* 26 (4), 2006–2014.

Yongqiang, Z., and Tianjing, W. (2017). Comparison of centralised and distributed energy storage configuration for AC/DC hybrid microgrid. *J. Eng.* 2017, 1838–1842. doi:10.1049/joe.2017.0649

Zhao, B., Yu, Q., Wang, L., and Xiao, Y. (2011). Bi-directional extensible converter and its distributed control strategy for battery energy storage grid-connected system. *Proc. CSEE* 31 (S1), 244–251.

Zhou, H., Bhattacharya, T., Tran, D., Siew, T. S. T., and Khambadkone, A. M. (2011). Composite Energy Storage System Involving Battery and Ultracapacitor with Dynamic Energy Management in Microgrid Applications. *IEEE Trans. Power Electron.* 26 (3), 923–930. doi:10.1109/tpel.2010.2095040

Conflict of Interest: Author KS was employed by State Grid Zhejiang Electric Power Co., Ltd.

The remaining authors declare that the research was conducted in the absence of any commercial or financial relationships that could be construed as a potential conflict of interest.

Publisher's Note: All claims expressed in this article are solely those of the authors and do not necessarily represent those of their affiliated organizations, or those of the publisher, the editors and the reviewers. Any product that may be evaluated in this article, or claim that may be made by its manufacturer, is not guaranteed or endorsed by the publisher.

frontiers in Energy Research

ORIGINAL RESEARCH
published: 29 November 2021
doi: 10.3389/fenrg.2021.723192

Cooperative Trading Mechanism and Satisfaction-Based Profit Distribution in a Multi-Energy Community

Jian Wang[1,2], *Ning Xie*[1]*, *Valentin Ilea*[2], *Cristian Bovo*[3], *Hao Xin*[1] and *Yong Wang*[1]

[1]Department of Electrical Engineering, Shanghai Jiao Tong University, Shanghai, China, [2]Department of Energy, Politecnico di Milano, Milan, Italy, [3]Department of Electrical, Computer and Biomedical Engineering, Università degli Studi di Pavia, Pavia, Italy

With the development of distributed generation and demand-side response, traditional consumers are now converted into prosumers that can actively produce and consume electricity. Moreover, with the help of energy integration technique, prosumers are encouraged to form a multi-energy community (MEC), which can increase their social welfare through inside multi-energy sharing. This paper proposes a day-ahead cooperative trading mechanism in a MEC that depends on an energy hub (EH) to couple electricity, natural gas, and heat for all prosumers. The model of the traditional uncooperative local integrated energy system (ULIES) is also built as a comparison. A satisfaction-based profit distribution mechanism is set according to prosumers' feelings about the extra cost they save or extra profit they gain in MEC compared with that in ULIES. Finally, case studies are set to analyze the utility of MEC in enlarging social welfare, after considering the effects of prosumers' electricity usage patterns and buy-and-sell prices in retail market. The results of satisfaction-based profit distribution are also analyzed to verify that it can save the cost or increase the profit of each prosumer and EH.

Keywords: prosumers, cooperative trading mechanism, multi-energy community, energy sharing, satisfaction-based profit distribution

OPEN ACCESS

Edited by:
Tao Huang,
Politecnico di Torino, Italy

Reviewed by:
Fei Xue,
Xi'an Jiaotong-Liverpool University, China
Ye Cai,
Changsha University of Science and Technology, China

***Correspondence:**
Ning Xie
xiening@sjtu.edu.cn

Specialty section:
This article was submitted to Smart Grids, a section of the journal Frontiers in Energy Research

Received: *10 June 2021*
Accepted: *12 October 2021*
Published: *29 November 2021*

Citation:
Wang J, Xie N, Ilea V, Bovo C, Xin H and Wang Y (2021) Cooperative Trading Mechanism and Satisfaction-Based Profit Distribution in a Multi-Energy Community. Front. Energy Res. 9:723192. doi: 10.3389/fenrg.2021.723192

INTRODUCTION

With the continuous integration of distributed energy resources, traditional passive consumers are now becoming proactive prosumers who can produce and consume energy at the same time (Parag et al., 2016; Hu et al., 2021). For example, household consumers are encouraged to install roof-top solar panels for self-supplying and to further sell electricity to the power grid when there exists energy surplus (Liu et al., 2018; Ancona et al., 2021).

A promising way to deal with the energy management of prosumers is to gather individual prosumers into a group-wide system, and the energy community (EC) is one of the most typical concepts that has attracted much attention (Cai et al., 2017; Firoozi et al., 2020). The paper of Bera et al. (2018) analyzes the formatting process of an EC from a dynamic perspective. The paper of Lilla et al. (2020) focuses on the day-ahead operational planning of an EC. The paper of Feng et al. (2020) introduces a coalitional game-based transactive energy management method of ECs. In the paper of Cui et al. (2021), cheating behaviors in benefit sharing of EC are analyzed, and a cheating equilibrium-based solution is proposed to ensure a stable community.

The development of local integrated energy system realizes the multi-energy operation among local prosumers, which can broaden the energy utilization scope and contribute to the holistic economy of the whole energy system (Liu et al., 2019; Cai et al., 2021). In Yang et al. (2016), Zhou

et al. (2018), and Xu et al. (2020), optimal operation models are proposed for the multi-energy systems interconnected by energy hubs (EHs), considering both technical and economic aspects.

From the viewpoint of trading, proactive prosumers are able to promote a demand side-centric market mechanism against the traditional top-down hierarchical one. For example, prosumers can directly transact energy with each other through a P2P trading mechanism (Oh and Son, 2020). However, individual trading cannot ensure the global expected efficiency and need some special trading methods. The papers of Liu et al. (2017) and Cui et al. (2020) focus on designing appropriate price functions based on demand–supply relationships among prosumers to improve social welfare. The paper of ZiboWang and YunfeiMu (2020) proposes a real-time double auction with a continuous bidding mechanism to achieve the coordination among prosumers and, therefore, improve the global efficiency. The paper of Le Cadre et al. (2020) designs game theory approaches of P2P energy market and proves the optimal social welfare of the equilibrium achieved.

In addition, forming an EC is an appropriate cooperation method for individual prosumers to improve global efficiency and social welfare. One of the key works of EC is to gain the maximum profit (or minimum cost) of the entire community. The paper of Ma et al. (2019) designs a cooperative trading mode to minimize the overall cost of an EC composed of heating and power generation (CCHP) devices and PV prosumers. In the paper of Pourakbari-Kasmaei et al. (2020), the integrated community energy system maximizes its profit by analyzing its interactions with the inside prosumers and the outside wholesale electricity market. The paper of Ye et al. (2017) designs an online algorithm for prosumers to share energy with others that can minimize the overall cost of EC. The other key work of EC is to guarantee the fairness of profit distribution inside, which is the distribution of the entire profit gained by EC to each individual prosumer inside EC. It can affect the participation willingness of prosumers (Xu et al., 2014). A Nash-type non-cooperative game theory approach distributes prosumers' profit by introducing a spontaneous competition among them (Long et al., 2019; Jing et al., 2020). The paper of Ye et al. (2017) designs a profit division algorithm based on the Nash bargaining theory to fairly share profit among prosumers. A few studies, like Shapley (1953), introduce fairness by using the Shapley value, which is a common method for profit distribution in cooperative games based on the participants' contribution in the cooperation. However, it can be computationally complex and time consuming when there are many participants. Therefore, Ma et al. (2019) propose a simplified profit distribution method, which also follows the contribution-based principle and verifies the validity of the method.

Despite those comprehensive works, there still exist some gaps, which the current work seeks to fill. The previous literatures comprehensively analyze the structures and behaviors of ECs with only electricity carrier (Cai et al., 2017; Ye et al., 2017; Bera et al., 2018; Feng et al., 2020; Firoozi et al., 2020; Lilla et al., 2020; Cui et al., 2021), but barely focus on building a multi-energy community (MEC) with multi-energy interactions and analyzing the trading mechanism of it. In Ma et al. (2019), an EH is proposed to interact different energy carriers in an EC, but it is viewed as an EC operator in the leading level, which means the EH is not on the same status as prosumers and can lead the transaction with prosumers. Moreover, the EH only owns CCHP devices, which is not a realistic scenario. However, with the development of energy integration, building a comprehensive MEC is a promising way to improve the global efficiency and social welfare in a wider scope. Additionally, the existing profit-distribution methods in the reviewed papers can be divided into two types, game-based methods (Ye et al., 2017; Long et al., 2019; Jing et al., 2020) and contribution-based methods (Ma et al., 2019). The former introduces individual competition, which may lose some market efficiency because of individual selfish behaviors. However, the latter relies too much on the EC operator to calculate the contribution and distribute the whole profit, which does not take prosumers' own will into consideration.

Given these gaps, this paper builds a MEC in which all prosumers and EH can share multi-energy carriers with each other freely. The two main points of the MEC are the cooperative trading mechanism in market-clearing process and the profit distribution mechanism in market settlement process. The main contributions of this paper are summarized as follows:

a. The model of cooperative trading mechanism is built, based on the physical structure of a MEC. In this mechanism, all prosumers and EH firstly share multi-energies with each other in the MEC and then transact with the outside retail market (RM). The mechanism can improve social welfare, compared with traditional uncooperative trading mechanism in uncooperative local integrated energy systems (ULIES).
b. The satisfaction-based profit distribution method is designed based on the principle that the results should maximize the overall satisfaction of all prosumers as well as meet the profit requirement of EH in the MEC. The method can meet the desire of saving the cost and increasing the profit of each prosumer and EH.
c. The model of uncooperative trading mechanism of ULIES is built in details as a comparison to show the advantages of a cooperative trading mechanism of MEC in enlarging social welfare and saving/improving the costs/profits of prosumers and EH.

The remainder of the paper is organized as follows. *Structure of the MEC* describes the structure of MEC. *Model of Cooperative Trading Mechanism for MEC* builds the cooperative trading mechanism model of MEC. *Profit Distribution Mechanism for MEC* proposes the satisfaction-based profit distribution method. *Case Study* analyzes the case study. *Conclusion and Prospective Works* draws the conclusion.

STRUCTURE OF THE MEC

Structure of the Trading Mechanism

The structure of a MEC is shown in **Figure 1A**. The community is operated by an independent community operator who aims at

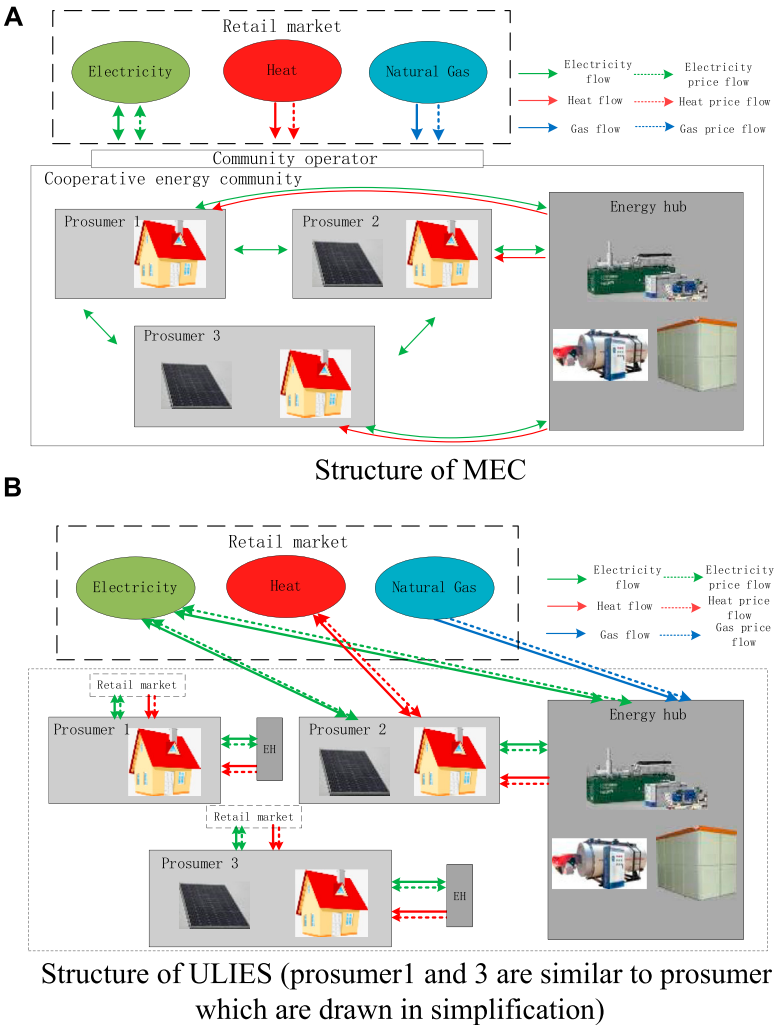

FIGURE 1 | Trading mechanism structure. **(A)** Structure of MEC. **(B)** Structure of ULIES (prosumers 1 and 3 are similar to prosumer 2, which are drawn in simplification). MEC, multi-energy community; ULIES, local integrated energy system

maximizing the total profit or minimizing the total cost of the entire community and then distributing the entire profit/cost fairly to each participant. The MEC is composed of two kinds of participants: prosumers and EH. Prosumers use solar panels to produce electricity and consume electricity and heat at the same time. A prosumer equals to a traditional consumer when there is no electricity generation. EH can convert energies through the conversion devices and store energies through the storage devices inside.

The cooperative trading mechanism of MEC is that all prosumers and EH firstly share energies with each other inside the community and then transact with the outside RM (including electricity RM, natural gas RM, and heat RM) as a whole. This is because energy sharing inside MEC is cost-effective, considering the fact that the cost of electricity generation of solar panels (PV generation) of each prosumer is very low and that EH can couple different energy carriers in an economical way. However, energy trading with the RM is always dominated by the RM operator. The price of buying electricity from RM is normally much higher than the price of selling electricity to RM. Once prosumers trade with the RM outside, prosumers will either pay high prices for energy consumed or receive low payments for energy sold, losing overall, while the RM operator will earn in both cases, being the price maker in both situations. Therefore, prosumers prefer sharing energies with each other and with EH, rather than transacting with the RM outside.

After that, the overall profit/cost is distributed by the community operator. Prosumers feel more satisfied and are more reliable to the community when they can gain more profit or save more cost according to the distribution. An energy hub can also be completely profit-driven like prosumers; however, it can also choose to help the development of MEC by giving up some of its profit after receiving an acceptable profit.

This trading mechanism is different from the mechanism of a traditional ULIES shown in **Figure 1B**. There does not exist any

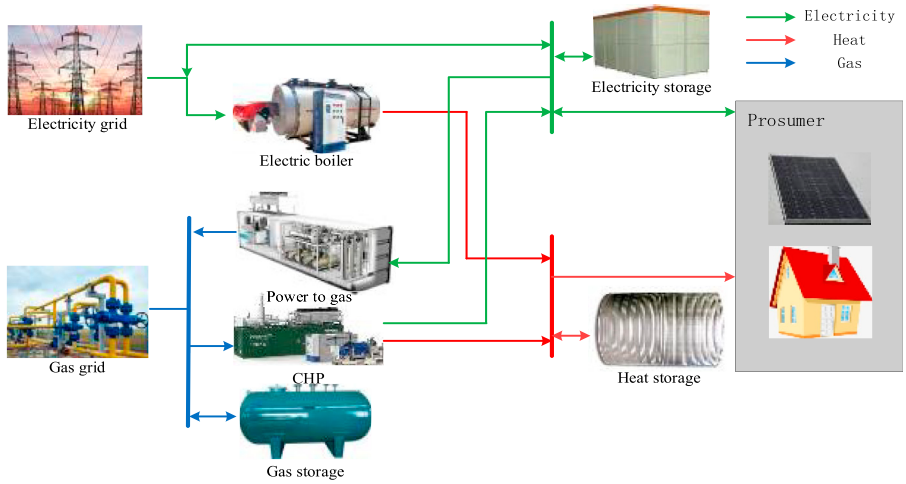

FIGURE 2 | structure of energy hub (EH) in MEC.

energy sharing on the demand side. All prosumers and EH work independently and are in competition, as each of them wants to maximize its own profit or minimize its own cost. In the competition, each prosumer transacts electricity and heat with EH or RM according to the corresponding prices. The EH, which can also be viewed as a kind of retailer, sets the prices for electricity and heat transactions with prosumers according to the demands, operation costs, and the prices in RM. The details of the uncooperative mechanism of ULIES are described in **Supplementary Appendix A**.

Prosumers and Energy Hub

Each prosumer inside the community is composed of solar panels and/or electricity demands and/or heat demands with a demand response. As shown in **Figure 1**, it can buy/sell electricity from/to RM, share electricity with other prosumers, and receive/send electricity from/to EH. It can also buy heat from RM and receive heat from EH. At each time point, prosumers can be divided into buy prosumers and sell prosumers, according to whether they have electricity demands or surpluses at that time.

In this paper, only solar panels are considered as the power production devices of prosumers in MEC as they are the most used among household consumers. However, the model can be extended to other distributed generators, including wind turbines, and electric vehicles. Since power generation mechanism is not considered in this paper, wind power can be judged the same as PV power with a difference in power output profile, which is, however, considered a constant parameter here. Electric vehicles, as a kind of controllable devices with the ability of charging, discharging, and storing electricity, can add some decision complexities inside MEC. However, this cannot affect fundamentally the cooperative trading mechanism and profit distribution mechanism of MEC. The goals and constraints of the model will be fundamentally the same as the ones presented here; the model of the electric vehicle for prosumer, if added, is fundamentally the same as the energy storage device that is here introduced for the energy hub.

As shown in **Figure 1**, EH can buy/sell electricity from/to RM, buy natural gas from RM, receive/send electricity from/to prosumers, and send heat to prosumers. The main task of EH is to convert different energy carriers in the most efficient and economical way. The structure of the EH inside MEC is shown in **Figure 2**. The energy conversion relationships are described in the following.

Combined heat and power unit (CHP) consumes natural gas and produces electricity and heat. The conversion relationship is expressed as:

$$h_{eh}^{CHP} = p_{eh}^{CHP} \cdot \left[k_{CHP}^{E} \cdot \left(1 - \eta_{CHP}^{E} - \eta_{CHP}^{LOSS}\right)\right] / \eta_{CHP}^{E}, \quad (1)$$

$$p_{eh}^{CHP} = \eta_{CHP}^{E} \cdot g_{eh}^{CHP}. \quad (2)$$

Eq. 1 represents the relationship between the electricity and heat CHP produces. **Eq. 2** represents the efficiency of the conversion between natural gas and electricity of CHP. Parameters k_{CHP}^{E}, η_{CHP}^{E}, and η_{CHP}^{LOSS} represent the heat exchange coefficient, electricity production efficiency coefficient, and heat loss coefficient of CHP, respectively. Since this paper only considers backpressure CHP, the heat-to-electricity ratio of the CHP, used to describe the relationship between the production of heat and electricity in **Eq. 1**, is a constant parameter given by $\eta_{CHP}^{H} = [k_{CHP}^{E} \cdot (1 - \eta_{CHP}^{E} - \eta_{CHP}^{LOSS})] / \eta_{CHP}^{E}$ (Xi et al., 2020).

A power-to-gas station (P2G) consumes electricity and produces natural gas. The conversion is expressed as follows:

$$g_{eh}^{P2G} = \eta_{P2G} \cdot p_{eh}^{P2G}, \quad (3)$$

where η_{P2G} is the gas production efficiency coefficient of P2G.

Gas furnace (GF) consumes gas and produces heat. The conversion is expressed as follows:

$$h_{eh}^{GF} = \eta_{GF} \cdot g_{eh}^{GF}, \quad (4)$$

where η_{GF} is the heat production efficiency coefficient of GF.

An electricity boiler (EB) consumes electricity and produces heat. The conversion is expressed as follows:

$$h_{eh}^{EB} = \eta_{EB} \cdot p_{eh}^{EB}, \tag{5}$$

where η_{EB} is the heat production efficiency coefficient of EB.

The general formulation of energy storage devices in EH (including electricity storage, natural gas storage, and heat storage) is uniformly written in a vector pattern. The limitations of them are also modeled:

$$\boldsymbol{SOC}_{eh,t} = \boldsymbol{SOC}_{eh,t-1} + \left(\boldsymbol{\gamma}_{Sc}\boldsymbol{r}_{eh,t}^{ch} - \frac{1}{\boldsymbol{\gamma}_{Sd}}\boldsymbol{r}_{eh,t}^{di}\right)/\boldsymbol{S}_S, t \in \mathbb{T} \tag{6}$$

$$\boldsymbol{SOC}_{eh,T} = \boldsymbol{SOC}_{eh,0} = 50\% \tag{7}$$

$$\boldsymbol{r}_{eh,t}^{ch}\boldsymbol{r}_{eh,t}^{di} = 0, t \in \mathbb{T} \tag{8}$$

$$0 \le \boldsymbol{r}_{eh,t}^{ch} \le \overline{\boldsymbol{R}_{eh}^{ch}}, t \in \mathbb{T} \tag{9}$$

$$0 \le \boldsymbol{r}_{eh,t}^{di} \le \overline{\boldsymbol{R}_{eh}^{di}}, t \in \mathbb{T} \tag{10}$$

$$0 \le \boldsymbol{SOC}_{eh,t} \le \overline{\boldsymbol{SOC}_{eh}}, t \in \mathbb{T}. \tag{11}$$

Eq. 6 indicates the discrete time storage dynamics. **Eq. 7** forces the states of storages at the end of 1 day to be equal to their states at the beginning of the day, which is 50% according to the convention. **Eq. 8** indicates the complementary relationship between the charge and the discharge. **Eqs. 9** and **10** indicate the lower and upper limitations of the charged and discharged energies. **Eq. 11** imposes the lower and upper limitations of the states of storages, which can be set at 0% and 100%, respectively. Vector $\boldsymbol{SOC}_{eh,t} = [SOC_{eh,t}^{E}, SOC_{eh,t}^{G}, SOC_{eh,t}^{H}]^T$ represents the states of charge of electricity, natural gas, and heat storages, respectively. Vectors $\boldsymbol{\gamma}_{Sc} = [\gamma_{Sc}^{E}, \gamma_{Sc}^{G}, \gamma_{Sc}^{H}]^T$, $\boldsymbol{\gamma}_{Sd} = [\gamma_{Sd}^{E}, \gamma_{Sd}^{G}, \gamma_{Sd}^{H}]^T$ represent the charge and discharge efficiencies of electricity, natural gas, and heat storages, respectively. Vector $\boldsymbol{S}_S = [S_S^E, S_S^G, S_S^H]^T$ represents the rated capacities of electricity, natural gas, and heat storages, respectively. Vectors $\boldsymbol{r}_{eh,t}^{ch} = [r_{eh,t}^{ch,E}, r_{eh,t}^{ch,G}, r_{eh,t}^{ch,H}]^T$, $\boldsymbol{r}_{eh,t}^{di} = [r_{eh,t}^{di,E}, r_{eh,t}^{di,G}, r_{eh,t}^{di,H}]^T$ represent the charging and discharging power of electricity, natural gas, and heat storages, respectively. Vectors $\overline{\boldsymbol{R}_{eh}^{ch}} = [\overline{R_{eh}^{ch,E}}, \overline{R_{eh}^{ch,G}}, \overline{R_{eh}^{ch,H}}]^T$, $\overline{\boldsymbol{R}_{eh}^{di}} = [\overline{R_{eh}^{di,E}}, \overline{R_{eh}^{di,G}}, \overline{R_{eh}^{di,H}}]^T$ represent the upper bounds of charging and discharging power of electricity, natural gas, and heat storages, respectively. Vector $\overline{\boldsymbol{SOC}_{eh}} = [\overline{SOC_{eh}^{E}}, \overline{SOC_{eh}^{G}}, \overline{SOC_{eh}^{H}}]^T$ represents the upper bounds of states of charge of electricity, natural gas, and heat storages, respectively.

MODEL OF COOPERATIVE TRADING MECHANISM FOR MEC

Based on the MEC structure described in *Structure of the MEC*, the principle of cooperative trading mechanism is that prosumers and EH share energies inside MEC before trading with the outside RM. The working procedure of cooperative trading consists in three parts: 1) prosumers and EH share energies inside the MEC and then send their energy shortage or surplus to MEC operator; 2) EH converts energies inside the MEC in the most profitable way; and 3) finally, MEC operator operates the MEC aiming at maximizing the overall profit or minimizing the overall cost of community operation and transaction with the outside RM. The corresponding mathematical model is built in the following.

The goal of the MEC operator is to maximize the overall profit or minimize the overall cost in MEC, which can be formulated as follows:

$$\min F_N^{CO} = F_N^{CO} + F_{eh}^{CO}, \tag{12}$$

$$F_N^{CO} = \sum_{i \in \mathbb{P}} F_i^{CO}, \tag{13}$$

$$F_i^{CO} = \sum_{t \in \mathbb{T}} \left(\lambda_t^{E,b} p_{i,t}^b - \lambda_t^{E,s} p_{i,t}^s + \lambda_t^{H,b} h_{i,t}^b + C_{i,t}^{dr}\right), \tag{14}$$

$$F_{eh}^{CO} = \sum_{t \in \mathbb{T}} \left[\lambda_t^{G,b}\left(g_{eh,t}^b + g_{eh,t}^{bs}\right) + \lambda_t^{E,b} p_{eh,t}^b - \lambda_t^{E,s} p_{eh,t}^s + C_{eh,t}^{op}\right]. \tag{15}$$

Eq. 12 represents the objective function of the MEC operator. **Eq. 13** imposes the total cost/profit of all prosumers in MEC. **Eq. 14** imposes the cost/profit of each prosumer in MEC, which is composed of cost of electricity buying from the RM, profit of electricity selling to the RM, cost of heat buying from the RM, and cost of demand response. **Eq. 15** represents the cost of EH, which is composed of cost of gas buying from the RM, cost of electricity buying from the RM, profit of electricity selling to the RM, and cost of device operation in the EH.

Constrains of prosumers' behaviors in the MEC include the following:

$$\begin{cases} \left[D_{i,t}^E - \Delta p_{i,t} - L_{i,t}^{pre}\right]^+ = p_{i,t}^b + p_{i,t}^{eh,fr} + \sum_j p_{i,j,t} \\ , i \in \mathbb{P}, j \in \mathbb{P}_{shp}(i), t \in \mathbb{T} \\ \left[D_{i,t}^E - \Delta p_{i,t} - L_{i,t}^{pre}\right]^- = -p_{i,t}^s - p_{i,t}^{eh,to} + \sum_j p_{i,j,t} \\ , i \in \mathbb{P}, j \in \mathbb{P}_{shp}(i), t \in \mathbb{T} \end{cases}, \tag{16}$$

$$\sum_i \sum_j p_{i,j,t} = 0, i \in \mathbb{P}, j \in \mathbb{P}_{shp}(i), t \in \mathbb{T}, \tag{17}$$

$$D_{i,t}^H - \Delta h_{i,t} = h_{i,t}^b + h_{i,t}^{eh,fr}, i \in \mathbb{P}, t \in \mathbb{T}, \tag{18}$$

$$0 \le \Delta p_{i,t} \le \overline{\Delta P_i}, i \in \mathbb{P}, t \in \mathbb{T}, \tag{19}$$

$$0 \le \Delta h_{i,t} \le \overline{\Delta H_i}, i \in \mathbb{P}, t \in \mathbb{T}, \tag{20}$$

$$p_{i,t}^b, p_{i,t}^s, h_{i,t}^b \ge 0, i \in \mathbb{P}, t \in \mathbb{T}, \tag{21}$$

$$p_{i,t}^{eh,fr}, p_{i,t}^{eh,to}, h_{i,t}^{eh,fr} \ge 0, i \in \mathbb{P}, t \in \mathbb{T}. \tag{22}$$

Eq. 16 represents the power balance of each prosumer. Each prosumer can either be a buy prosumer or a sell prosumer at a given time. Thus, when there exists energy requirement, the prosumer buys electricity from RM, gets electricity from EH, and gets electricity from other prosumers. When there exists energy surplus, the prosumer sells electricity to RM, sends electricity to EH, and sends electricity to other prosumers. **Eq. 17** imposes the electric energy flow balance among prosumers since the amount of electricity prosumer i sends to j equals to the negative amount prosumer j sends to i at the given time. **Eq. 18** represents the heat balance of each prosumer. **Eqs. 19** and **20** set limitations to the demand response ability of each prosumer. **Eqs. 21** and **22** set that the variables representing the energy prosumers transact with RM and share with EH are positive.

Constrains of EH in the MEC include the following:

$$\begin{cases} \left[\sum_i p_{i,t}^{eh,fr} - \sum_i p_{i,t}^{eh,to}\right]^+ = p_{eh,t}^b + \eta_{CHP}^E g_{eh,t}^{CHP,b} \\ -p_{eh,t}^{EB,b} - re_{eh,t}^{ch,b} + re_{eh,t}^{di,b}, i \in \mathbb{P}_{she}(eh), t \in \mathbb{T}, \\ \left[\sum_i p_{i,t}^{eh,fr} - \sum_i p_{i,t}^{eh,to}\right]^- = -p_{eh,t}^s - p_{eh,t}^{P2G,s} - p_{eh,t}^{EB,s} \\ -re_{eh,t}^{ch,s} + re_{eh,t}^{di,s}, i \in \mathbb{P}_{she}(eh), t \in \mathbb{T}, \end{cases}, \tag{23}$$

$$\sum_i h_{i,t}^{eh} = \eta_{CHP}^H g_{eh,t}^{CHP,b} + \eta_{GF} \cdot g_{eh,t}^{GF,bs} + \eta_{EB} \cdot \left(p_{eh,t}^{EB,b} + p_{eh,t}^{EB,s}\right) - rh_{eh,t}^{ch,bs} + rh_{eh,t}^{di,bs}, i \in \mathbb{P}_{she}(eh), t \in \mathbb{T}, \tag{24}$$

$$g_{eh,t}^{CHP,b} = g_{eh,t}^b - rg_{eh,t}^{ch,b} + rg_{eh,t}^{di,b}, t \in \mathbb{T}, \tag{25}$$

$$g_{eh,t}^{GF,bs} = g_{eh,t}^{bs} - rg_{eh,t}^{ch,bs} + rg_{eh,t}^{di,bs}, t \in \mathbb{T}, \tag{26}$$

$$p_{eh,t}^{P2G,s} = rg_{eh,t}^{ch,s}/\eta_{P2G}, t \in \mathbb{T}, \tag{27}$$

$$0 \le g_{eh,t}^{CHP,b} \le \overline{G_{CHP}}, t \in \mathbb{T}, \tag{28}$$

$$0 \le g_{eh,t}^{GF,bs} \le \overline{G_{GF}}, t \in \mathbb{T}, \tag{29}$$

$$0 \le p_{eh,t}^{EB,b}, p_{eh,t}^{EB,s} \le \overline{P_{EB}}, t \in \mathbb{T}, \tag{30}$$

$$0 \le p_{eh,t}^{P2G,s} \le \overline{P_{P2G}}, t \in \mathbb{T}, \tag{31}$$

$$p_{eh,t}^b, p_{eh,t}^s, g_{eh,t}^b, g_{eh,t}^{bs} \ge 0, t \in \mathbb{T}, \tag{32}$$

$$re_{eh,t}^{ch,b}, re_{eh,t}^{ch,s}, rg_{eh,t}^{ch,b}, rg_{eh,t}^{ch,bs}, rg_{eh,t}^{ch,s}, rh_{eh,t}^{ch,bs} \in \boldsymbol{r}_{eh,t}^{ch}, t \in \mathbb{T}, \tag{33}$$

$$re_{eh,t}^{di,b}, re_{eh,t}^{di,s}, rg_{eh,t}^{di,b}, rg_{eh,t}^{di,bs}, rh_{eh,t}^{di,bs} \in \boldsymbol{r}_{eh,t}^{di}, t \in \mathbb{T}. \tag{34}$$

Eq. 23 imposes the electricity balance of EH. The left side of the equation represents the net overall amount of electricity all prosumers receive from/give to EH. When it is positive, EH is in buying status. When it is negative, EH is in selling status. The right side represents the amount of electricity EH transacts with the RM and converts through its own devices. **Eq. 24** imposes the heat balance of energy hub. The left side of the equation represents the overall amount of heat all prosumers need. The right side represents the amount of heat EH converts through its own devices. What is worth mentioning is that, in this model, the dispatchable devices related to electricity carrier are different in a buying status and a selling status of EH. For example, CHP is only dispatchable in a buying status and P2G is only dispatchable in a selling status. If devices are not related to electricity carrier, there is no difference for them in buying and selling status, like GF and heat storage, and they are viewed as in a buying and selling status all the time. This is because energy buying and selling are two opposite directions for energy transmission. The electricity carrier can change the transmission directions in real time; therefore, prosumers and EH can buy and sell electricity freely. However, natural gas and heat carriers should follow the fixed direction because of the inertia of gas and heat flow. Therefore, when the dispatchable devices are related to the electricity carrier, their status of buying and selling needs to be distinguished. The superscripts *b*, *s*, and *bs* indicate buying, selling, and buying and selling status, respectively. **Eqs. 25** and **26** impose the compositions of gas used by CHP and GF. **Eq. 27** imposes that the gas P2G devices produce can only be stored by gas storage. **Eqs. 28–31** set limitations to the capacities of devices in EH. **Eq. 32** forces that the transaction amount with RM should be positive. **Eqs. 33** and **34** impose that the characteristics of electricity, natural gas, and heat storages in the EH follow constrains **Eqs. 6–11**.

PROFIT DISTRIBUTION MECHANISM FOR MEC

The profit distribution mechanism is of high importance in the settlement of MEC trading. According to the MEC structure described in *Structure of the MEC*, the aim of profit distribution is to ensure that each prosumer can have a lower cost or a higher profit in the MEC than in the traditional ULIES. Otherwise, prosumers have no incentive to cooperate with each other or to form a MEC. The procedure of profit distribution consists of two steps: Firstly, all prosumers send their satisfaction functions to the MEC operator. The functions should show the relationships between prosumers' satisfaction and the extra profit/cost they earn/save. Secondly, the MEC operator distributes the profit to maximize the overall satisfaction of all prosumers, considering the profit requirement of EH.

Satisfaction and Satisfaction Function

This paper introduces the concept of satisfaction function to reflect the satisfaction each prosumer in MEC feels about its cost or profit according to the results of profit/cost distribution. The satisfaction of each prosumer is related to the extra cost it can save or the extra profit it can earn when participating in MEC, compared to when participating in ULIES. Based on that relationship, the satisfaction function of each prosumer can be decided by the prosumer according to its own situation and sent to the MEC operator.

To be specific, the cost of each buy prosumer or the profit of each sell prosumer in the MEC after profit distribution can be formulated as follows:

$$CP_{i,t}^{CO,E} = \left(\lambda_t^{E,b} p_{i,t}^b - \lambda_t^{E,s} p_{i,t}^s + C_{i,t}^{dr,E}\right) + \lambda_t^{E,dit} p_{i,t}^{sh}, i \in \mathbb{P}, t \in \mathbb{T}, \tag{35}$$

$$CP_{i,t}^{CO,H} = \left(\lambda_t^{H,b} h_{i,t}^b + C_{i,t}^{dr,H}\right) + \lambda_t^{H,dit} h_{i,t}^{sh}, i \in \mathbb{P}, t \in \mathbb{T}, \tag{36}$$

$$p_{i,t}^{sh} = \sum_j p_{i,j,t} - p_{i,t}^{eh,to} + p_{i,t}^{eh,fr}, \ i \in \mathbb{P}, j \in \mathbb{P}_{shp}(i), t \in \mathbb{T}, \tag{37}$$

$$h_{i,t}^{sh} = h_{i,t}^{eh,fr}, i \in \mathbb{P}, t \in \mathbb{T}. \tag{38}$$

The cost/profit of electricity and heat is calculated separately by **Eqs. 35** and **36**, respectively. For both electricity and heat, the cost/profit of each prosumer after profit distribution is composed of two parts, the part of transaction with RM and the part of energy sharing inside MEC. The former part is already calculated before the profit distribution process, and the latter part is what needs to be calculated in this step. **Eq. 37** shows that $p_{i,t}^{sh}$ represents the total amount of electricity prosumer i shares with other prosumers and EH at time t. **Eq. 38** shows that $h_{i,t}^{sh}$ represents the total amount of heat prosumer i receives from EH. The extra cost/profit of each prosumer save/earn in electricity and heat can be formulated as follows:

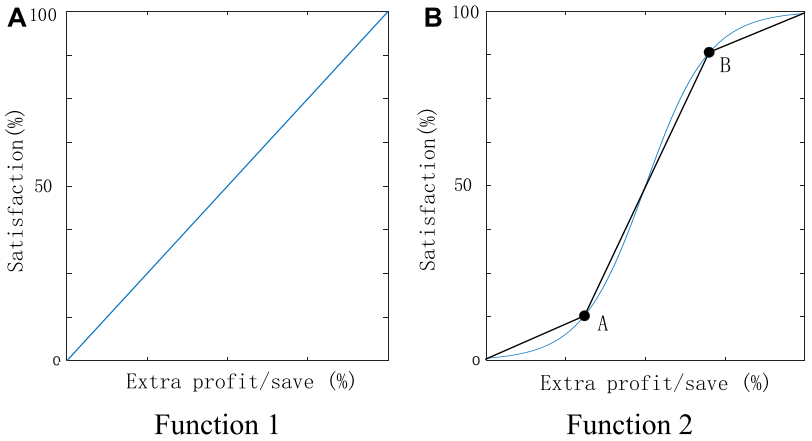

FIGURE 3 | Shapes of satisfaction function. **(A)** Function 1 and **(B)** function 2.

$$CP_i^{CO,ex,E} = -\sum_t CP_{i,t}^{CO,E} + \sum_t CP_{i,t}^{UL,E}, i \in \mathbb{P}, t \in \mathbb{T}, \quad (39)$$

$$CP_i^{CO,ex,H} = -\sum_t CP_{i,t}^{CO,H} + \sum_t CP_{i,t}^{UL,H}, i \in \mathbb{P}, t \in \mathbb{T}, \quad (40)$$

where $CP_{i,t}^{UL,E}$ and $CP_{i,t}^{UL,H}$ represent cost/profit of each prosumer in electricity and heat in ULIES. The calculation method of cost/profit in ULIES is shown in **Supplementary Appendix A**.

The satisfaction function can be formulated as follows:

$$SATI_i = \alpha \cdot SATI_i^E + \beta \cdot SATI_i^H, i \in \mathbb{P}, \quad (41)$$

$$\underline{SATI_i} = \alpha \cdot \underline{SATI_i^E} + \beta \cdot \underline{SATI_i^H}, i \in \mathbb{P}, \quad (42)$$

$$SATI_i^E = f_i^{SATI,E}\left(CP_i^{CO,ex,E}\right), i \in \mathbb{P}, \quad (43)$$

$$SATI_i^H = f_i^{SATI,H}\left(CP_i^{CO,ex,H}\right), i \in \mathbb{P}, \quad (44)$$

$$\underline{SATI_i^E} \geq f_i^{SATI,E}(0) = 0, i \in \mathbb{P}, \quad (45)$$

$$\underline{SATI_i^H} \geq f_i^{SATI,H}(0) = 0, i \in \mathbb{P}, \quad (46)$$

$$\alpha + \beta = 1. \quad (47)$$

Eqs. 41 and **42** indicate that the satisfaction of each prosumer is composed of the satisfaction coming from electricity transactions and the satisfaction coming from heat transactions with different weights α and β, so does the lower bound of satisfaction. In **Eqs. 43** and **44**, $f_i^{SATI,E}(\cdot)$ and $f_i^{SATI,H}(\cdot)$ represent the satisfaction functions from electricity and heat of prosumer i. Two typical function shapes may be used by prosumers as shown in **Figure 3**. The satisfaction under 0% or over 100% does not make sense and is ignored. Function 1 linearly relates the satisfaction to the extra profit/savings, while function 2 provides a certain level of indifference for very low or very high extra profit/savings. For calculation simplicity, the function should be linearized into piecewise if it is non-linear, which is shown by the black lines in **Figure 3B**. **Eqs. 45**, **46** indicate that the lowest satisfaction of each prosumer should be more than the satisfaction it can obtain when extra cost/profit is 0, and that is 0. **Eq. 47** forces the sum of weights equals one.

Profit Distribution Model

In this paper, the proposed objective of profit distribution is to maximize the overall satisfaction prosumers feel in MEC, under the condition that EH can achieve the minimum required profit, which is formulated as follows:

$$\max \sum_i SATI_i \quad (48)$$

$$(35) - (47) \quad (49)$$

$$\underline{SATI_i} \leq SATI_i \leq 100\%, i \in \mathbb{P} \quad (50)$$

$$F_{eh}^{CO,di} \geq \underline{F_{eh}^{CO,di}}. \quad (51)$$

Eq. 49 indicates the relationships between the satisfaction each prosumer feels and the extra cost/profit it can achieve through the satisfaction functions. **Eq. 50** represents the upper and lower limitations of satisfaction. **Eq. 51** represents the minimum required profit by EH, which can be calculated by the following:

$$F_{eh}^{CO,di} = \sum_t \left(-F_{eh,t}^{CO} - \lambda_t^{E,dit} \cdot \left(p_{i,t}^{eh,to} - p_{i,t}^{eh,fr} \right) + \lambda_t^{H,dit} h_{i,t}^{eh,fr} \right). \quad (52)$$

It should be noticed that, in this method, the variables are electricity and heat prices inside the MEC ($\lambda_t^{E,dit}$ and $\lambda_t^{H,dit}$). However, those prices are only a kind of virtual prices for the settlement process. They are only used for profit distribution after the market clearing and do not have any actual meaning or any impact on the market-clearing results.

CASE STUDY

Description of the Simulation System

In the simulation system, there exist five prosumers and an EH in the MEC. Each prosumer owns a solar panel. The structure of the EH is the same as in **Figure 2**. The time scale of the simulation is 24 h, with a time step of 1 h. Electricity demands and heat demands of all the prosumers are shown in **Figure 4A,B**. PV outputs are shown in **Figure 4C** (Zhou et al.,

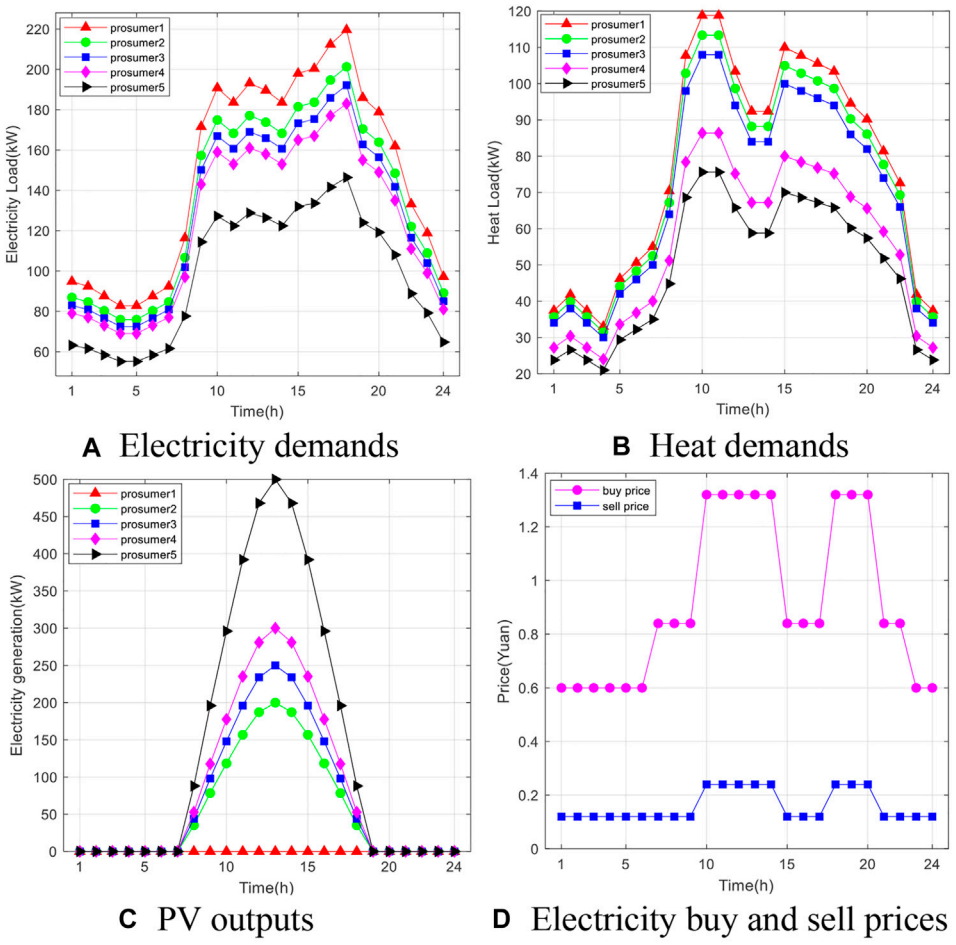

FIGURE 4 | Major parameters of simulation. **(A)** Electricity demands, **(B)** heat demands, **(C)** PV outputs, and **(D)** electricity buy and sell prices.

TABLE 1 | Other major parameters of simulation.

Parameters	Value	Unit	Parameters	Value	Unit	Parameters	Value	Unit
$\overline{G_{CHP}}$	100	kW	η^{E}_{CHP}	40	%	$\overline{SOC^{H}_{eh,t}}$	100	
$\overline{G_{GF}}$	100		η^{H}_{CHP}	45		S^{E}_{S}	200	kWh
$\overline{P_{EB}}$	70		η_{GF}	80		S^{G}_{S}	300	
$\overline{P_{P2G}}$	50		η_{EB}	85		S^{H}_{S}	300	
$\gamma^{E}_{Sc}, \gamma^{E}_{Sd}$	90, 90	%	η_{P2G}	40		$\overline{P^{ch,E}_{eh}}$	100	kW
$\gamma^{G}_{Sc}, \gamma^{G}_{Sd}$	95, 95		$\overline{SOC^{E}_{eh,t}}$	100		$\overline{P^{ch,G}_{eh}}$	100	
$\gamma^{H}_{Sc}, \gamma^{H}_{Sd}$	95, 95		$\overline{SOC^{G}_{eh,t}}$	100		$\overline{P^{ch,H}_{eh}}$	100	

2018). Parameters $\overline{\Delta P_i}$ and $\overline{\Delta H_i}$ are set as one-tenth of electricity (in **Figure 4A**) and heat demands (**Figure 4B**). To simplify the analysis and computation process, the units of heat and gas flow rate are converted into power unit as kilowatt (Zeng et al., 2016).

The retail prices of electricity (both buy price and sell price) in RM are shown in **Figure 4D** (Ma et al., 2019). Periods 10:00–14:00 and 18:00–20:00 are on-peak price periods; periods 7:00–9:00, 15:00–17:00, and 21:00–22:00 are mid-peak price period; and period 23:00–6:00 is off-peak price period. The retail prices of natural gas and heat in RM are the same in 24 h, which are 0.3 and 0.7 Yuan/kWh, respectively.

Other major parameters of the simulation are shown in **Table 1**.

The results of ULIES are used as a comparison to show the advantages MEC can achieve in enlarging social welfare and

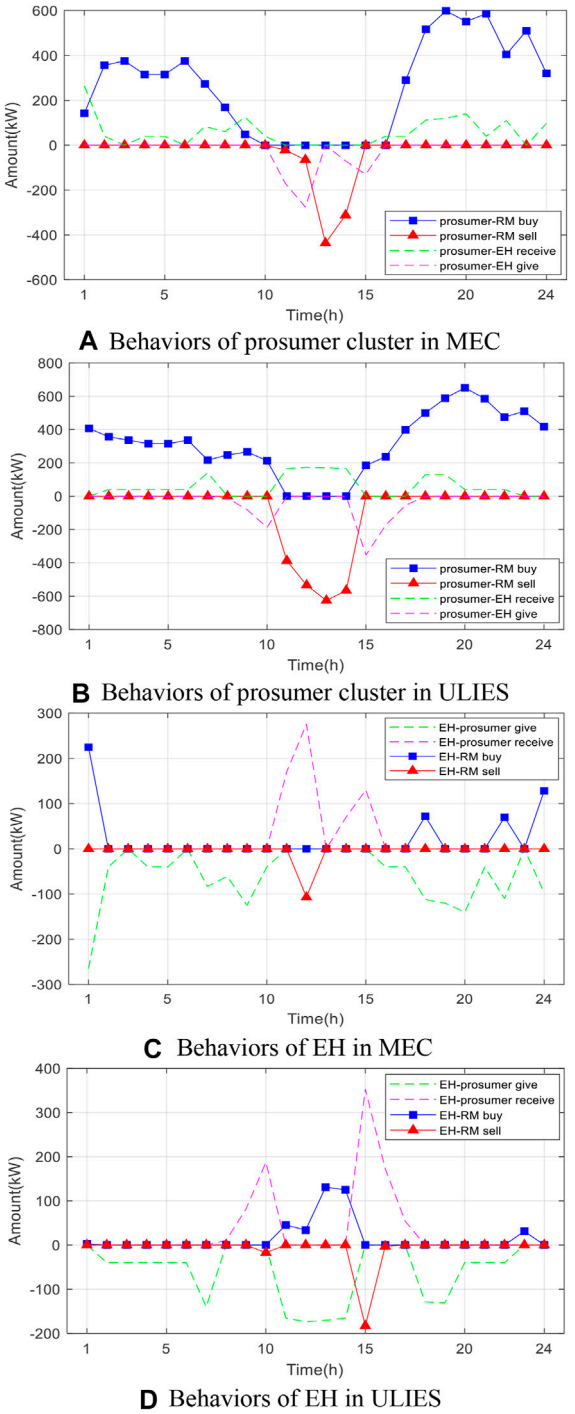

FIGURE 5 | Behaviors of prosumer cluster and EH. **(A)** Behaviors of prosumer cluster in MEC, **(B)** behaviors of prosumer cluster in ULIES, **(C)** behaviors of EH in MEC, and **(D)** behaviors of EH in ULIES.

improving profit/decreasing cost of prosumers. All parameters in ULIES are the same as MEC.

The problem is solved using Cplex under MATLAB on a laptop equipped with an i5-9300H CPU and an 8-GB RAM.

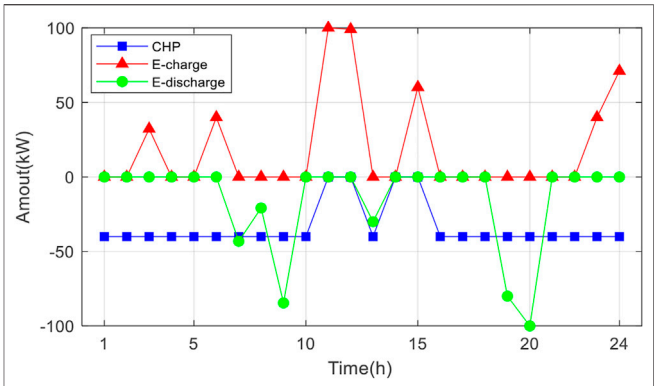

FIGURE 6 | EH operation.

Social Welfare and EH Operation of MEC

The overall cost of MEC is 10,815.99 Yuan. It is lower than the overall cost of ULIES, which is 11,993.72 Yuan. This means that MEC can achieve more social welfare than ULIES under the same conditions. To find the reasons, the behaviors of prosumer cluster and EH in MEC and ULIES are shown in **Figure 5**. The specific energy sharing behaviors among prosumers are shown in **Supplementary Appendix B**. It is mentioned in advance that, "prosumer-EH receive" and "prosumer-EH give" in **Figure 5A**, B are equal to negative "EH-prosumer give" and negative "EH-prosumer receive" in **Figure 5C**, D, respectively. This because they all refer to the same electricity transmission between prosumers and EH, but from the prospective in opposite.

Compare **Figure 5A** with **Figure 5B** and **Figure 5C** with **Figure 5D**, in periods 1:00–7:00 and 19:00–24:00, when there is no PV output, the behaviors of the prosumer cluster (can be viewed as consumers at that time) and EH in MEC and ULIES are similar. However, their behaviors change when there exists PV outputs and prosumers and EH in MEC begin to share energy. In MEC, when the amount of PV outputs is small in periods 8:00–10:00 and 15:00–18:00, it is firstly self-consumed and then sent to other prosumers who require it. This kind of inside balance decreases the overall electricity prosumers and EH need to buy from RM. When the amount of PV outputs is large in period 11:00–14:00, there exists electricity surplus after the inside balance among prosumers and EH, so prosumer cluster and EH stop buying and begin selling electricity to RM.

However, in ULIES, prosumers and EH are all in competitive situations; therefore, there does not exist any inside balance in ULIES. In the prosumer cluster, sell prosumers can only sell their electricity surplus to EH or RM, while buy prosumers can only buy electricity from EH or RM according to the price signals. Therefore, in the period 8:00–14:00, buy prosumers buy electricity in a high price while sell prosumers sell electricity in a low price.

To conclude, in MEC, prosumers and EH can balance themselves inside MEC before trading with RM, which can minimize the cost caused by the variations between selling price and buying price in RM, and therefore, improve the social welfare.

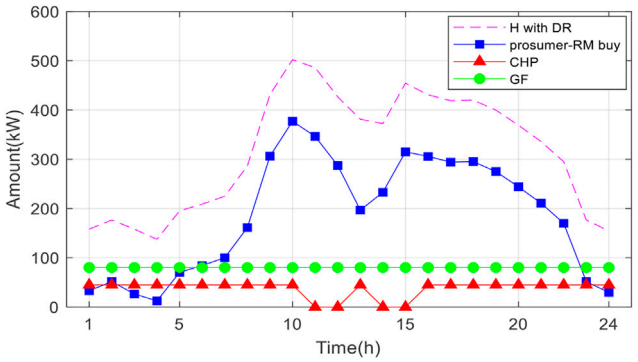

FIGURE 7 | Heat demand composition.

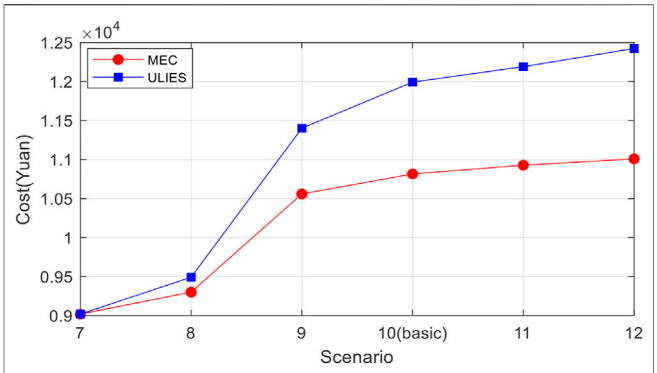

FIGURE 9 | Impacts of retail price differences in RM.

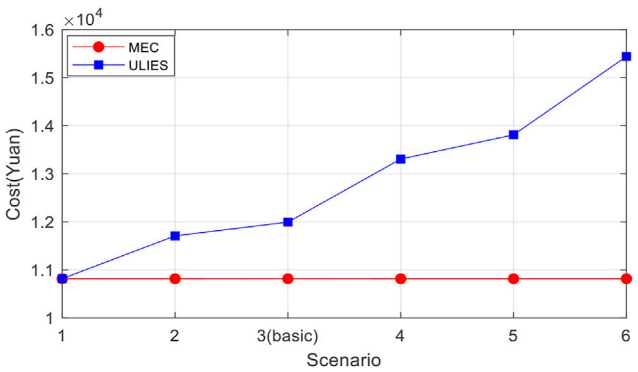

FIGURE 8 | Impacts of electricity usage patterns of prosumers.

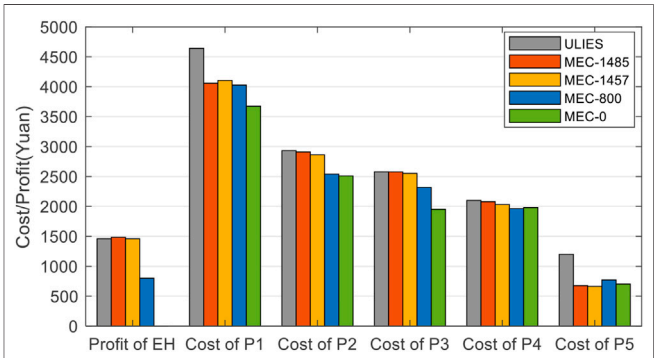

FIGURE 10 | Results of satisfaction-based profit distribution.

The operation of EH is shown in **Figure 6**. The CHP keeps working, because after considering the additional heat it can produce, it is cheaper than buying electricity and heat from RM, except during 11:00–12:00 and 14:00–15:00, when there exists electricity surplus in MEC. Electricity storage charges when there exists electricity surplus in MEC and during the off-peak price period. It discharges during the on-peak price and mid-peak price periods. The effects of EH operation on MEC can be noticed from **Figure 5A**,C that, during the on-peak period (18:00–20:00) and mid-peak period (7:00–9:00 and 16:00–17:00), prosumers decrease the overall amount of electricity bought from RM and use electricity from EH instead, which saves the overall cost of MEC and contributing to the improvement of its social welfare.

Moreover, a part of heat demands of all prosumers can also be supplied by CHP and GF in EH instead of buying from RM, which can further decrease the overall cost of MEC. The composition of heat demand is shown in **Figure 7**.

Impacts on the Utility of MEC

The utility of MEC refers to the social welfare MEC can increase (cost MEC can save) compared with ULIES. Electricity usage patterns and retail price differences can affect the utility of MEC. Five additional scenarios have been established for each of the two factors, besides the basic case described in the text above. In total, twelve scenarios have been obtained, and they are detailed in **Supplementary Appendix C**. To be more specific, electricity usage patterns indicate the differences among prosumers in their electricity demands. PV outputs can counteract prosumers' demands to increase or decrease the demand differences. The retail price differences indicate the variations or intervals between electricity buy and sell prices in RM.

Figure 8 shows the impact of the electricity usage patterns to MEC compared to the corresponding total cost of ULIES. The differences of prosumers' electricity demands and PV outputs are increasing from scenario 1 (no difference) to scenario 6. The results show that the cost of MEC does not change in any scenario because the total amount of electricity demands and PV outputs is the same in all scenarios. Since MEC firstly balance the energy inside and then trade with the RM, the total cost does not change when the total amount stays the same. However, the cost of ULIES is continuously growing and can be increased by about 50% in scenario 6: because there is no inside balance and prosumers' transactions with RM increase when the differences keep growing.

Figure 9 shows the impacts of the retail price differences in RM on MEC, with the comparison of the corresponding total cost of ULIES. The differences between buy and sell prices are increasing from scenario 7 (no difference) to scenario 12; to

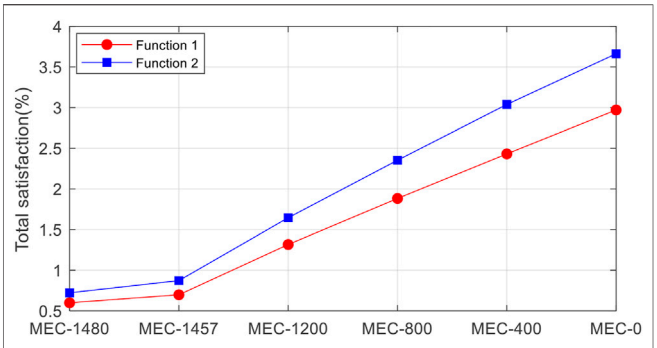

FIGURE 11 | Impacts of satisfaction functions.

be more specific, buy price stays the same while sell price keeps decreasing in all scenarios. The results show that the difference of the total cost between MEC and ULIES keeps enlarging, because social welfare loss of ULIES keeps increasing when prosumers transact with RM under growing variations between buy and sell prices.

To conclude, forming MEC has a larger utility size when the electricity usage patterns are more diverse or the retail price differences of RM are larger.

Profit/Cost Distribution Results

In advance, the lower bound of required profit of EH is set to 1,485 Yuan, 1,457 Yuan (the profit it earns in ULIES), 800 Yuan, and 0 Yuan, respectively. In the first two cases, EH requires at least the same profit it can earn in ULIES. In the last two cases, EH can give up some of its profit. What is more, we assume that prosumers all chose the linear satisfaction function, both for electricity and for heat, in **Figure 3A**, where satisfaction increases linearly from 0% where they receive the same cost/profit as in ULIES to 100% where $\lambda_t^{E,dit} = \lambda_t^{E,s}$ for buy prosumers, $\lambda_t^{E,dit} = \lambda_t^{E,b}$ for sell prosumers, and $\lambda_t^{H,dit} = 0.2 \cdot \lambda_t^{H,b}$. The cost of each prosumer and the profit of EH in MEC after profit distribution are shown in **Figure 10**, with the comparison of the situation in ULIES.

The costs of all prosumers in MEC are lower than in ULIES, even if EH does not give up any profit (shown in MEC-1457) or even earns more (shown in MEC-1485) compared to the ULIES, especially the costs of P1 and P5, who are composed of demands and PVs one much larger than the other. The cost drop of P5 can even reach about 40%. Moreover, if EH can give up some of its profit, the more it can give up, the lesser the cost all prosumers needs to pay, as is shown in MEC-800 and MEC-0. All prosumers' satisfactions are described through function 1, and the results are given in **Figure 11**, in which two more points MEC-1200 and MEC-400 are added. The lesser profit EH requires, the more satisfaction overall prosumers can feel.

We also change the satisfaction function from function 1 in **Figure 3A** to function 2 in **Figure 3B**, in which prosumers are not sensitive to the cost near 0% and 100% satisfaction. For linearization, in function 2, we suppose the point A and point B in **Figure 3B** as 10% and 0.5% and 90% and 99.5%. As is shown in **Figure 11**, prosumers' satisfaction is affected by the satisfaction function. When function 2 is used, the growth rate of the total satisfaction is faster than using function 1 when EH keeps giving up profit.

CONCLUSION AND PROSPECTIVE WORKS

This paper builds the cooperative trading mechanism model of MEC based on its physical structure consisting of prosumers and EH. A satisfaction-based profit distribution method is designed to distribute profit/cost of the entire MEC to each prosumer, which can maximize the satisfactions of all prosumers as well as meet the profit requirement of EH. The outcomes show prosumers and EH gaining advantages from forming an appropriate MEC in the future. In details, the paper's main results can be resumed in the following:

a. The cooperative trading mechanism of MEC can enlarge the social welfare, when compared with traditional uncooperative trading mechanism of ULIES, through energy sharing among prosumers and EH and energy conversion of EH inside MEC.
b. A satisfaction-based profit distribution method can ensure that all prosumers and EH pay less/earn more in MEC than in traditional ULIES. Moreover, if EH is willing to give up some profit, prosumers can achieve extra satisfactions, which can ensure a more solid MEC.
c. The utility size of MEC is larger when the differences of electricity usage patterns and/or buy-and-sell retail price intervals are larger.

In the future, the work can be improved mainly in two aspects:

a. The uncertainties of renewable energy can be taken into consideration, which also means that the real-time operation and ancillary service market can be combined with the day-ahead energy market. An analysis can focus on the short-time energy balancing, effects of physical limitations, and trading mechanisms in combined markets of MEC.
b. Prosumers' strategic behaviors on their satisfaction functions can be taken into consideration. An analysis can focus on how to design appropriate rules to ensure competition and fairness and avoid social welfare loss.

DATA AVAILABILITY STATEMENT

The original contributions presented in the study are included in the article/**Supplementary Material**. Further inquiries can be directed to the corresponding author.

AUTHOR CONTRIBUTIONS

JW, NX, and VI contributed to conception and design of the study. CB organized the database. HX conducted the statistical analysis. YW provided suggestions for amendments. All authors contributed to the article and approved the submitted version.

FUNDING

This work was supported by the National Key Research and Development Project of China under Grant 2018YFB1503000 and the China Scholarship Council.

SUPPLEMENTARY MATERIAL

The Supplementary Material for this article can be found online at: https://www.frontiersin.org/articles/10.3389/fenrg.2021.723192/full#supplementary-material

REFERENCES

Ancona, M. A., Bianchi, M., Branchini, L., De Pascale, A., Melino, F., Peretto, A., et al. (2021). Influence of the Prosumer Allocation and Heat Production on a District Heating Network. *Front. Mech. Eng.*, 7. doi:10.3389/fmech.2021.623932

Bera, S., Misra, S., and Chatterjee, D. (2018). C2C: Community-Based Cooperative Energy Consumption in Smart Grid. *IEEE Trans. Smart Grid* 9, 4262–4269. doi:10.1109/tsg.2017.2653245

Cai, Ye., Liu, Y., Tang, X., Tan, Y., and Cao, Y. (2021). Increasing Renewable Energy Consumption Coordination with the Monthly Inter-provincial Transaction Market. *Energ. Res.* 9, 355. doi:10.3389/fenrg.2021.719419

Cai, Y., Huang, T., Bompard, E., Cao, Y., and Li, Y. (2017). Self-Sustainable Community of Electricity Prosumers in the Emerging Distribution System. *IEEE Trans. Smart Grid* 8, 2207–2216. doi:10.1109/tsg.2016.2518241

Cui, S., Wang, Y.-W., Li, C., and Xiao, J.-W. (2020). Prosumer Community: A Risk Aversion Energy Sharing Model. *IEEE Trans. Sustain. Energ.* 11, 828–838. doi:10.1109/tste.2019.2909301

Cui, S., Wang, Y.-W., Shi, Y., and Xiao, J.-W. (2021). Community Energy Cooperation with the Presence of Cheating Behaviors. *IEEE Trans. Smart Grid* 12, 561–573. doi:10.1109/tsg.2020.3022792

Feng, C., Wen, F., You, S., Li, Z., Shahnia, F., and Shahidehpour, M. (2020). Coalitional Game-Based Transactive Energy Management in Local Energy Communities. *IEEE Trans. Power Syst.* 35, 1729–1740. doi:10.1109/tpwrs.2019.2957537

Firoozi, H., Khajeh, H., and Laaksonen, H. (2020). Optimized Operation of Local Energy Community Providing Frequency Restoration Reserve. *IEEE Access* 8, 180558–180575. doi:10.1109/access.2020.3027710

Hu, J., Wu, J., Ai, X., and Liu, N. (2021). Coordinated Energy Management of Prosumers in a Distribution System Considering Network Congestion. *IEEE Trans. Smart Grid* 12, 468–478. doi:10.1109/tsg.2020.3010260

Jing, R., Xie, M., Wang, F., and Chen, L. (2020). Fair P2P energy trading between residential and commercial multi-energy systems enabling integrated demand-side management. *Appl. Energ.* 262, 114550–114551. doi:10.1016/j.apenergy.2020.114551

Le Cadre, H., Jacquot, P., Wan, C., and Alasseur, C. (2020). Peer-to-peer electricity market analysis: From variational to generalized Nash equilibrium. *Eur. J. Oper. Res.* 282, 753–771. doi:10.1016/j.ejor.2019.09.035

Lilla, S., Orozco, C., Borghetti, A., Napolitano, F., and Tossani, F. (2020). Day-Ahead Scheduling of a Local Energy Community: An Alternating Direction Method of Multipliers Approach. *IEEE Trans. Power Syst.* 35, 1132–1142. doi:10.1109/tpwrs.2019.2944541

Liu, N., Cheng, M., Yu, X., Zhong, J., and Lei, J. (2018). Energy-Sharing Provider for PV Prosumer Clusters: A Hybrid Approach Using Stochastic Programming and Stackelberg Game. *IEEE Trans. Ind. Electron.* 65, 6740–6750. doi:10.1109/tie.2018.2793181

Liu, N., Wang, J., and Wang, L. (2019). Hybrid Energy Sharing for Multiple Microgrids in an Integrated Heat-Electricity Energy System. *IEEE Trans. Sustain. Energ.* 10, 1139–1151. doi:10.1109/tste.2018.2861986

Liu, N., Yu, X., Wang, C., Li, C., Ma, L., and Lei, J. (2017). Energy-sharing model with price-based demand response for microgrids of peer-to-peer prosumers. *IEEE Trans. Power Syst.* 32, 3569–3583. doi:10.1109/tpwrs.2017.2649558

Long, C., Zhou, Y., and Wu, J. (2019). A game theoretic approach for peer to peer energy trading. *Energ. Proced.* 159, 454–459. doi:10.1016/j.egypro.2018.12.075

Ma, L., Liu, N., Zhang, J., and Wang, L. (2019). Real-Time Rolling Horizon Energy Management for the Energy-Hub-Coordinated Prosumer Community from a Cooperative Perspective. *IEEE Trans. Power Syst.* 34, 1227–1242. doi:10.1109/tpwrs.2018.2877236

Oh, E., and Son, S.-Y. (2020). Peer-to-Peer Energy Transaction Mechanisms Considering Fairness in Smart Energy Communities. *IEEE Access* 8, 216055–216068. doi:10.1109/access.2020.3041838

Parag, Y., and Sovacool, B. K. (2016). Electricity Market Design for the Prosumer Era. *Nat. Energ.* 1, 16032. doi:10.1038/nenergy.2016.32

Pourakbari-Kasmaei, M., Asensio, M., Lehtonen, M., and Contreras, J. (2020). Trilateral Planning Model for Integrated Community Energy Systems and PV-Based Prosumers-A Bilevel Stochastic Programming Approach. *IEEE Trans. Power Syst.* 35, 346–361. doi:10.1109/tpwrs.2019.2935840

Shapley, L. S. (1953). 17. A Value for n-Person Games. *Ann. Math. Stud.* 2, 307–318. doi:10.1515/9781400881970-018

Xi, Y., Zeng, Q., Chen, Z., Lund, H., and Conejo, A. J. (2020). A market equilibrium model for electricity, gas and district heating operations. *Energy* 206, 1–11. doi:10.1016/j.energy.2020.117934

Xu, D., Wu, Q., Zhou, B., Li, C., Bai, L., and Huang, S. (2020). Distributed Multi-Energy Operation of Coupled Electricity, Heating, and Natural Gas Networks. *IEEE Trans. Sustain. Energ.* 11, 2457–2469. doi:10.1109/tste.2019.2961432

Xu, K., Zhong, Y., and He, H. (2014). Can P2P Technology Benefit Eyeball ISPs? A Cooperative Profit Distribution Answer. *IEEE Trans. Parallel Distrib. Syst.* 25, 2783–2793. doi:10.1109/tpds.2013.267

Yang, H., Xiong, T., Qiu, J., Qiu, D., and DongDong, Z. Y. (2016). Optimal operation of DES/CCHP based regional multi-energy prosumer with demand response. *Appl. Energ.* 167, 353–365. doi:10.1016/j.apenergy.2015.11.022

Ye, G., Li, G., Di, W., Chen, X., and Zhou, Y. (2017). Towards Cost Minimization with Renewable Energy Sharing in Cooperative Residential Communities. *IEEE Acess*, 2717923. doi:10.1109/access.2017.2717923

Zeng, Q., Fang, J., Li, J., and Chen, Z. (2016). Steady-state analysis of the integrated natural gas and electric power system with bi-directional energy conversion. *Appl. Energ.* 184, 1483–1492. doi:10.1016/j.apenergy.2016.05.060

Zhou, Y., Wei, Z., Sun, G., Cheung, K. W., Zang, H., and Chen, S. (2018). A robust optimization approach for integrated community energy system in energy and ancillary service markets. *Energy* 148, 1–15. doi:10.1016/j.energy.2018.01.078

ZiboWang, X., and YunfeiMu, H. (2020). A distributed peer-to-peer energy transaction method for diversified prosumers in urban community microgrid system. *Appl. Energ.* 260, 114326–114327. apenergy.2019.114327. doi:10.1016/j.apenergy.2019.114327

Conflict of Interest: The authors declare that the research was conducted in the absence of any commercial or financial relationships that could be construed as a potential conflict of interest.

Publisher's Note: All claims expressed in this article are solely those of the authors and do not necessarily represent those of their affiliated organizations or those of the publisher, the editors, and the reviewers. Any product that may be evaluated in this article, or claim that may be made by its manufacturer, is not guaranteed or endorsed by the publisher.

GLOSSARY

MEC Multi-energy community

ULIES Uncooperative local integrated energy system

RM Retail market, including electricity retail market, natural gas retail market and heat retail market

EH Energy hub

Indices and Sets

$i, j, \mathbb{P}$ Indices and set of prosumers

$eh, \mathbb{E}$ Index and set of energy hub

$t, \mathbb{T}$ Index and set of time

$\mathbb{P}_{shp}(i)$ Set of prosumers sharing electricity with prosumer i

$\mathbb{P}_{she}(eh)$ Set of prosumers sharing energies with EH eh

In cooperative trading problem

Parameters and Constants

$\lambda_t^{E,b}, \lambda_t^{E,s}$ Electricity buying price and electricity selling price in RM at time t

$\lambda_t^{H,b}$ Heat buying price in RM at time t

$\lambda_t^{G,b}$ Gas buying price in RM at time t

$D_{i,t}^{E}, D_{i,t}^{H}$ Electricity demand and heat demand of prosumer i at time t

$L_{i,t}^{pre}$ Predicted PV output of prosumer i at time t

$\overline{\Delta P_i}, \overline{\Delta H_i}$ Upper bounds of electricity and heat demand response of prosumer i

$\overline{G_{CHP}}, \overline{G_{GF}}\ \overline{P_{EB}}, \overline{P_{P2G}}$ Upper bounds of energy conversion of CHP, GF, EB and P2G

Variables

$p_{i,t}^{b}, p_{i,t}^{s}$ Electricity buying amount and selling amount from and to RM of prosumer i at time t

$h_{i,t}^{b}$ Heat buying amount from RM of prosumer i at time t

$p_{i,t}^{eh,fr}, p_{i,t}^{eh,to}$ Electricity amount getting from and sending to EH of prosumer i at time t

$h_{i,t}^{eh,fr}$ Heat amount getting from EH of prosumer i at time t

$p_{i,j,t}$ Electricity amount sharing between prosumer i and prosumer j at time t

$\Delta p_{i,t}, \Delta h_{i,t}$ Electricity and heat demand responses of prosumer i at time t

$p_{eh,t}^{b}, p_{eh,t}^{s}$ Electricity buying amount and selling amount from and to RM of EH at time t

$g_{eh,t}^{b}, g_{eh,t}^{bs}$ Gas buying amount from RM in buying status and buying and selling status of EH at time t

$g_{eh,t}^{CHP,b}$ Amount of gas CHP consumes in buying status in EH at time t

$g_{eh,t}^{GF,bs}$ Amount of gas GF consumes in buying and selling status in EH at time t

$p_{eh,t}^{P2G,s}$ Amount of electricity P2G consumes in selling status in EH at time t

$p_{eh,t}^{EB,b}, p_{eh,t}^{EB,s}$ Amount of electricity EB consumes in buying and selling statuses in EH at time t

$re_{eh,t}^{ch,b}, re_{eh,t}^{ch,s}$ Amount of electricity charging in buying and selling statuses in EH at time t

$re_{eh,t}^{di,b}, re_{eh,t}^{di,s}$ Amount of electricity discharging in buying and selling statuses in EH at time t

$rg_{eh,t}^{ch,b}, rg_{eh,t}^{ch,bs}$ Amount of gas charging in buying and buying and selling statuses in EH at time t

$rg_{eh,t}^{di,b}, rg_{eh,t}^{di,bs}, rg_{eh,t}^{ch,s}$ Amount of gas discharging in buying, buying and selling and selling statuses in EH at time t

$rh_{eh,t}^{ch,bs}, rh_{eh,t}^{di,bs}$ Amount of heat charging and discharging in buying and selling status in EH at time t

In profit distribution problem

Functions

$f_i^{SATI,E}(\boldsymbol{\Delta})\ f_i^{SATI,H}(\boldsymbol{\Delta})$ Satisfaction functions of electricity part and heat part of prosumer i

Parameters and Constants

$p_{i,t}^{sh}, h_{i,t}^{sh}$ Electricity and heat amount sharing with prosumer i at time t

$C_{i,t}^{dr,E}, C_{i,t}^{dr,H}$ Costs of electricity and heat demand response prosumer i spends at time t

$CP_{i,t}^{UL,E}, CP_{i,t}^{UL,H}$ Costs/profits prosumer i spends/gains in ULIES at time t

$\underline{SATI_i}, \underline{SATI_i^E}, \underline{SATI_i^H}$ Lower bounds of satisfaction prosumer i requires in a whole day

$\underline{F_{eh}^{CO,di}}$ Lower bound of profit EH in MEC requires in a whole day

Variables

$\lambda_t^{E,dit}, \lambda_t^{H,dit}$ Electricity and heat prices in MEC at time t

$CP_{i,t}^{CO,E}, CP_{i,t}^{CO,H}$ Costs/profits prosumer i spends/gains in MEC at time t

$CP_i^{CO,ex,E}\ CP_i^{CO,ex,H}$ Extra costs/profits prosumer i saves/gets from MEC in a whole day

$SATI_i, SATI_i^E, SATI_i^H$ Total satisfaction, satisfaction of electricity and satisfaction of heat prosumer i feels in a whole day

$F_{eh}^{CO,di}$ Profit EH gains in MEC in a whole day

Advantages of publishing in Frontiers

OPEN ACCESS
Articles are free to read for greatest visibility and readership

FAST PUBLICATION
Around 90 days from submission to decision

HIGH QUALITY PEER-REVIEW
Rigorous, collaborative, and constructive peer-review

TRANSPARENT PEER-REVIEW
Editors and reviewers acknowledged by name on published articles

Frontiers
Avenue du Tribunal-Fédéral 34
1005 Lausanne | Switzerland

Visit us: www.frontiersin.org
Contact us: frontiersin.org/about/contact

REPRODUCIBILITY OF RESEARCH
Support open data and methods to enhance research reproducibility

DIGITAL PUBLISHING
Articles designed for optimal readership across devices

FOLLOW US
@frontiersin

IMPACT METRICS
Advanced article metrics track visibility across digital media

EXTENSIVE PROMOTION
Marketing and promotion of impactful research

LOOP RESEARCH NETWORK
Our network increases your article's readership